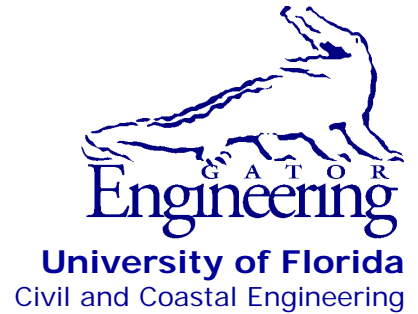


UF

**University of Florida
Civil and Coastal Engineering**

**Structures Research
Report 2014/87294**



Final Report

July 2014

Validation and Implementation of Bridge Design Specifications for Barge Impact Loading

Principal Investigator:

Gary R. Consolazio, Ph.D.

Research assistants:

Daniel J. Getter

George C. Kantrales

Department of Civil and Coastal Engineering
University of Florida
P.O. Box 116580
Gainesville, Florida 32611

Sponsor:

Florida Department of Transportation (FDOT)
Sam Fallaha, P.E. – Project manager

Contract:

UF Project No. 00087294
FDOT Contract No. BDK75-977-31

DISCLAIMER

The opinions, findings, and conclusions expressed in this publication are those of the authors and not necessarily those of the State of Florida Department of Transportation.

SI (MODERN METRIC) CONVERSION FACTORS
APPROXIMATE CONVERSIONS TO SI UNITS

SYMBOL	WHEN YOU KNOW	MULTIPLY BY	TO FIND	SYMBOL
LENGTH				
in	inches	25.4	millimeters	mm
ft	feet	0.305	meters	m
yd	yards	0.914	meters	m
mi	miles	1.61	kilometers	km
AREA				
in²	square inches	645.2	square millimeters	mm ²
ft²	square feet	0.093	square meters	m ²
yd²	square yard	0.836	square meters	m ²
ac	acres	0.405	hectares	ha
mi²	square miles	2.59	square kilometers	km ²
VOLUME				
fl oz	fluid ounces	29.57	milliliters	mL
gal	gallons	3.785	liters	L
ft³	cubic feet	0.028	cubic meters	m ³
yd³	cubic yards	0.765	cubic meters	m ³
NOTE: volumes greater than 1000 L shall be shown in m ³				
MASS				
oz	ounces	28.35	grams	g
lb	pounds	0.454	kilograms	kg
T	short tons (2000 lb)	0.907	Megagrams	Mg (or "t")
TEMPERATURE (exact degrees)				
°F	Fahrenheit	5(F-32)/9 or (F-32)/1.8	Celsius	°C
ILLUMINATION				
fc	foot-candles	10.76	lux	lx
fl	foot-Lamberts	3.426	candela/m ²	cd/m ²
FORCE and PRESSURE or STRESS				
kip	1000 pounds force	4.45	kilonewtons	kN
lbf	pounds force	4.45	newtons	N
lbf/in²	pounds force per square inch	6.89	kilopascals	kPa
psf	pounds force per square foot	47.88	pascals	Pa

1. Report No.		2. Government Accession No.		3. Recipient's Catalog No.	
4. Title and Subtitle Validation and Implementation of Bridge Design Specifications for Barge Impact Loading				5. Report Date July 2014	
				6. Performing Organization Code	
				8. Performing Organization Report No. 2014/87294	
7. Author(s) G. R. Consolazio, D. J. Getter, G.C. Kantrales				9. Performing Organization Name and Address University of Florida Department of Civil & Coastal Engineering P.O. Box 116580 Gainesville, FL 32611-6580	
12. Sponsoring Agency Name and Address Florida Department of Transportation Research Management Center 605 Suwannee Street, MS 30 Tallahassee, FL 32301-8064				10. Work Unit No. (TRAIS)	
				11. Contract or Grant No. BDK75-977-31	
				13. Type of Report and Period Covered Final Report	
15. Supplementary Notes				14. Sponsoring Agency Code	
16. Abstract Since 1991 in the United States, the design of highway bridges to resist collisions by errant waterway vessels has been carried out in accordance with design provisions published by AASHTO. These provisions have remained largely unchanged for more than 20 years, while numerous studies in recent years—conducted by researchers at the University of Florida (UF) and the Florida Department of Transportation (FDOT)—have greatly improved upon the analysis procedures in the AASHTO provisions. The focus of the work discussed in this report was the experimental validation of an improved UF/FDOT barge impact load-prediction model and the implementation of numerous other UF/FDOT procedures into a comprehensive risk assessment methodology that can be readily adopted for use in bridge design. To validate the UF/FDOT barge impact load model, two series of impact experiments were conducted, in which reduced-scale replicas of a typical barge bow were impacted by a high-energy impact pendulum to produce large-scale barge deformations. In support of the validation effort, a material testing program was carried out in order to characterize the strain rate-sensitive properties of steel materials from which the reduced-scale barge specimens were fabricated. Steel specimens were tested in uniaxial tension at strain rates covering seven orders of magnitude. To conduct high-rate material tests, a novel test apparatus was designed and employed that used an impact pendulum to impart the required energy. Data from the material testing program were used to develop constitutive models that were used in finite element barge impact simulations. Additionally in this study, a revised vessel collision risk assessment methodology was developed that incorporates various new UF/FDOT analysis procedures. The complete methodology was demonstrated for two real-world bridge cases, and the results were compared to the existing AASHTO risk assessment method. For these two cases, the revised procedure was found to predict higher levels of risk than the AASHTO procedure. However, it was also noted that the terms in the current AASHTO annual frequency of collapse (<i>AF</i>) expression that are associated with the probability of an impact event occurring may, in fact, overpredict this probability. Consequently, potential inaccuracies in these probability-related terms may account for the higher estimates of risk produced by the revised procedure.					
17. Key Words Barge, impact, collision, bridge pier, risk assessment, finite element analysis, dynamic analysis, probability of collapse, bridge design specifications			18. Distribution Statement No restrictions.		
19. Security Classif. (of this report) Unclassified		20. Security Classif. (of this page) Unclassified		21. No. of Pages 519	22. Price

ACKNOWLEDGEMENTS

The authors thank the Florida Department of Transportation (FDOT) for providing the funding that made this research project possible. Additionally, the authors would like to recognize that, without the contributions made by the staff of the FDOT Structures Research Center, this project would not have been successfully completed. Sam Fallaha, David Wagner, William Potter, Stephen Eudy, Chris Weigly, Paul Tighe, David Allen, Ben Allen, and Brandon Winter, were all exceptional participants in this research. Their expertise in testing, instrumentation, and test-article fabrication allowed the project to progress smoothly and efficiently.

EXECUTIVE SUMMARY

Since 1991 in the United States, the design of highway bridges to resist collisions by errant waterway vessels has been carried out in accordance with design provisions published by AASHTO. These provisions have remained largely unchanged for more than 20 years, while numerous studies in recent years—conducted by researchers at the University of Florida (UF) and the Florida Department of Transportation (FDOT)—have greatly improved upon the analysis procedures in the AASHTO provisions. The focus of the work discussed in this report was the experimental validation of the improved UF/FDOT barge impact load-prediction model and the implementation of numerous other UF/FDOT procedures into a comprehensive risk assessment methodology that can be readily adopted for use in bridge design.

To validate the UF/FDOT barge impact load model, two series of impact experiments were conducted, in which reduced-scale replicas of a typical barge bow were impacted by a high-energy impact pendulum to produce large-scale barge deformations. In support of the validation effort, a material testing program was carried out in order to characterize the strain rate-sensitive properties of steel materials from which the reduced-scale barge specimens were fabricated. Steel specimens were tested in uniaxial tension at strain rates covering seven orders of magnitude. To conduct high-rate material tests, a novel test apparatus was designed and employed that used an impact pendulum to impart the required energy. Data from the material testing program were used to develop constitutive models that were used in finite element barge impact simulations.

Additionally in this study, a revised vessel collision risk assessment methodology was developed that incorporates various new UF/FDOT analysis procedures. The complete methodology was demonstrated for two real-world bridge cases, and the results were compared to the existing AASHTO risk assessment method. For these two cases, the revised procedure was found to predict higher levels of risk than the AASHTO procedure. However, it was also noted that the terms in the current AASHTO annual frequency of collapse (AF) expression that are associated with the probability of an impact event occurring may, in fact, overpredict this probability. Consequently, potential inaccuracies in these probability-related terms may account for the higher estimates of risk produced by the revised procedure.

TABLE OF CONTENTS

DISCLAIMER	ii
CONVERSION FACTORS	iii
TECHNICAL REPORT DOCUMENTATION PAGE	iv
ACKNOWLEDGEMENTS	v
EXECUTIVE SUMMARY	vi
LIST OF FIGURES	xiv
LIST OF TABLES	xxiv
1. INTRODUCTION	1
1.1 Introduction	1
1.2 Motivation	1
1.3 Objectives	3
1.4 Scope of Work	3
2. BACKGROUND	5
2.1 Introduction	5
2.2 AASHTO Risk Assessment Procedure	5
2.3 UF/FDOT Research on Barge Collision	10
2.3.1 Full-scale barge impact experiments	10
2.3.2 Coupled vessel impact analysis (CVIA) procedure	11
2.3.3 Barge bow force-deformation curves	13
2.3.4 Collision-induced dynamic amplification phenomena	15
2.3.5 Other vessel impact analysis procedures	16
2.3.6 Revised probability of collapse (PC) expression	21
2.4 Observations	23
3. EXPERIMENTAL VALIDATION PLAN FOR UF/FDOT BARGE IMPACT LOAD- PREDICTION MODEL	24
3.1 Introduction	24
3.2 Validation Objectives	24
3.3 Overview of Experimental Program	25
3.3.1 Determination of barge bow model scale	27
3.3.2 Material testing program	28
3.4 Validation Simulations	29

4. STRAIN RATE-SENSITIVE CONSTITUTIVE RELATIONS FOR EXPERIMENTAL VALIDATION.....	32
4.1 Introduction.....	32
4.2 Materials and Methods.....	32
4.2.1 A1011 and A36 steel.....	32
4.2.2 Uniaxial tension testing (quasi-static).....	33
4.2.3 Uniaxial tension testing (high-strain rate).....	33
4.2.3.1 Pendulum-based high-rate test apparatus (HRTA).....	34
4.2.3.2 Instrumentation.....	37
4.2.4 Summary of testing program.....	38
4.3 Theory and Calculation Procedures.....	39
4.3.1 Quasi-static testing program.....	39
4.3.2 High-rate testing program.....	40
4.3.2.1 Single-degree-of-freedom data interpretation.....	40
4.3.2.2 Impulse-momentum data interpretation.....	41
4.4 Results and Discussion.....	44
4.4.1 Quasi-static testing program.....	45
4.4.2 High-rate testing program.....	48
4.5 Constitutive Model Details.....	56
4.5.1 Strain rate sensitivity.....	56
4.5.2 Failure strain considerations.....	56
4.5.3 Constitutive curves.....	58
4.5.4 Implementation in LS-DYNA.....	58
4.5.4.1 A1011-T11 model.....	59
4.5.4.2 A1011-T15 model.....	59
4.5.4.3 A36-T25 model.....	60
4.7 Concluding Remarks.....	60
5. PRELIMINARY FINITE ELEMENT SIMULATIONS OF REDUCED-SCALE BARGE IMPACT.....	62
5.1 Introduction.....	62
5.2 Implementation of Finite Element Constitutive Models.....	62
5.3 Barge Impact Simulations.....	62
5.3.1 Impact simulation results (flat-faced block).....	63
5.3.2 Sensitivity of results to steel constitutive model (flat-faced block).....	66
5.3.3 Impact simulation results (round nose block).....	70
5.3.4 Sensitivity of results to steel constitutive model (round nose block).....	73
6. REDUCED-SCALE BARGE BOW IMPACT TEST PROGRAM.....	75
6.1 Introduction.....	75
6.2 Experimental Components.....	75
6.2.1 Reduced-scale barge bow specimens.....	76
6.2.2 Barge bow reaction frame.....	78

6.2.3 Universal pendulum foundation.....	80
6.2.4 Impact block and cable support frame.....	84
6.3 Test Procedure.....	86
6.4 Test Instrumentation.....	88
6.4.1 Pressure sensitive tape switches.....	90
6.4.2 Infrared optical break beam sensors.....	91
6.4.3 Accelerometers.....	92
6.4.4 High-speed cameras.....	93
6.4.5 Optech ILRIS-3D laser scanner.....	94
7. REDUCED-SCALE BARGE BOW IMPACT TEST RESULTS.....	96
7.1 Introduction.....	96
7.2 Test RND1: Initial Round Nose Impact Test.....	96
7.2.1 Break beam and tape switch data.....	97
7.2.2 Acceleration and impact force data.....	99
7.2.3 Deformation data.....	100
7.2.4 Force-deformation relationship.....	101
7.3 Tests RND2-RND4: Subsequent Round Nose Impact Tests.....	103
7.3.1 Break beam and tape switch data.....	105
7.3.2 Acceleration and impact force data.....	105
7.3.3 Deformation data.....	108
7.4 Test FLT1: Initial Flat Nose Impact Test.....	112
7.4.1 Break beam and tape switch data.....	112
7.4.2 Acceleration and impact force data.....	113
7.4.3 Deformation data.....	114
7.4.4 Force-deformation relationship.....	114
7.5 Test FLT2-FLT4: Subsequent Flat Nose Impact Tests.....	116
7.5.1 Break beam and tape switch data.....	116
7.5.2 Acceleration and impact force data.....	116
7.5.3 Deformation data.....	121
7.6 Summary of Results from all Tests: RND1-RND4 and FLT1-FLT4.....	124
7.6.1 Discussion of overall round (RND) nose force-deformation relationship.....	125
7.6.2 Discussion of overall flat (FLT) nose force-deformation relationship.....	125
7.7 Validation of Finite Element Modeling and Analysis Procedures.....	125
8. REVISED RISK ANALYSIS PROCEDURES FOR VESSEL IMPACT WITH BRIDGES.....	130
8.1 Introduction.....	130
8.2 Options for Implementing UF/FDOT Research in Design Practice.....	130
8.2.1 Simplified LRFD approach to vessel collision design.....	130
8.2.2 Targeted revisions to AASHTO risk assessment procedure.....	131
8.2.3 Ship impact considerations.....	132
8.3 Overview of Revised Risk Analysis Procedure.....	133
8.4 Use of UF/FDOT PC Expression in Design.....	135

9. VESSEL COLLISION RISK ASSESSMENT OF THE BRYANT GRADY PATTON BRIDGE (SR-300) OVER APALACHICOLA BAY, FLORIDA	138
9.1 Introduction.....	138
9.2 Data Collection	138
9.3 Waterway Characteristics	139
9.3.1 General description	139
9.3.2 Navigation channel	140
9.3.3 Tide levels and tidal range	141
9.3.4 Currents.....	141
9.3.5 Water depths	142
9.4 Bridge Characteristics.....	144
9.4.1 Bridge piers.....	145
9.4.2 Superstructure	147
9.4.3 Soil conditions	149
9.4.4 Finite element models.....	149
9.5 Vessel Fleet Characteristics.....	150
9.5.1 Vessel categories.....	151
9.5.2 Vessel traffic growth.....	153
9.5.3 Vessel transit speeds	153
9.5.4 Vessel transit path.....	154
9.6 Vessel Impact Criteria.....	154
9.6.1 General requirements.....	154
9.6.2 Extreme event load combinations (scour).....	155
9.6.3 Minimum impact load criteria	155
9.6.4 Maximum impact load criteria.....	155
9.6.5 Operational classification.....	156
9.7 Maximum Impact Load (Method II) Analysis Methodology	156
9.7.1 Annual frequency of collapse (AF).....	156
9.7.2 Vessel frequency (N)	157
9.7.3 Probability of aberrancy (PA).....	157
9.7.4 Geometric probability (PG)	159
9.7.5 Probability of collapse (PC).....	160
9.7.5.1 AASHTO methods.....	161
9.7.5.1.1 AASHTO 1991 barge impact load model (as designed)	162
9.7.5.1.2 AASHTO 2009 barge impact load model.....	163
9.7.5.2 UF/FDOT methods	164
9.7.5.2.1 CVIA structural analysis.....	165
9.7.5.2.2 AVIL structural analysis	166
9.7.5.2.3 SBIA structural analysis	170
9.7.6 Protection factor (PF).....	173
9.8 Risk Analysis Results	176
9.8.1 AASHTO methods.....	176
9.8.1.1 AASHTO (1991) barge impact load model (as-designed)	176
9.8.1.2 AASHTO 2009 barge impact load model.....	179
9.8.2 UF/FDOT methods	182

9.8.2.1 CVIA.....	182
9.8.2.2 AVIL.....	185
9.8.2.3 SBIA.....	187
9.9 Discussion of Results.....	189
9.10 Suggestions for Mitigating Risk.....	191
9.11 Concluding Remarks.....	193
10. VESSEL COLLISION RISK ASSESSMENT OF THE LOUISIANA HIGHWAY 1 (LA 1) BRIDGE OVER BAYOU LAFOURCHE, LOUISIANA.....	195
10.1 Introduction.....	195
10.2 Data Collection.....	196
10.3 Waterway Characteristics.....	196
10.3.1 General description.....	196
10.3.2 Navigation channel.....	196
10.3.3 Tide levels and tidal range.....	198
10.3.4 Currents.....	198
10.3.5 Water depths.....	198
10.4 Bridge Characteristics.....	198
10.4.1 Bridge piers.....	200
10.4.2 Superstructure.....	202
10.4.3 Soil conditions.....	203
10.4.4 Finite element models.....	204
10.5 Vessel Fleet Characteristics.....	205
10.5.1 Vessel categories.....	205
10.5.2 Vessel traffic growth.....	208
10.5.3 Vessel transit speeds.....	208
10.5.4 Vessel transit path.....	208
10.6 Vessel Impact Criteria.....	208
10.6.1 General requirements.....	208
10.6.2 Extreme event load combinations (scour).....	209
10.6.3 Minimum impact load criteria.....	209
10.6.4 Maximum impact load criteria.....	209
10.6.5 Operational classification.....	210
10.7 Maximum Impact Load (Method II) Analysis Methodology.....	210
10.7.1 Annual frequency of collapse (AF).....	210
10.7.2 Vessel frequency (N).....	211
10.7.3 Probability of aberrancy (PA).....	211
10.7.4 Geometric probability (PG).....	213
10.7.5 Probability of collapse (PC).....	214
10.7.5.1 AASHTO methods.....	215
10.7.5.1.1 AASHTO (1991) barge impact load model (as designed).....	216
10.7.5.1.2 AASHTO (2009) barge impact load model.....	217
10.7.5.2 UF/FDOT methods.....	217
10.7.5.2.1 CVIA structural analysis.....	218
10.7.5.2.2 AVIL structural analysis.....	220

10.7.6 Protection factor (PF).....	224
10.8 Risk Analysis Results	224
10.8.1 AASHTO methods.....	224
10.8.1.1 AASHTO (1991) barge impact load model (as-designed)	224
10.8.1.2 AASHTO (2009) barge impact load model	226
10.8.2 UF/FDOT methods	229
10.8.2.1 CVIA.....	229
10.8.2.2 AVIL.....	231
10.9 Discussion of Results.....	233
10.10 Suggestions for Mitigating Risk	235
10.10.1 Pier footing retrofit	235
10.10.2 Pier protection system.....	237
10.10.3 Alternative foundation design.....	238
10.11 Concluding Remarks.....	242
11. CONCLUSIONS AND RECOMMENDATIONS	244
11.1 Concluding Remarks.....	244
11.2 Recommendations for Bridge Design.....	247
11.3 Recommendations for Future Research.....	247
REFERENCES	249
APPENDIX A: REVIEW OF EUROCODE PROCEDURES FOR VESSEL COLLISION.....	253
APPENDIX B: DERIVATION OF SCALE-MODEL SIMILITUDE EXPRESSIONS.....	264
APPENDIX C: PENDULUM-BASED HIGH-RATE TEST APPARATUS (HRTA) FABRICATION DRAWINGS	267
APPENDIX D: DEMONSTRATION OF IMPULSE-MOMENTUM THEORY FOR MULTIPLE DEGREE OF FREEDOM (MDF) SYSTEMS	292
APPENDIX E: SENSITIVITY OF REDUCED-SCALE BARGE IMPACT SIMULATION RESULTS TO STEEL FAILURE STRAIN.....	295
APPENDIX F: REDUCED-SCALE (0.4-SCALE) BARGE BOW FABRICATION DRAWINGS	299
APPENDIX G: BARGE BOW REACTION FRAME FABRICATION DRAWINGS	325
APPENDIX H: PENDULUM FOUNDATION FABRICATION DRAWINGS.....	342
APPENDIX I: IMPACT BLOCK FABRICATION DRAWINGS	362
APPENDIX J: HANGER FRAME FABRICATION DRAWINGS	398

APPENDIX K: INSTRUMENTATION PLAN419

APPENDIX L: CONSIDERATION OF LRFD APPROACH TO VESSEL COLLISION
DESIGN423

APPENDIX M: SR-300 BRIDGE VESSEL COLLISION RISK ASSESSMENT DATA429

APPENDIX N: LA-1 BRIDGE VESSEL COLLISION RISK ASSESSMENT DATA.....465

LIST OF FIGURES

<u>Figure</u>	<u>Page</u>
Figure 2.1 Determination of geometric probability of impact (PG) with a bridge pier (Source: AASHTO 2009)	7
Figure 2.2 Determination of probability of collapse (PC) (Source: AASHTO 2009)	9
Figure 2.3 Full-scale barge impact experiments at St. George Island, Florida: a) Stand-alone pier impact (superstructure removed), and b) Intact bridge impact (Consolazio et al. 2006).....	11
Figure 2.4 Coupled vessel impact analysis (CVIA) (Consolazio and Cowan 2005)	12
Figure 2.5 AASHTO barge bow force-deformation curve: P_B - a_B (AASHTO 2009).....	13
Figure 2.6 UF/FDOT barge bow force-deformation model (Getter and Consolazio 2011)	15
Figure 2.7 Dynamic amplification of pier column moments sorted by amplification mode (Davidson et al. 2010).....	16
Figure 2.8 Applied vessel impact loading (AVIL) (Consolazio et al. 2008)	18
Figure 2.9 Impact response spectrum analysis (IRSA) (Consolazio et al. 2008).....	19
Figure 2.10 Static bracketed impact analysis (SBIA) (Getter et al. 2011).....	21
Figure 2.11 Revised probability of collapse expression (Consolazio et al. 2010)	23
Figure 3.1 Impact pendulum at M.H. Ansley Structures Research Center in Tallahassee, FL.....	26
Figure 3.2 Test setup for barge bow impact experiments	27
Figure 3.3 Rendering of reduced-scale barge bow specimen showing internal truss structure	28
Figure 3.4 Rendering of barge bow finite element model with flat-faced pendulum impact block and reaction frame (mesh not shown for clarity).....	30
Figure 3.5 Barge bow finite element model showing mesh density	30
Figure 4.1 a) Specimen dimensions, and b) test setup and instrumentation for quasi-static tests	33
Figure 4.2 Impact pendulum facility at Florida Department of Transportation (FDOT) Structures Research Center in Tallahassee, Florida.....	34
Figure 4.3 Depictions of a) perfectly inelastic and b) perfectly elastic impact scenarios in tension testing that rely on impact energy for specimen elongation.....	35
Figure 4.4 High-rate testing apparatus (HRTA): a) horizontal configuration schematic and b) section view, and c) angled configuration schematic and d) section view.....	36
Figure 4.5 High-rate material testing apparatus (HRTA) before pendulum impact a) schematic and b) photograph, and after impact c) schematic and d) photograph.....	37

Figure 4.6	a) Specimen dimensions and gage marks, and b) instrumentation setup.....	38
Figure 4.7	Strain-displacement relation for test A1011-T11-R1-B, including parabolic fit.....	39
Figure 4.8	High-rate test apparatus (HRTA) as a damped SDF oscillator.....	40
Figure 4.9	Impulse-momentum-based optimization procedure for computing Cowper-Symonds coefficients C and P	43
Figure 4.10	Stretching and scaling of average R1 stress-strain relation [] to arrive at dynamic stress-strain relation for each test [], following procedure shown in Fig. 4.9.....	44
Figure 4.11	Engineering stress-strain curves for each quasi-static test series	46
Figure 4.12	Rate sensitivity of material parameters among quasi-static testing rates: (a) yield stress; (b) ultimate stress; and (c) failure elongation. (d) Representative variation in strain rate through the duration of a quasi-static test (data from test A36-T25-R3-C shown).....	47
Figure 4.13	Engineering strain rate (among three tests per trace) as a function of strain.....	49
Figure 4.14	Engineering stress-strain curves (computed by the process in Figs. 4.9 and 4.10) for each high-rate test series.....	50
Figure 4.15	Specimen and reaction force-time histories (computed by process in Fig. 4.9) for selected tests.....	51
Figure 4.16	Specimen and reaction impulse-time histories (computed by process in Fig. 4.9) for selected tests	52
Figure 4.17	Normalized histograms of impulse ratio (IR) for each material series (computed by process in Fig. 4.9).....	53
Figure 4.18	Sensitivity of dynamic stress to strain rate for each material test series.....	54
Figure 4.19	(a) Rate sensitivity of yield and ultimate stress from Manjoine study (1944), showing fitted Cowper-Symonds coefficients C and P. (b) Comparison between Manjoine data and rate sensitivity curves derived in this study	55
Figure 4.20	Static constitutive curves developed for the MAT_24 material model in LS DYNA.....	58
Figure 5.1	Finite element impact simulation of 0.4-scale barge bow (round nose impact block shown).....	63
Figure 5.2	Maximum barge bow deformation caused by each successive impact (flat-faced block)	64
Figure 5.3	Barge impact simulation data (flat-faced block).....	65
Figure 5.4	Empirical CDF of impact force data from first pendulum impact event.....	66
Figure 5.5	Comparison of maximum barge bow deformation (flat-faced block).....	69
Figure 5.6	Comparison of barge bow force-deformation curves (flat-faced block)	70

Figure 5.7	Maximum barge bow deformation caused by each successive impact (round nose block).....	71
Figure 5.8	Barge impact simulation data (round nose block).....	72
Figure 5.9	Comparison of maximum barge bow deformation (round nose block).....	73
Figure 5.10	Comparison of barge bow force-deformation curves (round nose block).....	74
Figure 6.1	Schematic of test setup for barge bow impact experiments.....	75
Figure 6.2	Photograph of test setup for barge bow experiments.....	76
Figure 6.3	Rendering of reduced-scale (40%) barge bow replicate showing internal truss structure	77
Figure 6.4	Fabrication of replicate barge bow model: a) Exploded view of replicate barge bow; b) Replicate barge bow during fabrication; c) Completed replicate barge bow.....	78
Figure 6.5	Exploded view of connection between replicate barge bow and reaction frame.....	79
Figure 6.6	Reaction frame structural members and general dimensions	80
Figure 6.7	Pendulum impact foundation: plan view dimensions	81
Figure 6.8	Embedded foundation anchor connection system	82
Figure 6.9	Site plan for universal pendulum impact foundation.....	83
Figure 6.10	Universal pendulum foundation construction stages (viewed from northwest corner): a) Anchor frames positioned; b) Reinforcement cage installed; c) Concrete cast (in 3 lifts); d) Soil backfilled.....	84
Figure 6.11	Impact block and cable support frame: exploded view	86
Figure 6.12	Instrumentation layout to be used in barge bow impact experiments: a) Elevation view; b) Plan view; c) Front view of instrumented impact block	89
Figure 6.13	Tape switches mounted to face of impact nose: a) Full view; b) Detail of end of single tape switch.....	90
Figure 6.14	Optical break beam sensor mounted on stand	92
Figure 6.15	Accelerometers mounted to bottom surface of impact block	93
Figure 6.16	High-speed digital video cameras.....	94
Figure 6.17	Laser scanner	95
Figure 7.1	Initial round nose impact test (RND1) of barge bow: a) Bottom view of impact zone; b) Side view of impact zone; c) Rear view of impact zone; d) Isometric view of impact zone.....	97
Figure 7.2	Sample break beam data from impact test RND1.....	98
Figure 7.3	Break beam data from impact test RND1	98
Figure 7.4	Tape switch data from impact test RND1.....	98

Figure 7.5	Averaged and filtered acceleration time-histories obtained from impact test RND1	99
Figure 7.6	Impact force time-histories computed for impact test RND1	100
Figure 7.7	3D scan of undeformed replicate barge bow (prior to round nose test series)	100
Figure 7.8	Permanent barge deformation following test RND1	101
Figure 7.9	Barge deformation at various stages of impact for impact test RND1: a) Incipient contact; b) Intermediate stage; c) At peak (maximum) deformation (prior to rebound); d) Residual deformation at rebound (zero force level)	102
Figure 7.10	Deformation time-history computed from high speed video for impact test RND1	102
Figure 7.11	Force-deformation relationship for impact test RND1	103
Figure 7.12	Distribution of absorbed energy for impact test RND1	103
Figure 7.13	Round nose impact test RND2 of barge bow: a) Bottom view of impact zone; b) Side view of impact zone; c) Rear view of impact zone; d) Isometric view of impact zone	104
Figure 7.14	Round nose impact test RND3 of barge bow: a) Bottom view of impact zone; b) Side view of impact zone; c) Rear view of impact zone; d) Isometric view of impact zone	104
Figure 7.15	Round nose impact test RND4 of barge bow: a) Bottom view of impact zone; b) Side view of impact zone; c) Rear view of impact zone; d) Isometric view of impact zone	105
Figure 7.16	Averaged and filtered acceleration time-histories obtained from impact test RND2	106
Figure 7.17	Averaged and filtered acceleration time-histories obtained from impact test RND3	106
Figure 7.18	Averaged and filtered acceleration time-histories obtained from impact test RND4	106
Figure 7.19	Impact force time-histories for test RND2	107
Figure 7.20	Impact force time-histories for test RND3	107
Figure 7.21	Impact force time-histories for test RND4	107
Figure 7.22	Permanent barge deformation following test RND2	108
Figure 7.23	Permanent barge deformation following test RND3	108
Figure 7.24	Permanent barge deformation following test RND4	108
Figure 7.25	Barge deformation at various stages of impact for impact test RND2: a) Incipient contact; b) Intermediate stage; c) At peak (maximum) deformation (prior to rebound); d) Residual deformation after rebound (zero force level)	109

Figure 7.26	Barge deformation at various stages of impact for impact test RND3: a) Incipient contact; b) Intermediate stage; c) At peak (maximum) deformation (prior to rebound); d) Residual deformation after rebound (zero force level).....	110
Figure 7.27	Barge deformation at various stages of impact for impact test RND4: a) Incipient contact; b) Intermediate stage; c) At peak (maximum) deformation (prior to rebound); d) Residual deformation after rebound (zero force level).....	110
Figure 7.28	Incremental deformation time-history for test RND2.....	111
Figure 7.29	Incremental deformation time-history for test RND3.....	111
Figure 7.30	Incremental deformation time-history for test RND4.....	111
Figure 7.31	Initial flat nose impact test (FLT1) of barge bow: a) Bottom view of impact zone; b) Side view of impact zone; c) Rear view of impact zone; d) Isometric view of impact zone	112
Figure 7.32	Averaged and filtered acceleration time-histories obtained from impact test FLT1	113
Figure 7.33	Impact force time-histories computed for impact test FLT1	113
Figure 7.34	3D scan of undeformed replicate barge bow (prior to flat-faced nose test series) .	114
Figure 7.35	Permanent barge deformation following test FLT1.....	114
Figure 7.36	Barge deformation at various stages of impact for impact test FLT1: a) Incipient contact; b) Intermediate stage; c) At peak (maximum) deformation (prior to rebound); d) Residual deformation after rebound (zero force level).....	115
Figure 7.37	Deformation time-history computed from high speed video for impact test FLT1	115
Figure 7.38	Force-deformation relationship for impact test FLT1	116
Figure 7.39	Flat-faced nose impact test FLT2 of barge bow: a) Bottom view of impact zone; b) Side view of impact zone; c) Rear view of impact zone; d) Isometric view of impact zone	117
Figure 7.40	Flat-faced nose impact test FLT3 of barge bow: a) Bottom view of impact zone; b) Side view of impact zone; c) Rear view of impact zone; d) Isometric view of impact zone	117
Figure 7.41	Flat-faced nose impact test FLT4 of barge bow: a) Bottom view of impact zone; b) Side view of impact zone; c) Rear view of impact zone; d) Isometric view of impact zone	118
Figure 7.42	Averaged and filtered acceleration time-histories obtained from impact test FLT2	118
Figure 7.43	Averaged and filtered acceleration time-histories obtained from impact test FLT3	119
Figure 7.44	Averaged and filtered acceleration time-histories obtained from impact test FLT4	119

Figure 7.45	Impact force time-histories for test FLT2.....	119
Figure 7.46	Impact force time-histories for test FLT3.....	120
Figure 7.47	Impact force time-histories for test FLT4.....	120
Figure 7.48	Permanent barge deformation following test FLT2.....	121
Figure 7.49	Permanent barge deformation following test FLT3.....	121
Figure 7.50	Permanent barge deformation following test FLT4.....	121
Figure 7.51	Barge deformation at various stages of impact for impact test FLT2: a) Incipient contact; b) Intermediate stage; c) At peak (maximum) deformation (prior to rebound); d) Residual deformation after rebound (zero force level).....	122
Figure 7.52	Barge deformation at various stages of impact for impact test FLT3: a) Incipient contact; b) Intermediate stage; c) At peak (maximum) deformation (prior to rebound); d) Residual deformation after rebound (zero force level).....	122
Figure 7.53	Barge deformation at various stages of impact for impact test FLT4: a) Incipient contact; b) Intermediate stage; c) At peak (maximum) deformation (prior to rebound); d) Residual deformation after rebound (zero force level).....	123
Figure 7.54	Incremental deformation time-history for test FLT2.....	123
Figure 7.55	Incremental deformation time-history for test FLT3.....	124
Figure 7.56	Incremental deformation time-history for test FLT4.....	124
Figure 7.57	Force-deformation relationship for impact series with round impactor.....	127
Figure 7.58	Backbone curve for impact series with round impactor.....	127
Figure 7.59	Force-deformation relationship for impact series with flat-faced impactor.....	128
Figure 7.60	Backbone curve for impact series with flat-faced impactor.....	128
Figure 7.61	Comparison of experimental and analytical backbone curves for RND series.....	129
Figure 7.62	Comparison of experimental and analytical backbone curves for FLT series.....	129
Figure 8.1	Current AASHTO vessel collision risk assessment procedure.....	134
Figure 8.2	Revised UF/FDOT vessel collision risk assessment workflow.....	135
Figure 8.3	Possible pier collapse mechanisms: a) Pier column collapse mechanism; b) Pile collapse mechanism.....	136
Figure 9.1	Bryant Grady Patton Bridge (SR 300) spanning Apalachicola Bay, Florida.....	140
Figure 9.2	High-rise portion of SR 300 Bridge, showing potential navigational obstructions.....	141
Figure 9.3	Current velocities in Apalachicola Bay at various tidal stages (Conner et al. 1982).....	142
Figure 9.4	Nautical chart including water depth soundings at MLLW (NOAA 2013a).....	144
Figure 9.5	High-rise portion of SR-300 Bridge, showing piers at risk for impact.....	145

Figure 9.6	Pier and foundation configurations for SR-300 Bridge (Arrows at pile locations indicate directions of pile batter)	146
Figure 9.7	Typical barge impact scenarios, showing possible headlog elevations	147
Figure 9.8	Overview of bridge span configurations.....	148
Figure 9.9	Superstructure cross-sections for the SR-300 Bridge	148
Figure 9.10	Locations of soil borings and piers to which each soil profile is assigned.....	149
Figure 9.11	FB-MultiPier models of selected piers from SR-300 Bridge	150
Figure 9.12	Computing the geometric probability of impact (PG) (after AASHTO 2009).....	159
Figure 9.13	Coupled vessel impact analysis (CVIA) method.....	165
Figure 9.14	Typical barge impact with pile cap, showing pertinent impact parameters.....	166
Figure 9.15	Applied vessel impact load (AVIL) method.....	167
Figure 9.16	Procedure for computing barge impact force-time histories in accordance with AVIL method (Consolazio et al. 2008)	168
Figure 9.17	Determination of lateral pier-soil stiffness (kP) by static analysis	169
Figure 9.18	Static load cases for SBIA method (Getter et al. 2011).....	171
Figure 9.19	Determination of lateral superstructure stiffness (ksup).....	172
Figure 9.20	Procedure for computing the probability that a navigational obstruction (island) will cause vessel grounding prior to pier impact (PGr) based on its orientation and path to the pier.....	174
Figure 9.21	Procedure for computing PGr for old bridge (fishing pier) navigational obstruction	175
Figure 9.22	Risk analysis results for each pier and vessel group: AASHTO (1991) methods ..	177
Figure 9.23	Percent contribution to AF: AASHTO (1991) methods	178
Figure 9.24	Risk analysis results for each pier and vessel group: AASHTO (2009) methods ..	180
Figure 9.25	Percent contribution to AF: AASHTO (2009) methods	181
Figure 9.26	Risk analysis results for each pier and vessel group: UF/FDOT methods, CVIA..	184
Figure 9.27	Percent contribution to AF: UF/FDOT methods, CVIA.....	185
Figure 9.28	Risk analysis results for each pier and vessel group: UF/FDOT methods, AVIL..	186
Figure 9.29	Percent contribution to AF: UF/FDOT methods, AVIL.....	187
Figure 9.30	Risk analysis results for each pier and vessel group: UF/FDOT methods, SBIA ..	188
Figure 9.31	Percent contribution to AF: UF/FDOT methods, SBIA	189
Figure 9.32	SR-300 Bridge pier footing end cap retrofit to reduce vessel collision risk (retrofitted end caps indicated in grey)	193
Figure 9.33	SR-300 Bridge pier alternative design with foundation consisting of (2) 9-ft diameter drilled shafts, connected by a strut or shear wall.....	193

Figure 10.1	Louisiana Highway 1 (LA-1) Bridge over Bayou Lafourche, Louisiana	197
Figure 10.2	LA-1 Bridge region of interest, showing navigation channel alignment.....	197
Figure 10.3	High-rise portion of LA-1 Bridge, showing piers at risk for impact	199
Figure 10.4	Pier and foundation configurations for LA-1 Bridge.....	201
Figure 10.5	Typical barge impact scenarios, showing possible headlog elevations	202
Figure 10.6	Overview of bridge span configurations ('E' indicates locations of expansion joints).....	202
Figure 10.7	Superstructure cross-sections for the LA-1 Bridge.....	203
Figure 10.8	Locations of soil borings and piers to which each soil profile is assigned.....	204
Figure 10.9	FB-MultiPier models of selected piers from LA-1 Bridge	204
Figure 10.10	Computing the geometric probability of impact (PG) (from AASHTO 2009)	213
Figure 10.11	Coupled vessel impact analysis (CVIA) method.....	219
Figure 10.12	Typical barge impact with pile cap, showing pertinent impact parameters.....	219
Figure 10.13	Applied vessel impact load (AVIL) method.....	221
Figure 10.14	Procedure for computing barge impact force-time histories in accordance with AVIL method (Consolazio et al. 2008)	222
Figure 10.15	Determination of lateral pier-soil stiffness (kP) by static analysis	223
Figure 10.16	Risk analysis results for each pier and vessel group: AASHTO (1991) methods ..	225
Figure 10.17	Percent contribution to AF: AASHTO (1991) methods	226
Figure 10.18	Risk analysis results for each pier and vessel group: AASHTO (2009) methods ..	227
Figure 10.19	Percent contribution to AF: AASHTO (2009) methods	228
Figure 10.20	Risk analysis results for each pier and vessel group: UF/FDOT methods, CVIA..	230
Figure 10.21	Percent contribution to AF: UF/FDOT methods, CVIA.....	231
Figure 10.22	Risk analysis results for each pier and vessel group: UF/FDOT methods, AVIL..	232
Figure 10.23	Percent contribution to AF: UF/FDOT methods, AVIL.....	233
Figure 10.24	LA 1 Bridge pier footing end cap retrofit to reduce vessel collision risk (retrofitted end caps indicated in grey).....	237
Figure 10.25	Plan view of LA-1 Bridge showing locations of protective dolphin structures.....	238
Figure 10.26	LA-1 Bridge alternative design with drilled shaft foundation: piers 2 – 4	239
Figure 10.27	LA-1 Bridge alternative design with drilled shaft foundation: piers 96 – 97	240
Figure 10.28	Pile-founded alternative design with submerged footing and shear wall (pier 4) ..	242
Figure A.1	Eurocode risk assessment framework (Source: EN 1991-1-7:2006 §B.1)	254
Figure A.2	Possible numerical risk acceptance scheme (Source: EN 1991-1-7:2006 §B.4.2)..	257

Figure A.3	Eurocode head-on impact case	259
Figure A.4	Eurocode glancing (lateral) impact case.....	260
Figure A.5	Head-on barge impact force comparison: AASHTO vs. Eurocode.....	261
Figure A.6	Eurocode sample force time-histories (Reproduced from EN 1991-1-7:2006).....	262
Figure D.1	Four degree-of-freedom system with damping, subject to dynamic excitation by time-varying specimen resultant force $FS(t)$	292
Figure E.1	Finite element impact simulation of 0.4-scale barge bow	296
Figure E.2	Comparison of barge bow deformation after one impact	297
Figure E.3	Barge bow force-deformation comparison	298
Figure M.1	Impact force-time histories: SR-300 Bridge, Pier 35	439
Figure M.2	Impact force-time histories: SR-300 Bridge, Pier 36	440
Figure M.3	Impact force-time histories: SR-300 Bridge, Pier 37	441
Figure M.4	Impact force-time histories: SR-300 Bridge, Pier 38	442
Figure M.5	Impact force-time histories: SR-300 Bridge, Pier 39	443
Figure M.6	Impact force-time histories: SR-300 Bridge, Pier 40	444
Figure M.7	Impact force-time histories: SR-300 Bridge, Pier 41	445
Figure M.8	Impact force-time histories: SR-300 Bridge, Pier 42	446
Figure M.9	Impact force-time histories: SR-300 Bridge, Pier 43	447
Figure M.10	Impact force-time histories: SR-300 Bridge, Pier 44	448
Figure M.11	Impact force-time histories: SR-300 Bridge, Pier 45	449
Figure M.12	Impact force-time histories: SR-300 Bridge, Pier 46	450
Figure M.13	Impact force-time histories: SR-300 Bridge, Pier 47	451
Figure M.14	Impact force-time histories: SR-300 Bridge, Pier 48	452
Figure M.15	Impact force-time histories: SR-300 Bridge, Pier 49	453
Figure M.16	Impact force-time histories: SR-300 Bridge, Pier 50	454
Figure M.17	Impact force-time histories: SR-300 Bridge, Pier 51	455
Figure M.18	Impact force-time histories: SR-300 Bridge, Pier 52	456
Figure M.19	Impact force-time histories: SR-300 Bridge, Pier 53	457
Figure M.20	Impact force-time histories: SR-300 Bridge, Pier 54	458
Figure M.21	Impact force-time histories: SR-300 Bridge, Pier 55	459
Figure M.22	Impact force-time histories: SR-300 Bridge, Pier 56	460
Figure M.23	Impact force-time histories: SR-300 Bridge, Pier 57	461
Figure M.24	Impact force-time histories: SR-300 Bridge, Pier 58	462

Figure M.25	Impact force-time histories: SR-300 Bridge, Pier 59	463
Figure M.26	Impact force-time histories: SR-300 Bridge, Pier 60	464
Figure N.1	Impact force-time histories: LA-1 Bridge, Pier 2, upbound traffic, fully loaded ...	474
Figure N.2	Impact force-time histories: LA-1 Bridge, Pier 2, upbound traffic, lightly loaded.....	475
Figure N.3	Impact force-time histories: LA-1 Bridge, Pier 2, downbound traffic, fully loaded.....	476
Figure N.4	Impact force-time histories: LA-1 Bridge, Pier 2, downbound traffic, lightly loaded.....	477
Figure N.5	Impact force-time histories: LA-1 Bridge, Pier 3, upbound traffic, fully loaded ...	478
Figure N.6	Impact force-time histories: LA-1 Bridge, Pier 3, upbound traffic, lightly loaded.....	479
Figure N.7	Impact force-time histories: LA-1 Bridge, Pier 3, downbound traffic, fully loaded.....	480
Figure N.8	Impact force-time histories: LA-1 Bridge, Pier 3, downbound traffic, lightly loaded.....	481
Figure N.9	Impact force-time histories: LA-1 Bridge, Pier 4, upbound traffic, fully loaded ...	482
Figure N.10	Impact force-time histories: LA-1 Bridge, Pier 4, upbound traffic, lightly loaded.....	483
Figure N.11	Impact force-time histories: LA-1 Bridge, Pier 4, downbound traffic, fully loaded.....	484
Figure N.12	Impact force-time histories: LA-1 Bridge, Pier 4, downbound traffic, lightly loaded.....	485
Figure N.13	Impact force-time histories: LA-1 Bridge, Pier 96, upbound traffic, fully loaded .	486
Figure N.14	Impact force-time histories: LA-1 Bridge, Pier 96, upbound traffic, lightly loaded.....	487
Figure N.15	Impact force-time histories: LA-1 Bridge, Pier 96, downbound traffic, fully loaded.....	488
Figure N.16	Impact force-time histories: LA-1 Bridge, Pier 96, downbound traffic, lightly loaded.....	489
Figure N.17	Impact force-time histories: LA-1 Bridge, Pier 97, upbound traffic, fully loaded .	490
Figure N.18	Impact force-time histories: LA-1 Bridge, Pier 97, upbound traffic, lightly loaded.....	491
Figure N.19	Impact force-time histories: LA-1 Bridge, Pier 97, downbound traffic, fully loaded.....	492
Figure N.20	Impact force-time histories: LA-1 Bridge, Pier 97, downbound traffic, lightly loaded.....	493

LIST OF TABLES

<u>Table</u>	<u>Page</u>
Table 4.1	Summary of experimental testing parameters and number of repetitions39
Table 4.2	Rate sensitivity parameters and impulse ratio (<i>IR</i>) statistics53
Table 4.3	Effective plastic strain at failure for each material series57
Table 5.1	Summary of barge bow impact response data (flat-faced block)65
Table 5.2	Comparison of constitutive model parameters68
Table 5.3	Summary of barge bow impact response data (round nose block)72
Table 6.1	Specifications for tape switches91
Table 6.2	Specifications for optical break beams92
Table 6.3	Specifications for accelerometers93
Table 6.4	Specifications for high-speed cameras94
Table 6.5	Specifications for laser scanner95
Table 7.1	Summary of test program96
Table 7.2	Tabular summary of data collected from impact series with round impactor127
Table 7.3	Tabular summary of data collected from impact series with flat impactor128
Table 9.1	Upbound vessel traffic for Apalachicola Bay (Wang and Liu 1999)152
Table 9.2	Downbound vessel traffic for Apalachicola Bay (Wang and Liu 1999)152
Table 9.3	Aggregated vessel traffic data for vessel collision risk assessment152
Table 9.4	Footing geometry and projected pier width (BP) for each pier160
Table 9.5	Minimum lateral pushover capacities (H) for each pier162
Table 9.6	Barge impact parameters for CVIA166
Table 9.7	Lateral pier-soil stiffness (kP) for each SR-300 pier169
Table 9.8	Maximum barge impact force (PBm) (kip) for each pier and barge vessel group169
Table 9.9	Input parameters for SBIA IRF equations172
Table 9.10	IRF values for SBIA Load Case 1172
Table 9.11	Summary of risk assessment results for each analysis procedure considered190
Table 10.1	Vessel traffic for LA-1 Bridge206
Table 10.2	Aggregated barge traffic data for LA-1 Bridge207
Table 10.3	Minimum lateral pushover capacities (H) for each pier216
Table 10.4	Barge impact parameters for CVIA220
Table 10.5	Lateral pier-soil stiffness (kP) for each LA-1 pier223

Table 10.6	Maximum dynamic impact force (PBm): UF/FDOT methods (AVIL).....	223
Table 10.7	Protection factors (PF).....	224
Table 10.8	Summary of risk assessment results for each analysis procedure considered.....	233
Table 10.9	Comparison of barge yield forces (PBY) for as-built and retrofitted designs.....	236
Table 10.10	Comparison of barge yield forces (PBY) for as-built and alternative designs.....	240
Table 10.11	Summary of UF/FDOT (CVIA) risk assessment results for each design considered.....	241
Table A.1	Indicative values for dynamic forces due to ship impact on inland waterways (adapted from EN 1991-1-7:2006).....	258
Table A.2	Indicative values for dynamic forces due to ship impact for sea waterways (adapted from EN 1991-1-7:2006).....	259
Table E.1	Effective plastic strain at failure for each material series.....	295
Table L.1.	Pier reliability index (75-year \square) for various numbers of piers.....	427
Table L.2.	Comparison of LRFD and AASHTO vessel collision design methodologies.....	428
Table M.1	Vessel impact velocities (v_i) (knots).....	430
Table M.2	Geometric probability of impact (PG).....	430
Table M.3	Vessel impact forces (kips): AASHTO (1991) methods.....	431
Table M.4	Capacity-demand ratios (H/P): AASHTO (1991) methods.....	431
Table M.5	Probability of collapse (PC): AASHTO (1991) methods.....	432
Table M.6	Vessel impact forces (kips): AASHTO (2009) methods.....	432
Table M.7	Capacity-demand ratios (H/P): AASHTO (2009) methods.....	433
Table M.8	Probability of collapse (PC): AASHTO (2009) methods.....	433
Table M.9	Maximum vessel impact forces (kips): UF/FDOT methods (CVIA).....	434
Table M.10	Demand-capacity ratios (D/C): UF/FDOT methods (CVIA). Cases highlighted in grey indicate that D/C was controlled by pier column demands rather than pile demands.....	434
Table M.11	Probability of collapse (PC): UF/FDOT methods (CVIA). Cases highlighted in grey indicate PC = 1.....	435
Table M.12	Maximum vessel impact forces (kips): UF/FDOT methods (AVIL).....	435
Table M.13	Demand-capacity ratios (D/C): UF/FDOT methods (AVIL). Cases highlighted in grey indicate that D/C was controlled by pier column demands rather than pile demands.....	436
Table M.14	Probability of collapse (PC): UF/FDOT methods (AVIL). Cases highlighted in grey indicate PC = 1.....	436
Table M.15	Maximum vessel impact forces (kips): UF/FDOT methods (SBIA).....	437

Table M.16	Demand-capacity ratios (D/C): UF/FDOT methods (SBIA). Cases highlighted in grey indicate that D/C was controlled by pier column demands rather than pile demands	437
Table M.1	Probability of collapse (PC): UF/FDOT methods (SBIA). Cases highlighted in grey indicate PC = 1	438
Table M.18	Protection factor (PF).....	438
Table N.1	Vessel impact velocities (vi) (knots)	466
Table N.2	Geometric probability of impact (PG).....	466
Table N.3	Barge impact forces (kips): AASHTO (1991) methods	467
Table N.4	Capacity-demand ratios (H/P): AASHTO (1991) methods.....	467
Table N.5	Probability of collapse (PC): AASHTO (1991) methods	468
Table N.6	Barge impact forces (kips): AASHTO (2009) methods	468
Table N.7	Capacity-demand ratios (H/P): AASHTO (2009) methods.....	469
Table N.8	Probability of collapse (PC): AASHTO (2009) methods	469
Table N.9	Minimum of barge width (BB) and pier width (BP) (ft)	470
Table N.10	Barge yield force (PBY) (kip)	470
Table N.11	Maximum barge impact forces (PBm) (kip): UF/FDOT methods (CVIA).....	471
Table N.12	Demand-capacity ratios (D/C): UF/FDOT methods (CVIA)	471
Table N.13	Probability of collapse (PC): UF/FDOT methods (CVIA).....	472
Table N.14	Maximum dynamic impact force (PBm): UF/FDOT methods (AVIL).....	472
Table N.15	Demand-capacity ratios (D/C): UF/FDOT methods (AVIL)	473
Table N.16	Probability of collapse (PC): UF/FDOT methods (AVIL)	473

CHAPTER 1 INTRODUCTION

1.1 Introduction

Any bridge that spans a navigable waterway is at risk of accidentally being struck by waterway vessels that traverse beneath it. The severity of vessel impact loads can be sufficient to cause structural failure and collapse of supported roadways or railways. Given the unpredictable timing of vessel collisions, such failures have the potential to result in serious injury or loss of life and therefore constitute a public safety concern. Furthermore, the economic losses associated with bridge repair or replacement and interruption of critical traffic channels are significant.

In 1980, the Sunshine Skyway Bridge over Tampa Bay, Florida, collapsed as a result of being impacted by an errant cargo ship. The incident highlighted the need for engineers to consider the vessel collision hazard when designing bridges that span navigable water and clearly emphasized the urgent need for vessel collision design guidance. Throughout the 1980s, multiple research studies were conducted with the goal of quantifying vessel impact loads and the associated risks of structural failure. Those studies culminated in the development of design requirements that were adopted by Association of State Highway and Transportation Officials (AASHTO) as a guide specification (AASHTO, 1991, and later, AASHTO, 2009), and also incorporated into the main LRFD bridge design specifications (initially in AASHTO, 1994, and most recently, in AASHTO, 2011). Therefore, since 1991, in the United States, the design of bridges to resist vessel collision loading has been governed by the various AASHTO vessel collision design specifications.

1.2 Motivation

Development and publication of the 1991 AASHTO vessel collision design procedures was a dramatic improvement to bridge design practice and public safety, given that uniform national specifications for the design of bridges to resist vessel collision loading did not previously exist. However, the AASHTO procedures were developed at a time when structural analysis tools (i.e., software) and computing power were significantly more rudimentary than they are today. Consequently, the AASHTO guidelines treat vessel impact as a static loading event, even though impacts are inherently dynamic in nature. At the time of the AASHTO specification development, this was a reasonable simplification, given that dynamic analysis of bridge structures was extremely time consuming and cost prohibitive in a design setting.

In the intervening years since the AASHTO vessel collision guidelines were first published, extraordinary advances in computing power have been made, coupled with corresponding improvements in the sophistication of design-oriented structural analysis software. Currently, commercially available software packages can perform static analyses of multiple-pier, multiple-span bridge structures in seconds, even using typical workstation computers. Therefore, transient dynamic analyses can be completed in five minutes to one hour (depending on model fidelity and complexity). Given the ever increasing availability of such analysis capabilities, a significant proportion of structural engineers are now trained in the areas of

structural dynamics, finite element analysis, and inelastic (nonlinear) analysis. Indeed, modal dynamic analysis is employed on a regular basis for seismic design, and transient (linear as well as nonlinear) seismic analysis is becoming increasingly common. Given the widespread availability of computing power, sophisticated structural analysis software tools, and specialized engineering expertise, it is no longer necessary to simplify dynamic events, such as vessel collisions, down to simple, static loading events.

In contrast to seismic (earthquake) loading events, in which structural response can be evaluated with relatively high accuracy using simplified dynamic analysis techniques like response spectrum analysis, accurately evaluating the response of a bridge to vessel impact loading requires consideration of a significant number of unique factors. These include the geometry, mass, and stiffness characteristics of the impacting vessel and the impacted structure, localized damage, impact velocity and direction, and the duration of the impact event. Recent research indicates that the influences that these factors have on bridge response to impact load are highly variable among different bridge configurations, primarily because dynamic interactions between the vessel and bridge cause the magnitude and duration of the impact loading event to be dependent on characteristics that are specific to both the vessel and the bridge. Traditionally, only high-resolution, nonlinear contact-impact finite element analyses could directly account for all the various uncertainties and dynamic interactions involved. Such analyses have historically only been possible using highly specialized software tools and supercomputers. While such tools are commercially available, they are not currently (and may never be) practical for use in typical bridge design settings. To date at least, these limitations have precluded design engineers from considering the *dynamic response* of bridges to vessel collisions.

However, over the past several years, UF/FDOT research has significantly improved the understanding of barge-bridge collisions and the nature of structural response to such collisions. As part of this past research, UF and FDOT have developed improved impact load-prediction models, a variety of static and dynamic structural analysis procedures, and an improved structural reliability (probability of collapse) expression. These tools empirically, or directly, take into account the various uncertainties and interactions identified above in such a way that they can be implemented by bridge designers. Therefore, they constitute considerable improvements to existing design practice. However, the UF/FDOT impact load model has yet to be fully validated against experimental measurements, particularly at high levels of barge deformation. Furthermore, while the UF/FDOT structural analysis techniques have been extensively compared to high-resolution contact-impact analysis (the most accurate tool currently available) with excellent agreement, the influence of employing such techniques on design efficiency and economy has yet to be evaluated. That is, to date it has not been clear whether these new, more accurate procedures will result in increased demands on design engineers, and increased design and construction costs; whether the opposite will be true; or whether implementation of the new procedures will be design-and-construction-cost-neutral (in an average sense across a spectrum of multiple bridges).

1.3 Objectives

The objectives of the research presented in this report were to: 1) validate the UF/FDOT load-prediction model using high-deformation pendulum-impact experimental testing; 2) develop a unified vessel collision risk assessment methodology that incorporates the UF/FDOT impact load model, structural analysis techniques, and probability of collapse expression; 3) demonstrate use of that methodology by assessing the vessel collision risk of two recently constructed highway bridges; and, 4) compare outcomes from the revised methodology to the existing AASHTO procedures. Completion of these tasks will enable implementation of past and current UF/FDOT vessel collision research results into design practice by the FDOT in Florida, and ultimately by AASHTO nationwide.

1.4 Scope of Work

- Experimental validation of barge impact load model: In two past research studies funded by FDOT (Consolazio et al. 2009, Getter and Consolazio 2011), researchers at UF developed a new barge impact load prediction model that is a significant improvement over the model currently employed in the AASHTO provisions. In addition to being based on barge types that are common to United States waterways (the AASHTO barge provisions were based on tests conducted on European pontoon barges), the new UF/FDOT model takes into account important contributors to the magnitude of impact forces: size, shape, and orientation of the bridge surface being impacted. However, the UF/FDOT model is based heavily on finite element simulations, and only experimental data at limited deformation levels (Consolazio et al. 2006) were available to validate the findings of these past studies. Therefore, a series of impact experiments were conducted in this study, in which reduced-scale replicas of the barge used in the simulation studies (a jumbo hopper barge) were impacted by a high-energy impact pendulum to achieve significant bow deformations. Behavioral trends observed during the experiments were compared to analogous impact simulations that employ the same finite element modeling and analysis techniques that were used to develop the barge impact load model, thereby validating the UF/FDOT model.
- Characterize strain rate-sensitive material properties for common steels: During preliminary finite element (FE) simulations of the barge impact experiments, the model barge bow sustained as much as 15 in. of deformation during impact events lasting less than 0.1 sec. Consequently, localized strain rates in the various steel barge components were very high. Because steels, like most materials, exhibit greater yield and ultimate strengths at high strain rates, the rate-sensitive properties of the barge materials needed to be determined prior to conducting the impact tests. In this study, these properties were quantified by conducting uniaxial tension tests on the barge materials (ASTM A36 steel and A1011 steel) over a wide range of strain rates ($7 \times 10^{-5} - 500 \text{ s}^{-1}$). To conduct the high-rate material tests, a novel mechanical apparatus was designed that employed an impact pendulum as the source of energy. Data from material tests conducted using the apparatus were combined with data from lower-rate tests conducted using a typical laboratory load frame and were used to develop stress-strain relations and strain rate-sensitive properties

for input into finite element constitutive models that were used in the validation simulations.

- Develop a revised barge impact design procedure: A revised design procedure was developed that implements the barge impact load model, impact analysis procedures, and probability of collapse expression that were developed from UF/FDOT research over the past several years. Alternative design methodologies to the comprehensive risk assessment procedure required by AASHTO were also considered, most notably an LRFD approach to vessel collision loading. Ultimately, it was determined that the uncertainties associated with vessel collision loading do not permit a simplified LRFD methodology to be employed without introducing considerable conservatism. Therefore, the existing AASHTO risk analysis framework was instead modified in a targeted way to incorporate UF/FDOT procedures.
- Demonstrate revised design procedure through real-world examples: The revised risk analysis procedure was demonstrated using two bridges that were designed in accordance with the AASHTO (1991) provisions and constructed within the past decade: the SR-300 Bridge over Apalachicola Bay, Florida, and the LA-1 Bridge over Bayou Lafourche, Louisiana. The latter bridge is the same structure that was used to demonstrate the AASHTO procedure in the second edition of the AASHTO Vessel Collision Guide Specification (AASHTO 2009). For comparison, both bridges were also evaluated using both the 1991 and 2009 editions of the AASHTO procedure. Differences between the various procedures (AASHTO 1991, AASHTO 2009, and UF/FDOT procedures) were documented in detail, both to act as a complete worked-out example for future engineers to refer to, and also to demonstrate the implications of implementing the proposed UF/FDOT procedures in design practice.

CHAPTER 2 BACKGROUND

2.1 Introduction

Multiple bridge collapses caused by vessel collision—most notably the collapse of the Sunshine Skyway Bridge near Tampa, Florida—prompted the development of the American Association of State Highway and Transportation Officials (AASHTO) *Guide Specifications and Commentary for Vessel Collision Design of Highway Bridges*, which was originally published in 1991 (AASHTO 1991) and updated with minor revisions in 2009 (AASHTO 2009). The guide specification provided a framework for estimating loads associated with vessel collisions and quantifying the risk of structural failure posed by errant vessels. A detailed review of the AASHTO (2009) vessel collision risk analysis procedure is provided in Section 2.2. In the years since the 1991 publication of the guide specification, a multitude of research projects have been conducted by UF/FDOT which have uncovered important limitations to the AASHTO procedures. This research has culminated in state-of-the-art impact load-prediction models and structural analysis procedures. A summary of UF/FDOT research findings and proposed methods is provided in Section 2.3.

2.2 AASHTO Risk Assessment Procedure

The AASHTO provisions (AASHTO 2009) are strongly focused on quantifying the risk of bridge collapse resulting from vessel collision. Three (3) design methodologies—with varying levels of complexity—are permitted by AASHTO:

- **Method I:** A simplified semi-deterministic procedure in which the bridge is designed to withstand impact from a pre-determined design vessel. The design vessel is chosen such that only a small percentage of vessel traffic in the waterway is larger. Method I is intended for smaller, less critical bridges, for which a comprehensive risk analysis (Method II) is impractical. Approval by the bridge owner is required to employ Method I.
- **Method II:** A comprehensive risk analysis procedure in which the annual frequency of bridge collapse (AF) is directly quantified. The Method II risk analysis requires consideration of *all* vessel types that are expected to traverse the bridge. Method II is the preferred design method, and is considered the default procedure for any bridge at risk for vessel collisions. Thus, Method II is the focus of the research addressed by this study.
- **Method III:** A cost-benefit analysis procedure in which vessel impact risk reduction measures are compared based on cost. Method III is permitted for cases in which the risk acceptance criteria of Method II are deemed to be technically or economically infeasible. Like Method I, approval by the bridge owner is required to employ Method III.

As stated above, the Method II risk analysis consists of quantifying the annualized probability that a bridge will undergo catastrophic structural failure (collapse) as a result of vessel collision with any bridge element. This probability, expressed as an annual frequency of collapse (AF), is defined as:

$$AF = N(PA)(PG)(PC)(PF) \quad (2.1)$$

where N is the number of vessel passages per year, PA is the probability that a given vessel will become aberrant—deviate from its intended transit path—per vessel passage, PG is the probability that a bridge element will be impacted by an aberrant vessel, PC is the probability that impact-induced bridge element collapse results from the collision, and PF is a protection factor for bridge elements that are shielded by protection systems or other navigational obstructions.

Because most navigable waterways are utilized by a great variety of different types of vessels—ranging from small pleasure craft to massive cargo ships—the AASHTO provisions suggest partitioning the total vessel traffic into representative vessel groups. The vessels represented in each group should be approximately equal in mass and type, and thus be expected to impart similar loads during impacts with a bridge element. Note also, that a bridge ‘element’ may be defined as either superstructure spans or supporting piers. Either type of element is at risk for vessel collision and collapse. However, low-profile vessels such as river barges generally cannot impact the superstructure, thus only pier elements are at risk for collision from such vessel types. In practice, AF is computed as a summation across all vessel groups ($i = 1 \dots N_{VG}$) and bridge elements ($j = 1 \dots N_{BE}$):

$$AF = \sum_{i=1}^{N_{VG}} \left[N_i (PA_i) \sum_{j=1}^{N_{BE}} (PG_{ij})(PC_{ij})(PF_{ij}) \right] \quad (2.2)$$

Note that the probability of vessel aberrancy (PA) is not dependent upon the bridge element of interest and is thus excluded from the internal summation.

Computed in accordance with Eqn. 2.2, AF represents the total annual probability that *any* bridge element will be struck by an errant vessel *and* collapse. AASHTO prescribes acceptable quantities for AF , depending upon the importance classification of the bridge. For critical or essential bridges—as defined by Social/Survival and Strategic Highway Network (STRAHNET) requirements— AF should be less than or equal to 0.0001. For typical bridges, AF is limited to 0.001. Stated alternatively, the return period for vessel collision-induced bridge collapse should be at least 10,000 years for critical/essential bridges, and 1,000 years for typical bridges.

The probability of vessel aberrancy (PA) is computed as:

$$PA = BR(R_B)(R_C)(R_{XC})(R_{RD}) \quad (2.3)$$

where BR is the base rate of aberrancy (0.00006 for ships and 0.00012 for barges), and R_B , R_C , R_{XC} , and R_{RD} are correction factors to account for bridge location, parallel currents, cross currents, and vessel traffic density, respectively. Expressions for the correction factors are provided in the AASHTO provisions (AASHTO 2009).

The geometric probability (PG) represents the conditional probability that a particular bridge element (e.g., a bridge pier) will be impacted by a vessel *given* that the vessel has become aberrant. Fig. 2.1 demonstrates how PG is computed for a bridge pier. Vessel position within the channel is assumed to be normally (Gaussian) distributed with the mean value at the centerline of the intended vessel transit path. The standard deviation of the Gaussian distribution is assumed to be equal to the overall vessel length (LOA). In the case of multiple-barge flotillas, LOA includes the length of all barges in a line plus the propelling push boat. The quantity PG is computed as the total area under the Gaussian distribution over the range of distance from the channel centerline which would lead to vessel impact with the pier of interest. Pertinent parameters for this integration are defined in Fig. 2.1. Note that because the Gaussian distribution is dependent on LOA , PG for a given pier must be computed for each vessel group. Hence, PG is denoted PG_{ij} in the Eqn. 2.2.

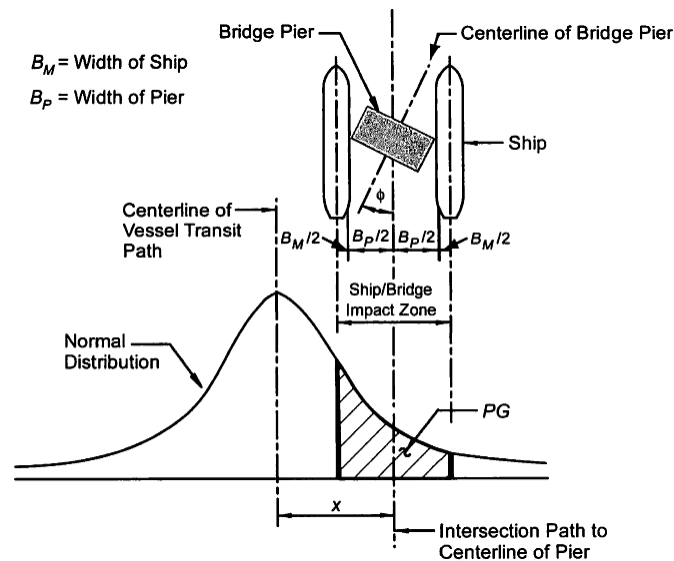


Figure 2.1 Determination of geometric probability of impact (PG) with a bridge pier
(Source: AASHTO 2009)

The probability of bridge element collapse (e.g., pier collapse) is computed as a function of the ratio of the lateral load carrying capacity of the bridge element (H) to the computed static vessel impact force (P). For bridge piers, H is usually defined as the static pushover capacity.

The impact force (P) is denoted P_S for ship impacts and P_B for barge impacts. Ship impact forces are computed (in kip) using the empirical expression:

$$P_S = 220(DWT)^{1/2} \left(\frac{V}{27} \right) \quad (2.4)$$

where DWT is the deadweight tonnage of the ship (tonnes, where 1 tonne = 2,205 lb), and V is the impact velocity (ft/s).

Barge impact forces are computed in a two-step process. First, the barge bow damage depth (a_B) is computed (in feet):

$$a_B = \left[\left(1 + \frac{KE}{5672} \right)^{1/2} - 1 \right] (10.2) \quad (2.5)$$

where KE is the kinetic energy (kip-ft) of the impacting barge or barge flotilla. Given a_B , the barge impact force (P_B) is computed (in kip) as:

$$P_B = \begin{cases} 4112(a_B) & a_B < 0.34 \text{ ft} \\ 1349 + 110(a_B) & a_B \geq 0.34 \text{ ft} \end{cases} \quad (2.6)$$

It is important to note that both P_S and P_B are considered by AASHTO to be equivalent-static impact forces, in that the forces are assumed to empirically include any dynamic amplification effects associated with the impacting vessel. While dynamic analysis of the impacted bridge is permitted by AASHTO, it is not required. Consequently, in typical practice, the static pushover capacity (H) of a given pier is compared to the equivalent-static impact force (P) to compute the probability of collapse (PC):

$$PC = \begin{cases} 0.1 + 9(0.1 - H/P) & 0.0 \leq H/P < 0.1 \\ 1 - H/P & 0.1 \leq H/P < 1.0 \\ 0 & H/P > 1.0 \end{cases} \quad (2.7)$$

It is also important to note that when the impact force is equal to the pier capacity (i.e., $H/P = 1$), according to AASHTO, the probability of collapse (PC) is equal to zero. Also, per AASHTO, the

impact force must greatly exceed the pier capacity before the probability of collapse grows larger than 10%. The AASHTO PC expression is illustrated graphically in Fig. 2.2.

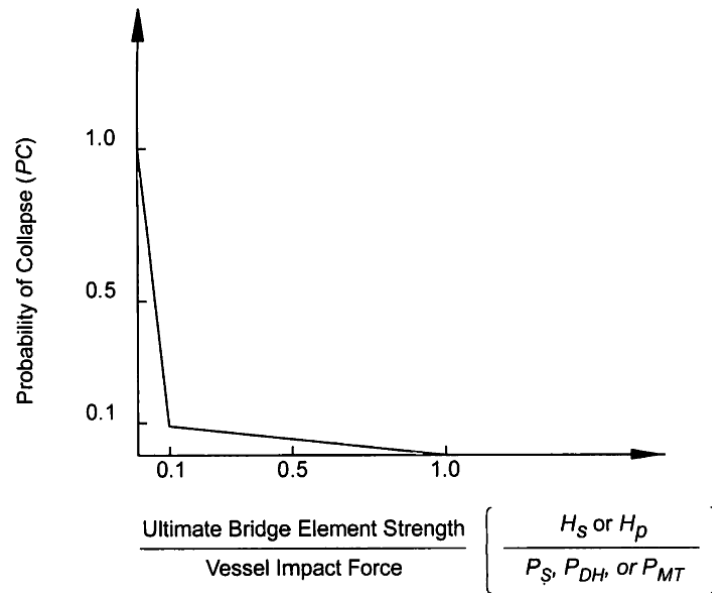


Figure 2.2 Determination of probability of collapse (PC) (Source: AASHTO 2009)

For cases in which a bridge pier is protected by fenders or other protection structures (e.g., dolphins), or by some other navigational obstruction (e.g., land masses), use of a protection factor (PF) is permitted. The value of PF can take a value between 0 and 1 and is a function of the percent protection provided such structures. Given the site-specific nature of pier protection, the development of appropriate values for PF is left to the discretion of the engineer and owner, though some limited guidance is provided in the AASHTO Guide Specification (2009). An example of how probabilistic analysis can be used to calculate PF is illustrated in Chapter 8.

Once PA has been computed for each vessel group, and PG , PC , and PF have been computed for each combination of vessel group and bridge element, the various probabilities are summed in accordance with Eqn. 2.2 to arrive at the annual frequency of collapse (AF). If AF is less than the limits noted earlier, then the bridge is deemed adequately resistant to vessel collision. If AF exceeds the specified limits, then the bridge must be appropriately strengthened, or protection systems must be installed. If neither option is economically or technically feasible, then the cost-effectiveness procedure (Method III) can be used to identify risk mitigation measures that are feasible.

It is noted that European design standards (CEN 2006) also prescribe a risk analysis based approach (similar to AASHTO) for vessel collision design of bridges. A comprehensive review of Eurocode provisions pertaining to vessel collision is provided in Appendix A.

2.3 UF/FDOT Research on Barge Collision

Over the past several years (2000 – present) multiple research studies have been conducted by the University of Florida (UF) and Florida Department of Transportation (FDOT), for the purpose of investigating limitations of the AASHTO provisions described above. Based on the results of these studies, design-oriented procedures have been developed to improve upon the AASHTO guidelines. The major findings from these studies are:

- During vessel impact, superstructure inertia results in dynamic amplification of pier column internal forces, and this phenomenon is not accounted for in the AASHTO-prescribed static analysis. Dynamic (transient or modal) and equivalent-static analysis procedures have been developed by UF/FDOT that account for superstructure inertia and resulting dynamic amplification;
- Barge impact forces are strongly dependent on the shape and size of the impacted pier and the angle of impact. These variables are not included in the AASHTO load-prediction expressions. An alternative barge impact load-prediction model has been developed that appropriately accounts for the parameters that strongly influence impact forces; and
- The AASHTO probability of collapse (*PC*) expression (Eqn. 2.7, Fig. 2.2) is based upon data gathered from ship-to-ship collisions (not ship-to-bridge collisions), and thus it can produce unrealistic predictions of *PC*. An alternative probability of collapse expression has been developed based upon rigorous reliability analysis of several bridges subjected to barge collision loading.

The UF/FDOT studies that led to these findings are summarized in the following sections.

2.3.1 Full-scale barge impact experiments

In 2004, Consolazio et al. conducted a series of full-scale barge impact experiments with multiple pier and partial bridge configurations (Consolazio et al. 2006). The experimental bridge was a decommissioned causeway leading to St. George Island, in northwest Florida. Prior to demolition of the old bridge, the researchers instrumented the channel pier and two adjacent piers with load cells, strain gauges, accelerometers, and displacement transducers, and impacted each structure multiple times with a full-sized barge. Impact experiments were conducted with a stand-alone pier with the superstructure removed (Fig. 2.3a) and a pier with the superstructure in place (Fig. 2.3b).



Figure 2.3 Full-scale barge impact experiments at St. George Island, Florida: a) Stand-alone pier impact (superstructure removed), and b) Intact bridge impact (Consolazio et al. 2006)

As part of these tests, impact forces, pier deflections, pier and barge accelerations, and impact velocities were measured. For safety and environmental reasons, Consolazio et al. were not permitted to collapse the tested structures. Thus, impact energies were lower than would be expected for a fully loaded barge flotilla. However, the experimental measurements revealed that inertial effects in the bridge—particularly from the superstructure—increase pier column member demands (i.e. shears, moments) relative to what the AASHTO-prescribed equivalent-static analysis procedures would predict.

Using dynamic finite element analysis of the experimental impact conditions—calibrated with the experimental data—Consolazio et al. (2006) demonstrated that immediately after impact, the superstructure mass provides inertial resistance to impact which acts as a significant source of dynamic amplification of column forces. Once the superstructure is accelerated to its maximum velocity and begins decelerating, the mass actually drives the pier to sway beyond the pier-top displacement predicted by AASHTO static analysis. Ultimately, it was demonstrated that while impact force magnitudes predicted by the AASHTO provisions were reasonably similar to those measured in the experiments, the AASHTO-prescribed static analysis procedure consistently underpredicted internal pier column structural demands (shear and moment). The discrepancy was attributed primarily to inertial effects resulting in dynamic amplification.

The full-scale impact experiments conducted at St. George Island provided valuable insights into dynamic structural response of bridges to barge impacts. Furthermore, the data from these experiments have been used on numerous occasions to validate finite element analysis results, newly developed analysis techniques, and impact load-prediction models.

2.3.2 Coupled vessel impact analysis (CVIA) procedure

Based on the results of the St. George Island experiments (Consolazio et al. 2006), it was concluded that only dynamic analysis techniques can adequately capture dynamic amplification effects during impact. However, methods available at the time—highly sophisticated contact-impact analyses involving tens or hundreds of thousands of finite elements—were not computationally efficient enough for use in bridge design. Thus, a novel dynamic analysis

technique was developed—coupled vessel impact analysis (CVIA)—in which barge motions and deformations are dynamically coupled to dynamic bridge response (Consolazio and Cowan 2005).

In CVIA (Fig. 2.4), the impacting barge is idealized as a single degree-of-freedom (SDF) system, consisting of a concentrated mass equal to the mass of the barge or flotilla and a nonlinear spring element which represents the crushable barge bow. This SDF system is coupled to a multi-degree-of-freedom (MDF) representation of the impacted bridge. To conduct CVIA, the barge mass is prescribed an impact velocity which initiates the analysis. At each timestep in the analysis, the impact load and bridge structural response are simultaneously computed based upon dynamic interaction between the SDF barge and MDF bridge models.

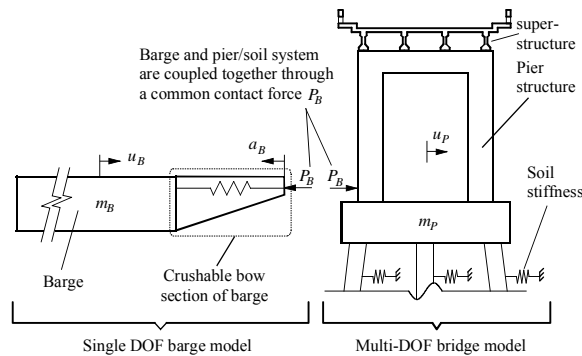


Figure 2.4 Coupled vessel impact analysis (CVIA) (Consolazio and Cowan 2005)

Impact forces and dynamic bridge response estimates provided by CVIA have been successfully validated against experimental data from the St. George Island impact experiments with excellent agreement (Consolazio and Cowan 2005). The CVIA method has been directly incorporated into the bridge finite element code FB-MultiPier (BSI 2010, Consolazio et al. 2008). In FB-MultiPier, multiple bridge piers and the connecting superstructure spans can be discretely modeled and analyzed. This approach permits dynamic interaction between the impacted pier, superstructure, and adjacent piers to be directly captured in the analysis.

Despite the efficiencies afforded by CVIA, dynamic analysis of a full bridge can still be computationally demanding. Thus, a simplified modeling procedure was developed in which the impacted pier and two adjacent spans are discretely modeled to form a one-pier two-span (OPTS) model (Consolazio and Davidson 2008). The stiffness and mass of the remaining portions of the bridge structure are represented with linear springs and concentrated masses placed at each end of the discretely modeled spans. When combined with the OPTS modeling technique, CVIA permits time-domain barge impact analysis to be completed within a few minutes with excellent accuracy on a typical workstation computer. Consequently, OPTS-CVIA represents the best currently available analysis tool for capturing dynamic amplification effects during barge impact events.

2.3.3 Barge bow force-deformation curves

A critical component of the CVIA method—and in fact, any barge impact analysis—is an accurate description of the strength and stiffness characteristics of the impacting barge bow. During even a moderate impact event, the barge bow undergoes significant plastic deformation, and the inelastic load-carrying capacity of the bow will determine impact force magnitudes. For design-oriented impact analysis, the impacting vessel is treated as a SDF system, so barge bow resistance can simply be described by a force-deformation curve (sometimes referred to as a ‘crush curve’).

The barge impact load-prediction model prescribed by AASHTO (2009) is based upon a series of barge bow crushing experiments performed in Germany in the early 1980s (Meier-Dörnberg 1983). The experiments included crushing—both statically and dynamically—reduced-scale models of European-style pontoon barge bows. A representative force-deformation curve (Fig. 2.5) was developed from the experimental results, and this curve was ultimately adopted by both AASHTO (2009) and the Eurocode (CEN 2006). The Meier-Dörnberg crush curve forms the basis for Eqs. 2.5 and 2.6 above.

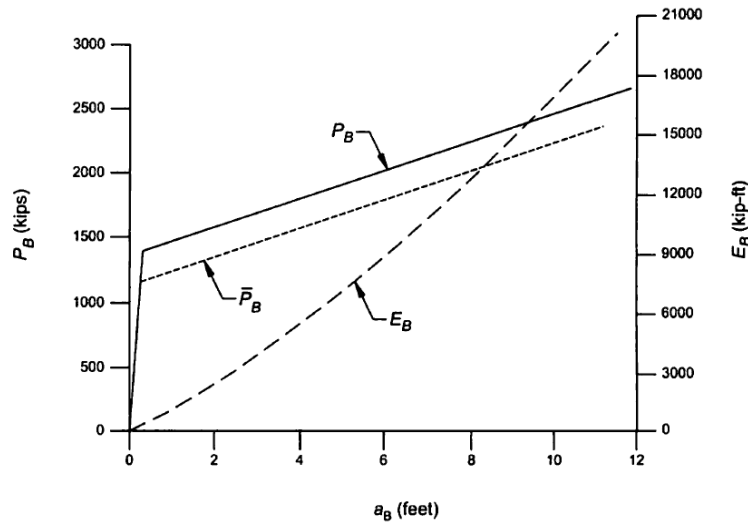


Figure 2.5 AASHTO barge bow force-deformation curve: P_B - a_B (AASHTO 2009)

In 2006, Consolazio et al. began studying, in detail, the mechanics of barge bow force-deformation behavior using fully-discretized high-resolution FE models and dynamic simulation tools (Consolazio et al. 2009). For this task, barge bow FE models were developed of the two most common barges in U.S. waterways, the jumbo hopper barge and the oversize tanker barge. The FE models were subjected to quasi-static crushing by rigid pier shapes of different shapes (round, flat) and widths (1 – 35 ft), and to very severe deformation levels (more than 15 ft). Force-deformation curves were then developed based on the simulation results. The study resulted in three primary findings:

- Force-deformation curves exhibit softening at large crushing deformations (approximately 12 in. or more). Thus, force-deformation curves can be conservatively idealized as elastic-perfectly plastic;
- Peak crushing forces are strongly dependent on the *width* of the impacted pier surface, where wide pier surfaces will develop larger forces than narrow surfaces;
- Peak crushing forces are strongly dependent on the *shape* of the impacted pier surface, where flat-faced (square or rectangular) shapes develop larger forces than round shapes.

These findings are significant because they demonstrate that crush curves—and the magnitude of corresponding barge impact forces—are dependent upon the geometry of the impacted pier. In contrast, AASHTO (2009) prescribes a single crush curve for all impact scenarios, independent of pier shape. Consequently, AASHTO-prescribed impact forces will be overly conservative for certain pier configurations and unconservative for others.

Consolazio et al. (2009) developed a design-oriented force-deformation model for barges based on data from the FE crushing simulations. However, a follow-up study (Getter and Consolazio 2011) demonstrated that impact forces with flat-faced piers are also strongly dependent upon the angle of impact: i.e., forces associated with oblique impact are smaller than head-on impact forces. Because the angle of impact is subject to significant uncertainty, a probabilistic approach was warranted. Getter and Consolazio combined force-deformation data from FE simulations of oblique crushing with a statistical description of impact orientation. Using Monte Carlo simulation, a new design-oriented force-deformation model was developed that probabilistically accounts for oblique impact scenarios. The revised crush model generally predicts smaller forces than the Consolazio et al. (2009) model, particularly for wide, flat-faced pier surfaces such as waterline footings.

The Getter-Consolazio (2011) barge force-deformation model is summarized in Fig. 2.6. If the impacted pier surface is round, a barge yield force (P_{BY}) is computed based only on the pier width (w_P). For flat-faced surfaces, P_{BY} is a function of both w_P and the most likely impact angle (θ). Generally, θ can be defined as the skew angle between the navigation channel and the pier alignment (the pier axis). Given P_{BY} , an elastic-perfectly plastic force-deformation curve is formed with a yield deformation (a_{BY}) equal to 2 in. The resulting force-deformation curve can be used directly as a description for barge bow stiffness in CVIA (recall Fig. 2.4) or as a basis for estimating equivalent-static impact loads.

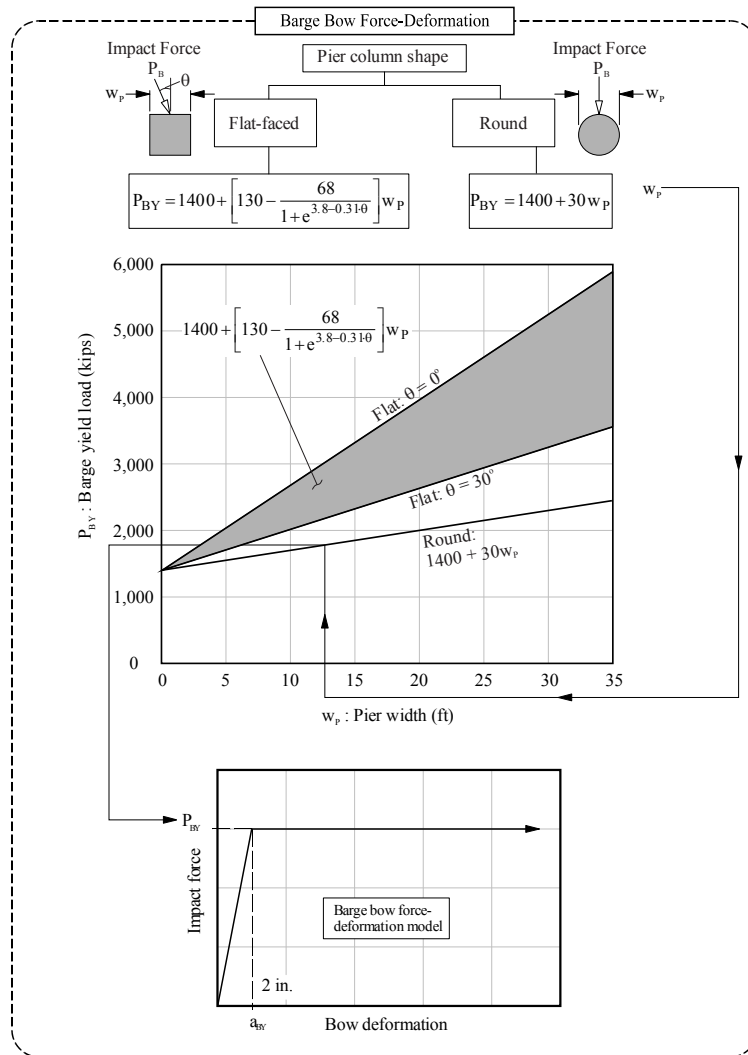


Figure 2.6 UF/FDOT barge bow force-deformation model (Getter and Consolazio 2011)

2.3.4 Collision-induced dynamic amplification phenomena

Given the development of an efficient and reliable dynamic impact analysis procedure (OPTS-CVIA) (Consolazio and Cowan 2005; Consolazio and Davidson 2008) and improved force-deformation relationships (Consolazio et al. 2009), a comprehensive study of barge impact-induced dynamic amplification phenomena was conducted (Davidson et al. 2010). In this study, a variety of bridges from around Florida were analyzed for barge impact using the best available dynamic analysis tool (OPTS-CVIA). Peak dynamic impact forces from each dynamic analysis were also applied statically to each bridge. The analysis results showed that pier column internal forces (shears, moments) obtained from dynamic analysis were significantly larger than those predicted by simple static analysis. In other words, dynamic amplification of pier column internal forces occurred during barge impact.

Detailed inspection of the analysis results showed that dynamic amplification is a consequence of superstructure inertial response during impact, as was observed during the full-scale barge impact experiments at St. George Island (Consolazio et al. 2006). The study (Davidson et al. 2010) uncovered two primary amplification modes: 1) superstructure inertial restraint, and 2) superstructure momentum-driven sway. Some bridges exhibited a mixed response in which both modes were present. [See Davidson et al. (2010) for detailed descriptions of each mode.]

Regardless of which amplification mode dominated the response, every bridge exhibited some level of dynamic amplification. Selected results from this study are provided in Fig. 2.7, sorted by amplification mode. Each bar represents a different bridge and impact energy. The data are presented as a ratio between the maximum dynamic and static pier column moments. Consequently, a ratio greater than 1.0 indicates dynamic amplification. Dynamic amplification ratios averaged between 1.5 and 2.0 (implying 50 – 100% amplification), and some cases exhibited much higher amplification levels. Consequently, dynamic amplification is a critical consideration in barge impact-resistant bridge design, and the phenomenon is not currently explicitly considered in the AASHTO (2009) provisions.

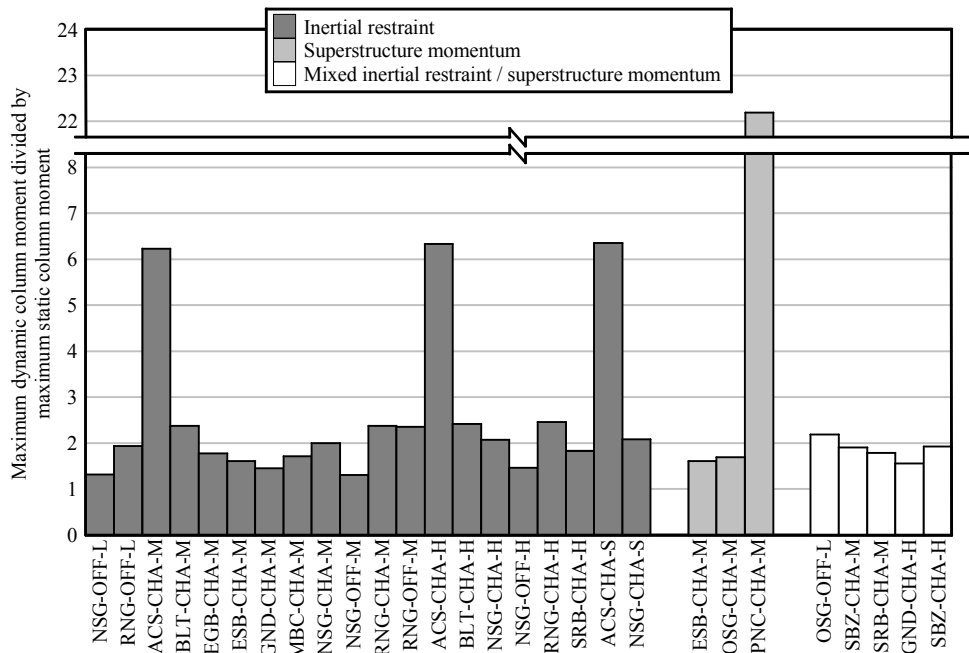


Figure 2.7 Dynamic amplification of pier column moments sorted by amplification mode (Davidson et al. 2010)

2.3.5 Other vessel impact analysis procedures

It has been demonstrated, both experimentally (Consolazio et al. 2006) and analytically (Davidson et al. 2010), that dynamic amplification is an important component of bridge response during vessel impact. Consequently, amplification effects must be considered when analyzing bridges for vessel impact loading. While the best available analysis tool (CVIA) can directly

account for dynamic amplification and is also reasonably efficient, time-domain dynamic analysis can be cumbersome in design, particularly during preliminary design stages. Accurate dynamic analysis requires well-defined descriptions of bridge stiffness and mass parameters, and time-domain analysis output requires significant post-analysis data processing to identify design member forces.

For this reason, UF and FDOT research has focused heavily on developing an array of vessel impact analysis procedures that are simple to use but which still account for important dynamic amplification effects. As a result, in addition to CVIA, three alternative analysis methods have also been developed:

- Applied vessel impact loading (AVIL): A time-domain dynamic analysis, in which the impact force time-history is computed *a priori* and applied to the bridge model;
- Impact response spectrum analysis (IRSA): A modal, frequency-domain (spectral) analysis;
- Static bracketed impact analysis (SBIA): An equivalent-static analysis that empirically accounts for dynamic amplification.

The applied vessel impact loading (AVIL) method involves pre-computing an impact force time-history—based upon the Getter-Consolazio (2011) force-deformation model—and then applying the load history to a bridge model using transient dynamic analysis (Consolazio et al. 2008). The AVIL method can serve as an adequate replacement for CVIA when bridge analysis software is used that does not include the necessary features to set up CVIA (e.g., concentrated masses or prescribed initial velocities).

The AVIL process is summarized in Fig. 2.8. Barge force-deformation parameters—barge yield force (P_{BY}) and yield deformation (a_{BY})—are determined in accordance with the Getter-Consolazio (2011) model (recall Fig. 2.6). Barge mass (m_B) and initial velocity (v_{Bi}) are determined based on the AASHTO provisions (AASHTO 2009) and site-specific vessel traffic and waterway current data. The lateral translational pier-and-soil stiffness (k_P) is determined by applying a static lateral load at the expected impact location and measuring the pier displacement at that location. Pier-soil stiffness (k_P) is combined in series with the barge bow stiffness to form a barge-pier-soil stiffness (k_S). With these parameters, an impact force time-history is formed, as illustrated in Fig. 2.6, that can be applied to the bridge model to conduct a time-domain dynamic analysis.

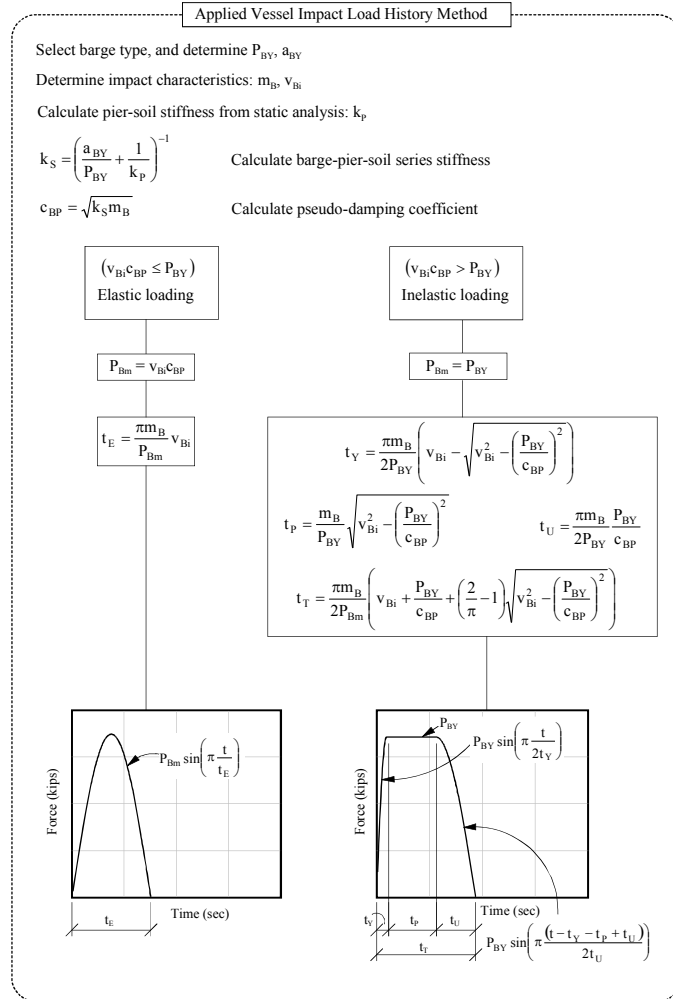


Figure 2.8 Applied vessel impact loading (AVIL) (Consolazio et al. 2008)

While methods such as CVIA and AVIL constitute the most accurate ways of quantifying vessel impact induced structural demands, such time-domain methods involve a number of disadvantages, foremost being computational time and output data processing effort. An alternative dynamic analysis approach is frequency-domain, also referred to as modal response spectrum analysis. Such methods are typically more computationally efficient than time-domain methods while still accounting for dynamic inertial phenomena. Given these benefits, a modal, frequency-domain analysis method—called impact response spectrum analysis (IRSA)—was developed for vessel impact analysis with bridges (Consolazio et al. 2008).

As summarized in Fig. 2.9, the IRSA procedure begins with developing vessel impact force time-history characteristics in accordance with the AVIL procedure (recall Fig. 2.8), including the maximum impact load (P_{Bm}) and load duration (T_I). The load duration is then used to form a design response spectrum. As with most response spectrum procedures, eigenanalysis is used to determine fundamental structural vibration periods and mode shapes. Modal displacements corresponding to each mode shape are magnified using DMFs computed from the response spectrum. For a given number of modes, magnified displacements and resulting internal

member forces are combined using either a square root sum of squares (SRSS) or complete quadratic combination (CQC) approach. If a sufficient number of modes are selected, combined displacements and internal forces constitute a reasonably accurate estimate of the peak dynamic structural response during vessel impact.

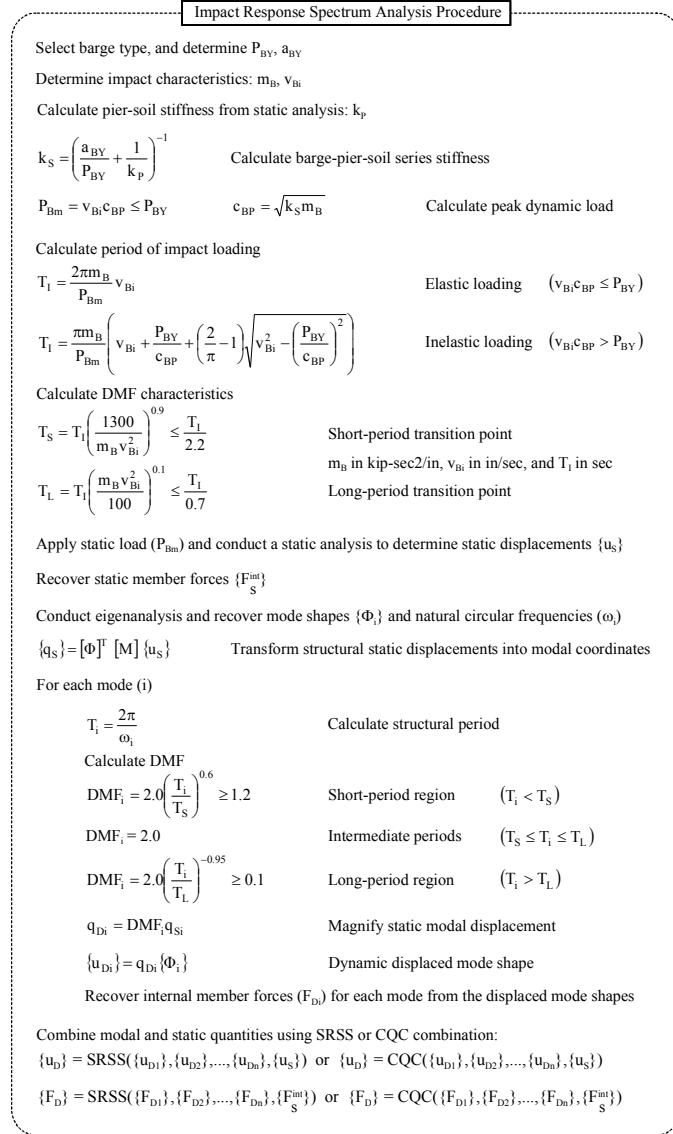


Figure 2.9 Impact response spectrum analysis (IRSA) (Consolazio et al. 2008)

While IRSA constitutes a significant advancement in simplified vessel impact analysis, key limitations have been identified which must be resolved before implementing the method in a design setting. Most importantly, it is unclear how to best determine the minimum number of vibration modes that should be considered. For seismic response spectrum analysis, the minimum number of modes is determined based on modal mass participation. Design codes for buildings (e.g., FEMA 2003, ASCE 7-10) and bridges (AASHTO 2011) require that a sufficient number of modes be included to achieve 90% modal mass participation. However, it has been

shown that IRSA method for vessel impact commonly underestimates structural demands at the 90% modal mass participation level (Consolazio et al. 2008). In many cases, more than 99% participation is necessary to achieve conservative results from IRSA when using eigenvectors. Further investigation into this issue, e.g. the possible use of Ritz vectors rather than eigenvectors, is necessary before IRSA can be safely suggested for bridge design.

Given the computational and data processing demands associated with dynamic analysis procedures such as CVIA, AVIL, and IRSA, a simpler static analysis method is desirable. However, it has been demonstrated that static impact analysis conducted in accordance with AASHTO (2009) consistently underestimates pier member structural demands (Consolazio et al. 2008) because dynamic amplification caused by superstructure inertia is neglected (Davidson et al. 2010). Consequently, an equivalent-static analysis procedure—called static bracketed impact analysis (SBIA)—was developed that empirically accounts for superstructure inertial effects (Getter et al. 2011).

As summarized in Fig. 2.10, SBIA consists of a series of static structural analyses in which all forces applied to the bridge pier are dependent upon the peak dynamic barge impact force (P_B). As with IRSA, P_B is computed in accordance with the AVIL procedure combined with the Getter-Consolazio (2011) barge force-deformation model. The SBIA method consists of two basic load cases. For Load Case 1, an amplified impact load ($1.45 \times P_B$) is applied at the expected impact location. Additionally, a load is applied at the superstructure elevation, which is calibrated to approximate the effect of superstructure inertial restraint that occurs immediately after impact. This pier-top force is equal to P_B times an inertial restraint factor (IRF). To minimize conservatism, IRF values are calibrated to estimate specific structural demand types: pier member moments (IRF_m); pier member shear forces (IRF_v); and bearing connection shear forces (IRF_b) at the substructure-superstructure interface. Load Case 2 simply consists of applying an amplified impact force ($1.85 \times P_B$) at the impact location. Maximum structural demands obtained between the two load cases are used for design.

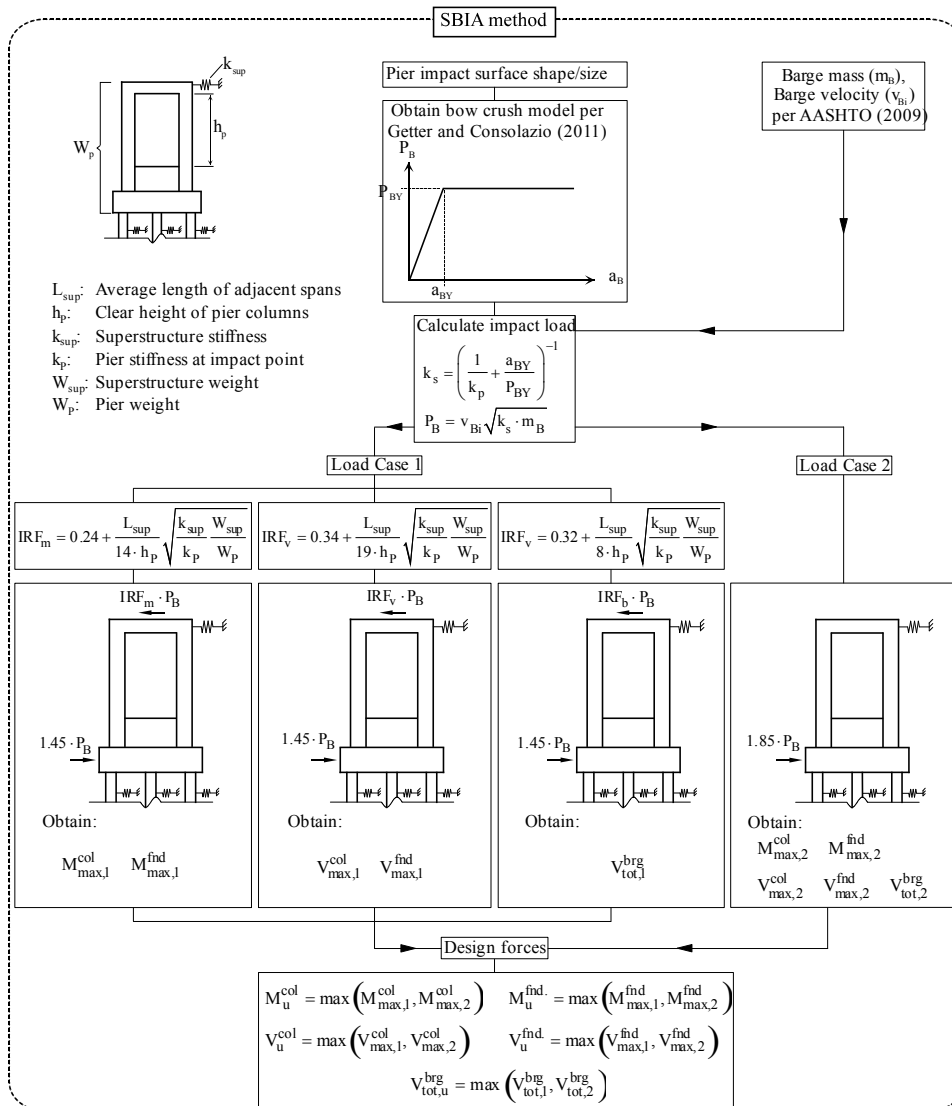


Figure 2.10 Static bracketed impact analysis (SBIA) (Getter et al. 2011)

2.3.6 Revised probability of collapse (PC) expression

Much of the UF/FDOT research summarized in previous sections was focused on accurately quantifying loads associated with barge impact and characterizing dynamic bridge response to impact. However, a critical step in vessel impact risk analysis is estimating the probability of catastrophic structural failure during an impact event. According to AASHTO (2009), the probability of collapse (PC) of a particular bridge element (e.g., a pier) is computed as (recall Fig. 2.2):

$$PC = \begin{cases} 0.1 + 9(0.1 - H/P) & 0.0 \leq H/P < 0.1 \\ 1 - H/P & 0.1 \leq H/P < 1.0 \\ 0 & H/P > 1.0 \end{cases} \quad (2.8)$$

where H/P (for a bridge pier) is the ratio of the static pushover capacity (H) to the maximum vessel impact force (P). Based on this expression, if the vessel impact force is *equal* to the capacity of the structure, then the probability of collapse is 0 (no chance of collapse). Furthermore, if $H/P = 0.1$ —i.e., the impact force is *10 times larger* than the bridge capacity— PC is only 0.1 (10%). Based on these observations, it is clear that the basis for the AASHTO PC expression warrants additional consideration. Scarce ship-to-bridge collision data were available at the time of the development of the AASHTO PC expression (prior to 1991). In fact, the AASHTO PC expression is based upon a historical analysis of ship-to-ship collisions, rather than ship-to-bridge (or, even more desirably, barge-to-bridge) collisions. A detailed discussion of the origins of the AASHTO PC expression can be found in Consolazio et al. (2010a).

Due to the clear limitations of the AASHTO PC expression, UF/FDOT researchers developed an updated PC expression based on rigorous reliability analysis of bridges subjected to barge impact (Consolazio et al. 2010a, Davidson et al. 2013). The probability of bridge collapse was directly quantified using well-established probabilistic analysis procedures (Monte Carlo simulation) paired with advanced sampling and sub-sampling methods. Bridge models were subjected to thousands of simulated barge impact events using dynamic impact analysis (CVIA) while accounting for important sources of statistical variability in impact loading and structural resistance. This approach was employed to quantify the probability of structural collapse (PC) for ten (10) different bridges of widely different structural characteristics. Each PC estimate was paired with the mean demand-to-capacity (D/C) ratio observed for each bridge. A detailed definition of D/C is provided in Davidson et al. (2013). As illustrated in Fig. 2.11, an exponential curve was fit to the data, and a 95% confidence upper bound envelope was established, resulting in a conservative PC - D/C expression that is suitable for use in bridge design:

$$PC = 2.33 \times 10^{-6} \cdot e^{13 \cdot D/C} \leq 1.0 \quad (2.9)$$

Consequently, a design engineer can conduct a single deterministic impact analysis—using the UF/FDOT methods described above (CVIA, AVIL, etc.)—to quantify the D/C ratio, and estimate the probability of collapse using the revised PC expression.

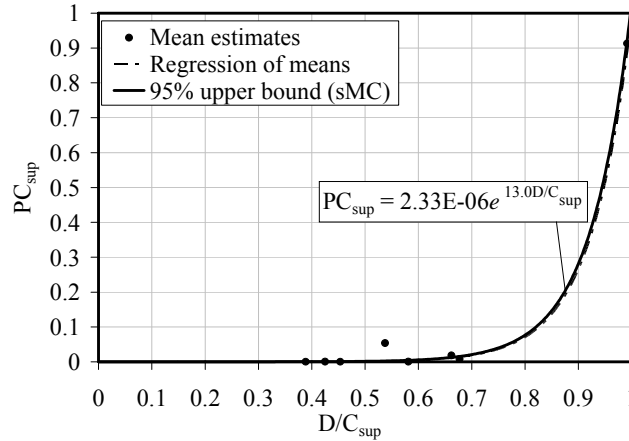


Figure 2.11 Revised probability of collapse expression (Consolazio et al. 2010a)

2.4 Observations

As summarized above, research conducted by UF and FDOT has resulted in the development of a more accurate barge impact load-prediction model, various structural analysis techniques that account for important dynamic structural response characteristics (CVIA, AVIL, IRSA, and SBIA), and a probability of collapse (PC) expression that properly accounts for barge impact and structural response uncertainties. These methods constitute significant advancements relative to the methods currently prescribed by AASHTO for bridge design for vessel collision. However, as noted in Chapter 1, the UF/FDOT barge impact load model is based primarily on high-resolution finite element simulations that have only been validated against experimental measurements at relatively moderate barge deformation levels. Therefore, additional experimental research is required to validate the UF/FDOT barge impact load model at higher barge deformation levels that are more consistent with impact severities commonly considered in bridge design. Furthermore, the UF/FDOT structural analysis techniques and PC expression have not yet been incorporated into a cohesive bridge design methodology. Therefore, while the individual UF/FDOT methods can be considered more accurate than those in the AASHTO provisions, the influence that the revised methods may have on design efficiency and economy is unknown. Consequently, the current study has been carried out to address methodology integration issues and thereby facilitate adoption of the UF/FDOT procedures in bridge design practice.

CHAPTER 3

EXPERIMENTAL VALIDATION PLAN FOR UF/FDOT BARGE IMPACT LOAD-PREDICTION MODEL

3.1 Introduction

As discussed in Chapter 2, past experimental validation of the UF/FDOT barge impact load-prediction model (Getter and Consolazio 2011) has been limited. In developing the originally conceived UF/FDOT load-prediction model (Consolazio et al. 2009) the authors compared finite element simulation results—the basis for the load-prediction model—to force and deformation measurements taken during the full-scale barge impact experiments at St. George Island (Consolazio et al. 2006). Reasonable agreement was observed between the numerical and experimental results. However, due to safety and environmental concerns, the barge impact experiments were only able to achieve barge deformations of approximately 16 in. Thus, the UF/FDOT load-prediction model has only been experimentally validated at relatively small deformations, while typical design impact conditions commonly correspond to barge bow deformations on the order of several feet. Consequently, a primary goal of the current study was to experimentally validate the UF/FDOT load-prediction model—and the finite element simulation techniques used to develop it—for higher level barge bow deformations.

3.2 Validation Objectives

Because the UF/FDOT load-prediction model was developed based on high-resolution finite element analyses, the primary goal of the experimental program is to validate that the finite element simulation techniques employed in prior research are theoretically and physically sound. This objective necessitates performing experiments that involve dynamic impact between a barge bow and nearly-rigid object, including large-scale, high-rate barge bow deformations (up to and including material failure). Impact force histories, dynamic motions of the various components, and barge bow deformations were measured as part of these experiments. Identical impact scenarios were simulated using the same type of finite element models, the same finite element code (LS-DYNA), and the same simulation techniques that were used to develop the UF/FDOT barge impact load-prediction model. Correspondence between the experimental measurements and finite element simulation results demonstrated that previously employed simulation tools adequately describe realistic barge impact behavior.

Recall that the UF/FDOT barge impact load model differs from the model currently employed in the AASHTO (2009) provisions in four primary ways. In the UF/FDOT model:

1. Barge impact forces are strongly dependent on the size of the impacted pier surface, in that larger pier surfaces result in larger forces than smaller pier surfaces (Consolazio et al. 2009);
2. Barge impact forces are strongly dependent on the shape of the impacted pier surface, in that flat-faced surfaces result in larger forces than similarly sized rounded surfaces (Consolazio et al. 2009);

3. Barge bow force-deformation behavior can be conservatively idealized as elastic-perfectly plastic (Consolazio et al. 2009, Getter and Consolazio 2011);
4. Barge impact forces are strongly dependent on the angle between the barge bow and pier surface for flat-faced piers (Getter and Consolazio 2011).

Consequently, the secondary objective of the experimental program is to validate as many of these previous research findings as possible within the time and budget constraints of the study. Given the material costs and labor effort associated with fabricating barge bow specimens, the program was limited to two series of impact experiments. One included impact with a rounded object (similar to impact with a rounded pier surface such as a circular pier column), and one included impact with a flat-faced object (similar to a rectangular pier column). Both objects had the same width. These two experimental series directly illustrated finding number 2 above, that flat-faced surfaces generate larger forces than equivalently sized rounded surfaces. Impact forces and dynamic barge bow deformations measured during the experiments were also used to form force-deformation curves. These curves validated finding number 3 listed above. It should be noted that the other two findings were implicitly validated by demonstrating that the finite element simulation techniques that were employed in this study (and in Consolazio et al. 2009 and Getter and Consolazio 2011) are generally sound.

3.3 Overview of Experimental Program

The barge bow impact experiments consisted of impacting reduced-scale replicas of a typical barge bow with a nearly-rigid object (impact block) that was swung from a large pendulum. The FDOT pendulum impact facility at the M.H. Ansley Structures Research Center, Tallahassee, Florida (Fig. 3.1) was used to conduct the impact experiments. The pendulum consists of three 50-ft-tall towers placed in a triangular pattern. The impacting object is suspended from two of the towers via four cables and lifted from the third tower to develop the desired energy potential. To initiate impact, a servo-actuated hook releases the lifting cable and the impact block begins swinging. The impacted specimen—a scale-model barge bow, in this case—is placed at the bottom of the pendulum swing to maximize the kinetic energy of the impact block. The FDOT impact pendulum is designed to accommodate (at maximum) a 9,000-lbf impact block swung from a maximum drop height of 35 ft. Thus, the maximum kinetic energy that the impact block can attain is 315 kip-ft.



Figure 3.1 Impact pendulum at M.H. Ansley Structures Research Center in Tallahassee, FL

For the barge impact experiments, a scale model barge bow was mounted to a reinforced concrete foundation via two steel reaction frames (Fig. 3.2). A steel support frame connected the impact block to four cables that are, in turn, connected to the pendulum towers. The support frame provided widely spaced cable connection points which improved the stability of the impact block before and during each pendulum swing.

Alternative testing scenarios were explored as part of preliminary planning for the impact experiments. One scenario that was considered involved swinging the barge specimen from the pendulum into a stationary object attached to the foundation, which would have been most similar to a barge impacting a stationary bridge pier. However, it was determined that the uneven mass distribution of the bow specimen and lack of adequate cable connection locations (to the bow model) made this scenario impractical. Furthermore, finite element simulations of both scenarios (swinging barge bow and stationary barge bow) indicated that impact forces were effectively identical between the two scenarios. The most important reason for not choosing to swing the barge bow from the pendulum, however, was the quality of the impact force data. The impact force (F) was computed by measuring (using accelerometers) the deceleration (a) of the pendulum mass (m) during impact, and then relying on the relation $F = m \times a$ (further discussed in Chapter 6). For this relation to be valid, the object to which the accelerometers are attached (i.e., the pendulum mass) must be effectively rigid. Because the barge bow was highly deformable, it was infeasible to obtain high-quality impact acceleration (and therefore force) data in this manner, using the barge bow as the pendulum mass. Given these various considerations, it was determined that the most effective testing scenario involved swinging an effectively rigid impact block from the pendulum to impact a stationary barge bow specimen, as shown in Fig. 3.2.

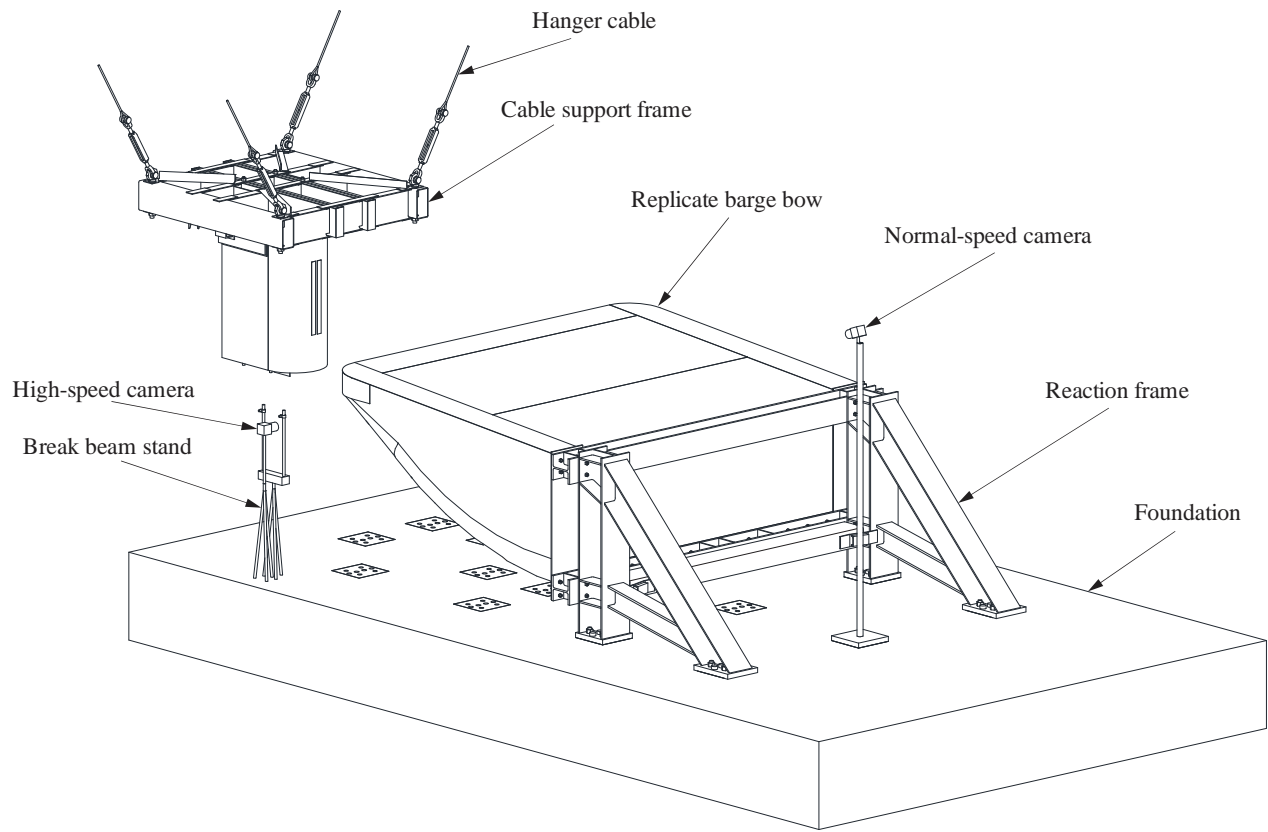


Figure 3.2 Test setup for barge bow impact experiments

3.3.1 Determination of barge bow model scale

Two reduced-scale specimens of the front portion (bow) of a typical jumbo hopper barge were fabricated from commercially available steel materials. One of the primary concerns in developing a reduced-scale bow model was choosing an appropriate model scale factor (β). Consequently, similitude expressions were derived that relate full-scale parameters to their corresponding model-scale values. The Buckingham π theorem (Jones 1997) was employed to derive the following similitude relations for the experimental program:

$$\Delta_{fs} = \beta \Delta_m; \quad P_{fs} = \beta^2 P_m; \quad E_{fs} = \beta^3 E_m \quad (3.1)$$

where Δ is displacement, P is force, and E is energy. Full-scale quantities are denoted with the subscript “ fs ” and model-scale quantities are denoted with “ m .” Note that β is the ratio of the full-scale size to model-scale size: i.e., $\beta = 4$ for a $1/4$ -scale model ($1:\beta$ scale). The full derivation of the above expressions is provided in Appendix B.

A primary objective of the impact experiments was to attain approximately 10 ft (at full scale) of bow deformation subject to design constraints of the FDOT impact pendulum (maximum energy of 315 kip-ft). Based on previously conducted simulation data (Consolazio et al. 2009), approximately 17,300 kip-ft of impact energy is required to achieve 10 ft of deformation at full scale (assuming perfectly inelastic collision). Using the energy similitude expression above and solving for β indicates that a 1:4 scale model ($\beta = 4$) would have been ideal for pendulum impact testing. However, many barge components, particularly steel angles and channels, are not commercially available at 1:4 scale. Consequently, milling of thicker stock members would have been required in order to attain the correct thicknesses; such fabrication was feasible, but cost prohibitive.

Therefore, a larger model scale of $\beta = 2.5$ (40%-scale) was selected. At this scale, internal steel angles and other components are commercially available with the correct thickness, which greatly reduced fabrication costs. The consequence of increasing the model scale was that the desired deformation could not be achieved with a single swing of the impact pendulum. Thus, individual bow specimens were subjected to *multiple* impacts in order to attain accumulated deformation equal to approximately 10 ft at full scale. At the model scale of $\beta = 2.5$, the jumbo hopper barge bow specimen measured approximately 14 ft wide by 11 ft long and 5 ft tall (Fig. 3.3). Additional details pertaining to the barge bow specimens are provided in Chapter 6.

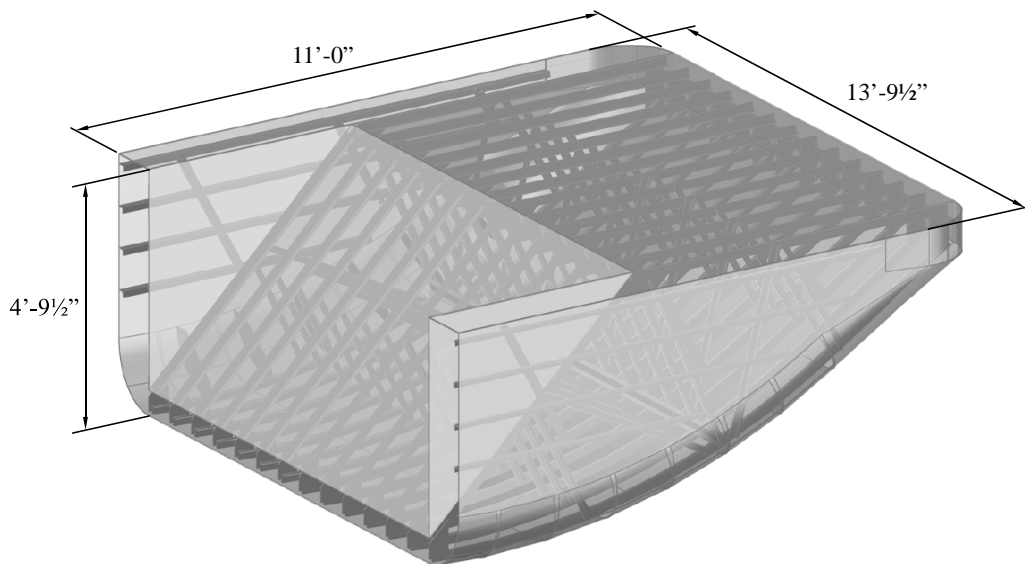


Figure 3.3 Rendering of reduced-scale barge bow specimen showing internal truss structure

3.3.2 Material testing program

Due to the large deformation rates anticipated, strain-rate sensitivity of the steel barge components was expected to be a significant contributor to the impact forces that were measured during the impact experiments, and thus, strain rate-sensitive constitutive models were developed for implementation in the FE model of the impact experiments. In the United States, barges are

typically constructed from ASTM A36 structural steel. Therefore, in prior studies (Consolazio et al. 2009, Getter and Consolazio 2011), a viscoplastic constitutive model for A36 was employed in the FE barge model, in which a representative stress-strain relation was adopted from the literature (Salmon and Johnson 1996). The Cowper-Symonds model was used to describe rate-sensitivity with parameters $C = 40.4 \text{ s}^{-1}$ and $P = 5$, as is common in practice (Jones 1997). However, it is recognized that these parameters vary widely among different studies of mild steel (Jones 1997, 2013, Hsu and Jones 2004, Jones and Jones 2002).

Furthermore, reduced-scale (40%) thicknesses of some barge components (mostly hull plates) were too thin to be addressed by the A36 specification (ASTM 2008). Therefore, ASTM A1011 hot-rolled carbon sheet steel (ASTM 2012a) was selected as the closest alternative to A36 that is available in the required thicknesses. The A1011 specification includes numerous material grades, of which, the most commonly available are CS (commercial steel) and DS (drawing steel). The specific grade that was used in the reduced-scale barge model was A1011 CS Type B. ASTM does not specify material properties for this grade.

To effectively carry out the FE model validation, it was necessary to characterize the materials out of which the reduced-scale barge bows were constructed, particularly given the uncertainty associated with the rate-sensitive material parameters and the fact that ASTM does not specify mechanical properties for A1011 steel. Therefore, uniaxial tension tests were conducted over a wide range of strain rates ($7 \times 10^{-5} - 500 \text{ s}^{-1}$) on A36 plate and A1011 sheet specimens. Chapter 4 documents the material testing program, including development of rate-sensitive constitutive models (implemented in LS-DYNA) for the materials that were evaluated.

3.4 Validation Simulations

Given that the purpose of the experimental program was to validate finite element modeling and simulation techniques that are the basis for the UF/FDOT barge impact load-prediction model (Getter and Consolazio 2011), a necessary component of the experimental program was to develop finite element simulations of each impact experiment. Behavioral trends obtained from these simulations were directly compared to the trends observed during the experiments. Demonstrating clear behavioral correspondence between the experiments and simulations will promote confidence in the UF/FDOT load model and facilitate its adoption as an AASHTO code procedure.

A finite element representation (Fig. 3.4) of the pendulum impact test setup—including reduced-scale barge bow, pendulum impact block, and reaction frame—was developed in LS-DYNA. The barge bow portion of the model is a 0.4-scale version of the same model that was used in the development of the UF/FDOT load-prediction model. As shown in Fig. 3.5, the finite element mesh of the reduced-scale barge bow consists of more than 120,000 nonlinear quadrilateral shell elements, in which each element is approximately 1.5 in. square or smaller. The barge bow zone is composed of fourteen (14) internal rake trusses and frames, transverse bracing members, and several external hull plates of varying thicknesses (see Chapter 6 for additional structural details).

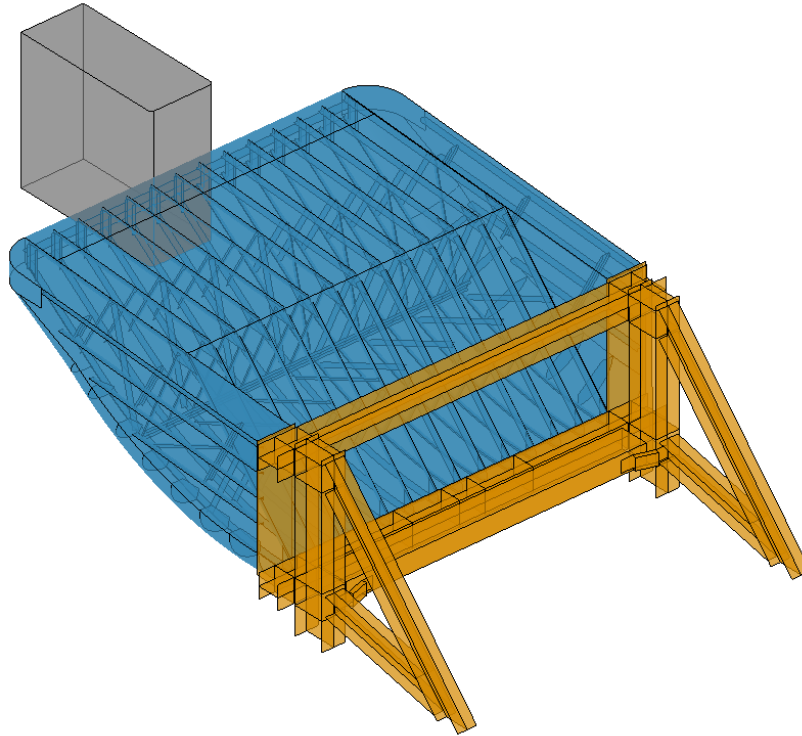
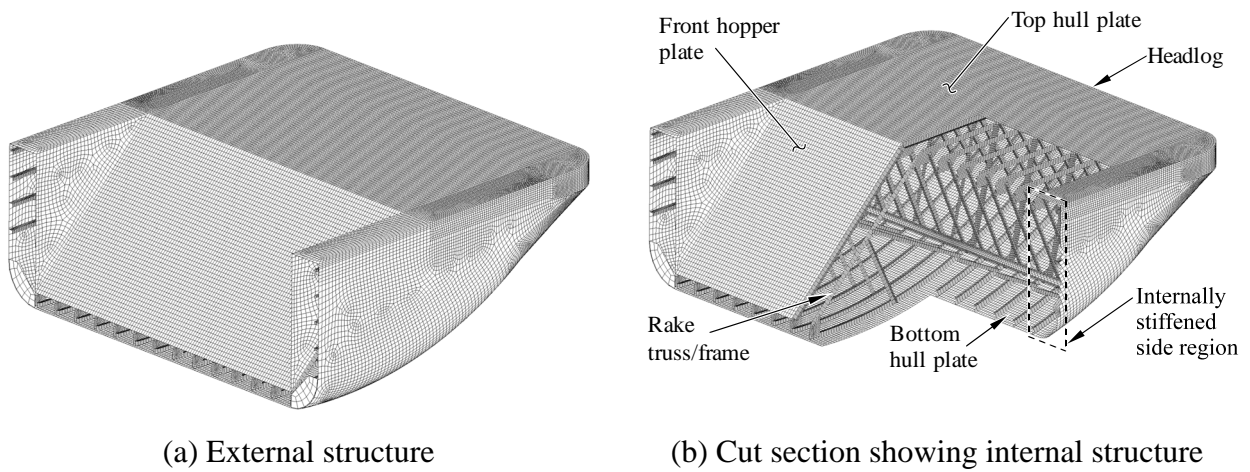


Figure 3.4 Rendering of barge bow finite element model with flat-faced pendulum impact block and reaction frame (mesh not shown for clarity)



(a) External structure

(b) Cut section showing internal structure

Figure 3.5 Barge bow finite element model showing mesh density

Quadrilateral 4-node, fully integrated shell elements were used to allow hull plate, gusset plate, and structural member (angles and channels) buckling to occur as appropriate throughout the barge. Additionally, the use of shell elements to model internal structural members of the barge permitted these components to undergo local material failure (discussed in detail in Chapter 4), which in LS-DYNA, results in element deletion. Angle and channel structural shapes were modeled with a sufficient number of elements so that reverse curvature can develop in the

event of local member buckling. In full-scale barge construction, steel components such as plates, angles, and channels are joined together by welds. In the FE model, localized welds (spot welds) were modeled by rigid beams that connect two nodes (from different structural members) together. Connection failure was accounted for through element deletion upon failure of the joined shell elements. Spot welds were introduced at a sufficient density to emulate welds present in the physical barge. Given these features, the barge bow FE model is capable of accurately simulating the response to dynamic impact events, including large-scale deformation and material failure. LS-DYNA also includes features which permit multiple successive impacts to be simulated by accurately accounting for residual stresses and accumulated material damage. Preliminary simulations of the experimental impact conditions are discussed in Chapter 5.

CHAPTER 4

STRAIN RATE-SENSITIVE CONSTITUTIVE RELATIONS FOR EXPERIMENTAL VALIDATION

4.1 Introduction

Given the deformation rates involved in preliminary FE analyses, strain-rate sensitivity of the steel barge components was anticipated to be a significant contributor to the impact forces that were measured, and thus, strain rate-sensitive constitutive models needed to be developed for implementation in the FE model that was validated. In the United States, barges are typically constructed from ASTM A36 structural steel. Therefore, in prior studies (Consolazio et al. 2009, 2010a, 2010b, 2012a, Consolazio and Walters 2012b, Getter and Consolazio 2011), a viscoplastic constitutive model for A36 was employed in the FE barge model, in which a representative stress-strain relation was adopted from the literature (Salmon and Johnson 1996). The Cowper-Symonds model was used to describe rate-sensitivity with parameters $C = 40.4 \text{ s}^{-1}$ and $P = 5$, as is common in practice (Jones 1997). However, it is recognized that these parameters vary widely among different studies on mild steel (Jones 1997, 2013, Hsu and Jones 2004, Jones and Jones 2002).

Thus, in preparation for the FE validation study, uniaxial tension tests were conducted over a wide range of strain rates ($7 \times 10^{-5} - 500 \text{ s}^{-1}$) on A36 plate specimens. Because reduced-scale thicknesses of some barge components (mostly hull plates) are too thin to be addressed by the A36 specification, these parts were constructed from ASTM A1011 hot-rolled sheet steel, the most similar alternative to A36. Therefore, A1011 sheet specimens were included in the material testing program as well. The remainder of this chapter documents the material testing program, including development of rate-sensitive constitutive models (implemented in LS-DYNA) for the materials that were evaluated. A novel testing apparatus was designed for this study that employed a large-scale impact pendulum to break specimens at high strain rates. Design features of the testing apparatus and associated data processing procedures are discussed in this chapter.

4.2 Materials and Methods

Experimental methods used to characterize the materials of interest are discussed in this section. Uniaxial tension tests were carried out in two series: (1) quasi-static tests utilizing conventional laboratory equipment and standardized procedures; and (2) high-strain rate tests utilizing a new pendulum-based high-rate testing apparatus (HRTA) designed specifically for this study. The design features and functionality of the HRTA are discussed in detail below.

4.2.1 A1011 and A36 steel

Materials evaluated in this study included ASTM A1011 (ASTM 2012a) hot-rolled carbon steel sheet and ASTM A36 (ASTM 2008) carbon steel plate. The A1011 specification includes numerous material grades, of which, the most commonly available are CS (commercial steel) and DS (drawing steel). The specific grade evaluated in this study was A1011 CS Type B. For this grade, no limits on the mechanical properties are specified by ASTM; however, yield

strength in the range of 30 – 50 ksi and elongation at failure exceeding 25% is generally expected (ASTM 2012a). Two thicknesses of A1011 steel were tested: 11 ga. (0.115 in.) and 9 ga. (0.155 in.). In contrast to A1011, where mechanical property limits are not specified, the ASTM A36 specification requires yield strength to exceed 36 ksi, ultimate strength to be between 58 – 80 ksi, and elongation to exceed 21% in a 2 in. gage length (ASTM 2008). A single thickness of A36 steel was tested: 0.25 in. Multiple test specimens of matching grade and thickness were cut from a single sheet or plate, which eliminated batch-to-batch variability in mechanical properties as a parameter considered in this study. The surface finish provided from the mill (including mill scale) was retained where possible.

4.2.2 Uniaxial tension testing (quasi-static)

Quasi-static uniaxial tension tests were performed in accordance with ASTM A370 (ASTM 2012b) using sub-sized flat specimens (as defined by ASTM) (Fig. 4.1a) and an Instron 3384 electromechanical testing system (Fig. 4.1b). Specimens were clamped in wedge action tension grips, and pulled to failure at a constant crosshead velocity. Specimen resistance was measured by a 33.75 kip load cell, and elongation was measured by an Instron 2360-114 clip-on extensometer with specimen clips modified to reduce the gage length from the stock length of 2 in. to a modified length of 1 in. Per manufacturer recommendations, the extensometer was removed prior to specimen failure to avoid damaging the instrument. Specifically, tests were paused to allow removal of the extensometer when the measured strain reached 0.15 in./in., after which tests were resumed until specimen failure (Section 4.3.1 provides details on how strain was measured beyond 0.15 in./in.). Data acquisition and test system control were performed using the ‘Partner’ software package provided by Instron.

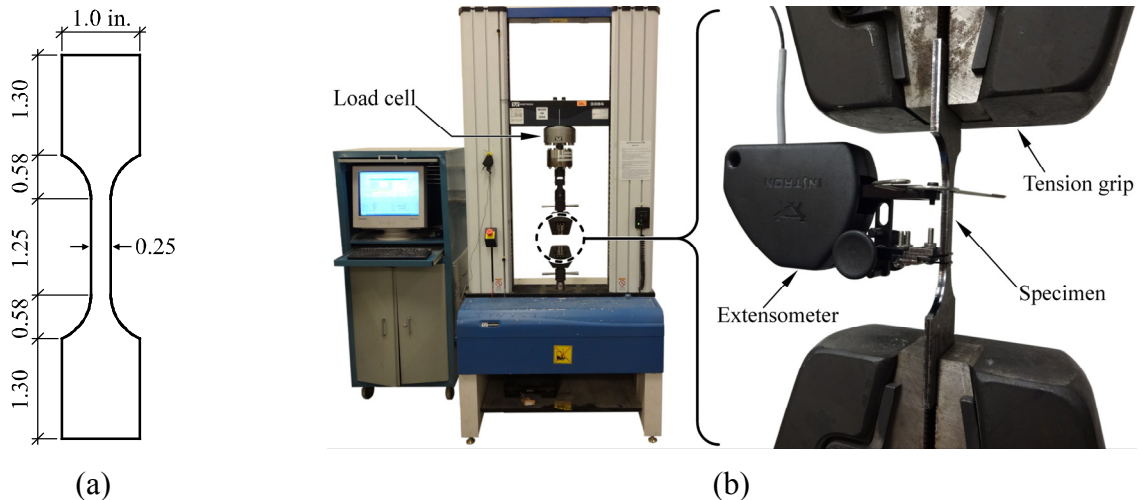


Figure 4.1 a) Specimen dimensions, and b) test setup and instrumentation for quasi-static tests

4.2.3 Uniaxial tension testing (high-strain rate)

Uniaxial tension tests at high strain rates ($1 - 500 \text{ s}^{-1}$) were conducted using a testing apparatus that employs an impact pendulum as the means of rapidly imparting energy. The

impact pendulum was designed by researchers at the University of Florida (UF) for the Florida Department of Transportation (FDOT) Structures Research Center located in Tallahassee, Florida (Consolazio et al. 2012c). As shown in Fig. 4.2a, the pendulum consists of three 50 ft tall towers. A pendulum mass (hereafter referred to as the impact block) is supported by four steel cables between two of the towers, and is lifted to the intended drop height by a cable, pulley, and winch system attached to the third tower. The pendulum is capable of dropping a 9,000 lb impact block from a maximum height of 35 ft. However, a 2,200 lb impact block was used for this study (Fig. 4.2b), with drop heights ranging from 1 – 25 ft to achieve different strain rates. The impact block consisted of a reinforced concrete core, surrounded on four sides by steel plates. A nearly-rigid nose assembly, built up from 0.5 – 1.0 in. thick steel plates, was attached to the impacting side of the block. Additional details pertaining to the pendulum facility and impact block can be found in Consolazio et al. (2012c).



a) Pendulum towers



b) Impact block

Figure 4.2 Impact pendulum facility at Florida Department of Transportation (FDOT) Structures Research Center in Tallahassee, Florida

4.2.3.1 Pendulum-based high-rate test apparatus (HRTA)

A novel testing apparatus was designed and employed in this study to perform uniaxial tension tests at high strain rates. The high-rate testing apparatus (HRTA) is similar in principle to commercially available testing devices, such as instrumented falling weight impact (IFWI) machines, that employ impact energy to initiate specimen extension. However, given the large scale of the pendulum facility, the design philosophy of the HRTA was different than that of IFWI devices previously employed in tensile testing (Shin et al. 2000, Thompson 2006, Bardelcik et al. 2012).

Fig. 4.3a presents a simplified depiction of the impact that occurs during an IFWI tension test. A relatively large striker mass, m_1 , is given an initial velocity $v_{1,0}$ by dropping it from a specified height. Mass m_1 strikes a lightweight anvil, m_2 , that is fixed to the specimen, ideally

resulting in a perfectly inelastic impact. Note that the impact is only inelastic because specimen resistance maintains contact between the striker and anvil. As might be expected, if the two surfaces are stiff, significant high-frequency ringing can occur, resulting in a highly oscillatory specimen response. Recent studies (Thompson 2006, Bardelcik 2012) employed RTV silicone damping pads between the striker and anvil to reduce ringing. However, damping the impact results in delayed anvil and specimen response, and thus a non-uniform strain rate through the test. Therefore, damping pad thickness must be carefully selected to balance the competing objectives of rapid anvil acceleration and minimal ringing vibration.

The HRTA designed in this study attempted to avoid these issues by employing an elastic impact instead. As illustrated in Fig. 4.3b, m_1 corresponds to the 2,200 lb pendulum impact block, which can attain a maximum velocity of 48 ft/s from a drop height of 35 ft. This magnitude of impact energy greatly exceeds what is typically possible in a laboratory setting. Consequently, m_2 in the HRTA can be considerably more massive than is possible in IFWI tension tests. In this study, $m_2 = 130$ lb. Given a perfectly elastic impact (and $m_1 \gg m_2$), the post-impact velocity of m_2 can approach two times the pre-impact velocity of m_1 . Thus, if the pendulum is dropped from the maximum height of 35 ft, then after impact, the velocity of m_2 is $v_{2,f} \approx 96$ ft/s. Even at lower drop heights, m_2 possesses sufficient momentum to break an ASTM-sized steel specimen without slowing appreciably. As a result, specimen extension is achieved through a single, nearly instantaneous impact, completely avoiding the ringing issue discussed above. Furthermore, the moving specimen end accelerates to the desired extension rate extremely rapidly.

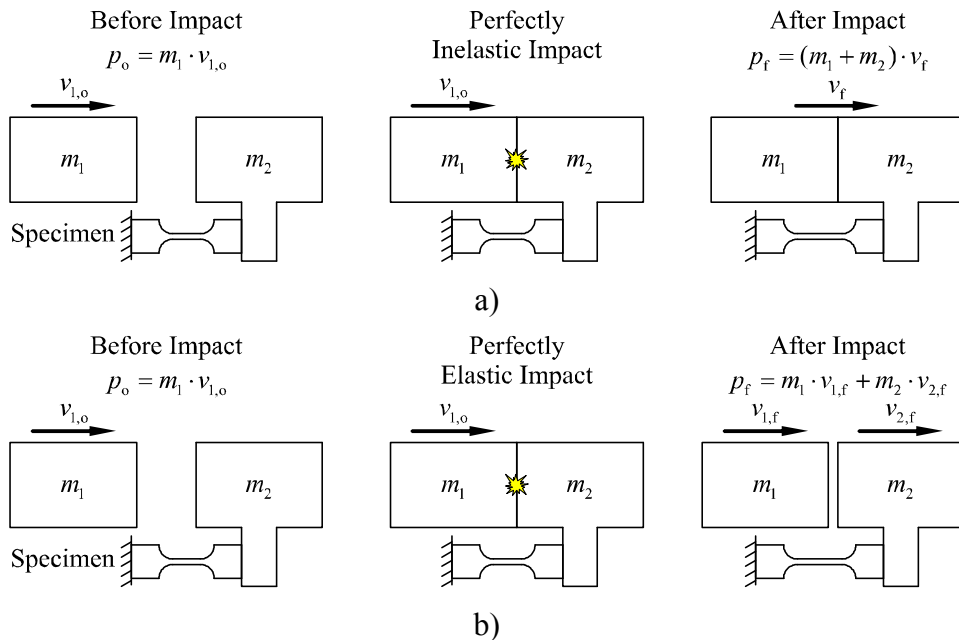


Figure 4.3 Depictions of a) perfectly inelastic and b) perfectly elastic impact scenarios in tension testing that rely on impact energy for specimen elongation

As shown in Fig. 4.4, the HRTA consisted of two main assemblies: 1) a rotating control arm with impact head (to be struck by the pendulum impact block), and 2) a main drive line consisting of a 1 in. diameter threaded rod with mass plates attached to the end (discussed below). Rocker plates supported the mass plates, allowing for unimpeded small displacements along the drive line axis. Test specimens were mounted between these two assemblies (Fig. 4.4b,d), anchored to the drive line and elongated by rotation of the control arm. To expand the range of strain rates that could be achieved, the HRTA can be assembled in two configurations: horizontal (Fig. 4.4a-b) for lower strain rates, and angled (Fig. 4.4c-d) for higher strain rates. Fine adjustments to the testing rate were achieved by varying the pendulum drop height.

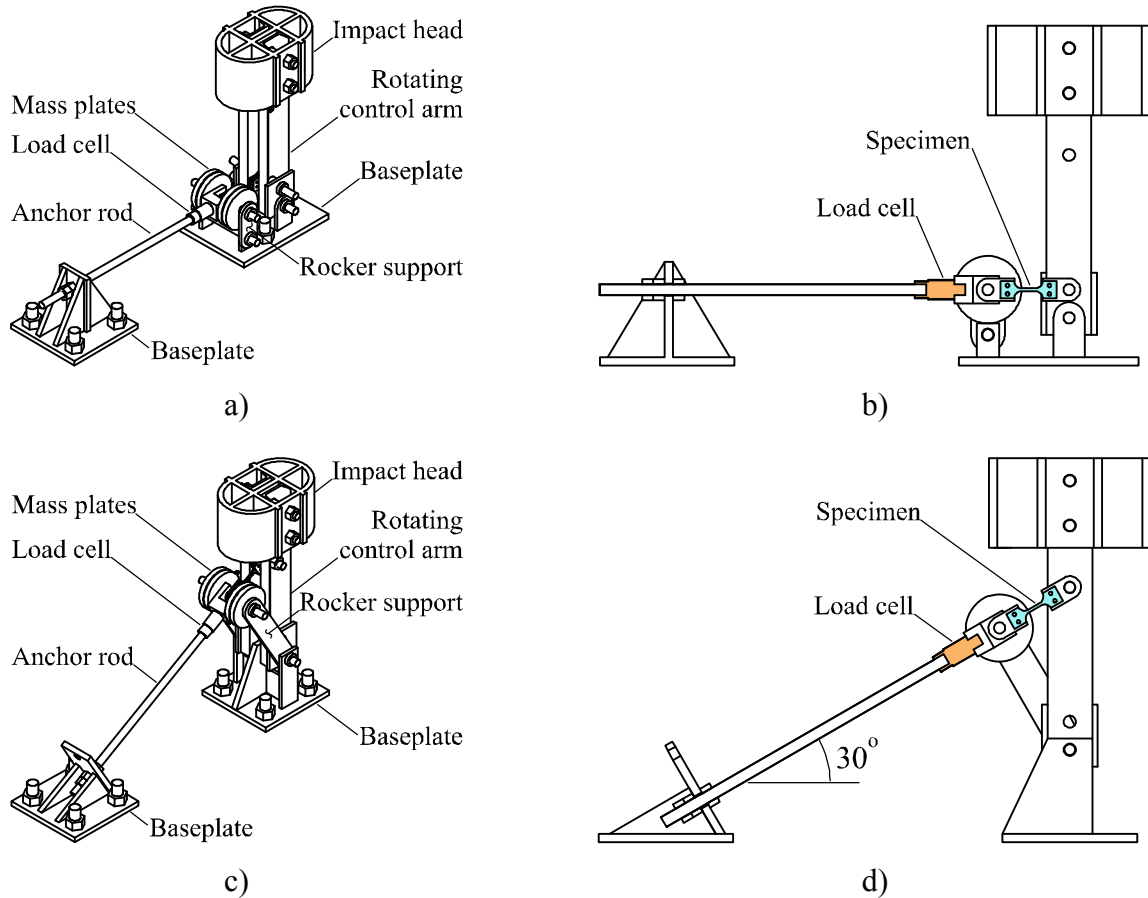


Figure 4.4 High-rate testing apparatus (HRTA): a) horizontal configuration schematic and b) section view, and c) angled configuration schematic and d) section view

To test a specimen at high rate, the impact block was released from the desired drop height, allowing it to swing down and strike the impact head of the HRTA (Fig. 4.5a-b). Because both the impact block and the HRTA impact head were constructed from thick steel plates, the impact event was elastic and nearly instantaneous. Post-impact momentum of the impact head caused the control arm to rotate, and this motion elongated and broke the specimen (Fig. 4.5c-d). The impact head mass was chosen to carry sufficient momentum that specimen resistance did not

appreciably slow rotation of the control arm. As a result, a nearly constant specimen elongation rate was achieved. After the control arm rotated approximately 90°, device momentum was arrested by sand bags.

The HRTA drive line was designed to act as a single-degree-of-freedom (SDF) oscillating system. By specifically tuning mass (provided by mass plates) and stiffness (provided by threaded anchor rod), drive line oscillation was dominated by the natural frequency of the SDF system. This design thereby minimized the influence of high-frequency vibrations that would result from anchoring the specimen to a more rigid reaction point. Furthermore, analyses conducted during the HRTA design stage indicated that if the drive line was permitted to undergo multiple oscillations during the specimen extension event, significantly non-uniform strain rates could result. Therefore, drive line mass and stiffness were selected such that the natural period was similar to or longer than typical test durations. Detailed fabrication drawings for the HRTA are provided in Appendix C.

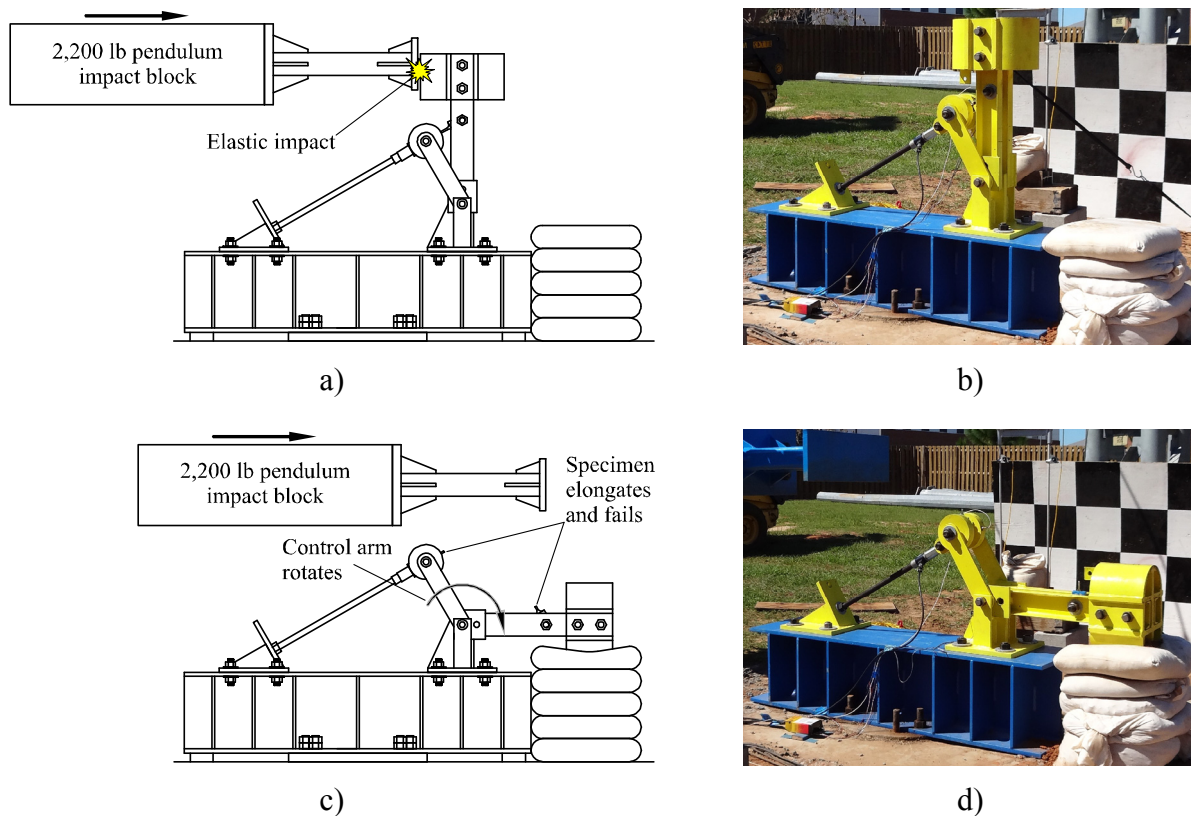


Figure 4.5 High-rate material testing apparatus (HRTA) before pendulum impact a) schematic and b) photograph, and after impact c) schematic and d) photograph

4.2.3.2 Instrumentation

As shown in Fig. 4.6a, specimens employed in the high-rate program had the same basic dimensions as the low-rate program to avoid introducing scaling discrepancies. Given the strain

rates that occurred in the high-rate test program, digital image correlation was used to quantify engineering strain in the specimen. Square 0.0625 in. gage marks were drawn on each specimen with a permanent marker, approximately 1 in. apart. The reduced gage specimen region was filmed at 50,000 frames per second with an IDT Redlake MotionXtra N3 high speed camera (Fig. 4.6b), and Xcitex ProAnalyst software was used to quantify gage mark displacements in two dimensions (in the plane of the pendulum swing motion). To improve contrast between the gage marks and specimen, the specimen surface was blasted with fine-grit sand.

Reaction force in the drive line was measured with an Interface REC-15K rod-end load cell, and acceleration of the mass plates at the end of the drive line was measured with a PCB Piezotronics 352A60 piezoelectric accelerometer (500g). Data from these sensors were acquired at a sampling rate of 50 kHz using a National Instruments cDAQ-9178 acquisition system. Balluff BLS 18KF-XX-1P-S4L infrared break beam sensors triggered the data acquisition and high speed camera to begin recording immediately prior to impact.

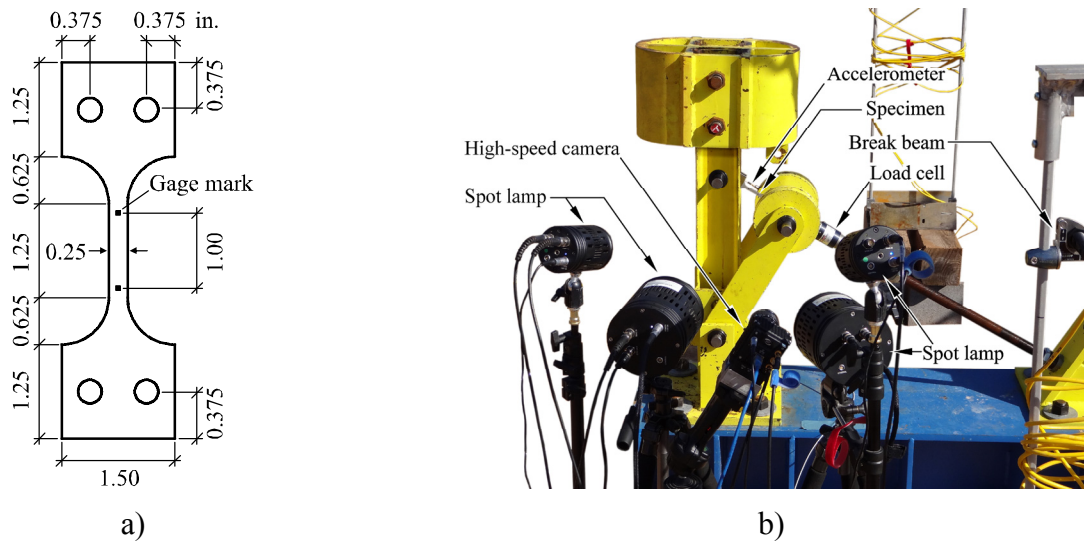


Figure 4.6 a) Specimen dimensions and gage marks, and b) instrumentation setup

4.2.4 Summary of testing program

A summary of the full testing program is provided in Table 4.1. As noted in Section 4.2.1, three main series of experiments were conducted: two involving A1011 steel (two thicknesses, denoted A1011-T11 and A1011-T15), and one involving A36 steel (denoted A36-T25). Within each material series, tests were conducted at eight strain rates (denoted R1 – R8) covering several orders of magnitude ($10^{-5} - 10^2 \text{ s}^{-1}$). Three or four repetitions of each test were conducted (denoted A, B, C, D). Tests at rates R1 – R4 were conducted in the laboratory using the Instron test machine, while tests at rates R5 – R8 utilized the impact pendulum and HRTA. A total of 84 tests were conducted (28 for each material series).

Table 4.1 Summary of experimental testing parameters and number of repetitions

Rate	Approximate strain rate (s ⁻¹)	Instron crosshead rate (in./min)	A1011-T11 0.115 in. thck.	A1011-T15 0.155 in. thck.	A36-T25 0.25 in. thck.
R1	7.0E-5	0.0075	A,B,C,D	A,B,C,D	A,B,C,D
R2	7.0E-4	0.075	A,B,C,D	A,B,C,D	A,B,C,D
R3	7.0E-3	0.75	A,B,C,D	A,B,C,D	A,B,C,D
R4	3.5E-2	3.5	A,B,C,D	A,B,C,D	A,B,C,D
		Apparatus configuration	Pendulum drop height (ft)		
R5	1.3E+1	Horizontal	1	A,B,C	A,B,C
R6	4.1E+1	Horizontal	15	A,B,C	A,B,C
R7	1.0E+2	Angled	4	A,B,C	A,B,C
R8	2.5E+2	Angled	25	A,B,C	A,B,C

4.3 Theory and Calculation Procedures

In this section, theoretical support for data-processing procedures that were employed in the study is discussed. A calculation framework is presented, in which Cowper Symonds coefficients C and P are determined for the materials tested by means of optimization.

4.3.1 Quasi-static testing program

One of the primary goals of the testing program was to characterize stress-strain behavior at all strains up to failure. However, as noted in Section 4.2.2, the extensometer utilized to measure strain in the quasi-static testing program had to be removed prior to specimen fracture. For each quasi-static test, the extensometer was removed at a measured strain of 0.15 in./in. The procedure illustrated in Fig. 4.7 was used to estimate larger strains, based on the crosshead displacement of the Instron machine. Specifically, a parabolic function was fit to measured strain-displacement data (for strains between 0.10 – 0.15 in./in.) and all strains larger than 0.15 in./in. were estimated by extrapolation along the fitted parabola. This procedure was found to predict the measured failure strains (quantified by placing the two pieces of each specimen together and measuring elongation of the gage region) to within 1 – 2% error.

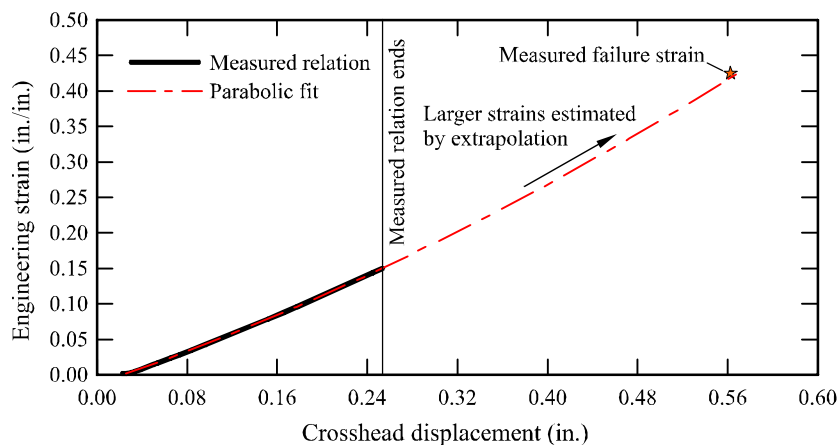


Figure 4.7 Strain-displacement relation for test A1011-T11-R1-B, including parabolic fit

4.3.2 High-rate testing program

Interpreting data measured from the high-rate testing program required consideration of inertial effects associated with the dynamic response of the HRTA. While engineering strain was readily quantified via digital image correlation, stress in the specimen could not be measured directly. To address this issue, two data interpretation methods are presented in the following sections: a direct method based on dynamic equilibrium of a SDF oscillating system, and an indirect method in which the strain rate-sensitive constitutive behavior is determined by iterative optimization. For reasons that are provided below, the latter method was employed in the interpretation of all HRTA test data.

4.3.2.1 Single-degree-of-freedom data interpretation

As noted in Section 4.2.3.1, the drive line of the HRTA was intended to act as a lightly damped SDF oscillating system (Fig. 4.8). During each test, the system was subjected to a time-varying force imparted by the specimen, $F_S(t)$, which was equal to the engineering stress times the original cross sectional area of the specimen.

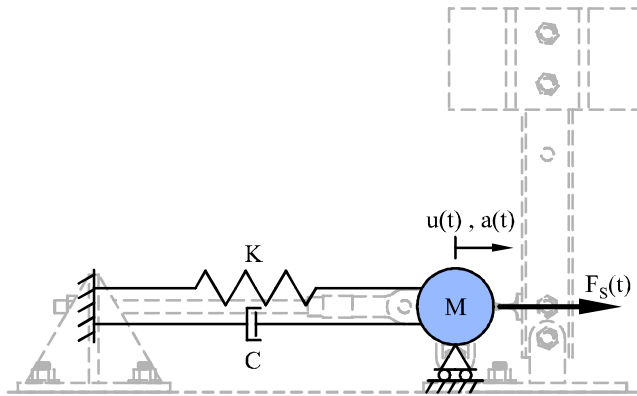


Figure 4.8 High-rate test apparatus (HRTA) as a damped SDF oscillator
 Subjected to forced vibration by $F_S(t)$, the damped SDF equation of motion is:

$$M \cdot a(t) + C \cdot v(t) + K \cdot u(t) = F_S(t) \quad (4.1)$$

where M is the mass of the plates attached to the end of the drive line, C is the damping coefficient resulting from natural damping in the drive line, and K is the stiffness of the drive line. Note that the load cell used during testing measured the *total* reaction force acting on the mass, $F_R(t)$, including *both* the stiffness and damping terms. Therefore, $F_R(t) = C \cdot v(t) + K \cdot u(t)$, and thus:

$$M \cdot a(t) + F_R(t) = F_S(t) \quad (4.2)$$

Because M is known, $a(t)$ is measured by an accelerometer, and $F_R(t)$ is measured by a load cell, $F_S(t)$ —and thus, engineering stress—can, theoretically, be easily computed. However, the validity of Eqn. 4.2 depends on the system responding as a SDF system. Unfortunately, connections between the mass plates and other elements of the drive line in the experimental setup were more flexible than intended. This additional source of flexibility resulted in localized oscillations that did not track temporally with the oscillations of the overall system, and the influence of these oscillations on instrument measurements could not be removed through signal processing. Therefore, an alternative data processing method (described below) was developed that does not depend on SDF response.

4.3.2.2 Impulse-momentum data interpretation

Consider integrating Eqn. 4.2 with respect to time, over the interval $[t_1, t_2]$:

$$\int_{t_1}^{t_2} [M \cdot a(t) + F_R(t)] dt = \int_{t_1}^{t_2} F_S(t) dt \quad (4.3)$$

where, t_1 is a time immediately prior to specimen extension, and t_2 is a time well after the specimen has broken and all oscillation in the HRTA has ceased. Evaluating the integral:

$$M \cdot [v(t_2) - v(t_1)] + \int_{t_1}^{t_2} F_R(t) dt = \int_{t_1}^{t_2} F_S(t) dt \quad (4.4)$$

Because $v(t_1) = v(t_2) = 0$,

$$\begin{aligned} \int_{t_1}^{t_2} F_R(t) dt &= \int_{t_1}^{t_2} F_S(t) dt \\ \Rightarrow J_R(t_2) &= J_S(t_2) \end{aligned} \quad (4.5)$$

where, J_R is the reaction impulse, and J_S is the impulse imparted by the specimen to the mass M . Note that Eqn. 4.5 does not imply that J_R and J_S are equal *at all times*. Indeed, while the system oscillates in free vibration (after the specimen has broken), system momentum, $M \cdot v(t)$, is continuously converted into reaction impulse, $J_R(t)$, and vice-versa, until motion eventually damps out. During this period, $J_R(t)$ is expected to oscillate about and eventually settle on the final value $J_R(t_2)$, which is equal to the specimen impulse $J_S(t_2)$ in accordance with Eqn. 4.5. Note that the validity of Eqn. 4.5 does not depend on the HRTA acting as a SDF system. It can

be readily demonstrated that Eqn. 4.5 holds for systems of any number of degrees of freedom that are anchored by a single point (the derivation is omitted here for brevity, but is provided in Appendix D).

It is also important to note that Eqn. 4.5 is insufficient to determine the stress-strain response of an arbitrary material. In fact, given a particular measured force-time history $F_R(t)$, there exist an infinite number of stress-strain relations for which Eqn. 4.5 can be satisfied. However, because quasi-static tension tests were conducted on the materials of interest, characteristics of the static stress-strain relations were well understood. Furthermore, for the high-rate tests, the strains, and by extension, the time-varying strain *rates* were known. Lastly, because the materials tested in this study were steels, the general manner in which plastic stresses were influenced by the strain rate were known from the literature. Specifically, numerous prior studies have demonstrated that the Cowper-Symonds expression describes rate sensitivity in many metals quite well, including steels (Jones 1997, 2013, Hsu and Jones 2004, Jones and Jones 2002).

Therefore, these known characteristics were combined with Eqn. 4.5 to form a calculation framework in which the Cowper-Symonds rate sensitivity parameters C and P were determined by iterative optimization. The calculation framework (summarized in Fig. 4.9) was used to determine optimal values of C and P that minimized the difference between an assumed constitutive response—based on the known stress-strain and rate sensitivity characteristics described above—and the measured HRTA response, in accordance with Eqn. 4.5.

As shown in Fig. 4.9, the calculation process begins with the average stress-strain curve calculated from the four test repetitions conducted at rate R1 (nearly-static, $\dot{\varepsilon} \approx 7 \cdot 10^{-5} \text{ s}^{-1}$). Given the typical dogbone specimen geometry employed in this study, strain rate was not constant through the specimen extension event, even for rate R1. As such, strain rate was computed as a function of strain, $\dot{\varepsilon}_{R1,avg}(\varepsilon)$, by numerically differentiating the strain-time histories from each R1 test and computing an interpolated average among the four tests. With this relation for R1, trial values of C and P were selected. Because rate R1, while extremely slow, was not truly static, the average R1 stress-strain relation, $\sigma_{R1,avg}(\varepsilon)$, was scaled down using the Cowper-Symonds expression to form a truly static constitutive curve, $\sigma_{st}(\varepsilon)$, that was representative of the material of interest (illustrated in Fig. 4.10). This static curve was used as a baseline for computing the response of other test strain rates in the study.

The steps enumerated below describe the process that was employed for computing a dynamic stress-strain curve, $\sigma_i(\varepsilon)$, for each test conducted ($i = 1 \dots 28$), based on the static curve, $\sigma_{st}(\varepsilon)$, experimental data, and the Cowper-Symonds expression. First, $\sigma_{st}(\varepsilon)$ was ‘stretched’ along the strain axis such that $\varepsilon_{st}^{max} = \varepsilon_i^{max}$, where ε_i^{max} was the maximum (failure) strain for test i (Fig. 4.10). This step accounted for differences in ductility between tests and was especially important, as significant increases in ductility were observed at higher strain rates in

this study. Given the variable strain rate, $\dot{\varepsilon}_i(\varepsilon)$ (computed from experimental data for test i), the ductility-adjusted static curve was ‘scaled up’ along the stress axis per the Cowper-Symonds expression to form a dynamic stress-strain relation, $\sigma_i(\varepsilon)$ (Fig. 4.10). It is important to note that each point in the $\sigma_i(\varepsilon)$ curve was individually scaled to reflect the strain rate *at that instant* during the test. Because such curves are specific to the conditions imposed on the specimens during each test, they are the most accurate possible representation of as-tested specimen response, given the information available and the assumptions made.

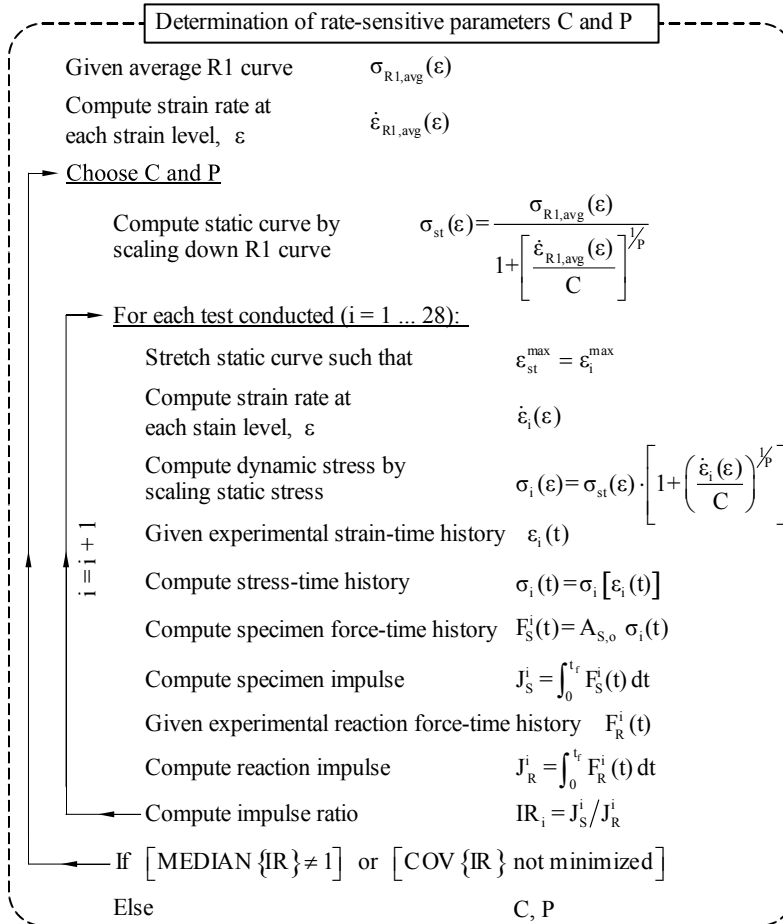


Figure 4.9 Impulse-momentum-based optimization procedure for computing Cowper-Symonds coefficients C and P

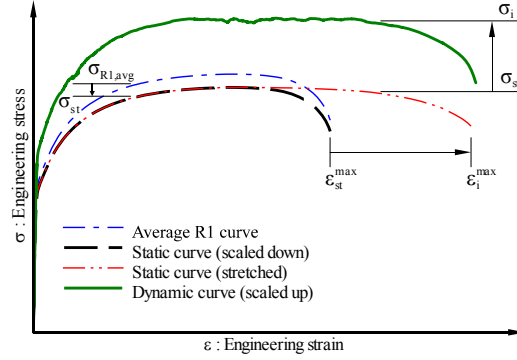


Figure 4.10 Stretching and scaling of average R1 stress-strain relation $[\sigma_{R1,avg}(\varepsilon)]$ to arrive at dynamic stress-strain relation for each test $[\sigma_i(\varepsilon)]$, following procedure shown in Fig. 4.9

From $\sigma_i(\varepsilon)$ and the measured strain-time history $\varepsilon_i(t)$, the specimen stress-time history, $\sigma_i(t)$, was computed and multiplied by the *original* specimen cross-sectional area, $A_{S,0}^i$, to compute the specimen force-time history, $F_S^i(t)$. Note that stresses were expressed as engineering stresses throughout the calculation process (rather than true stresses), therefore $A_{S,0}^i$ was the appropriate area quantity. To obtain total specimen impulse, J_S^i , the force-time history, $F_S^i(t)$, was numerically integrated. Similarly, the reaction force-time history, $F_R^i(t)$ (measured by the load cell), was integrated to obtain the total reaction impulse, J_R^i .

The final calculation step involved comparing the assumed specimen response to the measured reaction response in accordance with Eqn. 4.5. Rearranged, Eqn. 4.5 can be written $J_S/J_R = 1$. Therefore, a quantity termed impulse ratio (*IR*) was defined as $IR = J_S/J_R$. For a particular test, the condition $IR_i = 1$ suggests that the assumed values of C and P (and the other assumptions in the calculation framework) are correct for that test. It follows then, that if $IR_i = 1$ for *all* tests ($i = 1 \dots 28$), then optimal values of C and P have been determined. Given the presence of natural variability in the tested specimens, achieving $IR_i = 1$ for all tests is unlikely. Therefore, the objectives for optimizing C and P were instead that the median *IR* among all tests be equal to 1.0 and the coefficient of variation (COV) be minimized.

4.4 Results and Discussion

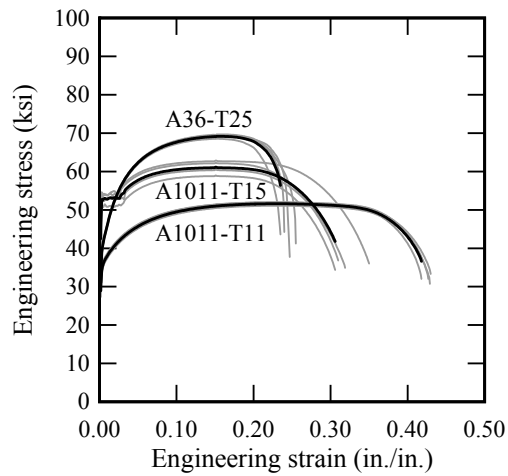
Results obtained from the quasi-static and high-rate test programs are described in the following sections. Using the methods described in Section 4.3.2.2, unique Cowper-Symonds coefficients C and P were computed for each of the three materials tested.

4.4.1 Quasi-static testing program

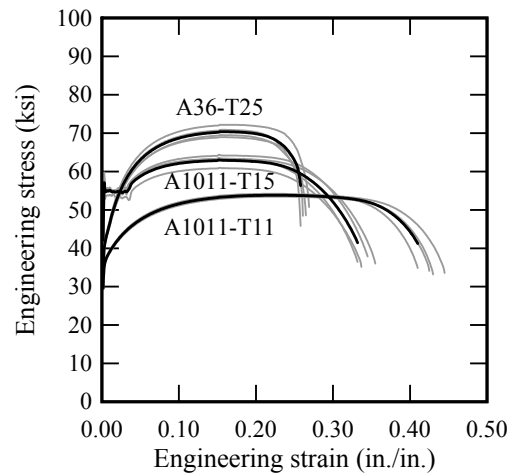
Engineering stress-strain curves obtained from the quasi-static testing program (rates R1 – R4) are provided in Fig. 4.11. Thinner grey traces correspond to individual repeated tests, while thicker black traces correspond to point-by-point interpolated averages of the four repetitions in each test series. Average curves were computed by re-sampling the curve for each repetition at strain increments equal to 10^{-4} in./in., then averaging stress values at each point of common strain. Average curves were terminated at the smallest breaking strain among the four curves being averaged.

The most striking observation is that stress-strain curves for the A1011-T11 and A1011-T15 series were largely dissimilar, even though the material grade was the same and only the thickness differed. The T11 curve exhibited a smooth shape, without a well-defined proportional limit, while the T15 curve included a clearly defined yield plateau followed by strain hardening. Additionally, the T15 material exhibited higher strength than T11, but with lower ductility. The A36-T25 series consistently had the highest ultimate tensile strength among the materials tested, and its mechanical properties conformed to the limits specified by ASTM.

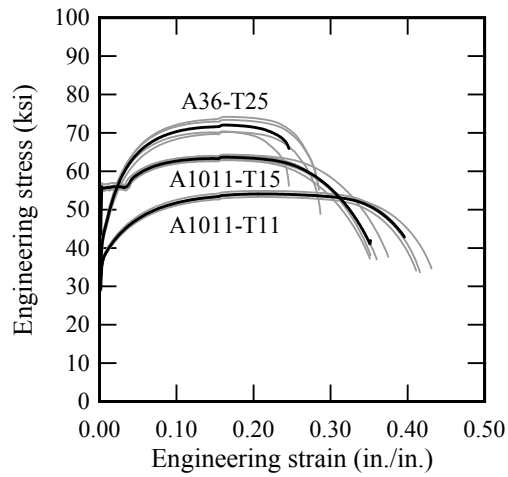
None of the materials that were tested exhibited a well-defined linear Young's modulus. While several methods were explored for determining a representative modulus for each material (e.g., curve fitting, numerical differentiation, visual methods), each method yielded unacceptably variable results from test-to-test, and none were deemed to be sufficiently reliable. The ASTM A370 standard acknowledges difficulty in establishing a linear modulus for many materials, and suggests a representative value of 30,000 ksi for carbon steels (ASTM 2012b). Given that the focus of this study was characterizing the *plastic* behavior of the materials tested, the representative *elastic* modulus value suggested by ASTM was adopted for further calculations (e.g., computing effective plastic strain) and employed in the finite element constitutive models discussed in Section 4.5.



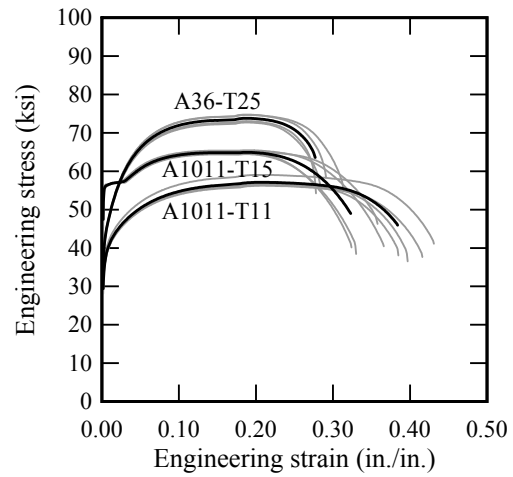
a) Rate R1



b) Rate R2



c) Rate R3



d) Rate R4

Figure 4.11 Engineering stress-strain curves for each quasi-static test series

The rate sensitivities of various physical properties observed from the quasi-static test program are shown in Fig. 4.12. Because the materials did not exhibit a well-defined modulus, yield stress was computed using the extension under load (EUL) method described in ASTM A370 (ASTM 2012b). Specifically, yield stress was taken to be the stress corresponding to an engineering strain of 0.005 in./in. (0.5% EUL), as suggested by ASTM for this class of materials. As shown in Fig. 4.12a, some increase in yield stress was observed for all three material series. Similar results were observed for ultimate stress (Fig. 4.12b). For each material series, yield and ultimate stress increased by approximately 5 – 10% from rate R1 ($\sim 7 \times 10^{-5} \text{ s}^{-1}$) to R4 ($\sim 5 \times 10^2 \text{ s}^{-1}$).

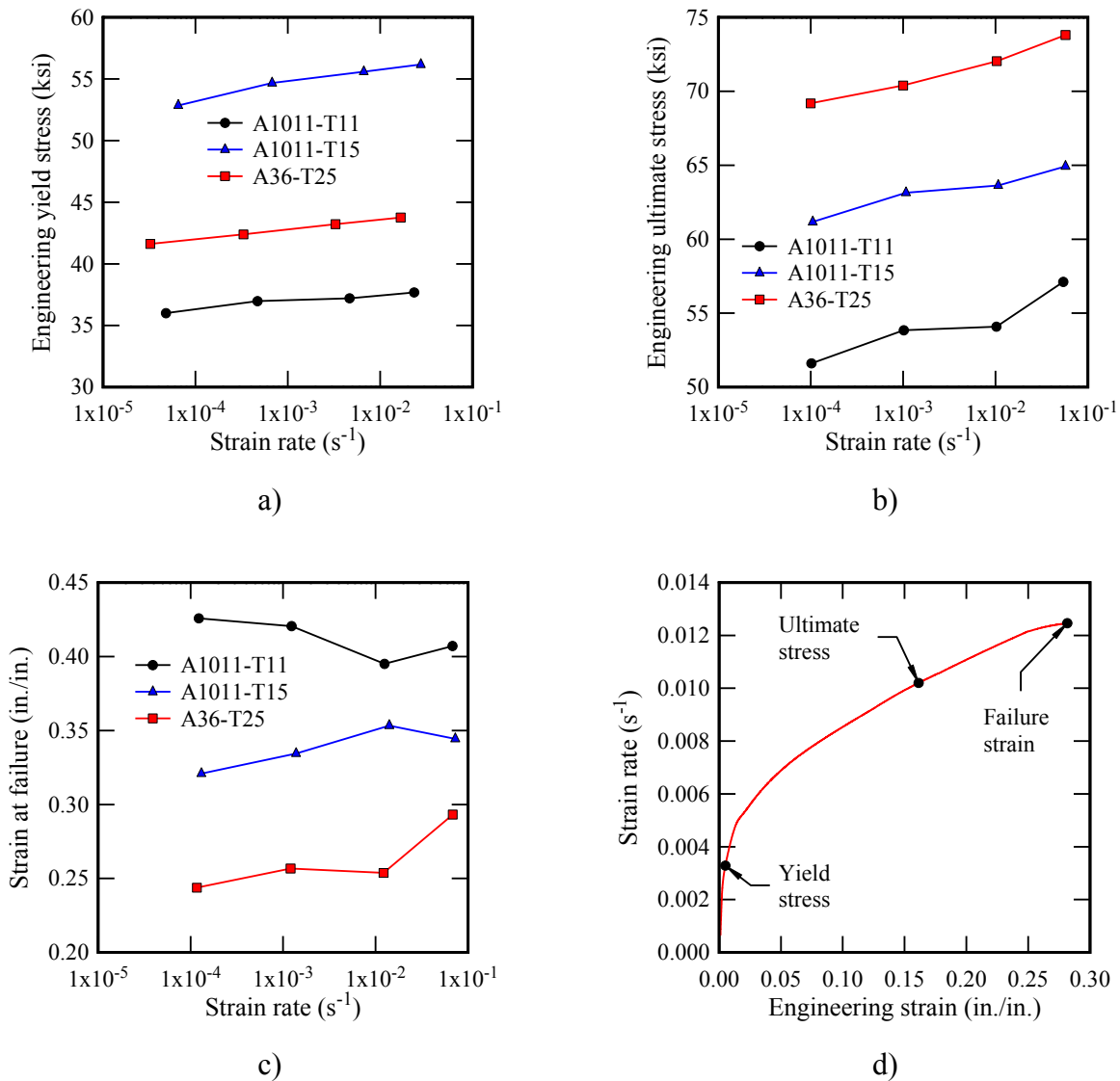


Figure 4.12 Rate sensitivity of material parameters among quasi-static testing rates: (a) yield stress; (b) ultimate stress; and (c) failure elongation. (d) Representative variation in strain rate through the duration of a quasi-static test (data from test A36-T25-R3-C shown)

As reported in Fig. 4.12c, strain at specimen failure (failure elongation) was determined by placing the two pieces of specimen together, measuring the change in length of the reduced gage region, and dividing by the original gage length, as specified by ASTM (ASTM 2012b). While ductility appeared to increase with increasing strain rate for the A1011-T15 and A36-T25 series, an apparent decrease was observed for A1011-T11. It is noted that clear increases in ductility were observed for all materials at higher strain rates in the pendulum testing program (see following section). Thus, the mixed results obtained during quasi-static testing can be attributed to typical variability in material ductility and error inherent in the method used to measure elongation.

It is important to note that measured strain rates were not perfectly constant through the duration of each quasi-static test. As a representative example, strain rate is plotted as a function of strain in Fig. 4.12d for test A36-T25-R3-C. As shown, strain rate increased rapidly in the near-elastic region, and continued to increase (less rapidly) throughout the test. Note that the crosshead velocity was extremely constant through the duration of each test. Thus, the consistently observed increase in strain rate was primarily a consequence of the dogbone-shaped specimen geometry and the continually varying stiffness of the reduced gage region. Such behavior could only be avoided if the testing machine was capable of continuously adjusting the crosshead velocity so as to maintain a constant strain rate in the gage region, which the Instron machine employed in this study was not able to do. Consequently, the strain rates plotted in Fig. 4.12a-c reflect the strain rate measured at the time that the event of interest occurred (e.g. yield).

4.4.2 High-rate testing program

As discussed in Section 4.3.2.2, during the high-rate tests, strain was quantified from displacements which were measured using digital image correlation, however, direct measurement of specimen stress was not possible using the HRTA. Consequently, data from the high-rate and quasi-static test programs were combined with the data processing method summarized in Figs. 4.9 and 4.10 to quantify rate-sensitive material behavior. Optimal Cowper-Symonds coefficients C and P that were a best fit to the experimental data were computed for each material series. This section presents and discusses results from key portions of the data processing methodology. Note that detailed data presented in this section correspond to the *final iteration* of the optimization procedure, and thus, correspond to the outcome of the procedure with optimal values of C and P (presented near the end of this section).

Strain rates measured from the high-rate tests are presented in Fig. 4.13 as a function of engineering strain. As before, thinner grey traces correspond to individual tests, and thicker black traces correspond to the interpolated average among the three repetitions for that test series. While strain rates were not perfectly uniform, variability was fairly small among tests in a given series, with the notable exception of the A1011-T11-R6 series (Fig. 4.13a). For all series, temporal fluctuations in strain rate were primarily attributed to vibrations within the HRTA. While the components of the HRTA were designed to be as stiff as practical, high-speed video of the overall system uncovered small motions in the base plate elements that supported the rotating control arm. These motions, combined with smaller-magnitude high-frequency vibrations contributed to oscillations in the strain rate. Regardless, oscillations of the magnitude shown in Fig. 4.13 were not considered detrimental because the data processing procedure (Fig. 4.9) accounted for temporal variations in strain rate by scaling stresses at each point in time through the duration of a test.

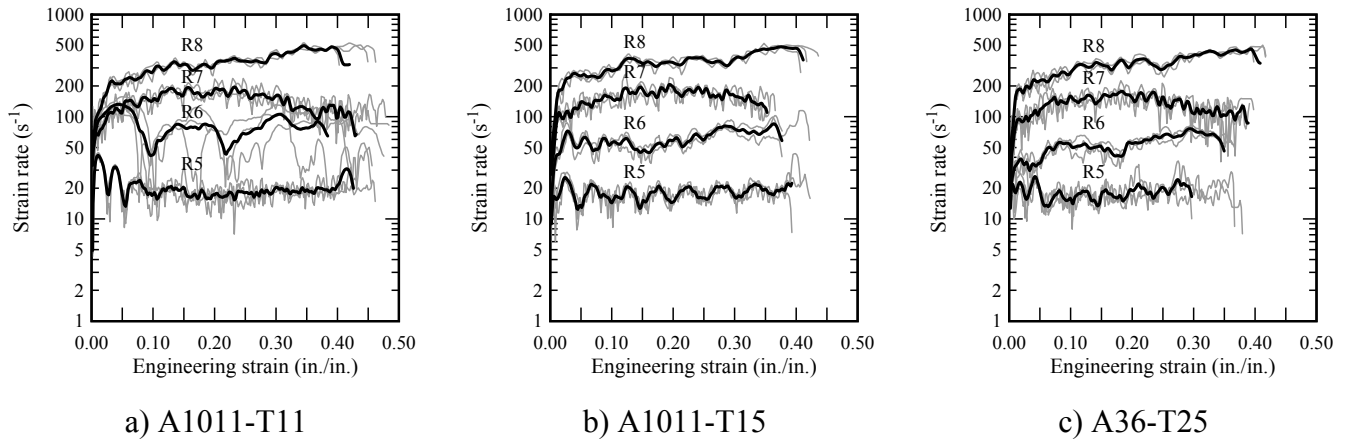


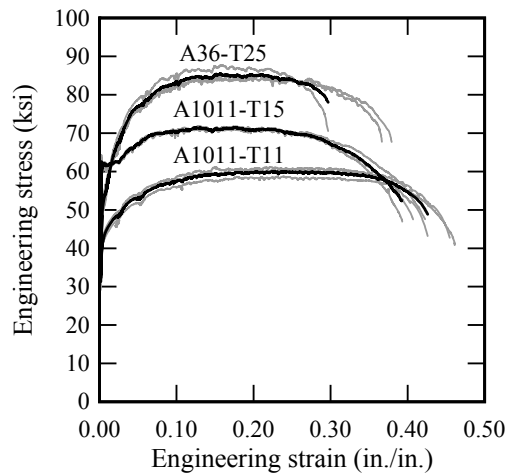
Figure 4.13 Engineering strain rate (among three tests per trace) as a function of strain

Engineering stress-strain curves computed for each high-rate test are presented in Fig. 4.14 (thin grey traces represent individual tests; black traces represent the interpolated average). In addition to increased strain rates producing increased stresses (as dictated by the scaling model employed), a clear increase in ductility was also observed as strain rate increased, particularly for the A36-T25 material. Indeed, at testing rate R8 (Fig. 4.14d) the ductility of all three materials was nearly identical, which is in stark contrast to the lowest rate, R1 (recall Fig. 4.11a), at which the A1011-T11 material was almost twice as ductile as the A36-T25 material.

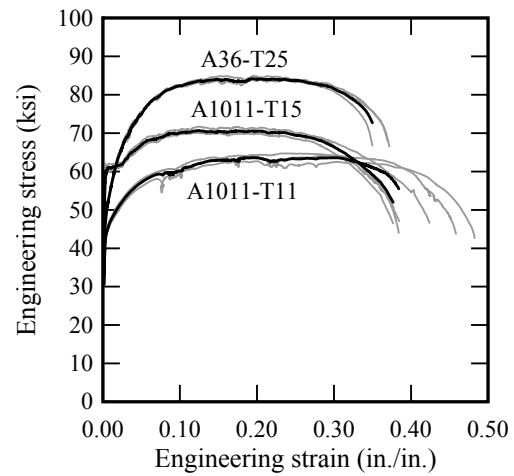
Using the procedure in Fig. 4.9, the computed stress-strain relations (presented in Fig. 4.14 for rates R5 – R8), were combined with measured strain-time histories, $\epsilon(t)$, to compute specimen force-time histories, $F_S(t)$, for every material test conducted in the study (rates R1 – R8) as:

$$F_S(t) = A_{S_0} \cdot \sigma[\epsilon(t)] \quad (4.6)$$

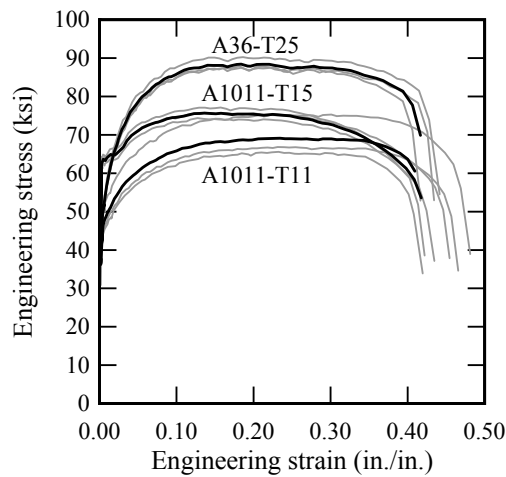
In Fig. 4.15, specimen force-time histories are compared to measured reaction force-time histories, $F_R(t)$, for two representative tests. The first example, A36-T25-R1-A (Fig. 4.15a), was conducted at the lowest testing rate using the Instron testing machine, while the second example, A36-T25-R6-A (Fig. 4.15b), was conducted using the HRTA.



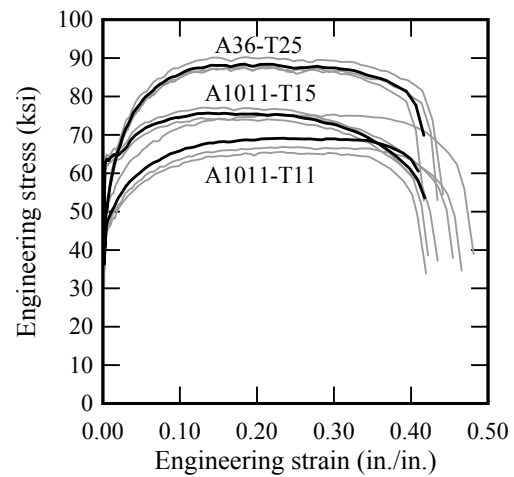
a) Rate R5



b) Rate R6



c) Rate R7



d) Rate R8

Figure 4.14 Engineering stress-strain curves (computed by the process in Figs. 4.9 and 4.10) for each high-rate test series

As expected, no dynamic oscillation was observed in F_R for the quasi-static test (Fig. 4.15a), and F_S was nearly equal to F_R throughout the test. Recall that in this context, F_S was computed within the calculation framework in Fig. 4.9, and is thereby approximate. Deviation between F_S and F_R observed near the end of the test can be attributed to assumptions made in the calculation framework and to deviations of physical specimen properties from the idealized rate-sensitivity model employed. The degree of deviation shown in Fig. 4.15a can be considered representative of the various quasi-static tests.

In contrast, significant dynamic oscillation was observed in F_R (Fig. 4.15b) for the high-rate tests and F_S was almost never equal to F_R . This oscillation can be attributed to the dynamic response of the HRTA drive line both during the specimen extension event ($t < 8$ msec), and

after failure of the specimen ($t > 8$ msec). As shown, the dynamic response damped out as the drive line came to rest, at which time $F_R = 0$. This example serves to illustrate the difficulty in directly determining force in the specimen, F_S , from the measured response, F_R , because vibrations within the HRTA partially obscured the intended measurement.

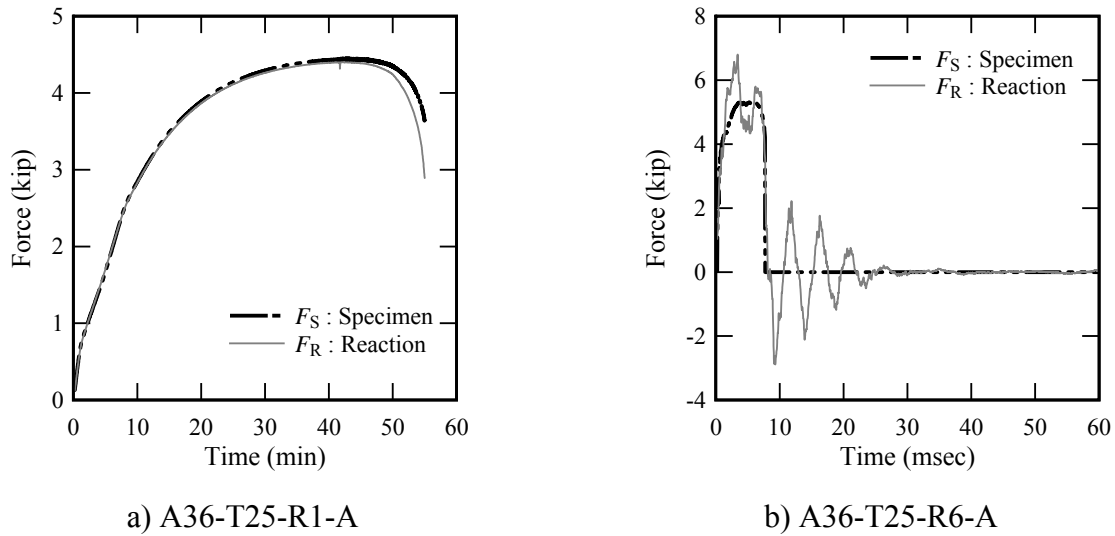


Figure 4.15 Specimen and reaction force-time histories (computed by process in Fig. 4.9) for selected tests

Consequently, specimen and reaction impulse (J_S and J_R , respectively) were computed by numerically integrating corresponding force-time histories. For the quasi-static case (Fig. 4.16a), J_S and J_R match closely, with a small deviation observed near the end of the test, caused by the difference between F_S and F_R discussed above. In contrast, for the dynamic case (Fig. 4.16b), deviations were observed between J_S and J_R throughout the specimen extension event and immediately after specimen fracture ($t < 25$ msec). However, as HRTA motion damped out, J_R oscillated about J_S in a rapidly decaying manner, and eventually settled to a value approximately equal to J_S . This behavior was expected in accordance with the impulse-momentum principle, as demonstrated by the derivation of Eqn. 4.5 in Section 4.3.2.2.

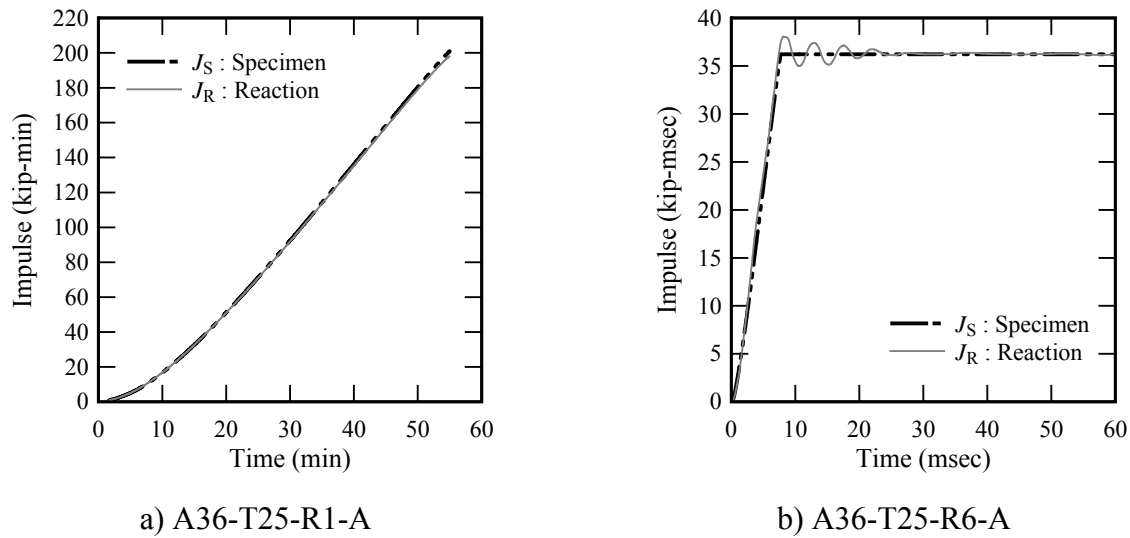


Figure 4.16 Specimen and reaction impulse-time histories (computed by process in Fig. 4.9) for selected tests

The final step in the calculation framework involved computing the impulse ratio ($IR = J_S/J_R$) for each test in the study. Recall that values of IR nearly equal to 1.0 indicate that the values for rate-sensitivity parameters C and P assumed at the beginning of the process are a good fit to the measured data. Significant deviations from 1.0 would suggest that C and P should be adjusted. Note that for quasi-static tests, the values of J_S and J_R used to compute IR were simply the values at the time that the specimen fractured (end of test). However, for dynamic tests, J_R oscillated about a terminal value as discussed above. Consequently, the mean value of the impulse-time history *after the specimen fractured* (corresponding to free vibration of the HRTA) was the J_R value used to compute IR for high rate tests.

For the optimal values of C and P computed for each test series, histograms of IR are presented in Fig. 4.17. A summary of basic IR statistics is also provided in Table 4.2 together with the computed optimal values of C and P for each series. As shown, IR values were tightly grouped around the ideal value of 1.0, rarely deviating by more than 5%. For each material series, the median value of IR was equal to 1.0, and coefficients of variation (COV) were 2.0 – 3.4%. This tight grouping in IR values suggests that the assumed rate-sensitivity model and optimal C and P values were a close fit to the experimentally measured response. Note that in the optimization process, P was limited to integer values for simplicity. No perceptible improvements in IR statistics were observed by permitting P to take on fractional values.

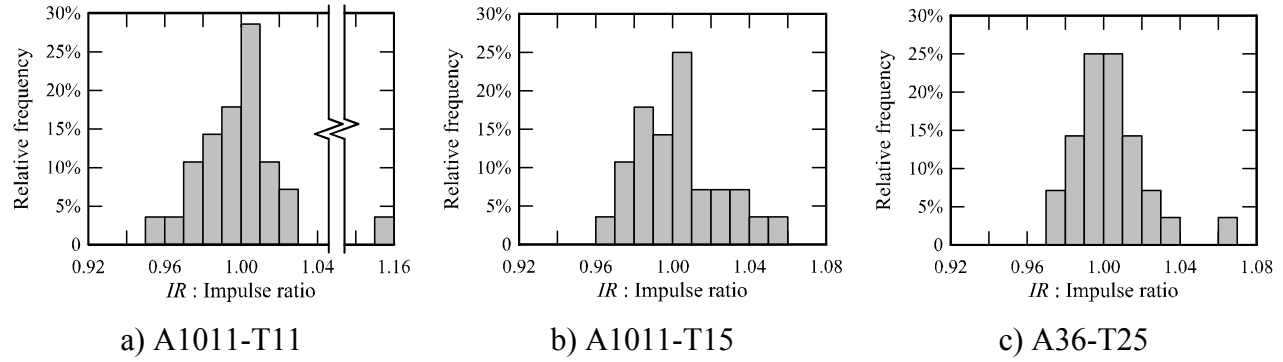


Figure 4.17 Normalized histograms of impulse ratio (IR) for each material series (computed by process in Fig. 4.9)

Table 4.2 Rate sensitivity parameters and impulse ratio (IR) statistics

Material series	C (s^{-1})	P	IR : Impulse ratio		
			Minimum	Maximum	COV
A1011-T11	9,200,000	10	0.958	1.154	3.4%
A1011-T15	20,500,000	10	0.966	1.058	2.3%
A36-T25	1,320,000	8	0.971	1.066	2.0%

Recall that, as employed in this study, the Cowper-Symonds expression states:

$$\frac{\sigma_{\text{dyn}}}{\sigma_{\text{st}}} = 1 + \left(\frac{\dot{\epsilon}}{C} \right)^{1/P} \quad (4.7)$$

where σ_{dyn} is the dynamic flow stress, and σ_{st} is the stress at a theoretical static state in which $\dot{\epsilon} = 0$. Eqn. 4.7 is plotted for each material series in Fig. 4.18, with optimal values for C and P from Table 4.2. Individual points shown in Figs. 4.18a-c are equal to the average impulse ratio for each testing rate (R1 – R8) multiplied by $\sigma_{\text{dyn}}/\sigma_{\text{st}}$. Error bars denote the minimum and maximum value within each rate series. Abscissa values for each point are the median strain rate through the duration of the test, averaged among the 3 – 4 tests within each series. Presented in this manner, Figs. 4.18a-c provide a visual representation of the degree of variability in each test series with respect to the optimal Cowper-Symonds curve. As shown, error was evenly distributed with respect to strain rate and insensitive to the method of testing (Instron machine versus HRTA). Confidence intervals (95%) were computed based on IR statistics, assuming uniform error with respect to strain rate.

Cowper-Symonds curves for each material series are compared in Fig. 4.18d. As shown, the three curves covered a relatively narrow band of $\sigma_{\text{dyn}}/\sigma_{\text{st}}$ over the range of strain rates considered. For example, at $10^{-5} s^{-1}$, $\sigma_{\text{dyn}}/\sigma_{\text{st}}$ was equal to 1.04 – 1.06 among the three curves, and at $10^3 s^{-1}$, $\sigma_{\text{dyn}}/\sigma_{\text{st}}$ was 1.37 – 1.40. This tight grouping suggests that a single Cowper-Symonds curve (with aggregated C and P values) would be acceptable, particularly given

significant overlap among the confidence intervals. However, absent any clear reason for aggregating the curves, individually derived Cowper-Symonds models were retained for each material series.

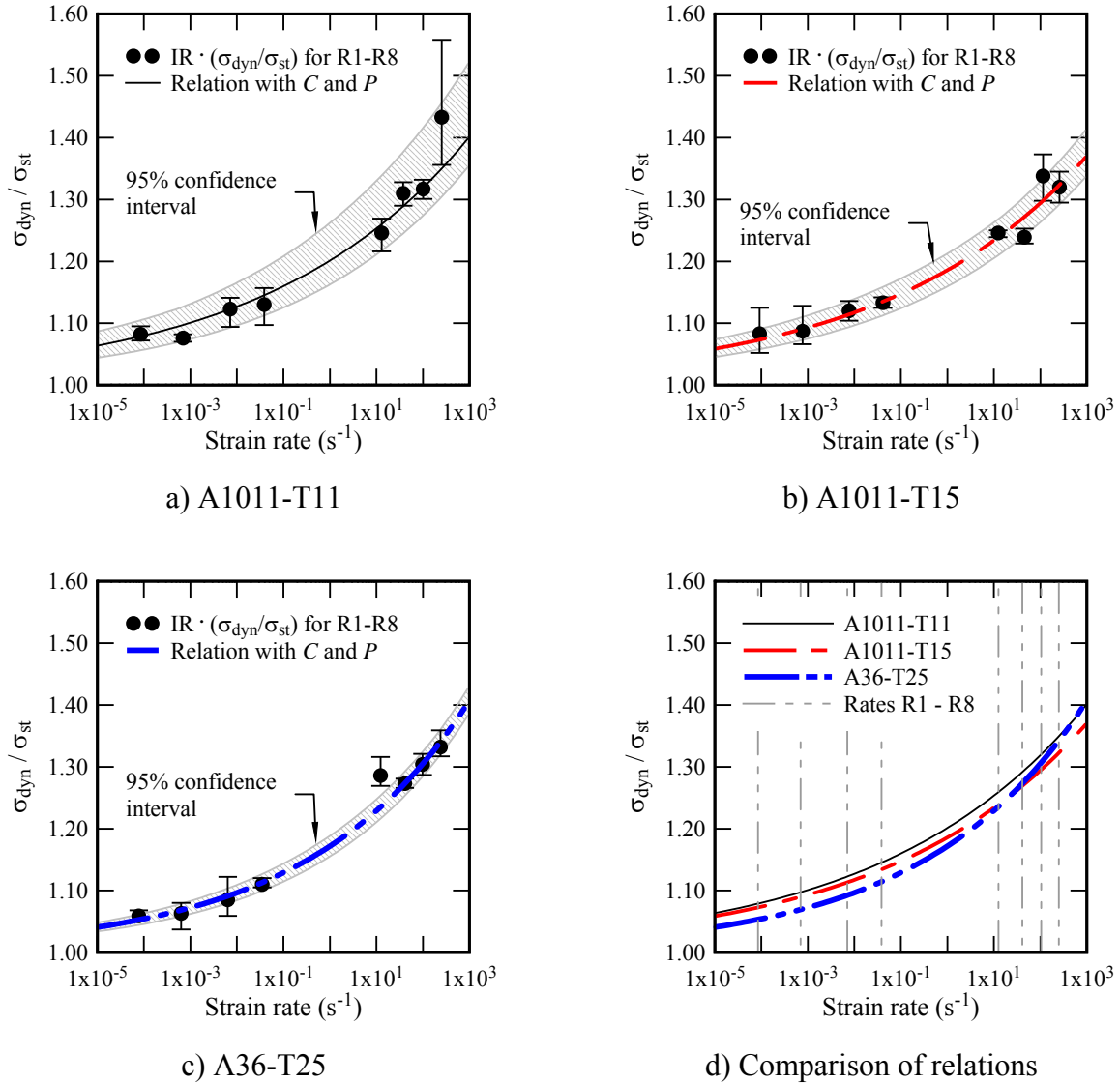


Figure 4.18 Sensitivity of dynamic stress to strain rate for each material test series

For all three materials tested, values of C and P were higher than those published in the literature (Jones 1997, 2013, Hsu and Jones 2004, Jones and Jones 2002). As noted previously, $C = 40.4 \text{ s}^{-1}$ and $P = 5$ are values commonly employed for steels (Jones 1997). It is important to acknowledge that the basis for these reference values is a survey of the dynamic stresses of various metals published by Symonds (1967), in which the author calculated $C = 40.4 \text{ s}^{-1}$ and $P = 5$ using the yield stress results of a *single study* on mild steel conducted by Manjoine (1944). Yield and ultimate stress results from Manjoine are reproduced in Fig. 4.19a. Evident from the figure, yield stresses were found to be significantly more sensitive to high strain rates than were

ultimate stresses, and the values $C = 40.4 \text{ s}^{-1}$ and $P = 5$ fit the yield stress data well. However, for ultimate stress, $C = 21,800 \text{ s}^{-1}$ and $P = 4.9$ fit the data better. Cowper-Symonds curves computed in the present study are compared to the range from Manjoine in Fig. 4.19b. It is observed that the materials evaluated in the present study were significantly less rate-sensitive than the *yield stresses* from Manjoine; however, the level of sensitivity of *ultimate stress* was fairly consistent with data from Manjoine.

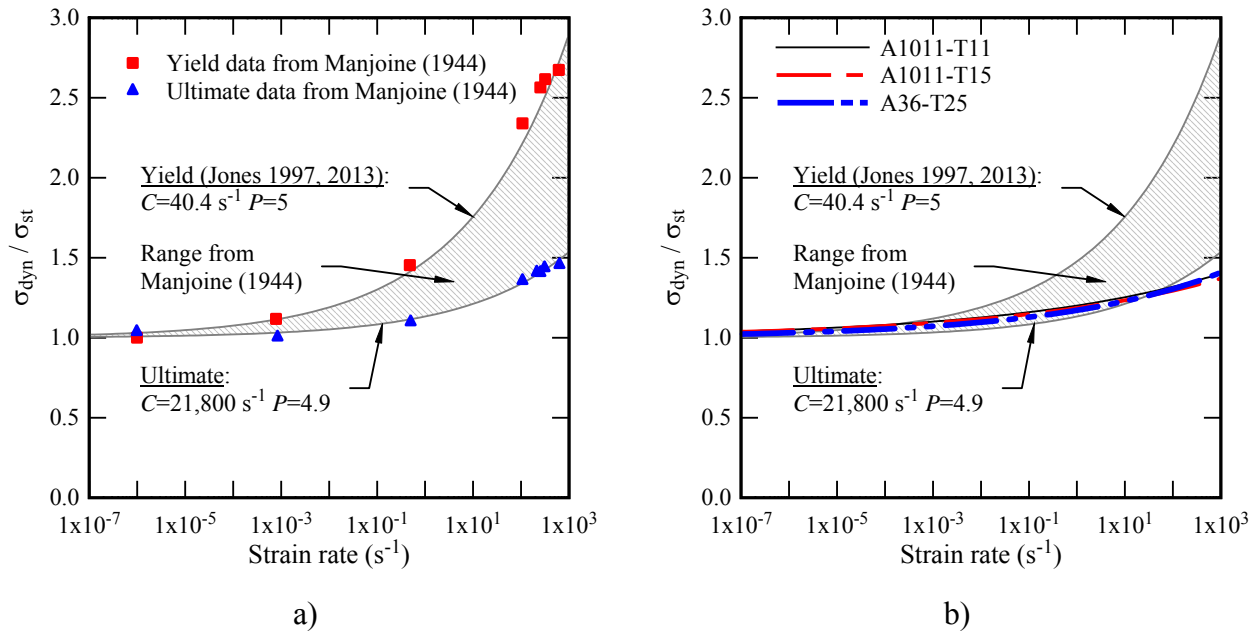


Figure 4.19 (a) Rate sensitivity of yield and ultimate stress from Manjoine study (1944), showing fitted Cowper-Symonds coefficients C and P . (b) Comparison between Manjoine data and rate sensitivity curves derived in this study

As discussed in Section 4.4.1, the materials evaluated in this study were found to have similar rate sensitivity for both yield and ultimate stress, and therefore the C and P values in Table 4.2 were derived to be the best fit to the experimental data for all strain levels (ranging from yield to failure). While dramatic differences in rate sensitivity at yield versus ultimate stress were observed in Manjoine (1944), the materials evaluated in the present study did not exhibit similarly dramatic rate sensitivity at small strains (near yield). Similar to Manjoine, numerous other studies (discussed Jones 1997) have found a difference in rate sensitivity at yield versus ultimate stress, however, the discrepancy was generally smaller than Manjoine. Reasons for the differing observations produced by Manjoine (1944) when compared to the current study are unclear. Certainly, steel chemistry, mill production processes, and experimental testing methods have undergone significant changes since the 1940s. Also, the steel specimens tested by Manjoine were bright annealed prior to testing, while in the present study, specimens were tested in the condition provided from the mill. As recently highlighted by Jones (2013), strain rate characteristics of mild steel vary significantly from study-to-study, and can be influenced by factors including surface finish, chemical content, and specimen geometry. However, in light of the potentially large degree of variability, it is notable that the specimens tested in this study—

taken from three material batches of two different material specifications—exhibited strain rate sensitivity that was strikingly similar.

4.5 Constitutive Model Details

As noted earlier, a primary goal of this study was to develop strain rate sensitive constitutive models for use in finite element simulations of vessel impact involving large-scale plastic deformations (using the LS-DYNA code). The LS-DYNA material database includes multiple isotropic plasticity models that follow well-established forms (e.g., Johnson-Cook). However, the most general model available is MAT_24 (MAT_PIECEWISE_LINEAR_PLASTICITY). This model permits the user to specify the stress-strain curve (in terms of true stress and effective plastic strain) as an arbitrary piecewise linear curve. Given that detailed experimental data were collected during this study, this feature is highly desirable.

4.5.1 Strain rate sensitivity

For rate-sensitivity, MAT_24 employs the Cowper-Symonds equation in two possible ways. First, if parameter SIGY > 0 (generally one would choose SIGY to be equal to the yield stress), then dynamic stress (σ_{dyn}) is computed as:

$$\sigma_{\text{dyn}}(\varepsilon_p, \dot{\varepsilon}_p) = \sigma_{\text{st}}(\varepsilon_p) + \text{SIGY} \cdot \left(\frac{\dot{\varepsilon}_p}{C} \right)^{1/P} \quad (4.8)$$

where, σ_{st} is the static stress (as defined by the user-specified material curve), ε_p is the effective plastic strain, $\dot{\varepsilon}_p$ is the effective plastic strain rate, and C and P are the Cowper-Symonds coefficients. If parameter SIGY = 0, then LS-DYNA employs an alternative scaling rule:

$$\sigma_{\text{dyn}}(\varepsilon_p, \dot{\varepsilon}_p) = \sigma_{\text{st}}(\varepsilon_p) \cdot \left[1 + \left(\frac{\dot{\varepsilon}_p}{C} \right)^{1/P} \right] \quad (4.9)$$

This latter rule is consistent with the scaling assumptions made in the formulation of C and P for this study, and will therefore be utilized in the constitutive models.

4.5.2 Failure strain considerations

Using MAT_24, material failure is simulated by element deletion when plastic strain within an element exceeds a specified threshold value (denoted FAIL in the material definition).

One of the limitations of MAT_24 is that this failure criterion cannot be defined as being strain rate sensitive. As noted in the prior section, ductility of the materials tested in this study tended to increase with increased strain rate. As such, the failure criterion limitation in MAT_24 required specific attention (discussed in more detail below).

The choice of an appropriate failure strain was further complicated by the size of the finite elements used in the mesh (relative to the size of the structural member being modeled). For the simulation scale of interest in this study, if elements were very small (i.e., on the order of 0.01 in. or smaller), then necking deformation prior to failure, and associated non-uniform stress distribution in the necked region, can be modeled directly. In this case, very high levels of localized strain (>1 in./in.) will occur in the necked region prior to failure, and a correspondingly high value of failure strain should be assigned in the FE model to avoid premature simulation of fracture. Conversely, if the finite elements are large (i.e., on the order of 0.25 in. or larger), then the finite element model cannot directly simulate necking effects. In this situation, each element represents material behavior in a macroscopic sense (similar to the manner in which material behavior is characterized in typical uniaxial tension testing, where stress and strain are calculated as average values over a finite size gage region) and the most appropriate failure strain for the FE constitutive model is the effective plastic strain at failure observed from uniaxial tension testing (0.2 – 0.4 in./in. for the materials tested in this study). For the FE model scales of interest in this study (dogbone material samples up to full-scale vessels), the element sizes were large enough that the latter approach to choosing failure strain was the most appropriate.

As noted above, in MAT_24, a value for failure strain must be selected that is constant with respect to strain rate, even though increased ductility was observed in the evaluated materials at higher strain rates. Table 4.3 summarizes minimum and maximum failure strains quantified from the experimental study, where the minimum was observed for rate R1, and the maximum was observed for R8. Simulations scenarios of interest in this study were not found to be strongly sensitive to the choice of failure strain over the range shown in Table 4.3. Consequently, the average of the R1 and R8 failure strains was selected for use in the FE constitutive models. For brevity, sensitivity simulations supporting this conclusion are not documented in this chapter; however, a complete discussion can be found in Appendix E. It is acknowledged that certain classes of problems (e.g., metal forming simulations) may be more sensitive to material ductility, and thus warrant a more detailed treatment of failure. For this reason, the MAT_24 constitutive model in LS-DYNA supports the use of user-defined failure subroutines that can be programmed to include strain rate sensitivity. However, this level of refinement was unwarranted for the impact problems of interest in the present study.

Table 4.3 Effective plastic strain at failure for each material series

Material series	Effective plastic strain at failure (in./in.)		
	Minimum (R1)	Maximum (R8)	Average
A1011-T11	0.342	0.384	0.363
A1011-T15	0.280	0.336	0.308
A36-T25	0.206	0.340	0.273

4.5.3 Constitutive curves

Static constitutive curves were developed for each material series by scaling down the interpolated average R1 curve to account for the non-zero strain rates at which specimens were tested, and stretching the curve along the strain axis to match the desired strain at failure (recall Figs. 4.9 and 4.10 for a description of this process). For input into MAT_24, the curve data were converted from engineering stress and strain to true stress and effective plastic strain. Lastly, the curves were decimated to include a minimal number of points. To minimize error with respect to experimental data, points on the curve were concentrated in regions of significant curvature. The resulting constitutive curves are presented in Fig. 4.20. Note that because the FE mesh size (greater than 0.25 in.) in the simulations supported by this study was significantly larger than the concentrated region formed by necking, it would have been ideal to retain material softening near failure (resulting from necking in the experimental specimens) in the FE constitutive curves. However, including softening in constitutive curves can cause numerical instabilities. Therefore, the FE constitutive curves were simplified such that the maximum stress was held constant until failure occurs, as shown in Fig. 4.20. If elements were sufficiently small to simulate necking behavior directly, it would be more appropriate to continue the constitutive curves at a constant positive slope from the point at which necking initiates.

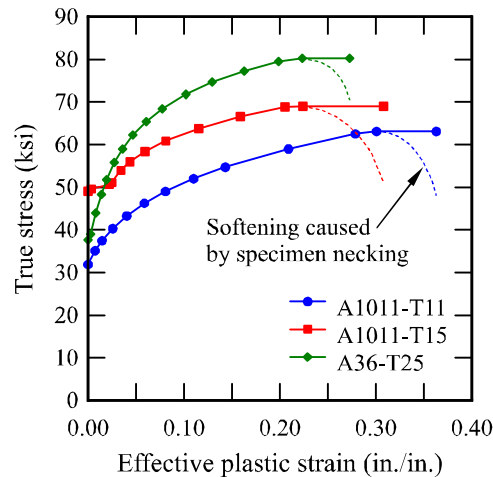


Figure 4.20 Static constitutive curves developed for the MAT_24 material model in LS-DYNA

4.5.4 Implementation in LS-DYNA

LS-DYNA input data for the three constitutive models developed in this study are provided in this section. Note that the models are expressed in terms of U.S. customary units (kip and in.). Each model consists of two parts: a material definition (denoted *MAT_PIECEWISE-_LINEAR_PLASTICITY), and a curve definition (denoted *DEFINE_CURVE) consisting of the true stress versus effective plastic strain curve. This curve is referenced by the parameter LCSS in the material definition. Cowper-Symonds coefficients are defined by parameters C and P in the material definition. For all three models, mass density (ρ_0) is equal to 7.34×10^7 kip/in./s² (490 pcf), Young's modulus (E) is equal to 30,000 ksi, and Poisson's ratio (PR) is equal to 0.30. See LSTC (2007) for details on other parameters in the material definitions.

4.5.4.1 A1011-T11 model

```

*MAT_PIECEWISE_LINEAR_PLASTICITY
$#      mid      ro      e      pr      sigy      etan      fail      tdel
      1 7.3400E-7 30000.000 0.300000 0.000 0.000 0.363000 0.000
$#      c      p      lcss      lcsr      vp
9.2000E+6 10.000000 1 0 1.000000
$#      eps1      eps2      eps3      eps4      eps5      eps6      eps7      eps8
      0.000      0.000      0.000      0.000      0.000      0.000      0.000      0.000
$#      es1      es2      es3      es4      es5      es6      es7      es8
      0.000      0.000      0.000      0.000      0.000      0.000      0.000      0.000
*DEFINE_CURVE
$#      LCID      SIDR      SFA      SFO      OFFA      OFFO      DATTYP
      1      0      0.000      0.000      0.000      0.000      0
$#
      A1      O1
      0.000      31.9029999
      0.0073300      35.1220016
      0.0146600      37.4809990
      0.0256600      40.3069992
      0.0403200      43.2869987
      0.0586400      46.2369995
      0.0806300      49.0439987
      0.1099600      51.9939995
      0.1429400      54.6850014
      0.2089200      58.9760017
      0.2785600      62.5239983
      0.3005500      63.0989990
      0.3628600      63.1989990

```

4.5.4.2 A1011-T15 model

```

*MAT_PIECEWISE_LINEAR_PLASTICITY
$#      mid      ro      e      pr      sigy      etan      fail      tdel
      2 7.3400E-7 30000.000 0.300000 0.000 0.000 0.308000 0.000
$#      c      p      lcss      lcsr      vp
2.0500E+7 10.000000 2 0 1.000000
$#      eps1      eps2      eps3      eps4      eps5      eps6      eps7      eps8
      0.000      0.000      0.000      0.000      0.000      0.000      0.000      0.000
$#      es1      es2      es3      es4      es5      es6      es7      es8
      0.000      0.000      0.000      0.000      0.000      0.000      0.000      0.000
*DEFINE_CURVE
$#      LCID      SIDR      SFA      SFO      OFFA      OFFO      DATTYP
      2      0      0.000      0.000      0.000      0.000      0
$#
      A1      O1
      0.000      49.0219994
      0.0031100      49.5880013
      0.0217900      50.6160011
      0.0249000      51.1139984
      0.0342400      53.9729996
      0.0435800      55.9269981
      0.0591400      58.3639984
      0.0809300      60.8370018
      0.1151600      63.7290001
      0.1587400      66.6259995
      0.2054300      68.9059982
      0.2241000      69.0049973
      0.3081400      69.1049973

```

4.5.4.3 A36-T25 model

```

*MAT_PIECEWISE_LINEAR_PLASTICITY
$#      mid      ro      e      pr      sigy      etan      fail      tdel
      3 7.3400E-7 30000.000 0.300000 0.000 0.000 0.273000 0.000
$#      c      p      lcss      lcsr      vp
1.3200E+6 8.000000 3 0 1.000000
$#      eps1      eps2      eps3      eps4      eps5      eps6      eps7      eps8
      0.000      0.000      0.000      0.000      0.000      0.000      0.000      0.000
$#      es1      es2      es3      es4      es5      es6      es7      es8
      0.000      0.000      0.000      0.000      0.000      0.000      0.000      0.000
*DEFINE_CURVE
$#      LCID      SIDR      SFA      SFO      OFFA      OFFO      DAT TYP
      3      0      0.000      0.000      0.000      0.000      0
$#
      A1      O1
      0.000      37.6539993
      0.0027600      38.9379997
      0.0082700      44.0110016
      0.0137800      48.3460007
      0.0192900      51.7560005
      0.0275600      55.7610016
      0.0358200      58.8940010
      0.0468500      62.1980019
      0.0606300      65.3919983
      0.0771600      68.3750000
      0.1019600      71.7929993
      0.1295200      74.7030029
      0.1625900      77.3229980
      0.1984100      79.5319977
      0.2232200      80.2129974
      0.2728200      80.3129974

```

4.6 Concluding Remarks

The strain-rate sensitive constitutive behavior of A36 and A1011 steel was investigated in this study by means of uniaxial tension testing at eight strain rates, covering seven orders of magnitude. A novel high-rate testing apparatus (HRTA) was designed which employed an impact pendulum as the source of energy. Finite element constitutive models were also developed that are appropriate for use in vessel impact analysis. The following conclusions can be drawn from the results presented in this chapter:

1. The yield and strain hardening behavior of the two thicknesses of A1011 steel tested differed significantly, while excellent repeatability was observed between specimens of the same thickness. The differences are more likely attributable to variability between steel batches than to any consequence of the difference in thickness;
2. The HRTA employed elastic impact as the means of breaking specimens, in which the momentum of the impacted object (anvil) provided the breaking energy, not the momentum of the impactor (striker). This design avoided the problem of ringing vibrations observed in prior studies that have employed impact-based test machines. No impact damping was required, resulting in rapid specimen acceleration;

3. The HRTA drive line was designed to act as a single degree of freedom (SDF) oscillating system, so that inertial effects in the drive line could be measured and removed from the data. However, flexibility between the SDF mass and drive line anchor rod resulted in a multiple degree of freedom (MDF) response. Because it was infeasible to redesign and reconstruct the HRTA within the scope of this study, an alternative data processing procedure (based on impulse-momentum principles that are not reliant on SDF behavior) was employed successfully. However, the SDF drive line concept does hold promise for future testing, as a way of mitigating the deleterious influence of drive line inertia on the measured data;
4. The materials tested in this study were found to be significantly less sensitive to strain rate than many prior studies. Consequently, calculated Cowper-Symonds coefficients were much larger than the values $C = 40.4 \text{ s}^{-1}$ and $P = 5$ commonly employed for mild steel;
5. Rate sensitivity, however, was very similar between the specimens tested in this study, despite being of different material grades.

CHAPTER 5

PRELIMINARY FINITE ELEMENT SIMULATIONS OF REDUCED-SCALE BARGE IMPACT

5.1 Introduction

As discussed in the previous chapters, the finite element (FE) simulation techniques that are the basis for the UF/FDOT barge impact load model were validated in this study against pendulum impact experiments involving reduced-scale barge bow specimens by comparing observed behavioral trends. As discussed in the present chapter, constitutive models that were developed based on experimental testing (Chapter 4) were incorporated into a reduced-scale version of the jumbo hopper barge bow FE model, and preliminary impact simulations were conducted in order to ascertain the behavioral influence of the revised constitutive models.

5.2 Implementation of Finite Element Constitutive Models

The finite element constitutive models (material models) described in Chapter 4 (referred to hereafter as the ‘revised constitutive models’) were integrated into the 0.4-scale FE barge model that was used in the planning stages of the experimental study (see Chapter 3). Specifically, the representative constitutive model for A36 that was employed in various prior studies (Consolazio et al. 2009, 2010a, 2010b, 2012a, Consolazio and Walters 2012, Getter and Consolazio 2011) with Cowper-Symonds coefficients $C = 40.4 \text{ s}^{-1}$ and $P = 5$ was replaced with the revised models. Note that the same LS-DYNA material model type (MAT_PIECEWISE-_LINEAR_PLASTICITY) was employed in both the original and revised constitutive models.

Each of the revised constitutive models was assigned to specific parts of the FE barge model based on the 0.4-scale thickness of the material. Hull, gusset, and stiffener plates with thicknesses equal to 0.115 in. were assigned the A1011-T11 constitutive model, plates with thickness equal to 0.155 in. were assigned the A1011-T15 constitutive model, and plates with thickness equal to 0.25 in. were assigned the A36-T25 constitutive model. While the internal structural members (angles and channels) have individual element thicknesses that are less than 0.25 in., such members are commercially manufactured and available from A36 steel. Therefore, the A36-T25 constitutive model was assigned to these parts.

5.3 Barge Impact Simulations

Using the revised FE model, preliminary impact simulations were conducted that were consistent with the impact conditions expected during the planning phase of the research program. As shown in Fig. 5.1, the simulations consisted of a 9,000-lbf rigid impact block and the fully-deformable 0.4-scale barge bow model. As will be discussed in later chapters, the actual impact block weight varied depending on which nose attachment was utilized (9,219-lbf with the round nose, and 9,700-lbf with the flat-faced nose). For simplicity, the impact block was assigned roller-type translating boundary conditions that only permit motion in the x-direction, and barge nodes at the rear-most interface were assigned fixed boundary conditions. While it is acknowledged that these simplified boundary conditions do not precisely represent the physical

support conditions of either the impact block (hanging from steel cables) or the barge bow (mounted to a reaction frame that is not perfectly rigid), they are sufficient to investigate the behavioral changes introduced by implementing the revised constitutive models.

To initiate each impact simulation, the impact block was assigned an initial velocity equal to 39.3 ft/s, which corresponds to a pendulum drop height of 24 ft (The actual impact tests were conducted at drop heights ranging from 14 ft to 20 ft). Subsequently, the block model impacted the barge bow model, causing several inches of bow deformation and ultimately arresting block motion. Elastic rebound of the barge bow caused the impact block motion to reverse, and contact between the objects eventually ceased. Recall that, in the impact experiments, multiple successive impacts were required in order to achieve target deformation levels. Therefore, to simulate this action, the analysis was stopped at the instant that contact ceased, and then restarted by assigning the impact block a new initial velocity of 39.3 ft/s. This process was repeated to simulate a total of five impacts, in which barge bow damage was accumulated with each successive impact. Two simulation series were conducted: one in which the impact block had a round nose (as shown in Fig. 5.1), and one with a flat-faced impact block with the same width as the round nose block. Results from these simulations are discussed in the following sections.

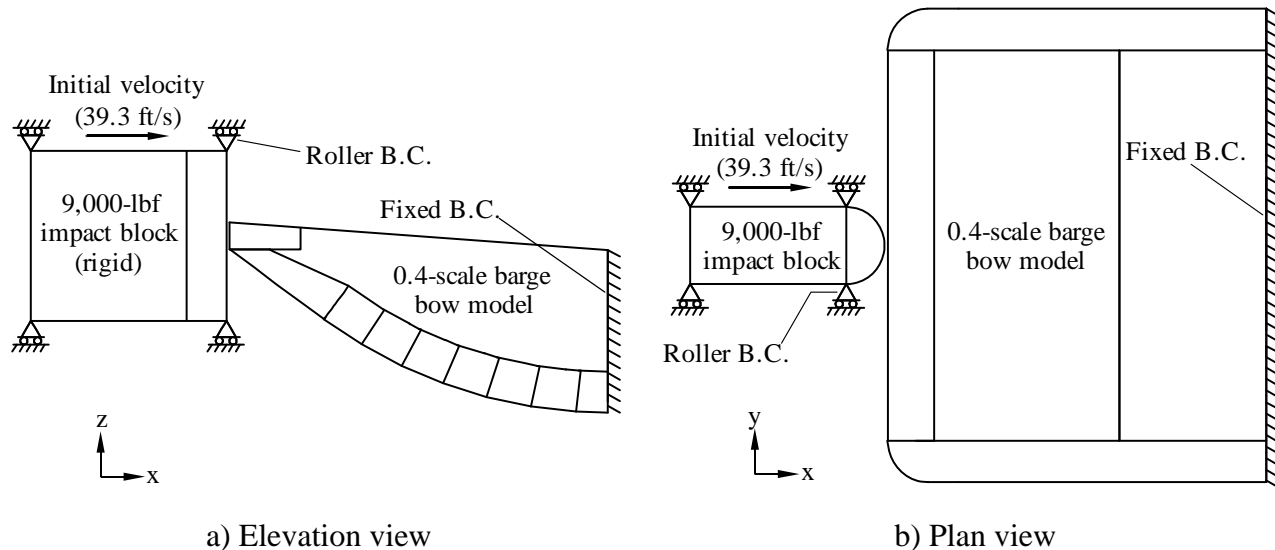


Figure 5.1 Finite element impact simulation of 0.4-scale barge bow (round nose impact block shown)

5.3.1 Impact simulation results (flat-faced block)

In Fig. 5.2, simulated barge bow deformations are presented for successive impacts with the flat-faced impact block. Each figure corresponds to the instant in time at which maximum bow deformation occurred (immediately prior to elastic rebound). As shown, deformation of the exterior of the barge was dominated by hull plate buckling and folding. Interior members (frames and trusses) failed by inelastic buckling. Significant yielding was observed throughout the damaged region, accompanied by localized fracture (characterized in the FE model by element

deletion). As crushing deformation increased, membrane action of the headlog plate pulled the bow corners inward toward the central damaged region. While localized fractures were present—generally resulting from extreme bending and folding of the steel plates—the headlog plate remained largely intact, which permitted continued membrane action. At 48 in. of bow deformation, 905 shell elements (0.75% of the total elements) had been deleted from the barge model. In general, barge bow crushing behavior observed in these simulations was found to be similar in nature to past studies (Consolazio et al. 2009, Getter and Consolazio 2011).

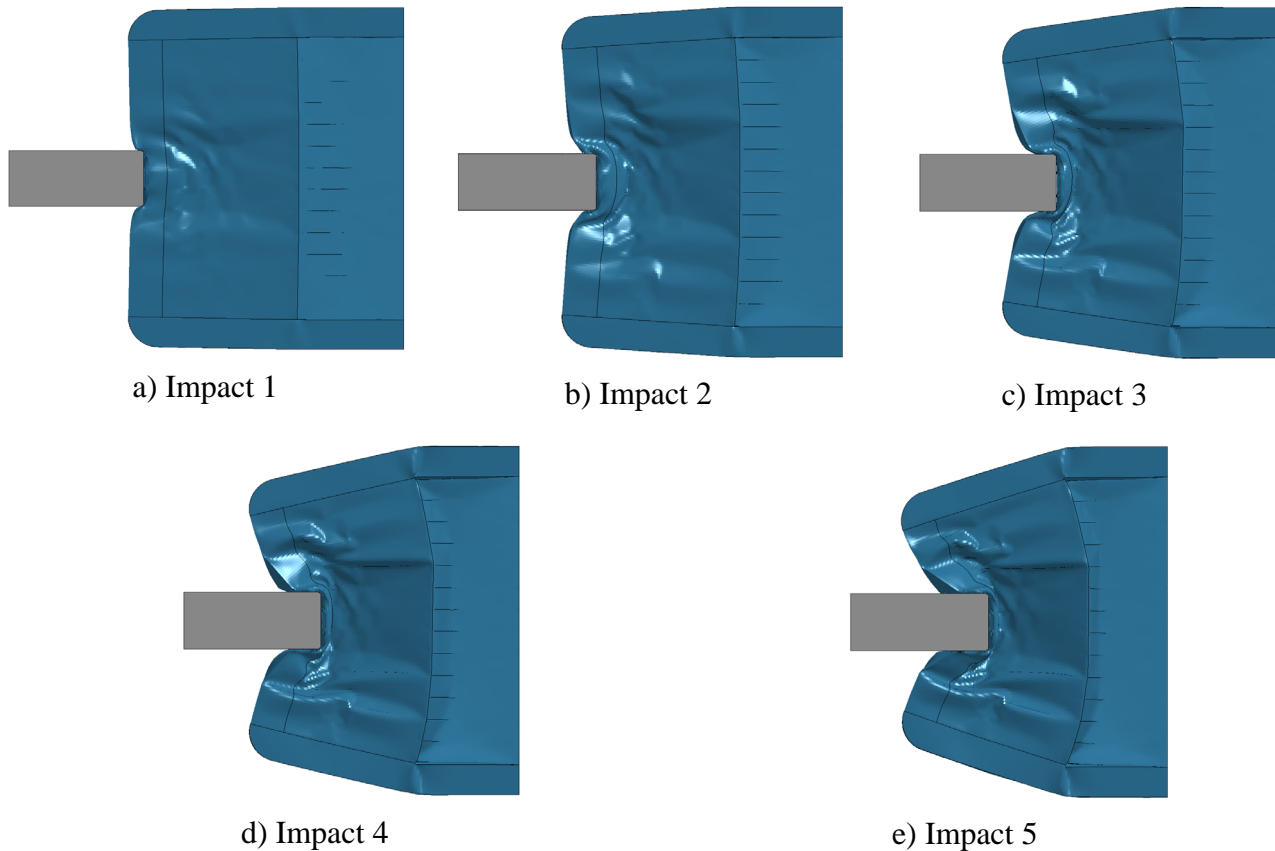
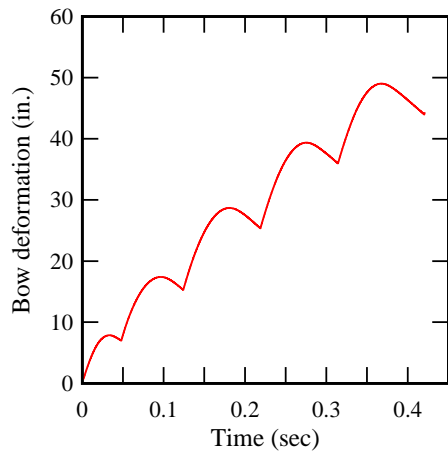
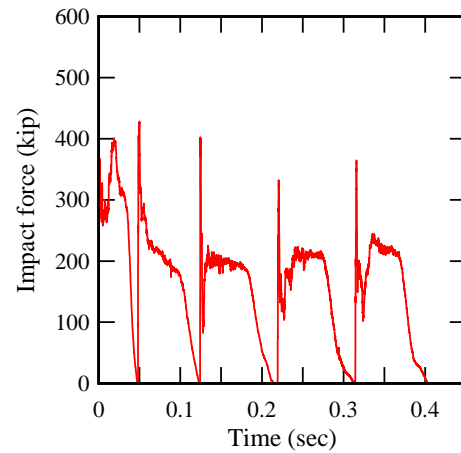


Figure 5.2 Maximum barge bow deformation caused by each successive impact (flat-faced block)

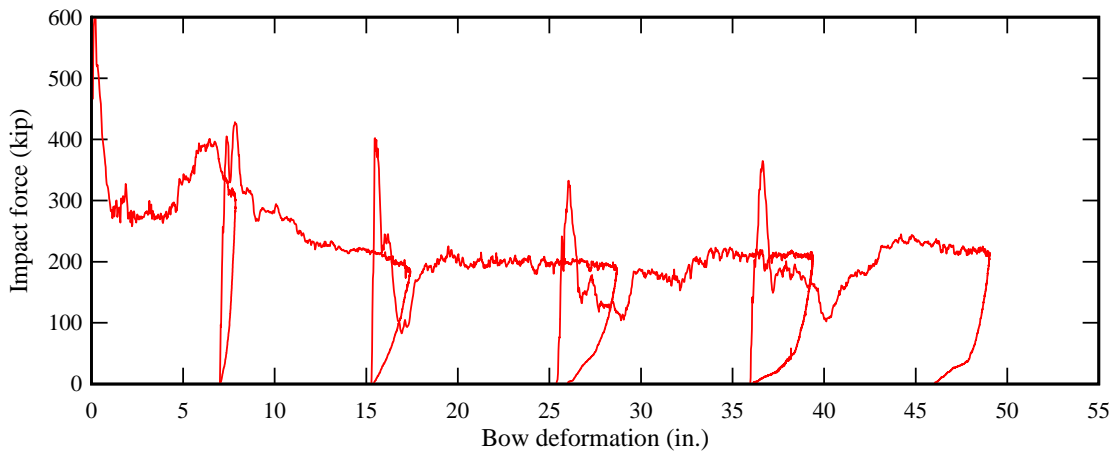
As shown in Fig. 5.3a, barge bow deformation increased with each successive impact, slightly exceeding the target deformation of 48 in. during the fifth impact. As shown in Table 5.1, each impact generated 8 – 11 in. of incremental barge deformation, with 1 – 5 in. of elastic rebound (note that the magnitude of elastic rebound increased with successive impacts). Impact force-time histories for all five impacts are shown in merged format Fig. 5.3b. Impact forces were higher for the first few impacts, after which forces were approximately constant. By merging force deformation data obtained from the five successive impact events, a reasonable approximation of the overall barge bow force-deformation curve is produced, as shown in Fig. 5.3c.



a) Deformation-time history



b) Force-time history



c) Force-deformation curve

Figure 5.3 Barge impact simulation data (flat-faced block)

Table 5.1 Summary of barge bow impact response data (flat-faced block)

Impact number	Maximum deformation (in.)	Residual deformation (in.)	Elastic rebound (in.)	Maximum impact force (kip)	5% exceedance impact force (kip)	Impact duration (msec)
1	7.9	7.0	0.9	1,070	394	48
2	17.4	15.3	2.1	428	292	76
3	28.7	25.4	3.3	402	206	95
4	39.4	36.0	3.4	333	217	95
5	49.0	44.0	5.0	365	233	106

Peak forces for each impact were significantly higher than the sustained portion of the impact event, but the peaks were extremely short in duration. It is important to point out that the magnitudes of such short-duration force peaks are of limited interest with regard to the model

validation, because they are likely a consequence of the idealized impact conditions in the finite element simulations (i.e., perfectly aligned head-on impact).

Therefore, a more meaningful measure of maximum impact force is the maximum of the sustained portion of the impact event. A variety of different methods could be employed to define the maximum sustained force, all of which include some level of subjectivity. It was observed that short-duration force peaks that were significantly higher in magnitude than the sustained portion of the curve. Therefore, for this study, such peaks were considered to be outliers with respect to the remainder of each impact force-time history. Therefore, the maximum *sustained* force was defined as the force corresponding to a 5% temporal probability of exceedance. To compute the 5% exceedance force, an empirical cumulative distribution function (CDF) was developed from the impact force data for each impact event, and the force value corresponding to 95% cumulative probability was selected. As a representative example, Fig. 5.4 illustrates this procedure for the first impact event. As summarized in Table 5.1, 5% exceedance forces were significantly smaller than raw peak forces, implying that raw peak forces were not a representative measure of physical impact force magnitude.

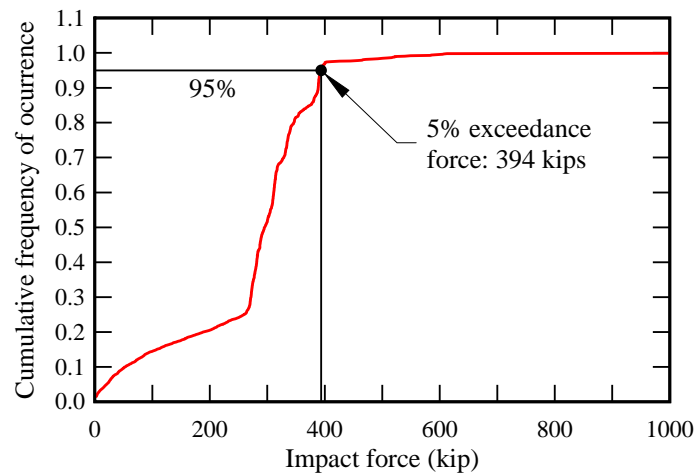


Figure 5.4 Empirical CDF of impact force data from first pendulum impact event

5.3.2 Sensitivity of results to steel constitutive model (flat-faced block)

As noted in Chapter 4, during the initial planning stages of this study, a representative constitutive model for ASTM A36 steel was adopted from available literature and employed in the reduced-scale impact simulations (this model is hereafter referred to as the ‘original constitutive model’). The original constitutive model employed a stress-strain relation published by Salmon and Johnson (1996), with a 36-ksi yield stress, 58-ksi ultimate stress, and failure strain equal to 0.2 in./in. The Cowper-Symonds model was used to model strain rate sensitivity, with coefficients $C = 40.4 \text{ s}^{-1}$, and $P = 5$ (Jones 1997). In preparation for the FE model validation, the original constitutive model was replaced with the material-specific revised constitutive models that were developed from material testing program (Chapter 4). The revised models are considered more accurate, because they were developed based on experimental

testing of the specific materials from which the reduced-scale barge specimens were fabricated. Given the differences between the two constitutive models, it was of interest to evaluate the level of sensitivity that the constitutive model selection (original or revised) had on impact simulation results obtained.

It is important to note that the Cowper-Symonds rate-sensitivity model can be employed in two possible ways in the LS-DYNA material model used in this study (MAT_24). First, if parameter $SIGY > 0$ (generally one would choose $SIGY$ to be equal to the yield stress), then dynamic stress (σ_{dyn}) is computed in LS-DYNA as:

$$\sigma_{dyn}(\varepsilon_p, \dot{\varepsilon}_p) = \sigma_{st}(\varepsilon_p) + SIGY \cdot \left(\frac{\dot{\varepsilon}_p}{C} \right)^{1/P} \quad (5.1)$$

where, σ_{st} is the static stress (as defined by the user-specified material curve), ε_p is the effective plastic strain, $\dot{\varepsilon}_p$ is the effective plastic strain rate, and C and P are the Cowper-Symonds coefficients. This stress scaling rule results in a shift (offset) of stress values in the stress-strain relation, where the shift is constant (does not vary) with respect to strain level. Consequently, for a material that exhibits strain hardening, yield stress is modeled as being more sensitive (in a ratio sense, σ_{dyn}/σ_{st}) to strain rate than ultimate stress (i.e., for a constant increase of stress, the percentage increase in yield stress will be larger than the percentage increase in ultimate stress). As discussed in Chapter 4, values for $C = 40.4 \text{ s}^{-1}$ and $P = 5$ (employed in the original constitutive model) are based on a study by Manjoine (1944) which found that yield stress was indeed more sensitive to high strain rates than ultimate stress (for the materials tested in the study). Therefore, the scaling rule defined by Eqn. 5.1 was appropriate for use in the original constitutive model employed during the planning stages.

However, if parameter $SIGY = 0$ in MAT_24, then LS-DYNA employs an alternative stress scaling rule:

$$\sigma_{dyn}(\varepsilon_p, \dot{\varepsilon}_p) = \sigma_{st}(\varepsilon_p) \cdot \left[1 + \left(\frac{\dot{\varepsilon}_p}{C} \right)^{1/P} \right] \quad (5.2)$$

For a particular strain rate, Eqn. 5.2 produces a uniform *scaling* of stress, rather than a uniform (constant) *shifting* of stress (as was the case in Eqn 5.1). Therefore, in a ratio sense (σ_{dyn}/σ_{st}), yield and ultimate stresses are modeled in Eqn. 5.2 as equally sensitive to strain rate. As discussed in Chapter 4, the steel materials tested in this study were found to have approximately equal levels of rate sensitivity for yield and ultimate stress. Therefore, the scaling rule defined by

Eqn. 5.2 was employed in the revised constitutive models. Detailed material model parameters for both the revised and original constitutive models are summarized in Table 5.2.

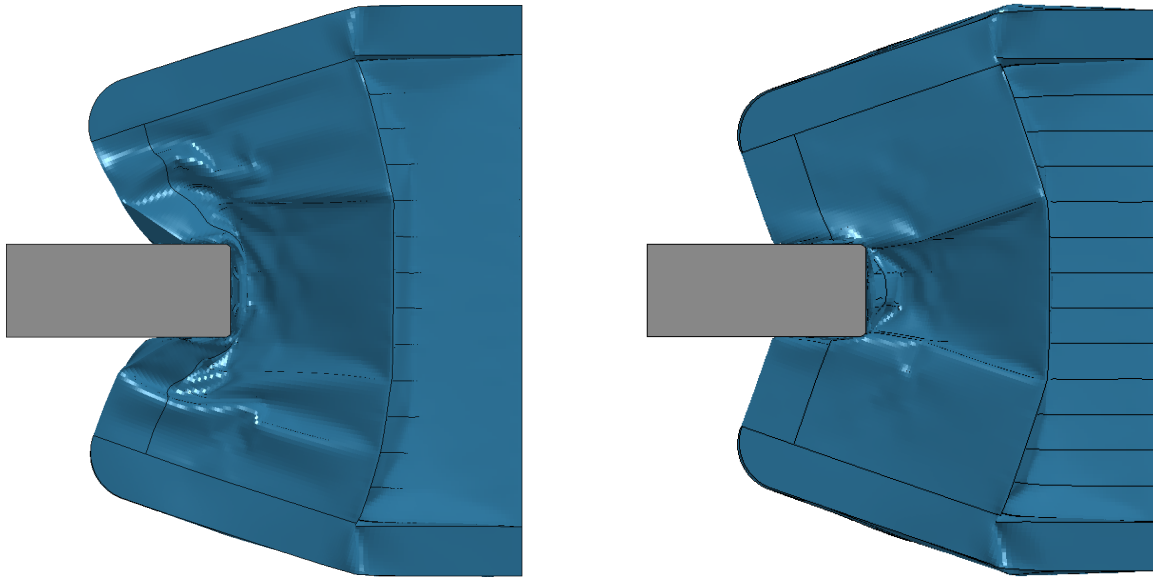
Table 5.2 Comparison of constitutive model parameters

Constitutive model	Barge bow components	Stress-strain relation	Dynamic stress scaling rule	C (s ⁻¹)	P	Failure strain (in./in.)
Revised	Selected	A1011-T11 ¹	Eqn. 5.2	9,200,000	10	0.363
	Selected	A1011-T15 ¹	Eqn. 5.2	20,500,000	10	0.308
	Selected	A36-T25 ¹	Eqn. 5.2	1,320,000	8	0.273
Original	All	Salmon & Johnson (1996) ²	Eqn. 5.1	40.4	5	0.200

¹ See Chapter 4 for details.

² See Consolazio et al. (2009, 2010a, 2010b, 2012a) and Consolazio and Walters (2012b) for details.

To evaluate the sensitivity of impact simulation results to the choice of constitutive model, two simulations were conducted: one with the revised constitutive models, and one with the original constitutive model. Both simulations included five repeated impacts by the 9,000-lbf flat-faced pendulum impact block, as discussed in the previous section. Fig. 5.5 compares large-scale barge bow deformations that were observed at the maximum deformation level (during the fifth impact). As shown, the simulation with the revised constitutive models (Fig. 5.5) developed more widespread damage across the width of the bow, including significant hull plate bending several feet to either side of the impact block. In contrast, the simulation with the original constitutive model had a damaged region that was only slightly wider than the impact block. However, wrapping of the bow corners toward the impact block (caused by membrane action) was more pronounced in the simulation with the original constitutive model. The differences in deformation were largely a consequence of increased ductility in the revised constitutive models. Specifically, internal structural members in the simulation with revised constitutive models were much less likely to fracture, thus permitting impact forces to flow into a wider area and cause more widespread damage.



a) Revised constitutive model

b) Original constitutive model

Figure 5.5 Comparison of maximum barge bow deformation (flat-faced block)

Force-deformation curves were computed for each impact simulation, and are compared in Fig. 5.6. Overall, differences between the force-deformation curves were relatively minor. The revised constitutive models resulted in slightly higher impact forces for the first and third impact, but lower forces for the fifth impact. Overall ductility of the barge bow was similar between the two simulations. Based on these results, it can be concluded that for flat-faced impact, introducing the revised constitutive models had limited influence on quantitative measures of system-wide impact response. However, qualitative differences in deformation patterns were observed.

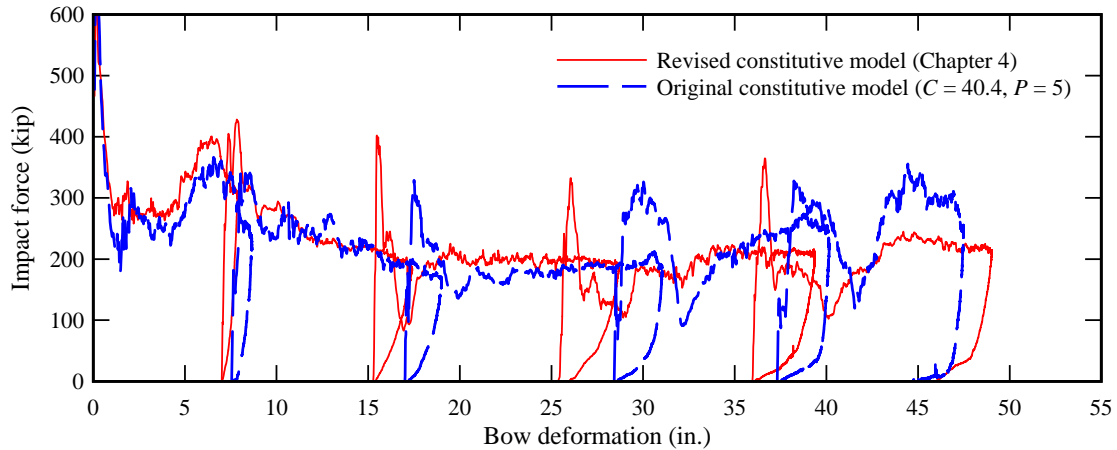


Figure 5.6 Comparison of barge bow force-deformation curves (flat-faced block)

5.3.3 Impact simulation results (round nose block)

In Fig. 5.7, simulated barge bow deformations are presented for successive impacts with the round nose impact block. Each figure corresponds to the instant in time at which maximum bow deformation occurred (immediately prior to elastic rebound). As with the flat-faced impact scenario, deformation of the exterior of the barge was dominated by hull plate buckling and folding. Interior members (frames and trusses) failed by inelastic buckling. Significant yielding was observed throughout the damaged region, accompanied by localized fracture (characterized in the FE model by element deletion). Again, as crushing deformation increased, membrane action of the headlog plate pulled the bow corners inward toward the central damaged region. While localized fractures were present—generally resulting from extreme bending and folding—the headlog plate remained largely intact, which permitted continued membrane action. At 48 in. of bow deformation, 969 shell elements (0.81% of the total elements) had been deleted from the barge model. In general, the barge bow crushing behavior observed in these simulations was found to be similar in nature to past studies (Consolazio et al. 2009, Getter and Consolazio 2011).

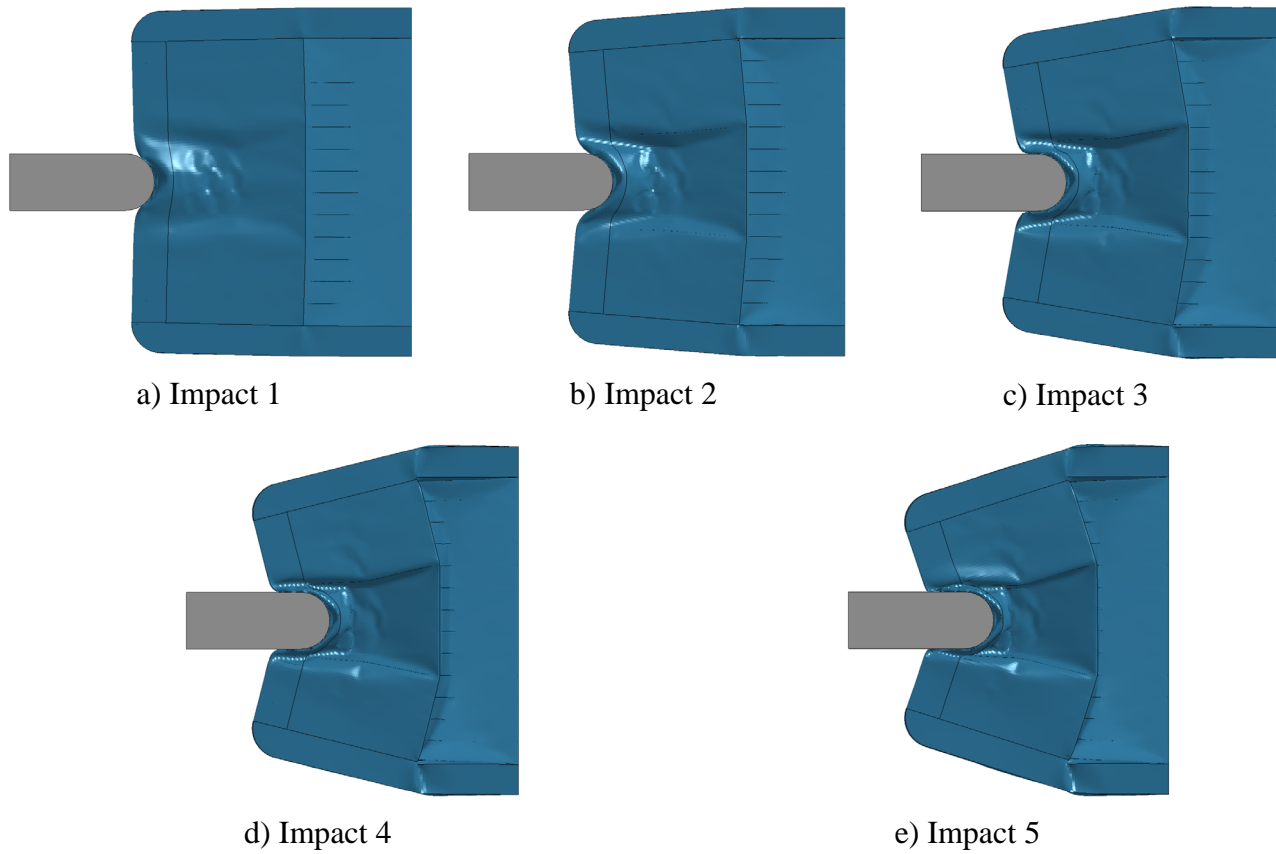
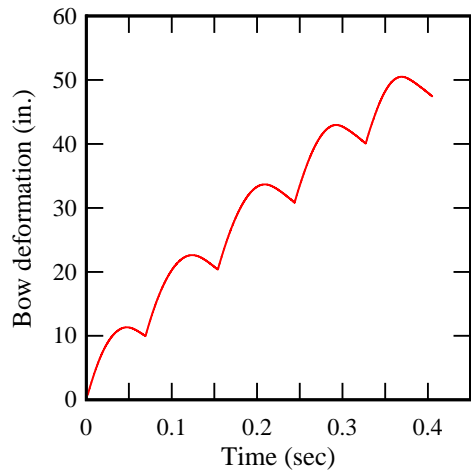
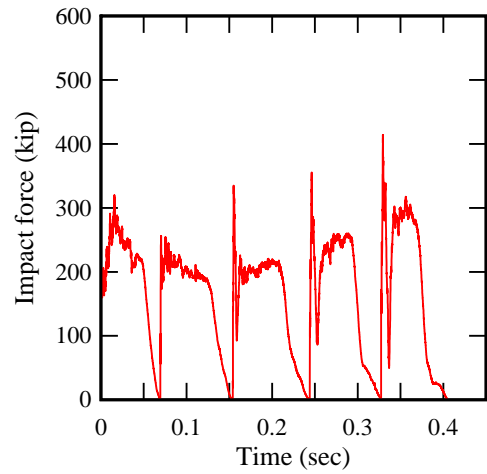


Figure 5.7 Maximum barge bow deformation caused by each successive impact (round nose block)

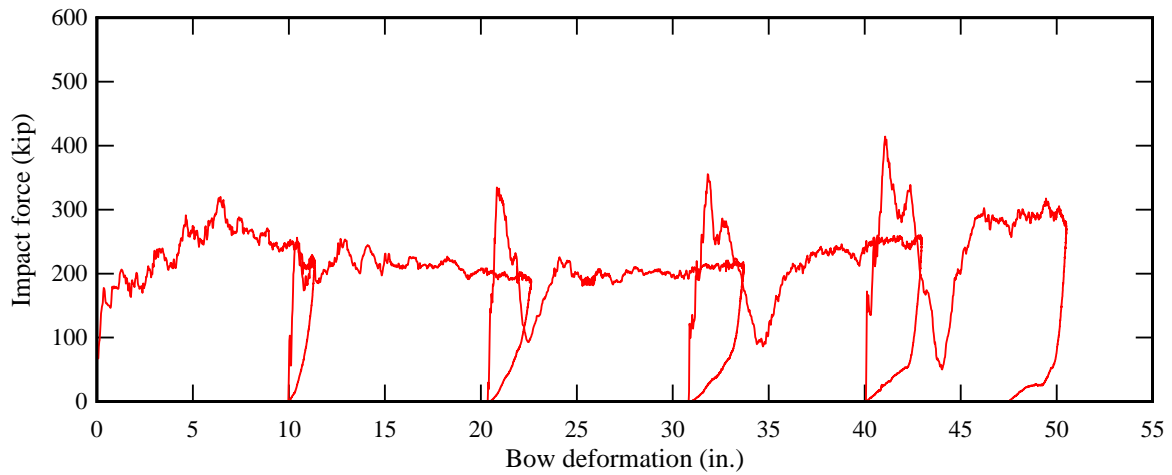
As shown in Fig. 5.8a, barge bow deformation increased with each successive impact, exceeding the 48 in. during the fifth impact. As shown in Table 5.3, each impact generated 8 – 11 in. of incremental barge deformation, with 1 – 3 in. of elastic rebound. The magnitude of elastic rebound increased with successive impacts, but less so than for the flat-faced impact scenario. Impact force-time histories are shown in Fig. 5.8b. During the second and third impacts, force magnitudes generally decreased; however, during the fourth and fifth impacts, forces increased and actually exceeded the initial (first) impact event. Peak forces for each impact were somewhat higher than the sustained portion of the impact event, but, as before, these peaks were short in duration. Therefore, as before, forces corresponding to a 5% temporal probability of exceedance were computed for each impact. As summarized in Table 5.3, 5% exceedance forces were 30 – 120 kips smaller than peak forces, which was a much smaller discrepancy than the flat-faced impact scenario. This outcome was expected, because during impact by a rounded object, barge materials become engaged by the impact block more gradually than a flat-faced impact scenario. Therefore, short-duration force peaks that are primarily caused by rapid engagement of a large region of the barge bow (as occurs during flat-faced impact) are not as prominent for rounded impacts. By merging force deformation data obtained from the five successive impact events, a reasonable approximation of the overall barge bow force-deformation curve is produced, as shown in Fig. 5.8c.



a) Deformation-time history



b) Force-time history



c) Force-deformation curve

Figure 5.8 Barge impact simulation data (round nose block)

Table 5.3 Summary of barge bow impact response data (round nose block)

Impact number	Maximum deformation (in.)	Residual deformation (in.)	Elastic rebound (in.)	Maximum impact force (kip)	5% exceedance impact force (kip)	Impact duration (msec)
1	11.3	10.0	1.3	320	282	69
2	22.6	20.4	2.2	256	226	85
3	33.7	30.8	2.9	335	217	90
4	43.0	40.1	2.9	355	258	83
5	50.5	47.5	3.0	414	308	78

5.3.4 Sensitivity of results to steel constitutive model (round nose block)

For the reasons discussed in Section 5.3.2, an additional round nose impact simulation was conducted with the original constitutive model (as described in Section 5.3.2) in order to assess the sensitivity of simulation results to the choice of constitutive model. Fig. 5.9 compares large-scale barge bow deformations that were observed at the maximum deformation level (during the fifth impact). As shown, overall deformation patterns were similar between the two simulations, with slightly more widespread hull plate buckling in the simulation with the revised constitutive model. Furthermore, where hull plates folded over themselves in the directly impacted headlog region, they remained largely intact in the revised model, while they fractured in the original model. In general, the deformation results indicate that the revised constitutive model resulted in a somewhat more ductile response, as would be expected.

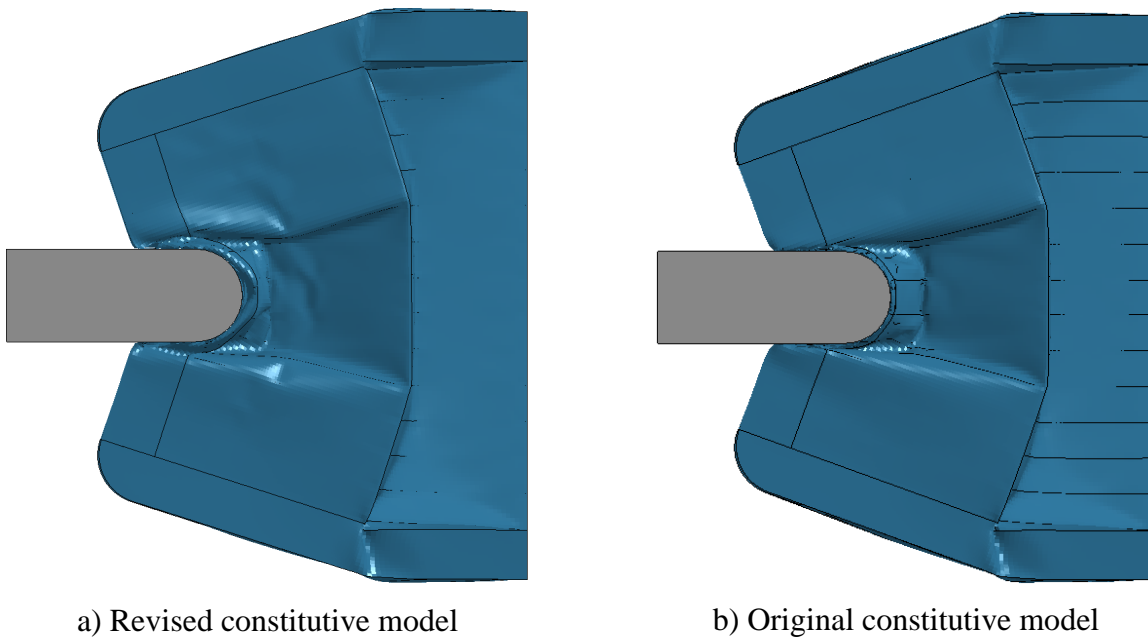


Figure 5.9 Comparison of maximum barge bow deformation (round nose block)

Force-deformation curves were computed for each impact simulation, and are compared in Fig. 5.10. As shown, impact forces were 5 – 10% lower at all deformation levels in the simulation with the original constitutive model. Furthermore, in the original simulation, maximum bow deformations were 1 – 2 in. larger for each individual impact, accumulating to an overall 6 in. difference in maximum deformation (after five impacts). These findings can be attributed to more widespread material fracture in both the hull plates and internal structural members of the simulation that used the original constitutive model. While the results shown in Fig. 5.10 were relatively similar, differences caused by the choice of constitutive model were more pronounced than for the flat-faced impact scenario (Section 5.3.2).

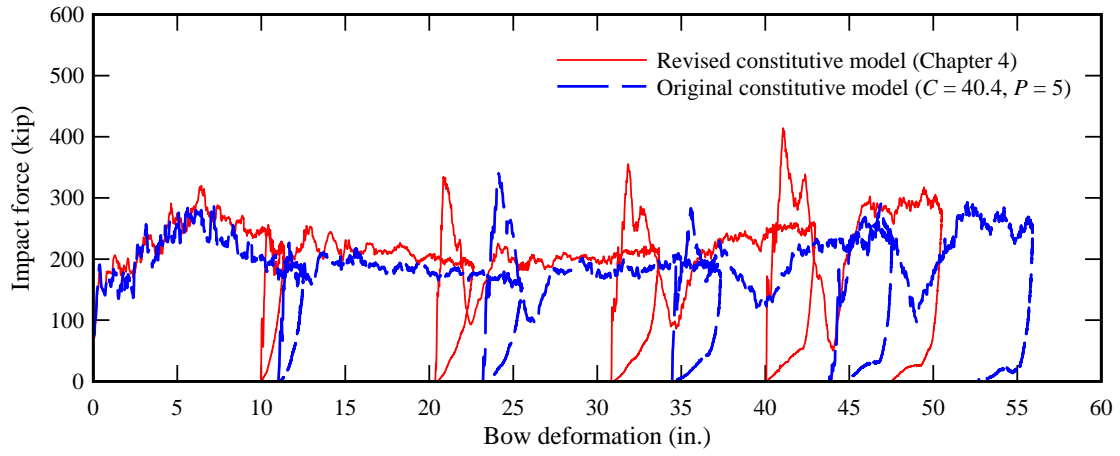


Figure 5.10 Comparison of barge bow force-deformation curves (round nose block)

CHAPTER 6 REDUCED-SCALE BARGE BOW IMPACT TEST PROGRAM

6.1 Introduction

As discussed in previous chapters, reduced-scale (40%-scale) barge bow impact experiments were conducted with the goal of validating the finite element modeling and simulation techniques that are the basis for the Getter and Consolazio (2011) barge impact load prediction model. The experiments involved impacting a stationary replica of a jumbo hopper barge bow with a high-energy impact pendulum to achieve barge bow deformations exceeding 10 ft at full scale (4 ft at pendulum impact model scale). This chapter discusses details pertaining to the components of the experimental setup and the array of instrumentation utilized.

6.2 Experimental Components

As shown in Figs. 6.1 and 6.2, the experimental test setup consisted of a 40%-scale barge bow specimen (referred to as a ‘replicate’ barge bow) supported by a steel reaction frame that was connected to a thick reinforced concrete foundation. The barge bow was impacted by a concrete-filled steel impact block that was suspended from pendulum support towers with a support frame and four cables. Each of these components was designed to resist sustained impact forces exceeding 200 – 300 kips without developing widespread damage (except in the barge bow). Each major component of the test setup is described in more detail in the following sections.

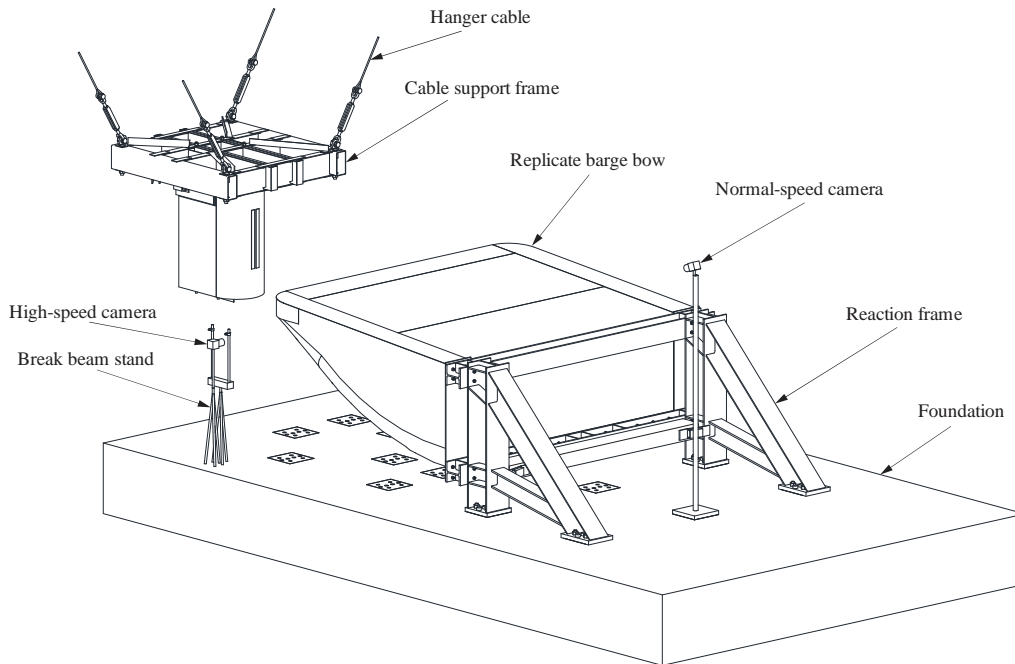


Figure 6.1 Schematic of test setup for barge bow impact experiments



b)

Figure 6.2 Photograph of test setup for barge bow experiments

6.2.1 Reduced-scale barge bow specimens

As discussed in Chapters 3 and 5, two series of impact experiments were conducted: one involving a round nose impact block and one involving a flat-face (rectangular) impact block. Therefore, two replicate barge bows were fabricated—one for each condition. At the model scale of 40%, each replicate barge bow measured approximately 14 ft wide by 11 ft long by 5 ft tall (Fig. 6.3), and had a total steel weight of approximately 3,800 lb. An exploded view of the component-parts of each barge bow is shown in Fig. 6.4a. The internal structure consisted of seven trusses and seven frames oriented along the longitudinal axis of the barge. The trusses and frames were fabricated from structural angle members connected by gusset plates and short channel members. Each sidewall of the barge was stiffened by a simple frame composed of three angles and three diagonal channels. Hull plates of varying thicknesses were provided around the entire bow region. Detailed fabrication drawings (including all dimensions) of the replicate barge bows are provided in Appendix F. Both replicate barge bows were fabricated (Figure 6.4b) by a partnership of Precision Tool and Engineering and All Steel Securities of Gainesville, Florida and then subsequently transported to the FDOT Structures Research Center (Figure 6.4c) in Tallahassee, Florida for impact testing.

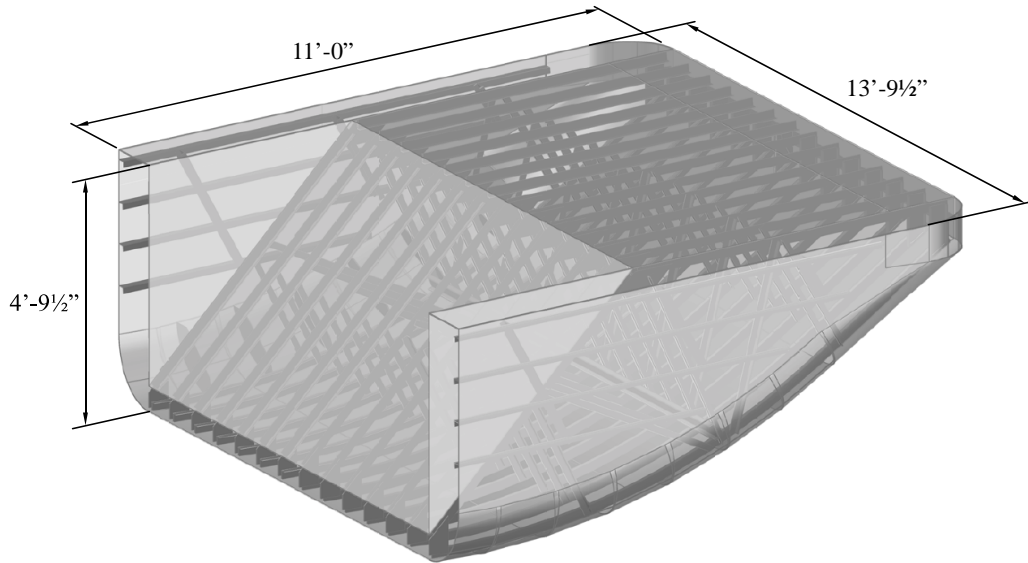
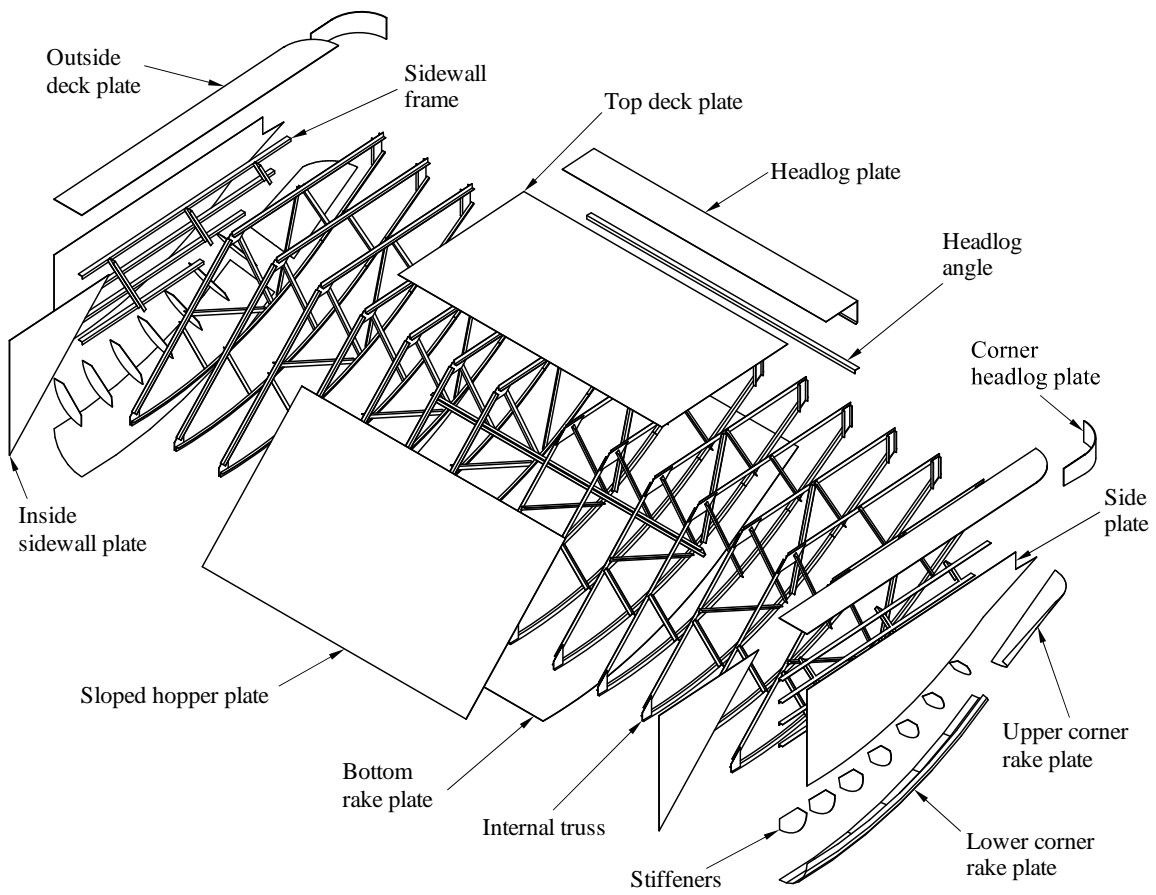


Figure 6.3 Rendering of reduced-scale (40%) barge bow replicate showing internal truss structure



a)



b)



Figure 6.4 Fabrication of replicate barge bow model:
a) Exploded view of replicate barge bow; b) Replicate barge bow during fabrication;
c) Completed replicate barge bow

6.2.2 Barge bow reaction frame

During impact testing, each replicate was supported by an essentially-rigid (relative to the bow stiffness) reaction frame, which was connected to a large structural foundation. As shown in Fig. 6.5, the rear interface of the barge bow was U-shaped. A watertight bulkhead plate covers this entire interface in the full-scale hopper barge from which the 40%-scale replicates were

derived. Therefore, a U-shaped adapter plate, similar in shape to the bulkhead, was welded to the rear face of the 40%-scale bow replicates and used to attach them to the reaction frame. Because the barge specimen needed to be removed and replaced between the two test series, bolted connections were used between the adapter plate and reaction frame.

As shown in Fig. 6.6, the reaction frame consisted of two triangular steel frames (spaced at 12 ft on center) connected transversely by upper and lower support beams. Because the lower support beam was subjected to significant flexural and torsional loads, it was additionally stiffened by attaching a hollow structural section (HSS). The lower support beam and HSS stiffening beam were welded together to act as a composite unit and connected to the reaction frame with a stiffened plate connection. The reaction frame was connected to the foundation using four 2-in. thick baseplates. Additional connection details regarding the frame-foundation connection are provided in the following section. Detailed structural drawings for the reaction frame are provided in Appendix G.

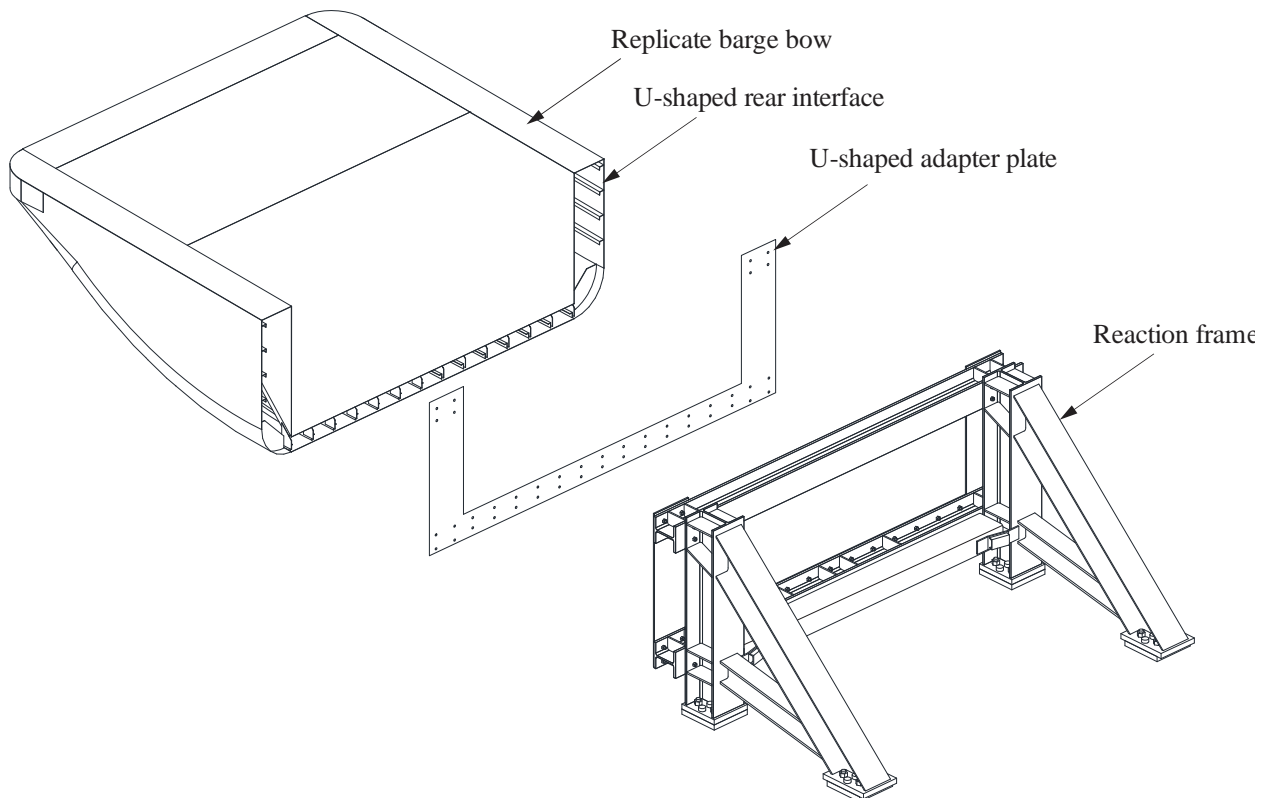


Figure 6.5 Exploded view of connection between replicate barge bow and reaction frame

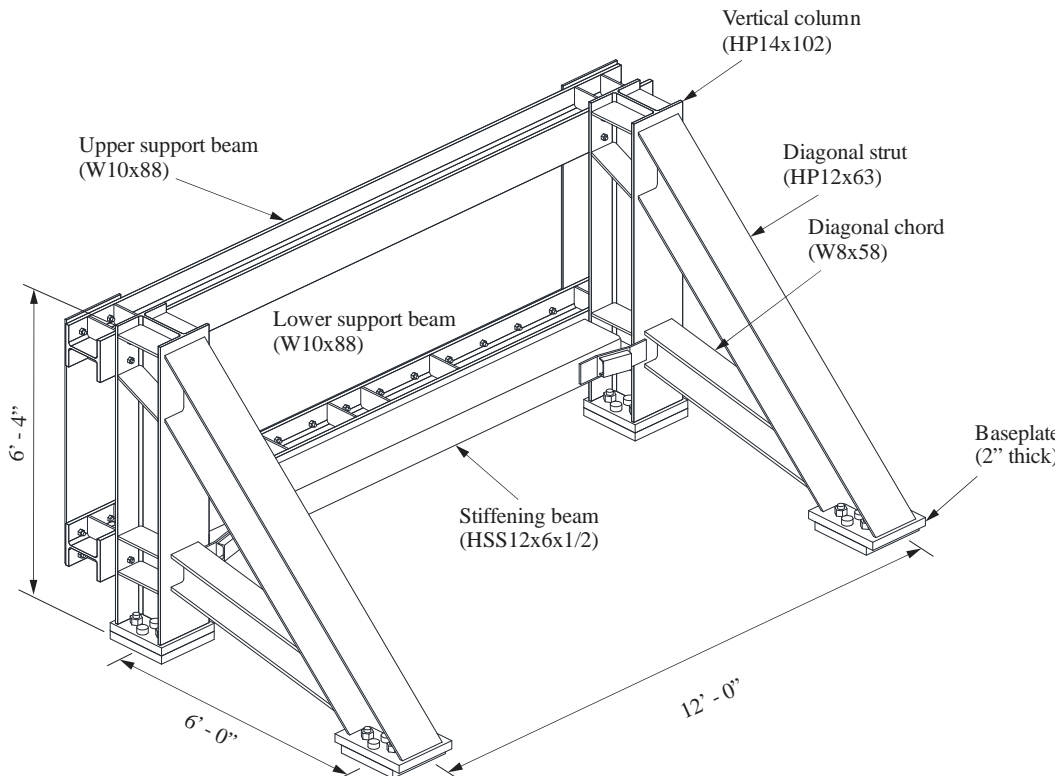


Figure 6.6 Reaction frame structural members and general dimensions

6.2.3 Universal pendulum foundation

The purpose of the reaction frame, which was anchored to a large foundation, was to transfer impact forces from the barge replicate to the soil with minimal horizontal movement in the direction of impact. Unlike traditional laboratory structural foundations, which are typically designed primarily to support vertical loads, the foundation for the barge impact experiments was subjected to horizontal impact loads, as well as moments caused by the vertical eccentricity of the applied impact loads. As a result, the foundation constructed in this study was designed to: develop sufficient lateral soil capacity to resist the applied impact loads; maintain stability against overturning; and minimize lateral movement. Because pendulum impacts generate relatively short-duration dynamic loads, inertial resistance provided by the mass of the foundation acted effectively as an additional source of resistance.

Several foundation design concepts—including deep foundations with one or more drilled shafts; embedded shallow mat foundations; and mat foundations with vertical shear key elements—were considered in the process of developing the design. For brevity, a detailed discussion of the various design concepts that were explored is excluded here. Ultimately, based on balancing lateral dynamic soil capacity, inertial resistance provided by foundation mass, and construction cost, a 3-ft-thick mat foundation was chosen. As shown in Fig. 6.7, the foundation was 34 ft long in the impact direction and 20 ft wide. The footing was fully embedded in the surrounding soil (i.e., the top surface falls at the finished grade elevation) and had a static lateral load capacity of approximately 400 kips, which was developed through skin friction on the bottom surface and side faces and passive soil resistance on the front face. As noted above,

additional lateral resistance was provided by dynamic soil resistance (damping) and the mass of the footing itself.

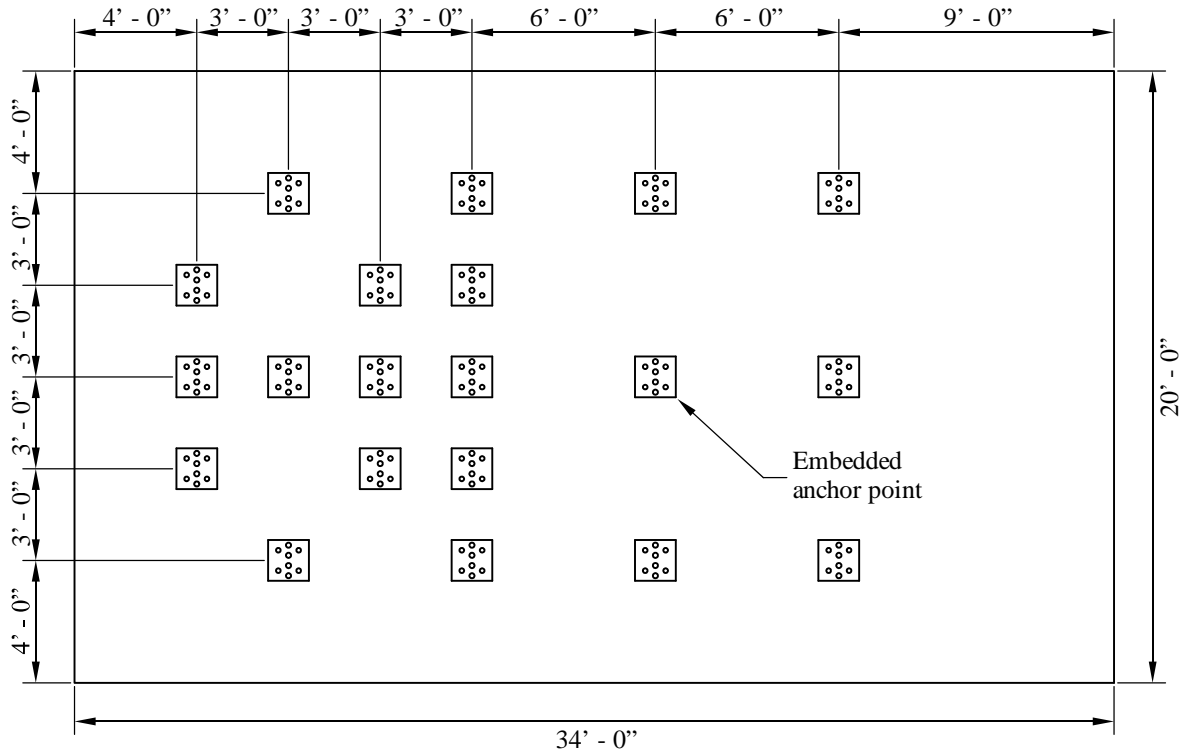


Figure 6.7 Pendulum impact foundation: plan view dimensions

Because the barge impact tests conducted in this study produced at, or near, the most severe loading scenarios that the pendulum is capable of producing (with regard to impact energy), the foundation was intended to be a permanent component of the FDOT pendulum impact test facility; one that will serve also as a ‘universal foundation’ for future FDOT-supported research projects. Consequently, a grid of additional anchor points were provided that were not necessary for the present study but which will enable a wide range of future test articles to be securely mounted for impact testing. The anchor layout shown in Fig. 6.7 (20 anchors total) was determined in coordination with FDOT laboratory staff.

During the barge impact experiments, the anchor system was simultaneously subjected to horizontal impact forces (shear forces) and uplift forces caused by overturning moments applied to the barge bow replicate. Both force components (horizontal and vertical) were expected to reach nearly 200 kips per anchor location (a total of four anchors were used during the barge impact tests to secure the reaction frames). Due to the large shear demand on each anchor, conventional concrete anchor designs that employ embedded bolts or headed studs were impractical. Therefore, each pendulum foundation anchor point (embedded within the 3 ft. thick footing) instead consisted of a triangular frame constructed from heavy structural steel, with a 2-in. thick anchor plate welded on top (Fig. 6.8a). At the base, each triangular frame was welded to a beam, oriented in the long direction of the foundation, that connected all anchors in a given

row together (see Appendix H for additional details). The anchor assemblies (triangular frames and longitudinal beams) were then embedded within the concrete footing.

As shown in Fig. 6.8a, fixtures (such as the barge bow reaction frame) attached to the anchor top plate using two types of fasteners: four 1.5-in. diameter threaded rods and up to four 1.9-in. diameter shear pins. Uplift and moment demands at the fixture-anchor interface were carried by the threaded rods, and shear forces are carried by the shear pins. As shown in Fig. 6.8b, threaded rods were threaded into hex nuts that were embedded in the foundation, underneath the anchor plate. As shown in Fig. 6.8c, holes for the shear pins were slightly oversized (approximately 0.1 in. in diameter) to allow for fabrication tolerances, while holes for the threaded rods were significantly oversized (approximately 0.3 in. in diameter) to avoid subjecting the threaded rods to unintended shear loading. This unique design decoupled the shear and uplift load paths with the intent of minimizing damage to the anchor system that could result from repeated impacts during the design life of the foundation.

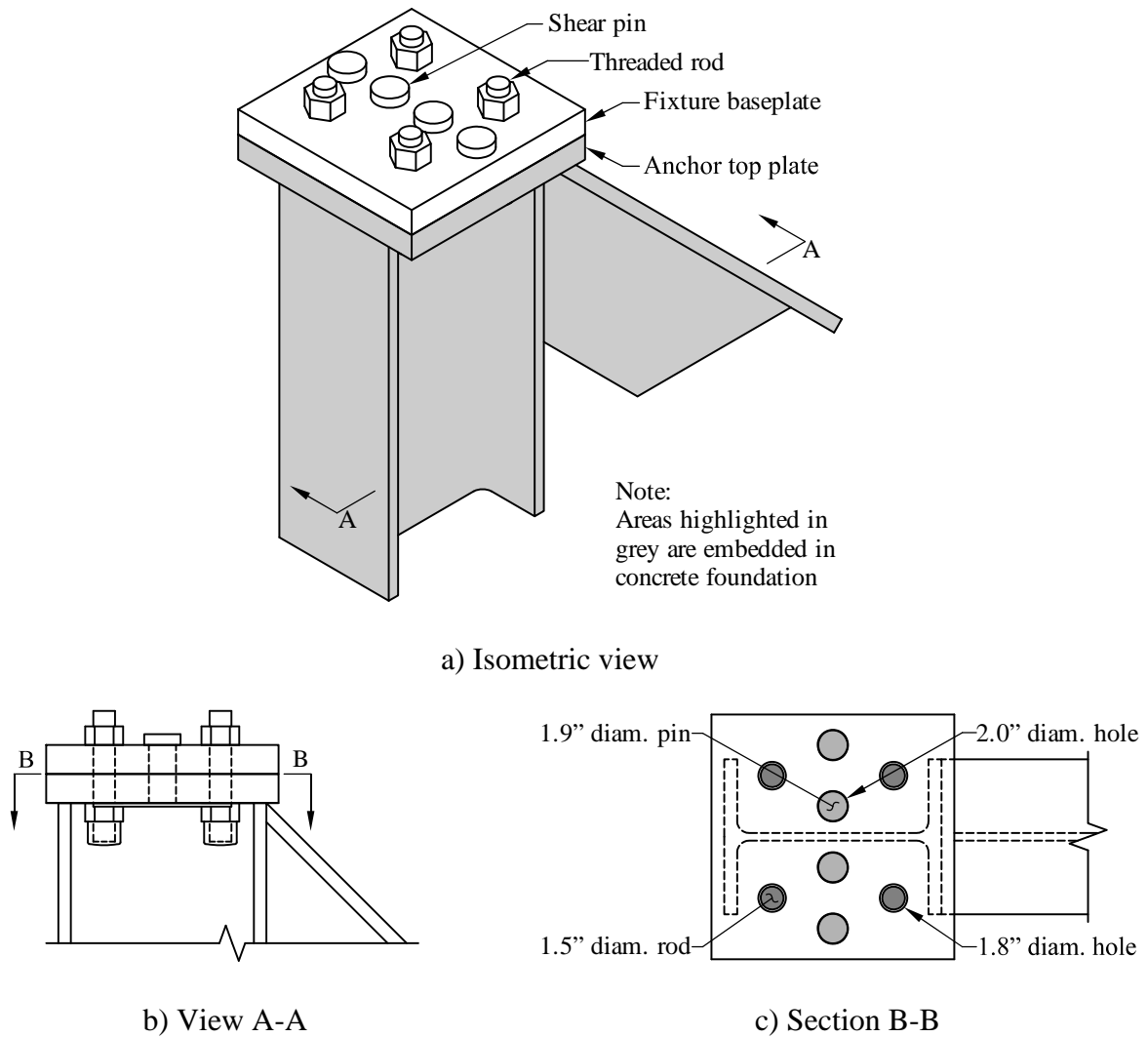


Figure 6.8 Embedded foundation anchor connection system

A site plan for the pendulum towers and universal foundation, located at the FDOT Structures Research Center in Tallahassee, Florida, is shown in Fig. 6.9. The universal foundation was constructed in the southern bay of the pendulum tower array, centered between two towers. Closely-spaced anchors near the leading edge of the foundation will be used in future impact testing of small specimens such as signs and roadside safety equipment. Larger specimens, such as the barge bow replicates tested in the present study, will be mounted to the rear-most anchor rows farthest from the pendulum towers.

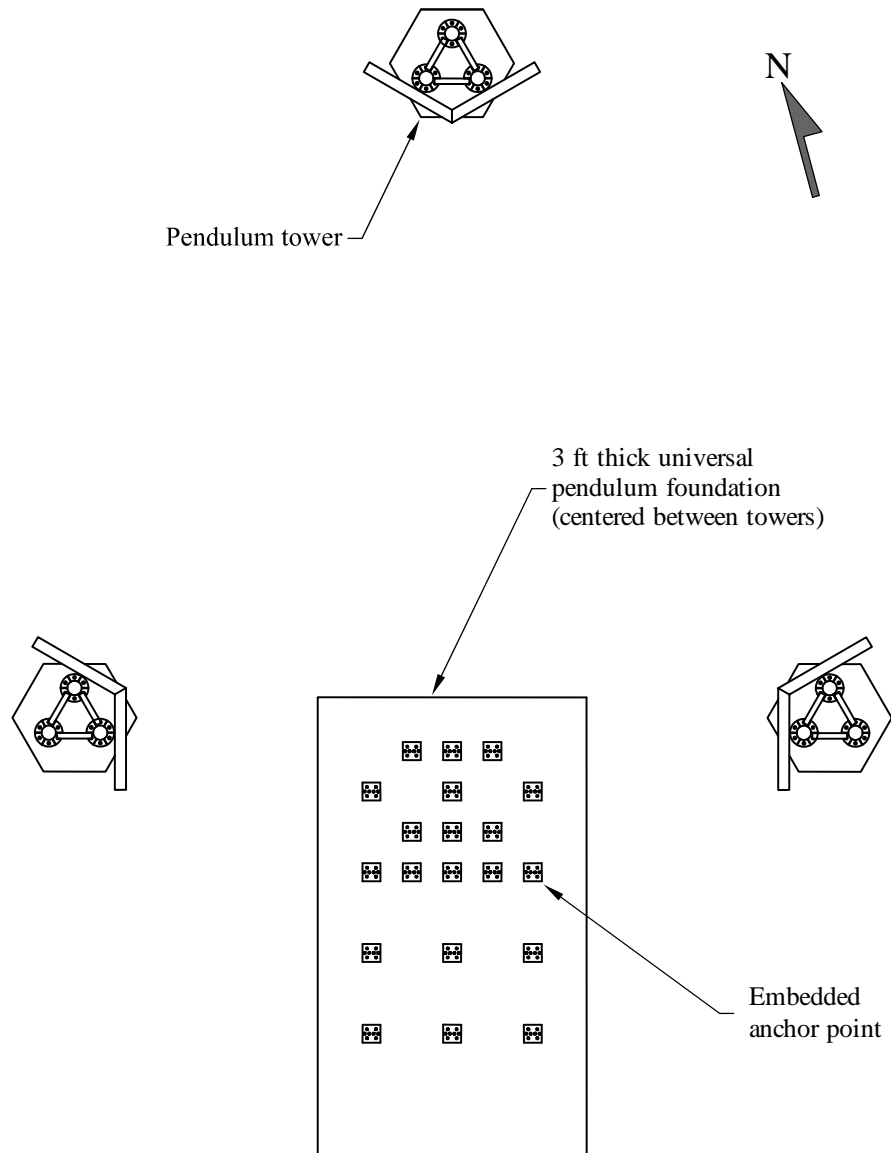


Figure 6.9 Site plan for universal pendulum impact foundation

Fig. 6.10 shows the construction sequence for the pendulum foundation. First, the anchor frames were fabricated, positioned, and fixed together with temporary structural members (Fig. 6.10a). Next, the rebar cage was fabricated (Fig. 6.10b), pre-fabricated steel formwork was installed (not shown), concrete was poured in three lifts separated by 3 – 4 days curing time, and

formwork was removed (Fig. 6.10c). Lastly, soil was backfilled around the finished foundation (Fig. 6.10d) and compacted to improve soil resistance on the vertical surfaces. Detailed fabrication drawings for the universal pendulum foundation are provided in Appendix H.



a)



b)



c)



d)

Figure 6.10 Universal pendulum foundation construction stages (viewed from northwest corner):
a) Anchor frames positioned; b) Reinforcement cage installed; c) Concrete cast (in 3 lifts);
d) Soil backfilled

6.2.4 Impact block and cable support frame

A schematic diagram of the pendulum impact block that was used in the barge impact experiments is shown in Fig. 6.11. The purpose of the block was to impart impact force to the barge bow over a surface area (and shape) that was representative of a bridge pier, and to generate crushing deformation of the barge bow replicate. The impact block was suspended from four cables (attached to two of the pendulum support towers). Using a pull-back cable, pulley, and winch system attached to the third pendulum tower, the block was raised to drop heights between 14 ft. and 20 ft. above the position at incipient contact with the barge replicate. To initiate impact, the block was released from the lifted position, allowing it to swing down and

impact the barge bow. Kinetic energy at the point of impact was thus equal to the stored potential (gravitational) energy at the elevated position prior to release.

As shown in Fig. 6.11, the impact block was constructed as separate pieces to facilitate installation of interchangeable front nose assemblies (Fig. 6.11): one with a round impact surface, and the other with a flat-faced surface. (Note that only *one* of the two nose assemblies was connected to the back block during any given test.) The single back block assembly was reused for both series of impact tests (i.e., round and flat). The components of the impact block—back block and nose—were secured together with two threaded rods and two shear keys located at the interface between the front and rear parts. Due to the raked geometry (i.e., the tapering depth) of the barge bow, a vertical (shear) component of impact force was imparted to the block during each impact event, which necessitated inclusion of a robust shear connection between the rear and front block components.

Each component of the impact block consisted of an internally reinforced, concrete-filled, steel shell structure. A cable support frame (hanger frame) was attached to the top surface of the impact block using four threaded rods which passed through the full depth of the impact block. In order to transfer the inertia of the hanger frame to the impact block during each impact test, a shear connection was provided between the frame and the block. This connection consisted of a series of steel plates welded to the back and sides of the impact block; the plates were extended vertically up from the back block and welded to the hanger frame. This connection transmitted the inertial force of the hanger frame to the block through a combination of shear and flexure in the vertical plates of the connection.

The four main support cables were connected to the hanger frame with swiveling eyebolts. Turnbuckles installed in-line with the cables allowed the vertical position of the impact block to be adjusted in the field. The entire assembly (impact block and hanger frame) weighed approximately 9,219 lbf with the round nose attached, and 9,700- lbf with the flat nose attached. Detailed fabrication drawings for both the impact block and the hanger frame are provided in Appendices I and J, respectively.

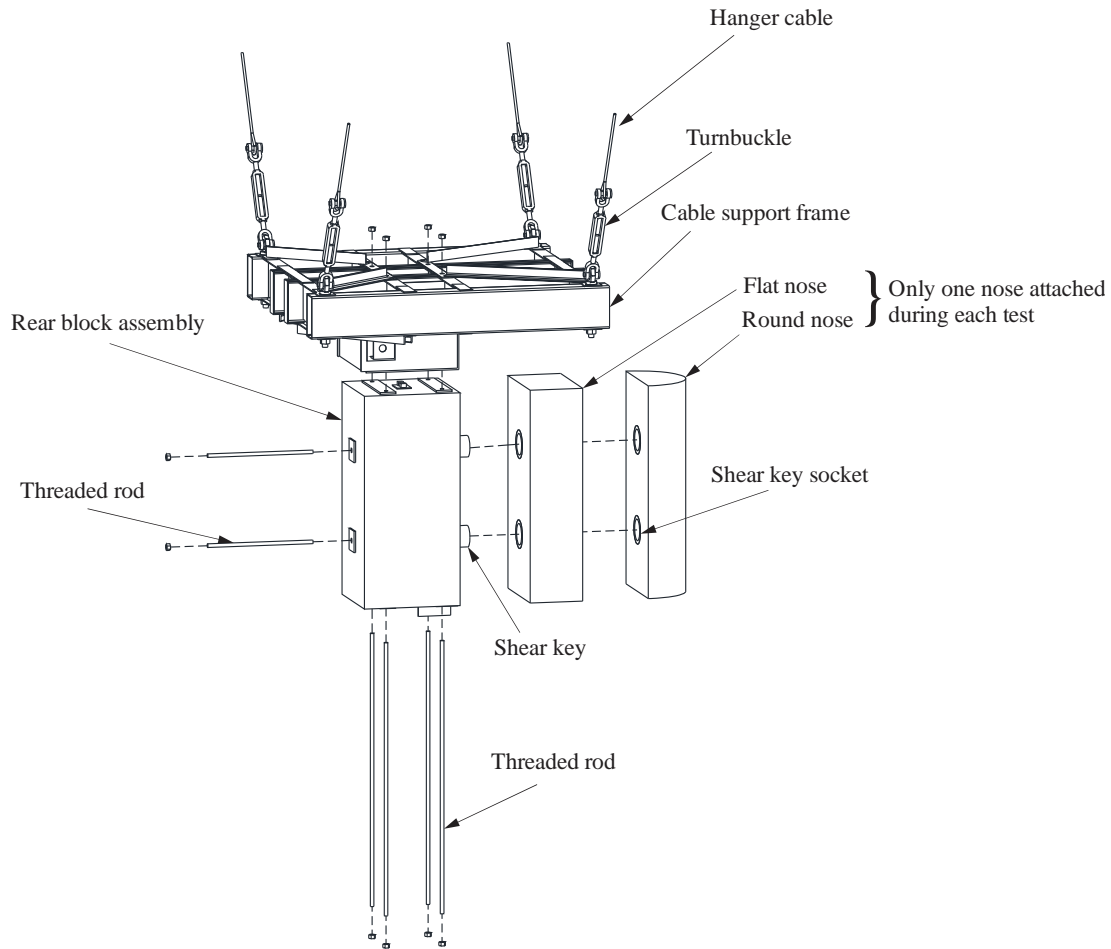


Figure 6.11 Impact block and cable support frame: exploded view

6.3 Test Procedure

The most important consideration in developing the test procedure was identifying the physical quantities that needed be measured in order to achieve the objectives of the study. Critical quantities that were identified included:

- Impact force: The time-varying contact force developed between the impact block and barge bow replicate during each impact event, and;
- Barge bow deformation: The time-varying deformation (crush-depth) of the barge bow during each impact experiment.

By combining these quantities, force-deformation curves, as previously discussed in Chapter 5, can be formed.

Due to the nature of the pendulum impact experiments, it was impractical to measure the impact force directly using load cells. Mounting load cells to either the impact block or the barge replicate would have modified the geometry and stiffness characteristics of the contact interface,

which would have altered the results. Therefore, the impact force was instead quantified indirectly, using accelerometers attached to the impact block. The time-varying impact force, $F(t)$, was calculated by measuring the deceleration of the impact block, $a(t)$, and multiplying by the known mass of the impact block and hanger frame, m , such that $F(t) = (m)(a(t))$. Note that this approach assumes that impact block motion is dominated by rigid body translation, and that the block undergoes no significant deformation. Finite element simulations indicated that these assumptions were valid. High frequency oscillations of acceleration data, resulting from the propagation of small-scale deformation waves in the block, were removed using a 800 Hz low-pass filter.

Similarly, the direct physical measurement of barge bow deformation was considered impractical. During each impact test, the bow specimen deformed more than 8 in. over a time span of approximately 0.1 sec. Such large scale and rapid deformations were too large to measure with displacement transducers, and too rapid to measure with most large-displacement string potentiometers. Therefore, time-varying deformations were quantified indirectly by monitoring impact block displacements via high-speed video and motion tracking (digital image correlation) software. Specific instrumentation that was utilized for these tasks is discussed in the following section.

The following additional physical quantities were also measured to further strengthen the validation effort:

- Impact velocity: The velocity of the impact block immediately prior to impact.
- Residual barge bow deformation: The plastic (permanent) barge bow deformation that remained after each impact had occurred and the damaged bow region had rebounded elastically.
- Barge bow deformation patterns: Qualitative inspection of local deformations in the barge bow, including hull plate bending and folding, and internal structural member buckling and plastic hinging.

Based on the considerations, characteristics, and physical quantities discussed above, the following test procedure was developed for the impact experiments:

1. Prepare instrumentation according to the layout described in the next section and detailed in Appendix K.
2. Align impact block, with round nose attached, with the impact face of the replicate barge bow.
3. Attach pick cable to impact block, and raise block to desired height, as measured from the center of gravity of the combined block and hanger frame.
4. Release lifting hook, initiating a swing and a subsequent impact event.
5. Inspect impact zone on barge bow replicate, and record desired characteristics (e.g. shape and extent of permanent deformation).

6. Prepare test components for subsequent impacts.
7. Repeat above steps until round nose impact series was completed.
8. Replace round nose with flat-faced nose and repeat steps above.

6.4 Test Instrumentation

Instruments that were used during each barge impact experiment are depicted in Fig. 6.12, and consisted of:

- Pressure sensitive tape switches (contact switches)
- Infrared optical break beam sensors
- Accelerometers
- High-speed video cameras
- Multiple normal-speed video cameras

In addition, after each impact test was completed, the residual (plastic) deformation pattern of the barge bow replicate was three-dimensionally mapped using:

- Optech ILRIS-3D laser scanner

Each instrument is described in greater detail in the following sub-sections. As discussed above, impact force was quantified indirectly by means of uniaxial accelerometers attached to the top and bottom surfaces of the impact block (Fig. 6.12a-b). The two accelerometers mounted at the top surface of the block were designated with the label “T”, while accelerometers mounted on the bottom surface were designated with the label “B”. Accelerations were generally expected to be less than 100 g, with very short-duration spikes possibly exceeding 250 g. Therefore, accelerometers with two ranges (250 g and 500 g) were employed. The accelerometers with a +/-250g range were given the label A250; correspondingly, accelerometers with a +/-500g range were given the label A500.

Impact block motions were monitored by two high-speed (2000 frames/sec) video cameras, one located on each side of the impact zone. Motion tracking (digital image correlation) software (ProAnalyst) was used to track the time-varying displacements of points on a checkerboard pattern painted on each side of the impact block. Motion tracking data were used to quantify impact block displacement, velocity, and acceleration (by time differentiation), and also barge bow deformations. Optical break beams, located a known distance (12 in.) apart, served as the primary means by which impact velocity was computed for each test (achieved by dividing the distance between the beams by the time that elapsed between each beam being triggered).

The data acquisition system was initiated just prior to release of the impact block. The high-speed cameras were triggered by tape switches affixed to the nose of the impact block. Two tape switches (designated TS-FR for the tape switch on the right side of the impact nose, and TS-FL for the corresponding tape switch on the left side) were used to identify the initiation of

contact between the impact block and the model barge bow. Data were acquired from all instruments (excluding the high-speed cameras) at a sampling rate of 10 kHz per sensor.

Each impact event was also visually recorded using several normal-speed video cameras, one of which was mounted on a support pole located behind the replicate barge bow (Fig. 6.12). Video obtained from the normal speed cameras captured the progression of the impact zone during each impact, and allowed for a qualitative assessment of barge bow deformation and behavior.

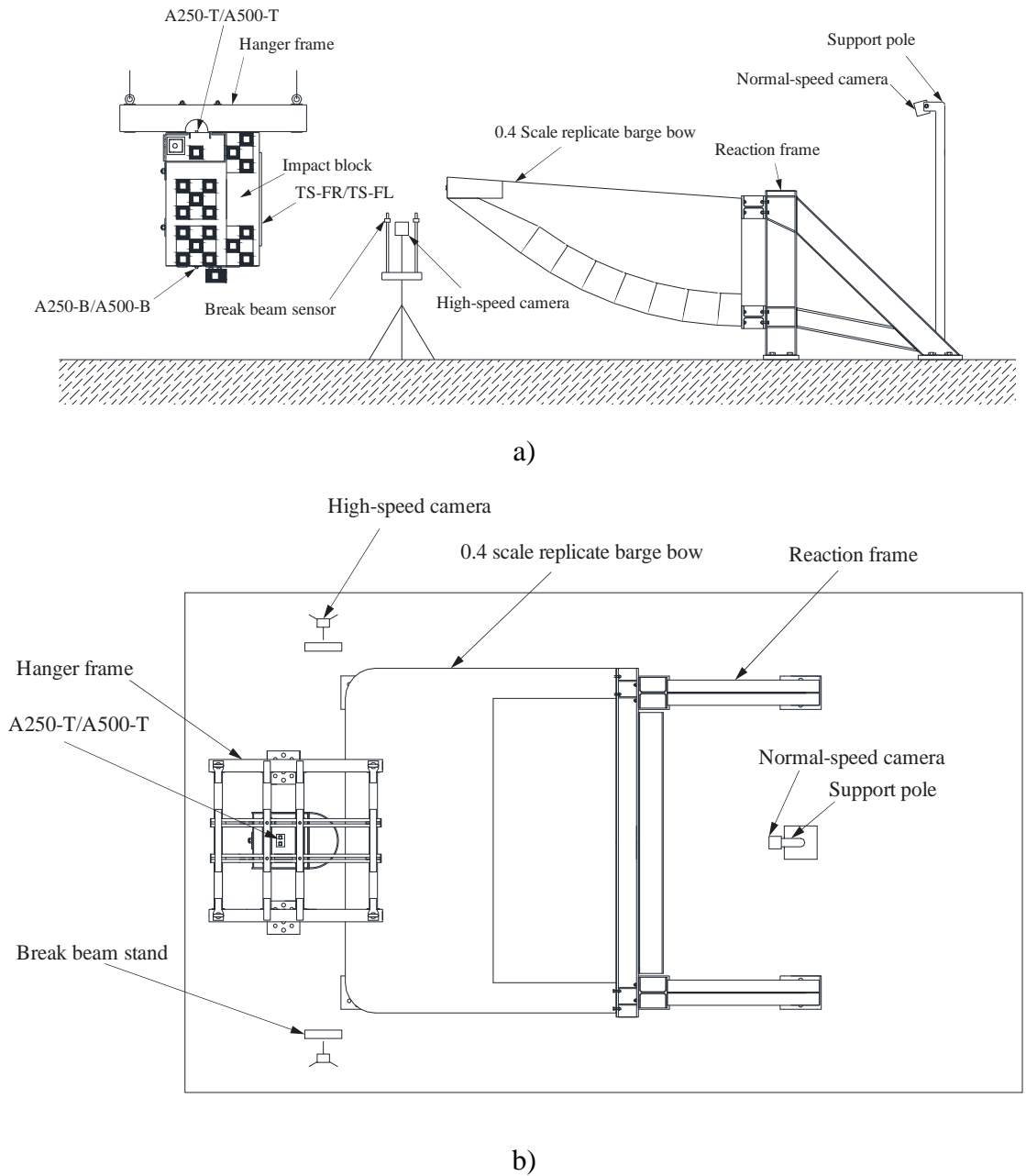


Figure 6.12 Instrumentation layout to be used in barge bow impact experiments:
a) Elevation view; b) Plan view; c) Front view of instrumented impact block

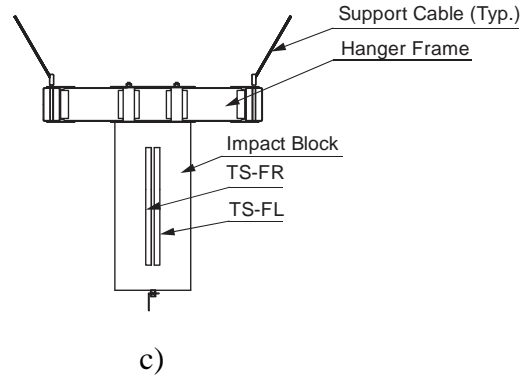


Figure 6.12, continued. Instrumentation layout to be used in barge bow impact experiments:
a) Elevation view; b) Plan view; c) Front view of instrumented impact block

6.4.1 Pressure sensitive tape switches

Tape switches are sensors that close an electrical circuit when compressed, and can therefore be used to detect contact without altering the dynamic response of the test article. In this study, two tape switches were affixed to the impact face of the block (Fig. 6.13), which were used to send a ‘zero time’ marker signal to the data acquisition system immediately upon impact. The ‘zero time’ marker provided a reference point showing the instant in time at which contact with the barge bow replicate occurred. Technical specifications for the tape switches are provided in Table 6.1. Note that the tape switches used in this study were sacrificial in nature; after sending the ‘zero time’ contact signal to the data acquisition system, the tape switches affixed to the face of the impact block were destroyed (due to the large force levels generated). Therefore, a new set of (low-cost) tape switches were used for each impact experiment.



a)

Figure 6.13 Tape switches mounted to face of impact nose:
a) Full view; b) Detail of end of single tape switch



b)

Figure 6.13, continued. Tape switches mounted to face of impact nose:
a) Full view; b) Detail of end of single tape switch

Table 6.1 Specifications for tape switches

Manufacturer	Tapeswitch Corporation
Ribbon switch type	131-A
Actuation force	60 oz.
Switch lengths used	42 in.
Dimensions	3/4" in. wide, 3/16 in. thick
Minimum bend radius	1 in.

6.4.2 Infrared optical break beam sensors

Optical break beams were used to quantify impact block speed for each test. Two pairs (four total) of infrared optical break beam sensors were used: one pair located near the impact point on the barge bow replicate and the other pair located 12 in. farther away (i.e., the separation distance between the sensor pairs was 12 in.). Each sensor pair consisted of a transmitter and receiver, mounted on an aluminum stand (see Figure 6.14), that was leveled with the impact zone on the barge bow. When the impact block passed between the transmitter and the receiver, the infrared beam was interrupted and the data acquisition system captured the time at which the interruption occurred. From the distance between the sensors, and the time duration between the two beam interruption events, the speed of the impact block just before contact with the barge replicate was accurately determined. Specifications for each optical break beam sensor are given in Table 6.2.



Figure 6.14 Optical break beam sensor mounted on stand

Table 6.2 Specifications for optical break beams

Manufacturer	Balluff
Receiver model	BLS 18KF-NA-1PP-S4-C
Transmitter model	BLS 18KF-XX-1P-S4-L
Range (ft)	65 ft.

6.4.3 Accelerometers

To measure acceleration, and to indirectly quantify time-varying impact force during each impact event, accelerometers were attached to the impact block. Based on acceleration results obtained from numerical impact analyses, accelerometers with two measurement ranges (0 - 250 g, and 0 - 500 g) were employed for the impact tests. A summary of accelerometer specifications is presented in Table 6.3. Each accelerometer was calibrated by Spectrum Sensors and Controls prior to usage in order to verify accuracy. Each impact test utilized four accelerometers attached to mounting plates on the top surface (two accelerometers) and bottom surface (two accelerometers) of the impact block, as shown in Fig. 6.15.

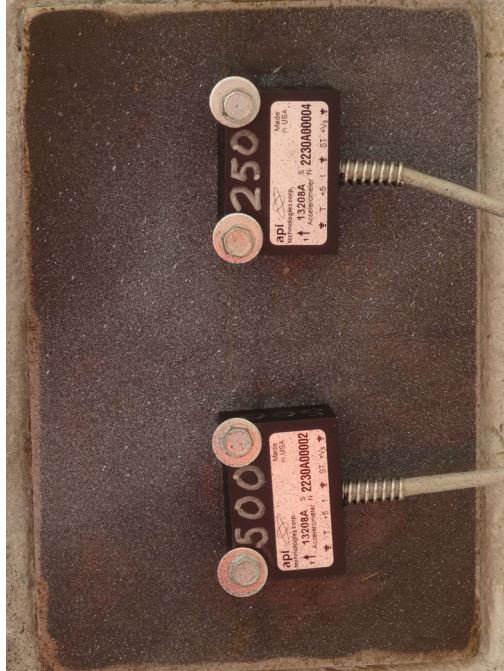


Figure 6.15 Accelerometers mounted to bottom surface of impact block

Table 6.3 Specifications for accelerometers

Manufacturer	Model number	Range (g)	Bandwidth (Hz)
Spectrum Sensors & Controls	13208A-R250	250	10,000
Spectrum Sensors & Controls	13208A-R500	500	10,000

6.4.4 High-speed cameras

During each impact test, two high-speed digital video cameras (Figure 6.16) were directed toward the barge replicate to enable the time-varying deformations of the replicate barge to be quantified, as well as to serve as a redundant means for determining the impact block speed at the point of contact. Each of the two cameras, positioned on either side of the replicate barge bow, was configured to produce a close-up side view of the impact zone. Each camera recorded each impact event at a rate of 2000 frames/second, as noted in the specifications in Table 6.4.



Figure 6.16 High-speed digital video cameras

Table 6.4 Specifications for high-speed cameras

Manufacturer	Integrated Design Tools (IDT)
Distributor	Dynamic Imaging, LLC
Camera model	MotionXtra N-3
Image resolution	1280 x 1024
Frame rate	1000 fps (frames/sec)
Frame rate (plus mode)	2000 fps (frames/sec)
Memory	1.25GB
Maximum recording time	0.76 sec.

6.4.5 Optech ILRIS-3D laser scanner

Prior to the first impact test, and following each impact test, a three-dimensional (3D) laser scan of the barge bow replicate was performed using an Optech ILRIS-3D laser scanner (Fig. 6.17). Raw data from each laser scan were processed, using the Rapidform XOR software into data formats typically employed by computer-aided design (CAD) software packages. The processed 3D scan data were used to measure plastic barge bow deformation, and to visualize the deformed state of the replicate barge bow after each test. Pertinent specifications for the ILRIS-3D laser scanner are provided in Table 6.5.



Figure 6.17 Laser scanner

Table 6.5 Specifications for laser scanner

Manufacturer	Optech, Inc.
Model	ILRIS-3D
Field of view	40° (+/- 20°)
Data sample rate	2000 points per second

CHAPTER 7 REDUCED SCALE BARGE BOW IMPACT TEST RESULTS

7.1 Introduction

As discussed in earlier chapters, a key objective of this research program was the experimental validation of analytical methods employed in previous UF/FDOT research projects. To achieve this objective, a series of pendulum impact experiments were conducted on two 0.4 scale replicate barge bows according to the procedures outlined in Chapter 6. In this chapter, results for the barge bow impact tests are described, and their implications are discussed in detail.

Results for the impact experiments are organized and discussed by impact series; each discussion is complemented with a detailed description of all employed data processing methods. Within the main discussion sections for each impact series, a subsection is provided which outlines the initial impact, and all commonalities between this event and subsequent impacts. Following the discussion of the initial impact, results from the remaining impacts are addressed summarily.

A summary of the overall test program is provided in Table 7.1. As described in Chapter 6, two series of impact experiments were conducted: one utilizing an impact block with a round nose, and one utilizing an impact block with a flat-faced nose.

Table 7.1 Summary of test program

Impact series	Test number	Test date	Test ID	Drop height (ft-in)	Impact speed (mph)	Impact energy (kip-in)	Barge replicate number
Round	1	2014/02/14	RND1	15'	20.9	1618	1
Round	2	2014/02/20	RND2	20'	24.9	2290	1
Round	3	2014/02/20	RND3	20'	24.7	2257	1
Round	4	2014/02/20	RND4	20'	25.3	2376	1
Flat	1	2014/03/11	FLT1	14'	20.5	1627	2
Flat	2	2014/03/11	FLT2	19'	24.1	2269	2
Flat	3	2014/03/11	FLT3	19'	24.3	2290	2
Flat	4	2014/03/11	FLT4	19'	24.3	2290	2

7.2 Test RND1: Initial Round Nose Impact Test

The first round nose impact experiment (RND1), conducted from a drop height of 15 ft, imparted sufficient force to buckle the internal trusses and frames of the replicate barge bow in the immediate vicinity of the impact zone. This behavior was evidenced by the bulged region on the bottom of the replicate (Fig. 7.1a), which was caused by the internal structural members buckling outward and pressing against the external steel hull plates. The pattern of deformation at the point of impact was relatively consistent with the shape of the impactor and the only notable material fracture in this region occurred in the weld material that joined the two portions of the headlog plate together.

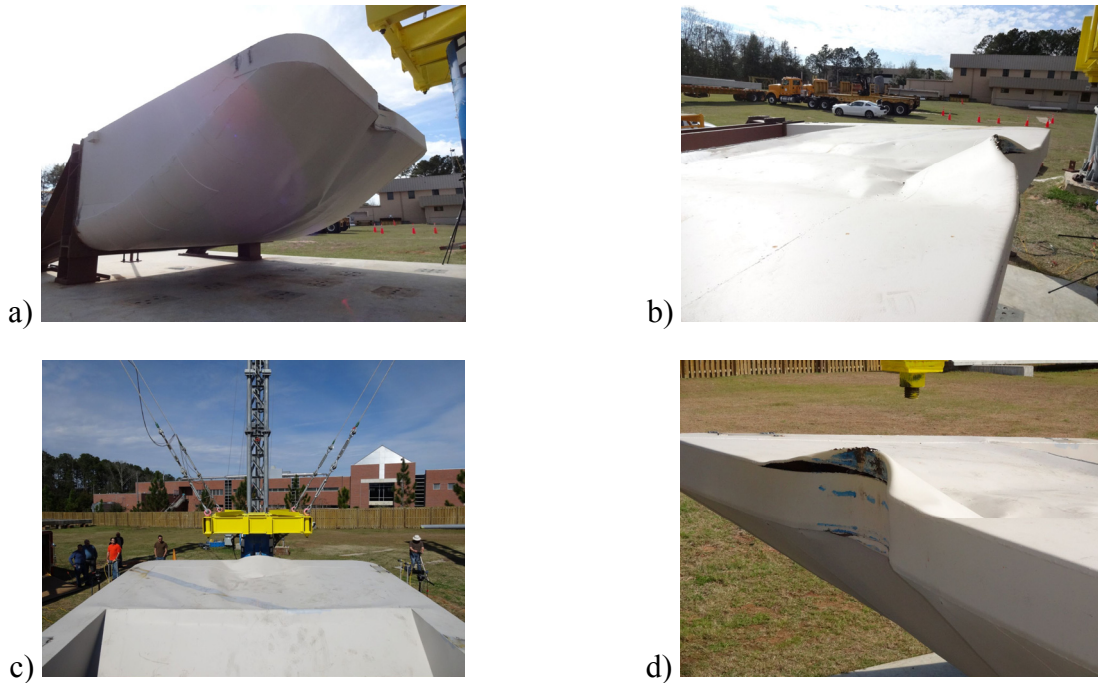


Figure 7.1 Initial round nose impact test (RND1) of barge bow:
 a) Bottom view of impact zone; b) Side view of impact zone; c) Rear view of impact zone;
 d) Isometric view of impact zone

7.2.1 Break beam and tape switch data

During each impact experiment, voltage data from the break beam sensors and the tape switches were recorded in order to ascertain the velocity of the impact block immediately prior to impact, and the time at which initial contact occurred.

Following release (denoted time = 0), when the impact block passed between two aligned optical break beam sensors (one transmitter and one receiver), interrupting the continuity of the signal passing between them, an abrupt rise in the voltage output occurred (Fig. 7.2). By identifying the time associated with the voltage change, the time at which the impact block passed between the break beam pair was determined. Tape switch data were similarly interpreted; however, in this case, the rise in voltage was attributed to activation of the tape switch due to direct contact between the impact block and the barge bow.

Voltage readings from both break beams during impact test RND1 are provided in Fig. 7.3; analogous voltage readings from the nose-mounted tape switches are provided in Fig. 7.4. As identified by the initial voltage rise in the tape switch data, the impact event was initiated 1.94 sec. after the release of the impact block. Likewise, the first break beam was triggered at 3.075 sec., and the second break beam was triggered at 3.108 sec. By taking the difference between the trigger times and dividing by the distance (12 in.) between the two pairs of sensors, an impact velocity of 368.1 in/sec (20.9 mph) was determined.

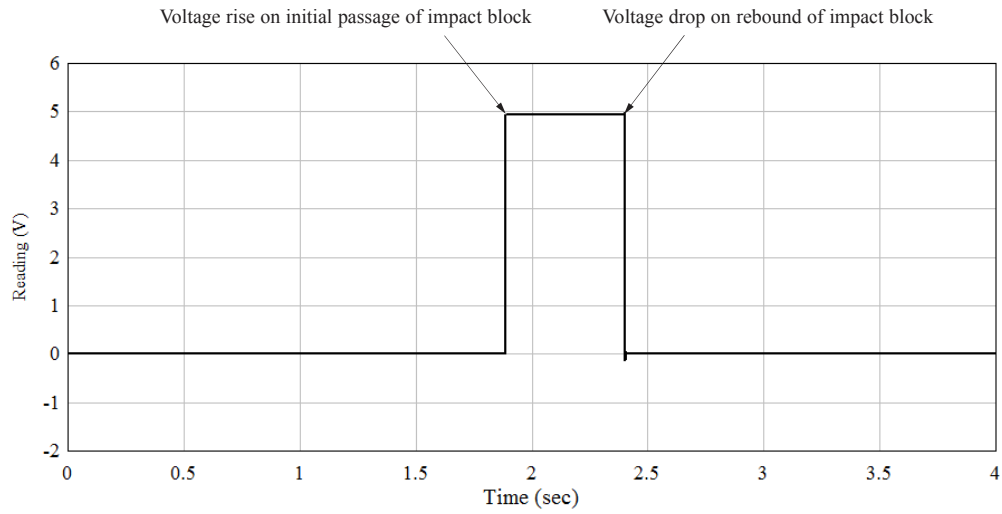


Figure 7.2 Sample break beam data from impact test RND1

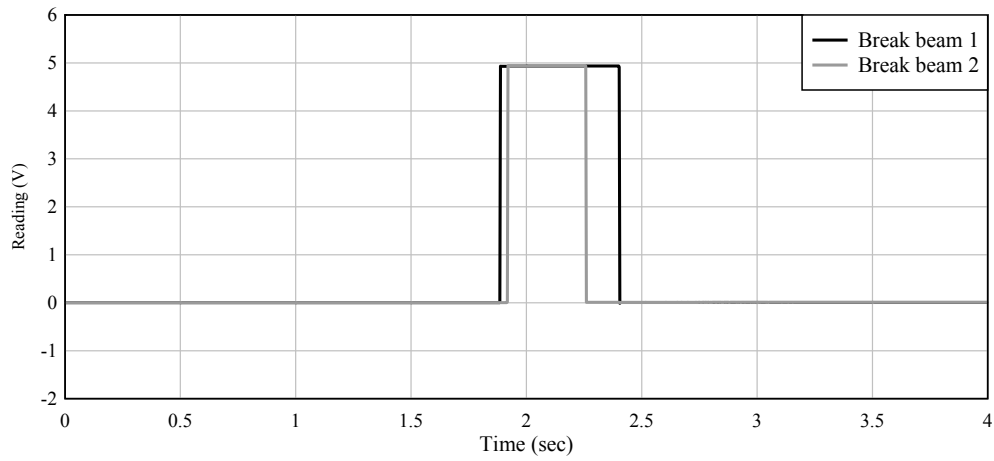


Figure 7.3 Break beam data from impact test RND1

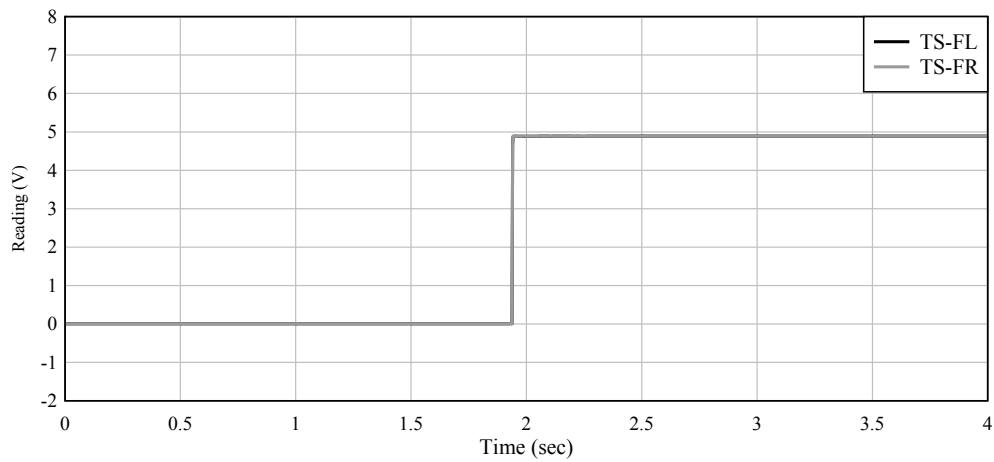


Figure 7.4 Tape switch data from impact test RND1

7.2.2 Acceleration and impact force data

As described in detail in Chapter 6, acceleration data were recorded by four surface-mounted accelerometers located on the top and bottom faces of the impact block. By combining the measured acceleration data with the known mass of the impact block (and attached hanger frame), time-histories of impact force acting on the barge bow could be computed. A primary goal of the testing program was to quantify the horizontal impact force (in the direction of impact) exerted by the impactor against the barge bow replicate. As such, to mitigate the possible influence of block rotation on the interpretation of acceleration data, all acceleration time-histories presented in this chapter were obtained by taking an average of output from analogous accelerometers mounted on the top and bottom of the impact block (i.e. the data from A250-T were averaged with the data from A250-B; data from A500-T were averaged with the data from A500-B). Moreover, in order to remove irrelevant high-frequency content, the averaged acceleration data were subsequently filtered using a low-pass fast-Fourier transform (FFT) filter; frequency content in excess of 800 Hz. was removed (Fig. 7.5). Impact force time-histories were then computed by multiplying the averaged and filtered acceleration time-histories by the impactor mass (Fig. 7.6).

The peak in the time-histories presented in Figs. 7.5 and 7.6 was unique to the *initial* impact event (RND1, as opposed to RND2, RND3, and RND4.), and was associated with the force required to initiate buckling of the internal trusses and frames inside the bow of the barge replicate in the vicinity of the impact zone. Once the internal trusses buckled, the bow crushed progressively at reduced force (load) levels until the kinetic energy of the impactor was completely absorbed and the block was brought to zero velocity before rebounding. As exhibited by the trends in Figs. 7.5 and 7.6, very good agreement was observed between the (averaged) A500 accelerometers and A250 accelerometers. Consequently, for the remainder of this chapter, each figure depicting acceleration or force data will consist of one trace representative of the data collected from both pairs of accelerometers (i.e., A500 data were averaged with A250 data).

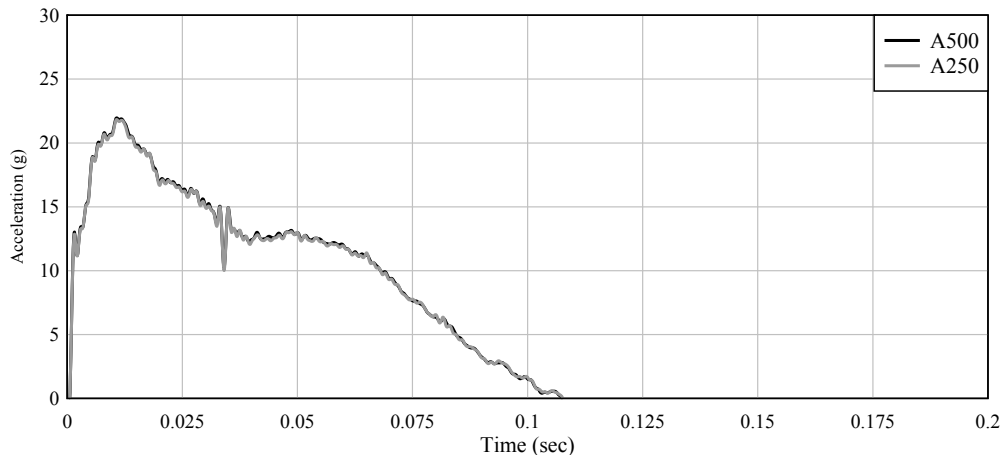


Figure 7.5 Averaged and filtered acceleration time-histories obtained from impact test RND1

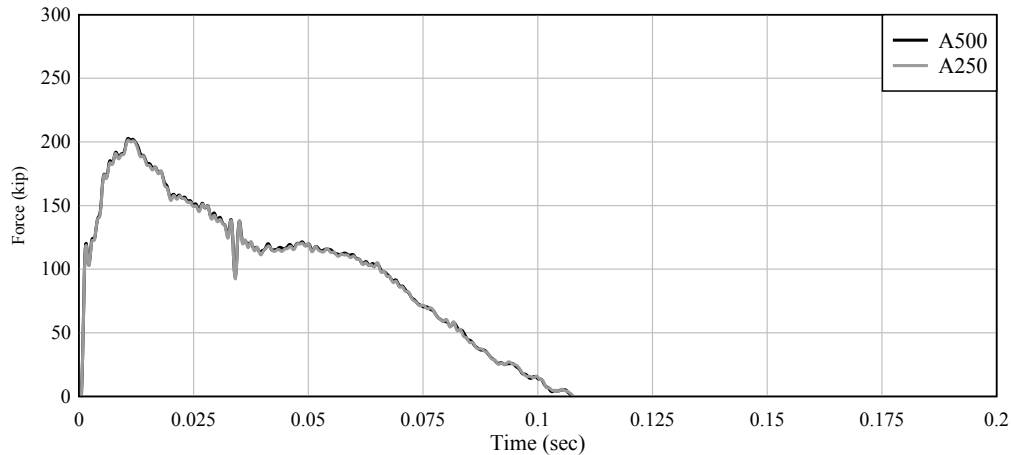


Figure 7.6 Impact force time-histories computed for impact test RND1

7.2.3 Deformation data

Permanent (plastic) barge deformation patterns produced by each impact event were quantitatively measured (mapped) using a 3D laser scanner. Prior to conducting any impact tests, however, the *undeformed* geometry of the barge bow replicate was first scanned (Fig. 7.7) to produce a datum against which subsequent geometric changes (caused by impact testing) could be referenced. After each impact test, the barge bow replicate was again scanned to produce a detailed quantitative 3D map of permanent barge deformation caused by the impact.

In Fig. 7.8, the permanent deformation pattern caused by the initial impact test (RND1) is presented. While the rounded geometry of the permanent deformation zone in Fig. 7.8 is expected—given the round shape of the impactor—the figure also reveals the presence, and influence of the stiffening trusses that make up the internal structure of the barge bow. Emanating from bottom tip of the permanent deformation zone, and extending along the bottom surface of the barge toward the back, is an apparent line of concentrated outward deflection. During impact test RND1, the two internal stiffening trusses that were located adjacent to the barge centerline inelastically buckled, thrust outward, and caused concentrated deflections in the outer hull plate. The concentrated line of deflection evident in Fig. 7.8 corresponds to the influence of one the two trusses in this area of the barge. (Further evidence that such lines correspond to internal stiffening trusses will be presented later for tests RND2 – RND4).

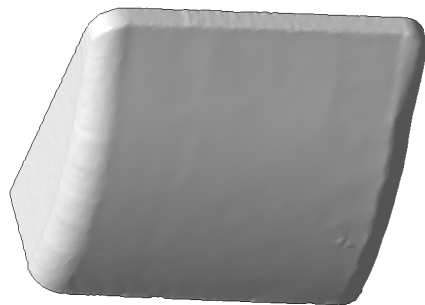


Figure 7.7 3D scan of undeformed replicate barge bow (prior to round nose test series)

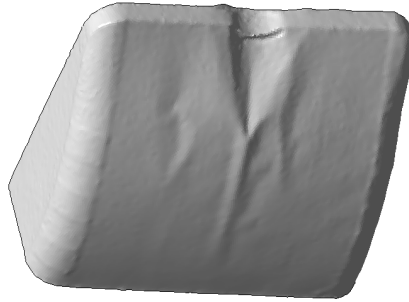


Figure 7.8 Permanent barge deformation following test RND1

To compute *time-varying* deformations for each impact event, the translational motion (displacement) of the block was tracked throughout each impact event using high speed video (Fig. 7.9) and the Xcitex ProAnalyst motion analysis software. By tracking well-defined points on the impact block—formed by checkered patterns painted on each side of the block—a ‘time-history’ of the motion (displacement) of the block was produced. Since the impact block was essentially rigid—particularly in comparison to the barge bow—the displacement of any point on the *side* of the block was known to be equal to the displacement of the impacting surface of the block *nose*. Thus, visually tracking the displacement of a point on the side of the block in the high speed video was equivalent to tracking the displacement of the nose itself; this is a very important fact given that the nose became visually obscured by the barge bow during each test.

Since the displacement of the front face of the impact block was directly correlative with barge crush depth once initial contact occurred, the deformation time-history for each test was produced by extracting the displacement obtained from the processed high speed video files. In Fig. 7.10, the peak deformation level reached—attributable to both plastic and elastic bow deformation—was 10.75 in. From 3D laser scanning (mapping) of the barge bow after impact, the final permanent (residual) plastic deformation level was determined to be 8 in. The difference between these two deformation values is attributed to elastic recovery of the material in the deformed region of the replicate barge.

7.2.4 Force-deformation relationship

To form a force-deformation relationship for impact test RND1, the time-varying force and time-varying deformation data described above were merged together (Fig. 7.11). In the force-deformation plot, the peak force is associated, as noted earlier, with the initiation of buckling of the internal frames and trusses. In Fig. 7.12, which graphically depicts the distribution of energy absorbed by the barge replicate, the area bounded by the force deformation curve was the amount of energy plastically dissipated as a result of permanent barge deformation. Similarly, the area under the curve between the peak deformation (10.75 in.) and the residual deformation (8 in.) was the elastically recovered energy. Summing these two quantities produced a total energy that was within 1.2% of the initial total kinetic energy of the impact block ($\frac{1}{2}mv^2$); as computed from the measure block mass (m) and impact speed (v). Additionally, the plastically dissipated energy was found to be 94% of the initial kinetic energy, whereas the rebound energy was found to be 6% of the initial kinetic energy. (Note: the

hypothetical impact block rebound velocity computed from the elastically recovered area indicated in Fig. 7.12 agreed well with the experimentally observed block rebound velocity; the two differed by only 6%).

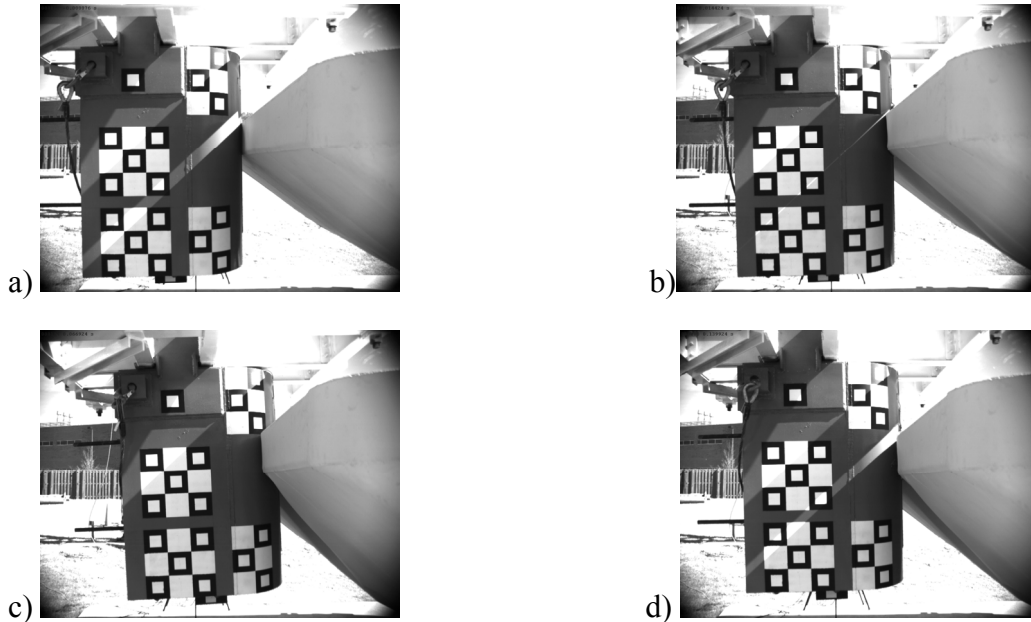


Figure 7.9 Barge deformation at various stages of impact for impact test RND1: a) Incipient contact; b) Intermediate stage; c) At peak (maximum) deformation (prior to rebound); d) Residual deformation at rebound (zero force level)

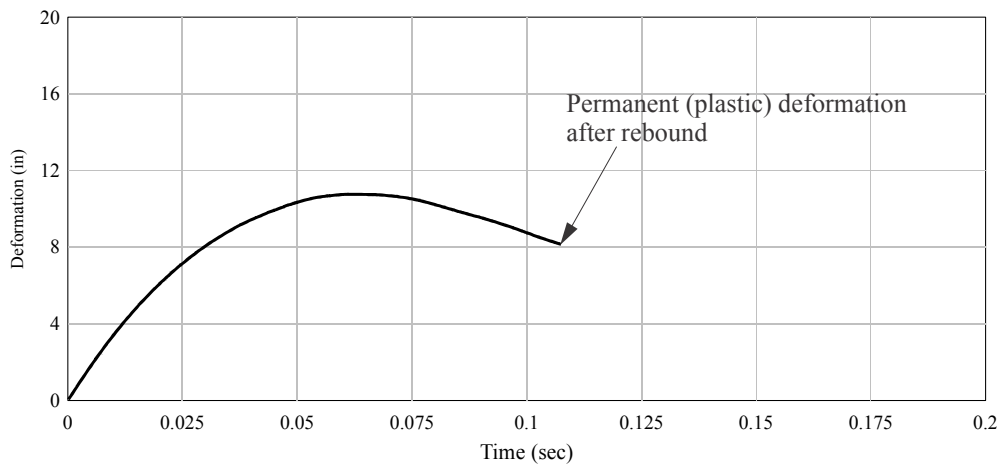


Figure 7.10 Deformation time-history computed from high speed video for impact test RND1

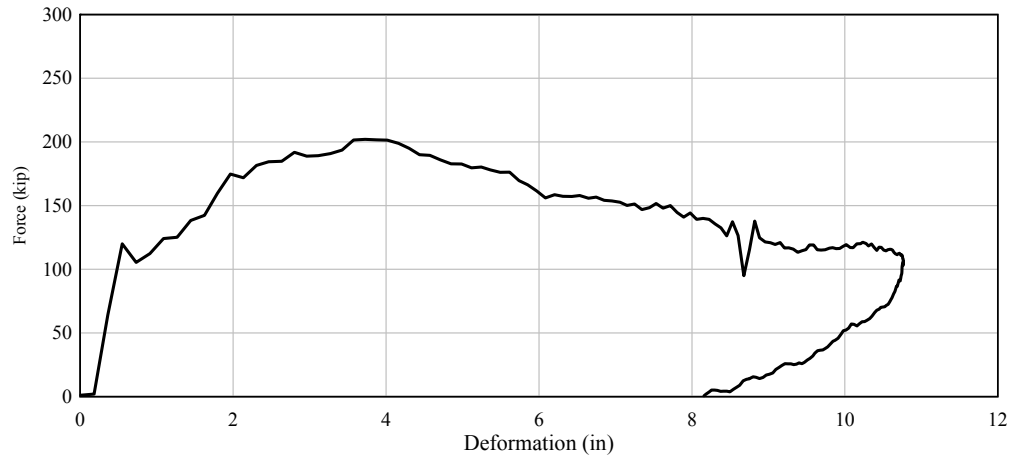


Figure 7.11 Force-deformation relationship for impact test RND1

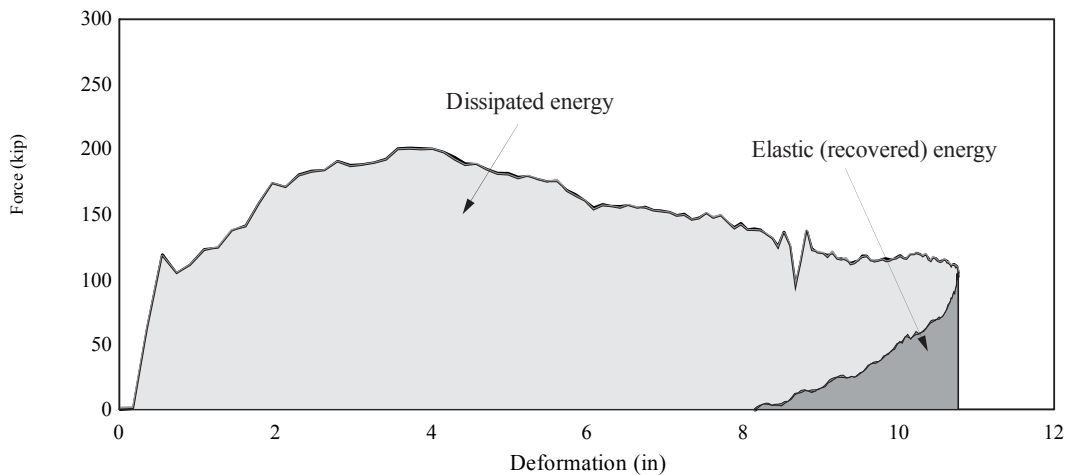


Figure 7.12 Distribution of absorbed energy for impact test RND1

7.3 Tests RND2-RND4: Subsequent Round Nose Impact Tests

Following the initial impact test (RND1) with the round nose impact block, three subsequent tests (RND2, RND3, RND4) were conducted from a drop height of 20 ft. By examining Figs. 7.13 – 7.15, it can be seen that the final three impact events with the round nose impact block produced substantial plastic deformation with little observed material fracture outside of the impact zone. By the fourth impact test, the entire height of the block had penetrated into the barge replicate. Consequently, since the contact surface of the impact block was fully utilized, subjecting the barge replicate to subsequent impacts would not result in the desired response. Additionally, since the target deformation level had been nearly reached, no further tests were conducted.

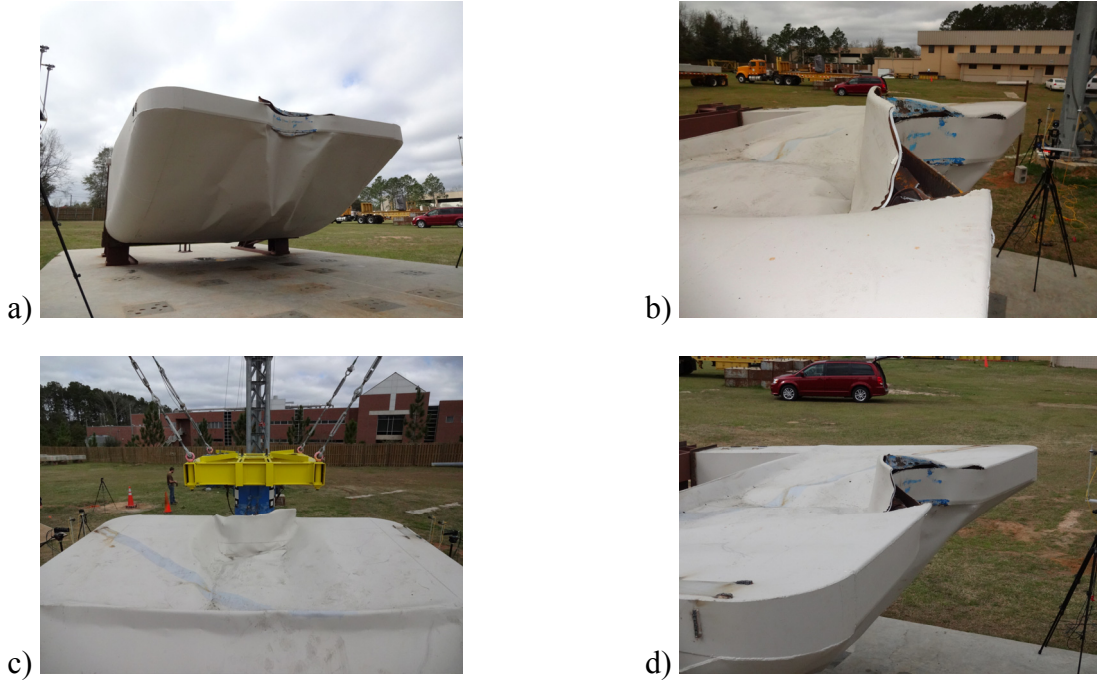


Figure 7.13 Round nose impact test RND2 of barge bow:
 a) Bottom view of impact zone; b) Side view of impact zone; c) Rear view of impact zone;
 d) Isometric view of impact zone

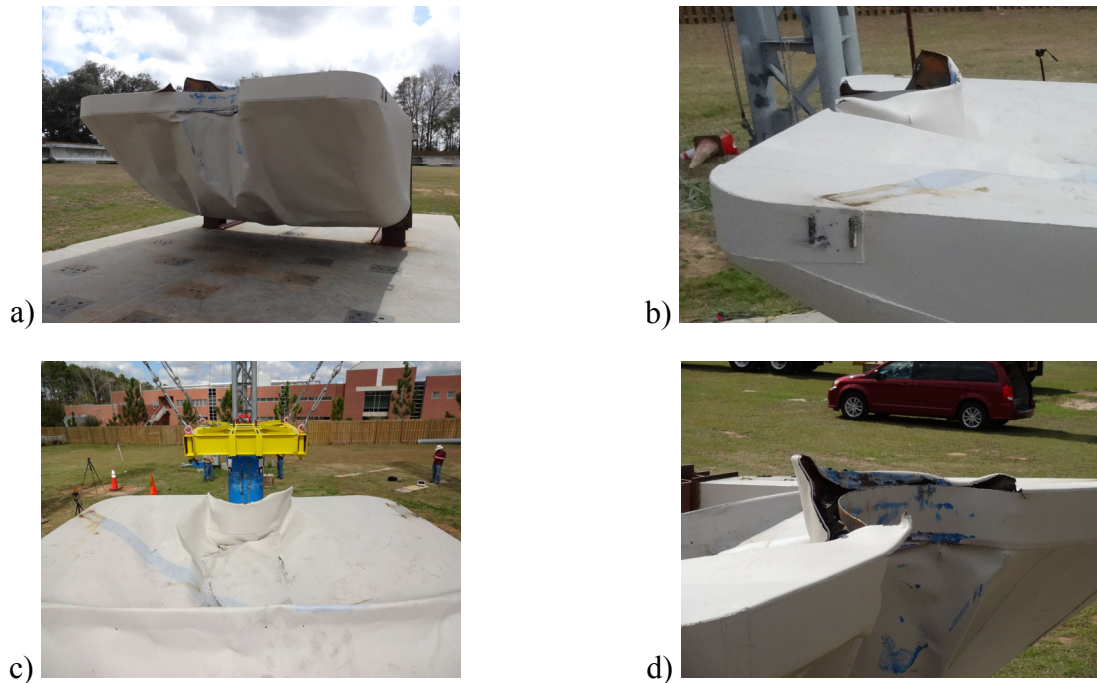


Figure 7.14 Round nose impact test RND3 of barge bow:
 a) Bottom view of impact zone; b) Side view of impact zone; c) Rear view of impact zone;
 d) Isometric view of impact zone

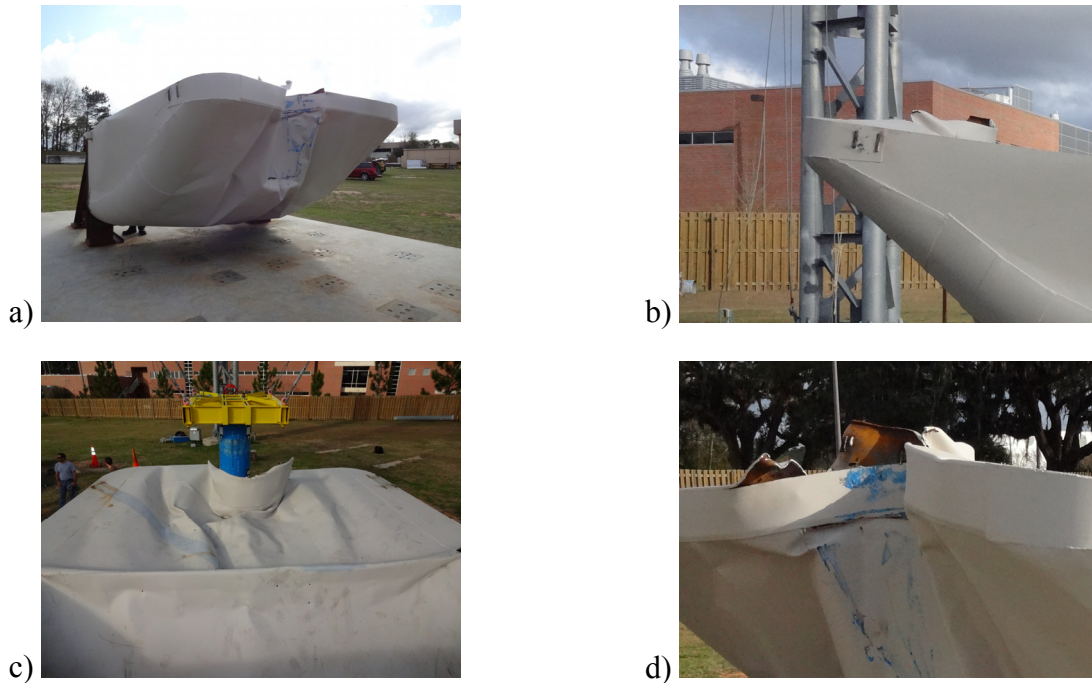


Figure 7.15 Round nose impact test RND4 of barge bow:
a) Bottom view of impact zone; b) Side view of impact zone; c) Rear view of impact zone;
d) Isometric view of impact zone

7.3.1 Break beam and tape switch data

Contact times and impact velocities for impact tests RND2 – RND4 were determined using the same procedures as outlined in Section 7.2.1.

7.3.2 Acceleration and impact force data

Acceleration time-histories (Figs. 7.16-7.18) and force time-histories (Figs. 7.19-7.21) for impact tests RND2 – RND4 were determined by employing the same data processing techniques described in Section 7.2.2. In general, the overall load pulse durations for tests RND2 – RND4 were somewhat longer than that noted during test RND1. Additionally, the force levels in the *sustained* portions in the force time-histories for tests RND2-RND4 generally grew in magnitude as each subsequent test was conducted.

As an aside, tests RND2 – RND4 exhibited a feature not strongly evident during test RND1: a very short duration, initial force spike at the beginning of each force time-history. These spikes were attributable to inertial resistance of the compacted mass of steel present in the ‘dented’ surface of the barge deformation zone. During each subsequent impact (RND2 – RND4), the impact block had to accelerate this mass of accumulated steel before generating additional barge deformation. Consequently, an initial, very short duration force spike was recorded. This feature, however, is simply an artifact of the testing procedure—i.e., using multiple, repeated impacts on a single barge bow replicate—and is of little relevance in terms of bridge design.

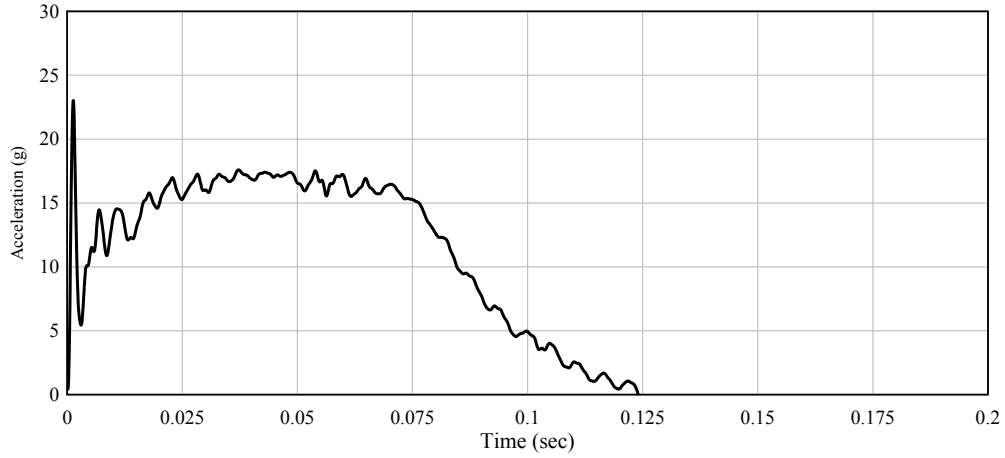


Figure 7.16 Averaged and filtered acceleration time-histories obtained from impact test RND2

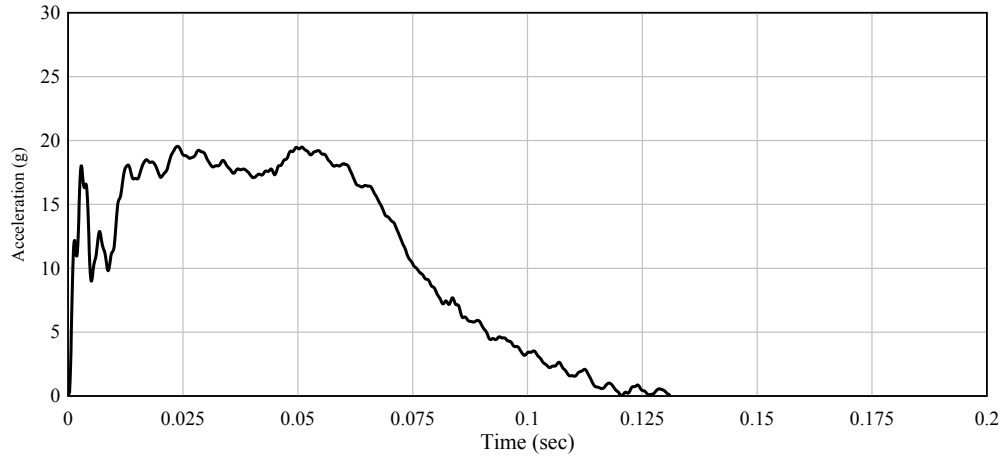


Figure 7.17 Averaged and filtered acceleration time-histories obtained from impact test RND3

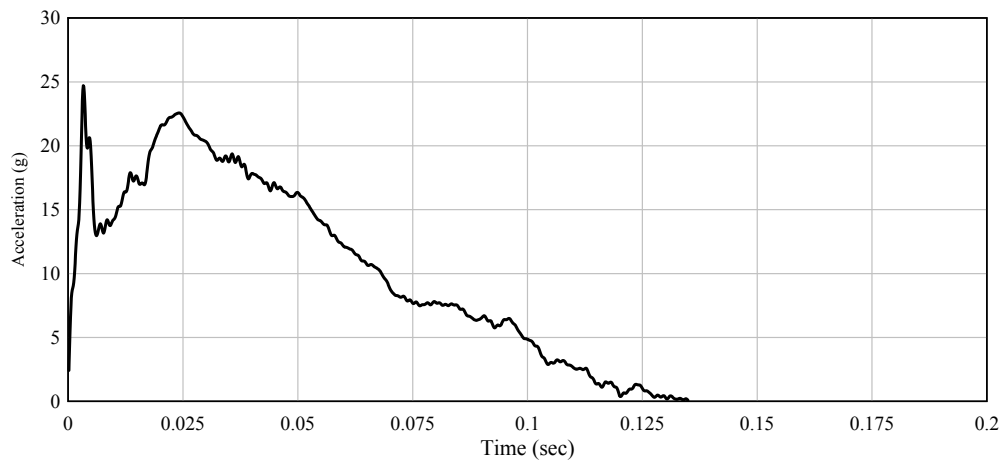


Figure 7.18 Averaged and filtered acceleration time-histories obtained from impact test RND4

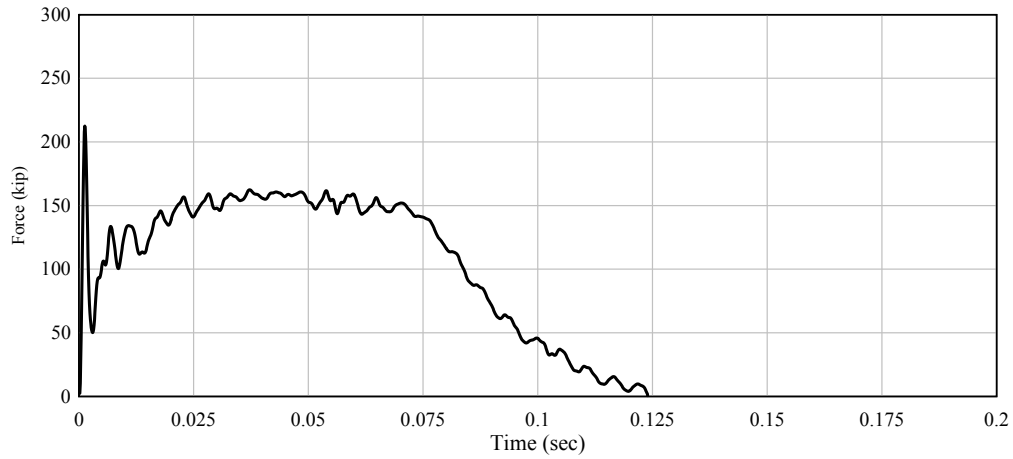


Figure 7.19 Impact force time-histories for test RND2

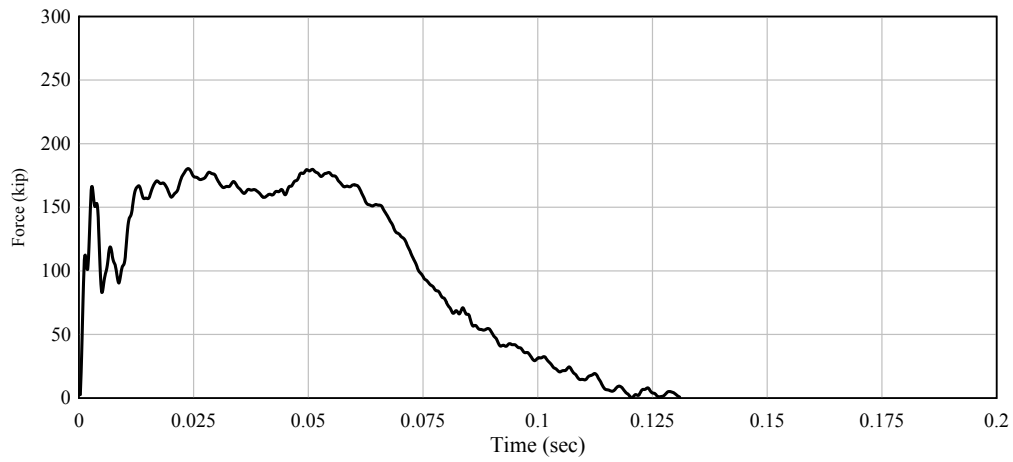


Figure 7.20 Impact force time-histories for test RND3

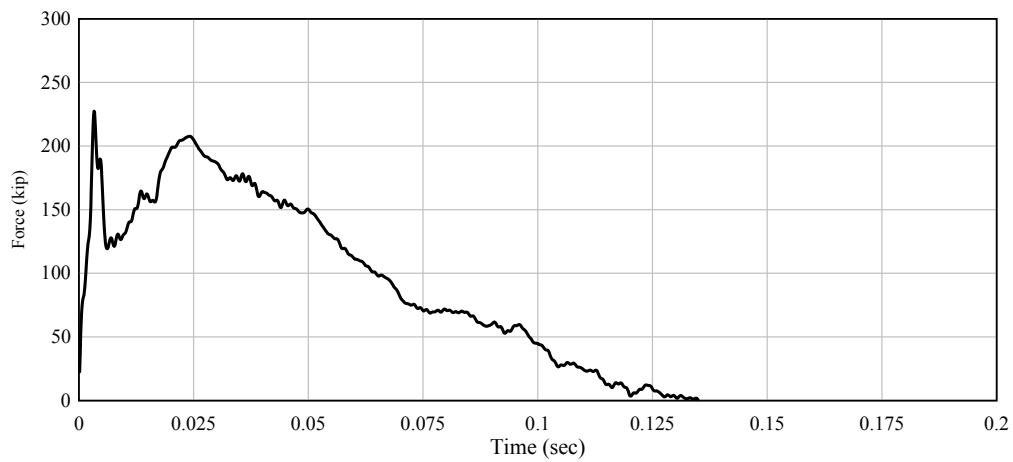


Figure 7.21 Impact force time-histories for test RND4

7.3.3 Deformation data

Visualizations of permanent barge deformations produced by impact tests RND2 – RND4 are shown in Figs. 7.22-7.24. With each subsequent impact test, the depth of penetration of the impactor into the barge bow (i.e., the ‘crush depth’) increased as damage was incrementally accumulated. Additionally, the presence—and influence—of stiffening trusses located inside the barge bow became increasingly evident. Earlier in this chapter, in Fig. 7.8 (corresponding to test RND1), a single concentrated line of deformation was identified as indicating the location of an internal stiffening truss. In Figs. 7.22-7.27, the presence and influence of *multiple* trusses, indicated by multiple crease lines (or ‘fold lines’) in the barge surface, is clearly evident. For comparison, these same truss lines are also clearly identifiable in photographs of barge deformation produced during testing; in particular, see Fig. 7.14a corresponding to test RND3.

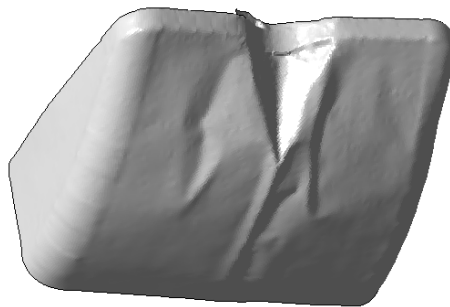


Figure 7.22 Permanent barge deformation following test RND2

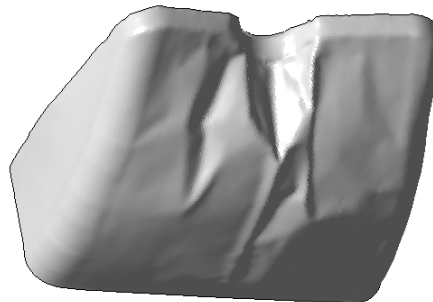


Figure 7.23 Permanent barge deformation following test RND3

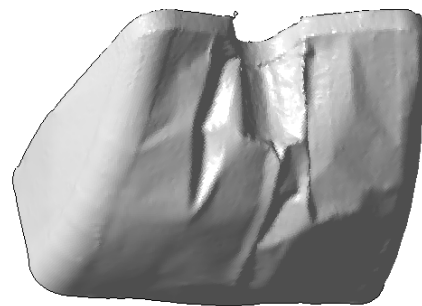


Figure 7.24 Permanent barge deformation following test RND4

By tracking the checkered pattern target points in the high speed videos of tests RND2-RND4 (Figs. 7.25-7.27), time-histories of *incremental* deformation were produced for all tests (Figs. 7.28-7.30). In this context, the term incremental indicates that the computed deformations are relative to the initially deformed state of the barge at the start of each new impact test. Consequently, to compute total deformations, the incremental deformations shown Figs. 7.28 - 7.30 are summed (accumulated), as will be discussed later in Section 7.6.

Although tests RND2-RND4 all employed the same drop height (20 ft), and therefore imparted the same impact energy, the maximum incremental barge deformations produced by each test gradually decreased in magnitude. That is, the increment of deformation produced by RND2 was larger than that produced by RND3, which was larger than that produced by RND4. The fact that the *incremental* deformations decreased in magnitude, as the *total* (accumulated) barge deformation increased, was an indication of stiffening (or hardening) of the barge bow. This phenomenon will be discussed in greater detail in Section 7.6 within the context of the overall (merged) force deformation curve for the entire RND test program.

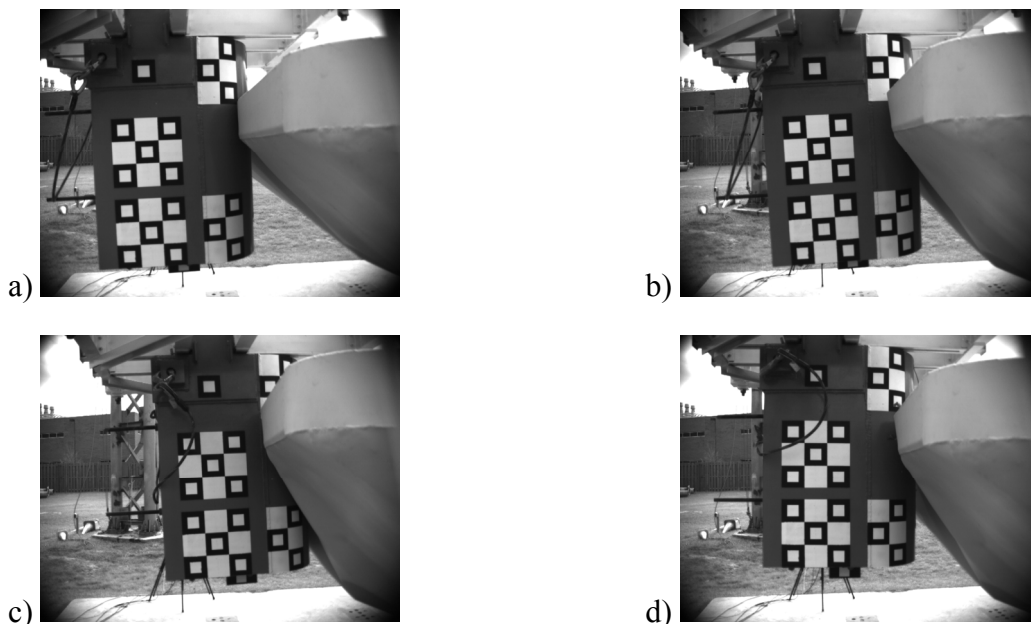


Figure 7.25 Barge deformation at various stages of impact for impact test RND2:
a) Incipient contact; b) Intermediate stage; c) At peak (maximum) deformation (prior to rebound); d) Residual deformation after rebound (zero force level)

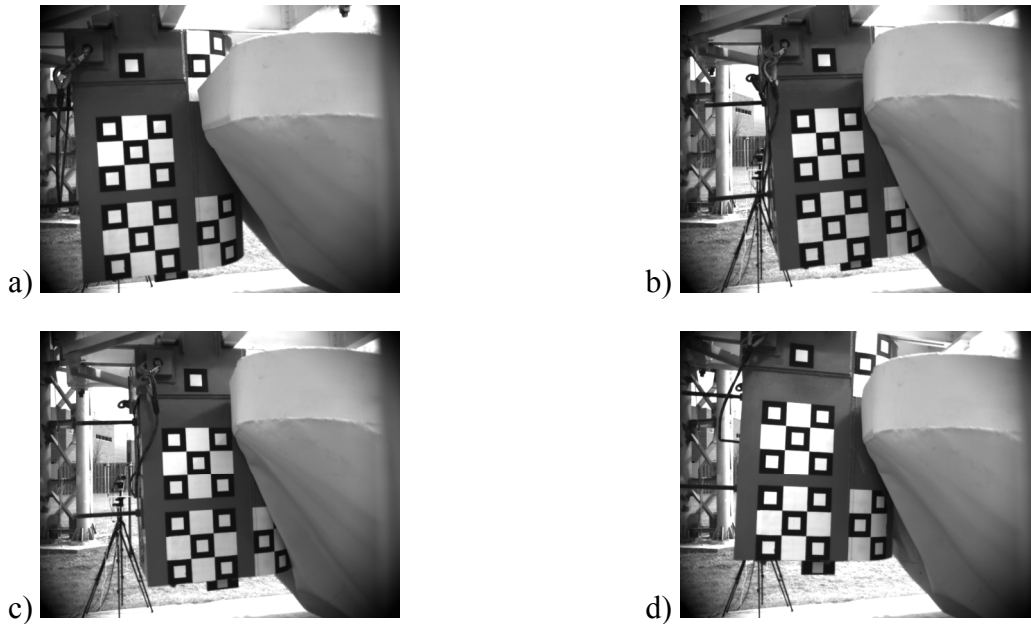


Figure 7.26 Barge deformation at various stages of impact for impact test RND3:
 a) Incipient contact; b) Intermediate stage; c) At peak (maximum) deformation (prior to rebound); d) Residual deformation after rebound (zero force level)

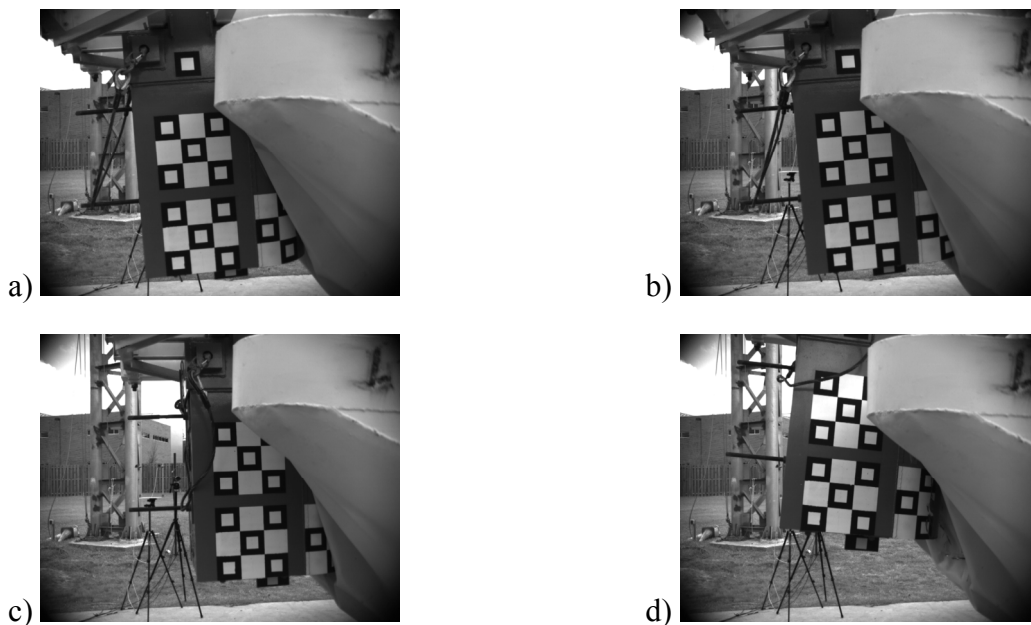


Figure 7.27 Barge deformation at various stages of impact for impact test RND4:
 a) Incipient contact; b) Intermediate stage; c) At peak (maximum) deformation (prior to rebound); d) Residual deformation after rebound (zero force level)

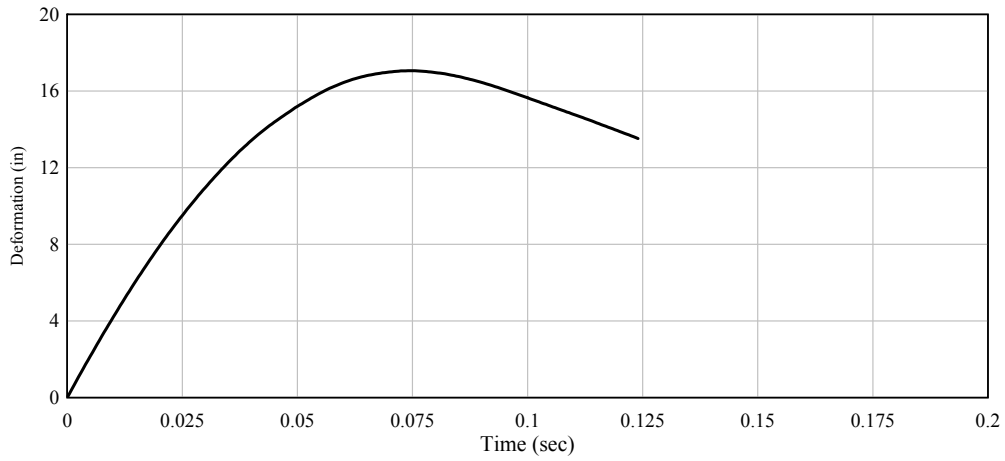


Figure 7.28 Incremental deformation time-history for test RND2

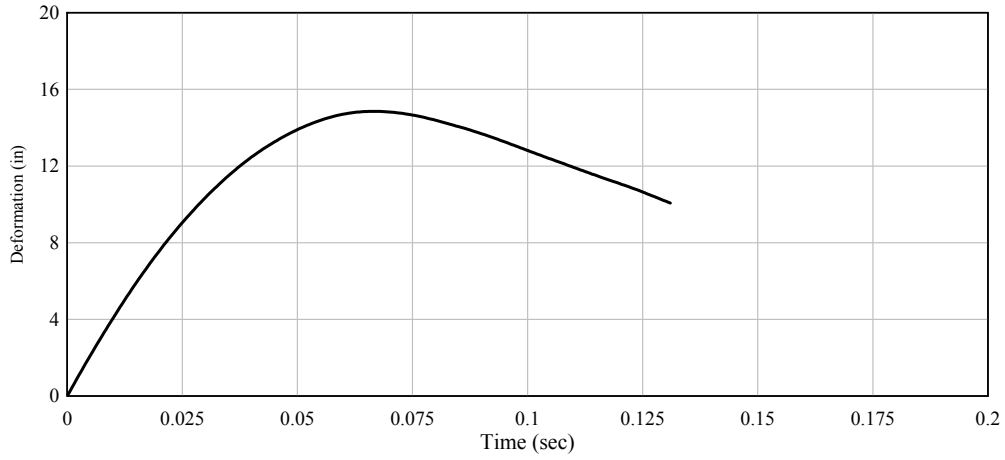


Figure 7.29 Incremental deformation time-history for test RND3

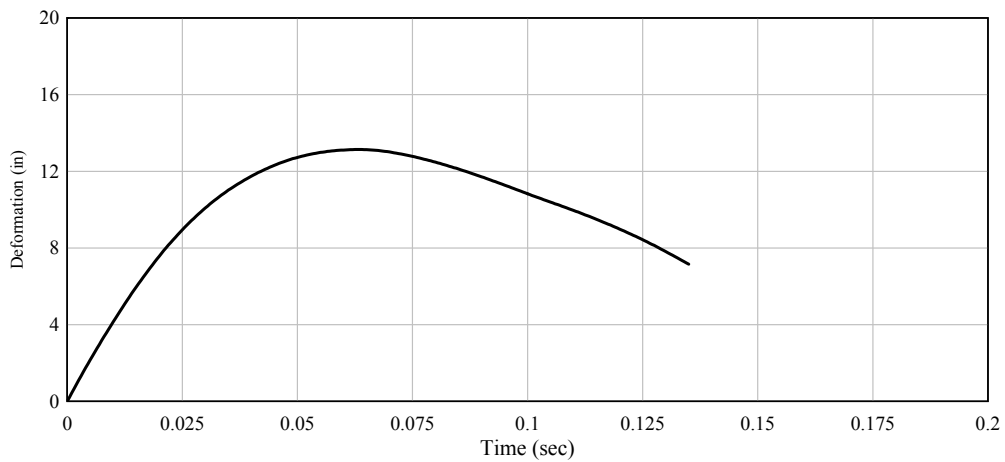


Figure 7.30 Incremental deformation time-history for test RND4

7.4 Test FLT1: Initial Flat Nose Impact Test

Whereas the weight of the impact block with the *round* nose attached was 9,219 lbf, the weight of the block with the *flat* nose attached was 9,700 lbf; nearly 500 lbf heavier due to the differing geometry and larger volume of the flat nose. As a result of the increase in weight, the first impact test with the flat nose (FLT1) was conducted using drop height of approximately 14 ft so as to impart the same impact energy as was generated by the lighter round nose when dropped from 15 ft. Moreover, while the impact energies for FLT1 and RND1 were the same, the impact momentums for these cases were also very close, differing by less than 2%.

Similar to test RND1, test FLT1 caused inelastic buckling of internal stiffening trusses (inside the barge) in the vicinity of the impact zone (Fig. 7.31). However, in contrast to RND1, test FLT1 caused a greater number of these trusses to be immediately engaged upon impact, due to the flat face on the impact block. Consequently, the deformation zone produced by test FLT1 appeared (qualitatively) more extensive than that produced by test RND1.

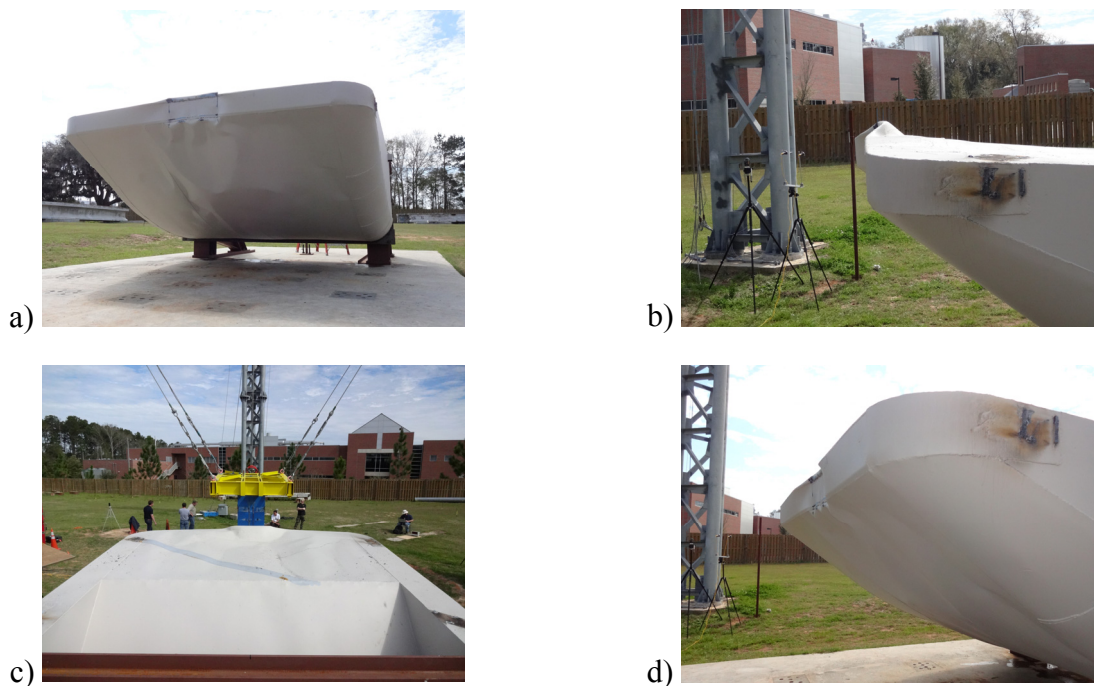


Figure 7.31 Initial flat nose impact test (FLT1) of barge bow:
a) Bottom view of impact zone; b) Side view of impact zone; c) Rear view of impact zone;
d) Isometric view of impact zone

7.4.1 Break beam and tape switch data

Procedures analogous to those previously outlined in Section 7.2.1 for round nose (RND) tests were used to collect and process break beam and tape switch data for all flat nose (FLT) impact tests.

7.4.2 Acceleration and impact force data

Acceleration and force time-history data from impact test FLT1 are shown in Figs. 7.32 and 7.33. Similar to the data previously shown in Fig 7.6 for test RND1, the peak value in Fig. 7.33 for test FLT1 is attributed to the force required to inelastically buckle the internal stiffening trusses in the vicinity of the impact zone. However, the force data in Fig. 7.33 also illustrate differences in response as compared to test RND1. Specifically, for test FLT1, the force level was 40% higher than for RND1, while the pulse duration was 20% shorter. These observations are consistent with the observed deformation pattern of the barge bow replicate following test FLT1. By engaging a greater number of the internal stiffening trusses immediately upon impact (in FLT1), a stiffer response was elicited, as characterized by higher forces and shorter load duration.

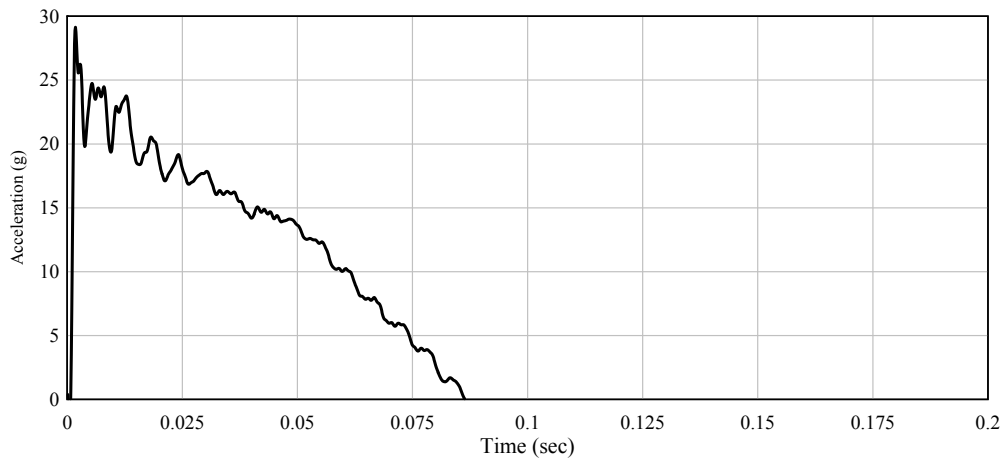


Figure 7.32 Averaged and filtered acceleration time-histories obtained from impact test FLT1

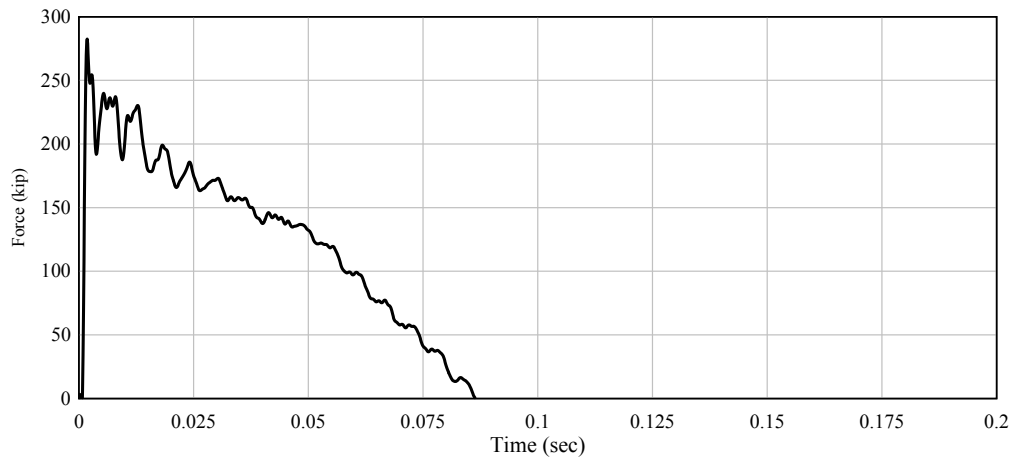


Figure 7.33 Impact force time-histories computed for impact test FLT1

7.4.3 Deformation data

As illustrated by 3D laser scans of the second replicate barge bow before (Fig. 7.34) and after (Fig. 7.35) test FLT1, the zone of deformation can be clearly identified. Maximum deformation depth at the center of the impact zone, prior to elastic recovery, was 8.5 in. (presented qualitatively in Fig. 7.36 and quantitatively in Fig. 7.37). After elastic recovery, the permanent deformation depth was found to be 6.25 in. Compared to test RND1, test FLT1 resulted in less maximum deformation, less permanent deformation, and less elastic recovery—all attributable to the width of the flat-faced nose.

7.4.4 Force-deformation relationship

The force-deformation relationship for impact test FLT1 (Fig. 7.38), constructed utilizing the methods outlined in Section 7.2.4, shows a very stiff initial response of the barge, resulting in the maximum impact force occurring at a low deformation level (less than 1 in.). This contrasts the response presented earlier for test RND1 (Fig. 7.11) in which a more gradual development of force was evident, with the maximum occurring after the barge had sustained almost 4 in. of deformation.



Figure 7.34 3D scan of undeformed replicate barge bow (prior to flat-faced nose test series)

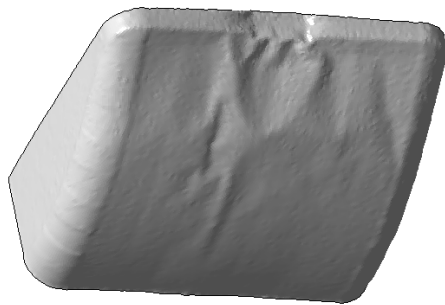


Figure 7.35 Permanent barge deformation following test FLT1

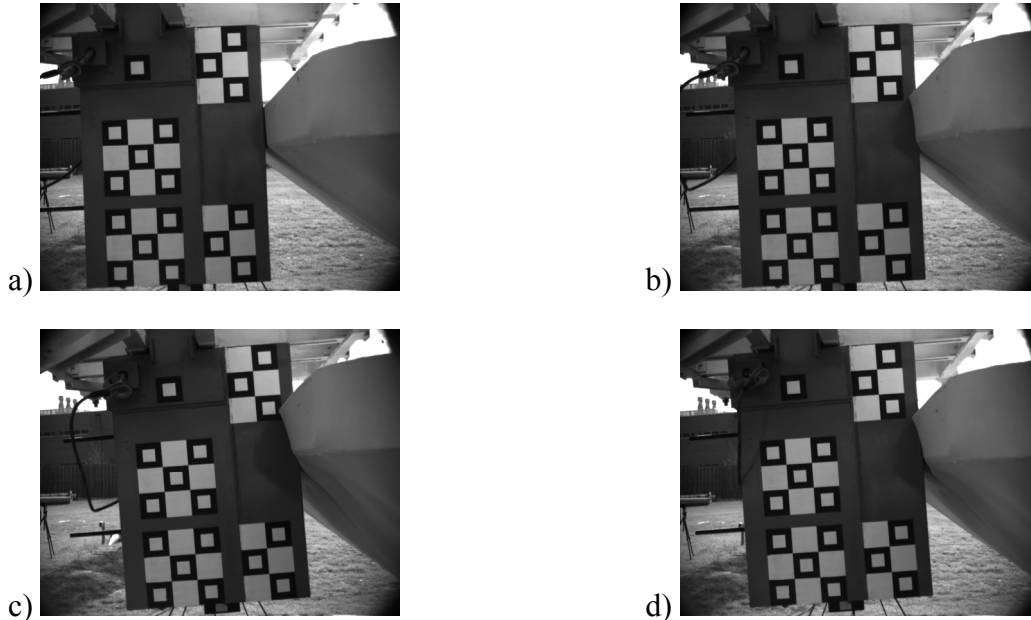


Figure 7.36 Barge deformation at various stages of impact for impact test FLT1:
 a) Incipient contact; b) Intermediate stage; c) At peak (maximum) deformation (prior to rebound); d) Residual deformation after rebound (zero force level)

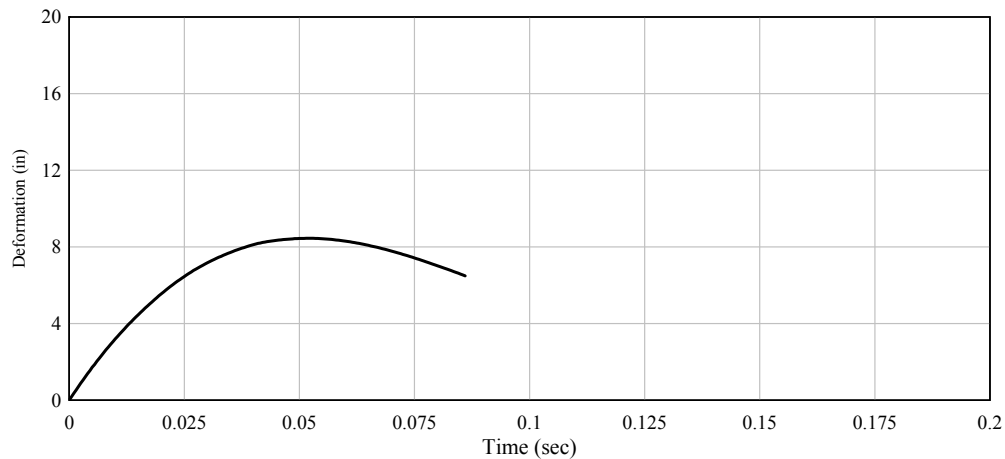


Figure 7.37 Deformation time-history computed from high speed video for impact test FLT1

Total energy absorbed by the barge replicate during test FLT1, determined by computing the area under the curve shown in Fig. 7.38, was found to be within 2% of the initial kinetic energy of the impact block. Additionally, identical to test RND1, the plastically dissipated energy in test FLT1 was found to be 94% of the initial kinetic energy, whereas the rebound energy was found to be 6% of the initial kinetic energy.

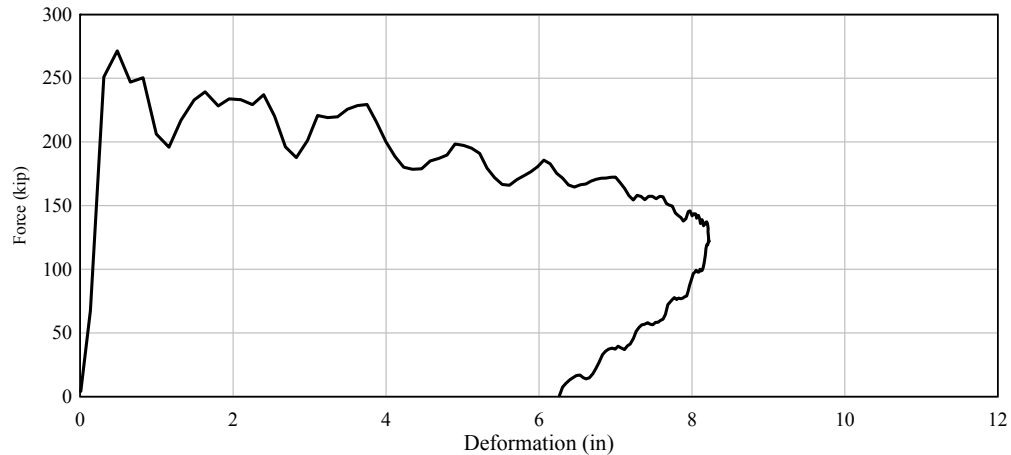


Figure 7.38 Force-deformation relationship for impact test FLT1

7.5 Test FLT2-FLT4: Subsequent Flat Nose Impact Tests

Following the initial impact test (FLT1) with the flat-faced impact block, three subsequent tests (FLT2, FLT3, FLT4) were conducted from a drop height of 19 ft. As for test FLT1, the drop height for tests FLT2-FLT4 was reduced—relative to that used for RND2-RND4, to account for the increased flat nose block weight. As illustrated in Figs. 7.39-7.41, tests FLT2-FLT4 produced more widespread deformation than tests RND2-RND4. At the end of test FLT3, the entire height of the impact block penetrated into the barge bow. For consistency with the RND test series, however, the decision was made to conduct a fourth flat nose impact test (FLT4), despite the fact that the height of the deformation zone somewhat exceeded the height of the impact block. Note that even under these conditions, comparisons could still be made between the two test series (RND and FLT). Finally, throughout most of the FLT test series, minimal material fracture was observed; however, following test FLT4, several fracture seams began to open near the bottom of the impact zone.

7.5.1 Break beam and tape switch data

Contact times and impact velocities (computed from optical break beam data) for impact tests FLT2-FLT4 were determined using the same procedures as outlined in Section 7.2.1.

7.5.2 Acceleration and impact force data

Acceleration time-histories (Figs. 7.42-7.44) and impact force time-histories (Figs. 7.45-7.47) for impact tests FLT2-FLT4 were determined by employing the same data processing techniques described in Section 7.2.2. In contrast to the RND test series, the sustained force levels were lower in the FLT test series, but with correspondingly longer pulse durations. In addition, increases in the sustained force levels recorded during repeated FLT impacts was not observed (as was the case in the RND test series). Finally, very short duration force spikes, caused by inertial resistance at the point of initial contact, were present in the FLT2-FLT4 force data, similar in nature to those noted in RND2-RND4 data.

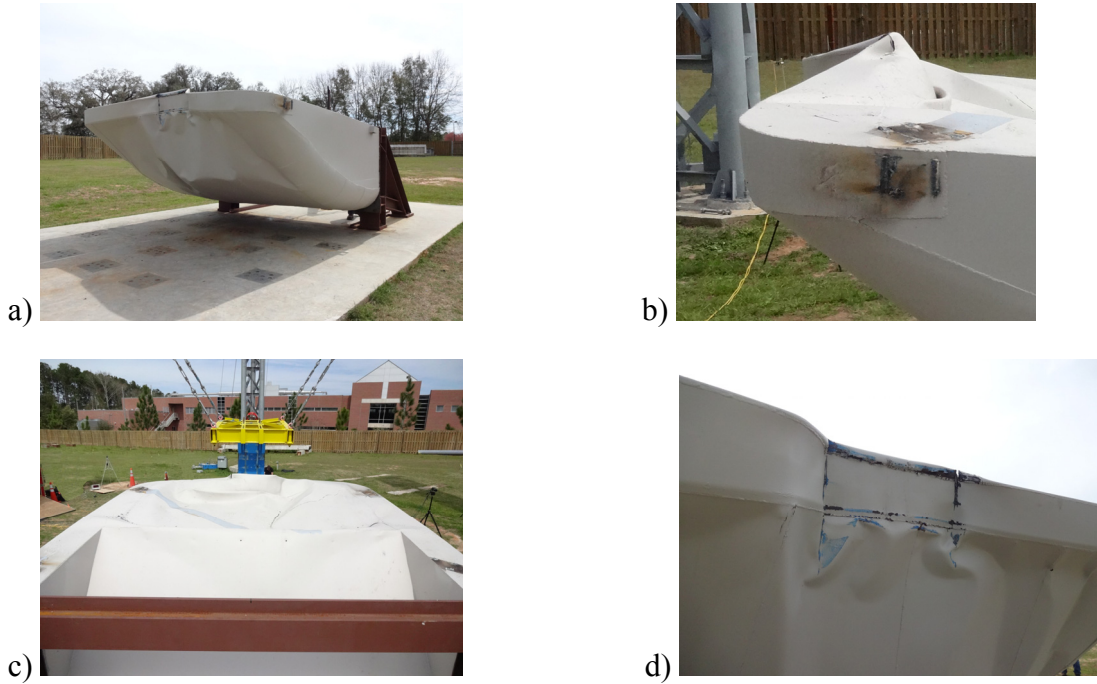


Figure 7.39 Flat-faced nose impact test FLT2 of barge bow:
 a) Bottom view of impact zone; b) Side view of impact zone; c) Rear view of impact zone;
 d) Isometric view of impact zone

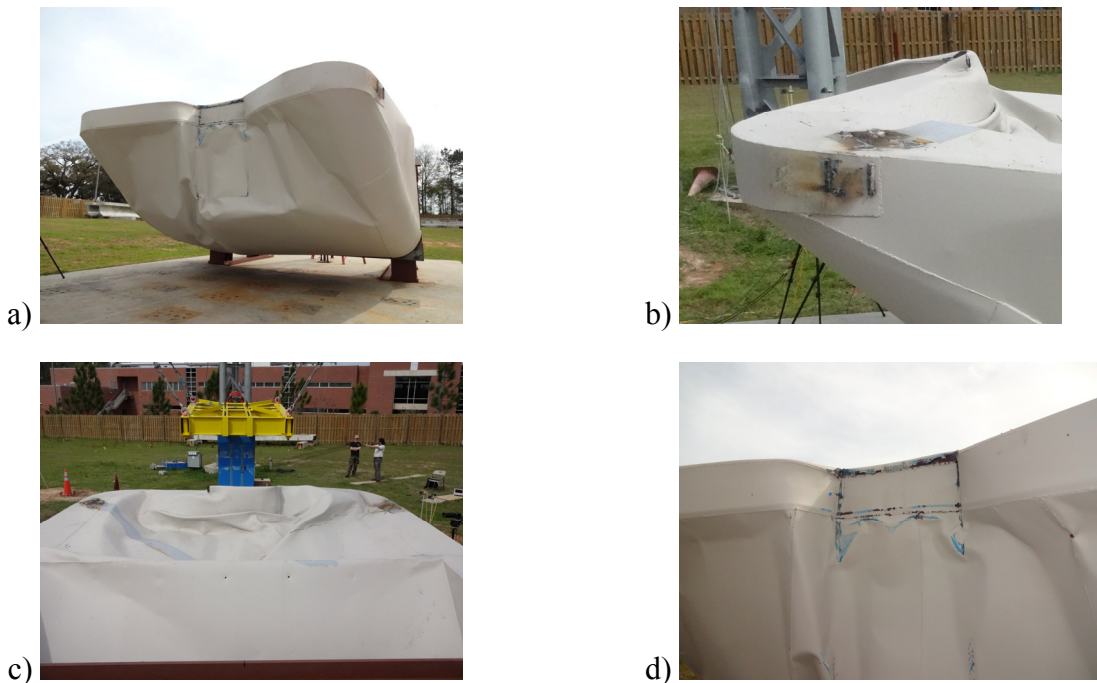


Figure 7.40 Flat-faced nose impact test FLT3 of barge bow:
 a) Bottom view of impact zone; b) Side view of impact zone; c) Rear view of impact zone;
 d) Isometric view of impact zone

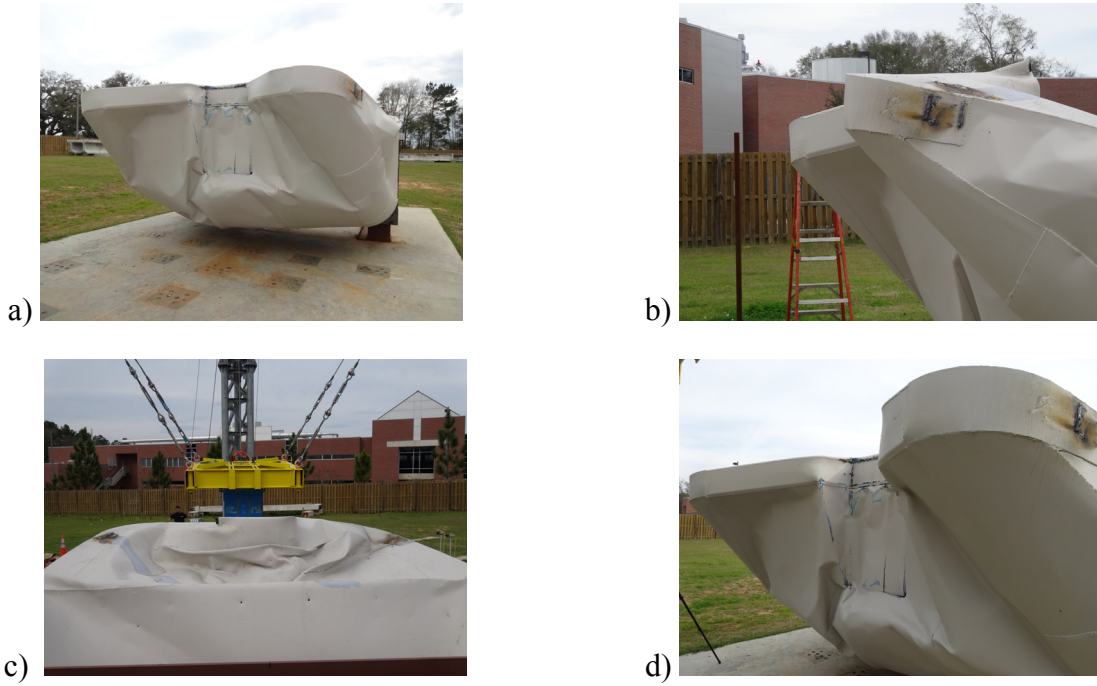


Figure 7.41 Flat-faced nose impact test FLT4 of barge bow:
 a) Bottom view of impact zone; b) Side view of impact zone; c) Rear view of impact zone;
 d) Isometric view of impact zone

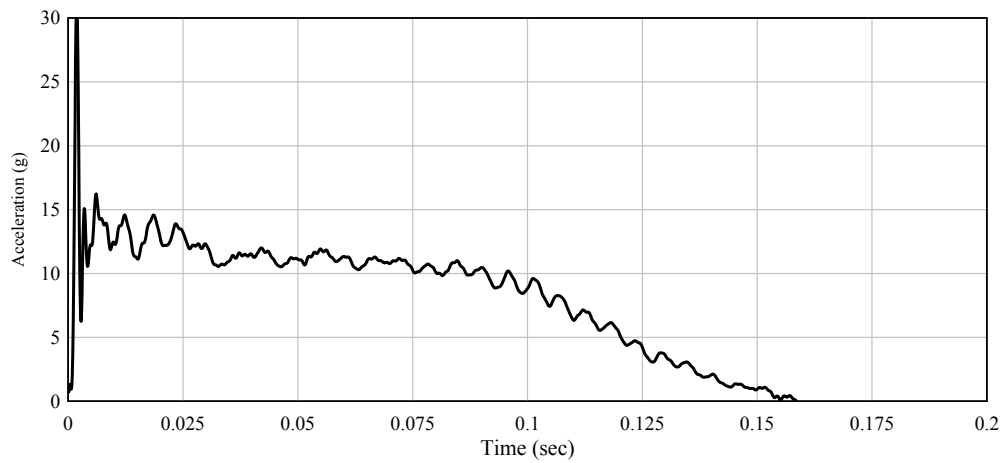


Figure 7.42 Averaged and filtered acceleration time-histories obtained from impact test FLT2

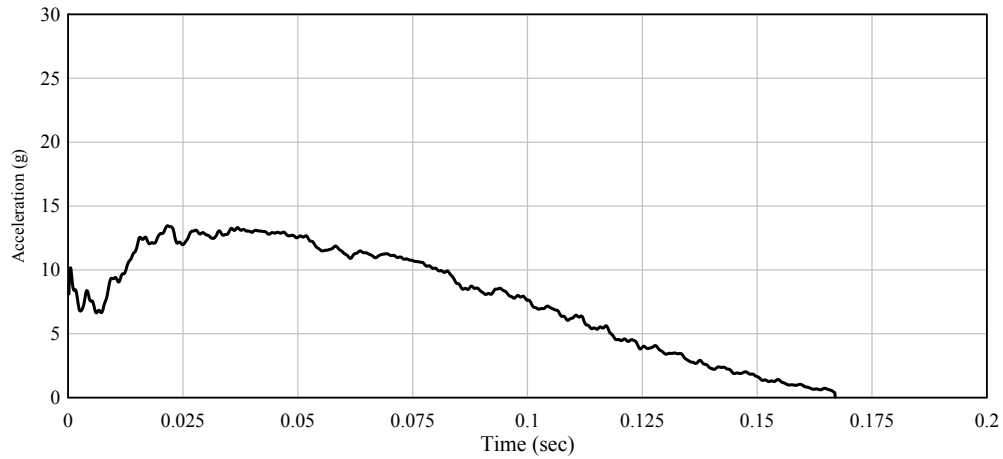


Figure 7.43 Averaged and filtered acceleration time-histories obtained from impact test FLT3

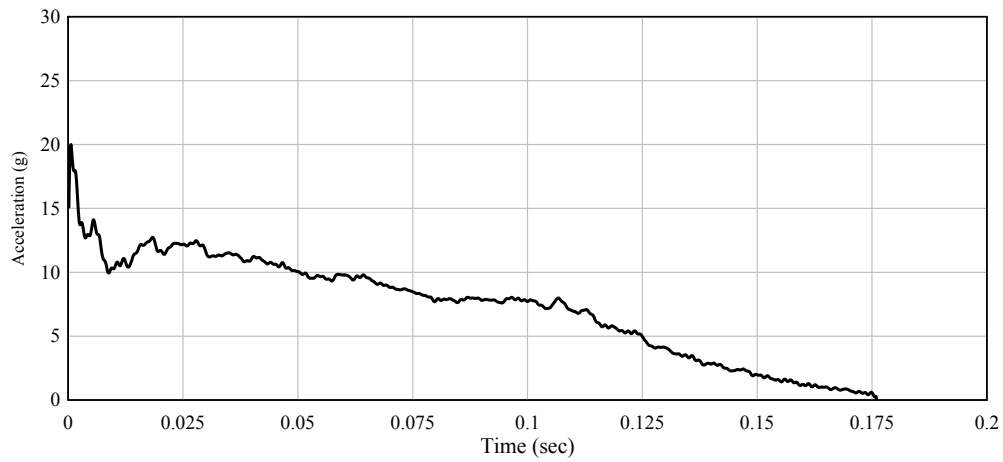


Figure 7.44 Averaged and filtered acceleration time-histories obtained from impact test FLT4

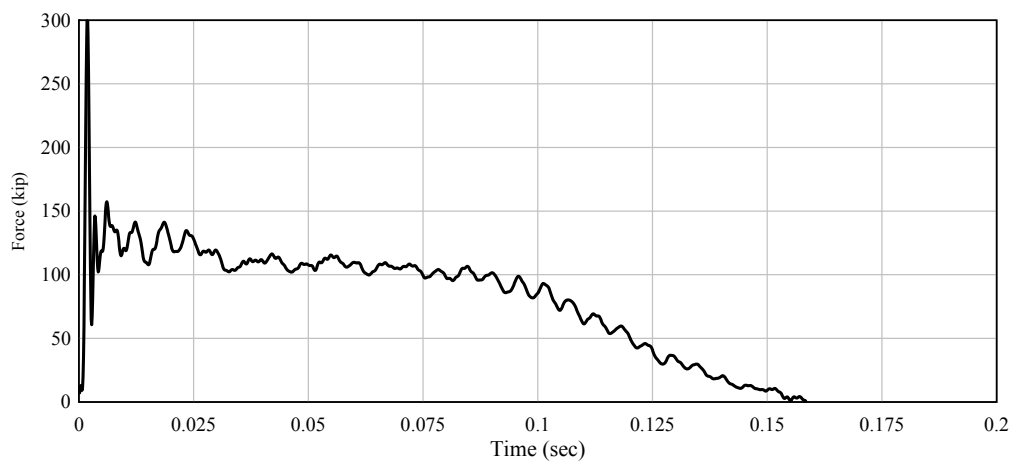


Figure 7.45 Impact force time-histories for test FLT2

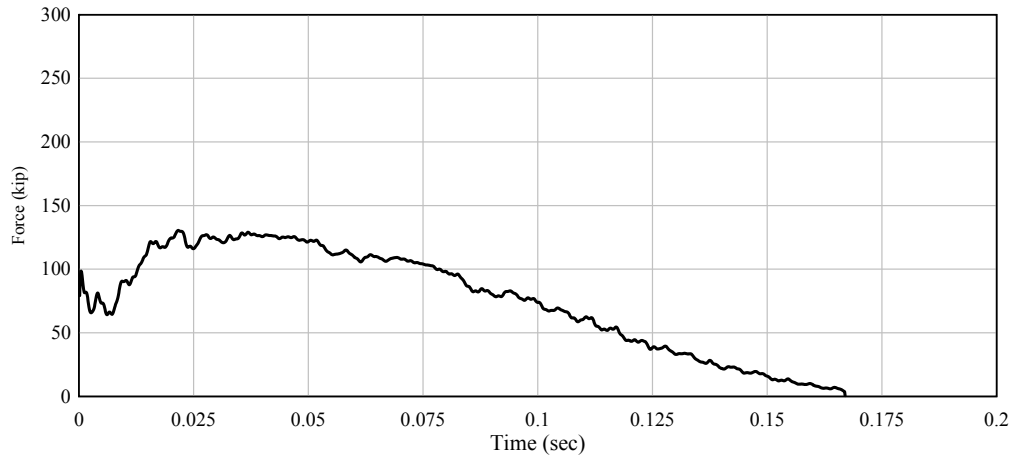


Figure 7.46 Impact force time-histories for test FLT3

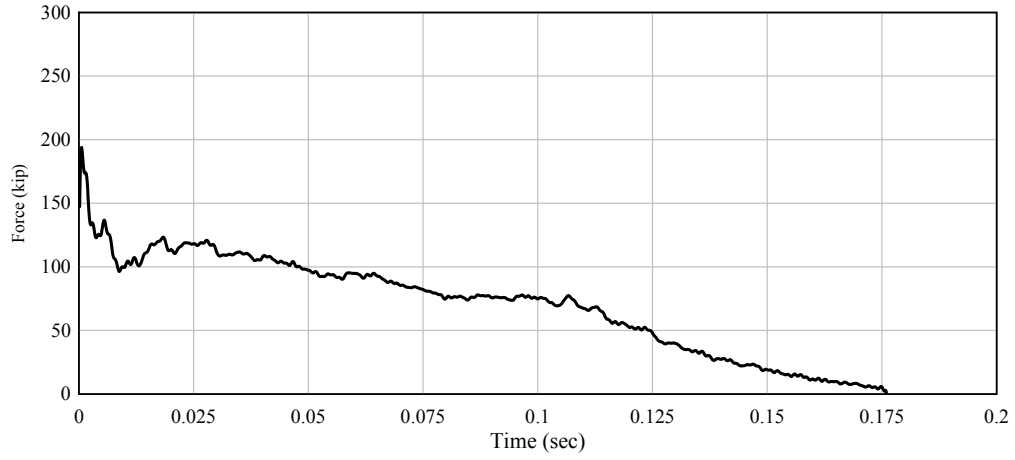


Figure 7.47 Impact force time-histories for test FLT4

7.5.3 Deformation data

As previously discussed, the deformation patterns on the barge bow following each experiment in the FLT test series (Figs. 7.48 – 7.50) showed a broader spread of deformation than that observed during the RND test series. In addition, significantly higher levels of plastic deformation were accrued during tests FLT2-FLT4 (presented qualitatively in Figs. 7.51-7.53 and quantitatively in Figs. 7.54-7.56) than occurred during RND; FLT plastic deformations were as much as 50% larger than corresponding RND plastic deformations.

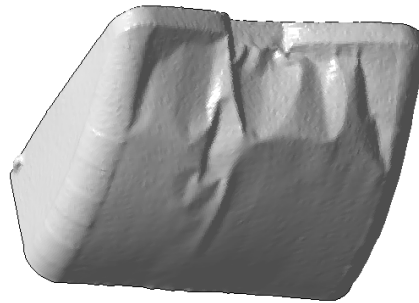


Figure 7.48 Permanent barge deformation following test FLT2

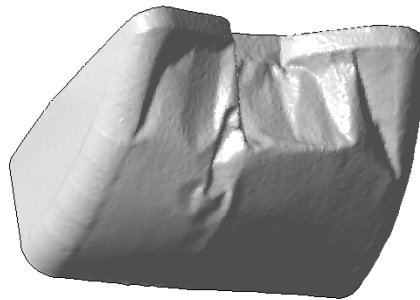


Figure 7.49 Permanent barge deformation following test FLT3

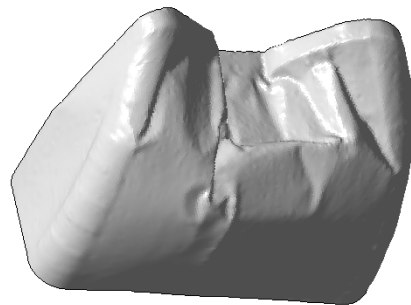


Figure 7.50 Permanent barge deformation following test FLT4

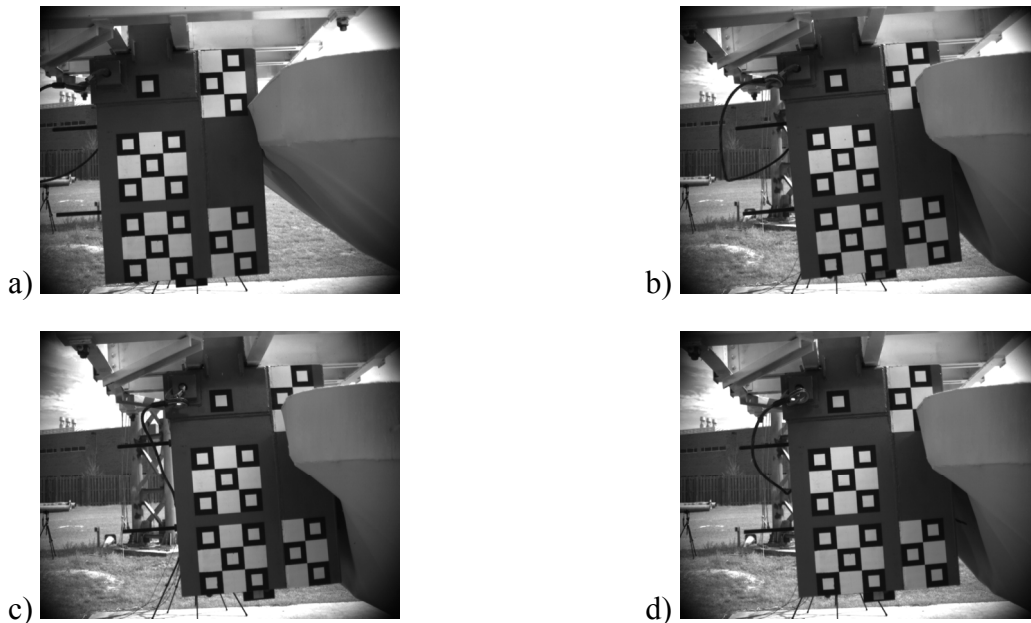


Figure 7.51 Barge deformation at various stages of impact for impact test FLT2:
 a) Incipient contact; b) Intermediate stage; c) At peak (maximum) deformation (prior to rebound); d) Residual deformation after rebound (zero force level)

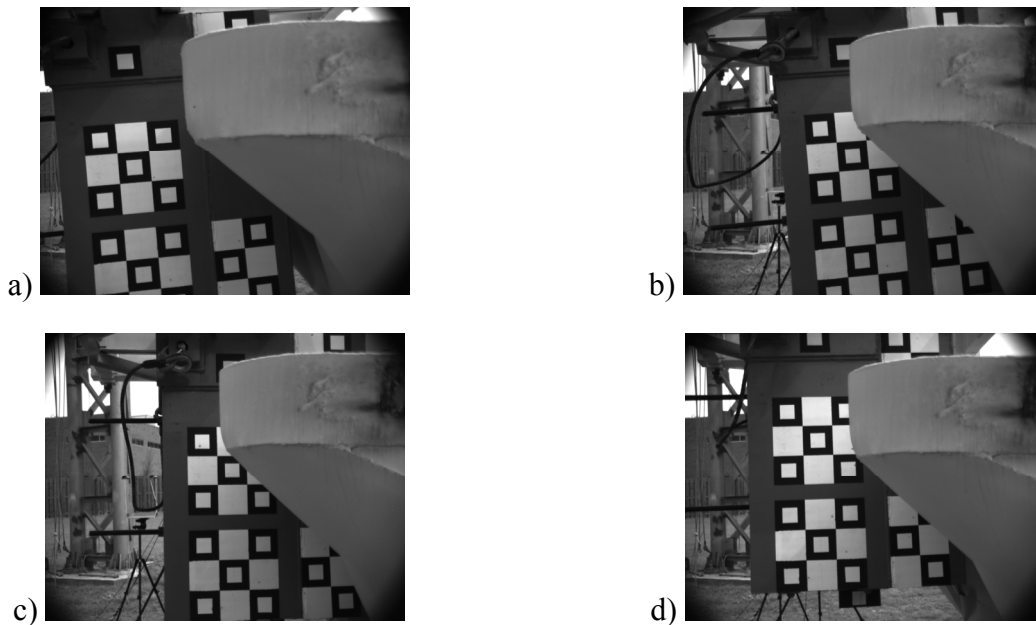


Figure 7.52 Barge deformation at various stages of impact for impact test FLT3:
 a) Incipient contact; b) Intermediate stage; c) At peak (maximum) deformation (prior to rebound); d) Residual deformation after rebound (zero force level)

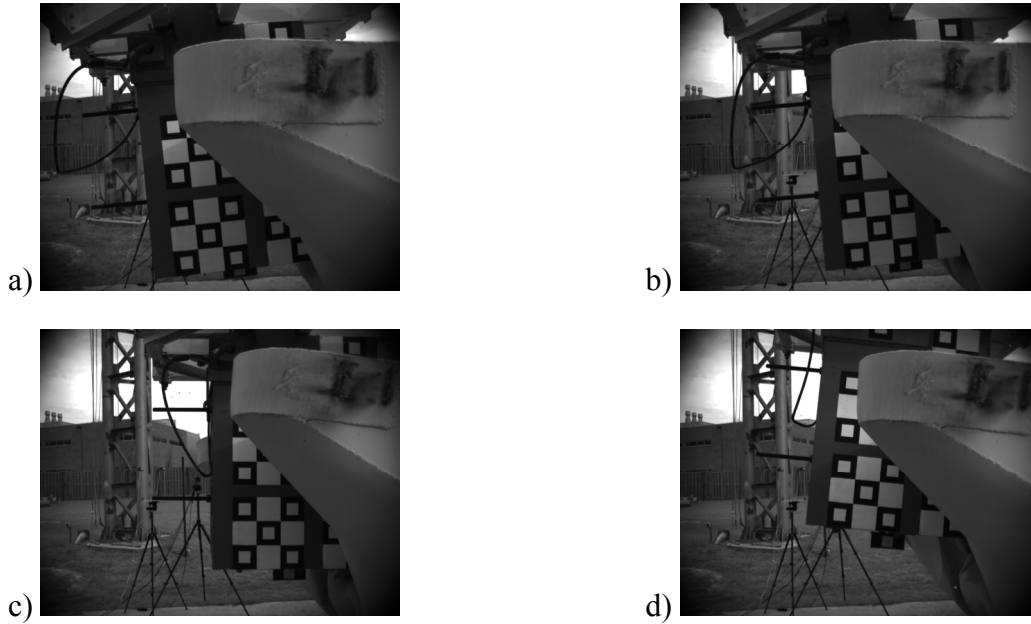


Figure 7.53 Barge deformation at various stages of impact for impact test FLT4:
 a) Incipient contact; b) Intermediate stage; c) At peak (maximum) deformation (prior to rebound); d) Residual deformation after rebound (zero force level)

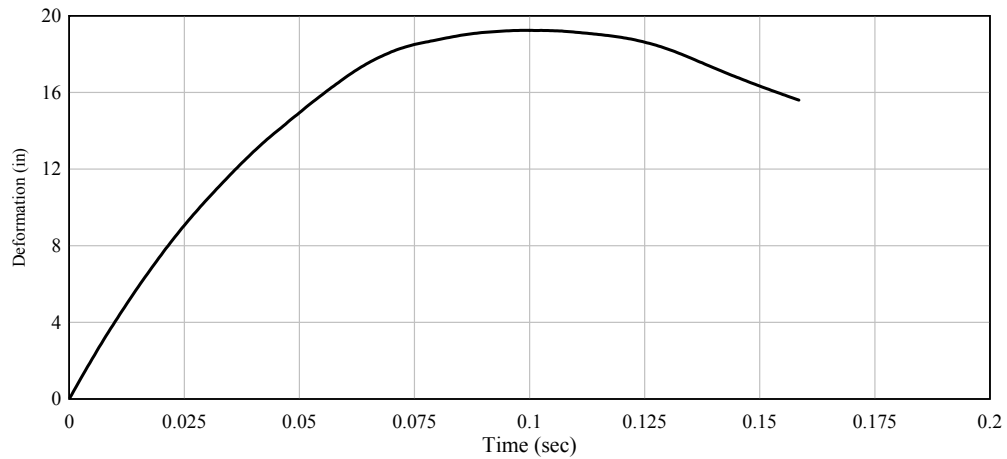


Figure 7.54 Incremental deformation time-history for test FLT2

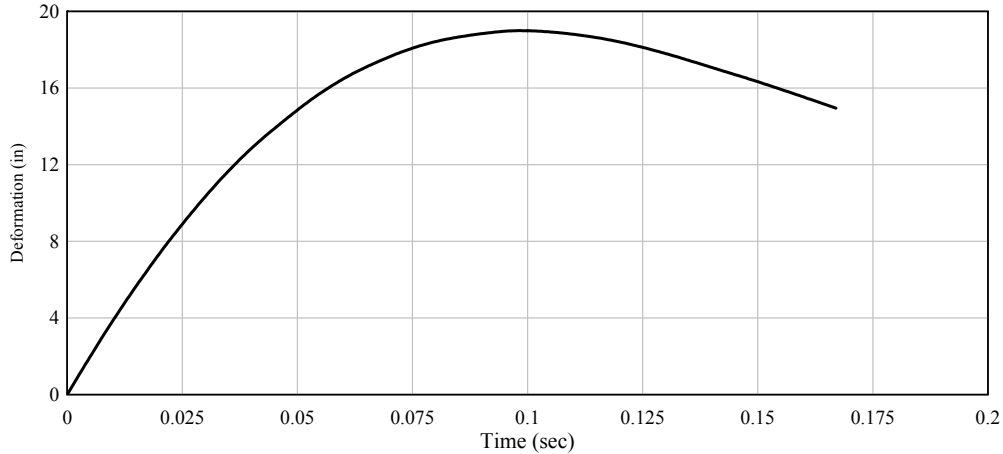


Figure 7.55 Incremental deformation time-history for test FLT3

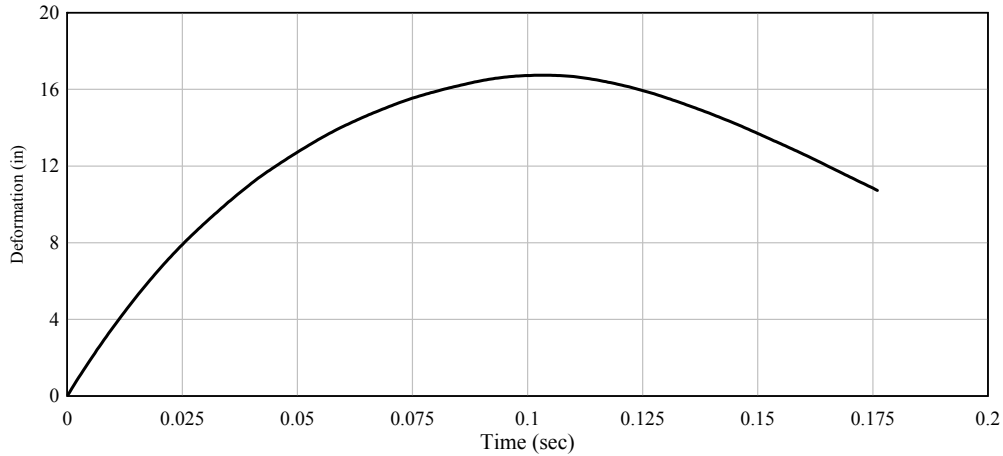


Figure 7.56 Incremental deformation time-history for test FLT4

7.6 Summary of Results from all Tests: RND1-RND4 and FLT1-FLT4

Tabular summaries of important test conditions (e.g., impact velocities) and test results (e.g., impact forces) are quantified for the round nose (RND) and flat nose (FLT) impact test series in Table 7.2 and Table 7.3, respectively. To provide additional insight into the test results, the force and incremental deformation data presented in previous sections for individual tests (RND1-RND4, FLT1-FLT4) are merged together to form force versus *total* deformation curves. Specifically, data from tests RND1-RND4 are merged to form an overall force versus total deformation curve for the round (RND) impactor, and data from tests FLT1-FLT4 are merged to form an overall force versus total deformation curve for the flat (FLT) impactor.

Merging the individual data sets for each test series was accomplished by accumulating (summing) the incremental deformations from one test to the next. For example, total deformations during test RND2 were computed by adding the permanent deformation at the end of test RND1 to the incremental deformations measured during test RND2. Likewise, total

deformations during test RND3 were computed by adding the permanent deformation at the end of test RND2 to the incremental deformations measured during test RND3. Concatenated curves of this form were thus formed for the round nose test series (Fig. 7.57) and the flat nose test series (Fig. 7.59).

Next, the *unloading* and *re-loading* portions of each curve were removed, forming an overall ‘backbone’ curve for each test series: round nose (Fig. 7.58) and flat nose (Fig. 7.60). Each of these backbone curves constitutes an overall force-deformation curve that is similar in form to the curve that would have been produced by a single, *very-high-energy* impact (a condition that was not feasible using the gravity pendulum due to practical limitations on pendulum height).

7.6.1 Discussion of overall round (RND) nose force-deformation relationship

In the round (RND) force-deformation curve shown Fig. 7.58, a transition in the resistance mechanism of the barge can be observed. Initially, at the lower deformation levels concordant with the response of the barge during the initial impact test (RND1), the resistance of the barge was derived from the stiffness of the internal trusses and frames. Once the internal trusses and frames buckled inelastically, larger deformations were accrued during successive impacts. The resulting large deformation levels led to the development of catenary force in the headlog plate and hull plates, with anchorage provided by the internal trusses and frames outside of the impact zone, in addition to the side-walls and side-frames of the barge. With increasing accumulation of deformation, this catenary resistance mechanism became more effective; as a result, impact forces increased (moderately) in magnitude with increasing deformation.

7.6.2 Discussion of overall flat (FLT) nose force-deformation relationship

The flat (FLT) force-deformation curve shown in Fig. 7.60 highlights a significant difference in the response—compared to the RND test series—due to the geometry of the flat-faced nose. As previously discussed, the maximum force occurred at a low deformation level (less than 1 in.). Following the occurrence of this maximum, force levels diminished until approximately 10 in. of deformation had been accrued. Force levels then remained relatively constant at approximately 120 kips as the barge crushed plastically. Unlike the round (RND) test series, no increase in force attributed to catenary action was observed. This difference can be explained by the deformation patterns on each barge. By virtue of the larger initial contact area afforded by the shape of the flat-faced nose, a greater number of internal stiffening trusses and frames inside the barge were buckled during the first impact test (FLT1). As a result, the level of restraint necessary to maintain catenary resistance was largely unavailable. Consequently, the sole mechanism available to absorb impact energy was additional crushing of internal trusses and frames in the immediate vicinity of the impact area, which resulted in a near perfectly plastic response (i.e., nearly constant force magnitude).

7.7 Validation of Finite Element Modeling and Analysis Procedures

Using the simulation techniques described in Chapter 5, finite element simulations were conducted using the same impact block masses and impact velocities that were used in experimental tests RND1-RND4 and FLT1-FLT4. Subsequently, all finite element time-history

data were post-processed using the same filtering methodology that was employed to process the experimental data. Backbone force-deformation curves were then constructed for the round and flat impact conditions based on finite element simulation results. Comparisons of finite element simulation results to corresponding experimental data (Figs. 7.61 and 7.62) indicate that several key aspects of the finite element model and analysis procedures are validated:

- Variations of forces, deformation levels, barge deformation patterns, resistance mechanisms, and energy dissipation characteristics indicated by the finite element results generally agreed well with those measured experimentally.
- Impact forces for flat face impact surfaces (e.g., rectangular pile caps and pier columns) were confirmed, experimentally, to be larger than forces generated on rounded impact surfaces, as predicted analytically using finite element simulations.
- Use of an elastic, perfectly-plastic force-deformation curve provides an appropriate level of conservatism for use in bridge design. For ranges of impact energy and barge deformation that are typical in bridge design, impact forces generated at lower deformation levels were not exceeded at high deformation levels, either experimentally or analytically. Thus the UF/FDOT elastic, perfectly-plastic force-deformation curve previously proposed is appropriate, and a force-deformation curve that hardens with increasing deformation, as is currently used in AASHTO, is unnecessary.

As noted above, force-deformation curves quantified experimentally and using finite element impact simulations (Figs. 7.61 and 7.62) were generally in very good agreement with each other, with the only significant discrepancy occurring in the very earliest portion of the data for the FLT impact series. Specifically, in Fig. 7.62 the finite element results revealed a low-deformation, and very short-duration, force spike that was not observed in the experimentally measured force data. Given the typical range of natural periods of bridge piers, such a short-duration force spike would have negligible influence on pier response and is therefore of little practical importance for bridge design. Nonetheless, the presence of the spike, as well as other observed differences between the experimental and finite element results, are most likely attributable to differences between the geometrically- and materially-‘perfect’ finite element barge model and the ‘as-built’ barge bow replicates. Due to practical limitations associated with physical barge fabrication, particularly at reduced (0.4) scale, some differences between the finite element models and the physical barge replicates were known to exist:

- Fabrication tolerances: Whereas the finite element models strictly adhered to the geometry specified in fabrication plans, the physical barge bow replicates, due to practical limitations on physical fabrication tolerances, deviated slightly from the intended geometry.
- Initial stress levels: Residual stresses, introduced by welding processes used in barge bow replicate construction, were not included in the finite element models.

Despite these differences, the observed agreement in behavior between physical experiment and finite element simulation indicates that the analytical methodology employed in the creation of the finite element models is reliable. By extension, since the same methods were utilized in the development of the UF/FDOT load prediction model, it can be concluded that the analytical basis for the UF/FDOT load model is valid.

Table 7.2 Tabular summary of data collected from impact series with round impactor

Impact test	Impact velocity (ft/s)	Impact energy (kip-ft)	Impact momentum (kip-sec)	Max force (kip)	Force pulse duration (sec)	Incremental plastic deformation (in)	Cumulative plastic deformation (in)	Drop height (ft)	Impact block weight (lbf)
RND1	30.6	135	9.20	203	0.1076	8	8	15	9,219
RND2	36.5	191	11.0	210	0.1240	13.5	21.5	20	9,219
RND3	36.2	188	10.9	181	0.1312	10.1	31.6	20	9,219
RND4	37.1	198	11.1	229	0.1351	7.2	38.8	20	9,219

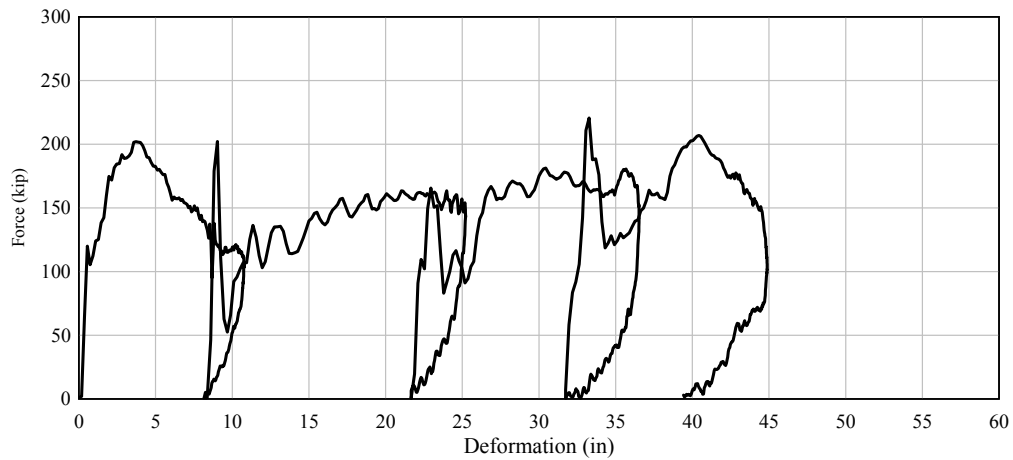


Figure 7.57 Force-deformation relationship for impact series with round impactor

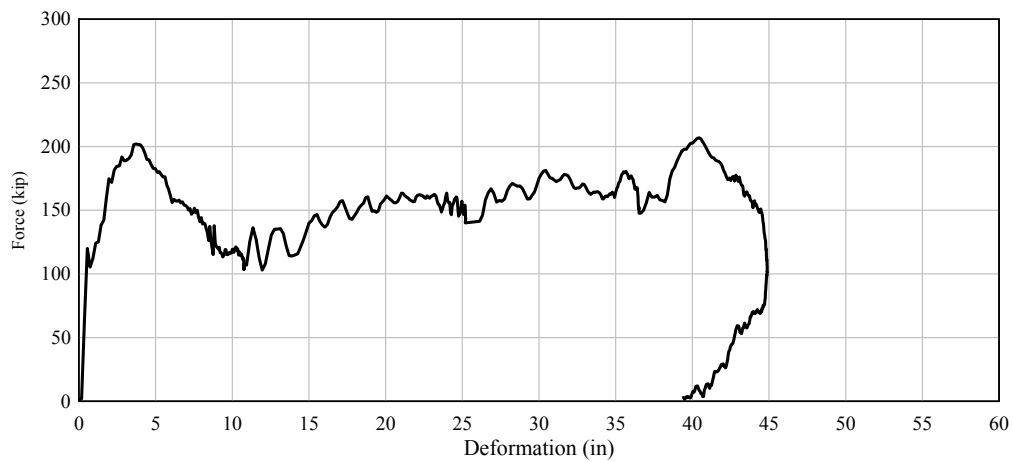


Figure 7.58 Backbone curve for impact series with round impactor

Table 7.3 Tabular summary of data collected from impact series with flat impactor

Impact test	Impact velocity (ft/s)	Impact energy (kip-ft)	Impact momentum (kip-sec)	Max force (kip)	Force pulse duration (sec)	Incremental plastic deformation (in)	Cumulative plastic deformation (in)	Drop height (ft)	Impact block weight (lbf)
FLT1	30	135	9.04	282	0.086	6.25	6.25	14	9,700
FLT2	35.4	189	10.62	304	0.159	15.5	21.75	19	9,700
FLT3	35.6	191	10.73	130	0.167	15	36.75	19	9,700
FLT4	35.6	191	10.73	195	0.176	10.75	47.50	19	9,700

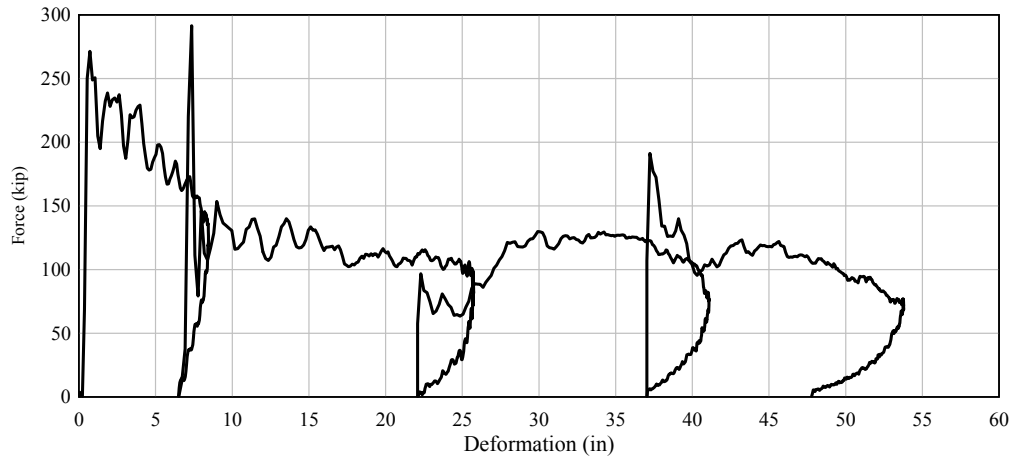


Figure 7.59 Force-deformation relationship for impact series with flat-faced impactor

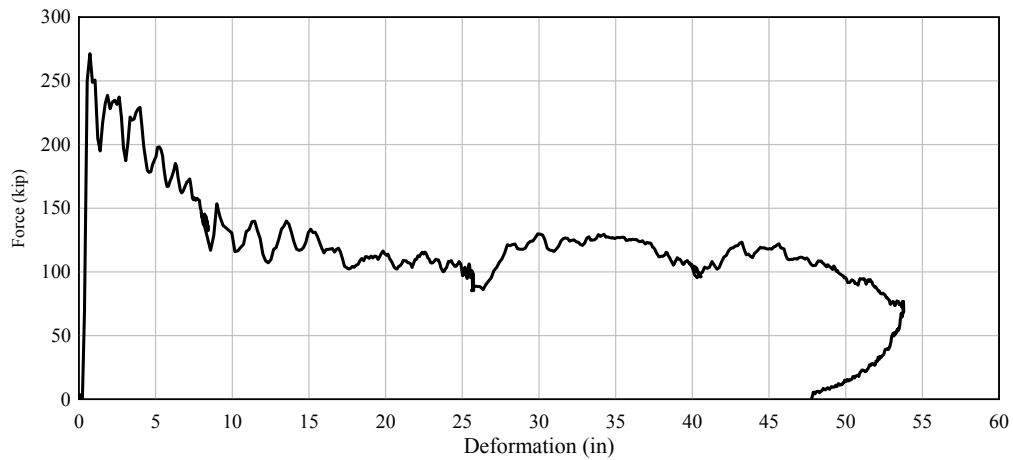


Figure 7.60 Backbone curve for impact series with flat-faced impactor

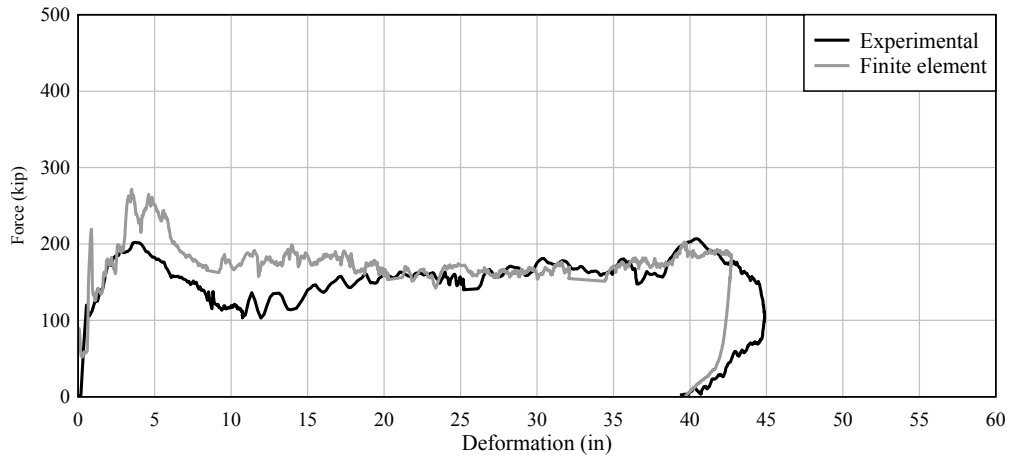


Figure 7.61 Comparison of experimental and analytical backbone curves for RND series

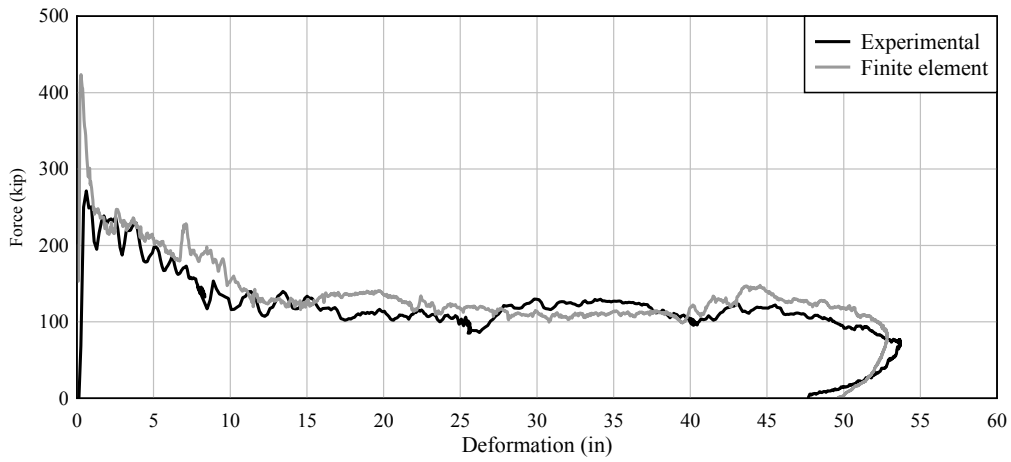


Figure 7.62 Comparison of experimental and analytical backbone curves for FLT series

CHAPTER 8

REVISED RISK ANALYSIS PROCEDURES FOR VESSEL IMPACT WITH BRIDGES

8.1 Introduction

A primary goal of the current study was to implement current and past UF/FDOT research findings into a format that can be adopted in the FDOT and AASHTO vessel collision design provisions. Research conducted by UF and FDOT (summarized in Chapter 2) has demonstrated the inadequacy of certain portions of the AASHTO procedures, and revised design and analysis tools have been developed to address these limitations. Thus, in the current study, a unified bridge design methodology was developed that incorporates these state-of-the-art structural and risk analysis procedures into the overall AASHTO risk assessment procedure without unduly complicating the bridge design process. Details of the revised methodology (hereafter referred to as “UF/FDOT methods”) are discussed in this chapter. In Chapters 8 and 9, the UF/FDOT methods are demonstrated and compared to the current AASHTO methodology using two bridges that are currently in service.

Throughout this chapter, numerous references are made to “AASHTO provisions/methods/procedures.” In each such instance, these refer to the *AASHTO Guide Specifications and Commentary for Vessel Collision Design of Highway Bridges* (2009). Furthermore, numerous references are made to “UF/FDOT methods/procedures.” These refer to a large body of work, comprising multiple publications (discussed in Chapter 2), and in general, refer to the modified risk assessment procedure outlined in Section 8.2.2. References to specific publications are provided where needed.

8.2 Options for Implementing UF/FDOT Research in Design Practice

Given the complexity and relative uncertainty associated with the vessel collision hazard, to date, vessel collision design (in accordance with AASHTO) involves conducting a comprehensive risk assessment in which the annual probability of bridge failure is directly quantified (recall Chapter 2). Thus, the current design process requires that practitioners gather a significant amount of site-specific vessel traffic and waterway alignment data, perform numerous structural analyses, and employ probabilistic analysis procedures that are not frequently used in structural engineering. In developing a new design methodology that incorporates UF/FDOT research findings—particularly including dynamic bridge analysis—significant attention was given to the prospect of adding complexity to a design process that is already relatively complicated. Two possible implementation strategies were considered: an LRFD approach in which the AASHTO risk assessment was replaced with a simpler deterministic procedure, and a targeted approach in which the AASHTO procedures were minimally revised to incorporate UF/FDOT methods. As discussed in the following sections, the latter approach was adopted.

8.2.1 Simplified LRFD approach to vessel collision design

Given the complexity of the current AASHTO risk assessment procedures, simplification of the overall vessel collision design process was considered in an effort to minimize the impact

of proposed changes on design complexity. One strategy considered was to develop a load and resistance factor design (LRFD) procedure in lieu of the rigorous risk analysis currently employed. Beginning in the early 1980s (Ellingwood et al. 1980), LRFD procedures were developed for various loading scenarios with the goal of obtaining uniform levels of structural reliability for all modes of failure (limit states). Statistical uncertainties associated with loads and structural resistance are included in the LRFD process by means of load and resistance factors. Use of such factors relieves the design engineer from having to directly quantify the probability of structural failure using complicated reliability analysis procedures.

The prospect of adapting an LRFD methodology to the problem of vessel collision with bridges was investigated in this study. For brevity, the full discussion is excluded here but is included in Appendix L. Ultimately, it was determined that the LRFD approach is infeasible for two primary reasons. First, statistical variability associated vessel impact loading is significantly larger than for other sources of loading (e.g., live load). Consequently, vessel impact load factors that account for all sources of uncertainty would need to be much larger than for other types of loads, which could result in unreasonably conservative designs. Secondly, in current design practice, the acceptable risk of structural failure due to vessel collision is defined differently than for other sources of loading. For vessel collision, acceptable risk is assessed based on the probability of *bridge* failure: i.e., catastrophic failure of multiple bridge elements resulting in collapse of the superstructure. In contrast, for typical LRFD, load and resistance factors are calibrated to achieve a desired probability of *member* failure (e.g., a single column). Currently for vessel collision, individual member failure is permitted, so long as the superstructure does not collapse. Thus, adapting LRFD principles to the vessel collision problem would require radical changes to the definition of acceptable risk. Fully understanding the cost implications of such a fundamental change would require additional research which was outside the scope of the current study. Consequently, targeted changes to the existing AASHTO risk assessment framework were developed that incorporated state-of-the-art methods developed by UF/FDOT.

8.2.2 Targeted revisions to AASHTO risk assessment procedure

Recall that the AASHTO risk assessment procedure involves quantifying the annual frequency of bridge collapse due to vessel collision (AF):

$$AF = N(PA)(PG)(PC)(PF) \quad (8.1)$$

where N is the number of vessel transits per year, PA is the probability of a given vessel becoming aberrant, PG is the geometric probability of an aberrant vessel impacting a given bridge element, PC is the probability of impact-induced bridge element collapse, and PF is a protection factor to account for navigational obstructions that may reduce impact risk.

Within the AASHTO risk assessment framework, prior UF/FDOT research has focused exclusively on improving the accuracy of procedures used to quantify PC . In the AASHTO

provisions, PC is computed as a function of the ratio H/P , where H is the ultimate static strength of a bridge element (generally a pier) and P is a static vessel collision force. While it is rational that PC should rely on measures of structural resistance and load magnitude, the form of the AASHTO PC expression is not conceptually consistent, in that it predicts relatively small failure probabilities for cases in which the impact load magnitude greatly exceeds bridge element capacity. Furthermore, the AASHTO definition of PC simplifies impact loading by treating it as a static load event, which neglects important dynamic structural response characteristics that commonly make the static approach unconservative. Therefore, UF/FDOT research has focused on developing an alternative expression for PC that is both consistent with reliability theory and that incorporates dynamic structural response into the definition of impact load and structural capacity.

To incorporate UF/FDOT research findings into the AASHTO procedures, the most targeted approach possible was to only modify selected provisions in the formulation of PC , and leave all other terms in the AF expression unmodified. To develop the revised risk assessment methodology, three primary modifications were made to the AASHTO procedure:

- The AASHTO barge impact load-prediction model was replaced with the model developed by Getter and Consolazio (2011).
- The AASHTO static analysis was replaced with analysis procedures that account for dynamic amplification effects in the impacted structure. A tiered approach was taken, in which an engineer can choose one of three analysis options, in order of increasing complexity and accuracy:
 - a. Static bracketed impact analysis (SBIA): An equivalent-static analysis method consisting of a small set of static load cases (Getter et al. 2011);
 - b. Applied vessel impact loading (AVIL): A transient dynamic analysis method incorporating an approximate impact load history that is computed prior to conducting the analysis (Consolazio et al. 2008), and;
 - c. Coupled vessel impact analysis (CVIA): A transient dynamic analysis method in which the vessel impact load and corresponding bridge response are coupled and computed simultaneously (Consolazio and Cowan 2005).
- The AASHTO probability of collapse (PC) expression was replaced with the UF/FDOT PC expression (Davidson et al. 2013).

The various methods mentioned above are discussed in detail in Chapter 2 and also in the demonstrative examples provided in Chapters 8 and 9. Therefore, detailed discussion is omitted here for brevity.

8.2.3 Ship impact considerations

Research conducted by UF/FDOT has focused almost exclusively on the problem of bridges being impacted by river barges, as opposed to larger seagoing ships such as bulk cargo carriers. Consequently, certain components of the proposed collision design framework are not

applicable to ship impact (e.g., the impact load-prediction model) or have simply not been tested for ship impact. Given the similarities between barge and ship collision, it is highly likely that the three UF/FDOT impact analysis methods (CVIA, AVIL, and SBIA) can be adapted to ship collision. However, additional research effort—outside the scope of the current study—would be necessary to validate these methods for ship collision. Similarly, the revised *PC-D/C* expression was developed based only on barge impact scenarios. However, it is unlikely that an analogous expression derived based on ship impact scenarios would be significantly different in nature. Further research should be conducted to demonstrate the applicability of the UF/FDOT *PC* expression to ship collision scenarios, or if necessary, develop a separate expression specifically for ship collision.

Because such activities were beyond the scope of the current study, it was necessary to create two separate analysis tracks within the UF/FDOT risk assessment procedure: one for barge collision and one for ship collision. In the ship impact track, the AASHTO ship collision load model, simple static analysis procedure, and existing AASHTO *PC* expression are still used. However, in the barge impact track, the UF/FDOT load model, three-tiered analysis approach, and revised *PC* expression are used. Because the proposed UF/FDOT barge collision risk assessment procedure follows the structure of the existing AASHTO risk assessment procedure, bridge failure estimates computed using the two tracks (ship and barge collision) can still be intermingled for bridges that are at risk for collision by both vessel types.

8.3 Overview of Revised Risk Analysis Procedure

It is recognized that implementing the revisions summarized above will result in significant changes to the current vessel collision risk analysis workflow. The existing AASHTO risk analysis workflow—effectively a summary of the discussion provided in Chapter 2—is shown in Fig. 8.1. Note that structural analysis falls outside the main risk analysis computations. Thus, for each combination of vessel group and exposed pier, it is not necessary to conduct any structural analysis. Commonly in practice, the pier pushover capacities (H_j) are determined *a priori* and are used to compute the probability of pier collapse for each combination of vessel group and pier (PC_{ij}). Indeed, the most common approach for a new design involves back-calculating pier pushover capacities (H_j) that both satisfy the overall acceptable level of risk (AF) and distribute risk evenly among the various piers at risk for impact. Piers are then designed such that the static pushover capacity exceeds the back-calculated values. The ability to take this approach is important, because limited information about the bridge design is required to back-calculate acceptable pushover capacities, thus minimizing the number of iterations required to arrive at an acceptable bridge design.

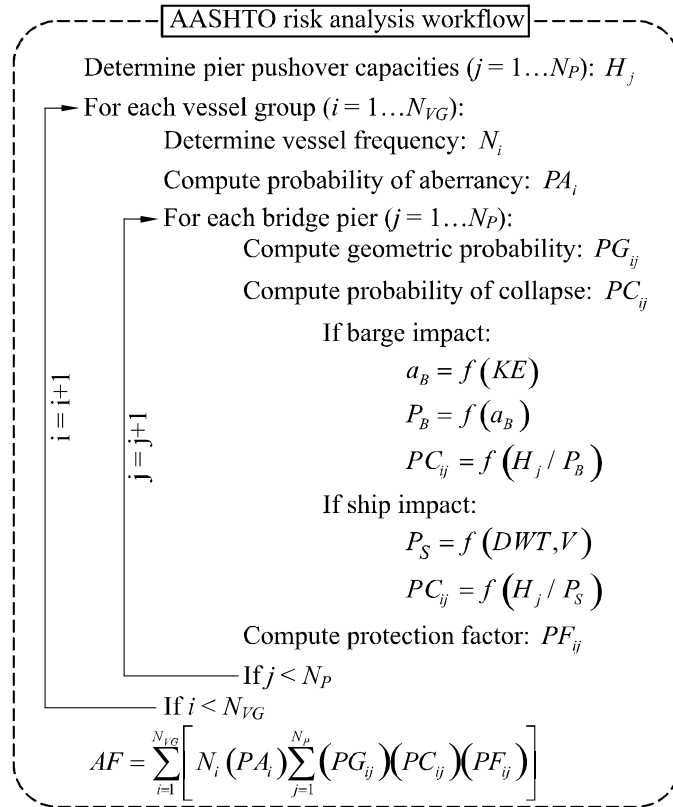


Figure 8.1 Current AASHTO vessel collision risk assessment procedure

The UF/FDOT risk analysis workflow is summarized in Fig. 8.2. The methodology differs from the existing AASHTO procedure in a few ways. First, a tiered structural analysis approach is employed, in which three analysis options—one static (SBIA) and two time-domain dynamic (AVIL, CVIA)—are available. The analysis options are shown in order of increasing complexity and accuracy. Note that these analysis procedures have been developed based on UF/FDOT research, and therefore account for important dynamic amplification effects that the AASHTO static analysis approach neglects. The UF/FDOT workflow (Fig. 8.2) also differs from the existing AASHTO process (Fig. 8.1) in that it employs the revised probability of collapse (PC) expression recently developed by UF/FDOT research.

Aside from modified analysis procedures, the UF/FDOT procedure differs from AASHTO in that a structural analysis must be conducted for every combination of pier and vessel group in order to arrive at estimates for PC and ultimately calculate AF . Therefore, when designing a new bridge, it is not possible to back-calculate acceptable minimum pier capacities, as is common practice with the AASHTO procedure (discussed above). Consequently, to design new bridges in accordance with the UF/FDOT procedure, it is first necessary to develop a trial design to the level of detail that is required to perform structural analyses using one of the three tiered methods (SBIA, AVIL, or CVIA). If the trial design is found to be inadequate (AF higher than the specified frequency), then the design must be strengthened in an iterative fashion until the bridge satisfies the acceptable level of risk. In developing strengthened alternative designs for the

example cases discussed in Chapters 9 and 10, iterating from an inadequate design to one that was acceptable was found to be a relatively time-efficient process.

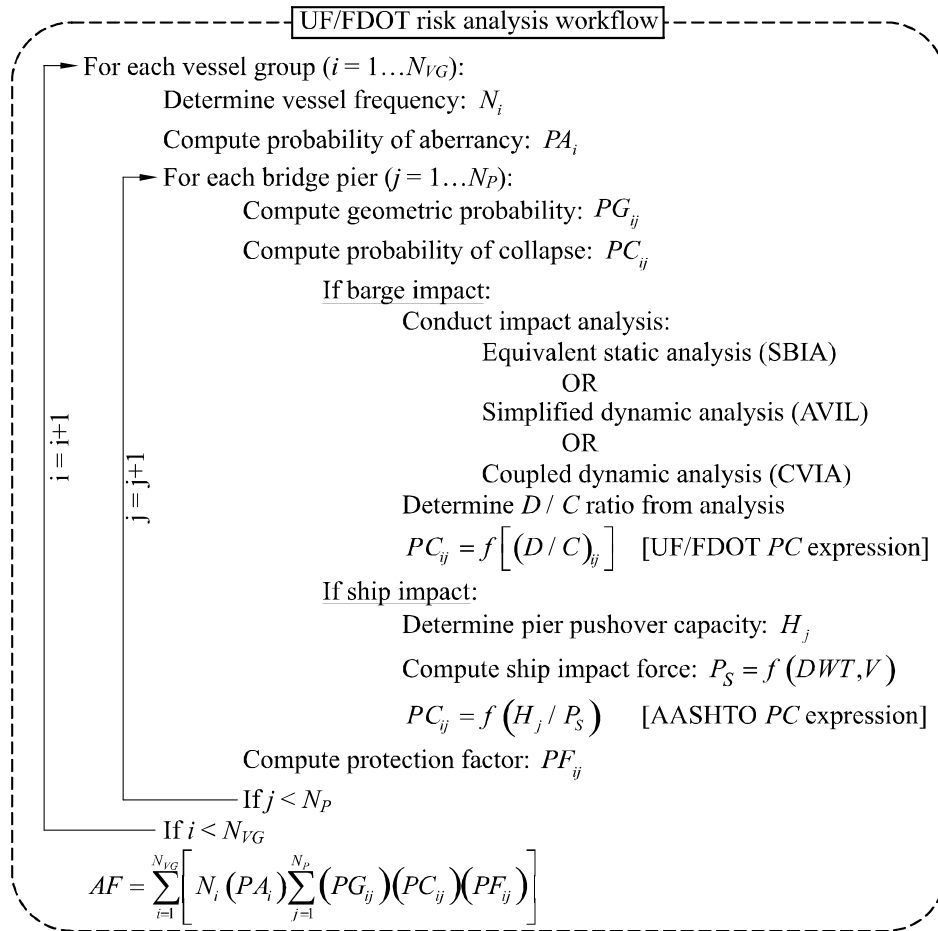


Figure 8.2 Revised UF/FDOT vessel collision risk assessment workflow

8.4 Use of UF/FDOT PC Expression in Design

An important aspect the UF/FDOT risk assessment procedure that must be considered is how to use the UF/FDOT probability of collapse (PC) expression in a design setting. Recall that the purpose of the PC expression is to allow design engineers to estimate the probability that a bridge element (e.g., a pier) will collapse by conducting a single deterministic impact analysis. Currently in the AASHTO provisions, PC is computed as:

$$PC = \begin{cases} 0.1 + 9(0.1 - H/P) & 0.0 \leq H/P < 0.1 \\ 1 - H/P & 0.1 \leq H/P < 1.0 \\ 0 & H/P > 1.0 \end{cases} \quad (8.2)$$

where H is the static pushover capacity of the pier, and P is the AASHTO static impact load. Thus, PC is a function of a static capacity-to-demand ratio.

Davidson et al. (2013) took a similar approach in the developing the UF/FDOT PC expression. In the revised expression, PC is computed as:

$$PC = 2.33 \times 10^{-6} \cdot e^{13 \cdot D/C} \leq 1.0 \quad (8.3)$$

where D/C is a demand-to-capacity ratio. Because the UF/FDOT expression was derived based on dynamic structural analysis (specifically CVIA), the AASHTO definitions of static capacity and demand cannot be used. Instead, Davidson et al. defined D/C as the percentage proximity to forming a structural mechanism that leads to instability and collapse, in which case, collapse occurs at $D/C = 1.0$.

To further illustrate the Davidson et al. (2013) D/C concept, consider the simplified bridge pier shown in Fig. 8.3. If the pier cap and pile cap are assumed to be effectively rigid, a structural collapse mechanism can occur in two possible ways: two plastic hinges form in all the pier columns (Fig. 8.3a), or two plastic hinges form in all the foundation piles (Fig. 8.3b). Either scenario would lead to catastrophic collapse of the superstructure. In terms of D/C , once either mechanism has fully formed, the pier has a D/C ratio of 1.0. Keeping in mind that the impact response is dynamic in nature, at times before the mechanism forms, D/C is less than 1.0. Also, if the impact severity is not sufficient to form a mechanism, then D/C observed throughout the impact event will always be less than 1.0.

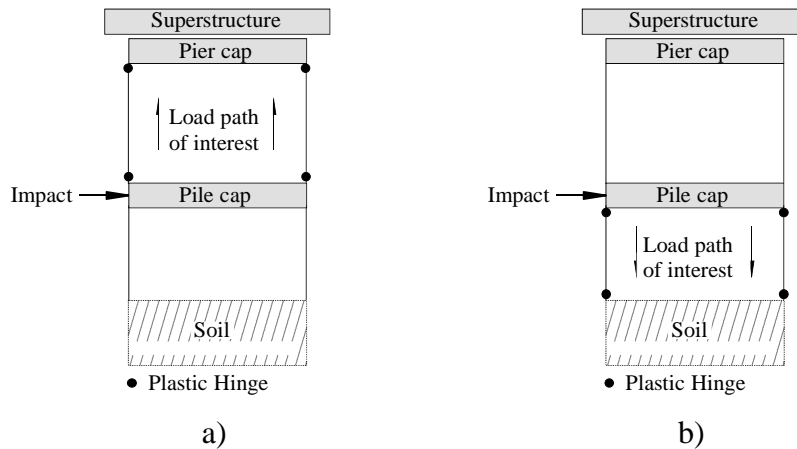


Figure 8.3 Possible pier collapse mechanisms: a) Pier column collapse mechanism; b) Pile collapse mechanism

Based on this concept, Davidson et al. (2013) devised a rigorous definition by which to quantify D/C in the context of time-varying structural response:

$$D/C = \max \left[\left(\frac{1}{m \cdot n} \sum_{i=1}^m \sum_{j=1}^n (D/C)_{ij}^{FBMP} \right)_{\text{columns}}, \left(\frac{1}{m \cdot n} \sum_{i=1}^m \sum_{j=1}^n (D/C)_{ij}^{FBMP} \right)_{\text{piles}} \right] \quad (8.4)$$

where m is the number of members (e.g., piers columns, piles) associated with a given collapse mechanism, n is the number of hinges per member that are necessary to form the corresponding collapse mechanism, and $(D/C)_{ij}^{FBMP}$ is the j th largest element demand-capacity ratio along member i , as reported by FB-MultiPier (internally computed based on biaxial load-moment interaction). See Consolazio et al. (2010a) and Davidson et al. (2013) for a more detailed description of D/C and its theoretical basis.

While this approach to computing D/C is the most rigorous and conceptually consistent definition possible, it is a complicated definition to employ in a design setting. Computing a time-varying estimate of D/C requires a considerable data-reduction effort that can only reasonably be achieved with automated data parsing routines. This effort is further complicated if an engineer employs a different software package than FB-MultiPier to perform the structural analysis, because assessments of load-moment interaction must be made for every column and pile element in the finite element bridge model in order to calculate element-level D/C ratios.

As part of this study, numerous attempts were made to develop a simpler, approximate definition for D/C . By virtue of being approximate, a simplified D/C ratio must be consistently conservative relative to the more rigorous definition suggested by Davidson et al. (2013) in order to maintain safe design outcomes. All simplified definitions considered in this study were found to be moderately conservative with respect to D/C . However, because the UF/FDOT PC expression is highly nonlinear, small increases in D/C estimates result in large (possibly order-of-magnitude) increases in PC . Thus, all simplified options that were considered were found to produce unduly conservative values of PC . Consequently, the rigorous definition described above was employed in all UF/FDOT risk assessment calculations in this study. However, it is worth noting that a simplified definition for D/C may indeed be achievable, and the topic thereby constitutes a potential area for future research.

CHAPTER 9

VESSEL COLLISION RISK ASSESSMENT OF THE BRYANT GRADY PATTON BRIDGE (SR-300) OVER APALACHICOLA BAY, FLORIDA

9.1 Introduction

In this chapter, detailed vessel collision risk assessments are presented for the Bryant Grady Patton Bridge (SR-300) over Apalachicola Bay, Florida. The annual frequency of bridge collapse (AF) was quantified using the revised methodology described in Chapter 8, employing two dynamic structural analysis techniques (CVIA and AVIL) and one equivalent-static analysis technique (SBIA). For comparison, AF was also computed using both the current AASHTO provisions (2009) and the AASHTO guidelines that were available at the time the bridge was designed (1991). Significant differences in AF were observed using the various methods. The final sections in this chapter identify the causes for such differences and provide suggestions for mitigating vessel collision risk within the context of the revised methodology.

The SR-300 Bridge was selected for this study for two primary reasons: 1) it was constructed fairly recently (2004), and was therefore designed to resist vessel collision in accordance with the 1991 AASHTO provisions, and 2) it was at relatively high risk for vessel collision (i.e., vessel collision was a controlling consideration in its design). Indeed, the current bridge was constructed to replace a bridge built in the 1960s, partially because the old bridge was determined to have insufficient strength to withstand high-energy vessel collisions. The new bridge spans approximately four miles over Apalachicola Bay, connecting St. George Island to the Florida mainland at Eastpoint. Vessel traffic that is of interest for quantifying collision risk consists primarily of barge tows and tug boats transiting between local ports, the Gulf Intracoastal Waterway, and the Gulf of Mexico. While vessel traffic volume for this site is relatively light (one or two large vessels per day, on average), the open nature of the waterway (when compared with a typical river crossing) allows for the possibility of vessels colliding with dozens of bridge piers. Consequently, risk to the total bridge is substantially higher than would be the case for a bridge crossing a narrow river with similar traffic volume.

Throughout this chapter, numerous references are made to “AASHTO provisions” or “AASHTO specifications.” These refer to the *AASHTO Guide Specifications and Commentary for Vessel Collision Design of Highway Bridges*. The specific edition (1991 or 2009) is referred to as needed, and if no date reference is given, it should be assumed to refer to the 2009 edition. Furthermore, numerous references are made to “UF/FDOT methods/procedures.” These refer to a large body of work, comprising multiple publications, and in general, refer to the modified risk assessment procedure outlined in Chapter 8. References to specific publications are provided where needed.

9.2 Data Collection

The critical first step in conducting a vessel collision risk assessment is gathering the relevant site data, including waterway, bridge, and vessel traffic characteristics. Because the Bryant Patton Bridge assessment involves an existing structure, a significant proportion of such

data is included in the as-built structural drawings. Specifically, the bridge plans were employed as a resource for:

- Waterway alignment, depth profile, and tidal fluctuations;
- Structural configuration of bridge piers, foundations, and superstructure, and;
- Soil layer profiles and scour estimates.

Waterway characteristics such as water depth and tidal fluctuations were investigated further using publicly available nautical charts of the Apalachicola Bay (NOAA 2013a). Such charts included depth soundings throughout the site and positions of underwater navigational obstructions. Such information was crucial to determining whether portions of the bridge could reasonably be impacted by errant vessels, or whether such vessels might run aground prior to impact. The magnitudes and directions of currents near the bridge were obtained from a comprehensive hydrographic study of Apalachicola Bay conducted in the 1980s (Conner et al. 1982). This information was critical to estimating vessel impact velocities and establishing any appropriate increase in collision risk resulting from crosscurrents.

Vessel traffic characteristics—i.e., vessel sizes, number of transits per year, and expected impact velocities—were obtained from a comprehensive survey of Florida waterways conducted by Wang and Liu (1999). The results of this survey have been compiled into an electronic database by the Florida Department of Transportation (FDOT), and are available as part of a vessel collision risk assessment Mathcad worksheet that is freely available on the FDOT website.

The data collection stage of this risk assessment was significantly aided by the availability of the documents mentioned above. For the design of a new bridge, a much more extensive data collection effort would be required, including site surveys and hydrological studies. Appropriate sources for such information are suggested in the AASHTO Guide Specification (2009).

9.3 Waterway Characteristics

9.3.1 General description

The Bryant Patton Bridge (hereafter referred to as the SR-300 Bridge), is located in Apalachicola Bay, in northwest Florida. The bridge crosses the easternmost end of the Gulf Intracoastal Waterway (GIWW), which is a maintained navigable waterway extending from Carrabelle, Florida (just east of the SR-300 bridge) to Brownsville, Texas. The GIWW primarily serves barge traffic, transporting petroleum products, chemicals, fertilizers, sand, gravel, cement, sulfur, grain, feeds, and logs (NOAA 2013b). The navigation channel passes approximately east-west under a high-rise section of the SR-300 Bridge, and extends east toward Carrabelle, Florida, and west then north to Apalachicola, Florida (Fig. 9.1).

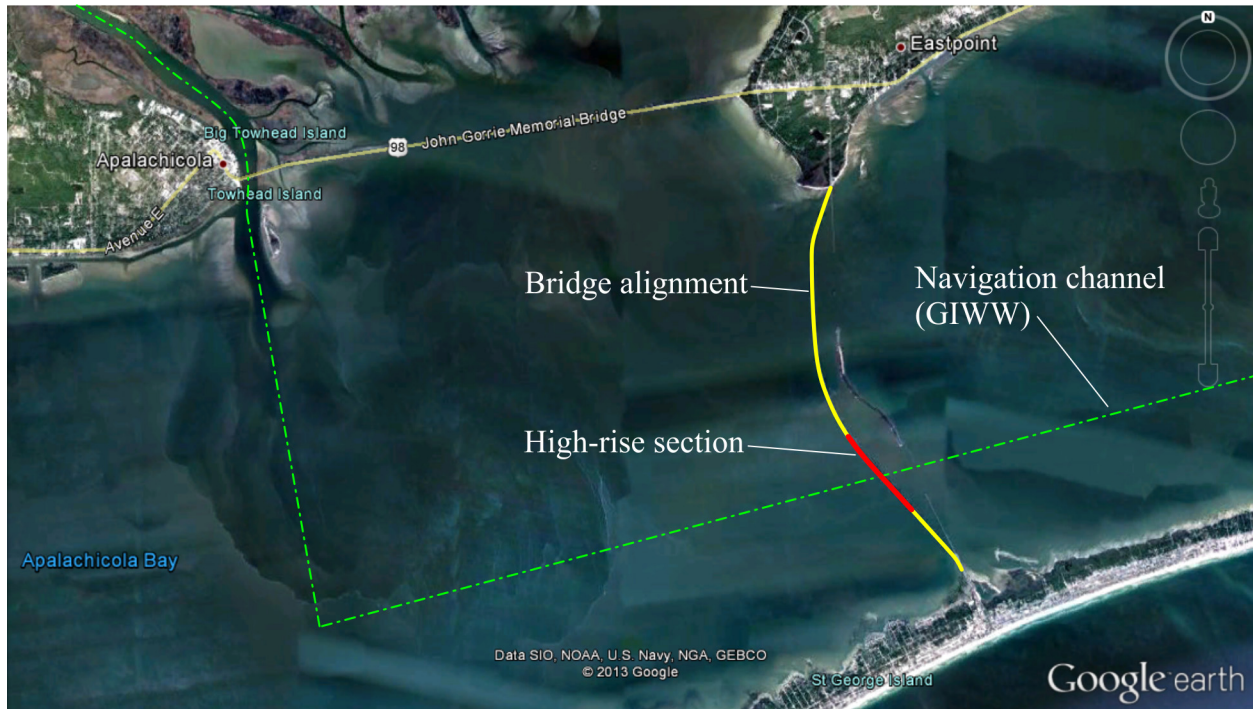


Figure 9.1 Bryant Grady Patton Bridge (SR-300) spanning Apalachicola Bay, Florida

9.3.2 Navigation channel

According to NOAA navigational charts (2013a), the navigation channel (GIWW) has a project depth of 12 ft along its entire length (Carrabelle, Florida to Brownsville, Texas). Water depths in numerous regions along the GIWW have depths exceeding 12 ft, including certain parts of Apalachicola Bay. As needed, the channel is periodically dredged by the U.S. Army Corps of Engineers to maintain the minimum project depth. Because channel width is limited to 100 ft in many areas and numerous tight bends exist, barge flotillas navigating the GIWW are limited to one, two, or three barges, oriented in a single string (one in front of the other). Therefore, the SR-300 Bridge is not at risk for being impacted by large, multi-barge flotillas that are more common on larger waterways.

As shown in Fig. 9.2, the navigation channel passes under the center bridge span at a 61.5° angle relative to the bridge alignment. Horizontal clearance of 150 ft and vertical clearance of 65 ft are provided through this passage. On the eastern side of the bridge, two potential navigational hazards are present: a manmade island to the north of the channel, and a segment of the old bridge (now a fishing pier) to the south. For westbound vessel traffic that is significantly off-course, these obstructions may provide some level of protection to bridge piers away from the channel. A methodology was developed to account for these obstructions in the risk assessment, as discussed in Section 9.7.6.

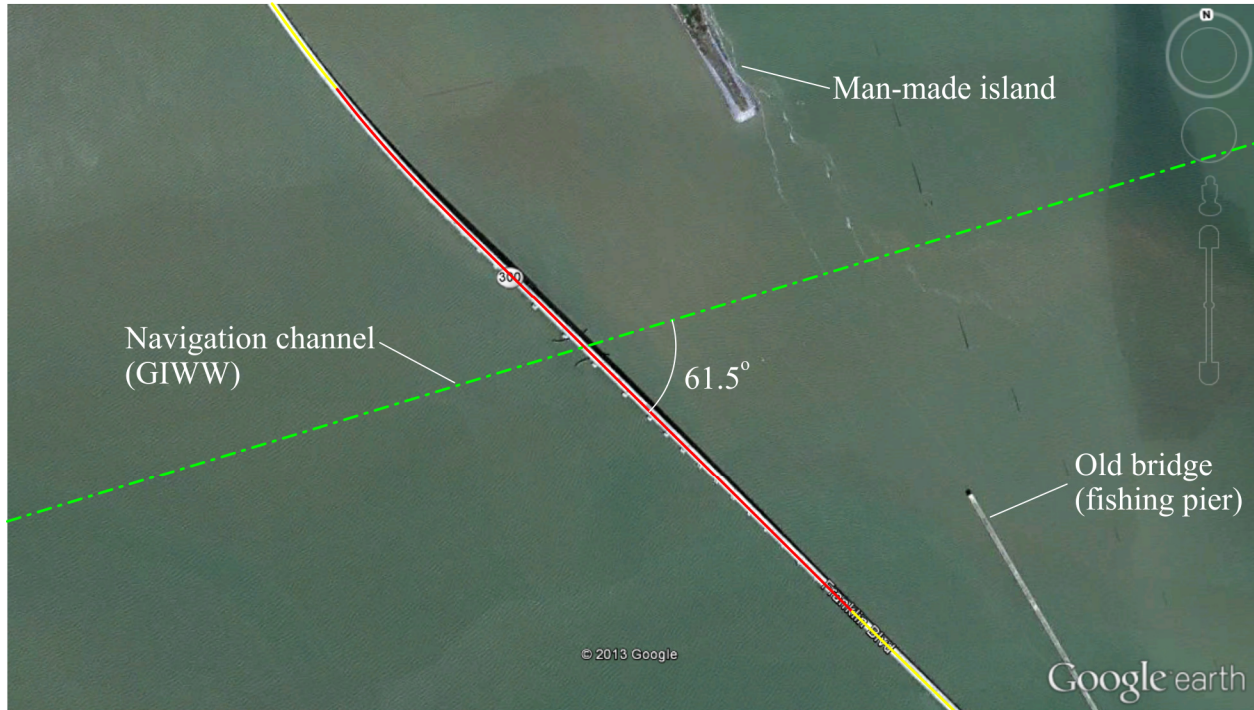


Figure 9.2 High-rise portion of SR-300 Bridge, showing potential navigational obstructions

9.3.3 Tide levels and tidal range

The SR-300 Bridge is subject to tidal variations in water level, by virtue of its vicinity to the Gulf of Mexico. For the purpose of the risk assessment, tidal range and elevations were taken from the bridge plans. Average tidal range is approximately 1.5 ft, with a mean low water (MLW) elevation of -0.87 ft, and mean high water (MHW) elevation of 0.62 ft. Elevations are referenced to the North American Vertical Datum of 1988 (NAVD88). For the purpose of the risk assessment presented in this chapter, MHW is taken as the reference water level for all calculations.

9.3.4 Currents

Currents in Apalachicola Bay are influenced by both periodic tidal flows and by outflow from the Apalachicola River. In 1982, Conner et al. published a detailed study of current flow velocities for the entire Apalachicola Bay. As shown in Fig. 9.3a, at low tide, currents are dominated by outflow from the river. In the vicinity of the bridge, currents are generally west-to-east at a velocity of approximately 0.25 knots. During flood tide (Fig. 9.3b), currents reverse direction near the bridge and flow east-to-west at approximately 0.35 knots. At high tide (Fig. 9.3c), currents continue east-to-west at 0.35 knots. During ebb tide (Fig. 9.3d), currents reverse again to flow approximately west-to-east at 0.25 – 0.35 knots, depending on location. Note that turbulence and crosscurrents are generally most pronounced during ebb tide, though crosscurrent velocity components are negligibly small. The average current velocity over one tidal cycle is provided in Fig. 9.3e. Note that flow is generally east-to-west, at a nominal velocity of less than 0.1 knots. For the purpose of this risk assessment, the current velocity parallel to the

navigation channel was conservatively taken to be 0.4 knots (east-to-west), and the crosscurrent velocity (perpendicular to the channel) was taken to be equal to 0.0 (zero) knots.

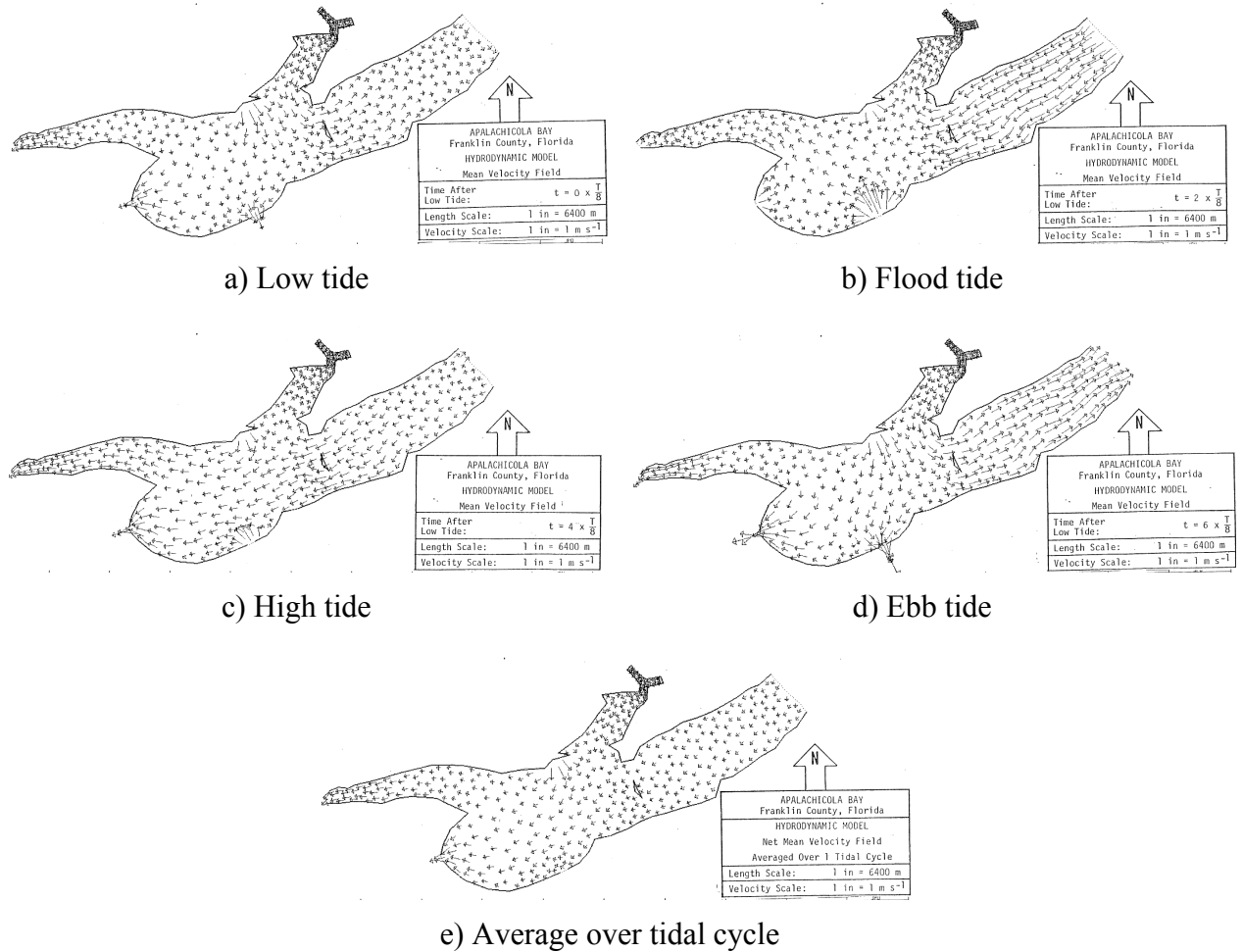


Figure 9.3 Current velocities in Apalachicola Bay at various tidal stages (Conner et al. 1982)

9.3.5 Water depths

Reasonable estimates of water depth are an important component of the vessel collision risk assessment. If insufficient water depth is available, then vessels may run aground prior to impacting components of the bridge. Indeed one of the most effective measures for protecting bridge piers from impact is constructing islands ahead of or around piers, forcing vessels to run aground, rather than impacting the protected piers. Water depth can be highly variable, depending on factors like tidal and seasonal water level and mudline scour. Because the bridge being evaluated is in a coastal region, water levels are primarily driven by tidal variations rather than seasonal fluctuations. As stated previously, MHW was conservatively taken as the waterline datum for the vessel collision risk assessment. Scour is likely to occur in the vicinity of each bridge pier, increasing the available water depth. However, such effects are generally localized

around the pier. If shallow water depths extend far from a given pier, then vessels may run aground well prior to reaching the scoured region.

A number of sources exist for determining water depths in the vicinity of the SR-300 Bridge. Detailed surveys were undertaken prior to bridge construction, and mudline elevations at the site are documented in the design drawings. Soil borings taken along the bridge alignment are another indication of water depth, albeit in discrete, widely spaced intervals. Based on these data, water depth along the high-rise portion of the bridge varies between 12 – 18 ft, with the deepest water near the navigation channel, and shallowest to the north. Such water depths are sufficient to allow nearly all vessels to strike piers in this region.

However, nautical charts prepared by the National Oceanic and Atmospheric Administration (NOAA 2013a) indicate that a shoal with water depths as low as 2 – 3 ft lies immediately to the east of the bridge (Fig. 9.4). Note that sounding depths provided in the chart are relative to mean lower low water (MLLW), which in the Apalachicola Bay, is 1.5 ft lower than MHW. Therefore, for the purpose of the risk assessment, water depths near the shoal were assumed to be uniform and equal to 4 ft. Such low water levels constitute a navigational obstruction for certain vessel types traveling east-to-west, and thus, vessels with a draft exceeding 4 ft were assigned a lower probability of impacting piers lying away from the navigation channel when approaching from the east. The specific methodology used for assigning this reduction in risk is discussed in Section 9.7.6. Note that, as shown in Fig. 9.4, sufficient water depth is available for all vessel types approaching from the west. A spoil area (area where dredging waste is deposited) is indicated south of the channel, which may result in reduced water depth. However, the depth in this region is not indicated on the chart. Furthermore, such features are highly localized, and a powered barge tow may simply “plow” through the raised mudline. For these reasons, the spoil area was neglected as a navigational obstruction in the risk assessment.

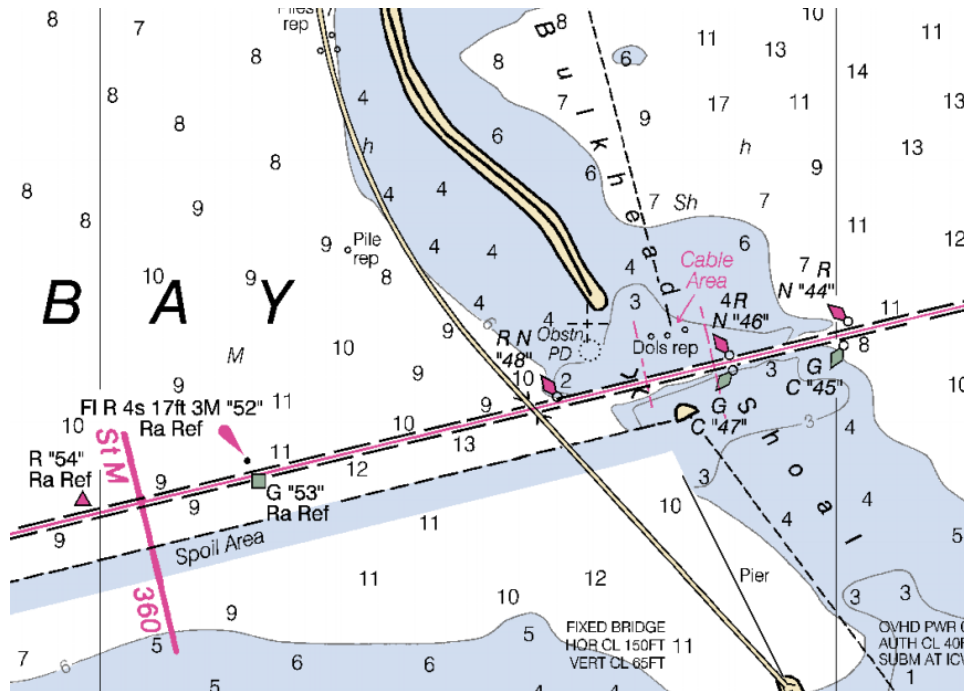


Figure 9.4 Nautical chart including water depth soundings at MLLW (NOAA 2013a)

9.4 Bridge Characteristics

The SR-300 Bridge consists of 165 spans, most of which are 125 ft long and supported by low-rise pile bents. Near the navigation channel, a high-rise portion is provided, which includes increased span lengths and vertical clearance. This section of the bridge (shown schematically in Fig. 9.5) consists of 30 pile-founded piers (numbered 33 – 62) that support spans that are 140 – 258 ft long. The AASHTO vessel collision provisions require that all piers located less than $3 \times LOA$ from the navigation channel be considered at risk for vessel collision, where LOA is the overall vessel length. For this location, the longest vessel type is a multi-barge flotilla (623 ft long), being pushed by a tugboat (75 ft long), resulting in a maximum $LOA = 698$ ft. Therefore, any piers located less than $3 \times LOA = 2,094$ ft from the channel centerline—specifically, piers 35 – 60—were considered in the risk assessment. In order to adequately analyze these piers for vessel collision, finite element models of two additional piers on each end of the central $6 \times LOA$ impact region were also prepared.

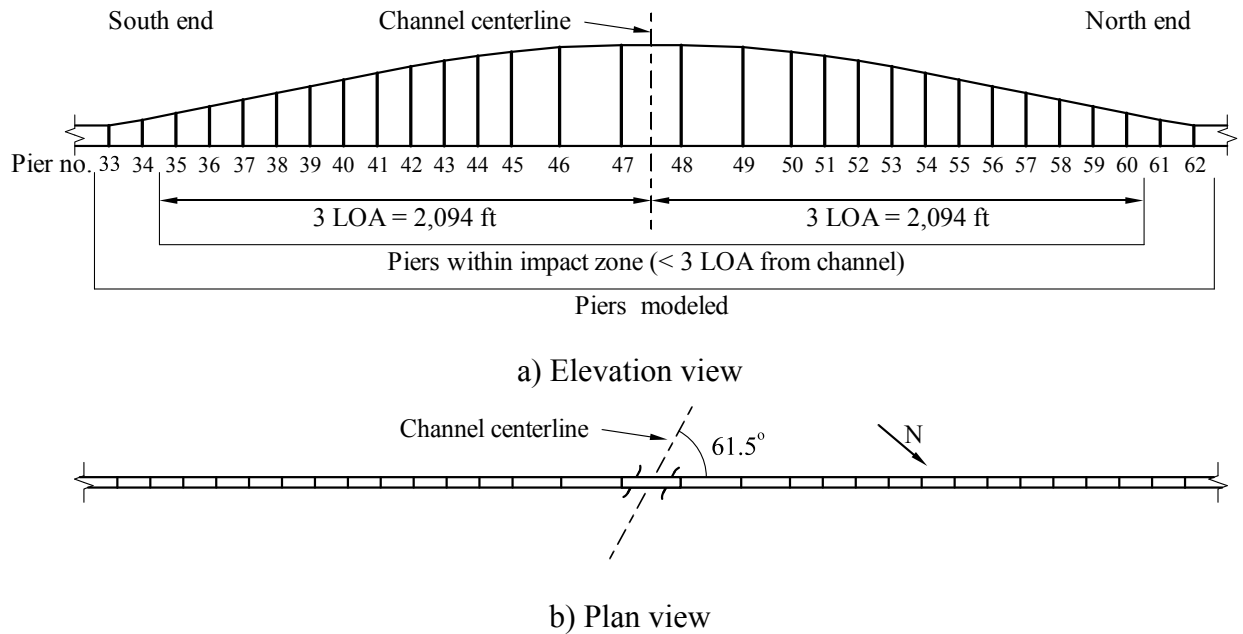


Figure 9.5 High-rise portion of SR-300 Bridge, showing piers at risk for impact

9.4.1 Bridge piers

Bridge pier configurations for the SR-300 Bridge are shown in Fig. 9.6. Piers consist of two circular columns (5 – 6 ft diameter) supporting a 6 ft deep pier cap beam. A strut is provided between the columns at the approximate mid-height for piers 43 – 52. All piers are founded on 54 in. diameter cylinder piles, with the smallest foundations (pile caps) being supported by only four piles, and the largest foundations (pile caps) being supported by fifteen. Many piles are battered at an inclination of 2 in. horizontal per 12 in. vertical, as indicated by arrows in Fig. 9.6. All footings are 6.5 ft thick and are positioned such that the top surface is approximately 5.5 ft above MHW. The smallest footing (Fig. 9.6d) is 18.5 × 39 ft in plan, and the largest footing (Fig. 9.6j) is 28 × 55 ft.

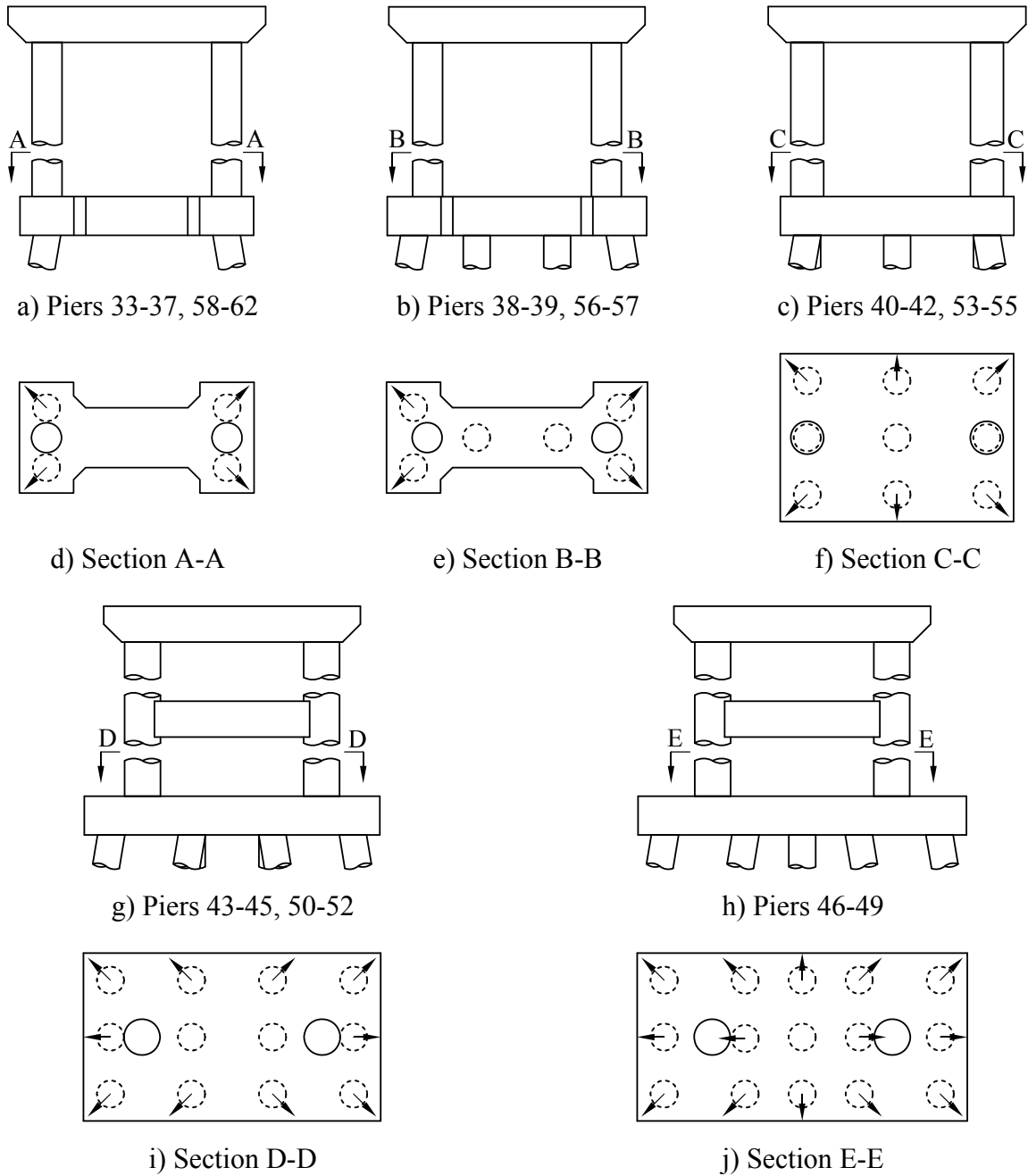


Figure 9.6 Pier and foundation configurations for SR-300 Bridge
 (Arrows at pile locations indicate directions of pile batter)

Based on these pier configurations, barges and most small ships are expected to impact pier footings rather than columns, though some column impacts are possible. Consider the two impact scenarios shown in Fig. 9.7. A fully loaded barge carries 6 – 12 ft of draft, with the most common being approximately 9 ft (Fig. 9.7a). In this scenario, the barge headlog impacts the pier at an elevation below the top of the pier footing. However, an empty barge (Fig. 9.7b) drafts only approximately 2 ft, and the headlog elevation is above the top of the footing. Depending on the barge bow and pier geometry, the impacting barge may make contact with the footing first.

However, the barge may slide up and over the footing edge, or given sufficient energy, simply crush into the top footing corner, ultimately striking a pier column.

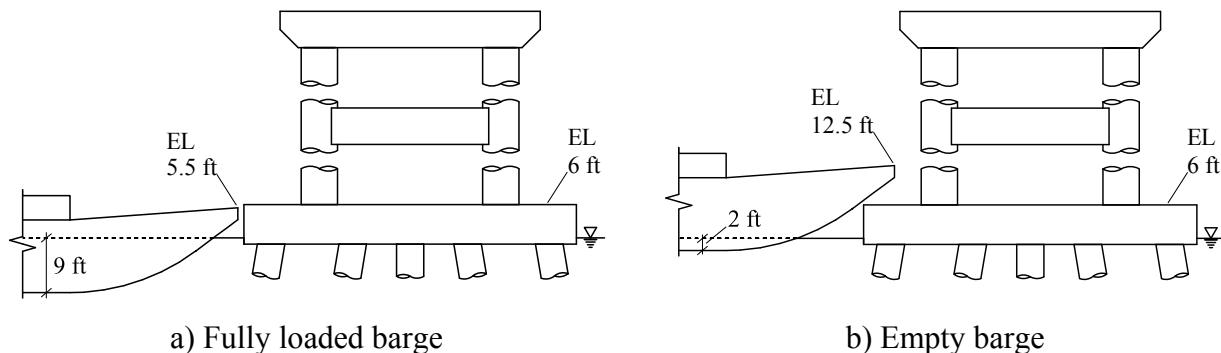


Figure 9.7 Typical barge impact scenarios, showing possible headlog elevations

Impact scenarios like the one shown in Fig. 9.7b are certainly of interest for design, in that all impacted pier components must be proportioned to resist impact loading. However, numerous factors—e.g., footing overhang distance, barge bow rake angle, vessel draft, water level, and impact angle—all influence the relative probability of a column impact occurring. Given the inherent variability of such factors, assessing the probability of column impact is difficult. Thus, for the purpose of the risk assessment, columns were assumed to have sufficient capacity to transmit impact loads to the footing. As such, for simplicity, impact forces were applied at the footing elevation in all impact analyses. For final design, it would be appropriate to choose the most severe column impact scenario possible and proportion or support the columns such that they can resist the loads imparted. A strut or shear wall between the columns is commonly employed for this purpose, though not on the SR-300 Bridge piers.

9.4.2 Superstructure

The superstructure for the SR-300 Bridge is typically supported by 78-in. Florida Bulb-T girders. In the region of interest for the risk assessment, the roadway (8.5-in. thick R/C slab) is supported by five girders, spaced at 9.5 ft on center. (The only portions of the superstructure that use four girders are the low-rise causeway sections of the bridge). As shown in Fig. 9.8, the high-rise portion consists of three superstructure zones. Spans between piers 33 – 45 and between piers 50 – 62 are 140 ft long, and consists of standard prestressed girders. Spans are cast contiguously with a R/C diaphragm at each pier. Expansion joints are provided every four spans. The central five spans (between piers 45 – 50) are between 207.5 ft and 257.5 ft in length (the center span is 250 ft), and include haunched sections over each pier, at which the girder depth increases from 78 in. to 144 in. The haunched girder segments and uniform-depth segments near midspan were individually precast and prestressed. During bridge construction, the various girder segments were post-tensioned together with tendons in harped profiles, to form a five-span continuous unit.

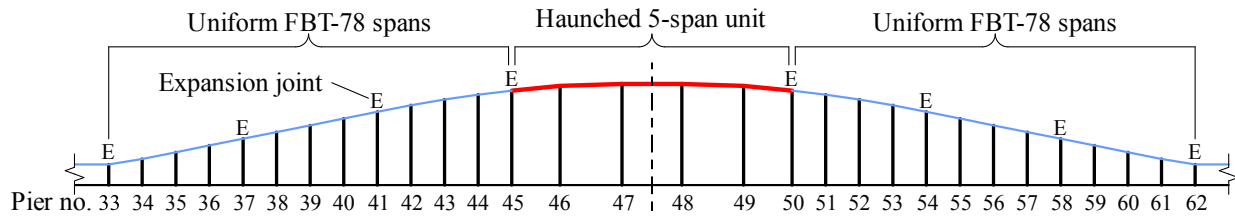


Figure 9.8 Overview of bridge span configurations

Typical superstructure cross-sections are shown in Fig. 9.9. The roadway slab is approximately 47 ft wide, with standard concrete barriers on each side. As discussed above, five evenly spaced girders support the roadway. Fig. 9.9a shows a typical section in a uniform-depth region of the superstructure (all 140-ft spans, and the midspan segments of the haunched spans). Fig. 9.9b shows a typical cross section at the piers with haunches. The girder depth is 144 in. at these locations.

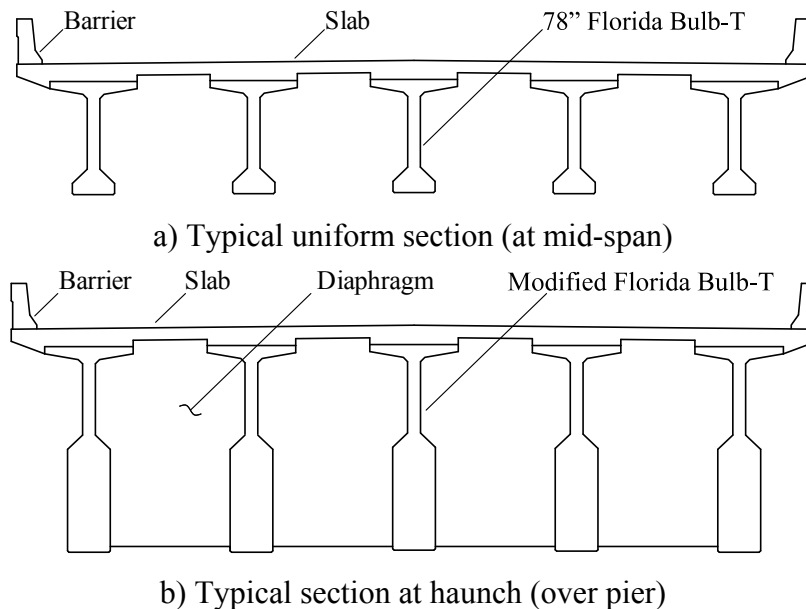


Figure 9.9 Superstructure cross-sections for the SR-300 Bridge

At all piers, girders rest on neoprene bearing pads. Two rows of bearing locations are provided at expansion joint piers, and a single row is provided at all other piers. At every bearing location, 4-in. diameter steel shear pins provide continuity between the girders and pier cap beam for lateral motions. These pins are particularly important for vessel collision loading, as they permit more than 1,500 kip of shear force to be carried across the substructure-superstructure interface. Consequently, when a pier is impacted, demand on the foundation is mitigated by permitting some portion of the lateral load to be shed through the superstructure and ultimately to adjacent piers. This action is important to consider when analyzing the piers for vessel impact, so the shear pin connection was included in finite element models of the piers and superstructure.

9.4.3 Soil conditions

In general, soil conditions at the site consist of layers of clean sand and silty and/or shelly sand. A thick layer of soft Florida limestone begins at a depth of approximately -60 ft, and is present across the entire bridge site. During construction, piles were generally driven a few feet into the limestone and terminated. Thus, pile embedment depths vary for each pier, depending on the depth of this limestone layer. For the purpose of developing finite element models of each pier, soil properties were determined from SPT boring logs taken prior to bridge construction. As shown in Fig. 9.10, eight boring logs were available in the vicinity of the piers of interest. Soil layer profiles were developed from these boring logs and assigned to each pier finite element model, as shown in Fig. 9.10. Finite element soil spring characteristics were derived by well-established equations that relate various important soil properties (e.g., internal friction angle, subgrade modulus) to the overburden-adjusted SPT blowcount. The specific methodology that was employed is omitted here for brevity, but has been documented in numerous prior publications (Consolazio et al. 2008, 2010a, 2010b). Additional information is also available in the user's manuals for FB-MultiPier and FB-Deep (BSI 2009, 2010).

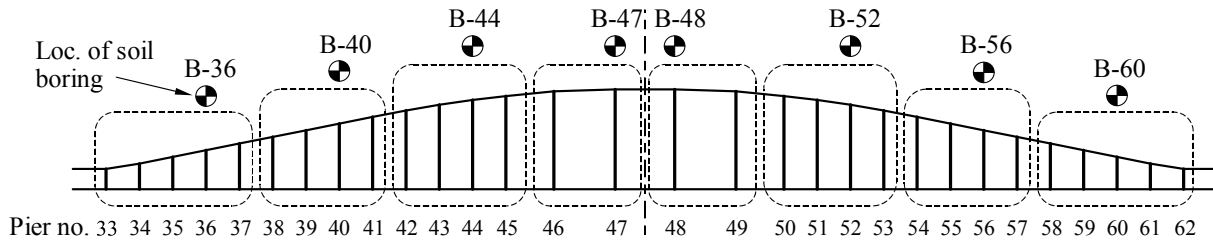


Figure 9.10 Locations of soil borings and piers to which each soil profile is assigned

9.4.4 Finite element models

Renderings of finite element models of selected piers (developed in FB-MultiPier) are shown in Fig. 9.11. Each pier shown is a representative example of the five pier configurations shown in Fig. 9.6. As discussed in Chapter 2, FB-MultiPier models piles, pier columns, struts, and pier caps with cross section-integrated nonlinear beam elements that can account for cracking, material plasticity, and plastic hinging behaviors. Soil is modeled in FB-MultiPier with nonlinear spring elements distributed down the embedded pile length, footings (pile caps) are modeled with linear-elastic shell elements, and the superstructure is modeled as a composite (girder/slab) unit with linear-elastic resultant beam elements that are connected to pier caps at discrete bearing locations. One-pier, two-span models of all piers within the impact zone (piers 35 – 60) were developed in accordance with the procedure discussed in Chapter 2 (Consolazio and Davidson 2008), and these models were employed for all structural impact analyses discussed in this chapter.

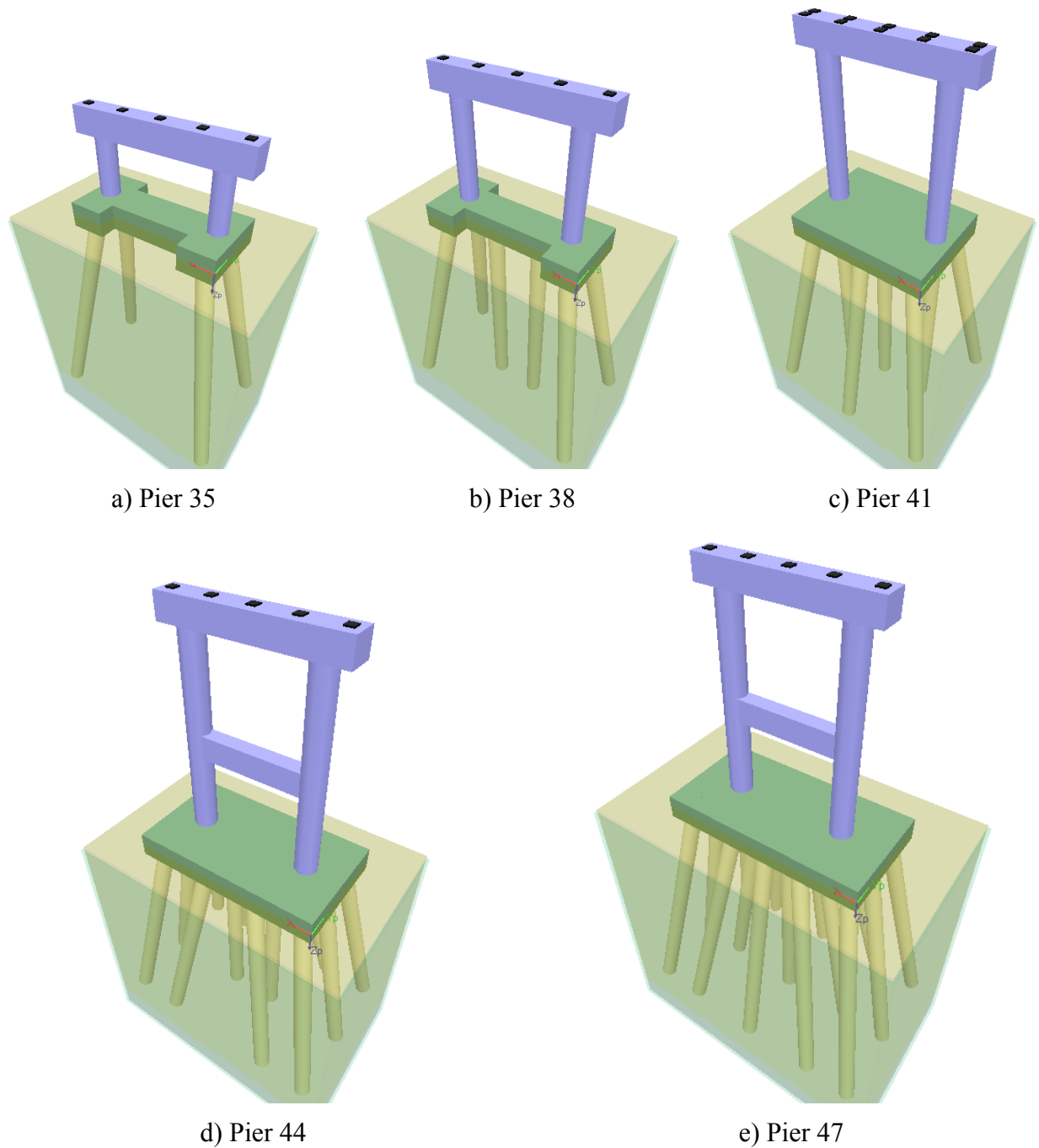


Figure 9.11 FB-MultiPier models of selected piers from SR-300 Bridge

9.5 Vessel Fleet Characteristics

As stated in Section 9.2, vessel traffic data were obtained from a comprehensive study of Florida vessel traffic conducted by Wang and Liu (1999). This study categorized vessel traffic for dozens of waterway “past points” in Florida into representative groups, and reported average vessel dimensions, vessel tonnage, and estimated transit velocities for each vessel group. The

SR-300 Bridge corresponds to past point number 15, as defined by the Florida Department of Transportation (FDOT). County-by-county past point maps are available on the FDOT website at <http://www.dot.state.fl.us/structures/pastpointmaps/vppm.shtm>. Vessel traffic data associated with each past point is integrated into the FDOT Vessel Impact Analysis Mathcad worksheet, which is freely available for download at <http://www.dot.state.fl.us/structures/proglib.shtm>.

9.5.1 Vessel categories

Vessel traffic data for the SR-300 Bridge site that were obtained from the Wang and Liu study (1999) are summarized in Table 9.1 for upbound traffic, and Table 9.2 for downbound traffic. Note that downbound traffic refers to vessels traveling east-to-west, as defined in the FDOT past point map for Franklin County. Vessel traffic was categorized by similar shapes and sizes of vessel, and the dimensions and tonnage listed in the tables correspond to the average values among the various vessels that were assigned to each vessel ID. It is clear from these data that the vast majority of vessel traffic reported by Wang and Liu consists of barge tows. Most upbound traffic (Table 9.1) consists of single barges being propelled by a tugboat, while downbound traffic (Table 9.2) generally consists of two-barge flotillas also being propelled by a tugboat. Because the beam (i.e., width) of single-vessels and combined flotillas are reportedly equal, it can be surmised that two-barge flotillas are oriented in a single string (one barge in front of the other). This observation is consistent with channel width limitations downstream.

It is notable that data reported by Wang and Liu include very little ship traffic. The self-propelled vessels indicated by Vessel ID 6 in Table 9.1 and Vessel ID 5 in Table 9.2 are assigned only six trips per year by Wang and Liu. However, the primary industry in Apalachicola Bay is fishing and oyster harvesting. Consequently, one would expect to see a large number of vessel transits by smaller fishing craft included in the traffic data. The sizes of the vessels listed as “self-propelled” (> 100 ft long) are larger than typical local fishing boats (30 – 60 ft long). It is noted by Wang and Liu (1999) that because such small fishing boats (50 – 150 tons) pose a negligible impact risk to bridges, they were excluded from the data set. This choice is warranted, given that vessel traffic data reported by Wang and Liu were gathered for specific purpose of assessing the risk of bridge collapse caused by vessel collisions. As such, no further investigation was conducted in order to quantify traffic volume for smaller self-propelled vessels.

For the purpose of the risk assessment, vessel types were reorganized into vessel groups (VG) with unique contiguous numbers. Pertinent data for each vessel group that were used in the risk assessment are summarized in Table 9.3. Note that barge vessel groups were assigned the lowest numbers (1 – 8), and ship groups were assigned the highest numbers (9 – 11). Barge vessel drafts are reported in Table 9.3 as the maximum draft between the barge and tug. In cases where the tug draft controlled (VG 1, 2, 5, and 6), the barge draft was used in assessing whether the vessel will run aground prior to impacting a particular pier. In doing so, it was assumed that the tug would run aground, lashings between the tug and barge would break, and the barge would impact the pier under its own momentum (see Section 9.7.6 for additional details).

Table 9.1 Upbound vessel traffic for Apalachicola Bay (Wang and Liu 1999)

Vessel ID	Vessel type	Description	Average single vessel size (ft)			Single vessel displacement (tons)	Average barge tow size		Tug size (ft)			Tug displacement (tons)	Length <i>LOA</i> (ft)	Beam (ft)	Total displacement (tons)
			L	W	D		# W	# L	L	W	D				
1	Barge	Barge tow	216	51	2	811	1	1	75	25	8	260	291	51	1,071
2	Barge	Barge tow	316	59	6	3,365	1	1	75	25	8	260	391	59	3,625
3	Barge	Barge tow	246	51	8	3,333	1	1	75	25	8	260	321	51	3,593
4	Barge	Barge tow	318	54	11	5,952	1	1	120	30	9	560	439	54	6,512
5	Ship	Free tug	75	25	9	336	N/A	N/A	N/A	N/A	N/A	N/A	75	25	336
6	Ship	Self-propelled	122	27	5	388	N/A	N/A	N/A	N/A	N/A	N/A	122	27	388

Table 9.2 Downbound vessel traffic for Apalachicola Bay (Wang and Liu 1999)

Vessel ID	Vessel type	Description	Average single vessel size (ft)			Single vessel displacement (tons)	Average barge tow size		Tug size (ft)			Tug displacement (tons)	Length <i>LOA</i> (ft)	Beam (ft)	Total displacement (tons)
			L	W	D		# W	# L	L	W	D				
1	Barge	Barge tow	267	51	2	894	1	1.9	75	25	8	260	582	51	1,959
2	Barge	Barge tow	328	62	5	3,360	1	1.9	75	25	8	260	698	62	6,644
3	Barge	Barge tow	251	45	8	3,313	1	1.9	75	25	8	260	552	45	6,555
4	Barge	Barge tow	256	72	12	6,969	1	1.9	120	30	9	560	606	72	13,611
5	Ship	Self-propelled	105	23	5	228	N/A	N/A	N/A	N/A	N/A	N/A	105	23	228

Table 9.3 Aggregated vessel traffic data for vessel collision risk assessment

<i>VG</i> Vessel group	Vessel ID from Tables 9.1 – 9.2	<i>N</i> No. transits (yr ⁻¹)	<i>v_i</i> Transit velocity (knot)	<i>D</i> Draft (ft)	<i>LOA</i> Overall length (ft)	<i>B_M</i> Beam (ft)	<i>W_B</i> Total displacement (tons)
1	1 (Table 9.1)	85	5.6	2 ¹	291	51	1,071
2	2 (Table 9.1)	25	4.6	5 ¹	391	59	3,625
3	3 (Table 9.1)	117	4.6	8	321	51	3,593
4	4 (Table 9.1)	92	4.7	11	439	54	6,512
5	1 (Table 9.2)	135	6.4	2 ¹	582	51	1,959
6	2 (Table 9.2)	22	5.4	5 ¹	698	62	6,644
7	3 (Table 9.2)	19	5.4	8	552	45	6,555
8	4 (Table 9.2)	28	5.4	12	606	72	13,611
9	5 (Table 9.1)	53	7.6	9	75	25	336
10	6 (Table 9.1)	4	7.6	5	122	27	388
11	5 (Table 9.2)	2	8.4	5	105	23	228

¹ Draft shown is for the barge itself. Tug draft is 8 ft.

9.5.2 Vessel traffic growth

For this risk assessment, vessel traffic was assumed to remain constant over time. Historical data compiled by Wang and Liu (1999) suggested a slight negative rate of growth for waterway through Apalachicola Bay. However, for design purposes, FDOT suggests zero growth for this particular waterway (FDOT 2013). Therefore, a vessel traffic growth factor equal to 1.0 (no growth) was assumed.

9.5.3 Vessel transit speeds

Vessel transit speeds were selected in accordance with FDOT recommendations, which are based on the traffic study by Wang and Liu (1999). Specifically, FDOT recommends a base transit velocity equal to 7 knots for barge tows, and 10 knots for self-propelled vessels and free tugs. This base velocity corresponds to ideal navigation conditions (straight channel and clear traffic). It is recommended that the base velocity be reduced by various amounts, depending on local conditions:

- 2 knot reduction for a curved navigation channel and/or crowded traffic;
- 2 knot reduction for self-propelled vessels on narrow canals or restricted intracoastal waterways;
- 1 knot reduction for barge tows on narrow canals or restricted intracoastal waterways, and;
- 1 knot reduction for loaded barge tows.

As shown above, the navigation channel is straight for several miles surrounding the SR-300 Bridge, and vessel traffic volume is relatively light. Therefore no reduction was taken for channel alignment or traffic volume reasons. While the Apalachicola Bay appears to be a wide-open body of water, the dredged channel is only 100 – 150 ft wide. In many locations in the bay (including near the bridge), the channel is surrounded by shallow water within which many commercial vessels would run aground. Therefore, it was assumed that vessel operators would treat the ICWW channel through Apalachicola Bay in the same fashion as other restricted intracoastal waterways, and reduce speeds for safety. Therefore, vessel speeds were reduced by 2 knots for self-propelled vessels and 1 knot for barge tows. A further 1 knot speed reduction was applied to loaded barge vessel groups. Specifically, the loaded condition was defined as any barge with a draft exceeding 4 ft.

Vessel speeds were further modified to account for the current velocity. Thus, 0.4 knots was subtracted from the velocity of upbound vessels and added to the velocity of downbound vessels. Refer to Table 9.3 for the final velocities after adjustments. Note that the AASHTO provisions suggest reducing the impact velocity for piers located away from the navigation channel, based on a linear function of vessel *LOA*. Therefore, the values shown in Table 9.3

correspond only to piers near the navigation channel. Impact velocities for every combination of pier and vessel group are provided in Appendix M.

9.5.4 Vessel transit path

The SR-300 Bridge was constructed such that the dredged navigation channel was centered between the main channel piers (piers 47 and 48). Because vessel traffic is fairly light, it is unlikely that vessels traveling opposite directions would pass each other under the bridge. Therefore, it was assumed that both upbound and downbound traffic is most likely to navigate along this channel centerline, and risk analysis parameters that rely on position relative to the vessel transit path (geometric probability, impact velocity) were computed assuming a common centerline for both traffic directions.

9.6 Vessel Impact Criteria

In designing a new bridge, AASHTO requires additional criteria that the design must satisfy, aside from the maximum impact load criteria defined by the probabilistic risk assessment. Given that the example presented in this chapter is an assessment of an existing structure, certain criteria (e.g., minimum impact load combined extreme event scour, impact with superstructure elements) are not fully explored. Furthermore, for this study, certain portions of the AASHTO procedure have been replaced with new methods, as discussed in Chapter 8. The following sections describe, in a broad sense, how the overall vessel impact criteria prescribed by AASHTO were assessed in this study.

9.6.1 General requirements

The adequacy of the SR-300 Bridge to resist vessel impact loading was assessed in accordance with the general requirements of the following provisions:

AASHTO (1991). *Guide Specification and Commentary for Vessel Collision Design of Highway Bridges*, American Association of State Highway and Transportation Officials, Washington DC.

AASHTO (2009). *Guide Specification and Commentary for Vessel Collision Design of Highway Bridges*, 2nd Edition, American Association of State Highway and Transportation Officials, Washington DC.

FDOT (2013). *FDOT Structures Manual Volume 1. Structures Design Guidelines* Florida Department of Transportation, Tallahassee.

Modifications to the AASHTO-prescribed requirements, including consideration of dynamic bridge response and the influence of pier geometry on impact forces, were made as described in Chapter 8 (referred to as UF/FDOT methods). Such modifications, as they pertain to

the SR-300 Bridge risk assessment, are documented in Section 9.7. Note that, because the UF/FDOT procedures reflect the most up-to-date published research, the intent of the analysis was to meet or exceed (generally exceed) the level of engineering rigor required by the AASHTO specifications. Furthermore, while the results presented in this chapter imply that the UF/FDOT procedures predict higher levels of vessel collision risk when compared to AASHTO methods, this outcome is not guaranteed. Indeed, as discussed in Section 9.9, commonly encountered impact scenarios exist for which UF/FDOT procedures may predict a lower vessel collision risk than the current AASHTO procedures.

9.6.2 Extreme event load combinations (scour)

The *FDOT Structures Design Manual* requires that two different scour and impact conditions be considered in the design of bridge substructures: 1) minimum vessel impact associated with an empty barge that has broken loose from its moorings during a storm event (including high water), and 2) maximum vessel impact associated with an aberrant vessel being driven into the bridge under normal environmental and operating conditions. Corresponding scour levels for each condition were obtained from the bridge design drawings, as determined by combined geotechnical and hydrological analysis performed when the bridge was designed.

9.6.3 Minimum impact load criteria

The minimum impact condition corresponds to the scenario in which an empty hopper barge (195 × 35 ft) that was moored in the vicinity of the bridge breaks loose from its moorings during a storm and strikes the bridge. Under such conditions, barge motion is driven by wind and wave action. For this assessment, the empty barge displacement was assumed to be 200 tons, and the wind-driven impact velocity was assumed to be equal to 1 knot. As required by the *FDOT Structures Design Manual*, this minimum impact condition was combined with one half the 100-year short-term scour level. While the minimum impact condition was a critical check on bridge pier performance under extreme environmental conditions, the maximum impact condition was found to control in all cases. Therefore, the minimum impact condition is omitted from further discussion.

9.6.4 Maximum impact load criteria

The maximum impact condition corresponds to the scenario in which a vessel being piloted under normal operating conditions becomes aberrant (by mechanical failure or other means) and impacts the bridge at full speed. Under such conditions, vessel motion is driven under its own power, or in the case of a barge tow, the power of a tug. For this assessment, vessel displacements and impact velocities were assumed to vary as discussed in Section 9.5.1. As required by the *FDOT Structures Design Manual*, the maximum impact condition was combined with one half the long-term ambient scour level. Note that in accordance with AASHTO procedures, the maximum impact load conditions can be determined using a simplified, deterministic procedure (Method I), or by conducting a probabilistic risk assessment (Method II). Only the latter analysis procedure was considered in this study.

9.6.5 Operational classification

The SR-300 Bridge was classified by the owner (FDOT) under the “critical/essential” operational classification. Consequently, structural collapse as a result of vessel collision should have a return period of 10,000 years, as required by the AASHTO provisions. This requirement is significantly more stringent than a normal bridge (return period of 1,000 years). However, the classification reflects the importance of the bridge to the region. Because the SR-300 Bridge is the only roadway between St. George Island and the Florida mainland, it constitutes the only hurricane evacuation route to residents of the island. Furthermore, access to hospitals and other emergency services require that the bridge be operational even under extreme conditions.

9.7 Maximum Impact Load (Method II) Analysis Methodology

As defined by AASHTO, Method II is a probabilistic risk analysis procedure that is used to quantify the annual frequency (annualized probability) that a bridge will collapse when subjected to vessel collision loading (denoted AF). In its formulation, Method II attempts to account for all major factors that contribute to vessel collision risk, including but not limited to vessel traffic volume, waterway characteristics, bridge geometry, and bridge element strength. The following sections detail analysis assumptions and the overall methodology that was used to quantify AF for the SR-300 Bridge. Risk assessments were completed both using strict AASHTO methodology (static loading and pushover analysis) and using the modified UF/FDOT methodology that incorporates dynamic structural analysis and other state-of-the art procedures from recent research. Risk measures that were computed using each method are compared in Section 9.8.

Because a significant portion of the risk assessment methodology was conducted in accordance with the AASHTO provisions, FDOT Vessel Impact Analysis software (version 3.1), implemented in Mathcad, was utilized extensively in various calculations. Structural analyses were carried out using FB-MultiPier (version 4.18), and custom Perl scripts (Perl 2013) were programmed to summarize relevant analysis data. Subsequent risk calculations were completed using Mathcad worksheets.

9.7.1 Annual frequency of collapse (AF)

The annual frequency of collapse (AF) was computed by the following expression:

$$AF = (N)(PA)(PG)(PC)(PF) \quad (9.1)$$

where:

AF = Annual frequency of pier collapse due to vessel collision,

- N = Annual number of vessel transits, as categorized by vessel type and transit direction,
 PA = Probability of vessel aberrancy,
 PG = Geometric probability of a pier being impacted by an aberrant vessel,
 PC = Probability of bridge element collapse subject to collision, and
 PF = Protection factor to account for land masses or other objects (e.g. structural dolphins) that may block vessels from colliding with the bridge ($PF=0$: bridge element fully protected; $0 < PF < 1$: bridge element partially protected; $PF=1$: bridge element unprotected).

Note that AF was more specifically computed as a summation of all possible combinations of bridge pier and vessel group. Therefore, a more detailed form of Eqn. 9.1 is:

$$AF = \sum_{i=1}^{N_{VG}} \sum_{j=1}^{N_p} (N_i)(PA_i)(PG_{ij})(PC_{ij})(PF_{ij}) \quad (9.2)$$

where, N_{VG} is the number of vessel groups ($N_{VG} = 11$ in this case, as defined in Table 9.3), and N_p is the number of bridge piers within the navigation zone ($N_p = 26$ in this case, piers 35 – 60).

9.7.2 Vessel frequency (N)

Vessel frequency (N) refers to the annual number of vessel transits by a particular vessel type and transit direction (as defined by the vessel groups listed in Table 9.3). On any of these transits, the vessel has some finite probability of becoming aberrant and striking a bridge pier. However, in order to collide with a pier, sufficient water depth must be available to accommodate the vessel draft. Otherwise, the vessel will run aground prior to impacting a pier. Premature vessel groundings caused by insufficient water depth can be accounted for in the risk assessment in two ways: 1) the value of N for relevant piers and vessel groups can be set equal to zero or reduced in some way, or 2) a protection factor (PF) can be assigned to relevant piers and vessel groups. The latter option was adopted in for this assessment, as discussed in Section 9.7.6. It should be noted that the example risk assessment published in the AASHTO Guide Specification employs the first option (setting $N=0$ for certain vessels to account for groundings).

9.7.3 Probability of aberrancy (PA)

Probability of aberrancy (PA) refers to the likelihood that a given vessel will stray off course (become aberrant), making collision with a bridge pier possible. Such events can occur due to pilot error, adverse environmental conditions (e.g. dense fog), or mechanical failure (e.g. loss of power). As it is unknown how often and for how long vessels typically veer off course and can be classified as aberrant, accurately quantifying PA can be extremely difficult. Furthermore, the aberrant condition can often be temporary, and may not occur anywhere in the

vicinity of a bridge. Certainly, aberrancy caused by pilot inattentiveness is likely to be reduced in the vicinity of a bridge, given that the pilot is aware of the risk of collision. No comprehensive studies have ever been conducted to quantify AF itself. Estimates have been posited by past engineers and researchers, based on analysis of historical vessel accident data (groundings, collisions, rammings), as discussed in the AASHTO Guide Specification. However, by definition, recorded accident data only include incidences of aberrancy that resulted in an accident. Commonly, the course of an aberrant vessel is corrected by the pilot, and an accident is avoided.

Depending on the amount of information available, two possible approaches can be taken to quantify AF : 1) gather available accident data for the waterway of interest and make a defensible estimate (prior studies should be consulted for guidance in preparing an estimate), or 2) if accident data are unavailable, use the simplified procedure provided in the AASHTO provisions. The latter option was employed in this study. Specifically, PA was computed as:

$$PA = (BR)(R_B)(R_C)(R_{XC})(R_D) \quad (9.3)$$

where:

- BR = Base rate of aberrancy (0.6×10^{-4} for ships, and 1.2×10^{-4} for barges),
- R_B = Correction factor for bridge location (related to waterway alignment),
- R_C = Correction factor for currents acting parallel to the navigation channel,
- R_{XC} = Correction factor for currents acting perpendicular to the navigation channel, and
- R_D = Correction factor for vessel traffic density.

As stated above, $BR = 1.2 \times 10^{-4}$ was used for barge vessel groups (1 – 8) and $BR = 0.6 \times 10^{-4}$ was used for ship vessel groups (9 – 11).

The correction factor for bridge location (R_B) was computed based on the relative location of the bridge in one of three possible waterway regions (straight, transition to a turn, or within a turn). Because the bridge is located in a straight region that is several miles long, $R_B = 1.0$ was selected.

The correction factor for currents acting parallel to the channel (R_C) was computed as $R_C = 1 + V_C/10$, where V_C is the current velocity (parallel) in knots. Given a parallel current velocity of 0.4 knots, $R_C = 1.04$. Because currents acting perpendicular to the channel were found to be negligibly small, $R_{XC} = 1.0$ was selected.

The correction factor for vessel traffic density (R_D) was computed based on the relative volume of traffic, and the likelihood of vessels overtaking each other near the bridge location. Because only 1 – 2 large vessels traverse under the bridge per day, it is highly unlikely that vessels would overtake each other under or nearby the bridge. Therefore, $R_D = 1.0$ was selected, corresponding to low traffic density.

Considering the various correction factors, $PA = 1.25 \times 10^{-4}$ was computed for barge vessel groups (1 – 8) and $PA = 0.624 \times 10^{-4}$ was computed for ship vessel groups (9 – 11).

9.7.4 Geometric probability (PG)

The geometric probability (PG) is the conditional probability that a vessel will collide with a particular bridge pier, given that it has become aberrant. The AASHTO provisions suggest assuming that the vessel position (perpendicular to the intended transit path), is a Gaussian distributed random variable, with mean equal to the channel centerline and standard deviation equal to the overall vessel length (LOA). Therefore, PG for a given pier is equal to the area under the Gaussian distribution bounded by the extents of the pier element width (B_P) and plus the vessel width or beam (B_M), as illustrated in Fig. 9.12.

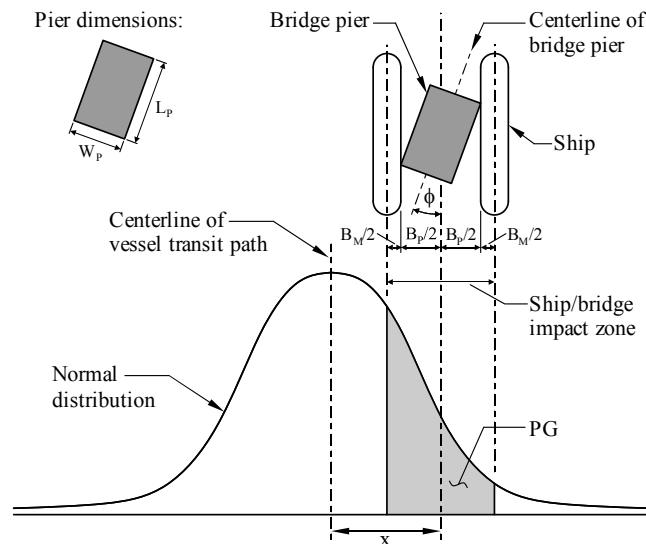


Figure 9.12 Computing the geometric probability of impact (PG) (after AASHTO 2009)

Based on the procedure illustrated in Fig. 9.12, projected pier widths (B_P) were computed as $B_P = W_P \cdot \cos(\phi) + L_P \cdot \sin(\phi)$, where W_P is the width of the pier footing parallel to the bridge alignment, L_P is the length of the footing perpendicular to the bridge alignment, and ϕ is the skew angle of the navigation channel relative to the bridge alignment ($\phi = 28.5^\circ$). Values of B_P for each pier are summarized in Table 9.4. Using these values of B_P , the positions of each pier relative to channel centerline, and the vessel beam (B_M) values for each vessel group, PG values varying between 0.0 (zero) and approximately 0.15 were computed for each combination of pier and vessel group. A table of computed PG values is provided in Appendix M.

Table 9.4 Footing geometry and projected pier width (B_p) for each pier

Pier number	W_p : Footing width (ft)	L_p : Footing length (ft)	B_p : Projected width (ft)
33 – 37, 58 – 62	18.5	39.0	34.9
38 – 39, 56 – 57	18.5	43.5	37.0
40 – 42, 53 – 55	28.0	39.0	43.2
43 – 45, 50 – 52	28.0	49.5	48.2
46 – 49	28.0	55.0	50.9

9.7.5 Probability of collapse (PC)

The probability of collapse (PC) refers to the likelihood that a particular bridge element (e.g., a pier) will collapse, given that it has been impacted by a particular vessel. Like any failure probability, PC is a function of both the loading characteristics and the structural capacity. Both the load and resistance are dependent on numerous parameters, each subject to random statistical variability. For example, vessel impact loads are a function of the vessel size, bow shape, impact velocity, direction of impact, vessel mass, and other parameters. Furthermore, the capacity of a pier to resist such impact loads is dependent upon structural configuration, pier member sizes, pier material strengths, and soil strength. To further complicate the process of predicting failure, impact events are dynamic in nature, and involve complex interactions between the impacting vessel and pier. Therefore, many of the load and resistance parameters listed above are correlated. For example, the magnitude and duration of dynamic impact forces (load characteristics) depend strongly upon the nonlinear lateral stiffness of the impacted pier (a resistance characteristic). Consequently, all of the important load and resistance characteristics, their statistical variability, and any possible correlations between them must be carefully considered in order to arrive at a reasonable estimate of PC .

The most accurate means of quantifying PC is through a structural reliability analysis (e.g., Monte Carlo simulation) that directly accounts for the statistical variability of the various load and resistance parameters. However, such an approach may require conducting tens of thousands dynamic structural analyses in order to arrive at a reliable PC estimate for just one pier and impact condition. Such an approach was demonstrated for eight different bridge piers by Davidson et al. (2013). Clearly, direct reliability analysis of this nature is overly burdensome for bridge designers to employ in practice.

As an alternative, PC has historically been computed (for vessel collision) using simplified equations that act as a surrogate for the complicated interactions and statistical variability discussed above. Such equations relate PC to a deterministically computed demand-to-capacity ratio. Structural demand (i.e., impact load magnitude) is computed using simplified equations that include the various parameters discussed above, and structural capacity is computed by structural analysis. Given the deterministically determined demand-capacity ratio (D/C), PC is computed from a surrogate equation.

Two surrogate equations for PC are available in the published literature: 1) the equation that is included in the AASHTO vessel collision provisions, and 2) an independently derived

equation recently developed by Davidson et al. (2013). Note that the AASHTO expression relies on a static treatment of both the impact load and structural capacity (i.e., static pushover analysis), while the Davidson expression employs a time-varying definition for the demand-capacity ratio, and can therefore be employed in conjunction with a dynamic definition of the impact load and structural response by means of transient structural analysis. The relative merits of the two expressions are discussed at length in Davidson et al. (2013) and Consolazio et al. (2010a).

The purpose of the current study was to compare the results of both procedures using the SR-300 Bridge as an example. As described in the following sections, PC values were computed using the AASHTO PC expression, employing AASHTO static load prediction models (from both the 1991 and 2009 specifications), and static pushover analysis of the piers. PC values were also computed using the Davidson PC expression, employing newly developed load prediction models and three new structural analysis techniques (two dynamic, one equivalent-static). It should be noted that the Davidson PC expression was derived exclusively for barge impact scenarios. Therefore, for ship-type vessel groups, PC was computed using the AASHTO procedures.

9.7.5.1 AASHTO methods

In accordance with the AASHTO guidelines, PC was computed as:

$$PC = \begin{cases} 0.1 + 9 \cdot [0.1 - (H/P)] & \text{for } 0.0 \leq H/P < 0.1 \\ [1 - (H/P)]/9 & \text{for } 0.1 \leq H/P \leq 1.0 \\ 0 & \text{for } H/P > 1.0 \end{cases} \quad (9.4)$$

where H is ultimate lateral pier resistance (as determined by static pushover analysis), and P is the vessel impact force (as determined by the equations below). From Eqn. 9.4, the following observations are made:

- For cases in which the lateral pier resistance exceeds the impact force, $PC = 0$.
- For cases in which the pier impact resistance is 10% to 100% of the impact force, PC varies linearly between 0.1 and 1.0. In other words, if the predicted impact force exceeds the pier capacity by *up to 10 times*, then PC varies between 0.1 and 1.0.
- For cases in which the pier impact resistance is below 10% of the impact force, PC varies linearly between 0.0 and 0.1. In other words, if the predicted impact force is *more than 10 times* the pier capacity, then PC varies between 0.0 and 0.1.

Lateral pier capacities (H) that were used to compute PC were taken from the bridge design drawings. Note that, as listed in the drawings, these capacities correspond to the *minimum* lateral capacity of each pier. Actual pushover capacities (determined by structural analysis in FB-MultiPier) were found to be higher than the minimum values. The degree of exceedance depended on soil conditions assigned to each pier. For consistency with the risk assessment methodology employed in the bridge design, the minimum values of H listed in the bridge drawings were adopted for the risk assessment (Table 9.5).

Table 9.5 Minimum lateral pushover capacities (H) for each pier

Pier number	H : Minimum lateral pushover capacity (kip)
33 – 37, 58 – 62	1,075
38 – 39, 56 – 57	1,500
40 – 42, 53 – 55	2,300
43 – 45, 50 – 52	2,750
46 – 49	3,255

In accordance with the AASHTO provisions, ship impact forces (P_S) were computed as:

$$P_S = 220(DWT)^{1/2} \left(\frac{V}{27} \right) \quad (9.5)$$

where DWT is the deadweight tonnage of the ship (tonnes), and V is the impact velocity (ft/s). In the given units, P_S was computed in kip. Ship impact forces varied between 198 kip and 1,670 kip, depending on ship type and pier distance from the navigation channel (see Appendix M)

9.7.5.1.1 AASHTO 1991 barge impact load model (as designed)

To compute barge impact forces (P_B) in accordance with the 1991 AASHTO provisions, vessel kinetic energy (KE) was first computed as:

$$KE = \frac{C_H W (V)^2}{29.2} \quad (9.6)$$

where, C_H is a hydrodynamic mass coefficient, W is the vessel weight (tonnes), and V is the impact velocity (ft/s). In the given units, KE was calculated in kip-ft. Hydrodynamic coefficients (C_H) were calculated based on underkeel clearance (distance between keel of vessel and bottom of waterway). For underkeel clearance $\geq 0.5 \times$ vessel draft, $C_H = 1.05$, and for underkeel clearance $\leq 0.1 \times$ vessel draft, $C_H = 1.25$. For clearances between those two limits, C_H was linearly interpolated. A table of C_H values for each pier and vessel group is provided in

Appendix M. Next, barge bow damage depth (a_B) (i.e., the depth of maximum crushing deformation) was computed as:

$$a_B = \left[\left(1 + \frac{KE}{5672} \right)^{1/2} - 1 \right] \left(\frac{10.2}{R_B} \right) \quad (9.7)$$

where, R_B is the ratio $B_B/35$, where B_B is the barge bow width (ft). In the given units, a_B was calculated in ft. Lastly, barge impact force (P_B) was computed as:

$$P_B = \begin{cases} [4112(a_B)](R_B) & \text{for } a_B < 0.34 \\ [1349 + 110(a_B)](R_B) & \text{for } a_B \geq 0.34 \end{cases} \quad (9.8)$$

In the given units, P_B was computed in kip. Barge impact forces computed using the 1991 AASHTO equations varied between 367 kip and 4,682 kip, depending on barge type and pier distance from the navigation channel (see Appendix M).

9.7.5.1.2 AASHTO 2009 barge impact load model

To compute barge impact forces (P_B) in accordance with the 2009 AASHTO provisions, vessel kinetic energy (KE) was also computed as before:

$$KE = \frac{C_H W (V)^2}{29.2} \quad (9.9)$$

In the given units, KE was calculated in kip-ft. The 2009 AASHTO provisions excluded the term R_B from all load equations. Therefore, barge bow damage depth (a_B) was computed as:

$$a_B = \left[\left(1 + \frac{KE}{5672} \right)^{1/2} - 1 \right] (10.2) \quad (9.10)$$

In the given units, a_B was calculated in ft. Lastly, barge impact force (P_B) was computed as:

$$P_B = \begin{cases} 4112(a_B) & \text{for } a_B < 0.34 \\ 1349 + 110(a_B) & \text{for } a_B \geq 0.34 \end{cases} \quad (9.11)$$

In the given units, P_B was computed in kip. Barge impact forces computed using the 2009 AASHTO equations varied between 367 kip and 3,241 kip, depending on barge type and pier distance from the navigation channel (see Appendix M).

As described above, the ratio H/P_S or H/P_B (depending on vessel group) was computed for each combination of pier and vessel group. Using Eqn. 9.4, corresponding estimates of PC were also calculated. Results are summarized in Section 9.8, and detailed results can be found in Appendix M.

9.7.5.2 UF/FDOT methods

In accordance with Davidson et al. (2013), PC was computed as:

$$PC = 2.33 \times 10^{-6} e^{13 \cdot D/C} \leq 1.0 \quad (9.12)$$

where, D/C is the maximum demand-to-capacity ratio from structural analysis. As defined by Davidson, D/C is a rational measure of the proximity of a structure to the formation of a structural mechanism that would result in instability and collapse. The ratio can take on any value from between 0 and 1, such that $D/C = 0$ for a pier under no load, and $D/C = 1$ for a pier which has formed a structural collapse mechanism and is at incipient collapse. It is important to note that D/C is a time-varying dynamic quantity. During a dynamic vessel impact event, D/C begins close to 0 (gravity loading will cause D/C to be nonzero even without impact load applied) and as the pier displaces, D/C increases (up to $D/C = 1$, if the pier collapses).

For this study, D/C was computed as:

$$D/C = \frac{\sum_{i=1}^m \sum_{j=1}^n (D/C)_{ij}^{FBMP}}{m \cdot n} \quad (9.13)$$

where m is the number of members (e.g., piers columns, piles) associated with a given collapse mechanism, n is the number of hinges per member that are necessary to form the corresponding collapse mechanism, and $(D/C)_{ij}^{FBMP}$ is the j th largest element demand-capacity ratio along member i , as reported by FB-MultiPier (internally computed based on biaxial load-moment

interaction). See Consolazio et al. (2010a) for a more detailed description of *D/C* and its theoretical basis.

9.7.5.2.1 CVIA structural analysis

The most accurate (design-oriented) vessel impact analysis method currently available is coupled vessel impact analysis (CVIA). As illustrated in Fig. 9.13, in CVIA, the impacting vessel is idealized as a single-degree-of-freedom (SDF) system, consisting of a concentrated mass that represents the vessel mass, and a nonlinear spring element that represents the crushing characteristics (force-deformation relation) of the vessel bow. The SDF barge model is coupled to a multiple-degree-of-freedom (MDF) finite element model of the impacted pier at a node corresponding to the expected impact location. To begin the analysis, the structure is pre-loaded with gravity and buoyancy forces, and then the vessel mass is prescribed an initial velocity equal to the impact velocity. Impact forces imparted on the pier are computed based on dynamic interaction between the SDF barge and MDF pier models, as would occur during a real impact event.

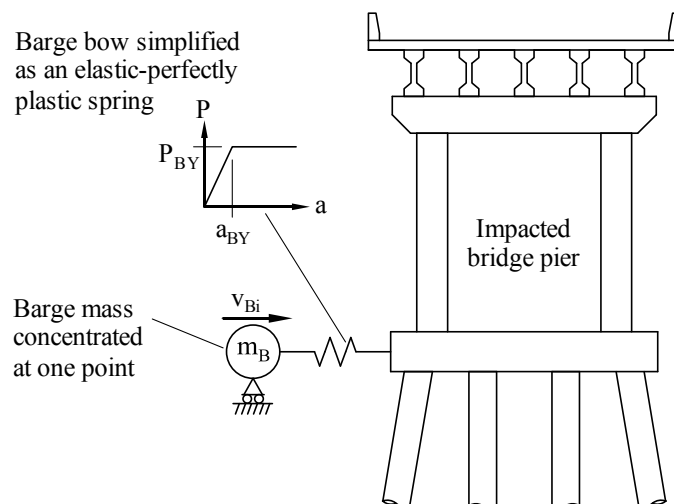


Figure 9.13 Coupled vessel impact analysis (CVIA) method

CVIA has been used extensively in numerous research projects (Consolazio et al. 2008, Davidson et al. 2010, Getter et al. 2011, and Davidson et al. 2013). As implemented in these prior studies, the barge force-deformation relation was assumed to be elastic, perfectly plastic (as shown in Fig. 9.13, using a force-deformation model from Consolazio et al. (2009). This model has since been updated to account for oblique impact scenarios (Getter and Consolazio 2011), like the one shown in Fig. 9.14.

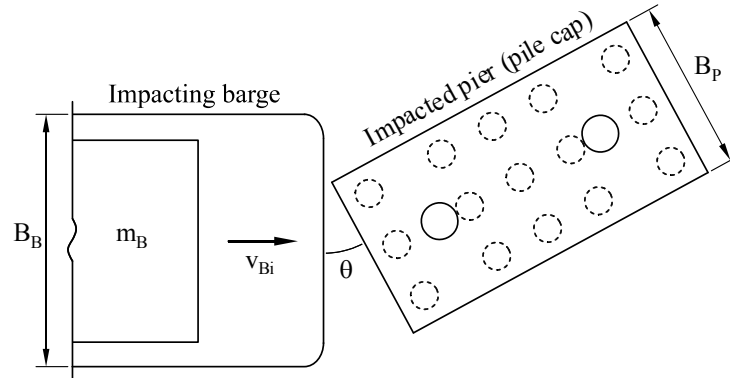


Figure 9.14 Typical barge impact with pile cap, showing pertinent impact parameters

The Getter-Consolazio force-deformation model was employed throughout this study for computing impact forces. Specifically pertaining to CVIA, force-deformation relations for the SDF barge models were taken to be elastic, perfectly plastic, with yield deformation $a_{BY} = 2$ in. Barge yield force (P_{BY}) was computed in accordance with the empirical Getter-Consolazio equations. For oblique impact with a flat-faced pier (the scenario for all piers in the SR-300 Bridge), P_{BY} was computed as:

$$P_{BY} = 1400 + \left(130 - \frac{68}{1 + e^{3.8 - 0.31 \cdot \theta}} \right) \cdot \min(B_B, B_P) \quad (9.14)$$

where θ is the smallest skew angle between the barge bow and pier surface (degrees), B_B is the vessel beam (width) (ft), and B_P is the width of the pier face associated with the smallest skew angle (ft). These quantities are illustrated for a typical impact condition in Fig. 9.14. Given the units shown, P_{BY} was computed in kip. A summary of relevant input data for CVIA simulations is provided in Table 9.6. Impact force-time histories computed by each CVIA simulation that was conducted (208 total) are provided in Appendix M. Finally, D/C values predicted by CVIA, and the associated values of PC are discussed in Section 9.8, and listed in detail in Appendix M.

Table 9.6 Barge impact parameters for CVIA

Pier	θ (deg)	$\min(B_B, B_P)$ (ft)	P_{BY} (kip)	W_B (tons)	v_{Bi} (knot)
35 – 39	28.5	18.5	2,555	1,071 – 13,611 ¹	Varies ²
40 – 55	28.5	28.0	3,148	1,071 – 13,611 ¹	Varies ²
56 – 60	28.5	18.5	2,555	1,071 – 13,611 ¹	Varies ²

¹ Varies by vessel group. See Table 9.3 for details.

² Varies by vessel group and pier location. See Table 9.3 and Appendix M for details.

9.7.5.2.2 AVIL structural analysis

The applied vessel impact load (AVIL) method was developed as a slightly simpler alternative to CVIA (Consolazio et al. 2008). The method consists of developing a pre-computed impact force-time history and applying it as a dynamic load in a transient analysis, as shown in

Fig. 9.15. It is recognized that many structural analysis packages do not include the features required to conduct CVIA (e.g., the ability to assign initial velocities), but the ability to analyze structures under prescribed time-varying loading is quite common. In such cases, AVIL is an excellent alternative analysis procedure to CVIA.

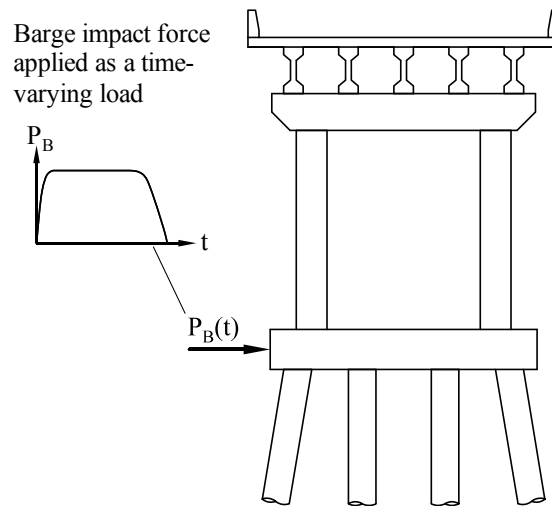


Figure 9.15 Applied vessel impact load (AVIL) method.

The AVIL method is summarized in Fig. 9.16. As implemented in this study, barge force-deformation characteristics (a_{BY} and P_{BY}) were established based on the Getter and Consolazio (2011) model, as discussed above for CVIA. Barge mass (m_B) and initial barge velocity (v_{Bi}) were also the same as CVIA (recall Table 9.6). As shown in Fig. 9.17, pier-soil stiffness (k_p) was determined by analyzing each pier finite element model subject to a lateral load (P), measuring the corresponding displacement (Δ), and computing $k_p = P/\Delta$. It is recognized that, due to soil and/or structural nonlinearity, k_p generally becomes smaller as P increases. Because the AVIL method is unable to account for changes in pier resistance during an impact event, a representative k_p must be selected for its formulation. It was observed in conducting this study, that using the *initial* pier stiffness (i.e., k_p corresponding to a very small value of P) resulted in analysis results that were very similar to CVIA and consistently conservative. Values of k_p that were determined for each pier are provided in Table 9.7, and maximum barge impact forces (P_{Bm}) for each pier and vessel group are shown in Table 9.8. Impact force-time histories that were computed for each AVIL analysis are compared to corresponding CVIA force histories in Appendix M. Finally, D/C values predicted by AVIL, and the associated values of PC are discussed in Section 9.8, and listed in detail in Appendix M.

Applied Vessel Impact Load History Method

Select barge type, and determine P_{BY}, a_{BY}

Determine impact characteristics: m_B, v_{Bi}

Calculate pier-soil stiffness from static analysis: k_p

$$k_S = \left(\frac{a_{BY}}{P_{BY}} + \frac{1}{k_p} \right)^{-1} \quad \text{Calculate barge-pier-soil series stiffness}$$

$$c_{BP} = \sqrt{k_S m_B} \quad \text{Calculate pseudo-damping coefficient}$$

$(v_{Bi} c_{BP} \leq P_{BY})$
Elastic loading

$(v_{Bi} c_{BP} > P_{BY})$
Inelastic loading

$$P_{Bm} = v_{Bi} c_{BP}$$

$$P_{Bm} = P_{BY}$$

$$t_E = \frac{\pi m_B}{P_{Bm}} v_{Bi}$$

$$t_Y = \frac{\pi m_B}{2P_{BY}} \left(v_{Bi} - \sqrt{v_{Bi}^2 - \left(\frac{P_{BY}}{c_{BP}} \right)^2} \right)$$

$$t_P = \frac{m_B}{P_{BY}} \sqrt{v_{Bi}^2 - \left(\frac{P_{BY}}{c_{BP}} \right)^2} \quad t_U = \frac{\pi m_B}{2P_{BY}} \frac{P_{BY}}{c_{BP}}$$

$$t_T = \frac{\pi m_B}{2P_{Bm}} \left(v_{Bi} + \frac{P_{BY}}{c_{BP}} + \left(\frac{2}{\pi} - 1 \right) \sqrt{v_{Bi}^2 - \left(\frac{P_{BY}}{c_{BP}} \right)^2} \right)$$

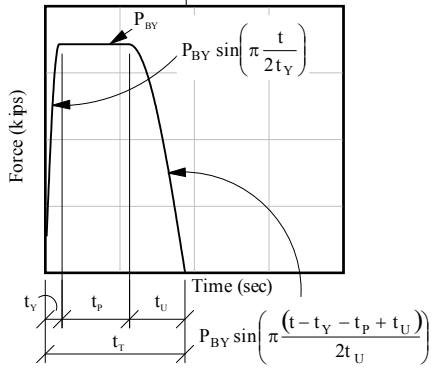
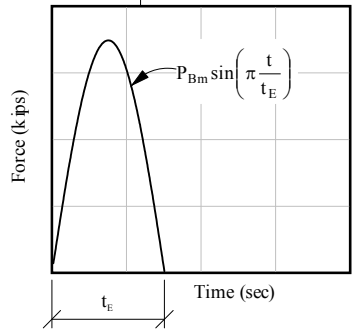


Figure 9.16 Procedure for computing barge impact force-time histories in accordance with AVIL method (Consolazio et al. 2008)

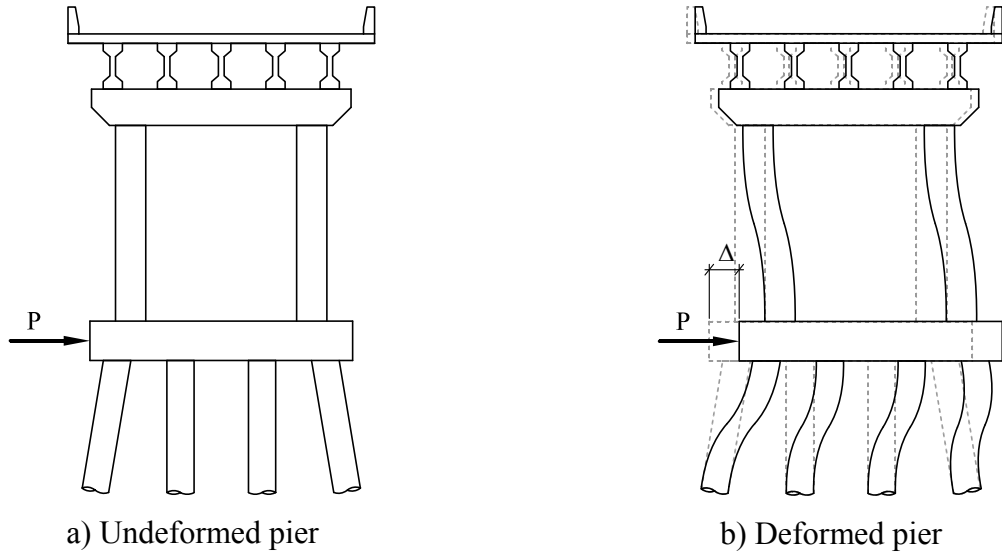


Figure 9.17 Determination of lateral pier-soil stiffness (k_p) by static analysis

Table 9.7 Lateral pier-soil stiffness (k_p) for each SR-300 pier

Pier no.	k_p (kip/in.)	Pier no.	k_p (kip/in.)	Pier no.	k_p (kip/in.)	Pier no.	k_p (kip/in.)
35	1,750	42	2,064	49	4,927	56	2,229
36	1,746	43	3,941	50	2,256	57	2,237
37	1,237	44	2,838	51	2,437	58	2,088
38	2,010	45	3,830	52	2,301	59	2,379
39	2,087	46	3,901	53	2,012	60	2,508
40	3,045	47	3,975	54	2,915		
41	2,929	48	4,932	55	3,041		

Table 9.8 Maximum barge impact force (P_{Bm}) (kip) for each pier and barge vessel group

VG	P35	P36	P37	P38	P39	P40	P41	P42	P43	P44	P45	P46	P47
1	1,298	1,297	1,197	1,335	1,345	1,539	1,528	1,427	1,630	2,770	3,148	3,148	3,148
2	2,388	2,387	2,203	2,456	2,474	2,831	3,028	3,148	3,148	3,148	3,148	3,148	3,148
3	2,378	2,376	2,193	2,445	2,463	2,818	2,799	2,614	3,148	3,148	3,148	3,148	3,148
4	2,555	2,555	2,555	2,555	2,555	3,148	3,148	3,148	3,148	3,148	3,148	3,148	3,148
5	1,755	1,755	1,811	2,555	2,555	3,148	3,148	3,148	3,148	3,148	3,148	3,148	3,148
6	2,555	2,555	2,555	2,555	2,555	3,148	3,148	3,148	3,148	3,148	3,148	3,148	3,148
7	2,555	2,555	2,555	2,555	2,555	3,148	3,148	3,148	3,148	3,148	3,148	3,148	3,148
8	2,555	2,555	2,555	2,555	2,555	3,148	3,148	3,148	3,148	3,148	3,148	3,148	3,148
VG	P48	P49	P50	P51	P52	P53	P54	P55	P56	P57	P58	P59	P60
1	3,148	3,148	3,148	2,692	1,486	1,420	1,527	1,538	1,361	1,362	1,345	1,377	1,390
2	3,148	3,148	3,148	3,148	3,148	3,148	3,026	2,830	2,504	2,506	2,474	2,534	2,555
3	3,148	3,148	3,148	3,148	3,148	2,600	2,797	2,818	2,493	2,495	2,463	2,522	2,545
4	3,148	3,148	3,148	3,148	3,148	3,148	3,148	3,148	2,555	2,555	2,555	2,555	2,555
5	3,148	3,148	3,148	3,148	3,148	3,148	3,148	3,148	2,555	2,555	2,034	1,862	1,879
6	3,148	3,148	3,148	3,148	3,148	3,148	3,148	3,148	2,555	2,555	2,555	2,555	2,555
7	3,148	3,148	3,148	3,148	3,148	3,148	3,148	3,148	2,555	2,555	2,555	2,555	2,555
8	3,148	3,148	3,148	3,148	3,148	3,148	3,148	3,148	2,555	2,555	2,555	2,555	2,555

9.7.5.2.3 SBIA structural analysis

The static bracketed impact analysis (SBIA) method is an equivalent-static analysis procedure that attempts to account for the inertial response of the impacted pier by means of a small number of static load cases (Getter et al. 2011). SBIA represents an improvement over static pushover analysis, in that it accounts for superstructure inertia and dynamic amplification of pier structural demands. It should be noted, however, that SBIA was specifically developed to produce conservative results relative to more refined procedures like CVIA or AVIL. It is therefore expected to produce D/C estimates that are larger than both dynamic methods. The purpose of including SBIA in this study was to evaluate its level of conservatism in the context of a vessel collision risk assessment.

The SBIA method is summarized in Fig. 9.18. As shown, the method consists of two overriding static load cases, of which one (Load Case 1, abbreviated LC1 hereafter) requires three separate analyses. The parameters of each LC1 analysis are specifically tuned to produce conservative analysis results for the corresponding structural demand type. From left-to-right in Fig. 9.18, the first analysis is intended to quantify pier column and/or foundation moments, the second analysis is intended to quantify pier shear forces, and the third analysis is used to quantify shear forces at the superstructure bearing locations (substructure-superstructure interface). For all three LC1 loading conditions, an amplified impact load ($1.45 \times P_B$) is applied at the impact location, and a load ($IRF \times P_B$) is applied at the superstructure elevation. The load $IRF \times P_B$ is intended to mimic superstructure inertial behavior that can only be directly quantified through dynamic analysis. Load Case 2 (LC2) consists of applying an amplified impact load ($1.85 \times P_B$) at the impact location, but no superstructure load.

As implemented in this study, P_B was computed using the same impact conditions, pier characteristics, and load equations as AVIL. However, because it is a static method, only the maximum dynamic impact load was of interest. As such, P_B for SBIA was equal to P_{Bm} from AVIL (recall Fig. 9.16, and Table 9.8). Values of inertial resistance factors (IRF_m , IRF_v , and IRF_b) were computed using the pier and superstructure characteristics and equations shown in Fig. 9.18. Superstructure stiffness was computed as shown in Fig. 9.19. A multiple-pier finite element model (including superstructure) was constructed, with the pier of interest (impact pier) in the center. The impact pier was removed from the analysis by removing connections between the pier and superstructure, and a lateral load equal to $0.25 \times P_B$ was applied to the superstructure at the location of the removed pier. Lateral deflection (Δ_{sup}) was computed, and superstructure stiffness was calculated as $k_{sup} = (0.25 \times P_B) / \Delta_{sup}$. Pier parameters that were used to compute IRF are summarized in Table 9.9, and computed IRF values are provided in Table 9.10.

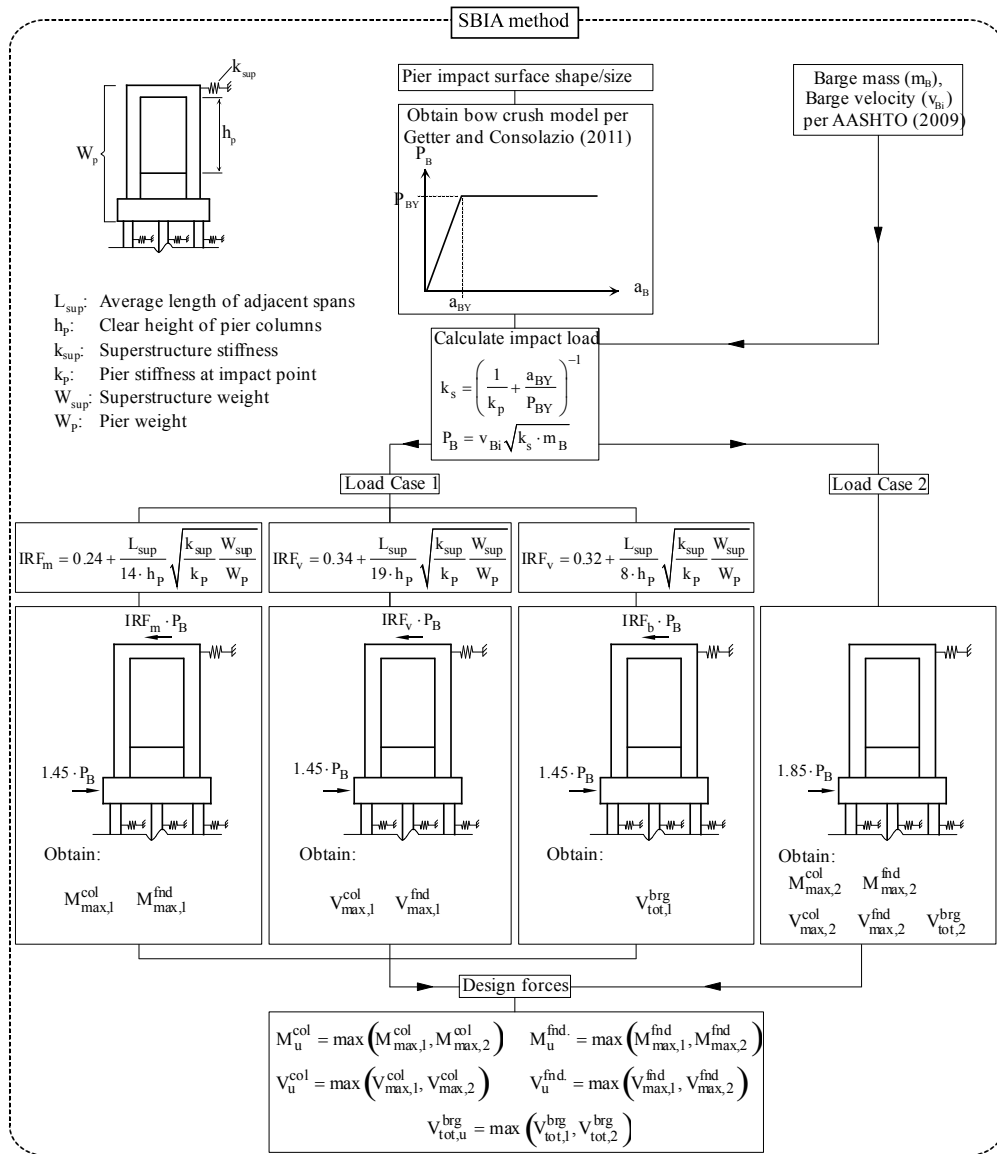


Figure 9.18 Static load cases for SBIA method (Getter et al. 2011)

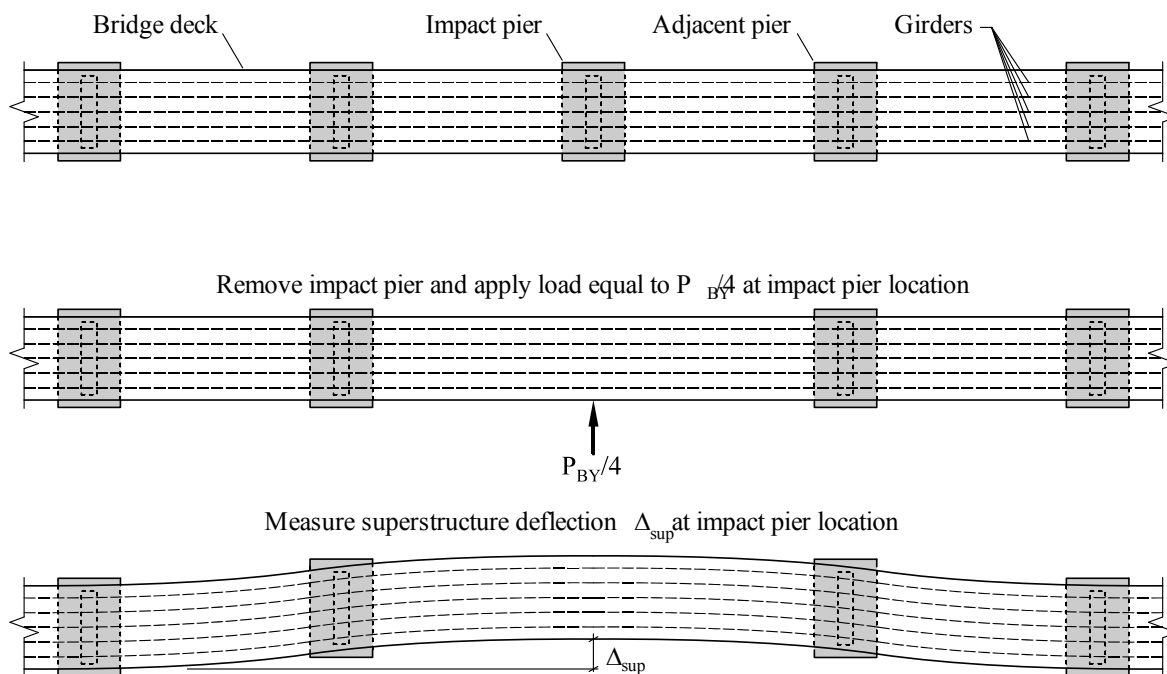


Figure 9.19 Determination of lateral superstructure stiffness (k_{sup})

Table 9.9 Input parameters for SBIA *IRF* equations

Pier no.	L_{sup} (ft)	h_p (ft)	k_{sup} (kip/in)	k_p (kip/in)	W_{sup} (kip)	W_p (kip)	Pier no.	L_{sup} (ft)	h_p (ft)	k_{sup} (kip/in)	k_p (kip/in)	W_{sup} (kip)	W_p (kip)
35	140	14.2	732	1,750	1,518	817	48	254	51.6	346	4,932	2,876	2,267
36	140	18.5	622	1,746	1,511	842	49	233	49.9	342	4,927	2,640	2,244
37	140	22.7	176	1,237	1,503	866	50	205	52.7	159	2,256	1,926	2,127
38	140	26.9	527	2,010	1,505	935	51	140	50.2	498	2,437	1,498	2,106
39	140	31.1	549	2,087	1,532	957	52	140	47.2	440	2,301	1,507	2,080
40	140	35.3	488	3,045	1,525	1,539	53	140	43.6	508	2,012	1,500	1,598
41	140	39.5	115	2,929	1,491	1,569	54	140	39.5	115	2,915	1,491	1,569
42	140	43.6	647	2,064	1,500	1,598	55	140	35.3	544	3,041	1,474	1,539
43	140	47.2	482	3,941	1,507	2,080	56	140	31.1	642	2,229	1,481	957
44	140	50.2	818	2,838	1,498	2,106	57	140	26.9	597	2,237	1,500	935
45	205	52.7	158	3,830	1,853	2,127	58	140	22.7	176	2,088	1,493	866
46	233	49.9	339	3,901	2,640	2,244	59	140	18.5	701	2,379	1,500	842
47	254	51.6	351	3,975	2,876	2,267	60	140	14.3	813	2,508	1,507	817

Table 9.10 *IRF* values for SBIA Load Case 1

Pier no.	IRF_m	IRF_v	IRF_b	Pier no.	IRF_m	IRF_v	IRF_b	Pier no.	IRF_m	IRF_v	IRF_b
35	0.86	0.80	1.41	44	0.33	0.41	0.48	53	0.35	0.42	0.52
36	0.68	0.66	1.08	45	0.29	0.38	0.41	54	0.29	0.38	0.41
37	0.46	0.50	0.71	46	0.35	0.42	0.51	55	0.36	0.43	0.53
38	0.48	0.52	0.74	47	0.36	0.43	0.53	56	0.45	0.50	0.70
39	0.45	0.49	0.69	48	0.34	0.42	0.50	57	0.48	0.52	0.75
40	0.35	0.42	0.52	49	0.34	0.41	0.49	58	0.41	0.46	0.61
41	0.29	0.38	0.41	50	0.31	0.39	0.44	59	0.63	0.63	1.01
42	0.36	0.43	0.54	51	0.32	0.40	0.45	60	0.78	0.74	1.27
43	0.30	0.39	0.43	52	0.32	0.40	0.46				

Note that primary purpose of the SBIA method is to quantify structural demands (shears, moments) for use in designing and proportioning various structural elements. In contrast, the goal of performing structural analysis in the context of this risk assessment was to quantify demand-capacity ratios (D/C) for input into the Davidson et al. (2013) PC expression (Eqn. 9.12). Because D/C , as defined by Davidson et al. (Eqn. 9.13), was computed based on load-moment interaction, only the LC1 analysis pertaining to pier moments (analyzed using IRF_m) and LC2 were used in computing D/C for the risk assessment. The other two LC1 analyses (utilizing IRF_v and IRF_b) would be useful for proportioning a new bridge, but such results had limited utility in the risk assessment. Values of D/C predicted by SBIA, and the associated values of PC are discussed in Section 9.8, and listed in detail in Appendix M.

9.7.6 Protection factor (PF)

The protection factor (PF) is a correction factor used in a vessel collision risk assessment to account for land masses and other navigational obstructions that may block bridge piers (either fully or partially) from being impacted by oncoming vessels. As noted in Section 9.3.2, two navigation obstructions exist to the east of the bridge: a man-made island in the vicinity of the northern piers, and a segment of a decommissioned bridge (now a fishing pier) in the vicinity of the southern piers (recall Fig. 9.2). It was therefore appropriate to assign protection factors (PF) to each pier in the vicinity of these obstructions to account for reduced collision risk. A rational calculation basis was developed to determine the probability that a vessel would run aground on the navigational obstructions (P_{Gr} , the probability of grounding) prior to impacting the bridge piers, and P_{Gr} was used to calculate PF for each pier.

To demonstrate the basis for calculating P_{Gr} , consider the scenario shown in Fig. 9.20, in which a barge tow is positioned such that impact is impending with a bridge pier to the north of the navigation channel. The orientation angle of the tow (relative to the bridge alignment) is assumed to be a Gaussian distributed random variable, with a mean equal to the orientation angle of the navigation channel (i.e., the most likely tow orientation is parallel to the navigation channel) and a standard deviation equal to 10° (Kunz 1998). As shown in Fig. 9.20, the orientation angle (θ) is taken to be equal to 0° when the tow is aligned parallel to the navigation channel, and thus θ can take on positive or negative values. Given the site geometry, a vessel would run aground on the island obstruction if it approached from a negative (signed) angle θ such that $\theta \leq \theta_{NO}$, where θ_{NO} is the negative (signed) angle, defined in Fig. 9.20, between the navigational obstruction and the most likely vessel orientation (parallel to the navigation channel). Note that because θ is defined as a Gaussian distributed random variable, it can take on values $\theta = [-\infty, \infty]$, which has little meaning in the polar domain ($\pm 180^\circ$). However, because the standard deviation is equal to a relatively small angle of 10° , the *practical* range of the Gaussian distribution is limited to realistic approach angles (i.e., $\theta = \pm 30^\circ$ spans three standard deviations on either side of the mean).

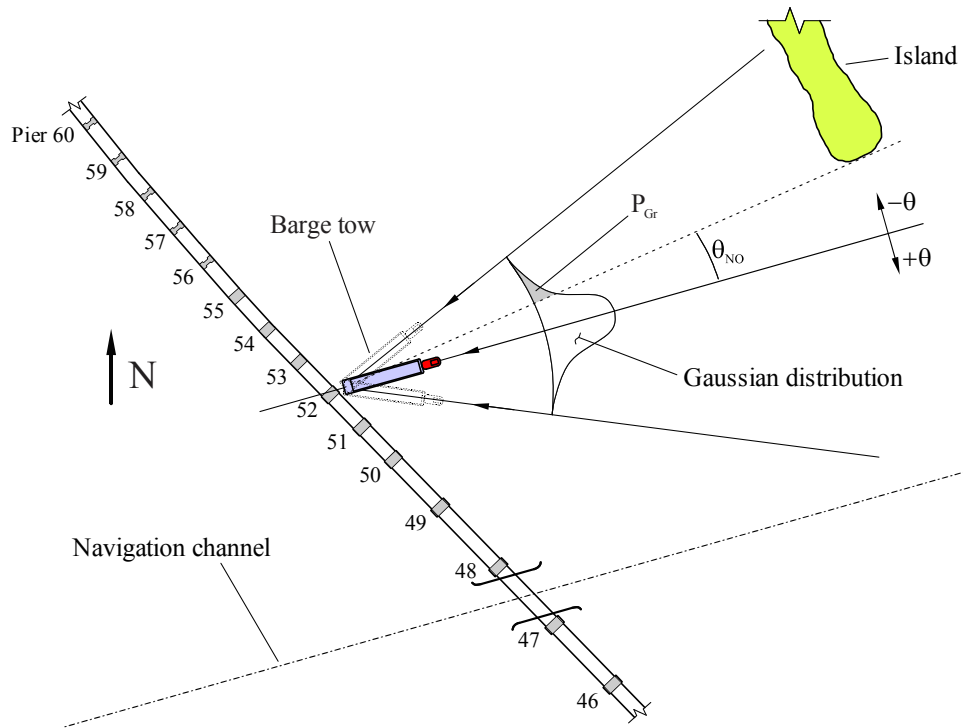


Figure 9.20 Procedure for computing the probability that a navigational obstruction (island) will cause vessel grounding prior to pier impact (P_{Gr}) based on its orientation and path to the pier

Given the scenario illustrated in Fig. 9.20, the total probability of the vessel grounding (P_{Gr}) was computed as:

$$P_{Gr} = \int_{-\infty}^{\theta_{NO}} P(\theta, \mu_{\theta}, \sigma_{\theta}) d\theta \quad (9.15)$$

where P is a Gaussian distribution with mean $\mu_{\theta} = 0^{\circ}$, and standard deviation $\sigma_{\theta} = 10^{\circ}$. For the example shown in Fig. 9.20, it is important to point out that P_{Gr} is nonzero even though the pier is located well south of the island. While this outcome may initially seem counterintuitive, the procedure appropriately takes into account low-probability impact scenarios in which the vessel approaches from a position north of the tip of the island and ultimately runs aground.

Fig. 9.21 shows an analogous scenario to Fig. 9.20, in which a barge tow instead approaches a pier located south of the navigation channel. As a vessel approaches a southern pier, the remaining segment of a decommissioned bridge (now a fishing pier) acts as a potential navigational obstruction. The old bridge obstructs possible approach angles such that a vessel would run aground (i.e., impact the old bridge) if $\theta \geq \theta_{NO}$ (where θ_{NO} is a positive signed angle, as defined in Fig. 9.21).

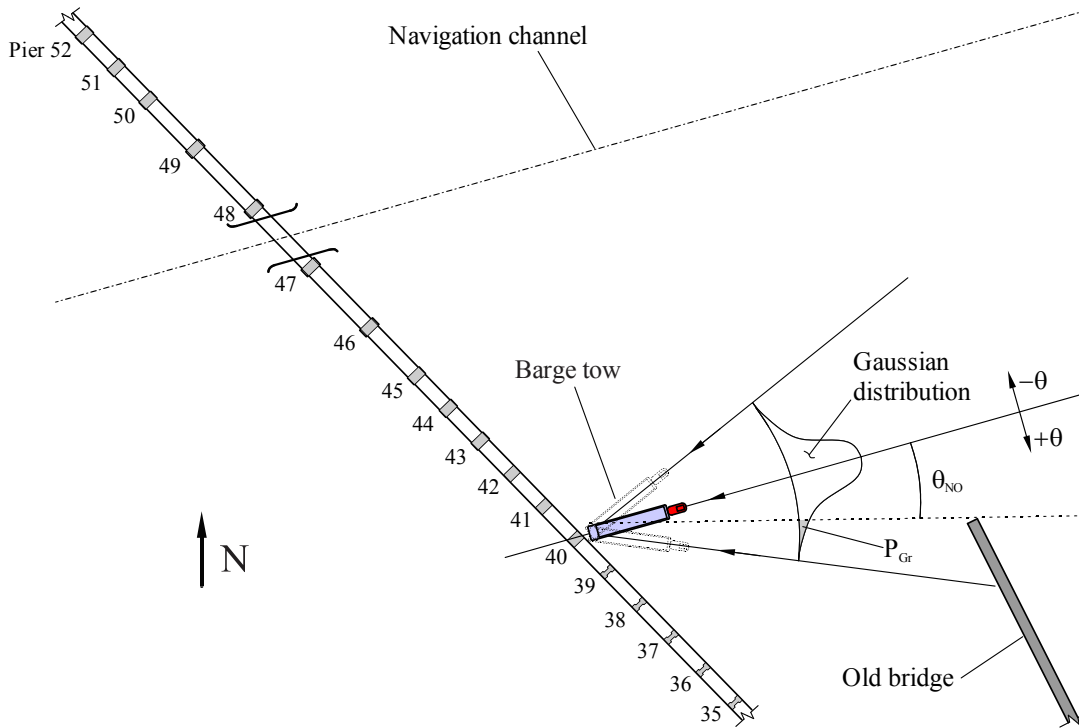


Figure 9.21 Procedure for computing P_{Gr} for old bridge (fishing pier) navigational obstruction

For the scenario shown in Fig. 9.21, probability of grounding (P_{Gr}) was computed as:

$$P_{Gr} = \int_{\theta_{NO}}^{\infty} P(\theta, \mu_{\theta}, \sigma_{\theta}) d\theta \quad (9.16)$$

Note that the integration limits in Eqn. 9.16 were changed (relative to Eqn. 9.15) to result in small values of grounding probability P_{Gr} for the northernmost piers and large values for the southernmost piers.

The procedure outlined above was repeated for each SR-300 pier in the impact zone, and for simplicity, $P_{Gr} = 0.0$ was conservatively assigned to any piers for which the computed value P_{Gr} was less than 0.001 (0.1%). Protection factors (PF) were subsequently computed as:

$$PF = 1 - P_{Gr} \quad (9.17)$$

Piers 44 – 48 (nearest the navigation channel) were afforded no meaningful protection by the obstructions (island or fishing pier), and were therefore assigned $PF = 1.0$ (corresponding to a zero probability of grounding, $P_{Gr} = 0.0$).

As discussed in Section 9.3.5, a shoal also exists immediately to the east of the SR-300 Bridge, restricting water depths to approximately 4 ft at MHW. As shown in a navigation chart (recall Fig. 9.4), reduced water depth from the shoal affects almost the entire eastern side of the bridge, with the exception of the dredged channel. Off-channel water depths do increase near the bridge (effectively widening the channel) with a more widespread increase in depth to the south of the channel. Therefore, vessels of any draft were assumed to be able to impact three piers south of the channel (piers 45 – 47) and one pier north of the channel (pier 48) without running aground. However, for all other piers, the probability of downbound vessels grounding on the shoal (P_{Gr}) was assumed to be equal to 0 for vessel draft ≤ 4 ft, and 1 for draft ≥ 12 ft. P_{Gr} was linearly interpolated between 0 and 1 for vessel drafts between 4 ft and 12 ft, respectively. Corresponding values of $PF = 1 - P_{Gr}$ were calculated and multiplied by the PF values corresponding to the island and fishing pier obstructions (i.e., the separate components of the protection factor were assumed to combine in the same manner as conditional probabilities—using multiplication). Final PF values for each pier and vessel group are tabulated in Appendix M.

9.8 Risk Analysis Results

As discussed in the prior section, vessel collision risk assessments were conducted for the SR-300 Bridge using the methodology prescribed by AASHTO (1991 and 2009 specifications). Additional assessments were conducted using the revised UF/FDOT methodology and three different structural analysis procedures (CVIA, AVIL, and SBIA). The results of each assessment are presented in this section, including probability of collapse (PC) and annual frequency of collapse (AF) estimates, as predicted by each method. Detailed results for each pier and vessel group are provided in Appendix M.

9.8.1 AASHTO methods

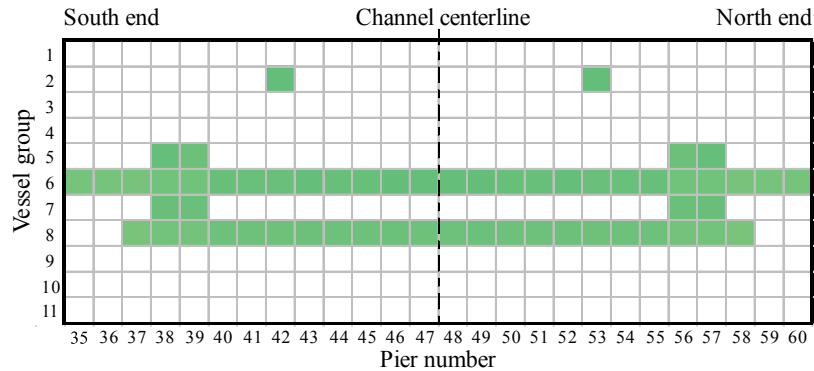
The following sections discuss results from the risk assessments conducted using AASHTO methodology with two different barge impact load equations: 1) from the 1991 AASHTO provisions (Eqns. 9.7 and 9.8), and 2) from the 2009 provisions (Eqns. 9.10 and 9.11).

9.8.1.1 AASHTO (1991) barge impact load model (as-designed)

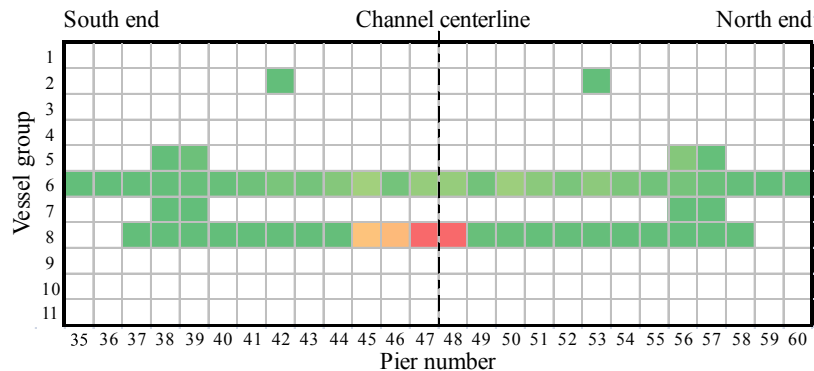
Estimates of PC values that were computed using the AASHTO (1991) methodology were very often equal to zero. Specifically, of the 289 combinations of pier and vessel group considered, PC was nonzero 58 times (approximately 20%). This occurred because, using the AASHTO expression, PC was only nonzero when the impact load P exceeded the lateral pier capacity H (i.e., $H/P < 1$). Furthermore, even nonzero values of PC were quite small. Indeed, the largest PC among all cases considered was 0.071, and for this case, the impact load exceeded pier capacity by 2.8 times. Among the nonzero cases, the average PC was 0.033, which corresponds to pier capacity being exceeded by 1.4 times.

Estimates of PC , as obtained by AASHTO (1991) methods, are presented qualitatively for every pier and vessel group in Fig. 9.22a. Note that in this format, white squares correspond to PC values that are exactly equal to zero. Green color indicates PC just greater than zero, and the color gradient fades to red at $PC = 1$. While all nonzero values are small, PC was slightly greater for piers far from the navigation channel. The majority of nonzero PC cases were in vessel groups 6 and 8.

Including all other terms in the AF expression (N , PA , PG , PF), the relative contribution to AF is shown for every pier and vessel group in Fig. 9.22b. Note that the color gradient is simply relative to the maximum contribution among all piers and vessel groups, having no specific numerical scale. The purpose of the gradient is to show, qualitatively, which piers and vessel groups contribute most to total risk (AF). As would be expected, piers nearest the centerline contributed most to AF , as they have the highest likelihood of being impacted. Most risk was concentrated in vessel group 8 (the largest vessel type in the fleet).



a) Probability of collapse (PC)
(white = 0, green \approx 0.0, red = 1.0)



b) Contribution to annual frequency of collapse (AF)
(colors are relative to maximum contribution among all piers and vessel groups)

Figure 9.22 Risk analysis results for each pier and vessel group: AASHTO (1991) methods

Fig. 9.23a shows the percent contribution to AF for each pier in the bridge (i.e., the contributions shown in Fig. 9.22b, summed across all vessel groups). As noted previously, the

majority of total risk was concentrated in piers near the navigation channel. Specifically, approximately 75% of risk was carried by the three piers south of the channel (piers 45 – 47) and one pier north of the channel (pier 48). Recall that these are the four piers that were assigned protection factors $PF = 1.0$ for downbound traffic (see Section 9.7.6). All other piers were assigned $PF < 1$, to account for navigational obstructions and shallow water depths to the east of the bridge, and therefore their percent contribution to total risk was correspondingly lower.

Fig. 9.23b shows the percent contribution to AF for each vessel group (i.e., the contributions shown in Fig. 9.22b, summed across all piers). The vast majority of risk (approximately 85%) came from vessel groups 6 and 8, as noted above.

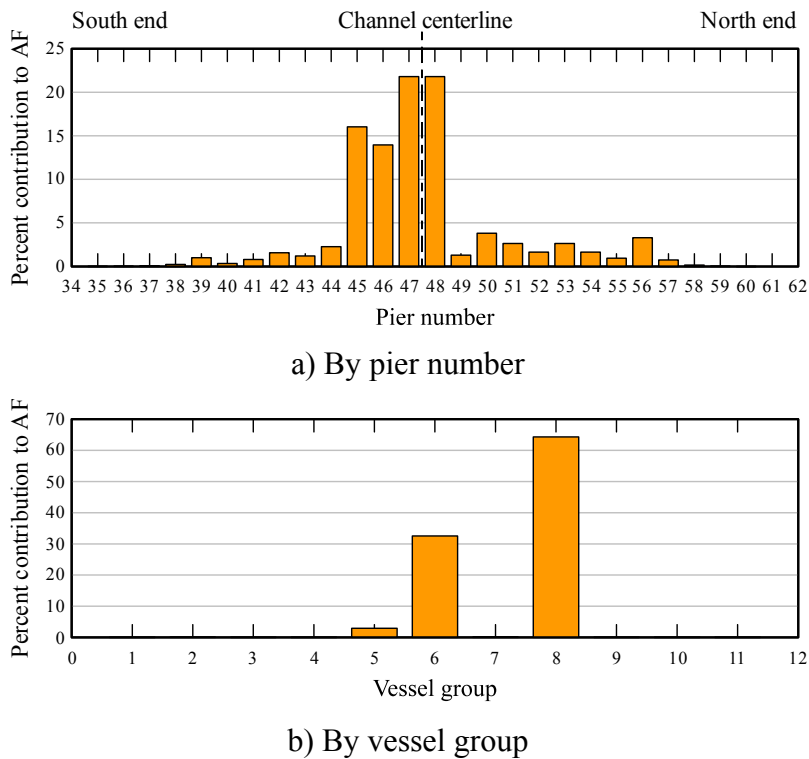


Figure 9.23 Percent contribution to AF : AASHTO (1991) methods

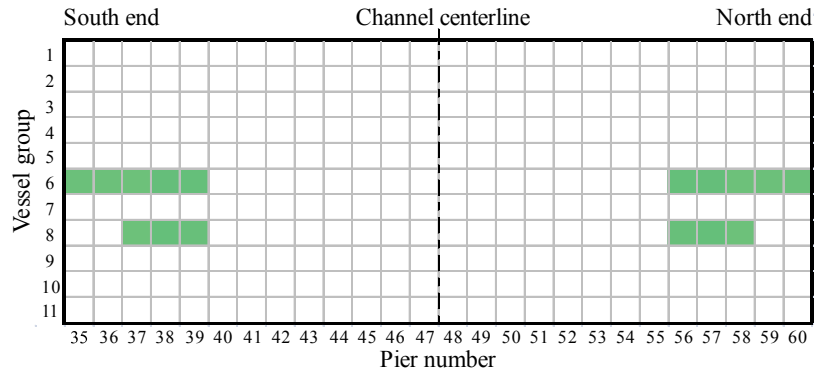
Summing AF among all piers and vessel groups, AF predicted by AASHTO (1991) methods was $4.96 \times 10^{-5} \text{ yr}^{-1}$, which corresponds to a return period $1/AF = 20,150$ years. Therefore, by the AASHTO definition, the bridge can be considered sufficiently robust to resist vessel collision loading, because the minimum acceptable return period is $1/AF = 10,000$ years for the “critical/essential” operational classification. It should be noted that the value for AF was strongly sensitive to assumptions made in the analysis. For example, if the possibility for vessel groundings for downbound traffic was neglected, the return period changed to $1/AF = 11,730$ years. This finding suggests that all assumptions made in performing the risk analysis should be stated clearly and explained thoroughly so that they may be effectively evaluated by peer engineers and the bridge owner. Furthermore, the sensitivity of AF to various

assumptions should be evaluated by the engineer to ensure that reasonably conservative choices are made.

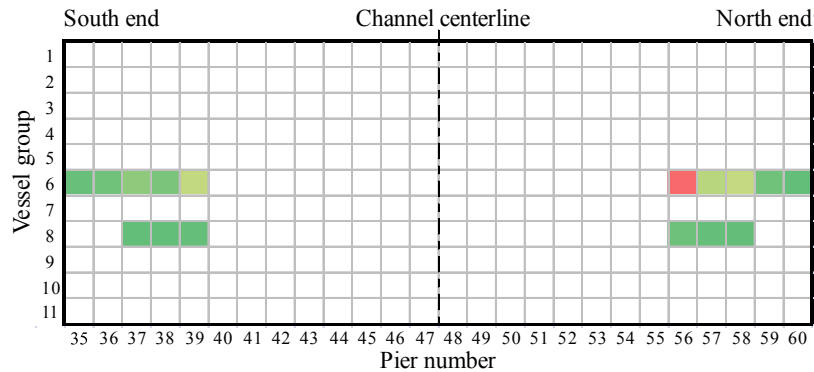
9.8.1.2 AASHTO 2009 barge impact load model

Estimates of PC that were computed using the AASHTO (2009) methodology were nearly always equal to zero. Specifically, of the 289 combinations of pier and vessel group considered, PC was nonzero 16 times (approximately 5%). This occurred because, compared to the 1991 AASHTO procedure, barge impact load magnitudes were lower, particularly for high-energy impact conditions experienced by piers near the navigation channel. Because the bridge was designed to resist relatively higher load magnitudes predicted by the 1991 AASHTO provisions, pier capacity was almost never exceeded ($H/P < 1$) using the 2009 provisions, and PC was equal to zero for 95% of impact cases considered.

Estimates of PC , as obtained by AASHTO (2009) methods, are presented qualitatively for every pier and vessel group in Fig. 9.24a. Note that PC was equal to zero for all piers between 40 and 55 for every vessel group. Consequently, PC was only nonzero for piers located far from the navigation channel, which are unlikely to be impacted. Including all other terms in the AF expression (N , PA , PG , PF), the relative contribution to AF is shown for every pier and vessel group in Fig. 9.24b. The largest single contributor to AF was pier 56 for vessel group 6, because, of the piers with nonzero PC , pier 56 had the highest probability of being impacted (as reflected by its PF value).



a) Probability of collapse (PC) (white = 0, green ≈ 0.0 , red = 1.0)



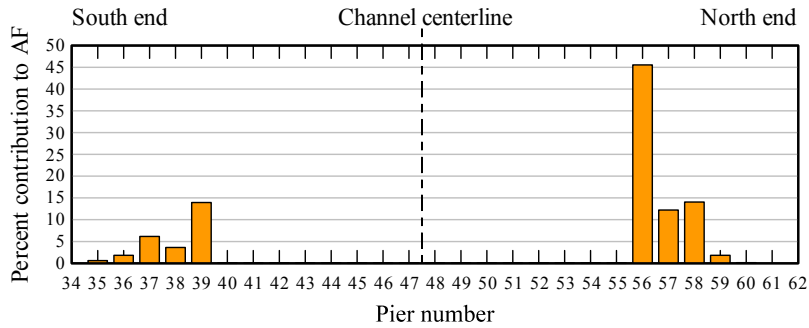
b) Contribution to annual frequency of collapse (AF)

(colors are relative to maximum contribution among all piers and vessel groups)

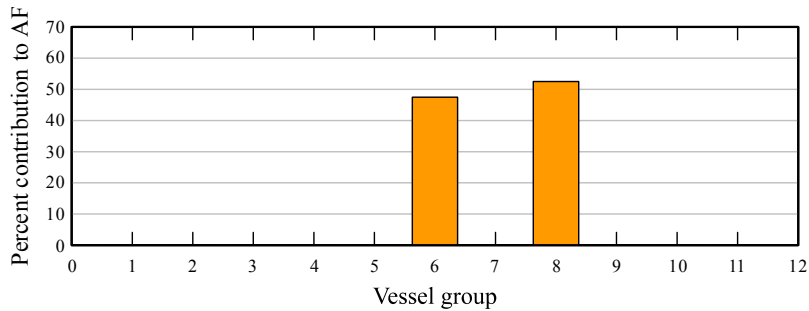
Figure 9.24 Risk analysis results for each pier and vessel group: AASHTO (2009) methods

Fig. 9.25a shows the percent contribution to AF for each pier in the bridge (i.e., the contributions shown in Fig. 9.24b, summed across all vessel groups). As discussed above, pier 56 accounted for more than 45% of the total risk to the bridge, and the next highest contributors were piers 39 and 58, each contributing less than 15%. This outcome differs substantially from the assessment using the 1991 AASHTO provisions, in which four piers near the navigation channel (piers 45 – 48) accounted for 75% of total risk (recall Fig. 9.23a). However, using the 2009 provisions, piers 45 – 48 had $PC = 0$, and therefore did not contribute to vessel collision risk at all.

Fig. 9.25b shows the percent contribution to AF for each vessel group (i.e., the contributions shown in Fig. 9.24b, summed across all piers). As with the 1991 AASHTO assessment, risk was concentrated in vessel groups 6 and 8. However, these vessel groups were the only contributors to AF in the 2009 AASHTO assessment.



a) By pier number



b) By vessel group

Figure 9.25 Percent contribution to AF: AASHTO (2009) methods

Summing AF among all piers and vessel groups, AF predicted by AASHTO (2009) methods was $6.85 \times 10^{-7} \text{ yr}^{-1}$, which corresponds to a return period $1/AF = 1,460,000$ years. Therefore, based on the 2009 provisions, the SR-300 Bridge is at no practical risk of collapsing due to vessel collision. As noted above, this outcome occurred because the only piers that had nonzero values for PC were those located very far from the navigation channel. Such piers had small PG values, because they were located at the tails of the probability distribution for vessel position relative to the channel. Also, nonzero PC values were very small for these distant piers, because vessel transit velocities (and thus, impact energies) decreased as the distance from the navigation channel increased (as required by AASHTO). Lastly, PF values were smallest for the distant piers because of the relatively large degree of protection afforded by navigational obstructions (island to the north and fishing pier to the south). Therefore, considering all these factors, AF was found to be nearly zero.

These results highlight how sensitive the AASHTO PC expression can be to changes in analysis assumptions. For this example case, vessel impact load magnitudes predicted by the 2009 equations were, on average, 17% smaller than those predicted by the 1991 equations. However, AF was found to be 72 times smaller, as a result. Indeed, if bridge pier capacities (H) are uniformly assumed to be 17% smaller to account for the reduction in loads, then the return period ($1/AF$) goes from 1,460,000 years to 37,400 years, a change of 39 times.

Such sensitivity is caused by the AASHTO PC equation allowing PC to be equal to zero if pier capacity (as estimated by engineering analysis) is greater than *or equal to* the estimated

impact load. Given the significant uncertainties associated with estimating both loads and capacities and statistical variability of material and soil strengths, as well as other factors, assigning a failure probability equal to zero cannot be reasonably justified. If one were to assume, for example, that when pier capacity exceeds the computed load, a 1 in 1,000 chance of collapse still exists, the return period for the SR-300 Bridge goes from 1,460,000 years to 31,700 years.

9.8.2 UF/FDOT methods

The following sections present risk analysis results (*PC* and *AF*) that were computed using UF/FDOT methods. The revised methods include a new *PC* expression, revised barge impact load prediction equations, and three structural analysis procedures (CVIA, AVIL, and SBIA). Recall that because these new UF/FDOT methods were primarily developed for barge impact, risk measures associated with ship vessel groups (9 – 11) were taken from the AASHTO procedures (discussed in the prior section). Note that since *PC* and *AF* for all *ships* (i.e., vessel groups 9 – 11; recall Table 9.3) were equal to 0.0 (zero), these vessel groups had no influence on the final results.

9.8.2.1 CVIA

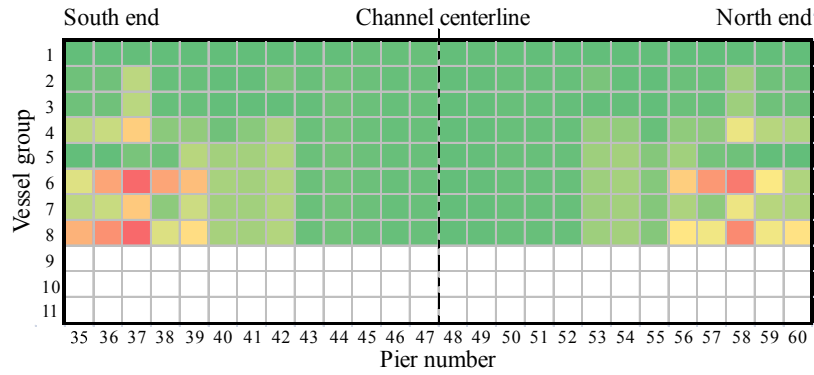
Estimates of *PC* computed using UF/FDOT methods were never equal to zero. This is because the minimum value that the *PC* equation (Eqn. 9.13) can take is 2.33×10^{-6} , when $D/C = 0$. Furthermore, by definition, $D/C = 1$ when the load carrying capacity of the pier has been reached or exceeded, at which point $PC = 1$. In the context of a CVIA dynamic structural analysis, such a condition typically results in the analysis failing to converge due to numerical (and structural) instability.

Estimates of *PC*, as obtained by UF/FDOT methods with CVIA structural analysis, are presented qualitatively for every pier and vessel group in Fig. 9.26a. Note that the color definitions are the same as stated in the previous section. As shown, *PC* values were highest for piers located away from the channel. Specifically, pier 38 had the largest *PC* values, being equal to 1.0 for vessel groups 6 and 8. Pier 58 (symmetrically opposite to pier 38) had the next largest *PC* values (equal to 0.93 and 0.88 for vessel groups 6 and 8, respectively). These piers had the highest *PC* because they were located at expansion joints in the superstructure. Therefore, superstructure resistance was a smaller component of the overall pier resistance (relative to surrounding piers), and this resulted in a higher *PC* estimates. This result also highlights the importance of including an accurate representation of superstructure resistance in vessel collision analyses. *PC* values were generally relatively small (0.001 – 0.02) for piers near the channel.

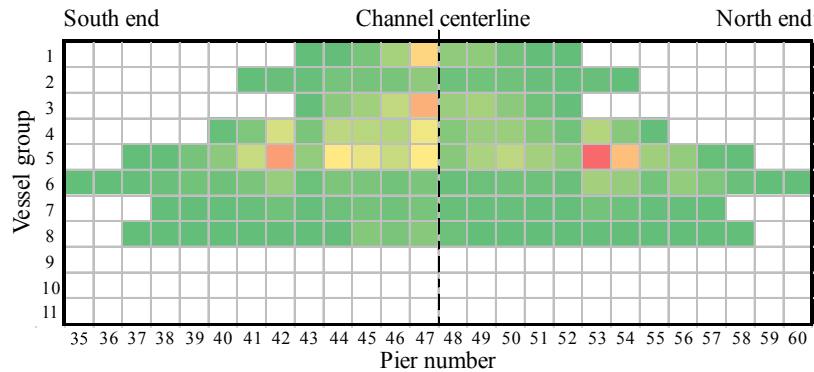
Considering other factors that contribute to overall risk (*N*, *PA*, *PG*, *PF*), relative contributions to *AF* are shown in 9.26b. Note that some piers did not contribute to *AF* for certain vessel groups (as defined by white coloring) because these piers fell outside the $6 \times LOA$ impact zone for the corresponding vessel groups. The largest *AF* contributions came from piers 42 and 53 for vessel group 5. This outcome is somewhat unexpected, as vessel group 5 refers to a flotilla

of empty barges (one of the lighter design vessels). However, because the barge force-deformation curve is elastic, perfectly plastic using UF/FDOT methods, the same peak impact force was generated for vessel group 5 as for much larger flotillas (only the impact duration was different). Consequently, *PC* values for vessel group 5 are approximately the same as vessel group 8 (the most massive design vessel). The higher level of risk associated with vessel group 5 then comes from the fact that vessel draft is only 2 ft. Therefore, it is likely to pass unimpeded through shallow water to the east of the pier. Thus, *PF* values associated with vessel group 5 were much higher (i.e., less protection) than for the larger downbound vessel groups (6 – 8), resulting in higher risk to the bridge. As discussed above, risk was highest for piers 42 and 53 because they were also located at expansion joints in the superstructure.

Fig. 9.27a shows the percent contribution to *AF* for each pier in the bridge (i.e., the contributions shown in Fig. 9.26b, summed across all vessel groups). As noted previously, piers 42 and 53 each contributed approximately 10% to *AF*. However, pier 47 (located adjacent to the navigation channel) was the largest single contributor to *AF*, because it was at moderate to high relative risk for many vessel groups. Comparing these results to the AASHTO (1991) procedures (9.23a), it is observed that risk is somewhat more evenly distributed among the piers when using the UF/FDOT procedures with CVIA. Using AASHTO procedures, approximately 75% of risk was concentrated in piers 45 – 48. However, using UF/FDOT procedures with CVIA, the proportion associated with piers 45 – 48 was only 39%.



a) Probability of collapse (PC) (white = 0, green \approx 0.0, red = 1.0)



b) Contribution to annual frequency of collapse (AF)

(colors are relative to maximum contribution among all piers and vessel groups)

Figure 9.26 Risk analysis results for each pier and vessel group: UF/FDOT methods, CVIA

Fig. 9.27b shows the percent contribution to AF for each vessel group (i.e., the contributions shown in Fig. 9.26b, summed across all piers). As shown, the largest contribution to AF (more than 40%) came from vessel group 5. As discussed above, this occurred because PF was higher for vessel group 5 than for some of the larger vessel groups, on account of its smaller draft. This result was completely different than the corresponding results from the AASHTO (1991) procedure (Fig. 9.23b), in that the AASHTO procedure predicted that vessel groups 6 and 8 dominated AF . This discrepancy is a consequence of the AASHTO impact load model and the AASHTO PC expression. The AASHTO equations predict larger and larger impact forces with increasing impact energy. Using the AASHTO load model, impact forces associated with vessel group 5 were small enough such that the AASHTO PC was equal to zero for almost all piers (recall Fig. 9.22a), whereas higher impact energy associated with vessel groups 6 and 8 resulted in nonzero PC values for most piers. Therefore, the disparity in AASHTO PC values between vessel group 5 and vessel groups 6 and 8 overcame the significant risk reduction taken for groups 6 and 8 to account for vessel grounding. In other words, AF predicted by AASHTO methods was primarily controlled by the magnitude of impact forces, while AF predicted by the UF/FDOT methods was controlled primarily by the probability of impacts occurring.

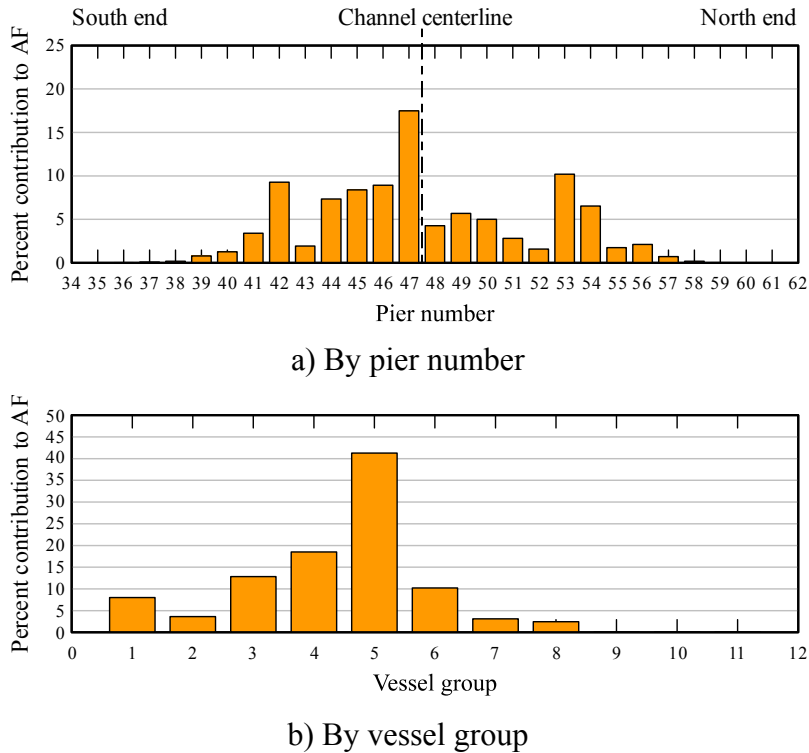


Figure 9.27 Percent contribution to AF : UF/FDOT methods, CVIA

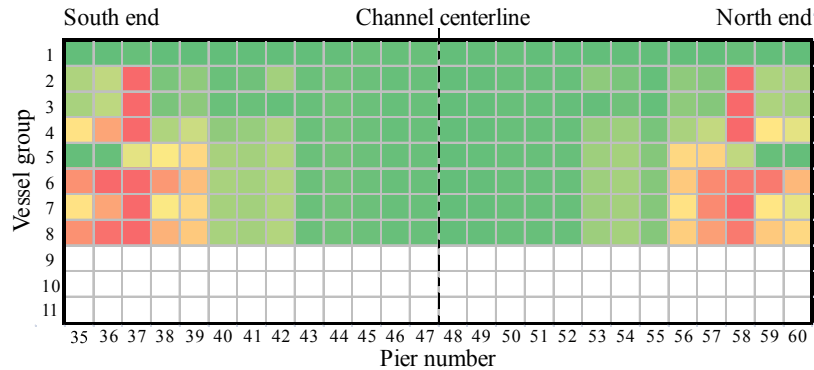
Summing AF among all piers and vessel groups, AF predicted by UF/FDOT methods (with CVIA) was $6.90 \times 10^{-4} \text{ yr}^{-1}$, which corresponds to a return period $1/AF = 1,448$ years. Consequently, the bridge was not found to be sufficiently robust to resist vessel collision, based on the AASHTO-specified minimum return period $1/AF = 10,000$ years for critical/essential bridges. Suggestions for mitigating collision risk using the UF/FDOT methods are provided later in Section 9.10. As with the AASHTO procedures, AF was found to be sensitive to assumptions made in the risk assessment. For example, if the possibility for vessel grounding is neglected, the return period drops to $1/AF = 1,285$ years. However, this difference (12.6%) is significantly smaller than the analogous difference observed using the AASHTO procedures (172%), indicating that the UF/FDOT results were much less sensitive to that particular assumption. The specific reasons why UF/FDOT methods predicted a higher level of risk than the AASHTO procedures ($1/AF = 20,150$ years) are discussed in detail in Section 9.9.

9.8.2.2 AVIL

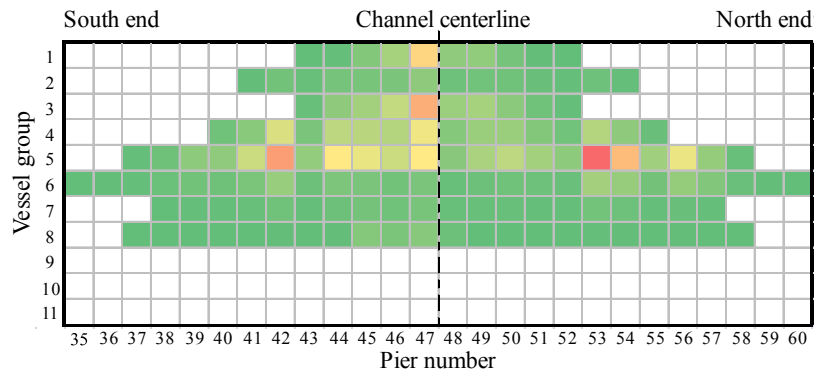
Estimates of PC , as obtained by UF/FDOT methods with AVIL structural analysis, are presented qualitatively for every pier and vessel group in Fig. 9.28a. As with CVIA, PC values were highest for piers 37 and 58, as a result of these piers being located at expansion joints. However, PC was equal or nearly equal to 1.0 for a larger number of vessel groups. This outcome was expected because the AVIL method (as employed in this study) was intended to be conservative relative to CVIA. Indeed, on average, PC values were 63% higher for AVIL than for CVIA. Note however, that D/C values predicted by AVIL were only 5.5% higher than CVIA.

Therefore, the 63% difference in PC was largely a consequence of the highly nonlinear (exponential) nature of the UF/FDOT PC expression.

Considering other factors that contribute to overall risk (N , PA , PG , PF), relative contributions to AF are shown in 9.28b. As with CVIA, the largest contributors to AF were piers 42 and 53 for vessel group 5. Reasons for this finding were discussed in the prior section. Indeed no notable differences in the distribution of risk were observed between AVIL and CVIA.



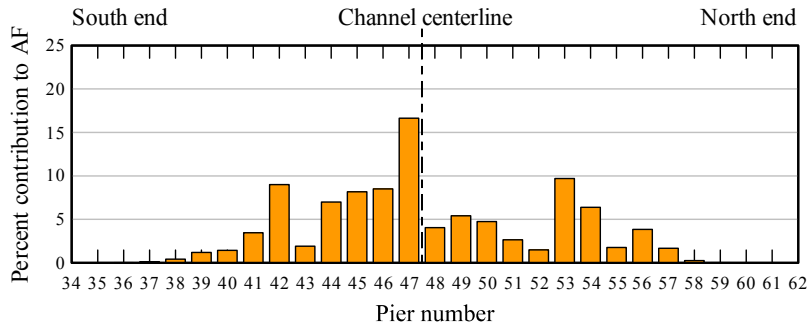
a) Probability of collapse (PC) (white = 0, green \approx 0.0, red = 1.0)



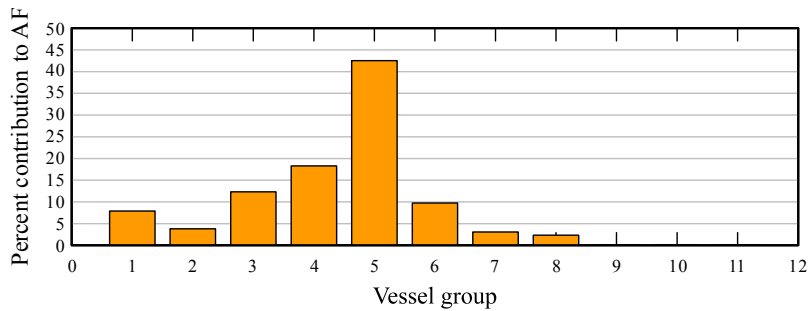
b) Contribution to annual frequency of collapse (AF)
(colors are relative to maximum contribution among all piers and vessel groups)

Figure 9.28 Risk analysis results for each pier and vessel group: UF/FDOT methods, AVIL

Fig. 9.29a shows the percent contribution to AF for each pier in the bridge (i.e., the contributions shown in Fig. 9.28b, summed across all vessel groups), and Fig. 9.29b shows the percent contribution to AF for each vessel group (i.e., the contributions shown in Fig. 9.28b, summed across all piers). The distribution of AF among the various piers and vessel groups was effectively identical to CVIA, with the largest contributions to AF coming from piers 42, 47, and 53, and, among all piers, vessel group 5.



a) By pier number



b) By vessel group

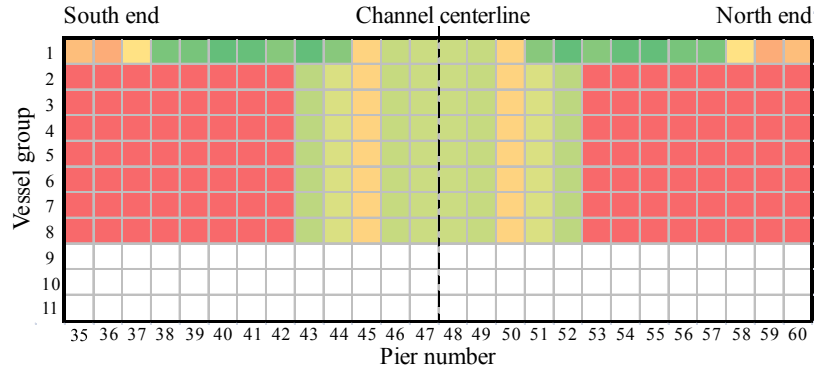
Figure 9.29 Percent contribution to *AF*: UF/FDOT methods, AVIL

Summing *AF* among all piers and vessel groups, *AF* predicted by UF/FDOT methods (with AVIL) was $6.90 \times 10^{-4} \text{ yr}^{-1}$, which corresponds to a return period $1/AF = 1,365$ years. Compared to CVIA ($1/AF = 1,448$ years), the outcome is surprisingly close (6.1% different), given that *PC* estimates were on average 65% higher for AVIL. It was observed that AVIL was most conservative relative to CVIA for impact cases that had a low or sometimes zero probability of occurrence (zero probability occurred because $PG = 0$ for piers located outside the $3 \times LOA$ impact zone). Furthermore, most of these cases were low-energy impacts that contributed little to the overall collision risk. Therefore, while *PC* values predicted by AVIL and CVIA differed by a large degree for these cases, their influence on *AF* was relatively small.

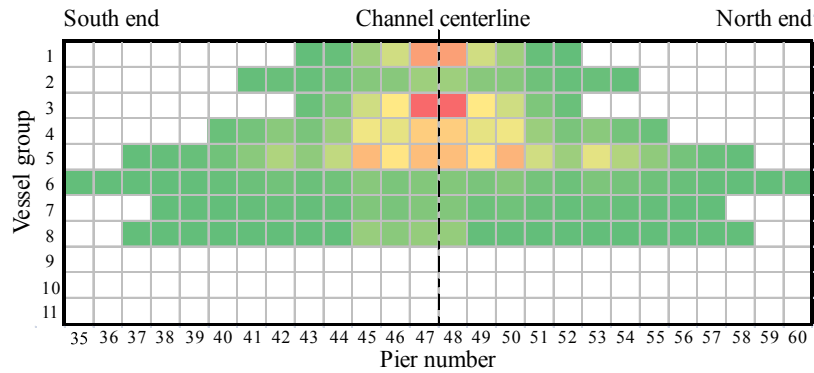
9.8.2.3 SBIA

Estimates of *PC*, as obtained by UF/FDOT methods with SBIA structural analysis, are presented qualitatively for every pier and vessel group in Fig. 9.30a. As shown, *PC* was equal to 1.0 for a large number of cases. Even for cases in which $PC < 1.0$, values are significantly higher than CVIA. Indeed, *PC* values predicted by SBIA were, in some cases, several hundred times higher than those predicted by CVIA. On average, with respect to *PC*, SBIA was 520% conservative relative to CVIA. However, with respect to *D/C*, SBIA was only 29% conservative. Again, this highlights how the exponential functional form of the UF/FDOT *PC* expression amplifies differences between analysis results.

Considering other factors that contribute to overall risk (N , PA , PG , PF), relative contributions to AF are shown in Fig. 9.30b. The distribution of risk predicted by SBIA was largely dissimilar from CVIA or AVIL. Vessel group 5 still provided a significant contribution to AF , but risk was not concentrated in piers 42 and 53, as it was with CVIA and AVIL. Indeed, the most significant risk came from piers 47 and 48 (vessel group 3), cases which were less prominent for CVIA and AVIL.



a) Probability of collapse (PC) (white = 0, green \approx 0.0, red = 1.0)



b) Contribution to annual frequency of collapse (AF)

(colors are relative to maximum contribution among all piers and vessel groups)

Figure 9.30 Risk analysis results for each pier and vessel group: UF/FDOT methods, SBIA

Fig. 9.31a shows the percent contribution to AF for each pier in the bridge (i.e., the contributions shown in Fig. 9.30b, summed across all vessel groups), and Fig. 9.31b shows the percent contribution to AF for each vessel group (i.e., the contributions shown in Fig. 9.30b, summed across all piers). As noted above, piers 47 and 48 were the most significant contributors to AF . Risk was somewhat more evenly distributed among vessel groups for SBIA, as compared to CVIA and AVIL.

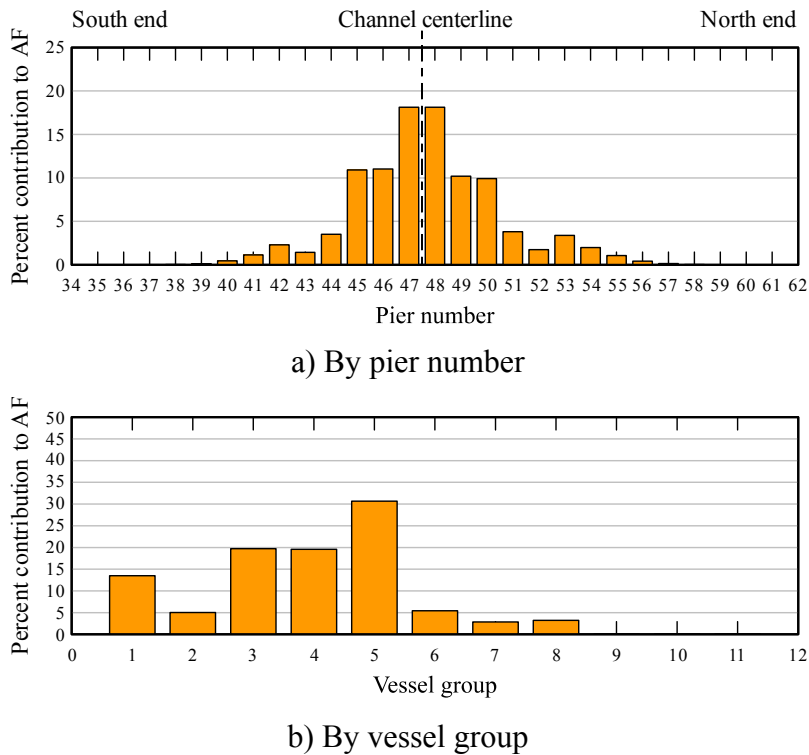


Figure 9.31 Percent contribution to AF : UF/FDOT methods, SBIA

Summing AF among all piers and vessel groups, AF predicted by UF/FDOT methods (with SBIA) was $1.14 \times 10^{-2} \text{ yr}^{-1}$, which corresponds to a return period $1/AF = 88$ years. Clearly, the SBIA method was unreasonably conservative relative to CVIA and AVIL, at least with regard to its use in the risk assessment. As discussed above, SBIA was only 29% conservative (relative to CVIA) with regards to pier structural demands (as reflected by D/C). However, a 29% increase in D/C resulted in an order of magnitude difference in PC . It is important to note that, in the development of SBIA, the method was found to predict pier demands that were, on average, 40 – 45% conservative relative to CVIA. Therefore, the level of conservatism in PC estimates could be more severe for other bridges than it was for this example. Given these results, it can be concluded that SBIA is not well suited for risk analysis. The SBIA method is more appropriately employed in analyses at the preliminary design stage, to aid in proportioning structural members. However, once proportioned, the vessel collision risk assessment should be completed with one of the dynamic analysis options (CVIA or AVIL).

9.9 Discussion of Results

Table 9.11 summarizes risk assessment results for the SR-300 Bridge, as determined by each analysis procedure that was considered in this study. As shown, impact loads computed using UF/FDOT methods were approximately 25% higher than those determined using the AASHTO (1991) procedure, while the maximum AASHTO load was 50% higher than UF/FDOT. The UF/FDOT barge force-deformation model is elastic, perfectly plastic, while the AASHTO model assumes an increase in load with increasing impact energy. Thus, at lower

impact energies, the UF/FDOT methods generally predicted loads higher than AASHTO, but at higher energies, the AASHTO loads were larger than the UF/FDOT loads.

Table 9.11 Summary of risk assessment results for each analysis procedure considered

	AASHTO (1991)	AASHTO (2009)	UF/FDOT (CVIA)	UF/FDOT (AVIL)	UF/FDOT (SBIA)
Minimum impact load (kip)	198	198	198	198	198
Average impact load (kip)	1,642	1,200	2,004	2,086	2,086
Maximum impact load (kip)	4,682	3,240	3,148	3,148	3,148
Average P/H or D/C	0.305	0.286	0.737	0.778	0.952
Average PC	0.00671	0.00122	0.136	0.222	0.702
Return period ($1/AF$) (yr)	20,150	1,460,000	1,448	1,365	88

In Table 9.11, AASHTO capacity-demand ratios (H/P) (used to compute PC) are inverted to be demand-capacity ratios (P/H) to facilitate comparison to D/C ratios computed by UF/FDOT methods. As shown, average D/C for the most accurate UF/FDOT method (CVIA) was approximately 2.4 times higher than P/H for the AASHTO (1991) method. This difference is primarily a consequence of higher UF/FDOT load magnitudes. However, dynamic amplification effects also contributed to this difference. Dynamic structural response was considered by the UF/FDOT methods, while AASHTO methods neglected inertial effects.

Average PC values obtained by UF/FDOT methods (CVIA) were 20 times higher than those obtained from AASHTO (1991). This is primarily a consequence of larger demand on the piers (caused by the larger UF/FDOT loads). However, another reason for the discrepancy is the difference between the PC expressions. As discussed in the prior section, PC was equal to zero for the majority of impact cases considered in the AASHTO risk assessment. In contrast, the UF/FDOT PC expression (by intentional design) cannot return a PC equal to zero. Consequently PC was greater than zero for every barge impact case considered in the UF/FDOT assessments. It should also be noted that PC values obtained using the UF/FDOT methods properly account for numerous statistical uncertainties associated with impact loading, structural capacity, and soil capacity, and are therefore a more rational estimate of collapse risk than the AASHTO PC values.

As shown in Table 9.11, AASHTO (1991) methods resulted in a return period for bridge collapse $1/AF = 20,150$ years, satisfying the acceptable risk criterion ($1/AF \geq 10,000$ years) for this critical bridge. This outcome is expected, given that the bridge was designed in accordance with the 1991 AASHTO provisions. However, the barge impact load model was modified slightly in the 2009 AASHTO provisions (i.e., elimination of the barge width modification factor), resulting in a significant reduction in load magnitude for most impact conditions. Accounting for this change, the return period increased dramatically to 1,460,000 years.

Return periods predicted by UF/FDOT methods imply that the bridge does not satisfy the level of acceptable risk. Indeed, AF predicted by the CVIA risk assessment was 14 times higher than the AASHTO (1991) method. This discrepancy is a consequence of the difference in PC

values predicted by each method, as discussed above. Predictions of AF were similar between CVIA and AVIL structural analysis, with AVIL being about 6% conservative. This suggests that AVIL is an adequate replacement for CVIA if appropriate analysis tools are not available to conduct CVIA. However, the return period predicted using SBIA structural analysis was only 88 years, indicating that the SBIA procedure is too conservative to be reasonably implemented in the context of risk assessment. Therefore, SBIA is better suited for preliminary analyses that are conducted for the purpose of roughly proportioning structural members. Once proportioned, the bridge should be evaluated for vessel collision risk using dynamic structural analysis methods (CVIA or AVIL).

Given that the SR-300 Bridge did not satisfy the acceptable risk level using UF/FDOT methods, it is important to consider whether the bridge could be economically retrofitted to improve its performance and thereby mitigate vessel collision risk within the context of the UF/FDOT assessment methodology. A possible retrofit solution is proposed in the following section (Section 9.10) that takes advantage of the fact that the UF/FDOT impact load model predicts significantly smaller forces if impacted pier surfaces are rounded rather than flat-faced. For demonstration purposes, an alternative pier design that would further mitigate risk is also discussed in Section 9.10.

The retrofit and alternative design examples presented in Section 9.10 are viable means of satisfying the required risk criteria if the UF/FDOT methodology were employed exactly as discussed in this chapter. However, results from the assessment of a different bridge considered in this study (see Chapter 9) suggest that the other terms in the expression for AF (specifically the PA and PG terms) may over-predict the likelihood that impacts will occur. Because these terms were adopted into the UF/FDOT methods directly from AASHTO, the value of AF computed using UF/FDOT methods may be unrealistically high. If this were the case, alternative designs or retrofits may not be necessary at all; this possibility is discussed further in Section 9.11.

9.10 Suggestions for Mitigating Risk

The primary reason that UF/FDOT methods predicted a higher risk level than AASHTO methods was the relative magnitude of impact loads. As discussed in Section 9.7.5.2.1, the barge force-deformation curve that is used as the basis for UF/FDOT predictions of impact force is elastic, perfectly plastic with yield deformation (a_{BY}) equal to 2 in. and yield force (P_{BY}) computed based on the Getter and Consolazio (2011) model. For a flat-faced impact surface, such as the pier footings of the SR-300 Bridge, P_{BY} is computed as:

$$P_{BY} = 1400 + \left(130 - \frac{68}{1 + e^{3.8 - 0.31 \cdot \theta}} \right) \cdot \min(B_B, B_P) \quad (9.18)$$

For the SR-300 Bridge, footings (pile caps) are either 28.0 ft or 18.5 ft wide. Given an impact angle $\theta = 28.5^\circ$, P_{BY} equals 3,148 kip for 28.0 ft wide footings and 2,555 kip for 18.5 ft wide footings. As demonstrated by the risk assessment, the barge bow yielded for most impact conditions, and thus, the maximum impact force was generally equal to P_{BY} .

However, the Getter-Consolazio force-deformation model states that, for rounded impact surfaces, P_{BY} is computed as:

$$P_{BY} = 1400 + 30 \cdot \min(B_B, B_P) \quad (9.19)$$

Therefore, if the SR-300 pier footings were the same size, but were rounded instead of flat-faced on the leading edge, P_{BY} would only equal 2,240 kip for 28.0 ft wide footings and 1,955 kip for 18.5 ft wide footings (a 29% and 23% reduction, respectively).

Choosing to round off the ends of footings would likely have little influence on construction cost, but could improve impact performance significantly. To evaluate this possibility, a risk assessment was conducted using UF/FDOT methods (CVIA) in which the SR-300 footings were assumed to be the same overall size, but the ends were rounded instead of flat (detailed analysis results are omitted here for brevity). Bridge structural demands were significantly reduced relative to the as-built condition, and the return period ($1/AF$) went from 1,448 years to 16,370 years. Consequently, the SR-300 Bridge was found to satisfy the level of acceptable risk using UF/FDOT methods if footings were round instead of flat. If deemed necessary by the bridge owner, footings could be readily be retrofitted with rounded caps made of reinforced concrete, as illustrated in Fig. 9.32. If the foundation does not have sufficient capacity to carry the additional concrete weight (262 kip and 600 kip for the 18.5 ft and 28.0 ft caps, respectively), a more lightweight design (steel or composite) with the same dimensions could be employed. This example illustrates that the UF/FDOT methods do not always predict significantly higher risk than the AASHTO procedures. Indeed, with the retrofit, AF is only 19% higher than predicted by AASHTO (1991).

An additional alternative design (illustrated in Fig. 9.33) could further mitigate collapse risk. In this alternative, piers could be supported by two large-diameter (9 ft, for example) drilled shafts (collinear with the pier columns), rather than with multiple driven piles. Consequently there is no longer a need for a large-footprint pile cap. Instead, a relatively narrow strut or shear wall could be provided between the shafts, as shown in Fig. 9.33. If two 9 ft diameter shafts were found to provide similar lateral capacity to the existing design, then vessel collision risk could be reduced, because the maximum barge impact force that could be developed (P_{BY}) is only 1,670 kip (see Eqn. 9.19) given that the impacted portion of the bridge is now only 9 ft. in diameter. The load of 1,670 kip corresponds to a 15 – 25% reduction in impact forces relative to the end cap retrofitted design shown above, and a 35 – 47% reduction relative to the as-built design. Clearly, given that the existing SR-300 Bridge was constructed in 2004 in accordance with the appropriate AASHTO provision, it is not proposed that the structure be replaced with an

alternative design. However, the alternatives described here demonstrate how careful design choices can mitigate vessel collision risk within the context of UF/FDOT risk assessment methodology.

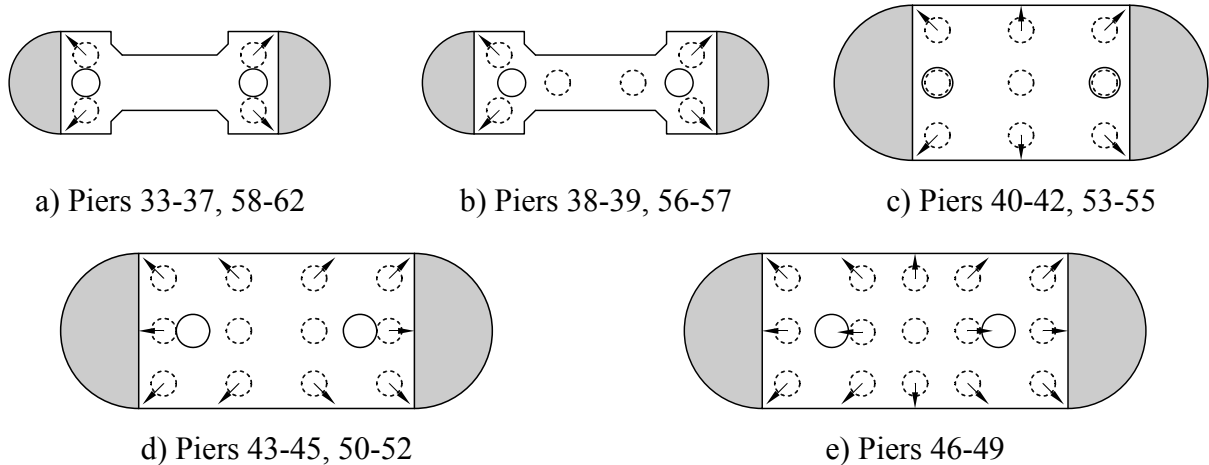


Figure 9.32 SR-300 Bridge pier footing end cap retrofit to reduce vessel collision risk (retrofitted end caps indicated in grey)

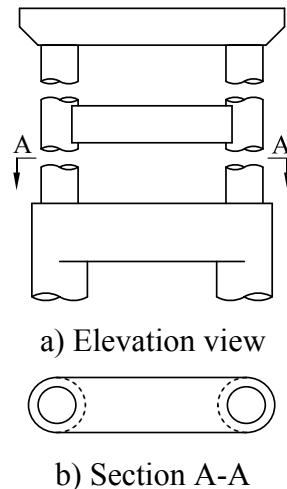


Figure 9.33 SR-300 Bridge pier alternative design with foundation consisting of (2) 9-ft diameter drilled shafts, connected by a strut or shear wall

9.11 Concluding Remarks

It is worth noting that no bridge that has been designed and constructed in accordance with the AASHTO vessel collision guidelines has collapsed due to vessel collision. However, the historical record (approximately 20 years) is short relative to the target return period for such events (1,000 – 10,000 years). Indeed, a bridge that was designed with the highest acceptable risk ($1/AF = 1,000$ years) has only a 2% chance of impact-induced collapse within its first 20 years of service. Therefore, the accuracy of the AASHTO procedure is difficult to assess.

As discussed above, the discrepancy between the AASHTO and UF/FDOT methods is entirely limited to PC . However, it is valuable to consider whether the other terms in the AF expression (N , PA , PG , PF) are historically accurate. Detailed records concerning the volume of commercial vessel traffic are readily available, thus N can be considered the most reliable value in the risk assessment. The accuracy of PA , PG , and PF are difficult to evaluate independently, but their combined result can be compared to available data. Specifically, if PC is removed from the expression for AF , the resulting probability is the annual frequency of impact (AFI):

$$AFI = \sum_{i=1}^{N_{VG}} \sum_{j=1}^{N_P} (N_i)(PA_i)(PG_{ij})(PF_{ij}) \quad (9.20)$$

Based on this definition, AFI represents the number of direct vessel collisions with the bridge piers that are expected to occur in a given year. For the SR-300 Bridge, $AFI = 0.0287$ impacts/yr (i.e., approximately one impact every 35 years). Given that the bridge has only been in service for nine years at present, according to the AASHTO-based AFI , there is only a 23% likelihood that the bridge would have been impacted to date.

The U.S. Coast Guard keeps detailed records on vessel casualties, which include (among other things) accidental impacts with bridges. These records are publicly available from an online database called the Coast Guard Maritime Information Exchange (CGMIX) (USCG 2013). A thorough review of the database—which includes complete records for the past 11 years and partial records for older incidents—uncovered no documented impact incidents involving either the current SR-300 Bridge or the older bridge that it replaced. This finding is reasonably consistent with the AASHTO-based estimate of AFI , which predicts a relatively low likelihood of a major impact occurring within the period considered. Therefore, for the SR-300 Bridge, is unclear whether the terms included within AFI are indeed accurate.

For the SR-300 Bridge, it can only be concluded that the AASHTO-predicted AFI is either accurate or it over-predicts the likelihood of impact events. Given the volume of vessel traffic in this particular waterway, the historical record is simply not long enough to draw a clear conclusion. Note however, that the AASHTO procedure almost certainly over-predicts AFI for the other case considered in this study (see Chapter 10). Additional research that is outside the scope of the current study would be required to determine conclusively whether the terms included in AFI should be modified in some way.

CHAPTER 10

VESSEL COLLISION RISK ASSESSMENT OF THE LOUISIANA HIGHWAY 1 (LA-1) BRIDGE OVER BAYOU LAFOURCHE, LOUISIANA

10.1 Introduction

In this chapter, detailed vessel collision risk assessments are presented for the Louisiana Highway 1 (LA-1) Bridge over Bayou Lafourche, Louisiana. The annual frequency of bridge collapse (AF) was quantified using the revised methodology described in Chapter 8, employing two dynamic structural analysis techniques (CVIA and AVIL). For comparison, AF was also computed using both the current AASHTO provisions (2009) and the AASHTO guidelines that were available at the time the bridge was designed (1991). Significant differences in AF were observed using the various methods. The final sections in this chapter identify the causes for such differences and provide suggestions for mitigating vessel collision risk within the context of the revised methodology.

The LA-1 Bridge was selected for this study for three primary reasons: 1) it was designed fairly recently (2003 – 2005), and is therefore designed to resist vessel collision in accordance with the AASHTO provisions, and 2) it is at relatively high risk for vessel collision, and 3) a vessel collision risk assessment was published for this bridge as an illustrative example in the 2009 AASHTO Guide Specification. The published example includes exhaustive discussion of all analysis assumptions and includes all the data required to reproduce the AASHTO risk assessment for the present study. In order to complete dynamic structural analyses of the LA-1 Bridge piers, the Louisiana Department of Transportation and Development (LaDOTD) graciously provided detailed structural drawings of the relevant bridge sections, soil boring logs, and a detailed scour report. These documents were crucial to the development of the risk assessments discussed in this chapter.

Throughout this chapter, numerous references are made to “AASHTO provisions” or “AASHTO specifications.” These refer to the *AASHTO Guide Specifications and Commentary for Vessel Collision Design of Highway Bridges*. The specific edition (1991 or 2009) is referred to as needed, and if no date reference is given, it should be assumed to refer to the 2009 edition. Also, many references are made to the “AASHTO example.” These refer to the example risk assessment of the LA-1 Bridge that is published in the 2009 AASHTO Guide Specification. Lastly, numerous references are made to “UF/FDOT methods/procedures.” These refer to a large body of work, comprising multiple publications, and in general, refer to the modified risk assessment procedure outlined in Chapter 8. References to specific publications are provided where needed.

Note that the format of this chapter is identical to Chapter 9, which described vessel collision risk assessments of a different bridge that were completed using the same methods discussed here. Consequently, many areas of discussion in this chapter are similar or identical to those in Chapter 9. Rather than referring back to Chapter 9 in such cases, pertinent discussions are repeated in this chapter, accounting for any bridge-specific modifications. While this approach introduces a level of redundancy into the discussion, it also permits this chapter to

serve as a standalone example of the various methods employed. However, in the interest of brevity, at times, references are made to the example risk assessment of the LA-1 Bridge published in the AASHTO Guide Specification, in lieu of repeating identical detailed discussions here.

10.2 Data Collection

The critical first step in conducting a vessel collision risk assessment is gathering the relevant site data, including waterway, bridge, and vessel traffic characteristics. As part of the bridge design effort, an exhaustive data collection effort was undertaken by the design engineers, the results of which are published in AASHTO (2009). The published data set was utilized in full in the risk assessment presented in this chapter. As noted above, structural and soil details that were required to develop finite element models of the relevant bridge piers and carry out structural analyses were taken from structural drawings and soil reports provided by LaDOTD.

10.3 Waterway Characteristics

10.3.1 General description

The LA-1 Bridge spans a navigable waterway (Bayou Lafourche) near Leeville, Louisiana. As shown in Fig. 10.1, the waterway runs approximately north-south, passing under the main fixed span of the LA-1 Bridge. The portion of the bridge at risk for vessel collision is highlighted in red in Fig. 10.1. The waterway serves a considerable volume of vessel traffic, including fishing and shrimp boats, crew and supply vessels, and barges of various kinds. Most vessels that pass under the LA-1 Bridge are transiting between the Gulf of Mexico (11 miles south of the bridge), and various inland communities and ports along the bayou. Furthermore, Bayou Lafourche intersects the Gulf Intracoastal Waterway (GIWW) approximately 23 miles upstream of the bridge, near the town of Larose. Thus, the bayou acts as a link between the Gulf of Mexico and the GIWW. See the AASHTO example (§1.2.1) for additional details.

10.3.2 Navigation channel

As shown in Fig. 10.2, the navigation channel passes under the center bridge span at a 70° angle relative to the bridge alignment. Horizontal clearance of 280 ft and vertical clearance of 76 ft are provided through this passage. Water depths along the navigation channel range from 3 – 12 ft, with larger depths available near the southern end of the bayou (near the LA-1 Bridge). See the AASHTO example (§1.2.2) for additional details.

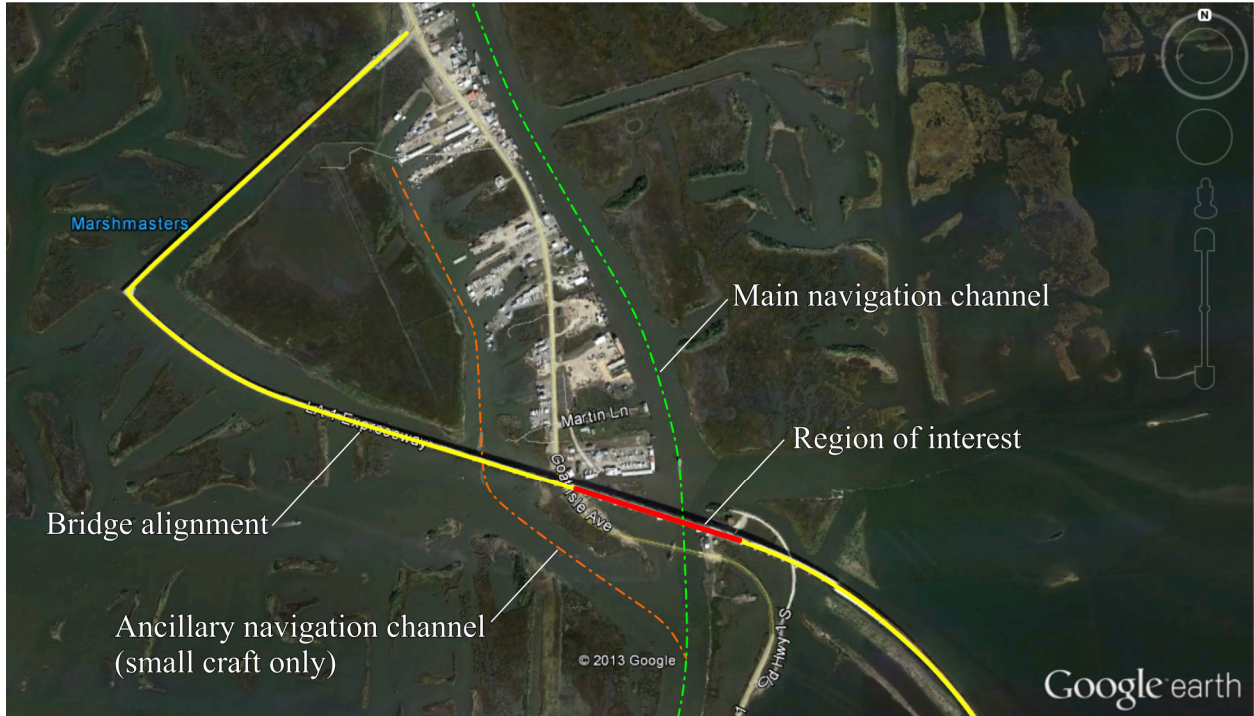


Figure 10.1 Louisiana Highway 1 (LA-1) Bridge over Bayou Lafourche, Louisiana

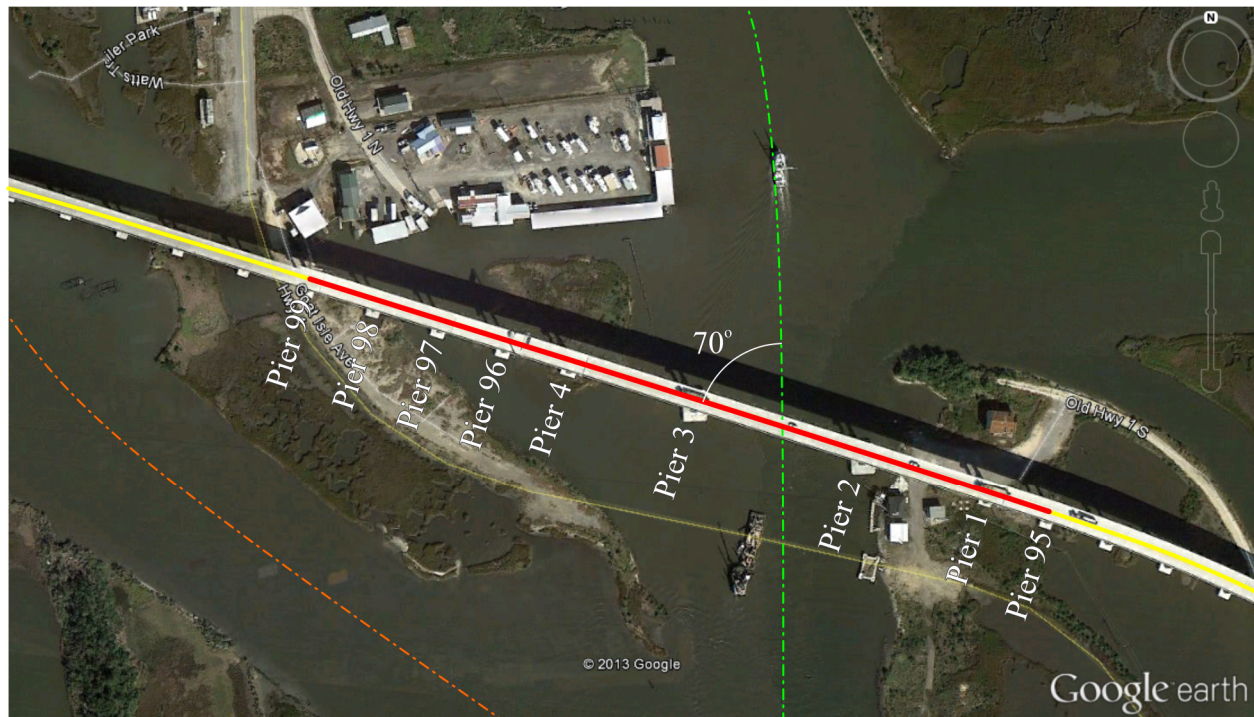


Figure 10.2 LA-1 Bridge region of interest, showing navigation channel alignment

10.3.3 Tide levels and tidal range

The LA-1 Bridge is subject to tidal variations in water level, by virtue of its vicinity to the Gulf of Mexico. The bayou has a tidal range between 1.0 and 1.8 ft, depending on the season. For the purpose of the risk assessment, MHW (elevation of 2.5 ft) was taken as the reference water level for all calculations. See the AASHTO example (§1.2.3) for additional details.

10.3.4 Currents

Currents in the vicinity of the LA-1 Bridge are primarily driven by tidal fluctuations. For the risk assessment, the current velocity parallel to the channel was taken to be 1.0 knot. The Southwestern Louisiana Canal—connecting Barataria Bay to the east and Terrebonne Bay to the west—crosses Bayou Lafourche at the LA-1 Bridge site. Differential tidal fluctuations between the two bays causes significant currents through the canal, resulting in strong crosscurrents at the bridge location. For the risk assessment, the crosscurrent velocity taken to be 2.5 knots. See the AASHTO example (§1.2.4) for additional details.

10.3.5 Water depths

Sufficient water depth is available for any vessel transiting the Bayou Lafourche to strike the two piers located immediately adjacent to the channel (piers 2 and 3). However, smaller depths are available at piers located away from the channel. The possibility for vessel grounding due to insufficient water depth was considered in the risk assessment. See the AASHTO example (§1.2.5) for additional details.

10.4 Bridge Characteristics

As constructed, the overall LA-1 Bridge consists of a short section of low-rise causeway to the north west of the waterway crossing (shown in Fig. 10.1), a high-rise section crossing the bayou, and another low-rise causeway section extending several miles south to Port Fourchon. Future plans include extending the northern causeway section several miles north to Golden Meadow. As indicated above, the bridge section of interest in this study is the high-rise section that crosses the Bayou Lafourche (shown schematically in Fig. 10.3). In the AASHTO example, the design team identified five piers as being at risk for impact by powered vessels: piers 2 – 4 and 96 – 97. All other piers were found to be fully protected by land masses in the vicinity, and were assigned zero risk by the designers. Therefore, the risk assessment presented in this chapter neglects such protected piers, even though they were considered in the AASHTO example, as appropriate for a new bridge. In order to adequately analyze these piers for vessel collision, finite element models of two additional piers on each end of the central impact region (piers 1, 95, and 98 – 99) were also prepared.

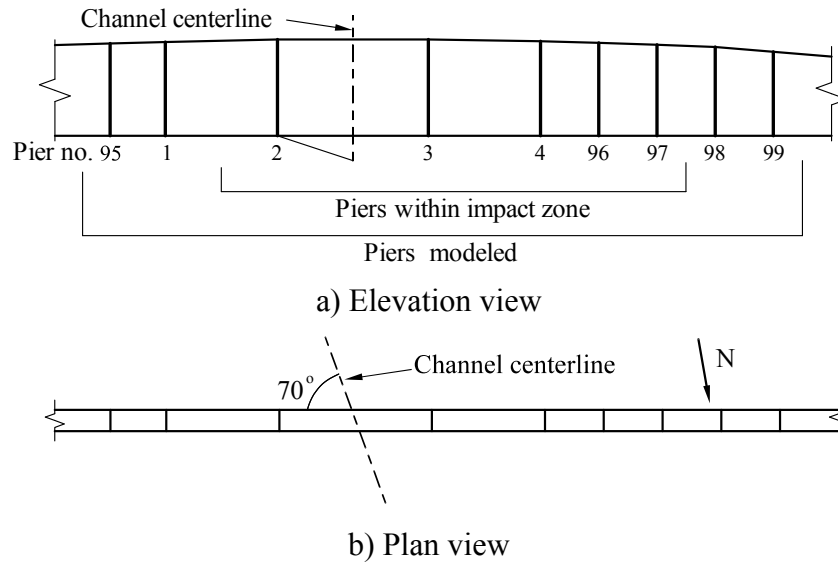


Figure 10.3 High-rise portion of LA-1 Bridge, showing piers at risk for impact

In the AASHTO example, the authors present a risk assessment of only one of the many bridge design alternatives: *Concrete Girder Alternative—Option A3*. However, the alternative that was ultimately constructed was *Steel Girder Alternative—Option D2*. This option included a superstructure consisting of four steel plate girders for the main spans, and piers supported by 30-in. square prestressed concrete piles. Comparing these two alternatives, it was found that differences in the designs had negligible influence on the various calculations included in the AASHTO risk assessment. Therefore, supporting data for the risk assessment published in the AASHTO example was simply adopted in this study as being valid for the design alternative that was considered.

The intent of this study was to evaluate the LA-1 Bridge as constructed (*Steel Girder Alternative—Option D2*). However, as described in more detail in the following sections, the footings of the two channel piers (piers 2 and 3) are skewed at 20° relative to the pier columns and bridge alignment, so that they are instead aligned with the navigation channel. In doing so, vessel impacts were most likely to occur in the direction of highest lateral foundation capacity, and horizontal clearance under the main span was improved. However, all structural analyses conducted in this study employed FB-MultiPier, which does not currently include features allowing foundations to be skewed relative to the pier columns. More specifically, in FB-MultiPier, the primary axes of the pile elements cannot be skewed relative to the primary axes of the pier columns. Because design *Option D2* employs square piles, this limitation in FB-MultiPier could not be overcome.

However, an alternative design (*Steel Girder Alternative—Option D1*) employs 54-in. diameter cylinder piles. Because such piles are circular, and therefore possess equal flexural stiffness and strength about all possible flexural axes, the orientation of the primary element axes is irrelevant. It was therefore possible to analyze *Option D1* in FB-MultiPier, by carefully defining the pile grid geometry and batter parameters in order to correctly define the relative

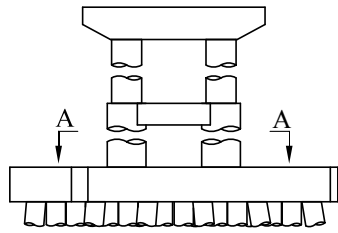
position and axial orientation of the pile elements. Consequently, the risk assessment presented in this chapter corresponds to *Steel Girder Alternative—Option D1*. Given that lateral foundation capacities are, by design, nearly equal between *Option D1* and *Option D2* (the latter being the design that was actually constructed), calculated measures of vessel collision risk are expected to be similar.

10.4.1 Bridge piers

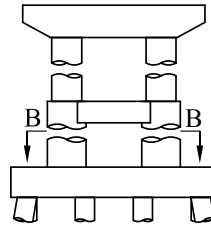
Bridge pier configurations for the LA-1 Bridge piers of interest are shown in Fig. 10.4. Piers consist of two 6 – 9 ft diameter circular columns supporting a 6.0 – 7.5 ft deep pier cap beam. A strut is provided between the columns at the approximate mid-height. As discussed above, piers 1 – 4 are founded on 54-in. diameter cylinder piles (corresponding to *Option D1*), while piers 95 – 99 are founded on 30-in. square piles. Many piles are battered at an inclination of 1.5 in. horizontal per 12 in. vertical, as indicated by arrows in Fig. 10.4. Footings (pile caps) are 6 – 8 ft thick and are positioned such that the top surfaces are approximately 4 – 5.5 ft above MHW. The largest footing (Fig. 10.4c) is 48×66.5 ft in plan, and the smallest footing (Fig. 10.4h) is 25×46 ft.

Based on these pier configurations, barges and most small ships are expected to impact pier footings (pile caps) rather than columns, though some column impacts are possible. Consider the two impact scenarios shown in Fig. 10.5. A fully loaded barge will draft 6 – 12 ft, with the most common draft being approximately 9 ft (Fig. 10.5a). In this scenario, the barge headlog impacts the pier at an elevation below the top of the pier footing. However, an empty barge (Fig. 10.5b) drafts only approximately 2 ft, and the headlog elevation is above the top of the footing. Depending on the barge bow and pier geometry, the impacting barge may make contact with the footing first. However, the barge may slide up and over the footing edge, or given sufficient energy, simply crush into the top footing corner, ultimately striking a pier column.

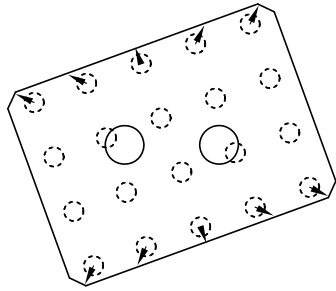
Impact scenarios like the one shown in Fig. 10.5b are certainly of interest for design, in that all impacted pier components must be proportioned to resist impact loading. However, numerous factors—e.g., footing overhang distance, barge bow rake angle, vessel draft, water level, and impact angle—all influence the relative probability of a column impact occurring. Given the inherent variability of such factors, assessing the probability of column impact is difficult. Thus, for the purpose of the risk assessment, columns were assumed to have sufficient capacity to transmit impact loads to the footing. As such, impact forces were applied at the footing elevation in all impact analyses. For final design, it would be appropriate to choose the most severe column impact scenario possible and proportion (or support) the columns such that they can resist the loads imparted. A supporting strut or shear wall between the columns is commonly employed for this purpose.



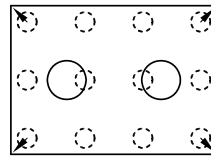
a) Piers 2 – 3



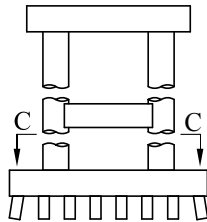
b) Piers 1, 4



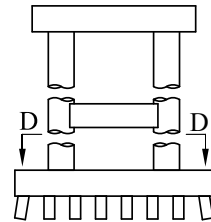
c) Section A-A



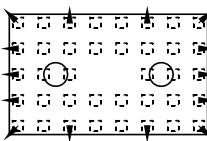
d) Section B-B



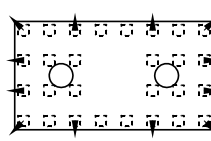
e) Piers 96 – 97



f) Piers 95, 98 – 99



g) Section C-C



h) Section D-D

Figure 10.4 Pier and foundation configurations for LA-1 Bridge

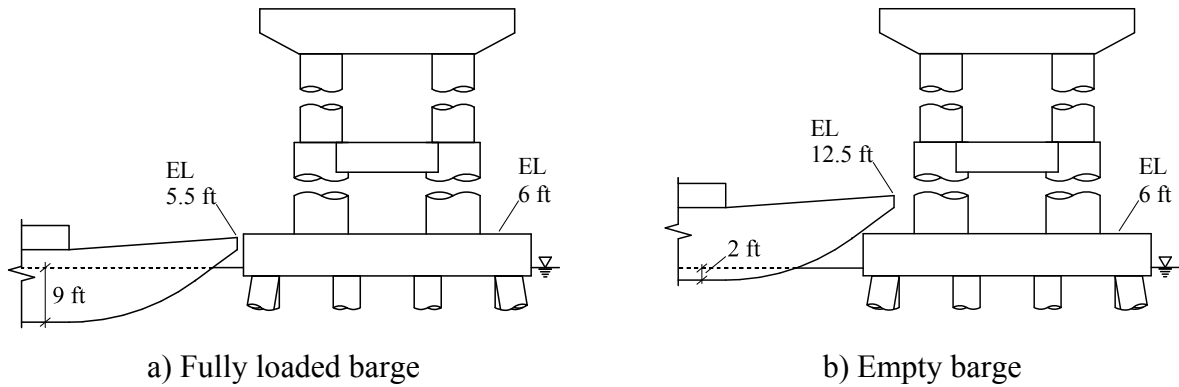


Figure 10.5 Typical barge impact scenarios, showing possible headlog elevations

10.4.2 Superstructure

As shown in Fig. 10.6, the region of interest of the LA-1 Bridge consists of three superstructure zones. Spans between piers 95 – 1 and between piers 4 – 99 are 128 – 135 ft long, and are supported by five (5) 78-in prestressed concrete Bulb-T girders. Spans were cast contiguously with a R/C diaphragm at each pier. Expansion joints were provided between every other span. The central three spans (between piers 1 – 4) are 260 – 350 ft long, and are supported by four (4) 117-in. deep steel plate girders.

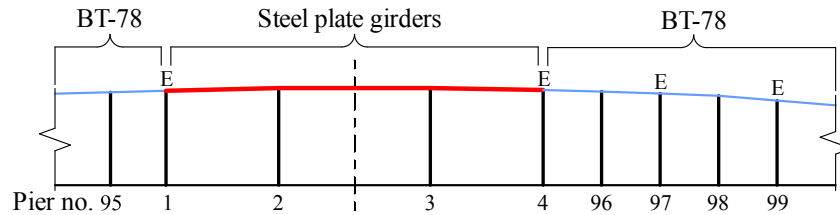


Figure 10.6 Overview of bridge span configurations ('E' indicates locations of expansion joints)

Typical superstructure cross-sections are shown in Fig. 10.7. The roadway slab is 42.5 ft wide, and 8.5 – 9 in. thick (depending on the span), with standard concrete barriers on each side. As discussed above, five (5) evenly spaced Bulb-T girders support the roadway on the approach spans (Fig. 10.7a), and four (4) steel plate girders support central spans (Fig. 10.7b).

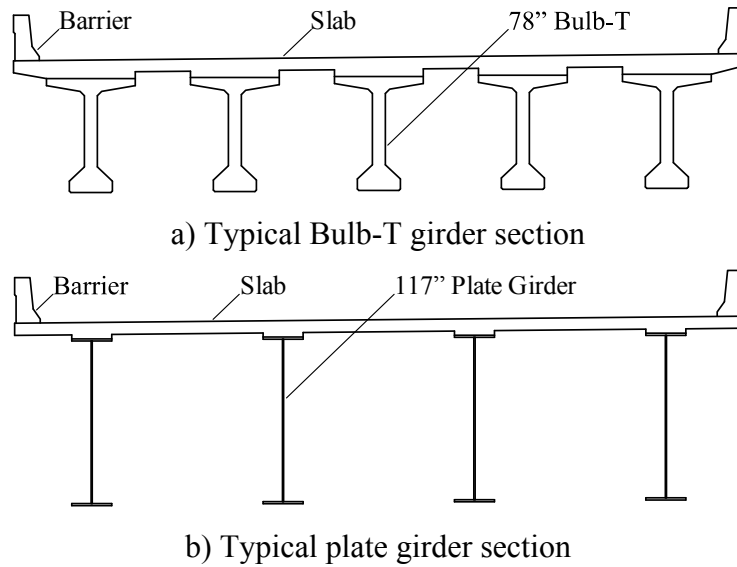


Figure 10.7 Superstructure cross-sections for the LA-1 Bridge

In this bridge, concrete girders are supported on neoprene bearing pads. At each concrete girder bearing location, (4) 1.25-in. diameter anchor bolts provide lateral continuity between the girders and pier cap beam, permitting impact-induced shear force to be carried across the substructure-superstructure interface. Steel girders are supported on pot bearings, which are bolted into the pier cap beam with four (4) 2.5-in. diameter anchor bolts and welded to the steel girders. Such bearings are also rated to carry impact-induced shear forces across the substructure-superstructure interface. Consequently, when a pier is impacted, demand on the foundation is mitigated by permitting a portion of the lateral load to be shed through the superstructure and ultimately to adjacent piers. This action is important to consider when analyzing the piers for vessel impact, so these connections were included in finite element models of the piers and superstructure.

10.4.3 Soil conditions

In general, soil conditions at the site consist primarily of layers sandy clay or silty clay, interspersed with thinner layers of silty sand or clayey sand. Sand density and clay consistency generally increased with increasing depth. Pile embedment depths varied for each pier, and were obtained from estimates provided in the design drawings. For the purpose of developing finite element models of each pier, soil properties were determined from SPT boring logs taken prior to bridge construction. As shown in Fig. 10.8, eight boring logs were available in the vicinity of the piers of interest. Soil layer profiles were developed from these boring logs and assigned to each pier finite element model, as shown in Fig. 10.8. Finite element soil spring characteristics were developed using well-established equations that relate various important soil properties (e.g., internal friction angle, subgrade modulus) to the overburden-adjusted SPT blowcount. The specific methodology that was employed is omitted here for brevity, but has been documented in numerous prior publications (Consolazio et al. 2008, 2010a, 2010b). Additional information is also available in the user's manuals for FB-MultiPier and FB-Deep (BSI 2009, 2010).

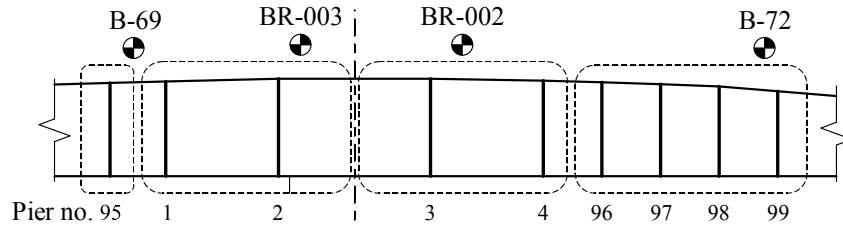


Figure 10.8 Locations of soil borings and piers to which each soil profile is assigned

10.4.4 Finite element models

Renderings of finite element models of selected piers (developed in FB-MultiPier) are shown in Fig. 10.9. Each pier shown is a representative example of the four pier configurations shown in Fig. 10.4. Note that because FB-MultiPier is unable to model skew between the pier columns and foundation, skewed footing geometry for piers 2 and 3 was approximated with a rectangular grid of shell elements that were oriented in the global (pier column) coordinate system, as shown in Fig. 10.9a. The ragged looking edge of the footing is a consequence of this approximation. Given the significant rigidity of the pile cap, the irregularity of the mesh has no notable influence on pier behavior. As noted previously, proper pile positioning and axial alignment was achieved by careful selection of pile grid spacing and batter parameters.

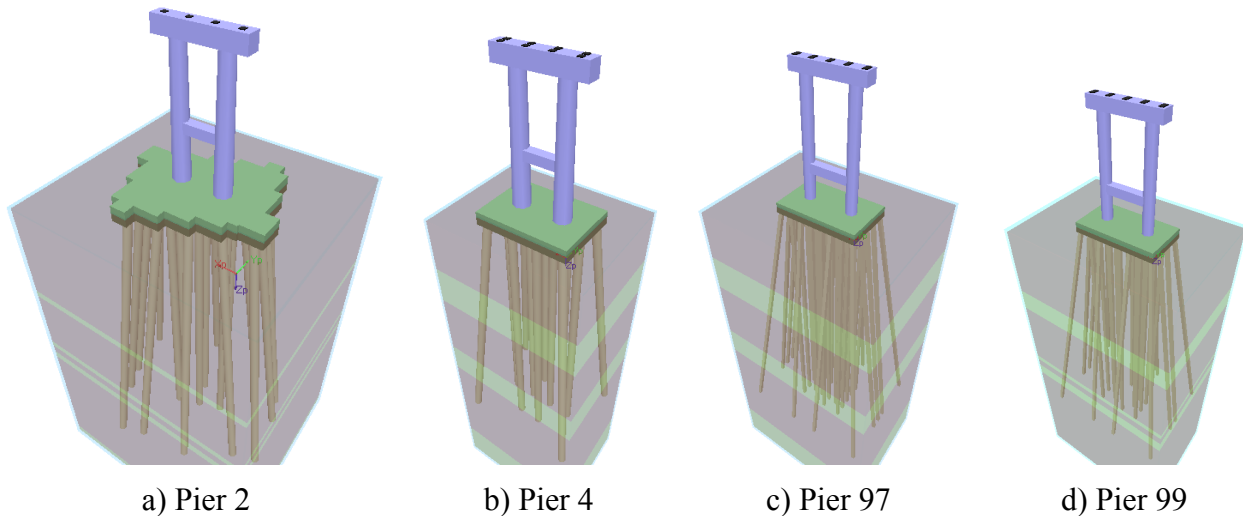


Figure 10.9 FB-MultiPier models of selected piers from LA-1 Bridge

As discussed in Chapter 2, FB-MultiPier models piles, pier columns, struts, and pier caps with cross-section integrated nonlinear beam elements that account for cracking, material plasticity, and plastic hinging behaviors. Soil is modeled in FB-MultiPier with nonlinear spring elements that are distributed down the embedded pile length, footings (pile caps) are modeled with linear-elastic shell elements, and the superstructure is modeled as a composite (girder/slab) unit with linear-elastic resultant beam elements that are connected to pier caps at discrete bearing locations. One-pier, two-span (OPTS) models of all piers within the impact zone (2 – 4, 96 – 97) were developed in accordance with the procedure discussed in Chapter 2 (Consolazio and

Davidson, 2008), and these models were employed for all structural impact analyses discussed in this chapter.

10.5 Vessel Fleet Characteristics

Vessel traffic data for this study were obtained from the AASHTO example (§1.4).

10.5.1 Vessel categories

Vessel traffic through Bayou Lafourche is fairly heavy. In 2003, on average, 13 barge vessels and 40 ships passed beneath the LA-1 Bridge per day. Ship traffic consists of supply vessels and crew boats headed to and from offshore oil facilities in the Gulf of Mexico and shrimp trawlers of various sizes. Barge traffic is a mix of hopper, tanker, and deck barges. In the AASHTO example, the authors organized vessel traffic by similar vessels into 17 categories, each with its own vessel ID number, as shown in Table 10.1. Traffic was further subdivided by transit direction (upbound or downbound), and load condition (lightly or fully loaded). Considering the subdivisions, 68 total impact scenarios are possible for each pier. Given that five piers are at risk for impact, $5 \times 68 = 340$ total impact cases are possible. See the AASHTO example (§1.4.1) for additional details.

To reduce the number of impact cases for this study, all ship vessel groups were omitted from the vessel fleet. Due to draft limitations, ship-type traffic on Bayou Lafourche excludes large cargo or tanker vessels that may pose a significant threat to the bridge. Indeed, it was noted in reviewing the AASHTO example that ship-type vessels did not contribute to vessel collision risk at all. Therefore, the vessel groups considered in this study include only the barge categories identified in the AASHTO example (vessel ID 1 – 8 in Table 10.1). The eight categories were separated into vessel groups corresponding to the subdivisions defined in the AASHTO example, as shown in Table 10.2. Vessel groups 1 – 8 correspond to fully loaded upbound traffic, vessel groups 9 – 16 correspond to lightly loaded upbound traffic, vessel groups 17 – 24 correspond to fully loaded downbound traffic, and vessel groups 25 – 32 correspond to lightly loaded downbound traffic.

Table 10.1 Vessel traffic for LA-1 Bridge

Vessel ID	Vessel type	Description	Average single vessel size (ft)			Single vessel capacity (tons)	Average barge tow size		Tug size (ft)			Length LOA (ft)	Beam (ft)	Total displacement (tons)	
			L	W	D ¹		# W	# L	L	W	D			Loaded	Light
1	Barge	Barge tow	264	50	9/2	3,153	1	1	72	30	7	336	50	4,012	860
2	Barge	Barge tow	210	44	9/2	2,194	1	1	72	30	7	282	44	2,899	705
3	Barge	Barge tow	195	35	9/2	1,631	1	1	65	24	6	260	35	2,105	474
4	Barge	Barge tow	160	42	8/2	1,400	1	1	65	24	6	225	42	1,874	474
5	Barge	Barge tow	150	30	8/2	779	1	2	50	20	5	350	30	2,189	631
6	Barge	Deck barge	140	40	5/2	408	1	1	50	20	5	190	40	904	496
7	Barge	Barge tow	140	35	7/2	860	1	1	50	20	5	190	35	1,168	309
8	Barge	Deck barge	120	30	4/2	154	1	1	50	20	5	170	30	518	364
9	Ship	Supply vessel	185	42	11/5	1,020	N/A	N/A	N/A	N/A	N/A	185	42	1,870	850
10	Ship	Supply vessel	165	36	9/4	650	N/A	N/A	N/A	N/A	N/A	165	36	1,168	518
11	Ship	Supply vessel	145	36	8/4	456	N/A	N/A	N/A	N/A	N/A	145	36	913	456
12	Ship	Crew boat	125	24	9/4	331	N/A	N/A	N/A	N/A	N/A	125	24	594	263
13	Ship	Utility boat	100	28	8/4	245	N/A	N/A	N/A	N/A	N/A	100	28	489	245
14	Ship	Shrimp boat	90	28	12/5	386	N/A	N/A	N/A	N/A	N/A	90	28	661	276
15	Ship	Crew boat	65	18	5/2	77	N/A	N/A	N/A	N/A	N/A	65	18	128	51
16	Ship	Shrimp boat	60	18	6/2	95	N/A	N/A	N/A	N/A	N/A	60	18	142	47
17	Ship	Shrimp boat	30	9	4/2	12	N/A	N/A	N/A	N/A	N/A	30	9	24	12

¹ [loaded draft]/[light draft]

Table 10.2 Aggregated barge traffic data for LA-1 Bridge

<i>VG</i> Vessel group	<i>N</i> Transits per year	v_i Velocity (knot)	<i>D</i> Draft (ft)	<i>LOA</i> Length (ft)	B_M Beam (ft)	W_B Displacement (tons)	<i>VG</i> Vessel group	<i>N</i> Transits per year	v_i Velocity (knot)	<i>D</i> Draft (ft)	<i>LOA</i> Length (ft)	B_M Beam (ft)	W_B Displacement (tons)
1	0	4.0	9	336	50	4,012	17	30	5.0	9	336	50	4,012
2	0	4.0	9	282	44	2,899	18	90	5.0	9	282	44	2,899
3	30	4.0	9	260	35	2,105	19	50	5.0	9	260	35	2,105
4	150	4.0	8	225	42	1,874	20	40	5.0	8	225	42	1,874
5	10	4.0	8	350	30	2,189	21	280	5.0	8	350	30	2,189
6	80	4.0	5	190	40	904	22	270	5.0	5	190	40	904
7	200	4.0	7	190	35	1,168	23	70	5.0	7	190	35	1,168
8	50	4.0	4	170	30	518	24	250	5.0	4	170	30	518
9	30	4.0	7 ¹	336	50	860	25	0	5.0	7 ¹	336	50	860
10	90	4.0	7 ¹	282	44	705	26	0	5.0	7 ¹	282	44	705
11	50	4.0	6 ¹	260	35	474	27	30	5.0	6 ¹	260	35	474
12	40	4.0	6 ¹	225	42	474	28	150	5.0	6 ¹	225	42	474
13	280	4.0	5 ¹	350	30	631	29	10	5.0	5 ¹	350	30	631
14	270	4.0	5 ¹	190	40	496	30	80	5.0	5 ¹	190	40	496
15	70	4.0	5 ¹	190	35	309	31	200	5.0	5 ¹	190	35	309
16	250	4.0	5 ¹	170	30	364	32	50	5.0	5 ¹	170	30	364

¹ Draft shown is for the tugboat. Barge draft is 2 ft.

10.5.2 Vessel traffic growth

In the AASHTO example (§1.4.2), vessel traffic volume was expected to grow by 2% per year. Two risk assessments were completed by the bridge designers, one corresponding to current vessel traffic (at the time, 2003), and one corresponding to future traffic (2053). A corresponding vessel traffic growth factor equal to 2.69 was applied to the 2003 data to estimate traffic volume in 2053. Detailed risk analysis results presented in the AASHTO example correspond to the future fleet (2053). Therefore, for this study, the growth factor was adopted, and thus the results correspond to the future (2053) fleet.

10.5.3 Vessel transit speeds

In the AASHTO example (§1.4.3) vessel transit velocities were assumed to be 5.0 knots for downbound traffic, and 4.0 knots for upbound traffic (all vessel types). However, as prescribed by AASHTO, impact velocities are expected to decrease as the distance from the channel increases. The decrease is also a function of overall vessel length (*LOA*). Impact velocities that were computed for every combination of pier and vessel group are provided in Appendix N.

10.5.4 Vessel transit path

The transit paths for both upbound and downbound traffic were taken to coincide with the centerline of the navigation channel (under the middle of the main span), as described in the AASHTO example (§1.4.4).

10.6 Vessel Impact Criteria

In designing a new bridge, AASHTO requires additional criteria that the design must satisfy, aside from the maximum impact load criteria defined by the probabilistic risk assessment. Given that the example presented in this chapter is an assessment of an existing structure, certain criteria were not fully explored. Furthermore, for this study, certain portions of the AASHTO procedure have been replaced with new methods, as discussed in Chapter 8. The following sections describe, in a broad sense, how the overall vessel impact criteria prescribed by AASHTO were assessed in this study.

10.6.1 General requirements

The adequacy of the LA-1 Bridge to resist vessel impact loading was assessed in accordance with the general requirements of the following provisions:

AASHTO (1991). *Guide Specification and Commentary for Vessel Collision Design of Highway Bridges*, American Association of State Highway and Transportation Officials, Washington DC.

AASHTO (2009). *Guide Specification and Commentary for Vessel Collision Design of Highway Bridges*, 2nd Edition, American Association of State Highway and Transportation Officials, Washington DC.

Modifications to the AASHTO-prescribed requirements, including consideration for dynamic bridge response and the influence of pier geometry on impact forces, were made as described in Chapter 8 (referred to as UF/FDOT methods). Such modifications, as they pertain to the LA-1 Bridge risk assessment, are documented in Section 10.7. Note that, because the UF/FDOT procedures reflect the most up-to-date published research, the intent of the analysis was to meet or exceed (generally exceed) the level of engineering rigor required by the AASHTO specifications. Furthermore, while the results presented in this chapter imply that the UF/FDOT procedures predict higher levels of vessel collision risk when compared to AASHTO methods, this outcome is not guaranteed. Indeed, as discussed in Section 10.10, commonly encountered impact scenarios exist for which UF/FDOT procedures may predict a lower vessel collision risk than the current AASHTO procedures.

10.6.2 Extreme event load combinations (scour)

The AASHTO example (§1.5.2) defines two different scour and impact conditions that must be considered in the design of bridge substructures: 1) minimum vessel impact associated with an empty barge that has broken loose from its moorings during a storm event (including high water), and 2) maximum vessel impact associated with an aberrant vessel being driven into the bridge under normal environmental and operating conditions. Corresponding scour levels for each condition were obtained from the bridge design drawings, as determined by hydrological and geotechnical analysis performed when the bridge was designed.

10.6.3 Minimum impact load criteria

The minimum impact condition corresponds to the scenario in which an empty hopper barge (195 × 35 ft) moored in the vicinity of the bridge breaks loose from its moorings during a storm and strikes the bridge. While the minimum impact condition was a critical check on bridge pier performance under extreme environmental conditions, the maximum impact condition was found to control in all cases. Therefore, the minimum impact condition is omitted from further discussion.

10.6.4 Maximum impact load criteria

The maximum impact condition corresponds to the scenario in which a vessel being piloted under normal operating conditions becomes aberrant (by mechanical failure or other means) and impacts the bridge at full speed. Under such conditions, vessel motion is driven under its own power, or in the case of a barge tow, the power of a tug. For this assessment, vessel displacements and impact velocities were assumed to vary as discussed in Section 10.5.1. As suggested in the AASHTO example (§1.5.4), the maximum impact condition was combined with one half the long-term ambient scour level. Note that in accordance with AASHTO procedures,

the maximum impact load conditions can be determined using a simplified, deterministic procedure (Method I), or by conducting a probabilistic risk assessment (Method II). Only the latter analysis procedure was considered in this study.

10.6.5 Operational classification

The LA-1 Bridge was classified by the owner (LaDOTD) under the “critical/essential” operational classification. Consequently, structural collapse as a result of vessel collision should have a return period of at least 10,000 years, as required by the AASHTO provisions. This requirement is significantly more stringent than a normal bridge (return period of 1,000 years or greater). However, the classification reflects the importance of the bridge to the region. Because the LA-1 Bridge is the only roadway heading inland from nearby coastal areas, it constitutes the only hurricane evacuation route to local residents. Furthermore, access to hospitals and other emergency services require that the bridge be operational, even under extreme conditions.

10.7 Maximum Impact Load (Method II) Analysis Methodology

As defined by AASHTO, Method II is a probabilistic risk analysis procedure that is used to quantify the annual frequency (annualized probability) that that a bridge will collapse when subjected to vessel collision loading (denoted AF). In its formulation, Method II attempts to account for all major factors that contribute to vessel collision risk, including but not limited to vessel traffic volume, waterway characteristics, bridge geometry, and bridge element strength. The following sections detail analysis assumptions and the overall methodology that was used to quantify AF for the LA-1 Bridge. Risk assessments were completed both using strict AASHTO methodology (static loading and pushover analysis) and using modified UF/FDOT methodology that incorporates dynamic structural analysis and other state-of-the art procedures from recent research. Risk measures that were computed using each method are compared in Section 10.8.

Structural analyses were carried out using FB-MultiPier (version 4.18), and custom Perl scripts (Perl 2013) were programmed to summarize relevant analysis data. Subsequent risk calculations were completed using Mathcad worksheets.

10.7.1 Annual frequency of collapse (AF)

The annual frequency of collapse (AF) was computed by the following expression:

$$AF = (N)(PA)(PG)(PC)(PF) \quad (10.1)$$

where:

AF = Annual frequency of bridge collapse due to vessel collision,

- N = Annual number of vessel transits, as categorized by vessel type and transit direction,
 PA = Probability of vessel aberrancy,
 PG = Geometric probability of a pier being impacted by an aberrant vessel,
 PC = Probability of bridge element collapse subject to collision, and
 PF = Protection factor to account for land masses or other objects that may block vessels from colliding with the bridge ($PF=0$: bridge element fully protected; $0 < PF < 1$: bridge element partially protected; $PF=1$: bridge element unprotected).

Note that AF was more specifically computed as a summation of all possible combinations of bridge pier and vessel group. Therefore, a more detailed form of Eqn. 10.1 is:

$$AF = \sum_{i=1}^{N_{VG}} \sum_{j=1}^{N_P} (N_i)(PA_i)(PG_{ij})(PC_{ij})(PF_{ij}) \quad (10.2)$$

where, N_{VG} is the number of vessel groups ($N_{VG} = 32$ in this case, as defined in Table 10.2), and N_P is the number of bridge piers within the navigation zone ($N_P = 5$ in this case, piers 2 – 4 and 96 – 97).

10.7.2 Vessel frequency (N)

Vessel frequency (N) refers to the annual number of vessel transits by a particular vessel type and transit direction (as defined by the vessel groups listed in Table 10.2). On any of these transits, the vessel has some finite probability of becoming aberrant and striking a bridge pier. However, in order to collide with a pier, sufficient water depth must be available to accommodate the vessel draft, otherwise the vessel will run aground prior to impacting the pier. Premature vessel groundings caused by insufficient water depth can be accounted for in the risk assessment in two ways: 1) the value of N for relevant piers and vessel groups can be set equal to zero or reduced in some way, or 2) a protection factor (PF) can be assigned to relevant piers and vessel groups. The example risk assessment published in the AASHTO Guide Specification employs the first option (setting $N=0$ for certain vessels to account for groundings), so this approach was adopted for this study. Note that vessel traffic volume shown in Table 10.2 was increased by a factor of 2.69 to account for traffic growth over time. Consequently, all risk results presented in this chapter correspond to the future annualized risk in the year 2053.

10.7.3 Probability of aberrancy (PA)

Probability of aberrancy (PA) refers to the likelihood that a given vessel will stray off course (become aberrant), making collision with a bridge pier possible. Such events can occur due to pilot error, adverse environmental conditions (e.g., dense fog), or mechanical failure (e.g., loss of power). As it is unknown how often and for how long vessels typically veer off course and can be classified as aberrant, accurately quantifying PA can be extremely difficult.

Furthermore, the aberrant condition can often be temporary, and may not occur anywhere in the vicinity of a bridge. Certainly, aberrancy caused by pilot inattentiveness is likely to be reduced in the vicinity of a bridge, given that the pilot is aware of the risk of collision. No comprehensive studies have ever been conducted to quantify *AF* itself. Estimates have been posited by past engineers and researchers, based on analysis of historical vessel accident data (groundings, collisions, rammings), as discussed in the AASHTO Guide Specification. However, by definition, recorded accident data only include incidences of aberrancy that resulted in an accident. Commonly, the course of an aberrant vessel is corrected by the pilot, and an accident is avoided.

Depending on the amount of information available, two possible approaches can be taken to quantify *AF*: 1) gather available accident data for the waterway of interest and make a defensible estimate (prior studies should be consulted for guidance in preparing an estimate), or 2) if accident data are unavailable, use the simplified procedure provided in the AASHTO provisions. As in the AASHTO example (§1.8.1.2) the latter option was employed in this study. Specifically, *PA* was computed as:

$$PA = (BR)(R_B)(R_C)(R_{XC})(R_D) \quad (10.3)$$

where:

- BR* = Base rate of aberrancy (0.6×10^{-4} for ships, and 1.2×10^{-4} for barges),
- R_B* = Correction factor for bridge location (related to waterway alignment),
- R_C* = Correction factor for currents acting parallel to the navigation channel,
- R_{XC}* = Correction factor for currents acting perpendicular to the navigation channel, and
- R_D* = Correction factor for vessel traffic density.

As stated above, $BR = 1.2 \times 10^{-4}$ was used for all vessel groups, given that ship-type vessels were omitted from this study.

The correction factor for bridge location (*R_B*) was computed based on the relative location of the bridge in one of three possible waterway regions (straight, transition to a turn, or within a turn). Due to a turn in the channel, $R_B = 2.11$, as computed in the AASHTO example (§1.8.1.2).

The correction factor for currents acting parallel to the channel (*R_C*) was computed as $R_C = 1 + V_C/10$, where V_C is the current velocity (parallel) in knots. Given a parallel current velocity of 1.0 knots, $R_C = 1.1$, as computed in the AASHTO example (§1.8.1.2).

The correction factor for currents acting perpendicular to the channel (R_{XC}) was computed as $R_{XC} = 1 + V_{XC}$, where V_{XC} is the current velocity (perpendicular) in knots. Given a crosscurrent velocity of 1.5 knots, $R_C = 2.5$, as computed in the AASHTO example (§1.8.1.2).

The correction factor for vessel traffic density (R_D) was selected based on the relative volume of traffic, and the likelihood of vessels overtaking each other near the bridge location. $R_D = 1.3$ was selected, corresponding to medium traffic density, as discussed in the AASHTO example (§1.8.1.2).

Consistent with the AASHTO example (§1.8.1.2), $PA = 9.0 \times 10^{-4}$ was computed for all vessel groups (1 – 32), given that ship-type vessels were omitted from this study.

10.7.4 Geometric probability (PG)

The geometric probability (PG) is the conditional probability that a vessel will collide with a particular bridge pier, given that it has become aberrant. The AASHTO provisions suggest assuming that the vessel position (perpendicular to the intended transit path), is a Gaussian distributed random variable, with mean equal to the channel centerline and standard deviation equal to the overall vessel length (LOA). Therefore, PG for a given pier is equal to the area under the Gaussian distribution bounded by the extents of the pier element width (B_P) and plus the vessel width or beam (B_M), as illustrated in Fig. 10.10.

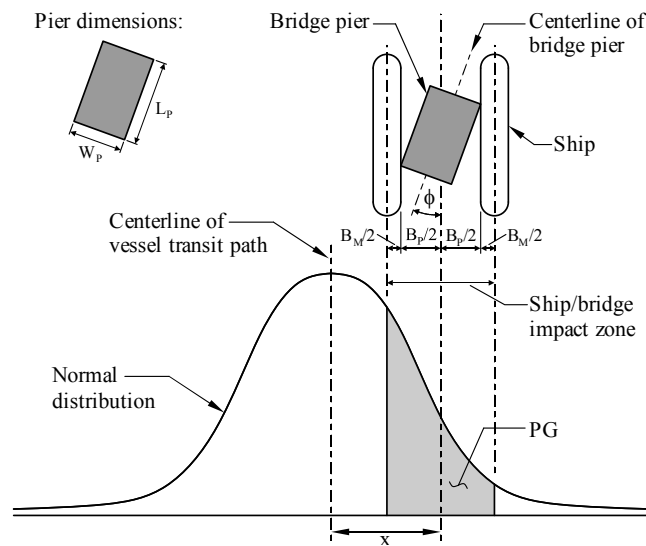


Figure 10.10 Computing the geometric probability of impact (PG) (from AASHTO 2009)

Based on the methodology illustrated in Fig. 10.10, PG values were computed by the design team, as documented in AASHTO example. These values were adopted in this study, and are summarized in Appendix N.

10.7.5 Probability of collapse (PC)

The probability of collapse (PC) refers to the likelihood that a particular bridge element (e.g., a pier) will collapse, given that it has been impacted by a particular vessel. Like any failure probability, PC is a function of both the loading characteristics and the structural capacity. Both the load and resistance are dependent on numerous parameters, each subject to random statistical variability. For example, vessel impact loads are a function of the vessel size, bow shape, impact velocity, direction of impact, vessel mass, and other parameters. Furthermore, the capacity of a pier to resist such impact loads is dependent upon structural configuration, pier member sizes, pier material strengths, and soil strength. To further complicate the process of predicting failure, impact events are dynamic in nature, and involve complex interactions between the impacting vessel and pier. Therefore, many of the load and resistance parameters listed above are correlated. For example, the magnitude and duration of dynamic impact forces (load characteristics), depend strongly upon the nonlinear lateral stiffness of the impacted pier (a resistance characteristic). Consequently, all of the important load and resistance characteristics, their statistical variability, and any possible correlations between them must be carefully considered in order to arrive at a reasonable estimate of PC .

The most accurate means of quantifying PC is through a structural reliability analysis (e.g., Monte Carlo simulation) that directly accounts for the statistical variability of the various load and resistance parameters. However, such an approach may require conducting tens of thousands dynamic structural analyses in order to arrive at a reliable PC estimate for just one pier and impact condition. Such an approach was demonstrated for eight different bridge piers by Davidson et al. (2013). Clearly, direct reliability analysis of this nature is overly burdensome for bridge designers to employ in practice.

As an alternative, PC has historically been computed (for vessel collision) using simplified equations that act as a surrogate for the complicated interactions and statistical variability discussed above. Such equations relate PC to a deterministically computed demand-to-capacity ratio. Structural demand (i.e., impact load magnitude) is computed using simplified equations that include the various parameters discussed above, and structural capacity is computed by structural analysis. Given the deterministically determined demand-capacity (D/C) ratio, PC is computed from a surrogate equation.

Two surrogate equations for PC are available in the published literature: 1) the equation that is included in the AASHTO vessel collision provisions, and 2) an independently derived equation recently developed by Davidson et al. (2013). Note that the AASHTO expression relies on a static treatment of both the impact load and structural capacity (i.e., static pushover analysis), while the Davidson expression employs a time-varying definition for the demand-capacity ratio, and can therefore be employed in conjunction with a dynamic definition of the impact load and structural response by means of transient structural analysis. The relative merits of the two expressions are discussed at length in Davidson et al. (2013) and Consolazio et al. (2010a).

The purpose of this portion of the study was to compare the results of both procedures using the LA-1 Bridge as an example. As described in the following sections, PC values were computed using the AASHTO PC expression, employing AASHTO static load prediction models (from both the 1991 and 2009 specifications) and static pushover analysis of the piers. PC values were also computed using the Davidson PC expression, employing newly developed load prediction models and two new dynamic structural analysis techniques (CVIA and AVIL). Note that the equivalent-static analysis method (SBIA) was not considered in the risk assessment of LA-1 Bridge. This is because it was found to be too conservative for use within the context of the risk assessment when assessing the previous bridge considered in this study (SR-300). As noted previously, SBIA is best suited to preliminary analyses in which pier structural members are approximately sized (proportioned). Once members are so proportioned, risk assessment should be completed using one of the more refined dynamic analysis methods (CVIA or AVIL).

10.7.5.1 AASHTO methods

In accordance with the AASHTO guidelines, PC was computed as:

$$PC = \begin{cases} 0.1 + 9 \cdot [0.1 - (H/P)] & \text{for } 0.0 \leq H/P < 0.1 \\ [1 - (H/P)]/9 & \text{for } 0.1 \leq H/P \leq 1.0 \\ 0 & \text{for } H/P > 1.0 \end{cases} \quad (10.4)$$

where H is the ultimate lateral pier resistance (as determined by static pushover analysis), and P is the vessel impact force (as determined by the equations below). From Eqn. 10.4, the following observations are made:

- For cases in which the lateral pier resistance exceeds the impact force, $PC = 0$.
- For cases in which the pier impact resistance is 10% to 100% of the impact force, PC varies linearly between 0.1 and 1.0. In other words, if the predicted impact force exceeds the pier capacity by *up to 10 times*, then PC varies between 0.1 and 1.0.
- For cases in which the pier impact resistance is below 10% of the impact force, PC varies linearly between 0.0 and 0.1. In other words, if the predicted impact force is *more than 10 times* the pier capacity, then PC varies between 0.0 and 0.1.

Lateral pier capacities (H) that were used to compute PC were taken from the AASHTO example. Note that, as listed in the example, these capacities correspond to the *minimum* lateral capacity of each pier. Actual pushover capacities (determined by structural analysis in FB-MultiPier) were found to be higher than the minimum values. The degree of exceedance

depended on soil conditions assigned to each pier. For consistency with the risk assessment methodology in the AASHTO example, the minimum values of H listed in the Appendix C of the AASHTO example were adopted for the risk assessment (Table 10.3).

Table 10.3 Minimum lateral pushover capacities (H) for each pier

Pier number	H : Minimum lateral pushover capacity (kip)
2	2,446
3	2,446
4	1,661
96	1,097
97	442

10.7.5.1.1 AASHTO (1991) barge impact load model (as designed)

To compute barge impact forces (P_B) in accordance with the 1991 AASHTO provisions, vessel kinetic energy (KE) was first computed as:

$$KE = \frac{C_H W (V)^2}{29.2} \quad (10.5)$$

where, C_H is a hydrodynamic mass coefficient, W is the vessel weight (tonnes), and V is the impact velocity (ft/s). In the given units, KE was calculated in kip-ft. Next, barge bow damage depth (a_B) (i.e., the depth of maximum crushing deformation) was computed as:

$$a_B = \left[\left(1 + \frac{KE}{5672} \right)^{1/2} - 1 \right] \left(\frac{10.2}{R_B} \right) \quad (10.6)$$

where, R_B is the ratio $B_B/35$, where B_B is the barge bow width (ft). In the given units, a_B was calculated in ft. Lastly, barge impact force (P_B) was computed as:

$$P_B = \begin{cases} [4112(a_B)](R_B) & \text{for } a_B < 0.34 \\ [1349 + 110(a_B)](R_B) & \text{for } a_B \geq 0.34 \end{cases} \quad (10.7)$$

In the given units, P_B was computed in kip. Barge impact forces computed using the 1991 AASHTO equations varied between 106 kip and 2,564 kip, depending on barge type and pier distance from the navigation channel (see Appendix N). As described above, the ratio H/P_B was computed for each combination of pier and vessel group. Using Eqn. 10.4, corresponding

estimates of PC were also calculated. Results are discussed in Section 10.8, and detailed results can be found in Appendix N.

10.7.5.1.2 AASHTO (2009) barge impact load model

To compute barge impact forces (P_B) in accordance with the 2009 AASHTO provisions, vessel kinetic energy (KE) was computed as before:

$$KE = \frac{C_H W (V)^2}{29.2} \quad (10.8)$$

In the given units, KE was calculated in kip-ft. The 2009 AASHTO provisions excluded the term R_B from all load equations. Therefore, barge bow damage depth (a_B) was computed as:

$$a_B = \left[\left(1 + \frac{KE}{5672} \right)^{1/2} - 1 \right] \quad (10.9)$$

In the given units, a_B was calculated in ft. Lastly, barge impact force (P_B) was computed as:

$$P_B = \begin{cases} 4112(a_B) & \text{for } a_B < 0.34 \\ 1349 + 110(a_B) & \text{for } a_B \geq 0.34 \end{cases} \quad (10.10)$$

In the given units, P_B was computed in kip. Barge impact forces computed using the 2009 AASHTO equations varied between 106 kip and 1,986 kip, depending on barge type and pier distance from the navigation channel (see Appendix N). As described above, the ratio H/P_B was computed for each combination of pier and vessel group. Using Eqn. 10.4, corresponding estimates of PC were also calculated. Results are discussed in Section 10.8, and detailed results can be found in Appendix N.

10.7.5.2 UF/FDOT methods

In accordance with Davidson et al. (2013), PC was computed as:

$$PC = 2.33 \times 10^{-6} e^{13 \cdot D/C} \leq 1.0 \quad (10.11)$$

where, D/C is the maximum demand-to-capacity ratio from structural analysis. As defined by Davidson, D/C is a rational measure of the proximity of a structure to the formation of a structural mechanism that would result in instability and collapse. The ratio can take on any value from between 0 and 1, such that $D/C = 0$ for a pier under no load, and $D/C = 1$ for a pier which has formed a structural collapse mechanism and is at incipient collapse. It is important to note that D/C is a time-varying dynamic quantity. During a dynamic vessel impact event, D/C begins close to 0 (gravity loading will cause D/C to be nonzero even without impact load applied) and as the pier displaces, D/C increases (up to $D/C = 1$, if the pier collapses).

For this study, D/C was computed as:

$$D/C = \frac{\sum_{i=1}^m \sum_{j=1}^n (D/C)_{ij}^{FBMP}}{m \cdot n} \quad (10.12)$$

where m is the number of members (e.g., piers columns, piles) associated with a given collapse mechanism, n is the number of plastic hinges per member that are necessary to form the corresponding collapse mechanism, and $(D/C)_{ij}^{FBMP}$ is the j th largest element demand-capacity ratio along member i , as reported by FB-MultiPier (internally computed based on biaxial load-moment interaction). See Consolazio et al. (2010a) for a more detailed description of D/C and its theoretical basis.

10.7.5.2.1 CVIA structural analysis

The most accurate (design-oriented) vessel impact analysis method currently available is coupled vessel impact analysis (CVIA). As illustrated in Fig. 10.11, in CVIA, the impacting vessel is idealized as a single-degree-of-freedom (SDF) system, consisting of a concentrated mass that represents the vessel mass, and a nonlinear spring element that represents the crushing characteristics (force-deformation relation) of the vessel bow. The SDF barge model is coupled to a multiple-degree-of-freedom (MDF) finite element model of the impacted pier at a node corresponding to the expected impact location. To begin the analysis, the structure is pre-loaded with gravity and buoyancy forces, and then the vessel mass is prescribed an initial velocity equal to the impact velocity. Impact forces imparted on the pier are computed based on dynamic interaction between the SDF barge and MDF pier models, as would occur during a real impact event.

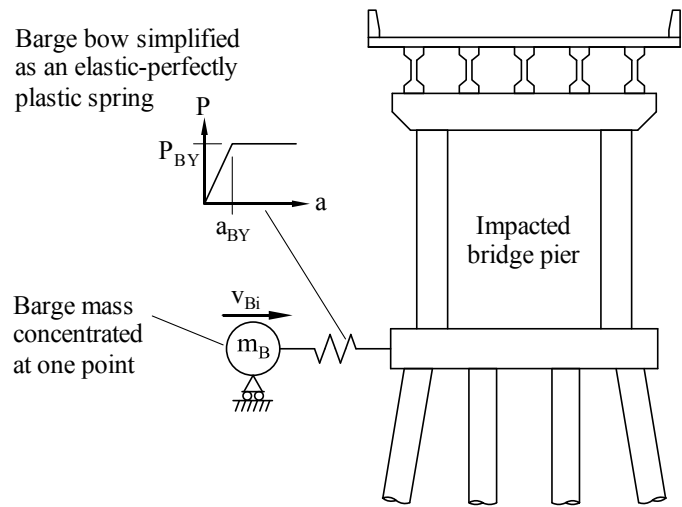


Figure 10.11 Coupled vessel impact analysis (CVIA) method

CVIA has been used extensively in numerous research projects (Consolazio et al. 2008, Davidson et al. 2010, Getter et al. 2011, and Davidson et al. 2013). As implemented in these prior studies, the barge force-deformation relation was assumed to be elastic, perfectly plastic (as shown in Fig. 10.11, using a force-deformation model from Consolazio et al. (2009). This model has since been updated to account for oblique impact scenarios (Getter and Consolazio 2011), like the one shown in Fig. 10.12.

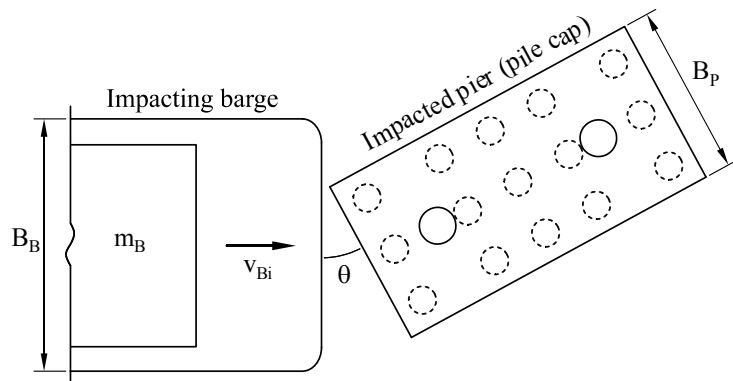


Figure 10.12 Typical barge impact with pile cap, showing pertinent impact parameters

The Getter-Consolazio force-deformation model was employed throughout this study for computing impact forces. Specifically pertaining to CVIA, force-deformation relations for the SDF barge models were taken to be elastic, perfectly plastic, with yield deformation $a_{BY} = 2$ in. Barge yield force (P_{BY}) was computed in accordance with the empirical Getter-Consolazio equations. For oblique impact with a flat-faced pier (the scenario for all piers in the LA-1 Bridge), P_{BY} was computed as:

$$P_{BY} = 1400 + \left(130 - \frac{68}{1 + e^{3.8 - 0.31 \cdot \theta}} \right) \cdot \min(B_B, B_P) \quad (10.13)$$

where θ is the smallest skew angle between the barge bow and pier surface (degrees), B_B is the vessel beam (width) (ft), and B_P is the width of the pier face associated with the smallest skew angle (ft). These quantities are illustrated for a typical impact condition in Fig. 10.12. Given the units shown, P_{BY} was computed in kip. A summary of relevant input data for CVIA simulations is provided in Table 10.4. Impact force-time histories computed by each CVIA simulation that was conducted (160 total) are provided in Appendix N. Finally, D/C values predicted by CVIA, and the associated values of PC are discussed in Section 10.8, and listed in detail in Appendix N.

Table 10.4 Barge impact parameters for CVIA

Pier	θ (deg)	$\min(B_B, B_P)$ (ft)	P_{BY} (kip)	W_B (tons)	v_{Bi} (knot)
2 – 3	0	30.0 – 48.0 ¹	5,255 – 7,569 ¹	308 – 4,012 ²	Varies ³
4	20	30.0 – 34.5 ¹	3,430 – 3,734 ¹	308 – 4,012 ²	Varies ³
96 – 97	20	28.0	3,294	308 – 4,012 ²	Varies ³

¹ Varies by vessel group and pier. See Table Appendix N.

² Varies by vessel group. See Table 10.2.

³ Varies by vessel group and pier. See Table 10.2 and Appendix N for details.

10.7.5.2.2 AVIL structural analysis

The applied vessel impact load (AVIL) method was developed as a slightly simpler alternative to CVIA (Consolazio et al. 2008). The method consists of developing a pre-computed impact force-time history and applying it as a dynamic load in a transient analysis, as shown in Fig. 10.13. It is recognized that many structural analysis packages do not include the features required to conduct CVIA (e.g., the ability to assign initial velocities), but the ability to analyze structures under prescribed time-varying loading is quite common. In such cases, AVIL is an excellent alternative analysis procedure to CVIA.

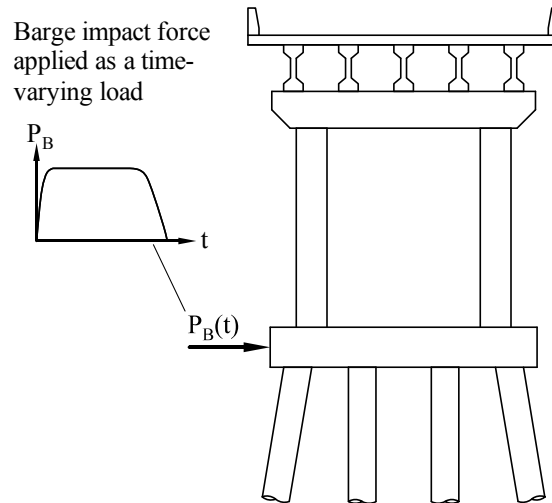


Figure 10.13 Applied vessel impact load (AVIL) method

The AVIL method is summarized in Fig. 10.14. As implemented in this study, barge force-deformation characteristics (a_{BY} and P_{BY}) were established based on the Getter and Consolazio (2011) model, as discussed above for CVIA. Barge mass (m_B) and initial barge velocity (v_{Bi}) were also the same as CVIA (recall Table 10.4). As shown in Fig. 10.15, pier-soil stiffness (k_p) was determined by analyzing each pier finite element model subject to a lateral load (P), measuring the corresponding displacement (Δ), and computing $k_p = P/\Delta$. It is recognized that, due to soil and/or structural nonlinearity, k_p generally becomes smaller as P increases. Because the AVIL method is unable to account for changes in pier resistance during an impact event, a representative k_p must be selected for its formulation. It was observed in conducting this study, that using the *initial* pier stiffness (i.e., k_p corresponding to a very small value of P) resulted in analysis results that were very similar to CVIA and consistently conservative. Values of k_p that were determined for each pier are provided in Table 10.5, and maximum barge impact forces (P_{Bm}) for each pier and vessel group are shown in Table 10.6. Impact force-time histories that were computed for each AVIL analysis are compared to corresponding CVIA force histories in Appendix N. Finally, D/C values predicted by AVIL, and the associated values of PC are discussed in Section 10.8, and listed in detail in Appendix N.

Applied Vessel Impact Load History Method

Select barge type, and determine P_{BY} a_{BY}

Determine impact characteristics: m_B v_{Bi}

Calculate pier-soil stiffness from static analysis: k_p

$$k_S = \left(\frac{a_{BY}}{P_{BY}} + \frac{1}{k_p} \right)^{-1} \quad \text{Calculate barge-pier-soil series stiffness}$$

$$c_{BP} = \sqrt{k_S m_B} \quad \text{Calculate pseudo-damping coefficient}$$

$(v_{Bi} c_{BP} \leq P_{BY})$
Elastic loading

$(v_{Bi} c_{BP} > P_{BY})$
Inelastic loading

$$P_{Bm} = v_{Bi} c_{BP}$$

$$P_{Bm} = P_{BY}$$

$$t_E = \frac{\pi m_B}{P_{Bm}} v_{Bi}$$

$$t_Y = \frac{\pi m_B}{2 P_{BY}} \left(v_{Bi} - \sqrt{v_{Bi}^2 - \left(\frac{P_{BY}}{c_{BP}} \right)^2} \right)$$

$$t_P = \frac{m_B}{P_{BY}} \sqrt{v_{Bi}^2 - \left(\frac{P_{BY}}{c_{BP}} \right)^2} \quad t_U = \frac{\pi m_B}{2 P_{BY}} \frac{P_{BY}}{c_{BP}}$$

$$t_T = \frac{\pi m_B}{2 P_{Bm}} \left(v_{Bi} + \frac{P_{BY}}{c_{BP}} + \left(\frac{2}{\pi} - 1 \right) \sqrt{v_{Bi}^2 - \left(\frac{P_{BY}}{c_{BP}} \right)^2} \right)$$

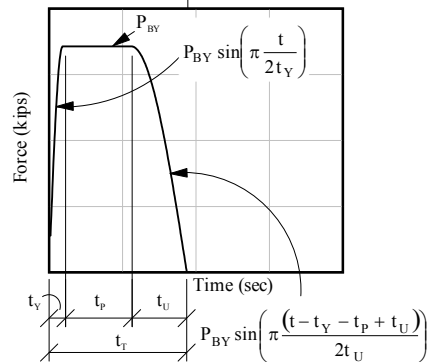
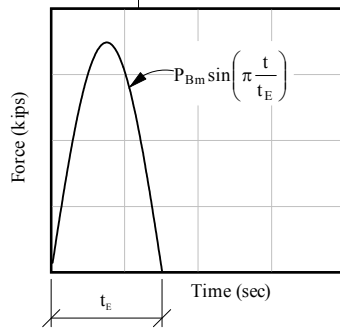


Figure 10.14 Procedure for computing barge impact force-time histories in accordance with AVIL method (Consolazio et al. 2008)

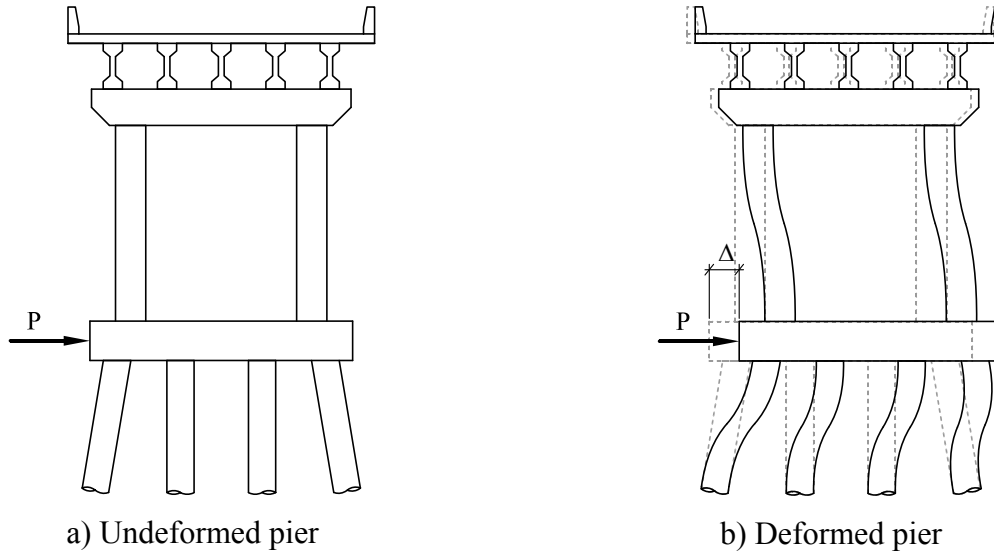


Figure 10.15 Determination of lateral pier-soil stiffness (k_p) by static analysis

Table 10.5 Lateral pier-soil stiffness (k_p) for each LA-1 pier

Pier no.	k_p (kip/in.)
2	2,181
3	2,911
4	2,479
96	2,388
97	2,288

Table 10.6 Maximum dynamic impact force (P_{Bm}): UF/FDOT methods (AVIL)

VG	P2	P3	P4	P96	P97	VG	P2	P3	P4	P96	P97
1	7,569	7,569	3,734	3,294	3,294	17	7,569	7,569	3,734	3,294	3,294
2	7,055	7,055	3,734	3,294	3,294	18	7,055	7,055	3,734	3,294	3,294
3	5,898	5,898	3,734	3,294	3,078	19	5,898	5,898	3,734	3,294	3,294
4	6,798	6,798	3,734	3,294	2,071	20	6,798	6,798	3,734	3,294	2,106
5	5,255	5,255	3,430	3,294	3,294	21	5,255	5,255	3,430	3,294	3,294
6	5,692	6,175	2,788	1,646	1,358	22	6,540	6,540	3,246	1,735	1,358
7	5,898	5,898	3,170	1,871	1,544	23	5,898	5,898	3,734	1,972	1,544
8	4,051	4,361	1,777	1,037	1,028	24	5,015	5,255	2,009	1,037	1,028
9	6,011	6,555	3,734	3,294	2,775	25	7,490	7,569	3,734	3,294	3,253
10	5,314	5,781	3,376	2,650	2,038	26	6,611	7,055	3,734	3,115	2,321
11	4,168	4,505	2,639	2,002	1,461	27	5,193	5,613	3,179	2,336	1,629
12	4,236	4,601	2,381	1,667	1,042	28	5,264	5,718	2,835	1,890	1,059
13	4,791	5,158	3,430	2,925	2,470	29	5,255	5,255	3,430	3,294	2,913
14	4,216	4,574	2,065	1,219	1,006	30	5,239	5,684	2,404	1,285	1,006
15	3,255	3,518	1,629	961	793	31	4,045	4,372	2,257	1,014	793
16	3,396	3,656	1,490	869	862	32	4,204	4,525	1,684	869	862

10.7.6 Protection factor (PF)

As documented in the AASHTO example (§1.8.1.5) protection factors (*PF*) were developed by the bridge design team to account for various land masses in the vicinity of the bridge. *PF* values (Table 10.7) provided in the AASHTO example were adopted for this study.

Table 10.7 Protection factors (*PF*)

	Pier 2	Pier 3	Pier 4	Pier 96	Pier 97
Upbound traffic (VG 1 – 16)	0.50	0.60	0.20	0.08	0.03
Downbound traffic (VG 17 – 32)	0.50	0.50	0.10	0.04	0.01

10.8 Risk Analysis Results

As discussed in the prior section, vessel collision risk assessments were conducted for the LA-1 Bridge using the methodology prescribed by AASHTO (1991 and 2009 specifications). Additional assessments were conducted using the revised UF/FDOT methodology and two different dynamic structural analysis procedures (CVIA, AVIL). The results of each assessment are presented in this section, including probability of collapse (*PC*) and annual frequency of collapse (*AF*) estimates, as predicted by each method.

10.8.1 AASHTO methods

The following sections discuss results from the risk assessments conducted using AASHTO methodology with two different barge impact load equations: 1) from the 1991 AASHTO provisions (Eqns. 10.6 and 10.7), and 2) from the 2009 provisions (Eqns. 10.9 and 10.10).

10.8.1.1 AASHTO (1991) barge impact load model (as-designed)

Estimates of *PC* values that were computed using the AASHTO (1991) methodology were very often equal to zero. Specifically, of the 160 combinations of pier and vessel group considered, *PC* was nonzero 47 times (approximately 29%). Including the ship-type vessel groups for which *PC* was always equal to zero (340 total cases), the percentage of nonzero *PC* cases was only 14%. This occurred because, using the AASHTO expression, *PC* was only nonzero when the impact load *P* exceeded the lateral pier capacity *H* (i.e., $H/P < 1$). Furthermore, even nonzero values of *PC* were quite small. Indeed, the largest *PC* among all cases considered was 0.088, and for this case, the impact load exceeded pier capacity by 4.9 times. Among the nonzero cases, the average *PC* was 0.039, which corresponds to pier capacity being exceeded by 1.5 times.

Estimates of *PC*, as obtained by AASHTO (1991) methods, are presented qualitatively for every pier and vessel group in Fig. 10.16a. Note that in this format, white squares correspond to *PC* values that are exactly equal to zero. Green color indicates *PC* just greater than zero, and

the color gradient fades to red at $PC = 1$. While all nonzero values were small, PC was slightly greater for piers far from the navigation channel (piers 96 and 97).

Including all other terms in the AF expression (N , PA , PG , PF), the relative contribution to AF is shown for every pier and vessel group in Fig. 10.16b. Note that the color gradient is simply relative to the maximum contribution among all piers and vessel groups, having no specific numerical scale. The purpose of the gradient is to show, qualitatively, which piers and vessel groups contribute most to total risk (AF). As would be expected, piers nearest the centerline (piers 2 and 3) contributed most to AF , as they have the highest likelihood of being impacted. These piers only contributed to AF for vessel group 17, the most severe impact case considered (fully loaded barge traveling downbound). Piers 4, 96, and 97 did contribute to AF , but only for some of the lightly loaded vessel groups. This occurred because only lightly loaded vessels had a small enough draft to permit impact these piers without running aground.

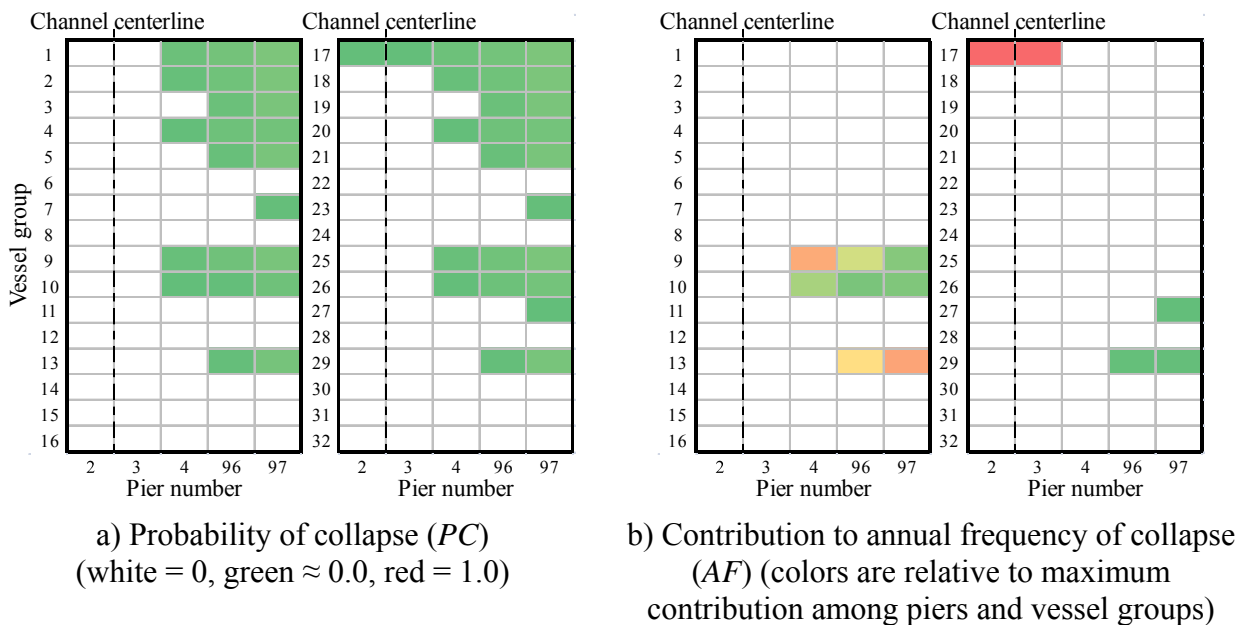
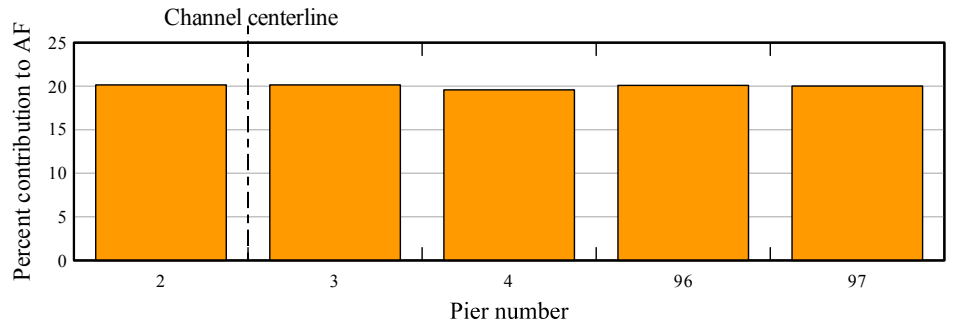


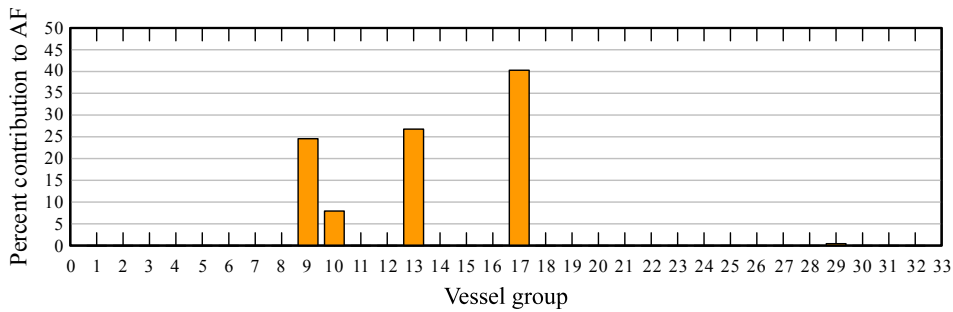
Figure 10.16 Risk analysis results for each pier and vessel group: AASHTO (1991) methods

Fig. 10.17a shows the percent contribution to AF for each pier in the bridge (i.e., the contributions shown in Fig. 10.16b, summed across all vessel groups). As intended by the bridge designers, each pier contributed equally to AF . See the AASHTO example for more details.

Fig. 10.17b shows the percent contribution to AF for each vessel group (i.e., the contributions shown in Fig. 10.16b, summed across all piers). Vessel group 17 (the most severe impact case) was the largest contributor to AF (approximately 40%). However, vessel groups 9 and 13 contributed approximately 25% each. Risk associated with groups 9 and 13 was primarily caused by their relatively high probability of impact. PC values for these groups were not particularly high compared to vessel groups that contributed nothing to AF .



a) By pier number



b) By vessel group

Figure 10.17 Percent contribution to *AF*: AASHTO (1991) methods

Summing *AF* among all piers and vessel groups, *AF* predicted by AASHTO (1991) methods was $9.98 \times 10^{-5} \text{ yr}^{-1}$, which corresponds to a return period $1/AF = 10,020$ years. Therefore, by the AASHTO definition, the bridge can be considered sufficiently robust to resist vessel collision loading, because the minimum acceptable return period is $1/AF = 10,000$ years.

10.8.1.2 AASHTO (2009) barge impact load model

Estimates of *PC* that were computed using the AASHTO (2009) methodology were nearly always equal to zero. Specifically, of the 160 combinations of pier and vessel group considered, *PC* was nonzero 37 times (approximately 23%). Including the ship-type vessel groups for which *PC* was always equal to zero (340 total cases), the percentage of nonzero *PC* cases was only 11%. This occurred because, compared to the 1991 AASHTO procedure, barge impact load magnitudes were lower, particularly for high-energy impact conditions experienced by piers near the navigation channel. Because the bridge was designed to resist relatively higher load magnitudes predicted by the 1991 AASHTO provisions, pier capacity was rarely exceeded ($H/P < 1$) using the 2009 provisions, and *PC* was equal to zero for 77% of impact cases considered.

Estimates of *PC*, as obtained by AASHTO (2009) methods, are presented qualitatively for every pier and vessel group in Fig. 10.18a. Note that *PC* was equal to zero for piers 2 and 3 for every vessel group. Consequently, *PC* was only nonzero for piers 4, 96, and 97, which are unlikely to be impacted. Including all other terms in the *AF* expression (*N*, *PA*, *PG*, *PF*), the

relative contribution to AF is shown for every pier and vessel group in Fig. 10.18b. Note that there was no risk contribution from fully loaded vessel groups (1 – 8 and 17 – 24), and no contribution from piers 2 – 4, regardless of vessel group. Therefore, only piers 96 and 97 had any vessel collision risk, and most of that risk was concentrated in vessel group 13.

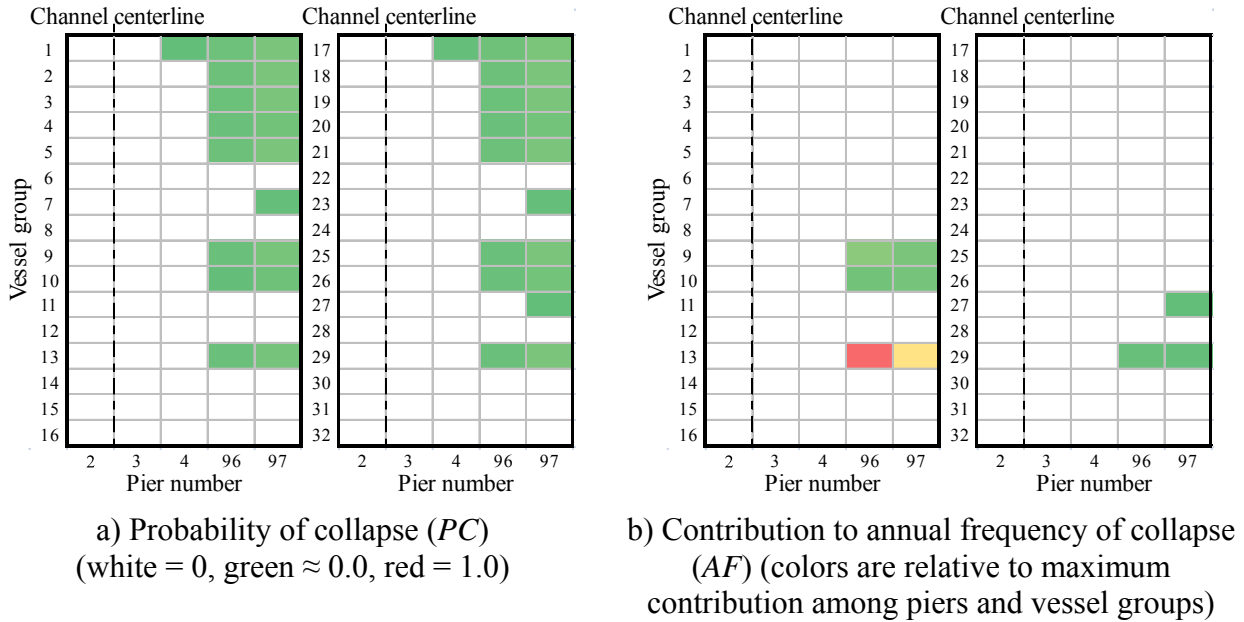
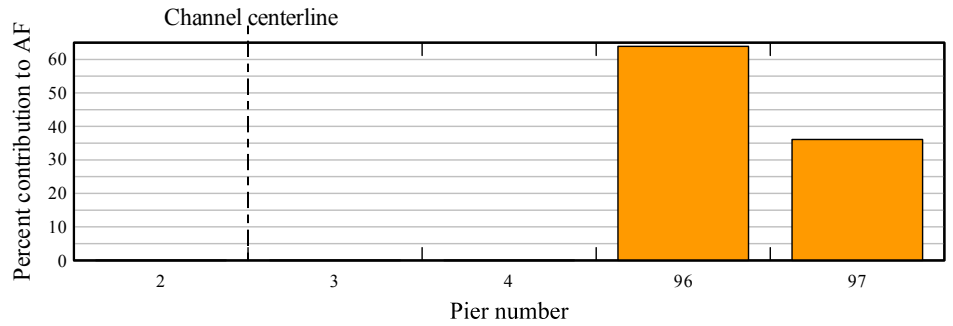


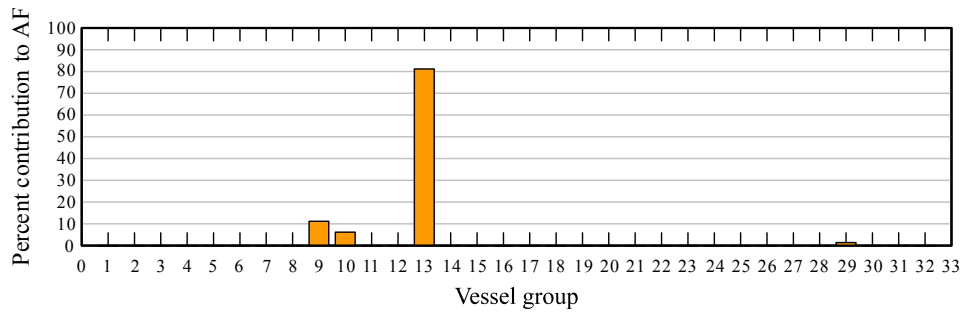
Figure 10.18 Risk analysis results for each pier and vessel group: AASHTO (2009) methods

Fig. 10.19a shows the percent contribution to AF for each pier in the bridge (i.e., the contributions shown in Fig. 10.18b, summed across all vessel groups). As discussed above, piers 96 and 97 together accounted for 100% of the total risk. This outcome differs substantially from the assessment using the 1991 AASHTO provisions, in which contributions to AF were distributed equally among the five piers (recall Fig. 10.17a). As noted above, this occurred primarily because 2009 AASHTO loads were smaller, causing PC to be equal to zero for the two channel piers (piers 2 and 3).

Fig. 10.19b shows the percent contribution to AF for each vessel group (i.e., the contributions shown in Fig. 10.18b, summed across all piers). In contrast to the 1991 AASHTO results, vessel group 13 accounted for more than 80% of total risk, and vessel groups 9 and 17 were significantly less important.



a) By pier number



b) By vessel group

Figure 10.19 Percent contribution to AF : AASHTO (2009) methods

Summing AF among all piers and vessel groups, AF predicted by AASHTO (2009) methods was $5.54 \times 10^{-5} \text{ yr}^{-1}$, which corresponds to a return period $1/AF = 18,060$ years. As noted above, this outcome occurred because the only piers that were found to be at risk for vessel collision (piers 96 and 97) were located relatively far from the navigation channel, resulting in lower geometric probability of impact (PG). Also, PF values were smallest for these piers because of the relatively large degree of protection afforded by navigational obstructions. Therefore, considering all these factors, AF was significantly smaller than predicted by the 1991 AASHTO procedure.

These results highlight how sensitive the AASHTO PC expression can be to changes in analysis assumptions. For this example case, barge impact load magnitudes predicted by the 2009 equations were, on average, only 7.8% smaller than those predicted by the 1991 equations. However, AF was found to be 55% smaller, as a result. Such sensitivity is caused by the AASHTO PC equation allowing PC to be equal to zero if pier capacity (as estimated by engineering analysis) is greater than *or equal to* the estimated impact load. Given the significant uncertainties associated with estimating both loads and capacities and statistical variability of material and soil strengths, as well as other factors, assigning a failure probability equal to zero cannot be reasonably justified.

10.8.2 UF/FDOT methods

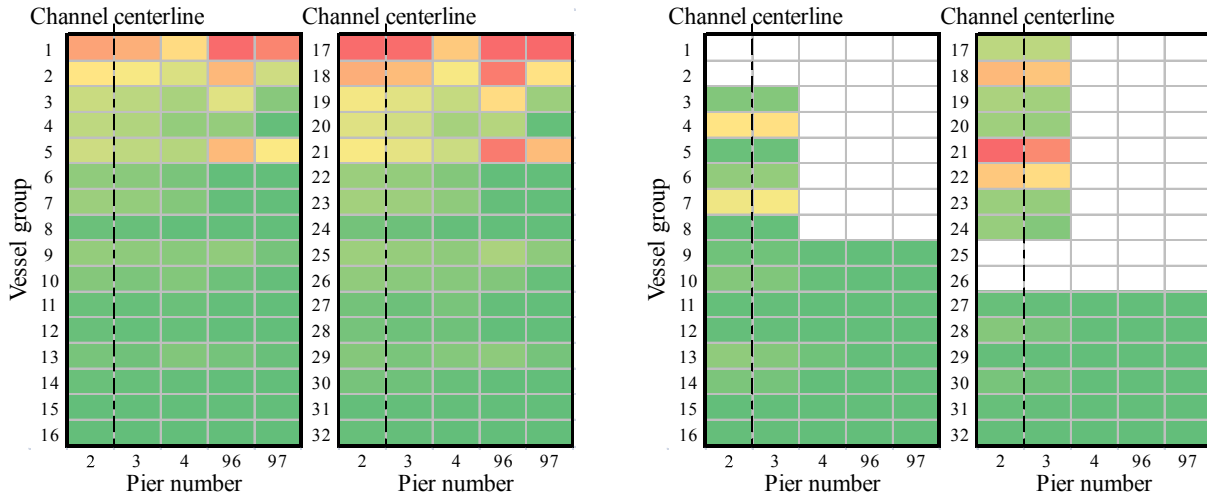
The following sections present risk analysis results (*PC* and *AF*) that were computed using UF/FDOT methods. The revised methods include a new *PC* expression, revised barge impact load prediction equations, and two dynamic structural analysis procedures (CVIA and AVIL).

10.8.2.1 CVIA

Estimates of *PC* computed using UF/FDOT methods were never equal to zero. This is because the minimum value that the *PC* equation (Eqn. 10.12) can take is 2.33×10^{-6} , when $D/C = 0$. Furthermore, by definition, $D/C = 1$ when the load carrying capacity of the pier has been reached or exceeded, at which point $PC = 1$. In the context of a CVIA dynamic structural analysis, such a condition typically results in the analysis failing to converge due to numerical (and structural) instability.

Estimates of *PC*, as obtained by UF/FDOT methods with CVIA structural analysis, are presented qualitatively for every pier and vessel group in Fig. 10.20a. Note that the color definitions are the same as stated in the previous section. As shown, the highest *PC* values were associated with vessel groups 1 – 5 and 17 – 21, which correspond to the most massive vessel types considered in this study. For a given vessel group, *PC* was relatively uniform among all the piers, indicating that pier capacity was approximately proportional to the impact demand. Compared to the AASHTO (1991) method results (Fig. 10.16a), *PC* values quantified by UF/FDOT methods using CVIA were much larger. The AASHTO procedure predicted an average $PC = 0.039$, while UF/FDOT average $PC = 0.19$. Furthermore, many impact cases had *PC* values equal to or nearly equal to 1.0, while their maximum AASHTO *PC* was only 0.088.

Considering other factors that contribute to overall risk (N , PA , PG , PF), relative contributions to *AF* are shown in 10.20b. Note that some piers did not contribute to *AF* for certain vessel groups (as defined by white coloring), because these piers were assigned $N = 0$. The largest *AF* contributions came from piers 2 and 3 for vessel group 21. This outcome is somewhat unexpected, as vessel group 21 refers to a moderate energy impact condition. However, this group is one of the most common on the waterway. Therefore, the high number of vessel trips (N) overcame the risk posed by more massive vessels by virtue of having a higher probability of impact occurring. Regardless of vessel group, piers 2 and 3 had the largest contribution to *AF*.



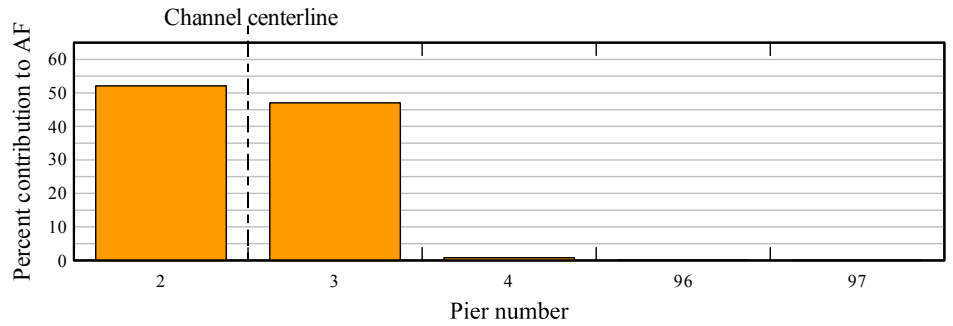
a) Probability of collapse (*PC*)
(white = 0, green \approx 0.0, red = 1.0)

b) Contribution to annual frequency of collapse
(*AF*) (colors are relative to maximum
contribution among piers and vessel groups)

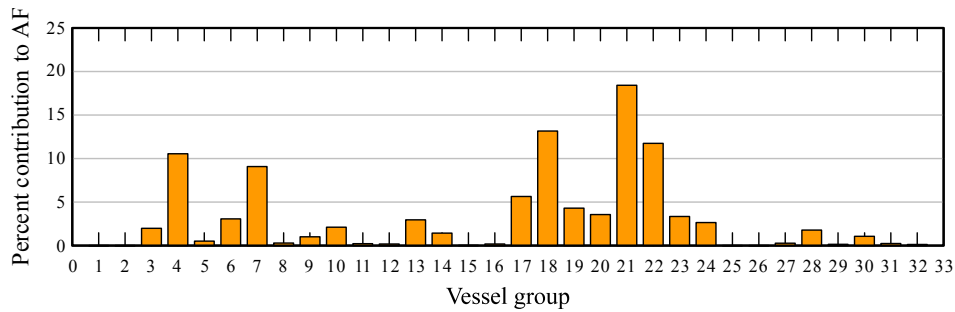
Figure 10.20 Risk analysis results for each pier and vessel group: UF/FDOT methods, CVIA

Fig. 10.21a shows the percent contribution to *AF* for each pier in the bridge (i.e., the contributions shown in Fig. 10.20b, summed across all vessel groups). As shown, piers 2 and 3 account for nearly 100% of total risk. This occurred for two reasons: 1) the piers are located adjacent to the channel, and are therefore most likely to be impacted, and 2) more importantly, vessel impact load magnitudes associated with piers 2 and 3 were significantly higher than for other piers. Load magnitudes were higher primarily because the pier footings are skewed, such that they are aligned with the navigation channel. Recalling the UF/FDOT load model (Eqn. 10.13), θ was equal to 0° for piers 2 and 3. Therefore, as shown in Table 10.4, impact loads were almost two times higher than the other piers, for which $\theta = 20^\circ$.

Fig. 10.21b shows the percent contribution to *AF* for each vessel group (i.e., the contributions shown in Fig. 10.20b, summed across all piers). As shown, the largest contribution to *AF* (approximately 18%) came from vessel group 21, and significant contributions (9 – 14%) came from vessel groups 4, 7, 18, and 22. Relative contributions to *AF* from each vessel group were influenced by a combination of impact severity and trip frequency. Many of the vessel groups with highest risk did not correspond to the most severe impact conditions. Indeed the most severe impact case was caused by vessel group 17, which only contributed 5% to *AF*.



a) By pier number



b) By vessel group

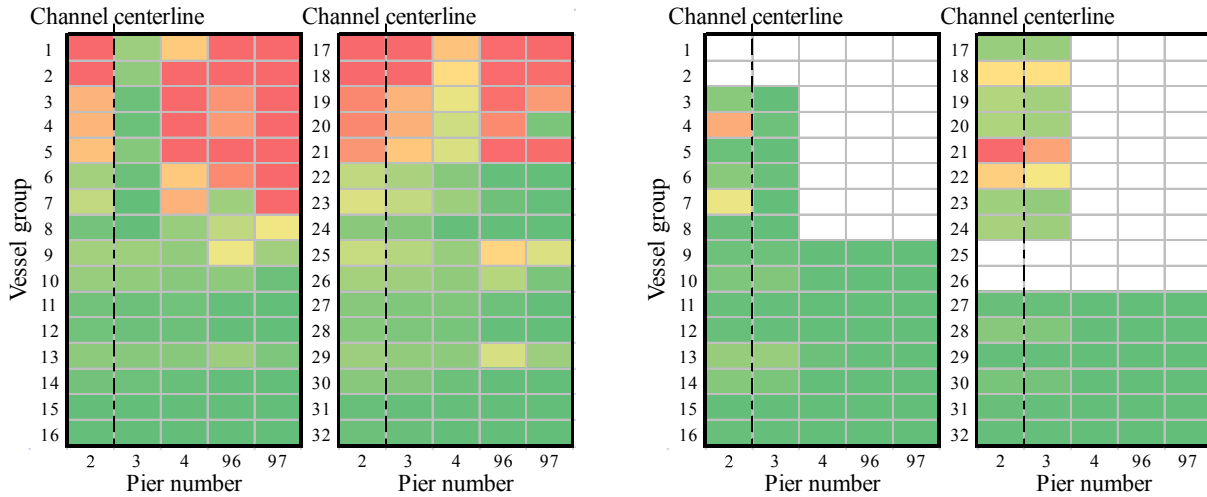
Figure 10.21 Percent contribution to *AF*: UF/FDOT methods, CVIA

Summing *AF* among all piers and vessel groups, *AF* predicted by UF/FDOT methods (with CVIA) was 0.137 yr^{-1} , which corresponds to a return period $1/AF = 7.3$ years. The specific reasons why the UF/FDOT methods predicted so much higher a level of risk than the AASHTO procedures ($1/AF = 10,020$ years) are discussed in detail in Section 10.9.

10.8.2.2 AVIL

Estimates of *PC*, as obtained by UF/FDOT methods with AVIL structural analysis, are presented qualitatively for every pier and vessel group in Fig. 10.22a. As with CVIA, the highest *PC* values were associated with vessel groups 1 – 5 and 17 – 21, which correspond to the most massive vessel types considered in this study. For a given vessel group, *PC* was relatively uniform among all the piers, indicating that pier capacity was approximately proportional to the impact demand.

Considering other factors that contribute to overall risk (*N*, *PA*, *PG*, *PF*), relative contributions to *AF* are shown in 10.22b. As with CVIA, the largest *AF* contributions came from piers 2 and 3 for vessel group 21. Regardless of vessel group, piers 2 and 3 had the largest contribution to *AF*.



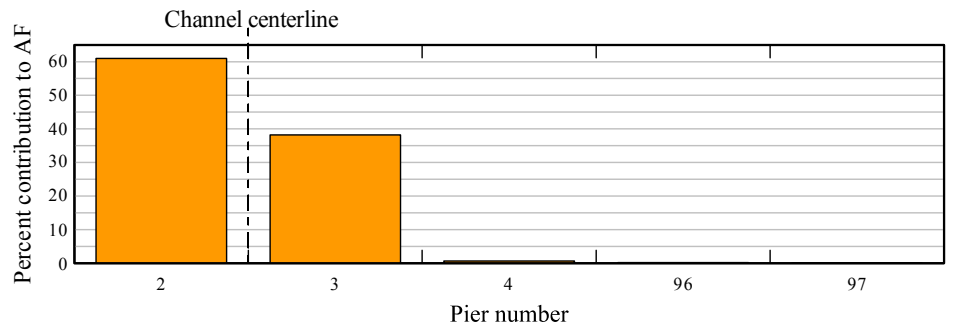
a) Probability of collapse (*PC*)
(white = 0, green \approx 0.0, red = 1.0)

b) Contribution to annual frequency of collapse (*AF*) (colors are relative to maximum contribution among piers and vessel groups)

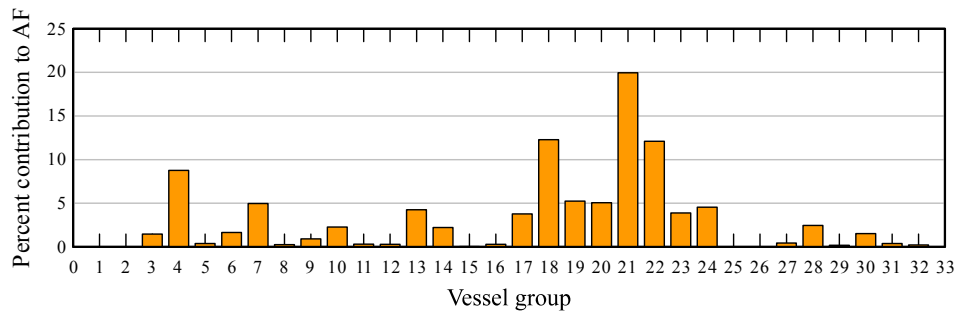
Figure 10.22 Risk analysis results for each pier and vessel group: UF/FDOT methods, AVIL

Fig. 10.23a shows the percent contribution to *AF* for each pier in the bridge (i.e., the contributions shown in Fig. 10.22b, summed across all vessel groups), and Fig. 10.23b shows the percent contribution to *AF* for each vessel group (i.e., the contributions shown in Fig. 10.22b, summed across all piers). The distribution of *AF* among the various piers and vessel groups was quite similar to CVIA, with piers 2 and 3 contributing almost 100% of total risk. Like CVIA, pier 2 contributed more to *AF* than pier 3. However, the difference is larger for AVIL.

Summing *AF* among all piers and vessel groups, *AF* predicted by UF/FDOT methods (with AVIL) was 0.206 yr^{-1} , which corresponds to a return period $1/AF = 4.8$ years. The specific reasons why the UF/FDOT methods predicted so much higher a level of risk than the AASHTO procedures ($1/AF = 10,020$ years) are discussed in detail in Section 10.9.



a) By pier number



b) By vessel group

Figure 10.23 Percent contribution to AF: UF/FDOT methods, AVIL

10.9 Discussion of Results

Table 10.8 summarizes risk assessment results for the LA-1 Bridge, as determined by each analysis procedure that was considered in this study. As shown, impact loads computed using UF/FDOT methods were approximately 3 times higher than those determined using the AASHTO (1991) procedure. As discussed above, this occurred primarily because the UF/FDOT impact load model tends to predict larger impact forces than the AASHTO model when piers have wide, flat-faced impact surfaces. Furthermore, impact forces predicted by the UF/FDOT model increase significantly when the impact angle is small (i.e., when the impact condition is nearly ‘head-on’). Because the footings of the two channel piers (2 and 3) in the LA-1 Bridge were skewed such that they aligned with the navigation channel, the expected impact angle was $\theta = 0^\circ$, resulting in significantly higher load magnitudes than the AASHTO model predicted.

Table 10.8 Summary of risk assessment results for each analysis procedure considered

	AASHTO (1991)	AASHTO (2009)	UF/FDOT (CVIA)	UF/FDOT (AVIL)
Minimum impact load (kip)	106	106	857	793
Average impact load (kip)	1,294	1,193	3,926	3,732
Maximum impact load (kip)	2,565	1,986	7,569	7,569
Average P/H or D/C	0.984	0.910	0.726	0.794
Average PC	0.01153	0.00981	0.190	0.336
Return period ($1/AF$) (yr)	10,020	18,060	7.3	4.8

In Table 10.8, AASHTO capacity-demand ratios (H/P) (used to compute PC) are inverted to be demand-capacity ratios (P/H) to facilitate comparison to D/C ratios computed by UF/FDOT methods. As shown, average D/C for the most accurate UF/FDOT method (CVIA) was approximately 26% lower than P/H for the AASHTO (1991) method, even though UF/FDOT load magnitudes were higher. This occurred because the piers, as designed, had significantly more lateral capacity than stated in the structural drawings, as evidenced by their ability to withstand dynamic impact loads on the order of 6,000 – 7,000 kip. Recall that the minimum pushover capacity stated in the structural drawings was only 2,446 kip for the channel piers. As discussed above, this minimum value was used for H in the AASHTO risk assessments for consistency with the published AASHTO risk assessment, in lieu of the capacity as estimated by pushover analysis of the finite element models used to perform the UF/FDOT assessments. Had the actual pushover capacities been employed in the AASHTO risk assessments, P/H would be lower than D/C from UF/FDOT assessments.

Average PC values obtained by UF/FDOT methods (CVIA) were more than 16 times higher than those obtained from AASHTO (1991). This is primarily a consequence of larger demand on the piers (caused by the larger UF/FDOT loads). However, another reason for the discrepancy is the difference between the PC expressions. As discussed in the prior section, PC was equal to zero for the majority of impact cases considered in the AASHTO risk assessment. In contrast, the UF/FDOT PC expression (by intentional design) cannot return a PC equal to zero. Consequently PC was greater than zero for every barge impact case considered in the UF/FDOT assessments. It should also be noted that PC values obtained using the UF/FDOT methods properly account for numerous statistical uncertainties associated with impact loading, structural capacity, and soil capacity and are therefore a more rational estimate of collapse risk than the AASHTO PC values.

As shown in Table 10.8, AASHTO (1991) methods resulted in a return period for bridge collapse $1/AF = 10,020$ years, satisfying the acceptable risk criterion ($1/AF \geq 10,000$ years) for this critical bridge. This outcome is expected, given that the bridge was designed in accordance with the 1991 AASHTO provisions. However, the barge impact load model was modified slightly in the 2009 AASHTO provisions (i.e., elimination of the barge width modification factor), resulting in a reduction in load magnitudes for most impact conditions. Accounting for this change, the return period increased to 18,060 years.

Return periods predicted by UF/FDOT methods imply that the bridge does not satisfy the level of acceptable risk. Indeed, AF predicted by the CVIA risk assessment was 1,370 times higher than the AASHTO (1991) method. This enormous discrepancy is a consequence of the difference in PC values predicted by each method, as discussed above. The AASHTO method had many PC values equal to zero, which may not be realistic, while the UF/FDOT methods had no PC values equal to zero, and all PC values were dramatically higher than AASHTO. From the available data, it is difficult to assess which estimate of AF is more realistic. Certainly, recent research indicates that impact load magnitudes should be higher than predicted by AASHTO for this particular bridge. Furthermore, it is difficult to defend PC being equal to zero (as AASHTO does) when the impact load estimated by an empirical equation is nearly equal to the pier

capacity estimated by engineering analysis. Given these factors, it is expected that AF would be greatly under-predicted by the AASHTO procedures for this bridge. Furthermore, additional evidence (discussed below) indicate that the UF/FDOT procedures likely over-predicted AF for this bridge.

Given that the LA-1 Bridge did not satisfy the acceptable risk level using UF/FDOT methods, it is important to consider whether the bridge could be economically retrofitted to improve its performance and thereby mitigate vessel collision risk within the context of the UF/FDOT assessment methodology. A possible retrofit solution is proposed in the following section (Section 10.10) that takes advantage of the fact that the UF/FDOT impact load model predicts significantly smaller forces if impacted pier surfaces are rounded rather than flat-faced. For demonstration purposes, a pier-protection system and two alternative pier designs that would further mitigate risk are also discussed in Section 10.10.

The retrofit, protection system, and alternative design examples presented in Section 10.10 are possible means of satisfying the required risk criteria if the UF/FDOT methodology were employed exactly as discussed in this chapter. However, a comparison of the LA-1 Bridge risk assessment data to historical incidents of vessel collision suggest that the other terms in the expression for AF (specifically the PA and PG terms) may over-predict the likelihood that impacts will occur. Because these terms were adopted into the UF/FDOT methods directly from AASHTO, the value of AF computed using UF/FDOT methods may be unrealistically high. If this were the case, alternative designs or retrofits may be less necessary. This possibility is discussed further in Section 10.11.

10.10 Suggestions for Mitigating Risk

The primary reason that UF/FDOT methods predicted a higher risk level than the AASHTO methods is the relative magnitude of impact loads. Three risk mitigation strategies are presented in this section: retrofits to the impacted piers, a protection system involving dolphin structures, and two alternative pier designs. The primary objective of the retrofits and alternative designs is to reduce the magnitude of impact forces by taking advantage of certain aspects of the UF/FDOT impact load model.

10.10.1 Pier footing retrofit

As discussed in Section 10.7.5.2.1, the barge force-deformation curve that was used as the basis for UF/FDOT predictions of impact force was elastic, perfectly plastic with yield deformation (a_{BY}) equal to 2 in. and yield force (P_{BY}) computed based on the Getter and Consolazio (2011) model. For a flat-faced impact surface, such as the pier footings of the LA-1 Bridge, P_{BY} was computed as:

$$P_{BY} = 1400 + \left(130 - \frac{68}{1 + e^{3.8 - 0.31 \cdot \theta}} \right) \cdot \min(B_B, B_P) \quad (10.14)$$

As summarized in Table 10.9, P_{BY} varied between 3,294 – 7,569 kip for the various piers and vessel groups. As demonstrated by the risk assessment, the barge bow yielded for most impact conditions, and thus, the maximum impact force was generally equal to P_{BY} .

However, the Getter-Consolazio force-deformation model states that, for rounded impact surfaces, P_{BY} should be computed as:

$$P_{BY} = 1400 + 30 \cdot \min(B_B, B_P) \quad (10.15)$$

Therefore, if the LA-1 pier footings (pile caps) were the same size, but were rounded instead of flat-faced on the leading edge, P_{BY} would vary between 2,240 – 2,840 (Table 10.9), corresponding to a 48% reduction in impact loads, on average.

Table 10.9 Comparison of barge yield forces (P_{BY}) for as-built and retrofitted designs

Pier	θ (deg)	$\min(B_B, B_P)$ (ft)	Flat footings (as-built)	Round footings (retrofit)
			P_{BY} (kip)	P_{BY} (kip)
2 – 3	0	30.0 – 48.0 ¹	5,255 – 7,569 ¹	2,300 – 2,840 ¹
4	20	30.0 – 34.5 ¹	3,430 – 3,734 ¹	2,300 – 2,435 ¹
96 – 97	20	28.0	3,294	2,240

¹ Varies by vessel group and pier. See Appendix N for details.

Choosing to round off the ends of footings would likely have little influence on construction cost, but could improve impact performance significantly. To evaluate this possibility, a risk assessment was conducted using UF/FDOT methods (CVIA) in which the LA-1 footings were assumed to be the same overall size, but the ends were rounded instead of flat (detailed analysis results are omitted here for brevity). Bridge structural demands were significantly reduced relative to the as-built condition, and the return period ($1/AF$) went from 7.3 years to 28.0 years, corresponding to a 74% reduction in risk. Therefore, significant risk reduction could be realized by retrofitting footings with rounded caps made of reinforced concrete, as illustrated in Fig. 10.24. If the foundation does not have sufficient capacity to carry the additional concrete weight, a more lightweight design (steel or composite) with the same dimensions could be employed.

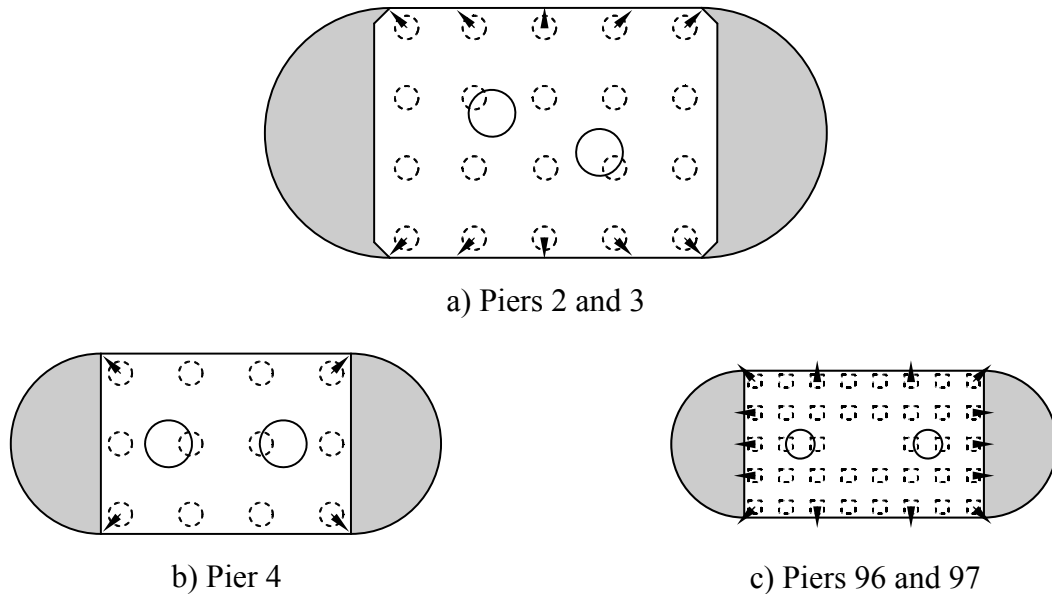


Figure 10.24 LA-1 Bridge pier footing end cap retrofit to reduce vessel collision risk (retrofitted end caps indicated in grey)

10.10.2 Pier protection system

Given that the retrofitted design had a return period $1/AF = 28.0$ years, the only practical means of achieving the specified return period of 10,000 years with the existing structure (using the UF/FDOT methodology) would be to construct protective structures that block oncoming vessels from impacting bridge piers near the navigation channel. Such structures can be designed to be permanent and thereby withstand numerous impacts in their design life, or they can be sacrificial, necessitating repair or reconstruction if they are significantly damaged by being impacted. As an illustrative example, consider the pier protection layout shown in Fig. 10.25, in which piers 2 – 4 are protected by dolphin structures. Dolphins are commonly constructed by driving a circular ring of steel sheet piling, filling the center with sand, rocks, and/or riprap, and casting a reinforced concrete cap on top (near the waterline). Such structures can be designed to withstand low-energy impacts without damage, while repair or replacement may be required following high-energy head-on impacts.

In the example shown in Fig. 10.25, piers 2 and 3 are protected by two 30-ft diameter dolphins on each side of the pier, and pier 4 is similarly protected by 20-ft. diameter dolphins. If positioned and designed carefully, such structures could provide effectively complete protection against vessel collisions. To evaluate the efficacy of the protection system, the UF/FDOT risk assessment (CVIA) was repeated but with $PF = 0$ (complete protection) for piers 2 – 4. The return period ($1/AF$) increased from 7.3 years in the as-built configuration to 8,160 years, which is close to the target of 10,000 years. If the protection system in Fig. 10.25 was combined with retrofitting piers 96 and 97 as shown in Fig. 10.24c, then the return period increases to 12,380 years. Alternatively, additional dolphins could be constructed to protect piers 96 and 97, and thereby reduce risk to effectively zero.

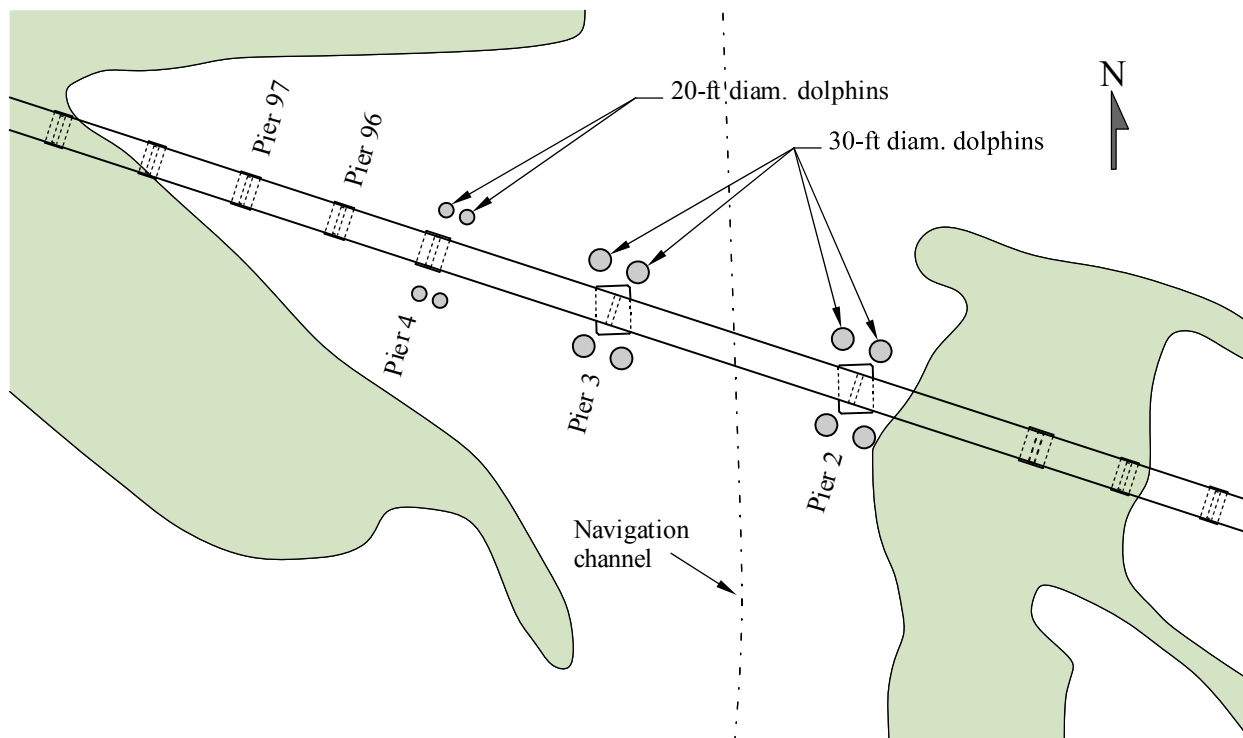


Figure 10.25 Plan view of LA-1 Bridge showing locations of protective dolphin structures

10.10.3 Alternative foundation design

In order to illustrate strategies for reducing vessel collision risk using UF/FDOT methods, an alternative foundation design was developed for the piers at risk for collision (piers 2 – 4 and 96 – 97). The alternative design employs two large-diameter drilled shafts in lieu of the driven pile foundations that were constructed. This design is advantageous because the portion of piers that would be impacted by barge vessels can be proportioned to be a relatively small-diameter (8 – 10 ft) cylinder, rather than a wide, flat-faced footing surface, as currently designed. This change in geometry can result in significant reductions in impact forces.

As shown in Fig. 10.26, the foundation for piers 2 – 4 (previously consisting of 54-in. driven cylinder piles) was replaced with two 9-ft diameter drilled shafts that are positioned collinearly with the pier columns (also 9 ft in diameter at the base) (Fig. 10.26a). Note that the spacing (22 ft) is less than three times the diameter of the shafts, and therefore lateral capacity is not optimal. However, the spacing was chosen such that no changes to the pier design were required. The shafts and pier columns are connected at the waterline with a 20-ft deep shear wall that is 10-ft wide and has cylindrically-shaped ends (Fig. 10.26b). The drilled shafts are reinforced with (48) No. 18 longitudinal bars and No. 8 ties spaced at 12 in. center-to-center (Fig. 10.26c), with 6 in. of clear concrete cover. Due to relatively weak soil conditions at the site, shafts must be drilled to an elevation of -185 ft, which is approximately 30 ft deeper than the driven piles in the as-built design.

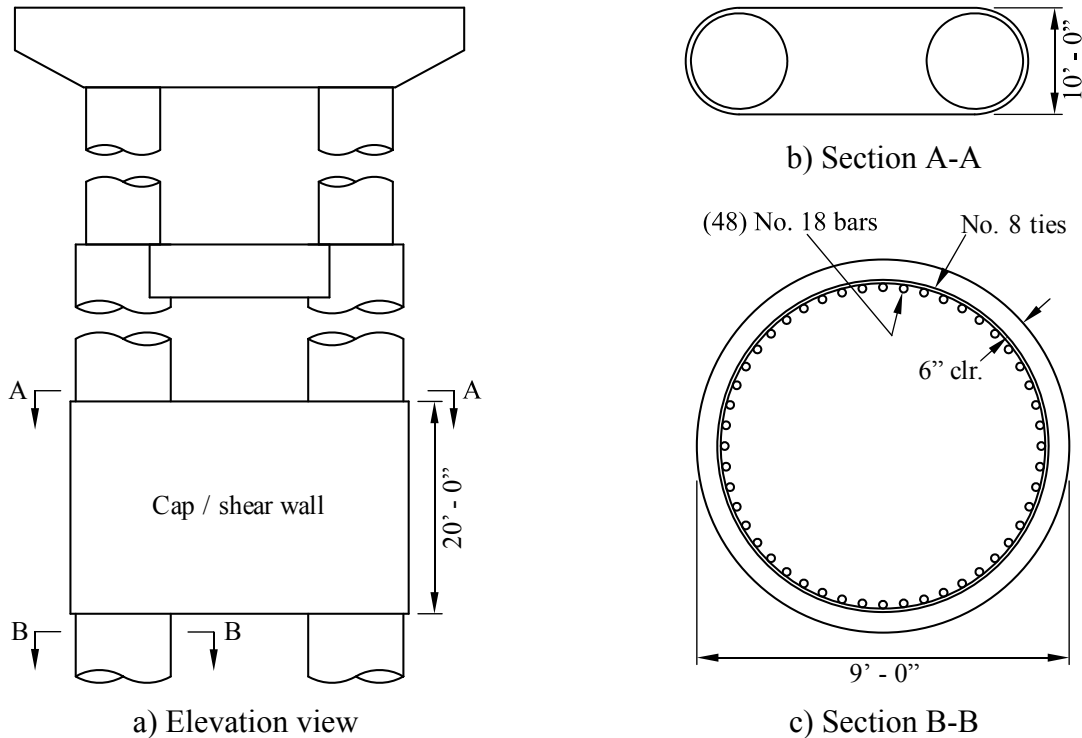


Figure 10.26 LA-1 Bridge alternative design with drilled shaft foundation: piers 2 – 4

As shown in Fig. 10.27, the foundation for piers 96 and 97 (previously consisting of 30-in. square driven piles) was replaced with two 7-ft diameter drilled shafts that are positioned collinearly with the pier columns (6 ft in diameter at the base) (Fig. 10.27a). The spacing (24.5 ft) was chosen such that no changes to the pier design were required, and exceeds three times the diameter of the shafts, which improves lateral capacity. The shafts and pier columns are connected at the waterline with a 20-ft deep shear wall that is 8-ft wide and has cylindrically-shaped ends (Fig. 10.27b). The drilled shafts are reinforced with (36) No. 18 longitudinal bars and No. 8 ties spaced at 12 in. center-to-center (Fig. 10.27c), with 6 in. of clear concrete cover. Again, shafts must be drilled to an elevation of -185 ft, which is approximately 25 ft deeper than the driven piles in the as-built design.

Because the impacted pier surfaces are rounded, P_{BY} was calculated as:

$$P_{BY} = 1400 + 30 \cdot \min(B_B, B_P) \quad (10.16)$$

where $\min(B_B, B_P)$ is equal to 10 ft for piers 2 – 4 and 8 ft for piers 96 and 97. As summarized in Table 10.10, P_{BY} was reduced by 63% on average (relative to the as-built design), and up to 77% for the piers that are adjacent to the navigation channel (piers 2 and 3).

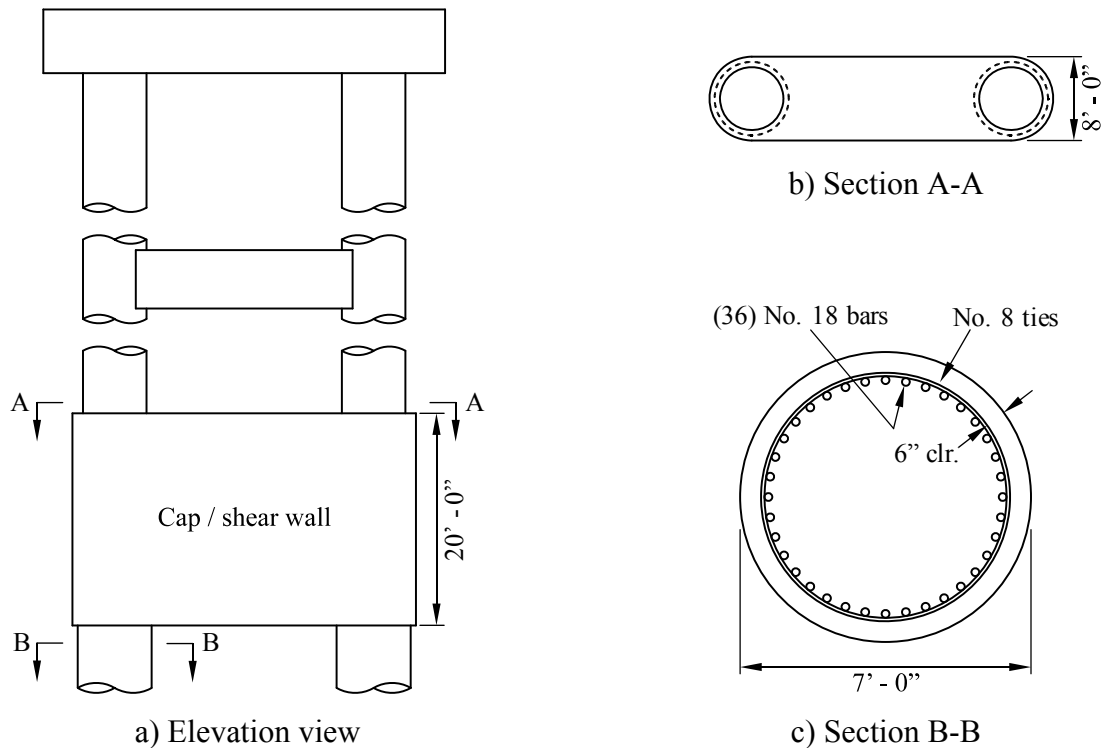


Figure 10.27 LA-1 Bridge alternative design with drilled shaft foundation: piers 96 – 97

Table 10.10 Comparison of barge yield forces (P_{BY}) for as-built and alternative designs

Pier	θ (deg)	Flat footings (as-built)		Drilled shafts (redesign)	
		$\min(B_B, B_P)$ (ft)	P_{BY} (kip)	$\min(B_B, B_P)$ (ft)	P_{BY} (kip)
2 – 3	0	30.0 – 48.0 ¹	5,255 – 7,569 ¹	10	1,700
4	20	30.0 – 34.5 ¹	3,430 – 3,734 ¹	10	1,700
96 – 97	20	28.0	3,294	8	1,640

¹Varies by vessel group. See Appendix N for details.

One of the requirements of the AASHTO provisions is that piers must be able to withstand 50% of the maximum vessel impact force applied in the direction longitudinal to the superstructure alignment, to account for glancing-type impacts. This requirement is a particular concern because the retrofitted design is relatively weak in that direction. However, static pushover analyses of each pier showed that the longitudinal capacity of the channel piers was approximately 3,300 kip. The weakest pier (97) is located at an expansion joint. Therefore, the entire longitudinal load must be carried by the foundation (i.e., no load path through the superstructure is available). Even in this extreme case, the pushover capacity was 1,400 kip, corresponding to 85% of the maximum impact force ($P_{BY} = 1,640$ kip). Consequently the alternative was considered adequate for glancing impacts.

Dynamic impact analyses (CVIA method) were conducted using FB-MultiPier models of the alternative pier designs with revised values of P_{BY} , and corresponding D/C ratios were computed from each analysis. As summarized in Table 10.11, average D/C was greatly reduced relative to both the as-built design (64%) and the retrofitted design (60%), with larger reductions observed for piers 2 and 3. Correspondingly, average PC values for the alternative design were more than *1,500 times* smaller than the as-built design, and *460 times* smaller than the retrofitted design. These examples demonstrate the highly nonlinear nature of the UF/FDOT PC expression, in that modest reductions in D/C can result in dramatic reductions in PC .

In addition to significantly reduced impact loads (and dramatically smaller PC values), the alternative design had a smaller overall footprint within the bridge alignment, and therefore had reduced likelihood of being impacted by aberrant vessels. In other words, horizontal clearance between piers was significantly increased with the alternative design. The geometric probability of impact (PG) was recalculated to account for the new pier geometry and was found to be 40% smaller, on average, than the as-built design. Combining the revised PC and PG values with the other terms in the AF expression (N , PA , PF) the return period ($1/AF$) was calculated to be equal to 10,230 years. Therefore, the alternative design was found to satisfy the level of acceptable vessel collision risk required by AASHTO for critical/essential bridges.

Table 10.11 Summary of UF/FDOT (CVIA) risk assessment results for each design considered

	As-built design (flat-faced footings)	Retrofitted design (rounded footings)	Alternative design (drilled shafts)
Minimum impact load (kip)	857	721	615
Average impact load (kip)	3,926	2,129	1,514
Maximum impact load (kip)	7,569	2,840	1,700
Average D/C	0.726	0.656	0.264
Average PC	0.190	0.0567	0.000122
Return period ($1/AF$) (yr)	7.3	28.0	10,230

The examples described above highlight how sensitive the results of the risk assessment can be to various design choices. The LA-1 Bridge design (as-built) constitutes effectively a worst-case scenario within the context of the UF/FDOT risk assessment procedures. Specifically, foundation footings are wide and flat-faced, which results in significantly larger impact forces than rounded footings of similar size. Furthermore, footings for the two piers adjacent to the navigation channel are skewed such that the flat pier faces are aligned with the channel (and impacting vessels). While this choice improves horizontal clearance and reduces the probability of impact somewhat, the as-built orientation increases impact forces by almost 60% (relative to footings that are aligned with the piers). When combined, these design choices resulted in impact forces that were 3 – 4 times higher than the alternative (drilled shaft) design described above, and collapse risk (AF) that is *1,400 times* higher than the alternative design.

It is important to note that the improved performance of the alternative design came primarily from the reduction in impact forces, and not from an increase in lateral capacity. Indeed, the lateral pushover capacity of the alternative design for piers 2 and 3 (channel piers) was approximately half the as-built design. For illustrative purposes, a second alternative design

concept is shown in Fig. 10.28. Rather than replacing the driven pile foundation with drilled shafts, the footing is simply moved downward to a submerged location, where it is unlikely to be impacted by vessels. A 10-ft wide shear wall that extends up to the maximum expected impact elevation transmits impact forces directly to the footing. Because the wall is the same width as the shear wall in the drilled shaft alternative, impact forces would be identical. However, the driven pile foundation is likely to have a larger lateral capacity than the drilled shaft foundation, and therefore the design would likely improve vessel collision performance even further.

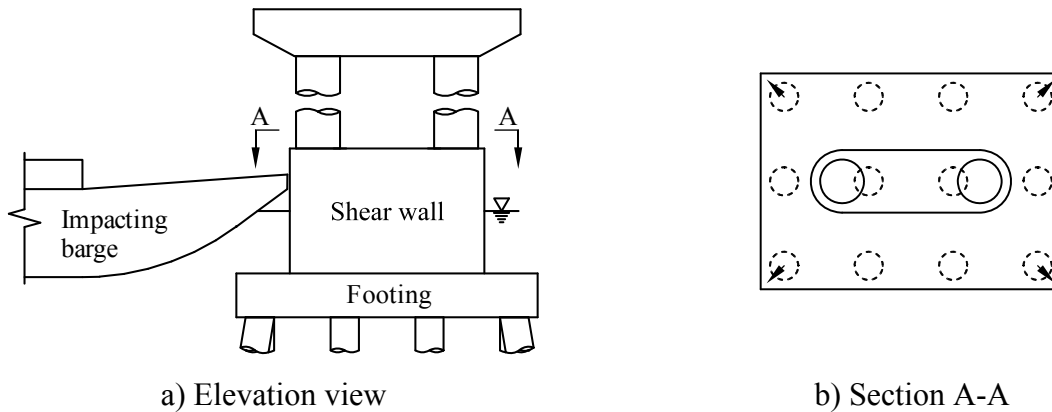


Figure 10.28 Pile-founded alternative design with submerged footing and shear wall (pier 4)

10.11 Concluding Remarks

As discussed previously, the discrepancy between the AASHTO and UF/FDOT methods is entirely limited to PC . However, it is valuable to consider whether the other terms in the AF expression (N , PA , PG , PF) are historically accurate. Detailed records concerning the volume of commercial vessel traffic are readily available, thus N can be considered the most reliable value in the risk assessment. The accuracy of PA , PG , and PF are difficult to evaluate independently, but their combined result can be compared to available data. Specifically, if PC is removed from the expression for AF , the resulting probability is the annual frequency of impact (AFI):

$$AFI = \sum_{i=1}^{N_{VG}} \sum_{j=1}^{N_p} (N_i)(PA_i)(PG_{ij})(PF_{ij}) \quad (10.17)$$

Based on this definition, AFI represents the number of direct vessel collisions with the bridge piers that are expected to occur in a given year. For the LA-1 Bridge, $AFI = 1.04$ impacts/yr. Given that the main piers and spans have been in place for more than five years at present, according to the AASHTO-based AFI it is extremely likely (99.5% probability) that a significant impact event should have already occurred to date.

The U.S. Coast Guard keeps detailed records on vessel casualties, which include (among other things) accidental impacts with bridges. These records are publicly available from an online database called the Coast Guard Maritime Information Exchange (CGMIX) (USCG 2013). Since 2008, only two incidents have been recorded at the LA-1 Bridge site, one of which involved the old lift bridge that has since been removed and replaced by the current high-rise bridge. Therefore, the only recorded incident of the new bridge being impacted by a vessel occurred on April 26, 2011 (CGMIX activity ID# 3997036), in which a fishing boat failed to lower its outriggers prior to traversing under the bridge, and the top 5 ft. of the outriggers impacted the center superstructure span. The incident resulted in no structural damage to the bridge.

Because no significant impact events have occurred at the site since the new bridge was constructed, it is highly *unlikely* that the annual frequency of vessel impact (*AFI*) is as high as predicted by the AASHTO procedure. However, it is unclear which factor in the expression (N , PA , PG , PF) contributed most to the divergence from historical data. Considering the likelihood that the AASHTO predicted *AFI* for the LA-1 Bridge is too large, it is not surprising that the UF/FDOT estimate for *AF*—which incorporates *AFI*—is also unrealistically high. Thus, the return period for vessel impact-induced collapse of the LA-1 Bridge is very likely longer than reported in Table 10.8. However, insufficient data are available for this particular bridge to determine how much longer the return period should be. Given this situation, it is recommended that additional research, outside the scope of the present study, be conducted to investigate the overall basis for the AASHTO terms (PA , PG , etc.) that make up *AFI*, and to propose appropriate alternatives.

CHAPTER 11 CONCLUSIONS AND RECOMMENDATIONS

11.1 Concluding Remarks

In the early 1990s, AASHTO published the first set of national design requirements for vessel collision design of bridges in the U.S.: the *Guide Specifications and Commentary for Vessel Collision Design of Highway Bridges*. Since the original publication, the AASHTO procedures have remained largely unchanged, even though a significant amount of research has been conducted pertaining to vessel collision with bridges, particularly by researchers at the University of Florida (UF), under sponsorship by the Florida Department of Transportation (FDOT). Revised analysis procedures have been developed—based on UF/FDOT research findings—that are significant improvements over the corresponding AASHTO provisions, particularly in the area of structural dynamics. Specifically, the UF/FDOT procedures include a more accurate barge impact load prediction model, dynamic and equivalent-static structural analysis techniques, and a more rational expression for the probability of bridge collapse (PC).

In the current study, a series of barge impact experiments were conducted, in which a reduced-scale (40%-scale) barge bow was impacted by a high-energy pendulum to achieve barge deformation levels close to 10 ft at full scale. The impact experiments demonstrated that the geometry of an impacted pier (i.e., round or flat) influences the magnitude of impact force transmitted during a barge-bridge collision event. Moreover, it was shown that even under high levels of deformation, the elastic perfectly-plastic assumption utilized in the UF/FDOT barge impact load prediction model remains conservative. Finally, it was demonstrated that the analytical simulation techniques used to develop the UF/FDOT load model were able to replicate the deformation (crush) patterns observed in the physical barge bow replicates during pendulum impact testing. Confirmation of these principal concepts serves to validate the UF/FDOT load prediction model.

In support of the barge impact experiments, a series of material tests were conducted, in which the stress-strain relations and strain rate-sensitive properties were determined for the materials (ASTM A36 and A1011 steel) from which the reduced-scale barge specimens will be fabricated. To conduct high-strain rate tests, a novel high rate testing apparatus (HRTA) was designed that employed an impact pendulum to generate the required energy. The HRTA is similar in some ways to impact-based devices that employ a heavy flywheel or drop hammer. However, the HRTA design overcame some important limitations that have been observed with such devices in prior material-evaluation studies. Additionally, a robust optimization-based data processing scheme, based on impulse-momentum theory (see Chapter 4), was developed that permitted extraction of usable test data despite some remaining design limitations.

Data quantified from the material testing program were used to develop stress-strain relations and strain rate-sensitive material parameters based on the Cowper-Symonds model. The materials tested in this study were found to be less sensitive to high strain rates than in prior studies conducted on similar materials. However, rate sensitivity was found to be similar among the multiple specimens tested in this study, despite being of different material grades. The

material parameters that were quantified from the experimental study were then used in representative finite element constitutive models. These constitutive models were then employed in impact simulations of the barge impact experiments.

Complementing the experimental components of this study, a revised vessel collision risk assessment procedure was developed in which the UF/FDOT barge impact load model, structural analysis procedures, and *PC* expression were inserted in place of analogous provisions of the AASHTO risk analysis framework. Because the various UF/FDOT methods are specific to, or have only been evaluated for, barge impact (and not ship impact), the revised risk assessment procedure includes two analysis tracks: one for ship impact and one for barge impact. For ship impact, all existing AASHTO procedures were retained, including the AASHTO *PC* expression. However, for barge impact, the impact load model was replaced with the UF/FDOT model, the *PC* expression was replaced with the UF/FDOT expression, and the AASHTO static structural analysis approach was replaced with the choice of two UF/FDOT dynamic analysis procedures: coupled vessel impact analysis (CVIA) and applied vessel impact loading (AVIL). The static bracketed impact analysis (SBIA) method was also evaluated but found to be too conservative for use in the risk assessment procedure, though it can be helpful for initially proportioning structural members during preliminary design stages.

Use of the revised UF/FDOT risk assessment procedure was demonstrated by applying it to the calculation of annual frequency of bridge collapse (*AF*) for two recently-constructed bridges: the SR-300 Bridge over Apalachicola Bay, Florida and the LA-1 Bridge over Bayou Lafourche, Louisiana. For comparison, *AF* was also computed using both the 1991 and 2009 editions of the AASHTO provisions. For both bridges, *AF* was found to be significantly higher when using the UF/FDOT procedures than when using the AASHTO procedures. This outcome was a consequence of two primary factors: (1) for piers of the bridges considered, the UF/FDOT barge impact load model typically predicted larger impact forces than the AASHTO load model; and (2) *PC* values computed using the UF/FDOT expression were higher than those computed using the AASHTO *PC* expression.

As discussed in Chapters 9 and 10, UF/FDOT barge impact forces were higher than AASHTO for the bridges considered in this study primarily due to the specific structural configuration of the bridge piers. Specifically, the piers in both bridges include wide, flat-faced pile caps (footings) that lie at the waterline and are therefore the most likely pier component to be impacted by barge vessels. Based on the UF/FDOT load model, the footing geometry resulted in larger impact forces than would be generated if the impacted pier surface were rounded or narrower. Retrofit and alternative design solutions were presented in Chapters 9 and 10 which employed rounded and narrower impact geometry. These retrofits and alternative designs were shown to have dramatically reduced collapse risk (smaller *AF*) relative to the as-built designs.

As noted above, and discussed at length in Chapters 9 and 10, the UF/FDOT *PC* expression uniformly resulted in higher *PC* values than the AASHTO expression. This outcome is partially a consequence of higher impact loads associated with the UF/FDOT load model, as discussed above. However, the primary cause of higher *PC* values was that, for the majority of

impact cases considered in the study (for both bridges), PC was calculated to be equal to 0.0 (zero) using the AASHTO expression. Note that such cases commonly involved scenarios in which the impact load was *nearly equal* to the maximum lateral pier resistance. Assigning a zero PC value to such situations (as AASHTO does) is unrealistic, in that it neglects numerous uncertainties associated with the strength of bridge materials, workmanship in construction, soil strength, impact angle, and dynamic interactions between the barge and bridge. As demonstrated by Davidson et al. (2013), when such factors were properly taken into account, the probability of structural collapse was non-zero even for cases in which the deterministically calculated (expected) impact load was much less than the expected pier resistance. Indeed, the UF/FDOT PC expression was specifically developed to account for these and many other relevant sources of uncertainty in impact loading and structural resistance, and accordingly, PC cannot be *equal* to 0.0 using the UF/FDOT expression. Consequently, while the UF/FDOT PC values were higher than the corresponding AASHTO values, the UF/FDOT values are a more rational and representative measure of collapse risk, by virtue of accounting for unavoidable statistical uncertainties.

As discussed at the end of Chapter 10, other terms in the AF expression (N , PA , PG , and PF), all of which were directly adopted into the UF/FDOT risk assessment methodology, may over-predict the probability of occurrence of vessel collision events in certain cases (and potentially all cases). For both example bridges examined in this study (Chapters 9 and 10), the terms N , PA , PG , and PF were combined to define the annual frequency of impact (AFI). Based on the available risk assessment data, the LA-1 Bridge is expected to undergo a significant vessel impact event approximately once per year ($AFI \approx 1.0$). However, no major impact events have occurred to date, even though the main bridge piers and spans have been in place in the waterway for more than five years. This finding strongly suggests that, when combined, the terms included in AFI over-predict the probability of occurrence of vessel impacts for certain cases, though it is unclear which term contributes most strongly to the discrepancy. For the SR-300 Bridge, which has less vessel traffic than the LA-1 Bridge, the historical record was not long enough to draw conclusions about the accuracy of AFI . As discussed below, additional research is warranted in this area.

A major concern in implementing the UF/FDOT methods in bridge design has been the necessary use of dynamic structural analysis. This requirement does indeed increase the effort associated with developing an adequate design. However, in preparing the demonstration cases for this study, the effort required to carry out the required structural analyses was found to be significant but not unreasonable. To carry out the example risk assessments, 208 structural analyses were required for the SR-300 Bridge, and 160 were required for the LA-1 Bridge. Quite clearly, automation of the analysis process—in which models were populated with the relevant case-specific data, analyzed, and post-processed to extract the important data by automated scripts—was crucial to completing the analyses in a timely manner. Once the process was automated, the analyses could be completed within 8 – 12 hours total using a typical workstation computer. In this study, most of the automation was accomplished using custom-developed programs written in the Perl programming language (Perl 2013). Alternatively, such automation could be programmed with a variety of general-purpose languages (e.g., C++, FORTRAN, etc.) or with more engineering-specific tools such as Matlab or even Mathcad. Developing the

automation framework was the most time-consuming aspect of carrying out the example risk assessments. However, once the framework was developed for the first bridge considered, it was readily and quickly adapted for use on the second bridge case. While creating and debugging such automation procedures constitutes significant effort on the part of engineers, the level of programming expertise required is relatively modest. Therefore, while the UF/FDOT methods are a significant departure from the current AASHTO provisions, the steps required to implement them could be completed by most bridge engineers without issue. Also, as recommended below, the transition to UF/FDOT methods could be greatly facilitated by implementing the required automation tasks in design-oriented analysis packages such as FB-MultiPier.

The results of this study demonstrate that the state-of-the-art analysis methods developed from UF/FDOT research over the past several years can feasibly be implemented in the design of bridges for vessel collision. The methods produced outcomes that were more rational than the existing AASHTO procedures and that included consideration for many additional factors that are important contributors to barge impact loads and dynamic structural response. Most importantly, it was demonstrated that UF/FDOT methods can predict a higher level of risk than the AASHTO procedures for *some* bridge configurations, while risk levels that are lower than AASHTO predicts can be achieved at similar construction cost by making careful design choices. However, in spite of this finding, it was noted that the terms in the current AASHTO *AF* expression associated with the probability of an impact event occurring may, in fact, overpredict this probability, thereby inflating risk estimates.

11.2 Recommendations for Bridge Design

- It is recommended that UF/FDOT vessel collision risk assessment procedure summarized in Chapter 8 and demonstrated in Chapters 9 and 10 be adopted for use in the design of future bridges.
- It is recommended that only *transient dynamic* structural analysis methods (CVIA, AVIL, or more refined methods) be used in conjunction with the UF/FDOT risk assessment procedure.
- It is recommended that the equivalent-static analysis method (SBIA) be used only for preliminary design, because the method is too conservative to be reasonably employed in the context of a risk assessment. Final structural assessment should be completed using transient dynamic methods (CVIA or AVIL).

11.3 Recommendations for Future Research

- Evidence from this study suggests that the AASHTO risk assessment procedure—and by extension, the UF/FDOT procedure—may over-predict the likelihood that bridges are impacted by errant vessels, which in this study, was expressed as the annual frequency of impact (*AFI*). In this study *AFI* was computed as the summation of every term in the

expression for the annual frequency of collapse (AF), excluding PC (i.e., N , PA , PG , and PF). For one of the bridges considered in this study (the LA-1 Bridge), AFI was found to be much higher than historical evidence would indicate. Therefore, the level of vessel collision risk was likely overestimated by the UF/FDOT risk assessment methods for this case (i.e., the actual risk for collapse is likely less than was calculated). Given these findings, further research is suggested in order to: (1) compare estimates of AFI to historical records of impact incidents for a wider spectrum of bridges; 2) determine if widespread discrepancies exist; and (3) should discrepancies exist, develop revised expressions for the terms that form AFI (e.g., PA , PG) using statistical analysis of relevant factors which contribute to the risk of an impact event occurring.

- A significant amount of the total effort required to carry out the UF/FDOT risk assessments was spent developing an automated analysis framework in which bridge pier finite element models were populated with the relevant case-specific impact parameters, analyses were carried out, and results were post-processed to extract data relevant to the risk assessment. Given that 150 – 200 transient dynamic impact analyses were required to complete the risk assessment for each bridge, this automated approach was crucial to completing the assessments in a timely manner. Analysis automation would be even more critical during the design of a new bridge, in which case the risk assessment might be conducted multiple times as the design is refined. Therefore, further research is suggested to implement similar analysis and data-reduction schemes into commercial bridge analysis software. The benefit of this effort would be to reduce the amount of programming that would be required of design engineers in order to implement the UF/FDOT risk analysis methodology. Given the collaborative research relationship that exists between UF, FDOT, and the Bridge Software Institute (BSI), FB-MultiPier would be an ideal candidate software package for this effort.
- As discussed in Chapter 8, the UF/FDOT structural analysis methods and PC expression have only been evaluated for barge impact scenarios, whereas ship impact scenarios are also common for many bridges. Consequently, the risk assessment methodology proposed in Chapter 8 includes two analysis tracks, in which UF/FDOT methods are suggested for barge impact, and the existing AASHTO methods are suggested for ship impact. Given the important limitations of the AASHTO methods (highlighted in both current and past studies), further research is suggested in order to: (1) validate the applicability of the various UF/FDOT methods to ship impact scenarios; or (2) develop similar alternative methods. From such research, a unified, single-track risk assessment procedure could be developed.

REFERENCES

- American Association of State Highway and Transportation Officials (AASHTO). (1991). *Guide specification and commentary for vessel collision design of highway bridges*, 1st Ed., Washington, DC.
- AASHTO. (1994). *LRFD bridge design specifications*, 1st Ed., Washington, DC.
- AASHTO. (2009). *Guide specification and commentary for vessel collision design of highway bridges*, 2nd Ed., Washington, DC.
- AASHTO. (2011). *LRFD bridge design specifications*, 5th Ed., Washington, DC.
- American Society of Civil Engineers (ASCE). (2010). *ASCE/SEI 7-10 Minimum design loads of buildings and other structures*, Reston, VA.
- American Society for Testing and Materials (ASTM). (2008). *A36/A36M-08 Standard specification for carbon structural steel*. West Conshohocken, PA.
- ASTM. (2012a). *A1011/A1011M-12b Standard specification for steel, sheet and strip, hot-rolled, carbon, structural, high-strength low-alloy and high-strength low-alloy with improved formability*, West Conshohocken, PA.
- ASTM. (2012b). *A370-12a Standard test methods and definitions for mechanical testing of steel products*, West Conshohocken, PA.
- Bardelcik, A., Worswick, M. J., Winkler S., and Wells, M.A. (2012) “A strain rate sensitive constitutive model for quenched boron steel with tailored properties.” *Int. J. Impact Eng.*, 50, 49-62.
- Bridge Software Institute (BSI). (2009). *FB-Deep user’s manual*, Univ. of Florida, Gainesville, FL.
- BSI (2010). *FB-MultiPier user’s manual*, Univ. of Florida, Gainesville, FL.
- European Committee for Standardization (CEN). (2006). *Eurocode 1: Actions on structures – Part 1-7: General actions – Accidental actions (EN 1991-1-7:2006)*, Brussels, Belgium.
- Conner, C., Conway, A., Benedict, B. A., and Christensen, B. A. (1982). *Modeling the Apalachicola system*. Technical Paper No. 23. Univ. of Florida, Gainesville, FL.
- Consolazio, G. R., and Cowan D. R. (2005). “Numerically efficient dynamic analysis of barge collisions with bridge piers.” *J. Struct. Eng.*, 131(8), 1256-1266.
- Consolazio, G. R., Cook, R. A., and McVay, M. C. (2006). *Barge impact testing of the St. George Island Causeway Bridge - Phase III: Physical testing and data interpretation*. Structures Research Report No. 26868, Engineering and Industrial Experiment Station, Univ. of Florida, Gainesville, FL.

- Consolazio, G. R., and Davidson, M. T. (2008). "Simplified dynamic barge collision analysis for bridge design." *Transportation Research Record 2050*, Transportation Research Board, Washington, DC, 13-25.
- Consolazio, G. R., McVay, M. C., Cowan, D. R., Davidson, M. T., and Getter, D. J. (2008). *Development of improved bridge design provisions for barge impact loading*. Structures Research Report No. 51117, Engineering and Industrial Experiment Station, Univ. of Florida, Gainesville, FL.
- Consolazio, G. R., Davidson, M. T., and Cowan, D. R. (2009). "Barge bow force-deformation relationships for barge-bridge collision analysis." *Transportation Research Record 2131*, Transportation Research Board, Washington, DC, 3–14.
- Consolazio, G. R., Davidson, M. T., and Getter, D. J. (2010a). *Vessel crushing and structural collapse relationships for bridge design*. Structures Research Report No. 72908/74039, Engineering and Industrial Experiment Station, Univ. of Florida, Gainesville, FL.
- Consolazio, G. R., Davidson, M. T., and Getter, D. J. (2010b). *Development and support of dynamic numerical modeling of aberrant rake barges impacting hurricane protection structures subjected to forces from a hurricane environment*. Structures Research Report No. 83710, Engineering and Industrial Experiment Station, Univ. of Florida, Gainesville, FL.
- Consolazio, G. R., Walters, R. A., and Harper, Z. S. (2012a). *Development of finite element models for studying multi-barge flotilla impacts*. Structures Research Report No. 87754, Engineering and Industrial Experiment Station, Univ. of Florida, Gainesville, FL.
- Consolazio, G. R., and Walters, R. A. (2012b). *Development of multiple-barge flotilla finite element models for use in probabilistic barge impact analysis of flexible walls*. Structures Research Report No. 94753, Engineering and Industrial Experiment Station, Univ. of Florida, Gainesville, FL.
- Consolazio, G. R., Bui, L. H., and Walters, R. A. (2012c). *Pendulum impact testing of an impact-breakaway, wind-resistant base connection for multi-post ground signs*. Structures Research Report No. 92174, Engineering and Industrial Experiment Station, Univ. of Florida, Gainesville, Fla.
- Davidson, M. T., Consolazio, G. R., and Getter, D. J. (2010). "Dynamic amplification of pier column internal forces due to barge-bridge collision." *Transportation Research Record 2172*, Transportation Research Board, Washington, DC, 11-22.
- Davidson, M. T., Consolazio, G. R., Getter, D. J., and Shah, F. D. (2013). "Probability of collapse expression for bridges subject to barge collision." *J. Bridge Eng.*, 18(4), 287-296.
- Ellingwood, B., Galambos, T. V., MacGregor, J. G., and Cornell, C. A. (1980). *Development of a probability based load criterion for American National Standard A58*. National Bureau of Standards, Washington, DC.

- Federal Emergency Management Agency (FEMA) (2003). *NEHRP Recommended provisions for seismic regulations for new buildings and other structures (FEMA 450)*, Washington, DC.
- Florida Department of Transportation (FDOT). (2013). *Structures manual - Volume 1: Structures design guidelines*, Tallahassee, FL.
- Getter, D. J., Consolazio, G.R., and Davidson, M. T. (2011), “Equivalent static analysis method for barge impact-resistant bridge design.” *J. Bridge Eng.*, 16(6), 718-727.
- Getter, D. J., and Consolazio, G. R. (2011). “Relationships of barge bow force-deformation for bridge design: Probabilistic consideration of oblique impact scenarios.” *Transportation Research Record 2251*, Transportation Research Board, Washington, DC, 3-15.
- Hsu, S. S., and Jones, N. (2004). “Quasi-static and dynamic axial crushing of thin-walled circular stainless steel, mild steel, and aluminum alloy tubes.” *Int. J. Crashworthiness*, 9(2), 195-217.
- Jones, N. (1997). *Structural Impact*, Cambridge Univ. Press, New York, NY.
- Jones, N. (2013). “The credibility of predictions for structural design subjected to large dynamic loadings causing inelastic behaviour.” *Int. J. Impact Eng.*, 53, 106-114.
- Jones, N., and Jones, C. (2002). “Inelastic failure of fully clamped beams and circular plates under impact loading.” *J. Mech. Eng. Sci.*, 216(C), 133-149.
- Kunz, C. U. (1998). “Ship bridge collision in river traffic, Analysis and design practice.” *Ship Collision Analysis* (H. Gluwer and D. Olsen, eds.), Balkema, Rotterdam, Netherlands, 13-22.
- Livermore Software Technology Corporation (LSTC). (2007). *LS-DYNA keyword user’s manual*, Livermore, CA.
- Manjoine, M. J. (1944). “Influence of rate of strain and temperature on yield stresses of mild steel.” *J. Appl. Mech. T. ASME*, 66, A211-A218.
- Meier-Dörnberg, K. E. (1983). *Ship collisions, safety zones, and loading assumptions for structures in inland waterways*. Verein Deutscher Ingenieure (Association of German Engineers) Report No. 496, Düsseldorf, Germany, 1–9.
- National Oceanic and Atmospheric Association (NOAA). (2013a). *Coast pilot 5: Gulf of Mexico, Puerto Rico, and Virgin Islands*, 41st Ed., Washington, DC.
- NOAA. (2013b). *Nautical chart 11404: Intracoastal waterway, Carrabelle to Apalachicola Bay*, Washington, DC.
- Nowak, A. S. (1999). “Calibration of LRFD bridge design code.” *NCHRP Report Volume 368*, Transportation Research Board, Washington, DC.

- Nowak, A. S., Szerszen, M. M., Szeliga, E. K., Szwed, A., and Podhorecki, P. J. (2008). "Reliability-Based Calibration for Structural Concrete, Phase 3." *PCA R&D Serial No. 2849*, Portland Cement Association and Precast/Prestressed Concrete Institute, Skokie, IL.
- Pedersen, P. T., Valsgard, S., Olsen, D., and Spangenberg, S. (1993). "Ship impacts: bow collisions." *Int. J. Impact Eng.*, 13(2), 163-187.
- Perl Foundation (Perl). (2013). *Perl 5 version 16.2 documentation*, Walnut, CA.
- Salmon, C. G., and Johnson, J. E. (1996). *Steel structures: Design and behavior*, 4th Ed., Harper Collins College Publishers, New York, NY.
- Shin, H. S., Lee, H. M., and Kim, M. S. (2000). "Impact tensile behaviors of 9% nickel steel at low temperature," *Int. J. Impact Eng.*, 24, 571-581.
- Symonds, P. S. (1967). "Survey of methods of analysis for plastic deformation of structures under dynamic loading." *Division of Engineering Report No. BU/NSDRG/1-67*, Brown Univ., Providence, RI.
- Thompson, A. C. (2006). *High strain rate characterization of advanced high strength steels*. Master's thesis, Univ. of Waterloo, Waterloo, Ontario.
- United States Coast Guard (USCG). (2013). *United States Coast Guard Maritime Information Exchange (CGMIX)*, Washington, DC, (<http://cgmix.uscg.mil>).
- Wang, T. L., and Liu C. (1999). *Synthesizing commercial shipping (barge/tug trains) from available data for vessel collision design*. Florida International Univ., Miami, FL.
- Woisin, G. (1976). "The collision tests of the GKSS." *Jahrbuch der Schiffbautechnischen Gesellschaft*, 70, 465-487.

APPENDIX A REVIEW OF EUROCODE PROCEDURES FOR VESSEL COLLISION

A.1 Introduction

European design and analysis procedures (in accordance with the Eurocode) for vessel collision with bridges are in many ways similar to those prescribed by AASHTO in the U.S. In the Eurocode, vessel collision is classified as an accidental action on structures and is consequently covered in *Eurocode 1: Actions on Structures Part 1-7: Accidental Actions* (CEN 2006). As with all Eurocode provisions, values for certain design parameters are not explicitly codified within the main Eurocode document. Such parameters are deemed Nationally Determined Parameters (NDPs) and are independently specified by each EU member nation by means of a National Annex (NA). Other nation-specific documents may exist to provide further design guidance or recommendations. For example, vessel collision design in the United Kingdom requires consideration of three (3) documents:

- *BS EN 1991-1-7:2006 Eurocode 1: Actions on Structures Part 1-7: Accidental Actions:* The core Eurocode provision, in part, pertaining to vessel collision with bridges. This provision may provide indicative design values for NDPs that can be used in lieu of guidance from the appropriate NA. This document is legally binding for all EU member nations.
- *NA to BS EN 1991-1-7:2006 National Annex to Eurocode 1: Actions on Structures Part 1-7: Accidental Actions:* UK-specific National Annex document, specifying NDPs that are relevant to *BS EN 1991-1-7*. This document is legally binding for the United Kingdom only.
- *PD 6688-1-7:2009 Recommendations for the Design of Structures to BS EN 1991-1-7:* UK-specific document providing additional recommendations pertaining to *BS EN 1991-1-7*. This document is not regarded as a British Standard, and recommendations provided herein are therefore not legally binding.

A.2 Risk Assessment

As with the AASHTO provisions, the Eurocode suggests that design for accidental actions (of which vessel collision is one) should be conducted within the context of a comprehensive risk assessment (risk analysis). It should be noted that the Eurocode risk assessment approach is significantly more open-ended than the procedure prescribed by AASHTO. Specific procedures related to quantifying risk are left to the discretion of the owner and design team.

The risk assessment framework proposed in the Eurocode is summarized in Figure A.1. In general, the process involves iterative qualitative and/or quantitative risk analysis, interspersed with reconsideration of the analysis scope and assumptions and design modifications. As part of each design iteration, the risk is re-evaluated, allowing the design team to identify economical risk mitigation schemes which may involve:

- Eliminating or reducing of the hazard by modifying the design concept;
- By-passing the hazard by changing the design concept or protecting the structure;
- Controlling the hazard by warning systems or monitoring;
- Overcoming the hazard by providing sufficient strength or structural redundancy such that overall structural failure does not occur, or;
- Permitting controlled structural collapse such that injury or fatality is reduced.

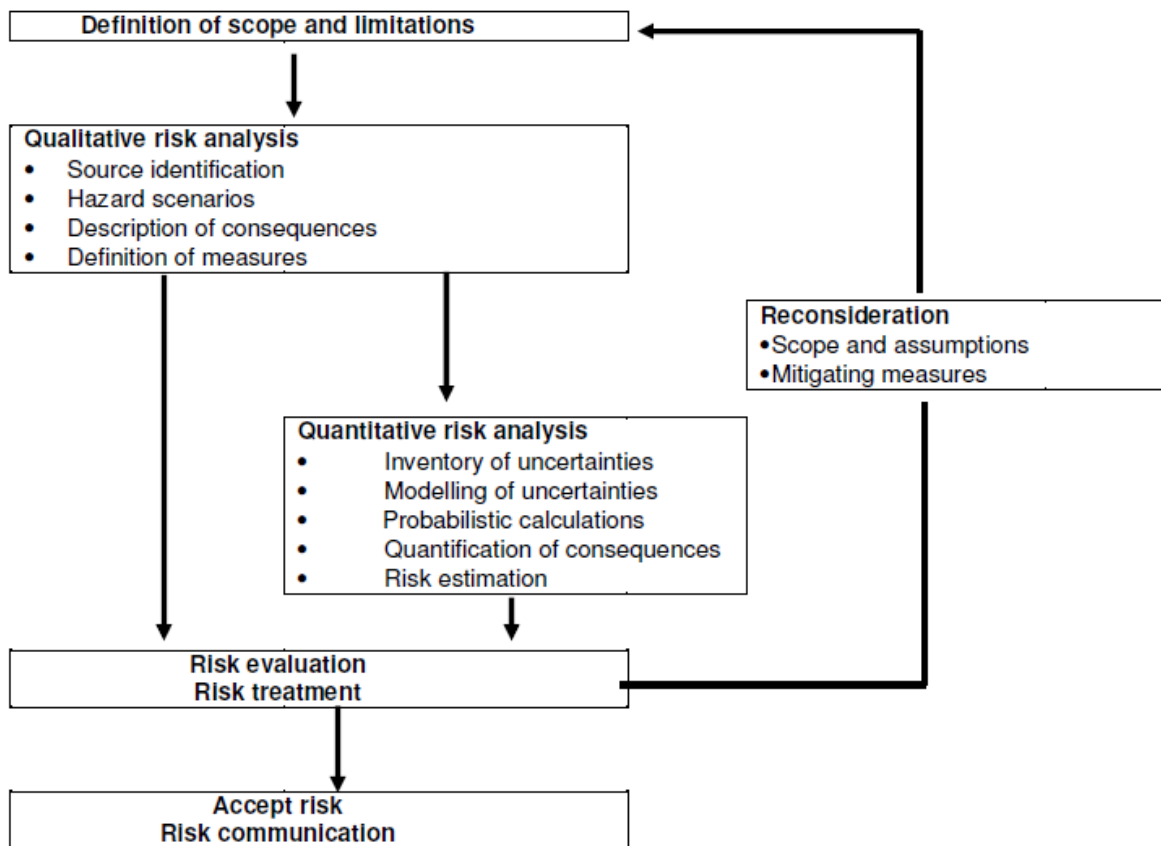


Figure A.1 Eurocode risk assessment framework (Source: *EN 1991-1-7:2006 §B.1*)

At the level of detail illustrated in Fig. A.1, the risk assessment may uncover economical means to mitigate risk (e.g., layout changes, protection systems, or warning systems) that are unrelated to structural strength. However, the risk of bridge failure as a result of vessel collision cannot be adequately assessed in a purely qualitative sense. As such, a quantitative risk analysis is necessary. The Eurocode provision EN 1991-1-7:2006 §B.9.2 states that risk (R), in general, can be quantified as a summation of conditional probabilities:

$$R = \sum_{i=1}^{N_H} p(H_i) \sum_{j=1}^{N_D} \sum_{k=1}^{N_S} p(D_j | H_i) \cdot p(S_k | D_j) \cdot C(S_k) \quad (\text{A.1})$$

where $p(H_i)$ is the probability of the i^{th} hazard (of total hazards N_H) occurring in a given time interval (typically one year), $p(D_j | H_i)$ is the probability of j^{th} damage state (of total number N_D) occurring as a result of the i^{th} hazard, $p(S_k | D_j)$ is the probability of the k^{th} adverse structural performance (of total number N_S) occurring as a result of the j^{th} damage state, and $C(S_k)$ is the consequence of the k^{th} adverse structural performance. Given the comprehensive nature of this expression, its direct applicability to vessel collision risk analysis is limited. Thus, an expression specific to vessel collision is given in §B.9.3.3:

$$P_f(T) = n \lambda T (1 - p_a) \int P(F_{\text{dyn}}(x) > R) dx \quad (\text{A.2})$$

where $P_f(T)$ is the probability of structural failure within a given time period (T), n is the ship traffic intensity, λ is the probability of navigation failure per unit traveling distance, p_a is the probability that collision can be avoided by human intervention, F_{dyn} is the dynamic impact force as a function of the coordinate (x) where navigation failure occurred, and R is the structural resistance. Note that if $T = 1$ year, then $P_f(T)$ is the annual frequency of collapse (parameter AF in the AASHTO provisions).

While §C.4 proposes load models to quantify F_{dyn} (described below), the provision provides no guidance into how F_{dyn} is influenced by the position of navigation failure (x). Furthermore no Eurocode provision, National Annex, or other official document provides guidance on quantifying λ , p_a , or the probability that F_{dyn} exceeds R . Sufficient records are typically available to estimate traffic intensity (n). Consequently, implementation of the above expression would require a significant degree of judgment and/or very sophisticated probabilistic analysis.

A.3 Risk Acceptance Criteria

As part of any risk assessment, risk acceptance criteria must be set forth which define (usually quantitatively) the maximum reasonable risk to the public of injury or death posed by a given structural hazard. Such criteria can be based on monetary loss (including repair and litigation costs), loss of life, or annual probabilities of structural failure. Most commonly, acceptable probabilities for structural failure (or damage) are set forth by government agencies and industry groups. For example, AASHTO specifies that the annual frequency of bridge collapse due to vessel collision should be, at most, 0.001 for non-critical bridges, and 0.0001 for

critical bridges. In other words, structural failure should, on average, occur once every 1,000 years for non-critical bridges and once every 10,000 years for critical bridges.

In the Eurocode provisions (*EN 1991-1-7:2006*), no value is specified for the acceptable frequency of bridge collapse due to vessel collision. Eurocode §3.2(1) states:

Levels of acceptable risks may be given in the National Annex as non contradictory, complementary information.

Additionally, §B.5(4) states:

Acceptance criteria may be determined from certain national regulations and requirements, certain codes and standards, or from experience and/or theoretical knowledge that may be used as a basis for decisions on acceptable risk. Acceptance criteria may be expressed qualitatively or numerically.

One quantitative risk acceptance scheme is provided in §B.4.2, primarily for illustration purposes, not as a direct recommendation (Fig. A.2). Note that, in this example, the maximum acceptable probability of structural collapse is 0.00001 (1 in 100,000 years), which is 10 times more stringent than the AASHTO requirement for critical structures. Larger maximum acceptable probabilities are assigned to less severe consequences.

Severe	X				
High	X				
Medium		X			
Low			X		
Very low				X	
consequence					
probability	0,00001	0,0001	0,001	0,01	> 0,1
X represents examples of maximum acceptable risk levels					

Clarification: The severity of potential failure is identified for each hazard scenario and classified as Severe, High, Medium, Low or Very Low. They may be defined as follows:

- Severe Sudden collapse of structure occurs with high potential for loss of life and injury.
- High Failure of part(s) of the structure with high potential for partial collapse and some potential for injury and disruption to users and public.
- Medium Failure of part of the structure. Total or partial collapse of structure unlikely. Small potential for injury and disruption to users and public.
- Low Local damage
- Very Low Local damage of small importance

Figure A.2 Possible numerical risk acceptance scheme (Source: *EN 1991-1-7:2006 §B.4.2*)

Given the ambiguity associated with this important parameter, the British National Annex to *EN 1991-1-7:2006 (NA to BS EN 1991-1-7:2006)* was consulted for further guidance. Note that the British NA is the only readily available NA to *EN 1991-1-7:2006* in English. §NA.2.3 (Level of acceptable risk) states:

The level of acceptable risk should be determined on a project specific basis. Recommendations for acceptable risk levels for road, footway, and cycletrack bridges are contained in *PD 6688-1-7*.

Thus, British Published Document *PD 6688-1-7* was consulted for such recommended values. §2.3.1 of *PD 6688-1-7* (Levels of acceptable risk) states:

The design of bridge support structures should ensure that the risks of an HGV [Heavy Goods Vehicle] striking a bridge support and causing structural collapse are as low as reasonably practicable (ALARP) taking account of site conditions.

This provision is the only section in *PD 6688-1-7* pertaining to risk acceptance criteria, and the language is specifically targeted at impact by Heavy Goods Vehicles (HGVs) and other vehicular traffic. In fact, no additional guidance for *any* parameter related to waterway vessel impact is provided in either *NA to BS EN 1991-1-7:2006* or *PD 6688-1-7*. All sections of the NA pertaining to vessel collision refer back to the main Eurocode provision (*EN 1991-1-7:2006*). For example, §NA.2.38 (Dynamic impact forces from seagoing ships) reads:

Values of frontal and lateral dynamic impact forces from seagoing ships should be agreed for the individual project. The recommended and indicative value may be used for preliminary design.

Thus, final design ship impact forces are to be determined at the discretion of the design team and owner. This pattern is consistent for virtually all British NA sections. In a few cases, the *EN 1991-1-7:2006* indicative value is simply accepted, without allowing for project-specific determination (e.g., friction coefficient for glancing impact). Consequently, as it pertains to vessel impact, the *NA to BS EN 1991-1-7:2006* and *PD 6688-1-7* documents are unnecessary. The core Eurocode (*EN 1991-1-7:2006*), combined with the judgment of the engineers and owner, are legally sufficient to define all vessel impact risk and structural demand parameters.

A.4 Vessel Impact Forces on Bridge Piers

Eurocode *EN 1991-1-7:2006* provides a fairly comprehensive treatment of vessel (barge and ship) impact loading on bridge piers. The provisions are similar, in many ways, to the AASHTO provisions. However, additional emphasis is placed on dynamic structural analysis. In general, vessel impact is defined as “hard impact,” in that the impacted pier is assumed to be rigid, and *all* kinetic energy is absorbed by elastic or plastic deformation of the vessel (§C.4.1). In lieu of dynamic analysis, indicative static force values are provided for both inland waterway vessels (Table C.3) and seagoing vessels (Table C.4). These two tables have been adapted here in Table A.1 and Table A.2, respectively.

Table A.1 Indicative values for dynamic forces due to ship impact on inland waterways (adapted from *EN 1991-1-7:2006*)

Class	Ship type	Length: l (m)	Mass: m (ton)	Force: F_{dx} (kN)	Force: F_{dy} (kN)
I		30-50	200-400	2,000	1,000
II		50-60	400-650	3,000	1,500
III	“Gustav-König”	60-80	650-1,000	4,000	2,000
IV	Class “Europe”	80-90	1,000-1,500	5,000	2,500
Va	Big ship	90-110	1,500-3,000	8,000	3,500
Vb	Tow + 2 barges	110-180	3,000-6,000	10,000	4,000
VIa	Tow + 2 barges	110-180	3,000-6,000	10,000	4,000
VIb	Tow + 4 barges	110-190	6,000-12,000	14,000	5,000
VIc	Tow + 6 barges	190-280	10,000-18,000	17,000	8,000
VII	Tow + 9 barges	300	14,000-27,000	20,000	10,000

Table A.2 Indicative values for dynamic forces due to ship impact for sea waterways (adapted from EN 1991-1-7:2006)

Class	Length: l (m)	Mass: m (ton)	Force: F_{dx} (kN)	Force: F_{dy} (kN)
Small	50	3,000	30,000	15,000
Medium	100	10,000	80,000	40,000
Large	200	40,000	240,000	120,000
Very large	300	100,000	460,000	230,000

Note that two independent impact cases are considered as part of Eurocode analysis: head-on impact (Fig. A.3) and glancing (lateral) impact (Fig. A.4). In the head-on case, force F_{dx} (as defined in Tables A.1 and A.2) is applied perpendicular to the bridge superstructure. In the glancing case, F_{dy} is applied parallel to the superstructure, and a friction force ($F_R = \mu F_{dy}$) is applied perpendicular to the superstructure. Friction coefficient, μ , is taken to be 0.4.

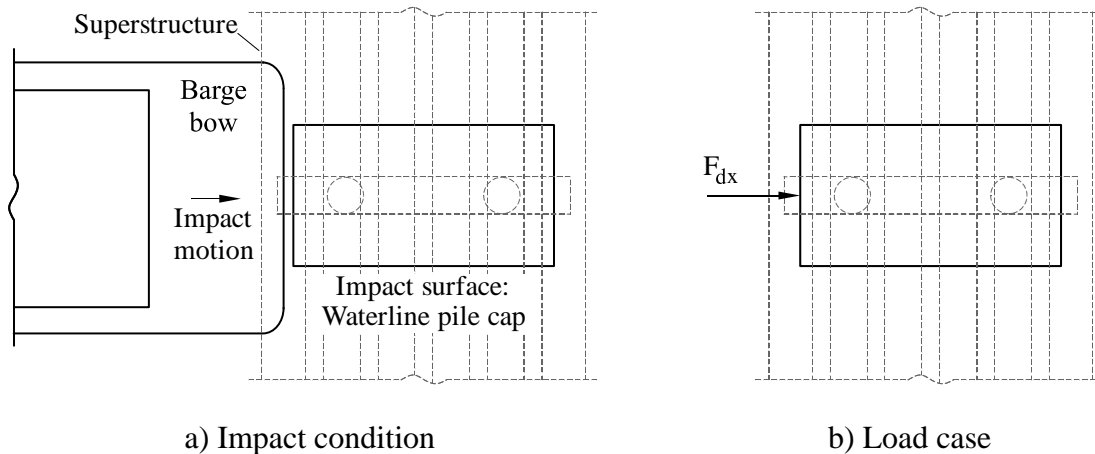


Figure A.3 Eurocode head-on impact case

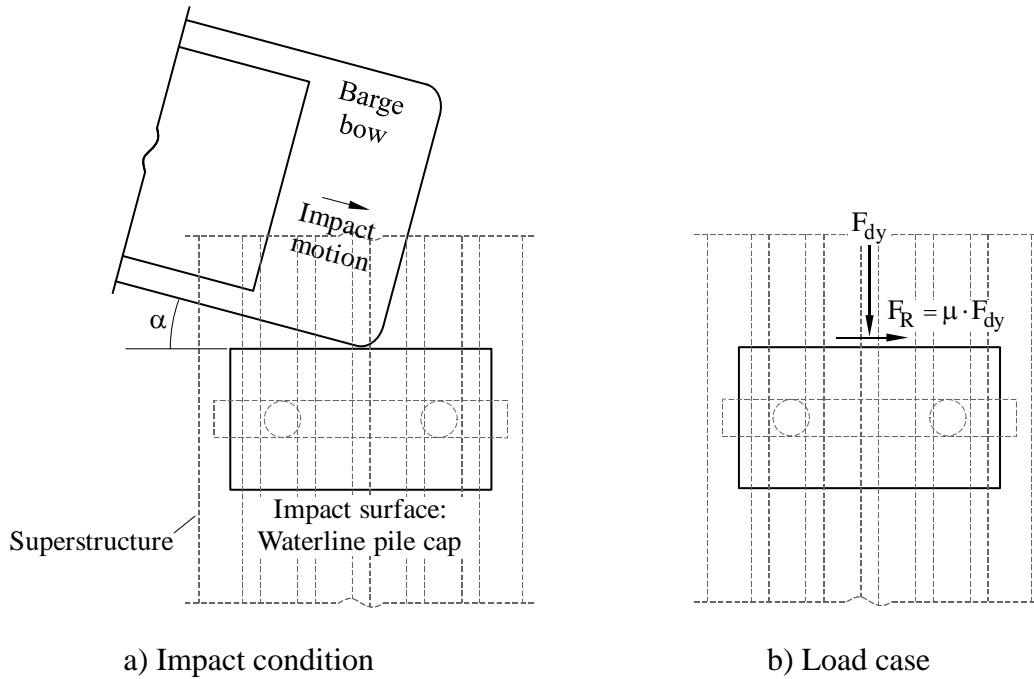


Figure A.4 Eurocode glancing (lateral) impact case

More refined methods are provided for computing both barge and ship impact forces, and, to some extent, force time-histories for dynamic analysis. Such procedures are detailed below and, where possible, compared to forces predicted by the AASHTO provisions.

A.4.1 Barge impact

Both the AASHTO and Eurocode provisions utilize the barge force-deformation relationship proposed by Meier-Dörnberg (1983), but with slightly varying formulations. In the Eurocode, all barge kinetic energy is assumed to be absorbed by the bridge pier through elastic and/or plastic deformation during head-on impact. Thus, deformation energy (E_{def}) is simply equal to the kinetic energy, and peak dynamic impact force (F_{dyn}) can be computed as:

$$\begin{aligned}
 F_{\text{dyn}} &= 10.95\sqrt{E_{\text{def}}} && \text{if } E_{\text{def}} \leq 0.21 \text{ MNm} \\
 F_{\text{dyn}} &= 5.0\sqrt{1+0.128 \cdot E_{\text{def}}} && \text{if } E_{\text{def}} > 0.21 \text{ MNm}
 \end{aligned}
 \tag{A.3}$$

where F_{dyn} is in MN and E_{def} is in MNm. E_{def} can simply be calculated as the initial kinetic energy of the impacting vessel:

$$E_{\text{def}} = \frac{1}{2} m^* v_{\text{rd}}^2 \quad (\text{A.4})$$

where v_{rd} is the impact velocity (3 m/s is recommended, increased by water velocity), and m^* is the sum of the vessel mass (m_1) and hydrodynamic mass (m_{hydr}). For head-on impact, m_{hydr} is taken as 10% of m_1 . Thus, $m^* = 1.1m_1$.

For static analysis, it is recommended that F_{dyn} be multiplied by a dynamic magnification factor of 1.3. The magnified F_{dyn} is then applied as shown in Figure A.3, as F_{dx} . The AASHTO impact force expression can also be expressed as a function of kinetic energy, and is shown in comparison to the Eurocode expression in Figure A.5 (Eurocode quantities have been converted to U.S. customary units). Note that the Eurocode F_{dyn} is lower than the AASHTO P_B (in the plastic range). However, once magnified by 1.3, Eurocode forces are higher than AASHTO.

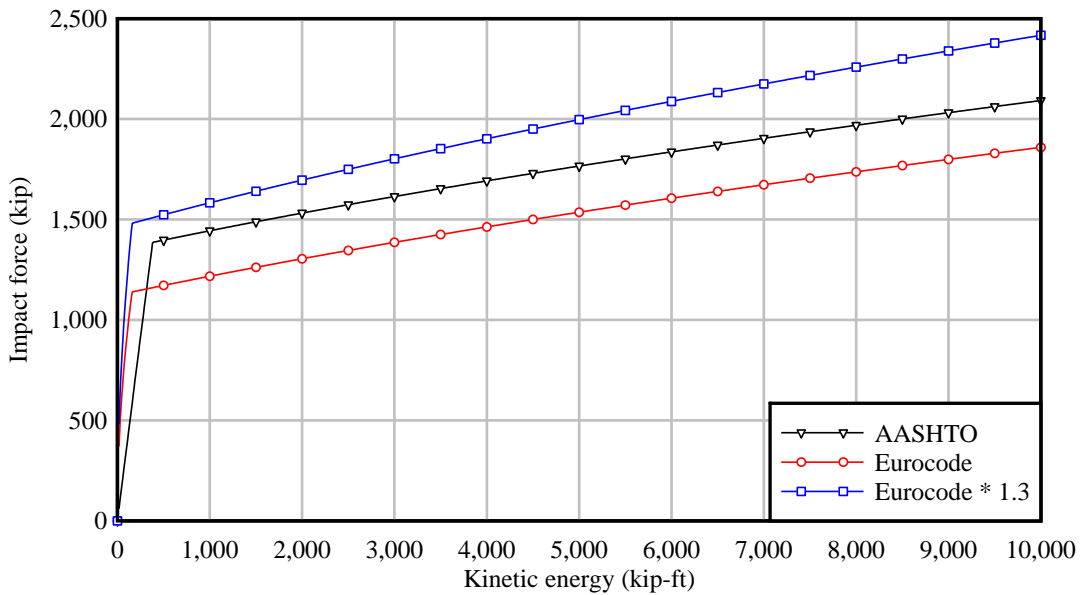


Figure A.5 Head-on barge impact force comparison: AASHTO vs. Eurocode

For glancing (lateral) impact, forces are computed using the $F_{\text{dyn}}(E_{\text{def}})$ expression above. However, E_{def} is reduced based on the impact angle, α (recall Fig. A.4):

$$E_{\text{def}} = E_a (1 - \cos \alpha) \quad (\text{A.5})$$

where E_a is the total kinetic energy. As with head-on impact, E_a is computed as:

$$E_a = \frac{1}{2} m^* v_{rd}^2 \quad (A.6)$$

However, for lateral impact:

$$m^* = \frac{m_1 + m_{hydr}}{3} = 0.367 m_1 \quad (A.7)$$

For cases in which α is not known, α can be assumed as 20° . For static analysis, the Eurocode suggests a dynamic magnification factor of 1.7 for glancing impact. The magnified F_{dyn} is applied as shown in Figure A.4, as F_{dy} . A friction force ($F_R = \mu F_{dy}$) is also applied, where $\mu = 0.4$.

For dynamic analysis, *a priori* formation of the impact force time-history is suggested. Force histories differ, depending on whether the plastic force (5 MN) is exceeded. Sample elastic and plastic force histories are given in the code (shown in Fig. A.6). Note that no expressions are provided to quantify important time quantities (e.g., t_r , t_e , t_p). However, these quantities can be derived, as needed, using energy and momentum conservation laws.

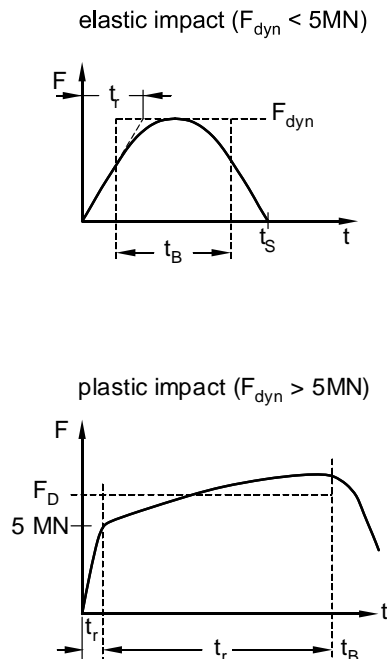


Figure A.6 Eurocode sample force time-histories (Reproduced from *EN 1991-1-7:2006*)

A.4.2 Ship impact

For ship impact, the AASHTO and Eurocode provisions differ substantially. The ship load model proposed in AASHTO is based upon impact tests conducted by Woisin (1976), whereas the Eurocode provisions use a newer model proposed by Pedersen et al (1993). According to the latter, the ship impact load (F_{bow}) is computed as:

$$F_{\text{bow}} \begin{cases} F_0 \cdot \bar{L} \left[\bar{E}_{\text{imp}} + (5.0 - \bar{L}) \bar{L}^{1.6} \right]^{0.5} & \text{for } \bar{E}_{\text{imp}} \geq \bar{L}^{2.6} \\ 2.24 \cdot F_0 \left[\bar{E}_{\text{imp}} \bar{L} \right]^{0.5} & \text{for } \bar{E}_{\text{imp}} < \bar{L}^{2.6} \end{cases} \quad (\text{A.8})$$

where:

$$\bar{L} = L_{\text{pp}} / 275 \text{ m}$$

$$\bar{E}_{\text{imp}} = E_{\text{imp}} / 1425 \text{ MNm}$$

$$E_{\text{imp}} = \frac{1}{2} m_x v_o^2$$

F_{bow}	is the maximum bow collision force (MN)
F_0	is the reference collision force = 210 MN
E_{imp}	is the energy absorbed by plastic deformations
L_{pp}	is the length of the vessel (m)
m_x	is the mass plus hydrodynamic mass (10^6 kg)
v_o	is the initial vessel speed = 5 m/s

For dynamic analysis, the impact duration (T_o) can be computed as:

$$T_o \approx 0.83 \frac{\pi E_{\text{imp}}}{F_{\text{bow}} v_o} \quad (\text{A.9})$$

However, no guidance is provided as to the shape of the load-history curve. Given the significant difference in formulation between the AASHTO and Eurocode ship impact force models, a direct graphical comparison (as shown in Figure A.5 for barge impact) cannot be readily produced.

APPENDIX B DERIVATION OF SCALE-MODEL SIMILITUDE EXPRESSIONS

In this appendix, an energy similitude expression is derived using the Buckingham π theorem (Jones 1997). Consider barge impact with a rigid object. The magnitude of impact force (P) is a function of a variety of system variables:

$$P = P(f_y, \Delta, w, h) \quad (\text{B.1})$$

where f_y is the yield strength of the barge steel, Δ is barge bow deformation, w is the width of the impacted object, and h is a representative barge dimension (e.g., a plate thickness). As such, there are $k = 4$ system variables (f_y, Δ, w, h). The force-length-time (FLT) reference unit system is chosen, but none of the relevant variables are time-dependent. Thus, there are $r = 2$ reference variables (F and L).

The Buckingham π theorem states that the problem can be described using $r + 1 = 3$ dimensionless groups of variables (π groups) such that:

$$\pi_1 = \phi(\pi_2, \pi_3) \quad (\text{B.2})$$

where ϕ represents an arbitrary function. To form each π group, choose $k - r = 2$ repeating variables from among the list of system variables. In this case, f_y and h are chosen. Thus:

$$\pi_1 = \pi_1(P, f_y, h); \quad \pi_2 = \pi_2(\Delta, f_y, h); \quad \pi_3 = \pi_3(w, f_y, h) \quad (\text{B.3})$$

By inspection or by more systematic means, the π groups are formed by arranging the dependent variables into dimensionless combinations. For this case:

$$\pi_1 = \frac{P}{f_y h^2}; \quad \pi_2 = \frac{\Delta}{h}; \quad \pi_3 = \frac{w}{h} \quad (\text{B.4})$$

Consequently,

$$\frac{P}{f_y h^2} = \phi\left(\frac{\Delta}{h}, \frac{w}{h}\right) \quad (\text{B.5})$$

Once derived, the π groups can be used to compute scale factors that relate model-scale physical quantities (denoted with the subscript m) to full-scale physical quantities (denoted with the subscripts fs). Consider a reduced-scale barge impact experiment in which the length scale factor is $\beta = h_{fs}/h_m$. A scale factor for impact force (P) can be derived using π_1 from above. Because π_1 is dimensionless,

$$\pi_{1,m} = \pi_{1,fs} \Rightarrow \left(\frac{P}{f_y h^2}\right)_m = \left(\frac{P}{f_y h^2}\right)_{fs} \quad (\text{B.6})$$

Rearranging:

$$P_{fs} = \left(\frac{f_{y,fs}}{f_{y,m}}\right) \left(\frac{h_{fs}}{h_m}\right)^2 P_m \quad (\text{B.7})$$

In most experiments, material parameters cannot be scaled along with the dimensions, thus $f_{y,fs}/f_{y,m} = 1$. Recall $h_{fs}/h_m = \beta$. Therefore:

$$P_{fs} = \beta^2 P_m \quad (\text{B.8})$$

Therefore, forces measured during a reduced-scale model can be multiplied by a factor of β^2 to obtain equivalent full-scale forces. Repeating a similar derivation, it can be shown that barge bow deformations (Δ) are related by:

$$\Delta_{fs} = \beta \Delta_m \quad (\text{B.9})$$

Combining Eqns. B.8 and B.9, a scaling expression for deformation energy (E) is derived:

$$\begin{aligned} E_{fs} &= P_{fs} \Delta_{fs} = (\beta^2 P_m)(\beta \Delta_m) = \beta^3 P_m \Delta_m \\ E_{fs} &= \beta^3 E_m \end{aligned} \tag{B.10}$$

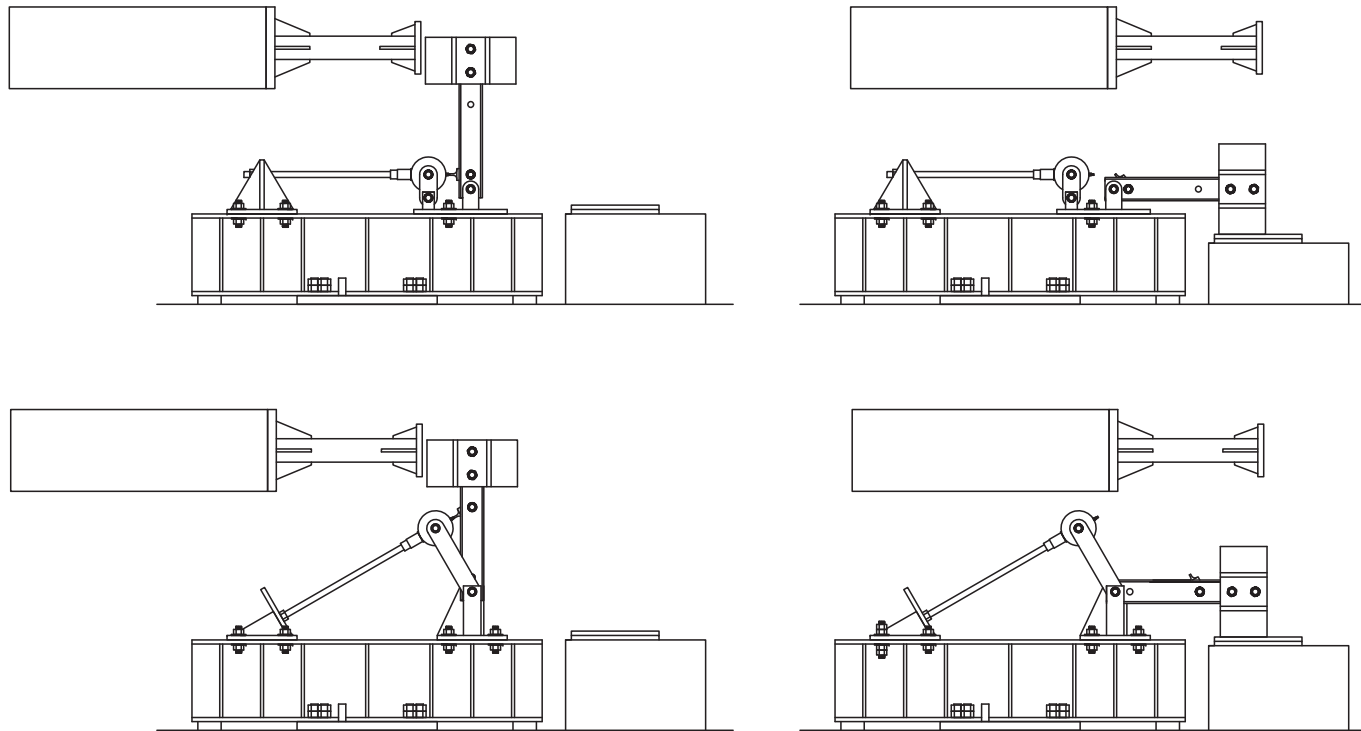
APPENDIX C
HIGH-RATE TEST APPARATUS (HRTA) FABRICATION DRAWINGS

Pendulum-Based High-Rate Test Apparatus (HRTA)

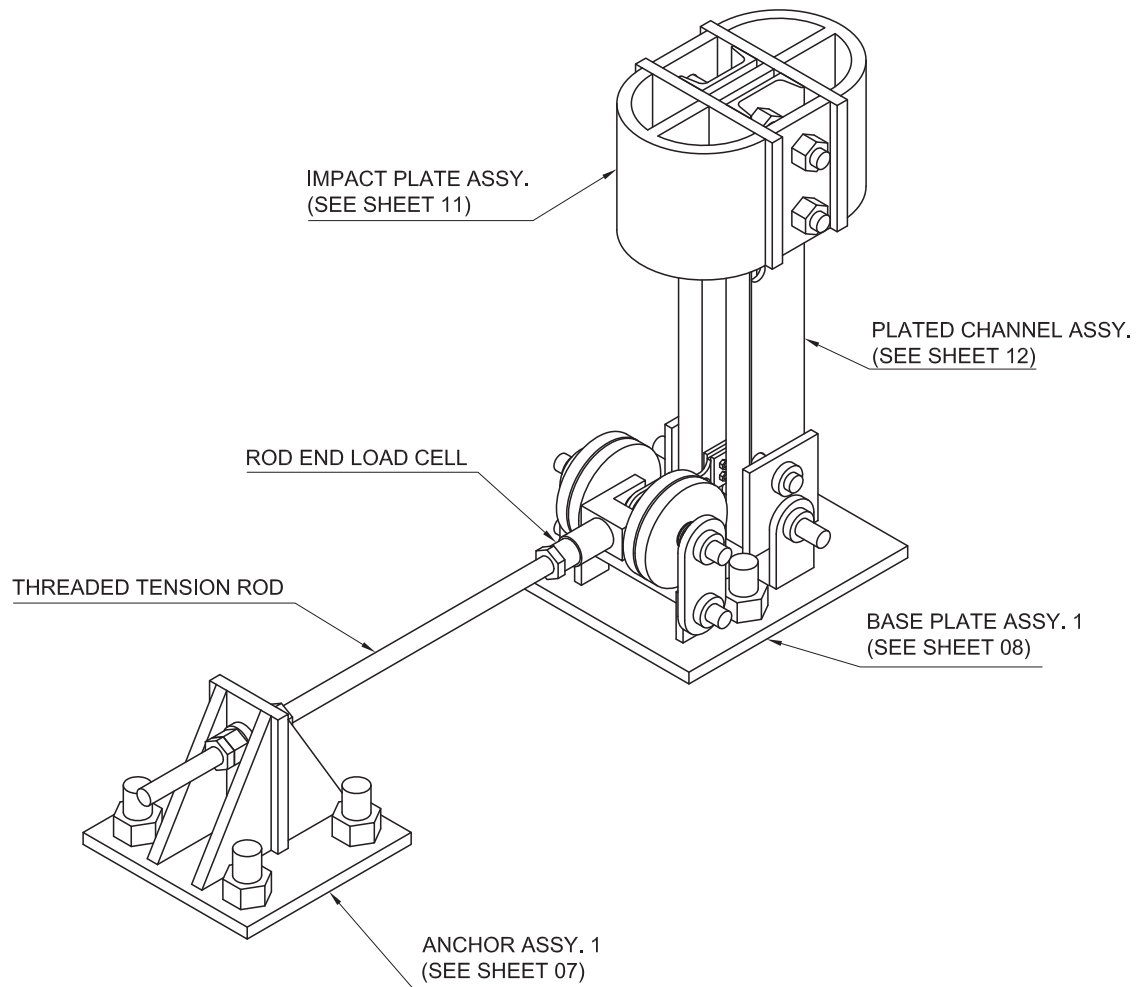
GENERAL NOTES:

All 1" diameter holes shall be machined fit with hardened steel shafts.

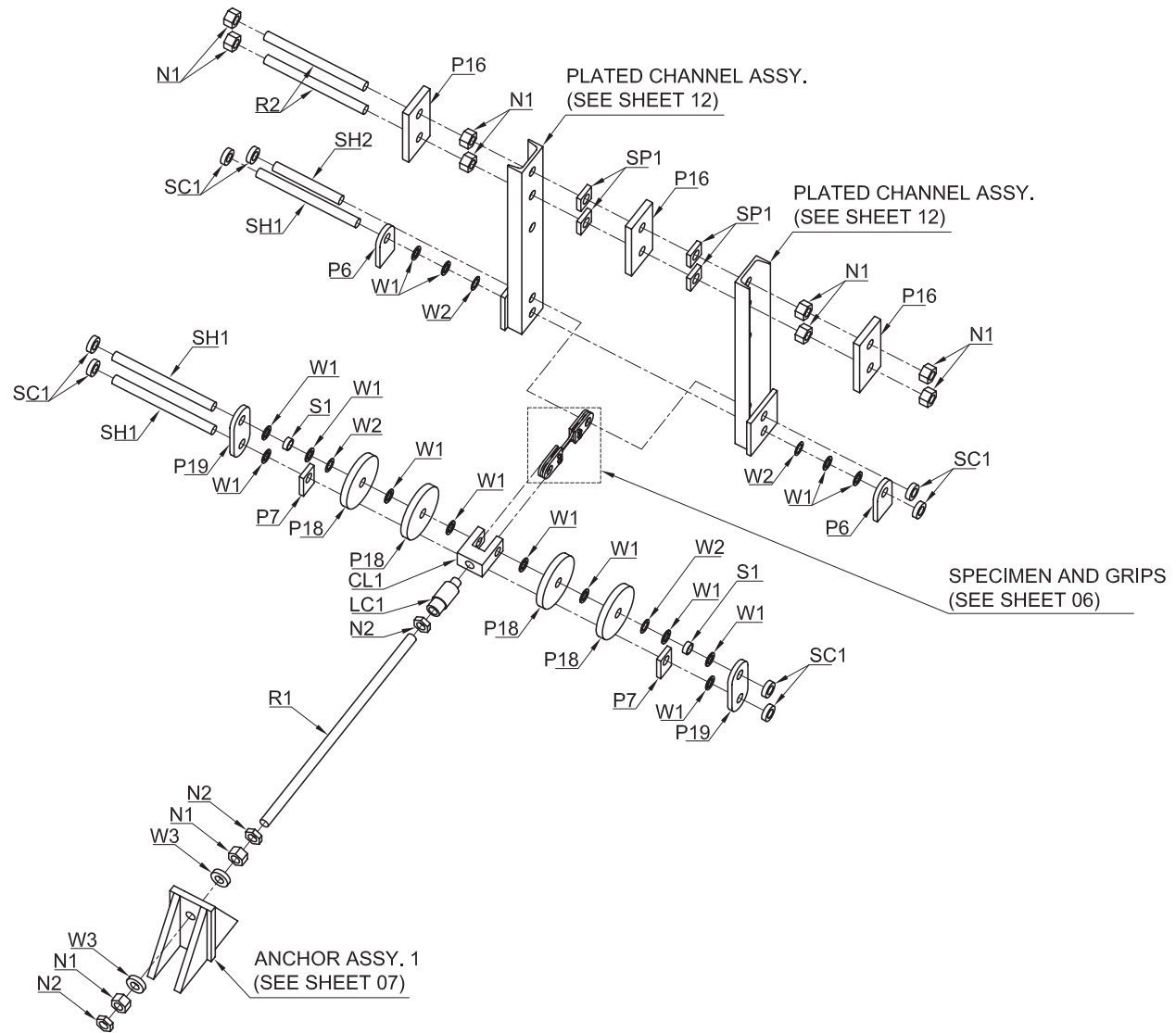
Standard washers may not be substituted in place of lubricated thrust bearing washers (W1, W2).



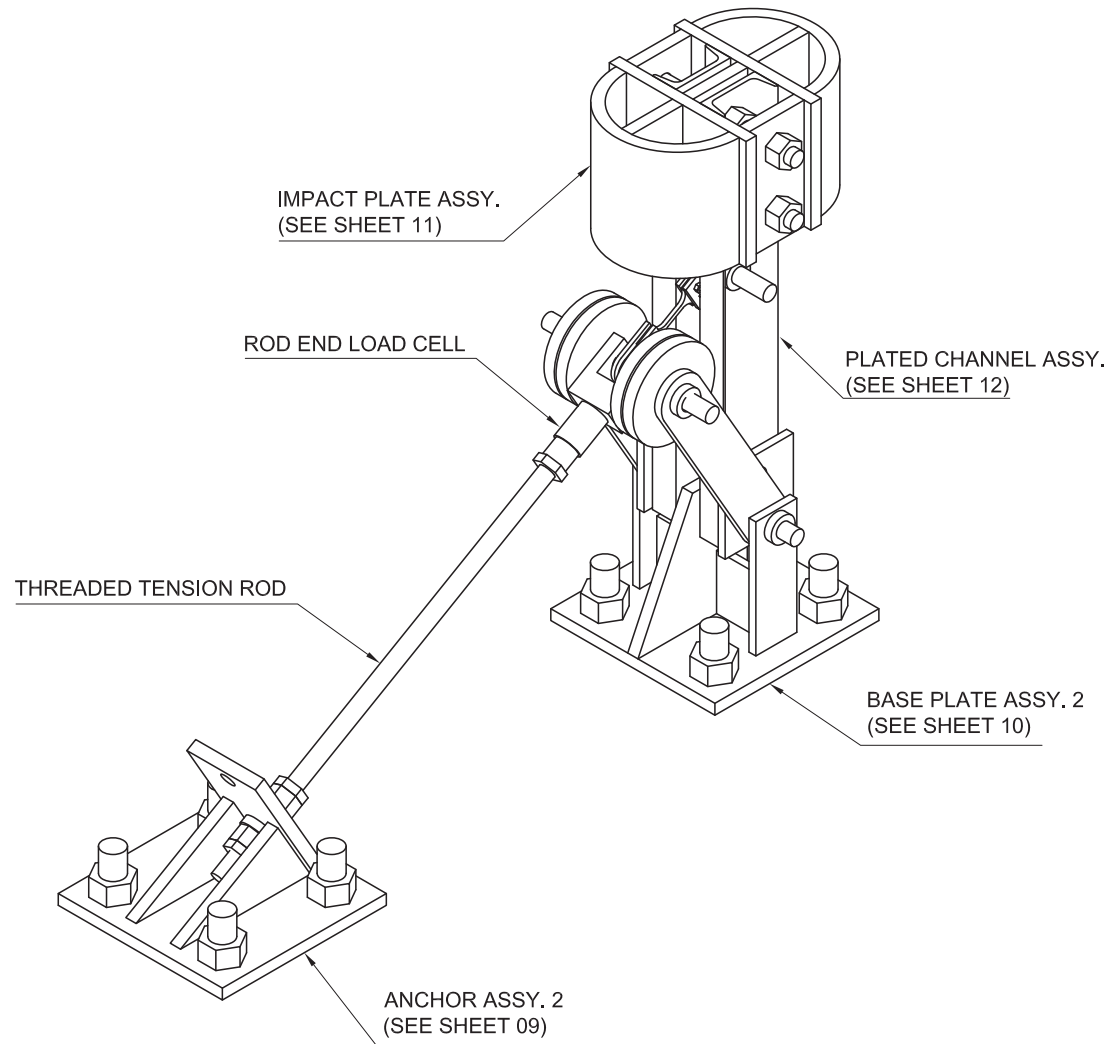
<i>Pendulum-Based High-Rate Test Apparatus (HRTA)</i>				<i>Revisions:</i>	<i>2012-03-30</i>	
<i>General Notes</i>	<i>2013-06-24</i>	<i>University of Florida</i>	<i>Sheet 01 of 24</i>			



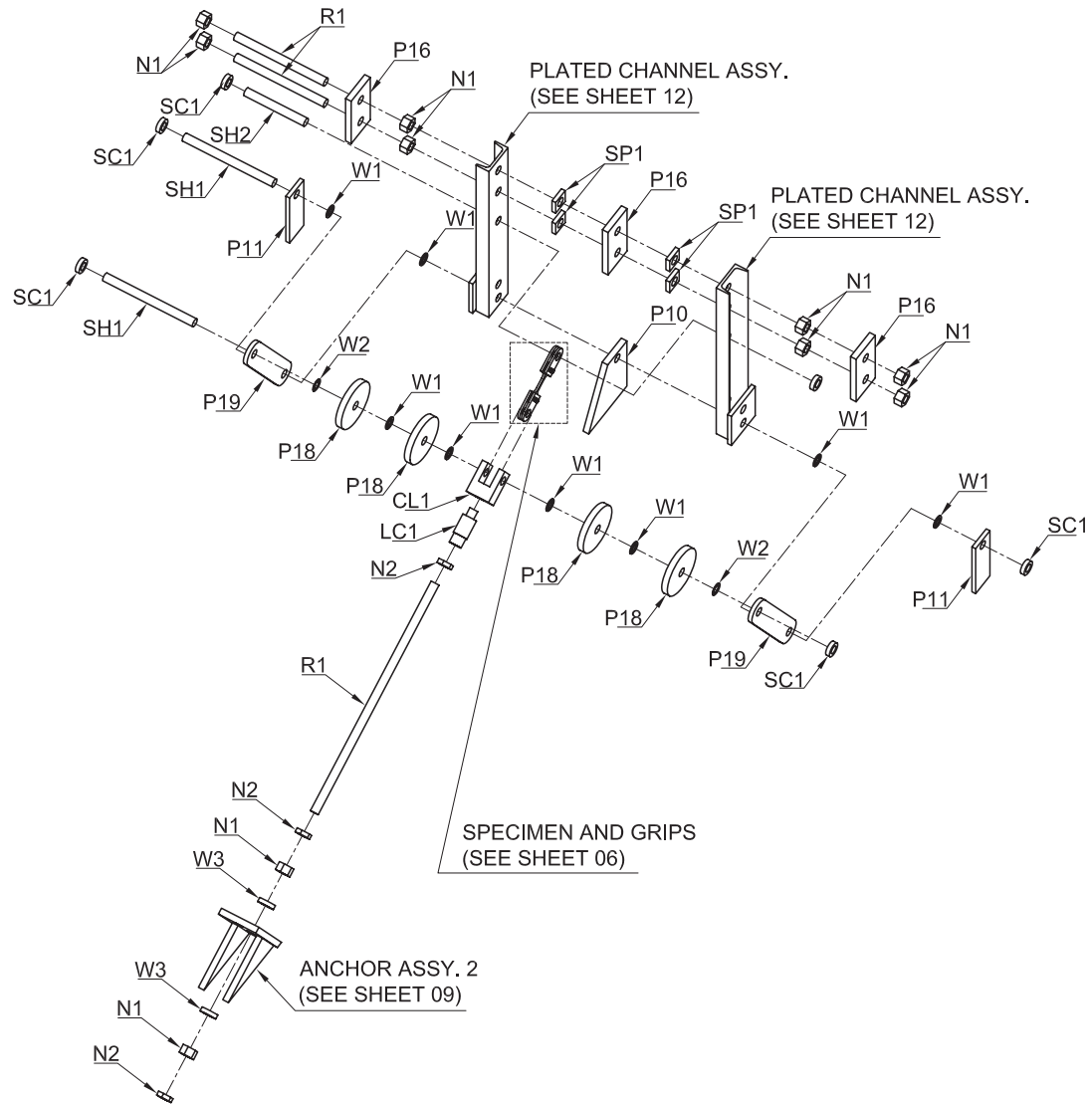
<i>Pendulum-Based High-Rate Test Apparatus (HRTA)</i>				<i>Revisions:</i>		
<i>Configuration 1 Overview</i>	<i>2013-06-24</i>	<i>University of Florida</i>	<i>Sheet 02 of 24</i>			



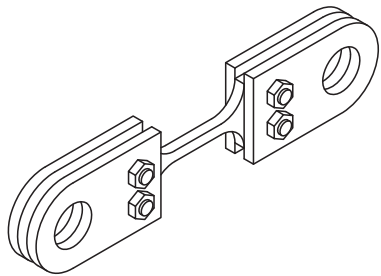
<i>Pendulum-Based High-Rate Test Apparatus (HRTA)</i>				<i>Revisions:</i>		
<i>Configuration 1 Details</i>	<i>2013-06-24</i>	<i>University of Florida</i>	<i>Sheet 03 of 24</i>			



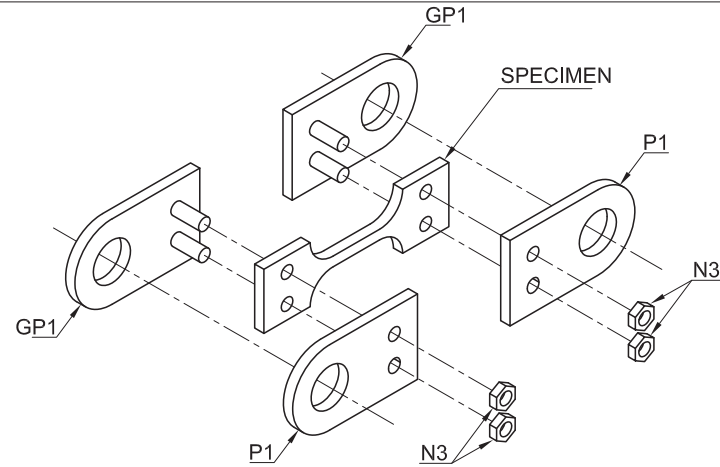
<i>Pendulum-Based High-Rate Test Apparatus (HRTA)</i>				<i>Revisions:</i>		
<i>Configuration 2 Overview</i>	<i>2013-06-24</i>	<i>University of Florida</i>	<i>Sheet 04 of 24</i>			



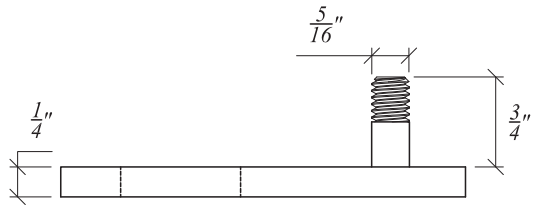
<i>Pendulum-Based High-Rate Test Apparatus (HRTA)</i>				<i>Revisions:</i>		
<i>Configuration 2 Details</i>	<i>2013-06-24</i>	<i>University of Florida</i>	<i>Sheet 05 of 24</i>			



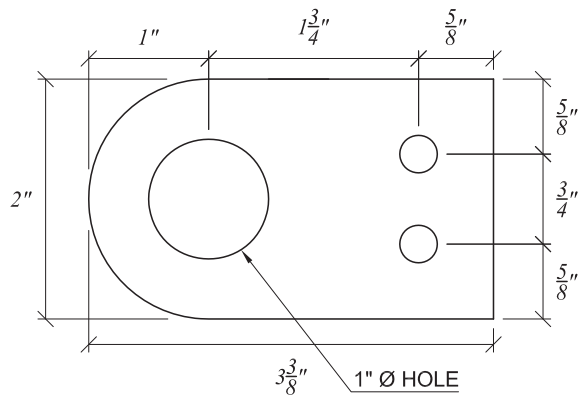
SPECIMEN AND GRIPS
ISOMETRIC VIEW



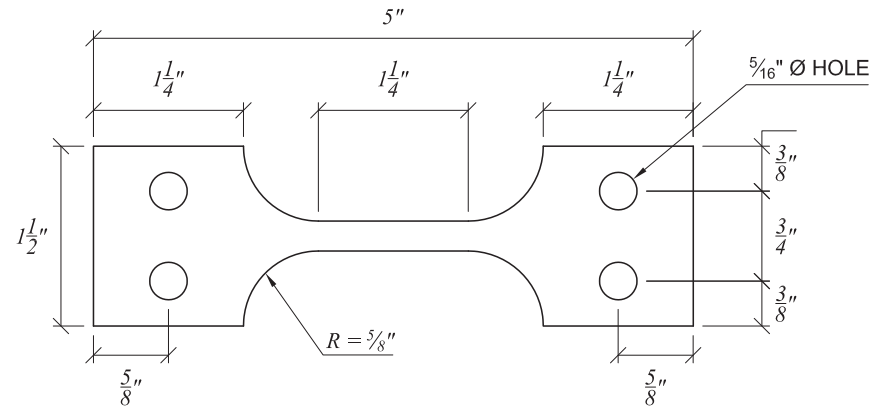
SPECIMEN AND GRIPS
EXPLODED VIEW



GRIP PLATE GP1
SIDE VIEW

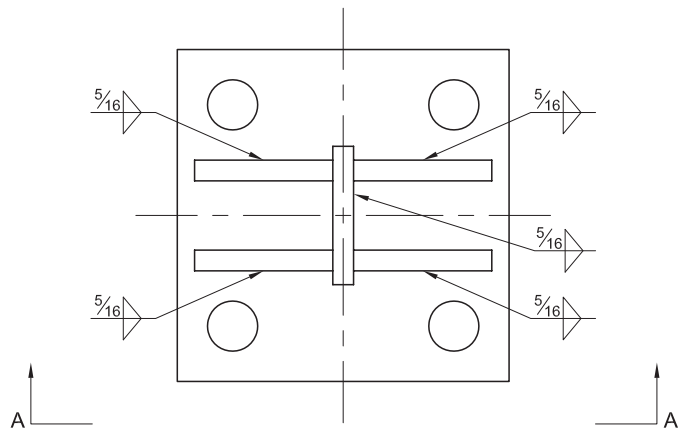


GRIP PLATE GP1
FRONT VIEW

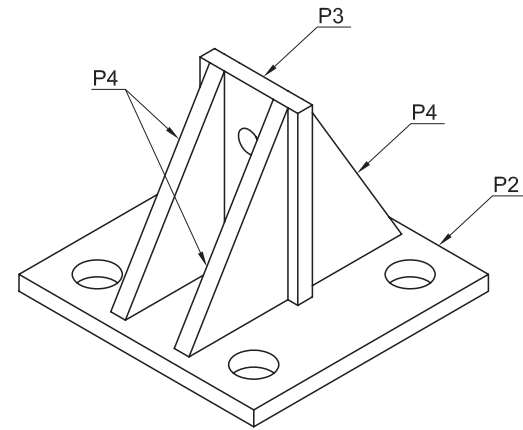


TEST SPECIMEN
t = 0.12" or 0.15" or 0.25"

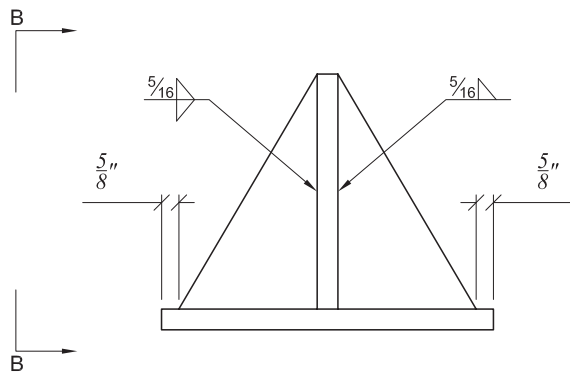
<i>Pendulum-Based High-Rate Test Apparatus (HRTA)</i>				Revisions:		
<i>Specimen and Grip Details</i>	2013-06-24	<i>University of Florida</i>	<i>Sheet 06 of 24</i>			



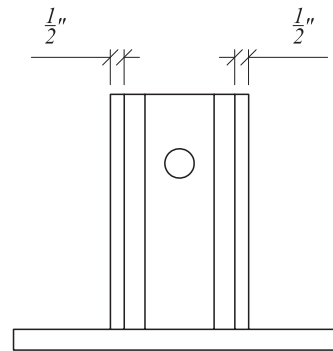
PLAN VIEW



ISOMETRIC VIEW

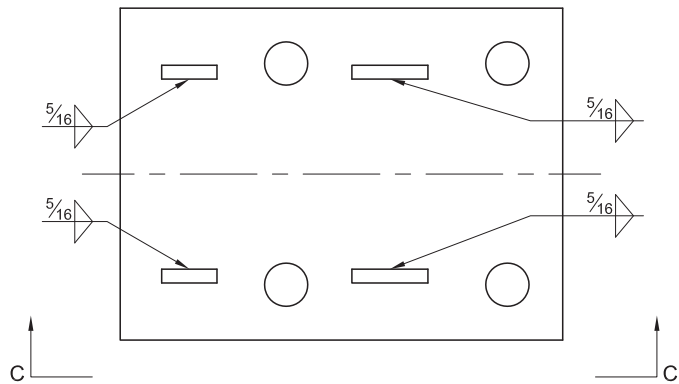


VIEW A-A

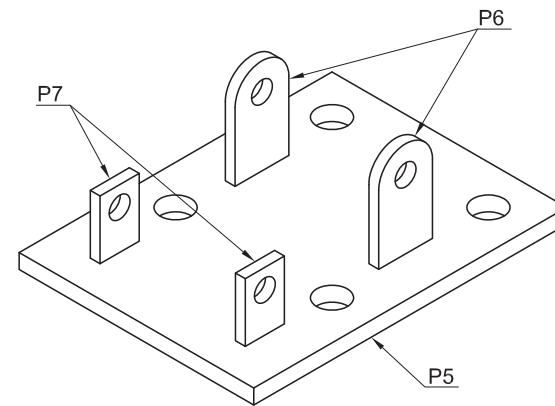


VIEW B-B

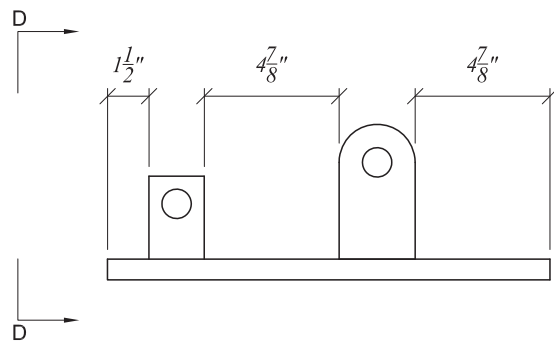
<i>Pendulum-Based High-Rate Test Apparatus (HRTA)</i>				<i>Revisions:</i>		
<i>Anchor Assembly 1</i>	<i>2013-06-24</i>	<i>University of Florida</i>	<i>Sheet 07 of 24</i>			



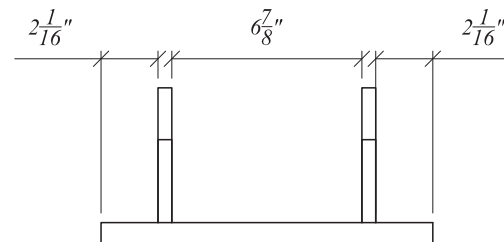
PLAN VIEW



ISOMETRIC VIEW

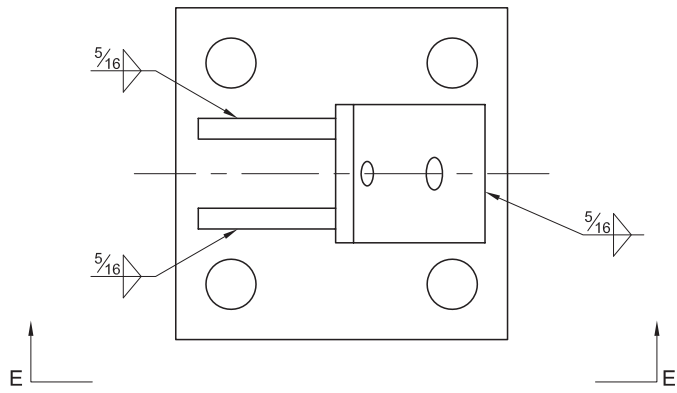


VIEW C-C

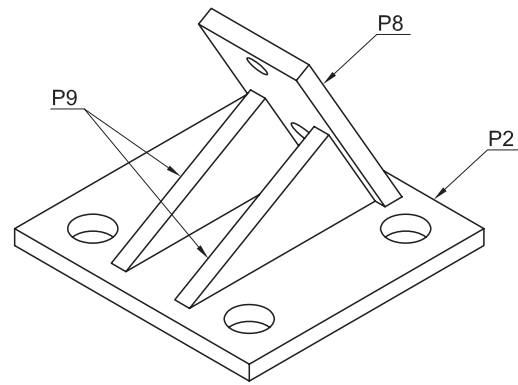


VIEW D-D

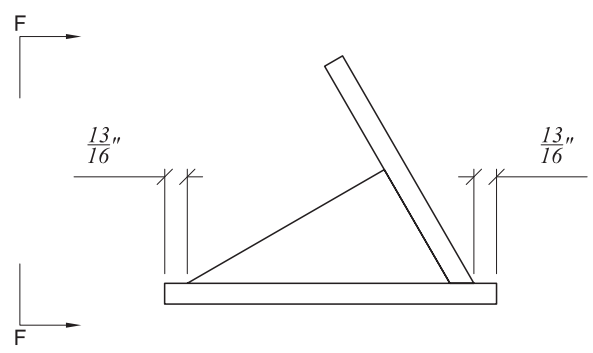
<i>Pendulum-Based High-Rate Test Apparatus (HRTA)</i>				<i>Revisions:</i>		
<i>Base Plate Assembly 1</i>	<i>2013-06-24</i>	<i>University of Florida</i>	<i>Sheet 08 of 24</i>			



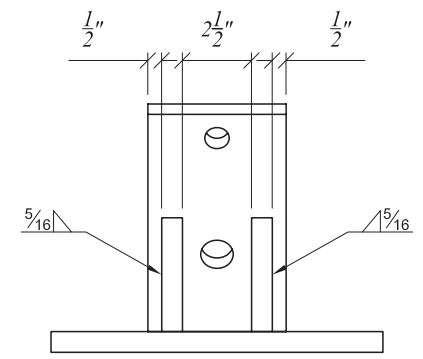
PLAN VIEW



ISOMETRIC VIEW

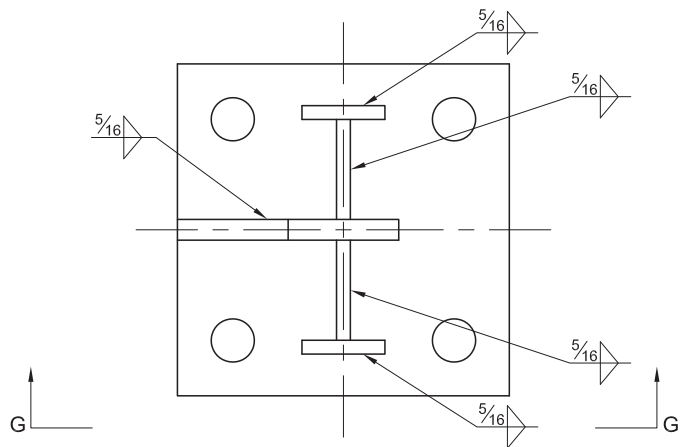


VIEW E-E

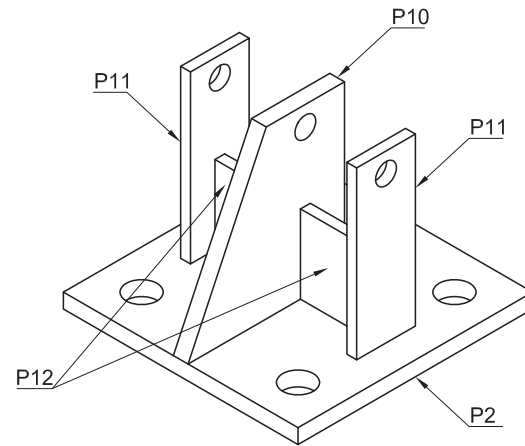


VIEW F-F

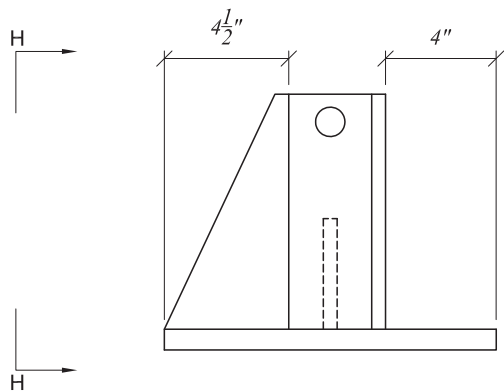
<i>Pendulum-Based High-Rate Test Apparatus (HRTA)</i>				<i>Revisions:</i>		
<i>Anchor Assembly 2</i>	<i>2013-06-24</i>	<i>University of Florida</i>	<i>Sheet 09 of 24</i>			



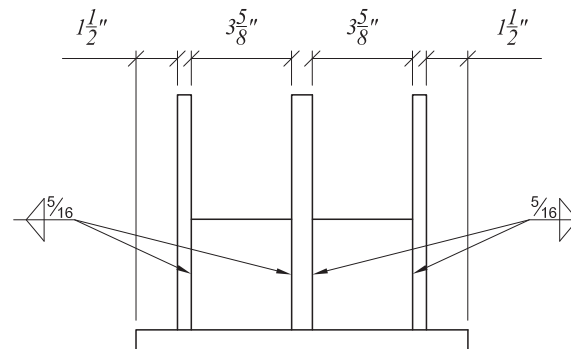
PLAN VIEW



ISOMETRIC VIEW

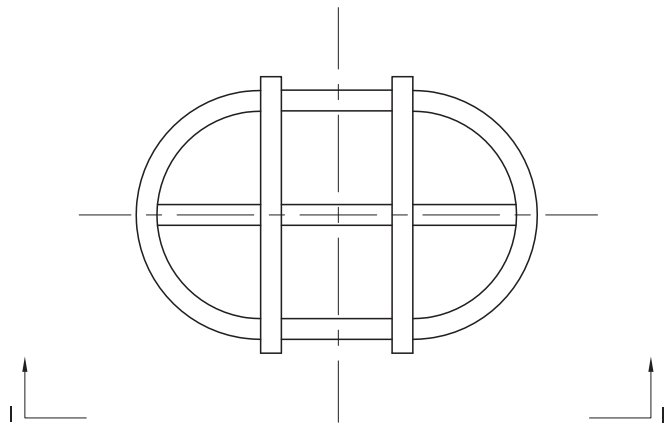


VIEW G-G

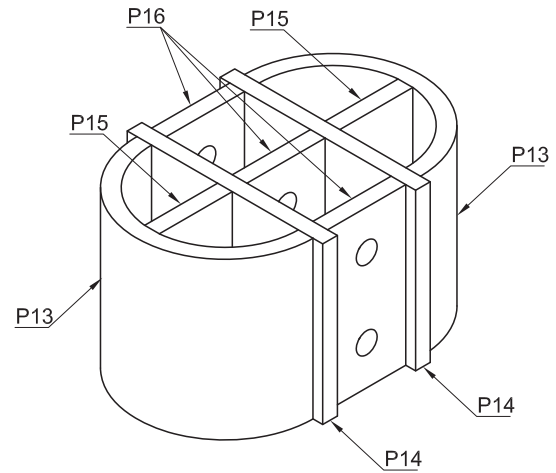


VIEW H-H

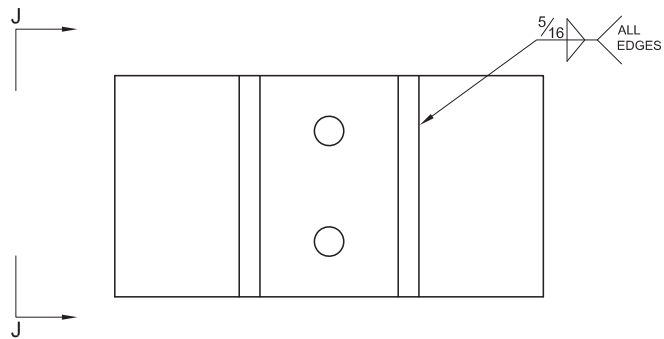
<i>Pendulum-Based High-Rate Test Apparatus (HRTA)</i>				<i>Revisions:</i>		
<i>Base Plate Assembly 2</i>	<i>2013-06-24</i>	<i>University of Florida</i>	<i>Sheet 10 of 24</i>			



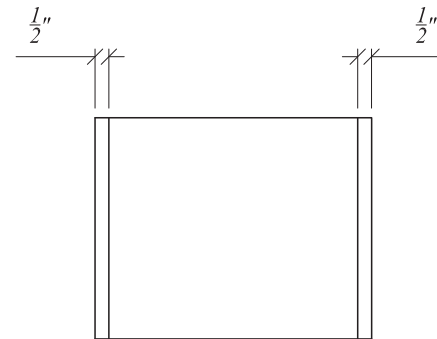
PLAN VIEW



ISOMETRIC VIEW

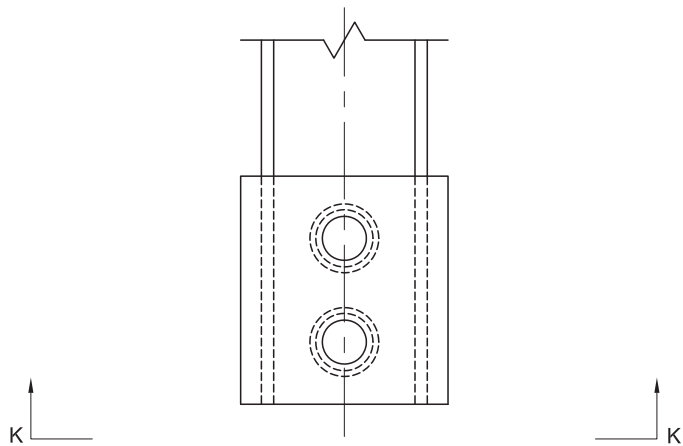


VIEW I-I

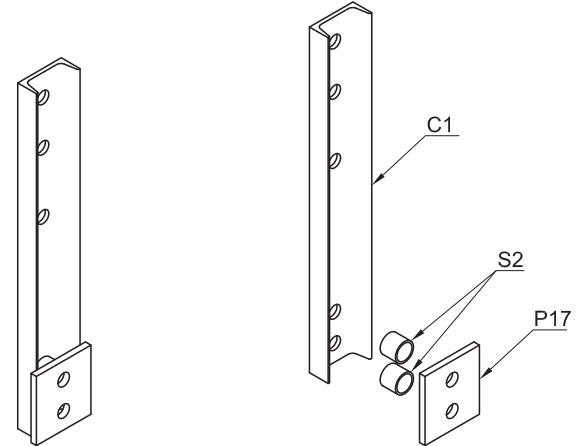


VIEW J-J

<i>Pendulum-Based High-Rate Test Apparatus (HRTA)</i>				<i>Revisions:</i>		
<i>Impact Plate Assembly</i>	<i>2013-06-24</i>	<i>University of Florida</i>	<i>Sheet 11 of 24</i>			

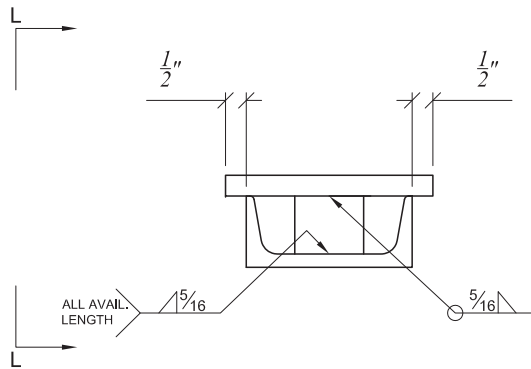


ELEVATION VIEW

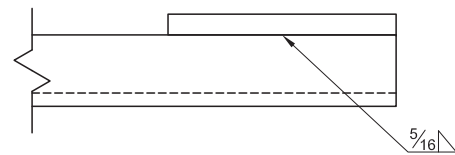


ISOMETRIC VIEW

EXPLODED VIEW

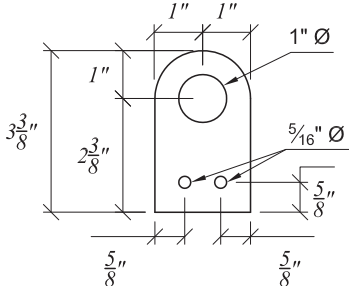
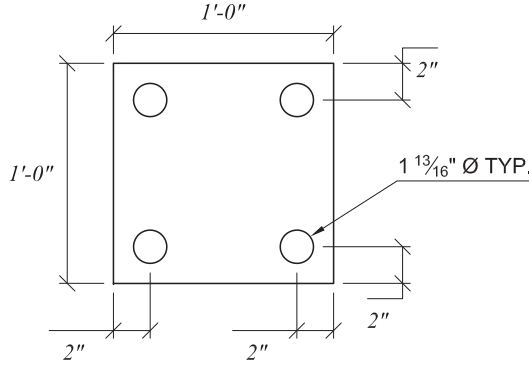
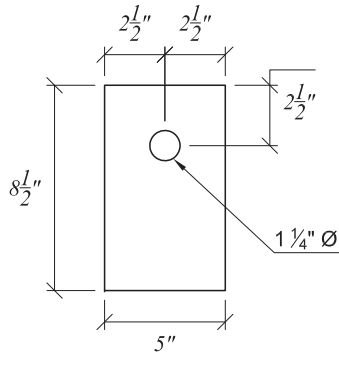


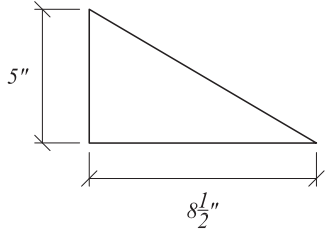
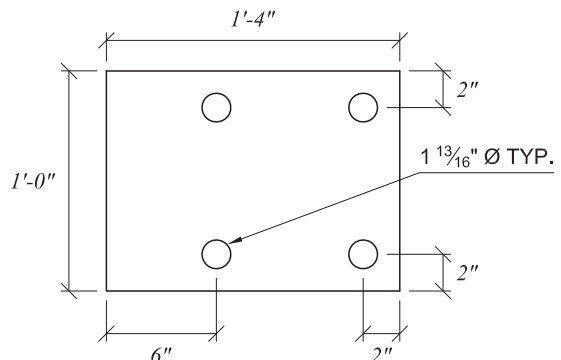
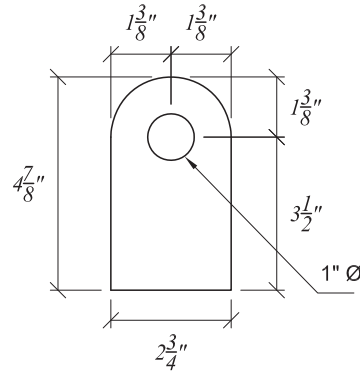
VIEW K-K

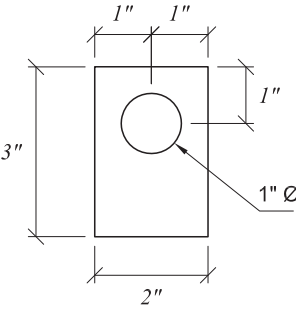
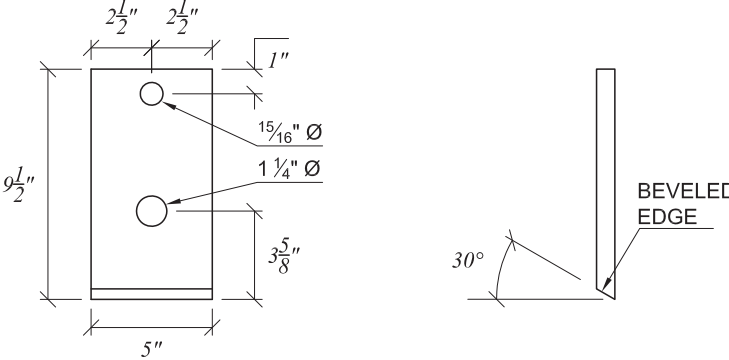
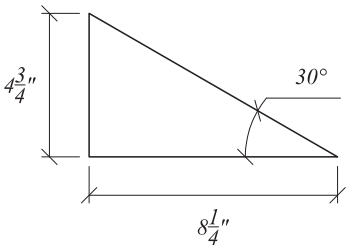


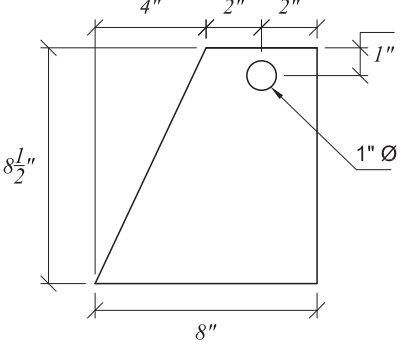
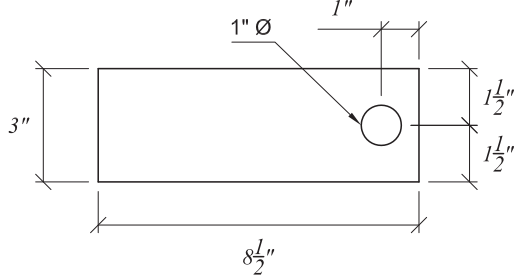
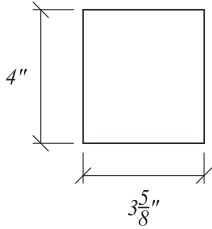
VIEW L-L

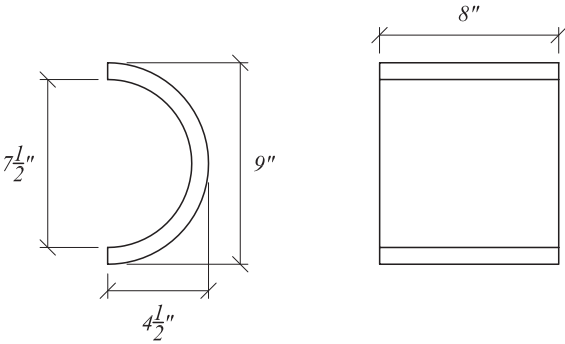
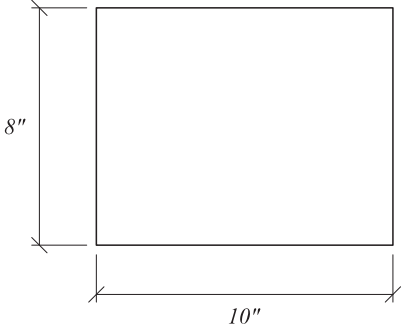
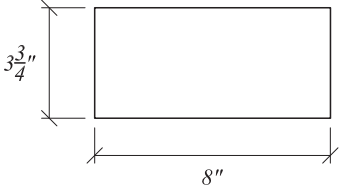
<i>Pendulum-Based High-Rate Test Apparatus (HRTA)</i>				<i>Revisions:</i>	<i>2012-03-30</i>	
<i>Plated channel assembly</i>	<i>2013-06-24</i>	<i>University of Florida</i>	<i>Sheet 12 of 24</i>			

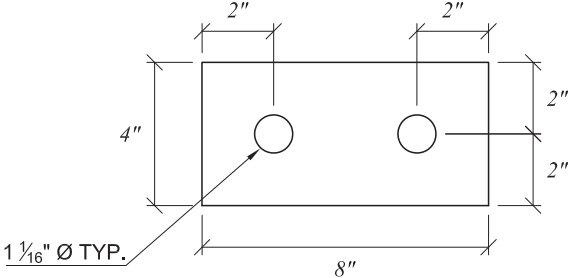
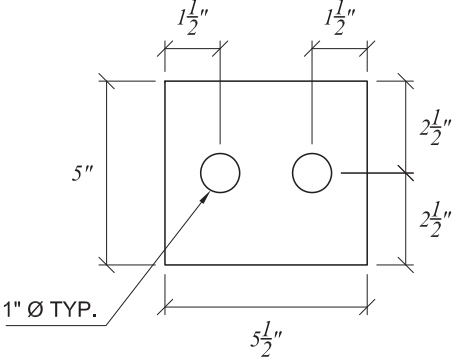
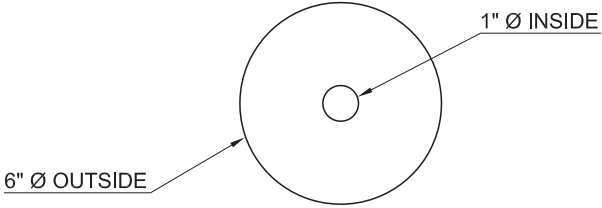
MARK	QTY.	DRAWING	NOTES
P1	4		ASTM A 36 t = 1/4"
P2	3		ASTM A36 t = 3/4"
P3	1		ASTM A 36 t = 3/4"
		Pendulum-Based High-Rate Test Apparatus (HRTA)	
Plate List	2013-06-24	University of Florida	Sheet 13 of 24
		Revisions:	

MARK	QTY.	DRAWING	NOTES
P4	4		ASTM A 36 t = 3/4"
P5	1		ASTM A36 t = 3/4"
P6	2		ASTM A 36 t = 1/2"
		Pendulum-Based High-Rate Test Apparatus (HRTA)	
Plate List	2013-06-24	University of Florida	Sheet 14 of 24
			Revisions:

MARK	QTY.	DRAWING	NOTES
P7	2		ASTM A 36 t = 1/2"
P8	1		ASTM A 36 t = 3/4"
P9	2		ASTM A 36 t = 3/4"
		Pendulum-Based High-Rate Test Apparatus (HRTA)	
Plate List	2013-06-24	University of Florida	Sheet 15 of 24
		Revisions:	

MARK	QTY.	DRAWING	NOTES
P10	1		ASTM A 36 t = 3/4"
P11	2		ASTM A 36 t = 1/2"
P12	2		ASTM A 36 t = 1/2"
		<i>Pendulum-Based High-Rate Test Apparatus (HRTA)</i>	
<i>Plate List</i>	2013-06-24	University of Florida	Sheet 16 of 24
		<i>Revisions:</i>	

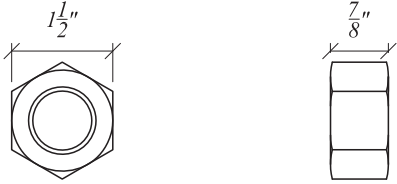

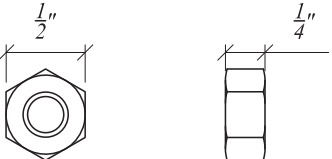
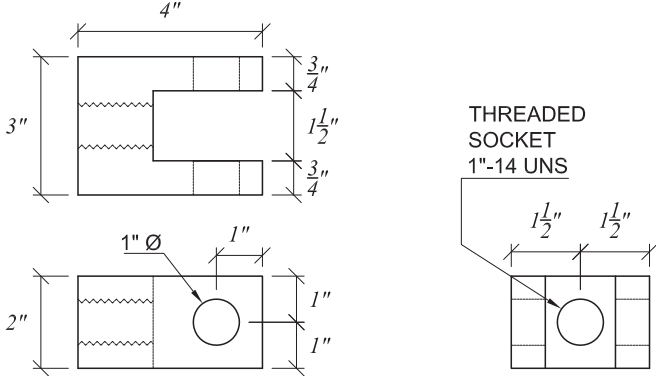
MARK	QTY.	DRAWING	NOTES
P13	2		ASTM A 519 COLD DRAWN MECHANICAL TUBING 9" O.D. 3/4" THICK CUT LENGTHWISE TO FORM (2) PIECES
P14	2		ASTM A 36 $t = \frac{3}{4}"$
P15	2		ASTM A 36 $t = \frac{3}{4}"$
		<i>Pendulum-Based High-Rate Test Apparatus (HRTA)</i>	
<i>Plate List</i>	2013-06-24	University of Florida	Sheet 17 of 24
		<i>Revisions:</i>	

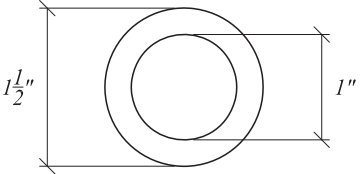
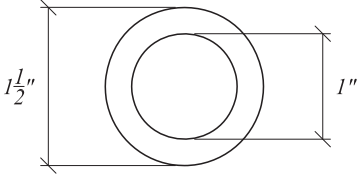
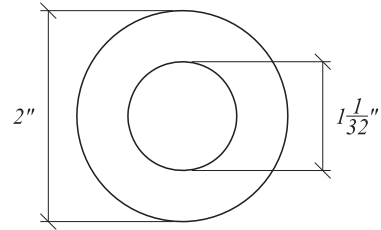
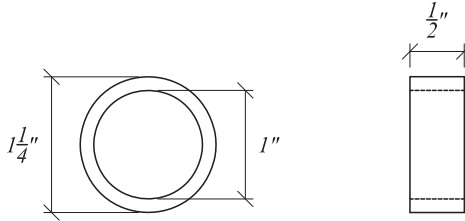
MARK	QTY.	DRAWING	NOTES
P16	3		ASTM A 36 t = 3/4"
P17	2		ASTM A 36 t = 1/2"
P18	4		ASTM A 36 t = 3/4"
		Pendulum-Based High-Rate Test Apparatus (HRTA)	
Plate List	2013-06-24	University of Florida	Sheet 18 of 24 Revisions:

MARK	QTY.	DRAWING	NOTES
P19	2		ASTM A 36 t = 1/2"
P20	2		ASTM A 36 t = 1/2"
P21	1		ASTM A 36 t = 5/8"
		Pendulum-Based High-Rate Test Apparatus (HRTA)	
Plate List	2013-06-24	University of Florida	Sheet 19 of 24 Revisions:

MARK	QTY.	DRAWING	NOTES
P22	1		ASTM A 36 t = 1/4"
C1	2		ASTM A 36 C 4x7.2
Pendulum-Based High-Rate Test Apparatus (HRTA)		Revisions:	2012-04-24
Plate List	2013-06-24		University of Florida

MARK	QTY.	DRAWING	NOTES
SH1	3		HARDENED PRECISION STEEL SHAFT AISI 1566 MCMaster-CARR: 6061K35
SH2	1		HARDENED PRECISION STEEL SHAFT AISI 1566 MCMaster-CARR: 6061K606
SC1	8		CLAMP-ON SHAFT COLLAR MCMaster-CARR: 6435K18
R1	1		THREADED ROD ASTM A193 B7 1"-14 UNS McMaster-CARR: 92580A114
R2	2		THREADED ROD ASTM A193 B7 1"-14 UNS McMaster-CARR: 98957A412
		<i>Pendulum-Based High-Rate Test Apparatus (HRTA)</i>	
<i>Miscellaneous Parts 1</i>		<i>2013-06-24</i>	<i>University of Florida</i>
		<i>Sheet 21 of 24</i>	<i>Revisions:</i>

MARK	QTY.	DRAWING	NOTES
N1	10		HEX NUT SAE J995 Gr. 5 1"-14 UNS McMASTER-CARR: 95505A621
N2	3		JAM NUT SAE J995 Gr. 2 1"-14 UNS McMASTER-CARR: 91078A255
N3	9		HEX NUT SAE J995 Gr. 2 5/16"-8 UNC McMASTER-CARR: 90473A030
CL1	1	 <p>THREADED SOCKET 1"-14 UNS</p>	CUSTOM MACHINED CLEVIS 6061-T6 ALUMINUM
		<i>Pendulum-Based High-Rate Test Apparatus (HRTA)</i>	
Miscellaneous Parts 2	2013-06-24	University of Florida	Sheet 22 of 24
		Revisions:	

MARK	QTY.	DRAWING	NOTES
W1	14		SAE 841 BRONZE PTFE/OIL-LUBRICATED THRUST BEARING $t = \frac{1}{8}$ " McMASTER-CARR: 7421K26
W2	8		SAE 841 BRONZE PTFE/OIL-LUBRICATED THRUST BEARING $t = \frac{1}{16}$ " McMASTER-CARR: 7421K25
W3	2		SELF-ALIGNING WASHER 18-8 STAINLESS STEEL $t = \frac{1}{2}$ " McMASTER-CARR: 91944A032
S1	4		SAE 841 BRONZE LUBRICATED SLEEVE BEARING McMASTER-CARR: 6391K281
		<i>Pendulum-Based High-Rate Test Apparatus (HRTA)</i>	
<i>Miscellaneous Parts 3</i>	<i>2013-06-24</i>	<i>University of Florida</i>	<i>Sheet 23 of 24</i>
		<i>Revisions:</i>	

MARK	QTY.	DRAWING	NOTES
R3	1		ASTM A193 B7 $\frac{3}{4}$ " - 10 UNC McMASTER-CARR: 98957A638
RE1	1		ROD END CLEVIS $\frac{3}{4}$ " - 10 UNC McMASTER-CARR: 6071K34
LC1	1		15-KIP ROD END LOAD CELL 1"-14 UNS INTERFACE: REC15K
SP1	4		SPACER PLATE ASTM A36
S1	8		SAE 841 BRONZE LUBRICATED SLEEVE BEARING McMASTER-CARR: 6391K281
		<i>Pendulum-Based High-Rate Test Apparatus (HRTA)</i>	
<i>Miscellaneous Parts 4</i>		<i>2013-06-24</i>	<i>University of Florida</i>
		<i>Sheet 24 of 24</i>	<i>Revisions:</i>

APPENDIX D
DEMONSTRATION OF IMPULSE-MOMENTUM THEORY FOR MULTIPLE
DEGREE OF FREEDOM (MDF) SYSTEMS

As discussed in Chapter 4, the high-rate material testing apparatus (HRTA) drive line was designed to respond as a single degree of freedom (SDF) system, and instrumentation for the device was selected accordingly. However, flexibility in the connections between various parts of the HRTA caused it to respond as a multiple degree of freedom (MDF) system instead. Consequently, an alternative data interpretation procedure was developed (Section 4.3.2.2) that is based on impulse-momentum theory. The derivation presented in this appendix demonstrates that the impulse-momentum data interpretation is indeed valid for MDF systems with an arbitrary number of degrees of freedom that are anchored by a single point.

Consider the damped MDF system shown in Fig. D.1a, consisting of four masses ($m_1 - m_4$), each connected by springs ($k_1 - k_4$) and dashpots ($c_1 - c_4$). The system (initially at rest) is subjected to dynamic excitation by a time-varying force, $F_S(t)$, which is equal to the resultant force imparted by the specimen during a high-rate material test (equal to the specimen stress times its original cross sectional area). The resulting free body diagrams of each mass are shown in Fig. D.1b.

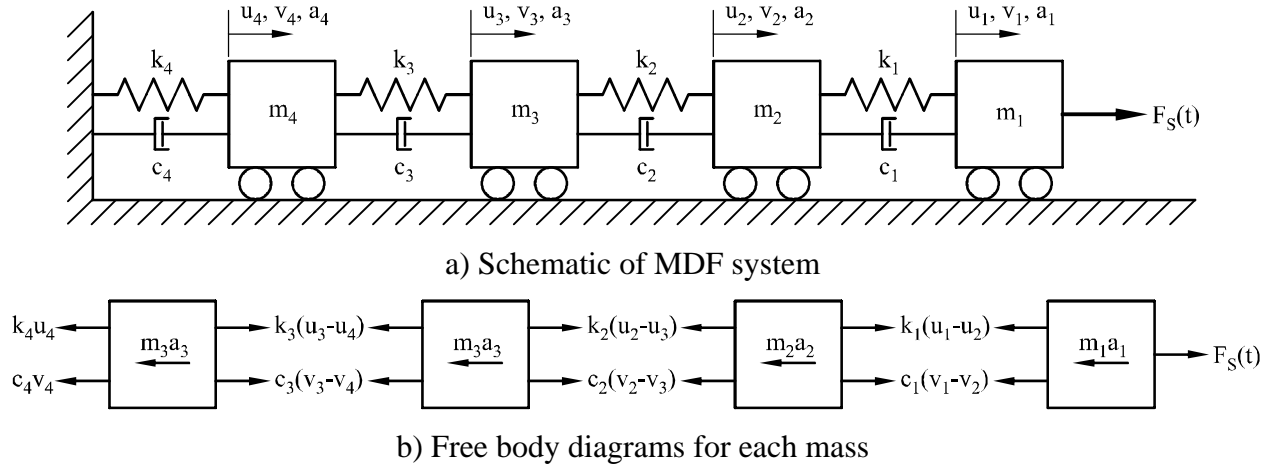


Figure D.1 Four degree-of-freedom system with damping, subject to dynamic excitation by time-varying specimen resultant force $F_S(t)$

In accordance with Fig. D.1b, four equilibrium equations are defined:

$$k_1(u_1 - u_2) + c_1(v_1 - v_2) = F_S(t) - m_1 a_1 \quad (D.1)$$

$$k_1(u_1 - u_2) + c_1(v_1 - v_2) = m_2 a_2 + k_2(u_2 - u_3) + c_2(v_2 - v_3) \quad (D.2)$$

$$k_2(u_2 - u_3) + c_2(v_2 - v_3) = m_3 a_3 + k_3(u_3 - u_4) + c_3(v_3 - v_4) \quad (\text{D.3})$$

$$k_3(u_3 - u_4) + c_3(v_3 - v_4) = m_4 a_4 + k_4 u_4 + c_4 v_4 \quad (\text{D.4})$$

Setting the right hand sides of Eqns. D.1 and D.2 equal to each other, and rearranging:

$$k_2(u_2 - u_3) + c_2(v_2 - v_3) = F_S(t) - m_1 a_1 - m_2 a_2 \quad (\text{D.5})$$

Setting the right hand sides of Eqns. D.5 and D.3 equal to each other, and rearranging:

$$k_3(u_3 - u_4) + c_3(v_3 - v_4) = F_S(t) - m_1 a_1 - m_2 a_2 - m_3 a_3 \quad (\text{D.6})$$

Setting the right hand sides of Eqns. D.6 and D.4 equal to each other, and rearranging:

$$k_4 u_4 + c_4 v_4 = F_S(t) - m_1 a_1 - m_2 a_2 - m_3 a_3 - m_4 a_4 \quad (\text{D.7})$$

Because the load cell in the HRTA measures the *total* reaction force, $F_R(t)$, including both the stiffness and damping components:

$$F_R(t) = k_4 u_4 + c_4 v_4 \quad (\text{D.8})$$

Substituting Eqn. D.8 into Eqn. D.7:

$$F_R(t) = F_S(t) - m_1 a_1 - m_2 a_2 - m_3 a_3 - m_4 a_4 \quad (\text{D.9})$$

It is readily observed from the repeated pattern of steps above that Eqn. D.9 can be generalized to be valid for any arbitrary number of degrees of freedom (N_{DOF}):

$$F_R(t) = F_S(t) - \sum_{i=1}^{N_{\text{DOF}}} m_i a_i \quad (\text{D.10})$$

Integrating Eqn. D.10 over the interval $[t_1, t_2]$:

$$\int_{t_1}^{t_2} F_R(t) dt = \int_{t_1}^{t_2} F_S(t) dt - \sum_{i=1}^{N_{\text{DOF}}} \int_{t_1}^{t_2} m_i a_i dt \quad (\text{D.11})$$

where t_1 is a time immediately prior to specimen extension, and t_2 is a time well after the specimen has broken and all oscillation in the HRTA has ceased. For these conditions, evaluating the integral produces:

$$\int_{t_1}^{t_2} F_R(t) dt = \int_{t_1}^{t_2} F_S(t) dt - \sum_{i=1}^{N_{\text{DOF}}} m_i [v_i(t_2) - v_i(t_1)] \quad (\text{D.12})$$

Because $v_i(t_1) = v_i(t_2) = 0$ for all degrees of freedom $i = 1 \dots N_{\text{DOF}}$,

$$\begin{aligned} \int_{t_1}^{t_2} F_R(t) dt &= \int_{t_1}^{t_2} F_S(t) dt \\ \Rightarrow J_R(t_2) &= J_S(t_2) \end{aligned} \quad (\text{D.13})$$

The resulting equation (Eqn. D.13) is exactly the same as Eqn. 4.5, which is the theoretical basis for the data processing procedure presented in Chapter 4. Therefore, even though flexibility in the various connections of the HRTA caused it to respond as an MDF system, the data processing procedure presented in Chapter 4 is valid.

APPENDIX E SENSITIVITY OF REDUCED-SCALE BARGE IMPACT SIMULATION RESULTS TO STEEL FAILURE STRAIN

E.1 Introduction

As discussed in Chapter 4, one of the constitutive model parameters that must be considered in the finite element (FE) validation simulations is the strain at which material failure occurs. In LS-DYNA, material failure is simulated by deleting individual finite elements from the model when the effective plastic strain exceeds a specified value. As noted in Chapter 4, in MAT_24, the FE constitutive (material) model employed for the steel barge components in this study—a value for failure strain must be selected that is constant with respect to strain rate, even though increased ductility was observed in material evaluations performed in this study at higher strain rates. Table E.1 summarizes minimum and maximum failure strains quantified from the experimental study, where the minimum was observed for testing rate R1, and the maximum was observed for testing rate R8. The purpose of this appendix is to evaluate the influence of failure strain on the results of reduced-scale barge impact simulations for the range of failure strains shown in Table E.1.

Table E.1 Effective plastic strain at failure for each material series

Material series	Effective plastic strain at failure (in./in.)		
	Minimum (R1)	Maximum (R8)	Mean
A1011-T11	0.342	0.384	0.363
A1011-T15	0.280	0.336	0.308
A36-T25	0.206	0.340	0.273

E.2 Barge Impact Simulations

To evaluate the sensitivity of response to failure strain, impact simulations were conducted that were consistent with the impact conditions described in Chapter 5. As shown in Fig. E.1, the simulations consisted of a 9,000-lbf rigid impact block and the fully-deformable 0.4-scale barge bow model. For simplicity, the impact block was assigned roller-type translating boundary conditions that only permit motion in the x-direction, and barge nodes at the rear-most interface were assigned fixed boundary conditions.

To initiate each impact simulation, the impact block was assigned an initial velocity equal to 39.3 ft/s, which corresponds to a pendulum drop height of 24 ft. Subsequently, the block model impacted the barge bow model, causing several inches of bow deformation and ultimately arresting block motion. Elastic rebound of the barge bow caused the impact block motion to reverse, and contact between the objects eventually ceased. For this investigation, only one impact was simulated.

Steel plates and structural members in the FE barge model were assigned one of the three constitutive models developed in Chapter 4 (A1011-T11, A1011-T15, A36-T25), depending

upon which material specification the part in question will be constructed from in the physical 0.4-scale barge specimens. Three simulations were conducted for this investigation, in which the failure strain in each FE constitutive model was set equal to the: 1) minimum, 2) mean, and 3) maximum values shown in Table E.1.

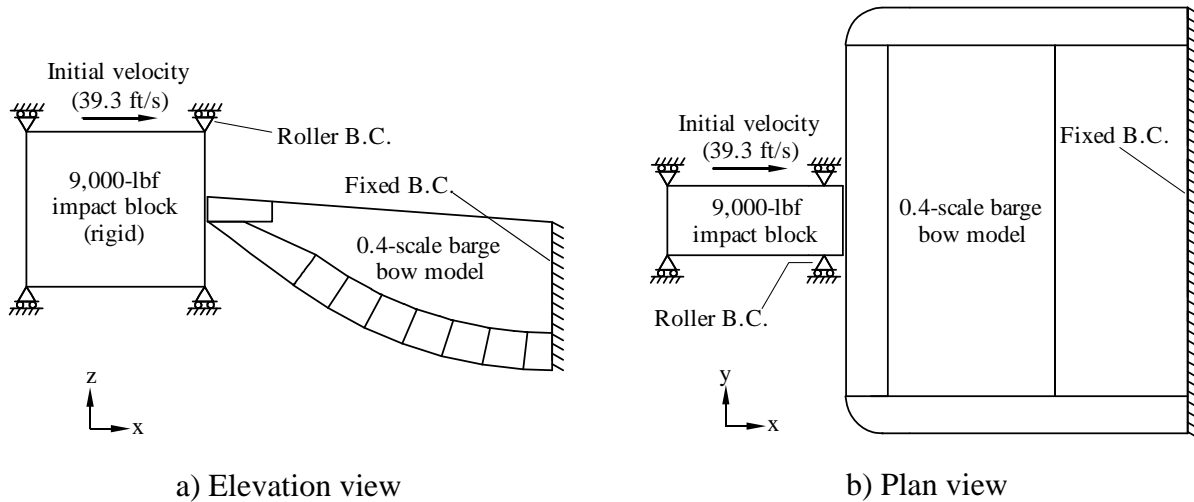


Figure E.1 Finite element impact simulation of 0.4-scale barge bow

E.3 Results and Discussion

Maximum barge bow deformations for the three simulations are compared in Fig. E.2. No significant qualitative differences are observed among the three simulations. For each case, deformation of the exterior of the barge was dominated by hull plate buckling. Interior members (frames and trusses) failed by inelastic buckling. Yielding was observed throughout the damaged region, accompanied by some localized fracture (characterized in the FE model by element deletion). As might be expected, the largest number of elements (342) failed in the model with the minimum failure strain, while 211 and 148 elements failed in the models with the mean and maximum failure strain, respectively. Nearly all of the failed elements were located in the exterior hull plates, particularly the headlog plate (on the leading edge of the barge bow). Widespread fracture did not occur in the internal structural elements for any of the simulations.

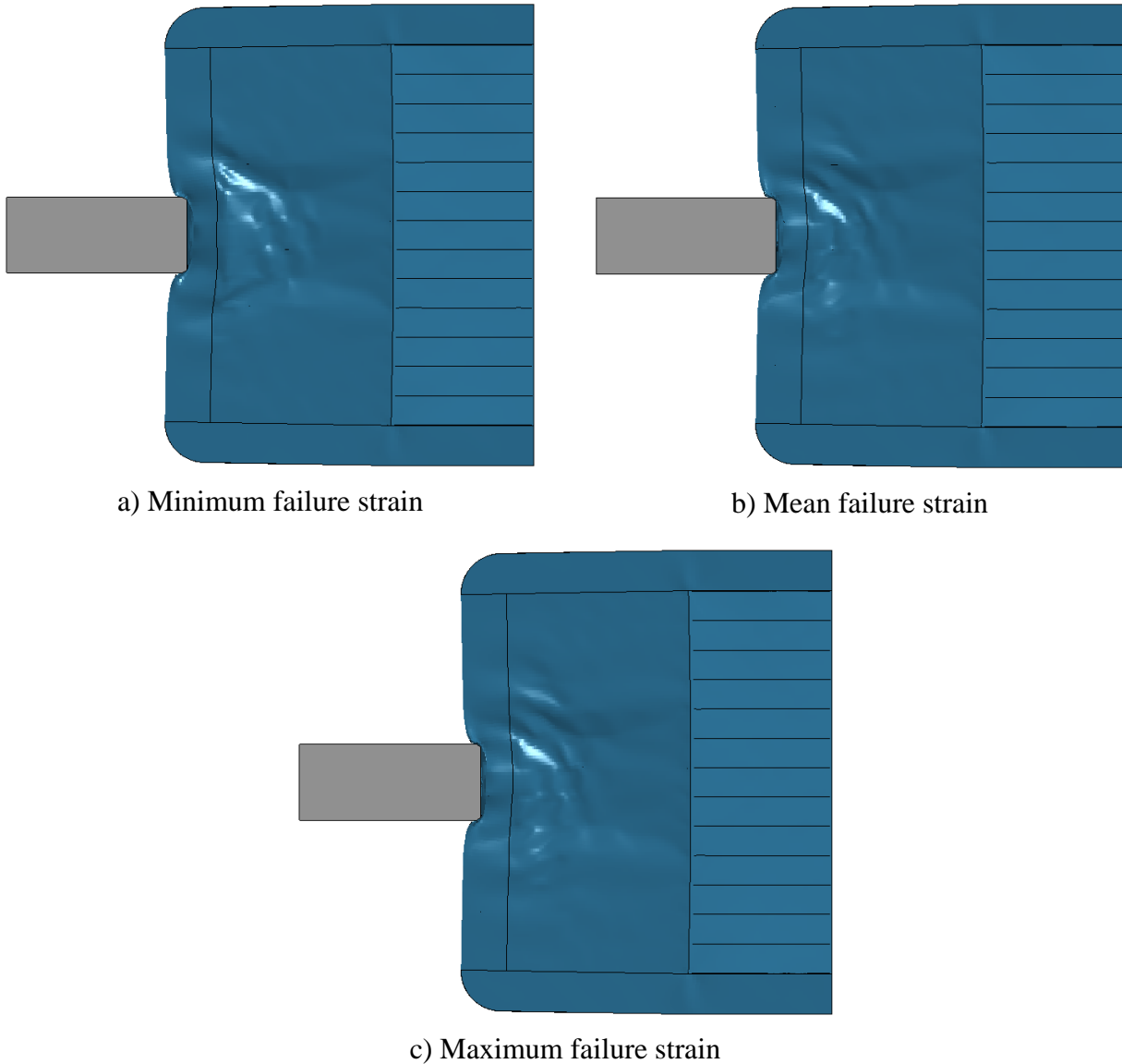


Figure E.2 Comparison of barge bow deformation after one impact

Fig. E.3 compares barge bow force-deformation curves that were developed based on the simulation results. As shown, impact forces were nearly identical for deformations up to 1 in. At larger deformations, impact forces diverged, but remained in a similar range (250 – 400 kips). Differences observed between each case can be attributed to relatively small differences in the degree of material fracture. Because fractures were concentrated in localized regions, differences in the total impact force generated on the barge model were not significant. Indeed each of the three force-deformation curves intersected and crossed over the others multiple times during the course of the impact event, indicating that there was no notable correlation between failure strain and the magnitude of impact forces. The most notable difference between the force-deformation curves is the maximum barge bow deformation. As expected, the model with the minimum failure strain experienced the largest bow deformation (8.3 in.), while the models with mean and maximum failure strains had smaller peak deformations equal to 7.9 in. and 7.5 in., respectively.

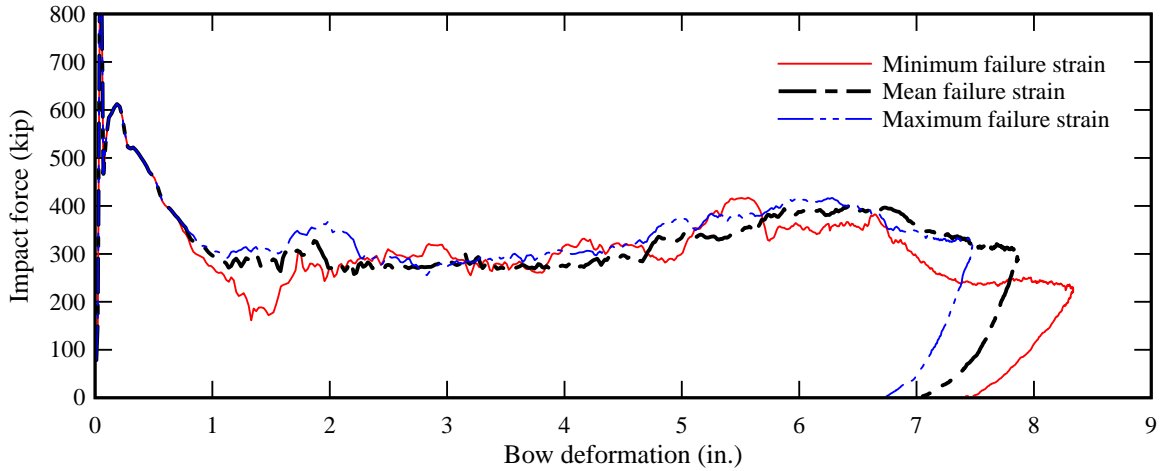


Figure E.3 Barge bow force-deformation comparison

In general, differences observed between the three simulations were fairly modest, and therefore the impact simulation results computed in this study can be considered relatively insensitive to the choice of failure strain. Over the full range of failure strains considered, impact forces and barge bow deformations differed by 10% or less, with the mean-failure strain model falling approximately in the middle. Therefore, if mean values for failure strain are selected for use in the validation simulations, the magnitude of error introduced by this approximation is approximately $\pm 5\%$. For the analysis of such a complex structural system under severe impact loading, this level of error was deemed acceptable, and therefore the mean failure strains shown in Table E.1 were employed in the FE constitutive models for all simulations of reduced-scale barge impact in this study.

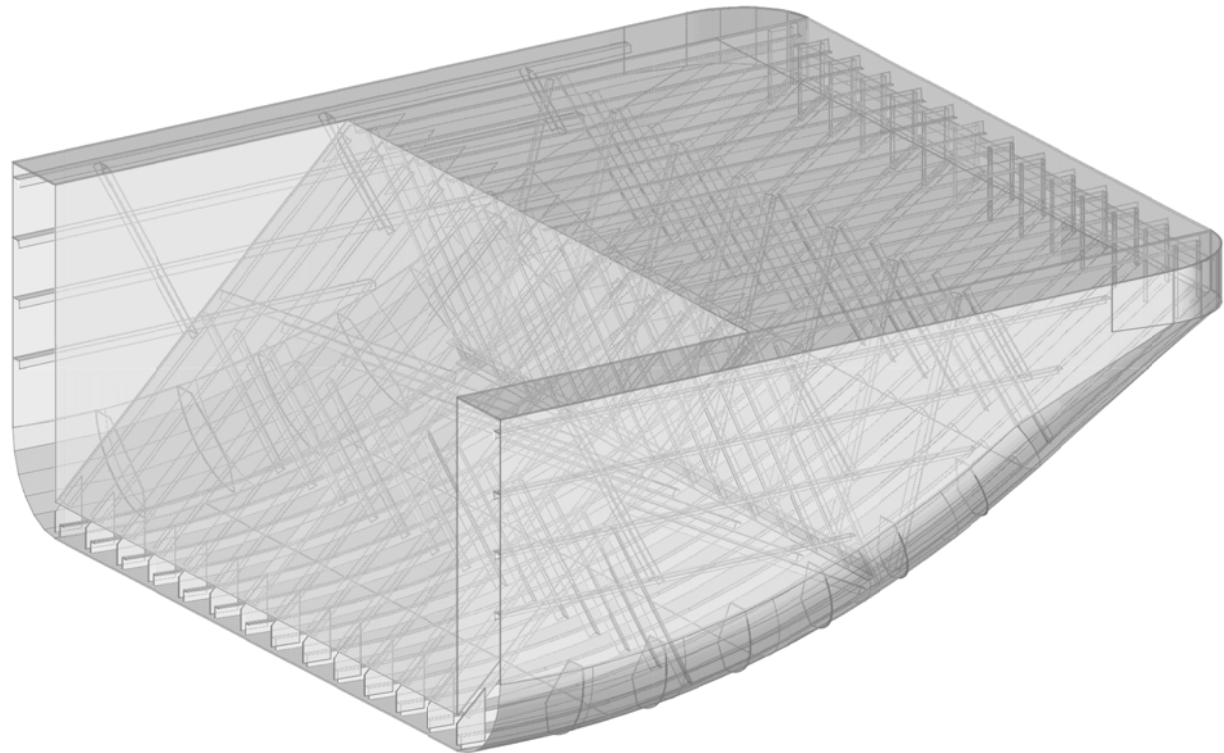
APPENDIX F
REDUCED-SCALE (0.4-SCALE) BARGE BOW FABRICATION DRAWINGS

Reduced Scale Barge Bow Fabrication Plans

TABLE OF CONTENTS	
1	TITLE PAGE
2	ISOMETRIC VIEW
3	VIEW OF COMPONENTS
4	PLAN VIEW
5	ELEVATION VIEW
6	SECTION VIEW A-A
7	SECTION VIEW B-B
8	SECTION VIEW C-C
9	SECTION VIEW D-D
10	TRUSS MEMBER LAYOUTS
11	TRUSS CHORD DIMENSIONS
12	TRUSS WEB DIMENSIONS
13	TRUSS DETAILS
14	SIDE FRAME DETAIL D
15	SIDE FRAME DETAIL E
16	PLATE DIMENSIONS 1
17	PLATE DIMENSIONS 2
18	PLATE DIMENSIONS 3
19	BENT PLATE I
20	BENT PLATE J
21	BENT PLATE K
22	BENT PLATE L
23	BENT PLATE M
24	BENT PLATE N
25	SCHEDULE OF MEMBERS

GENERAL NOTES

1. ALL OUTSIDE HULL PLATES A, B, C, D, E, H, I, AND J WELDED TOGETHER WITH FULL PENETRATION BUTT WELDS
2. TWO SPECIMENS OF THE BARGE BOW DESCRIBED IN THIS PLAN SET WILL BE BUILT. THEREFORE, ALL MATERIAL QUANTITIES INDICATED IN THIS PLAN SET SHALL BE DOUBLED.



Reduced Scale Barge Bow Fabrication Plans

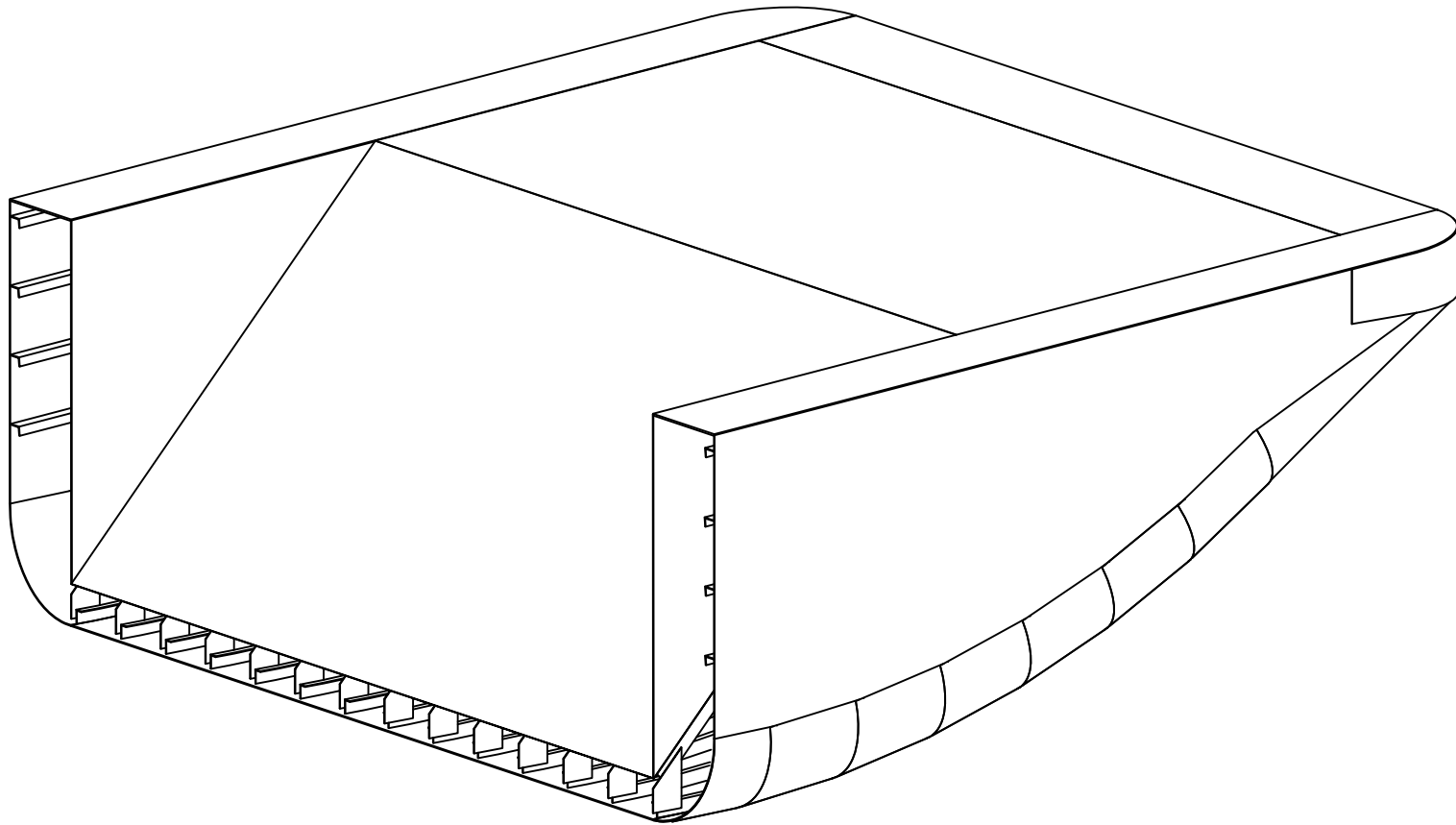
Title page

2013-12-11

University of Florida

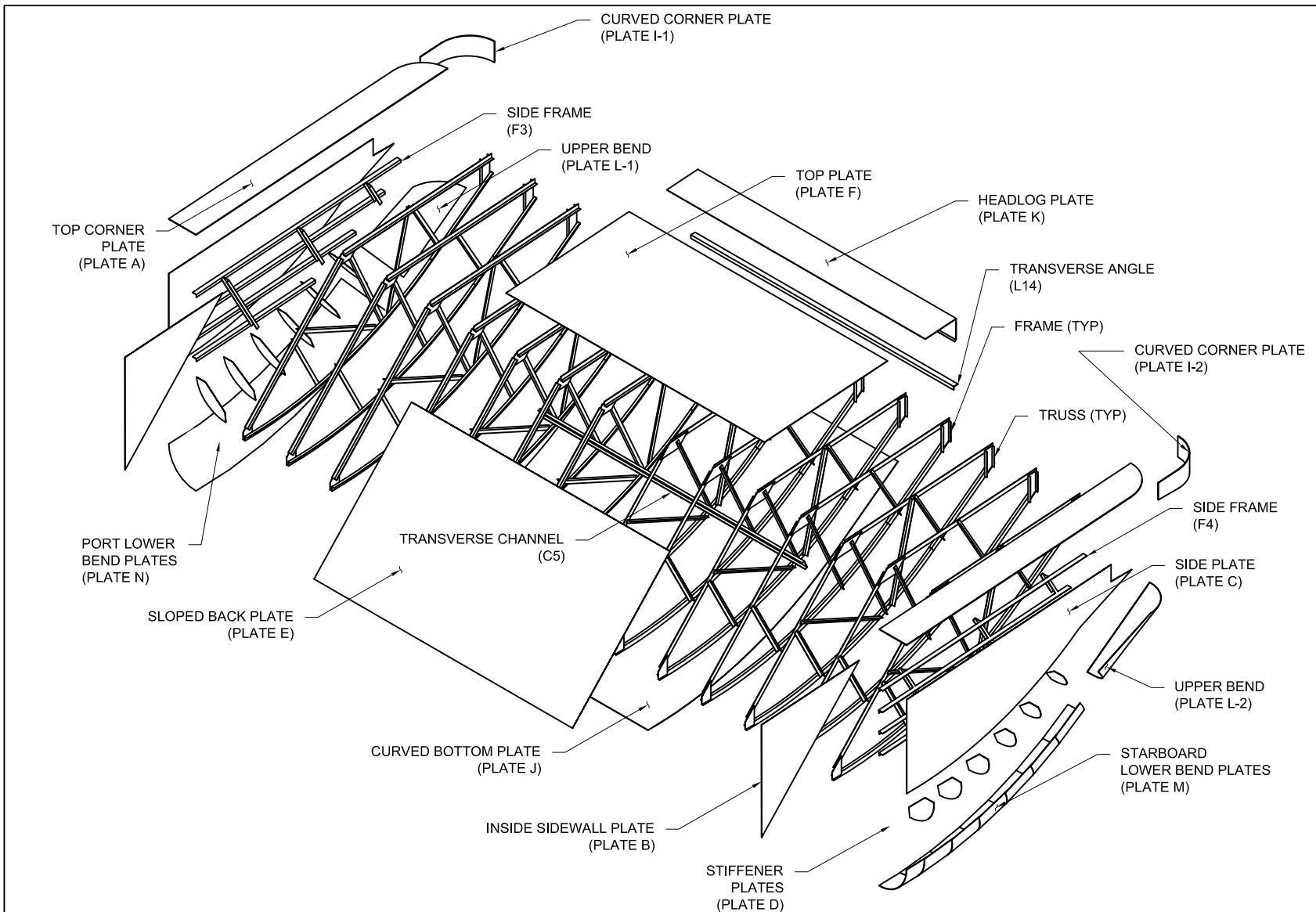
Sheet 01 of 25

Revisions:



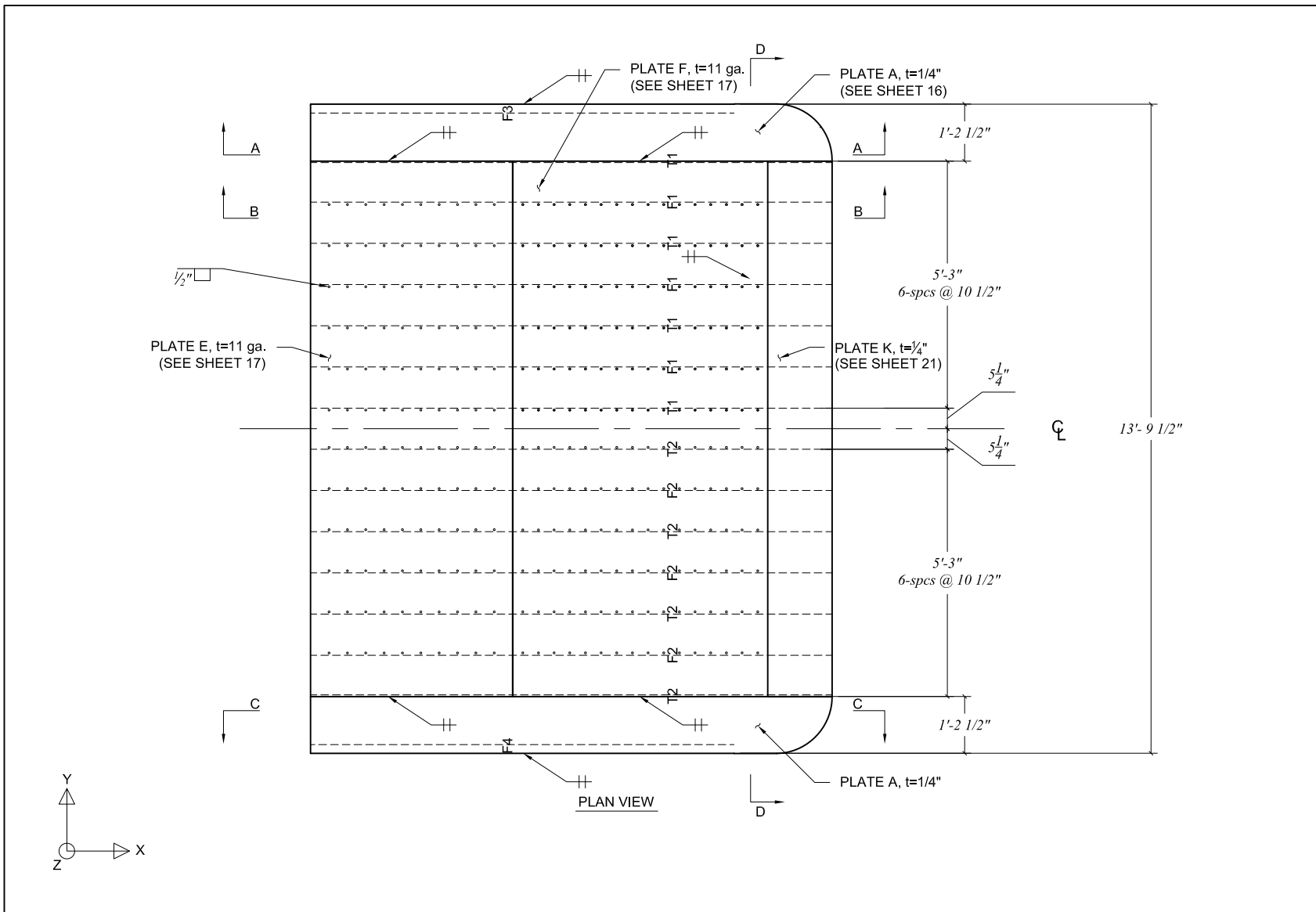
ISOMETRIC VIEW

<i>Reduced Scale Barge Bow Fabrication Plans</i>				<i>Revisions:</i>		
<i>Isometric view</i>	<i>2013-12-11</i>	<i>University of Florida</i>	<i>Sheet 02 of 25</i>			

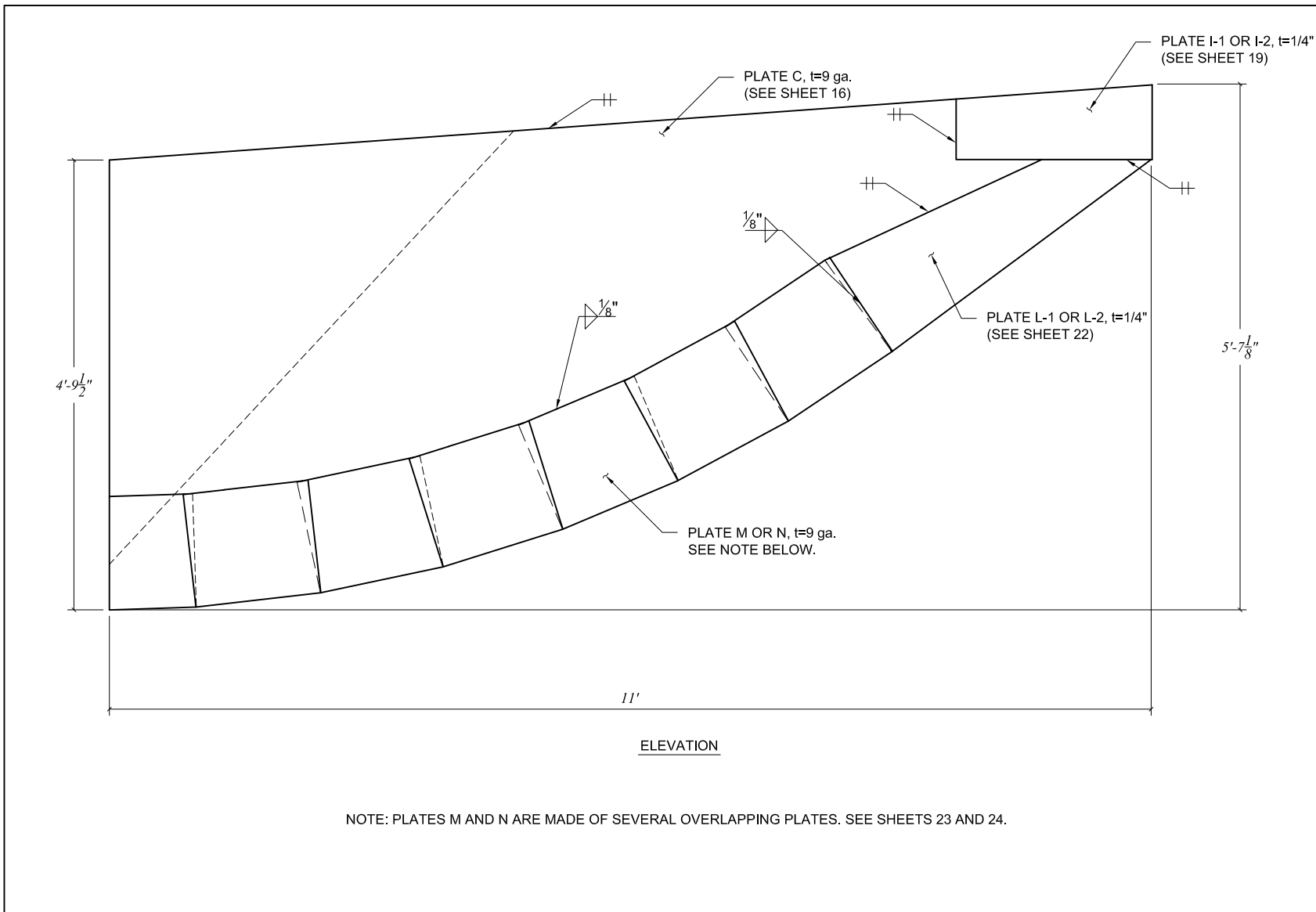


Reduced Scale Barge Bow Fabrication Plans

<i>View of components</i>	<i>2013-12-11</i>	<i>University of Florida</i>	<i>Sheet 03 of 25</i>	<i>Revisions:</i>		

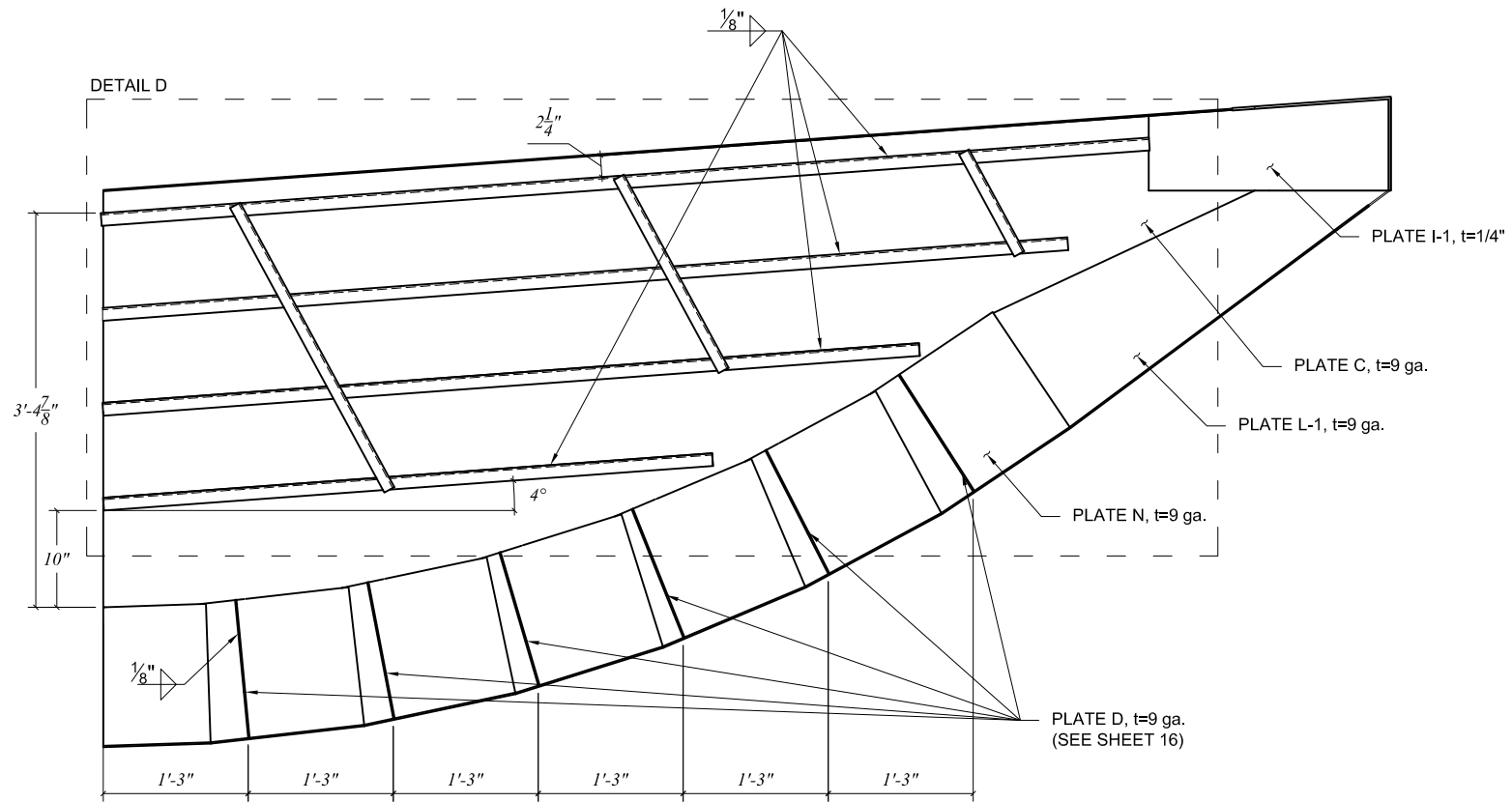


<i>Reduced Scale Barge Bow Fabrication Plans</i>				<i>Revisions:</i>	2013-08-26	
<i>Plan view</i>	2013-12-11	<i>University of Florida</i>	<i>Sheet 04 of 25</i>		2013-09-17	



NOTE: PLATES M AND N ARE MADE OF SEVERAL OVERLAPPING PLATES. SEE SHEETS 23 AND 24.

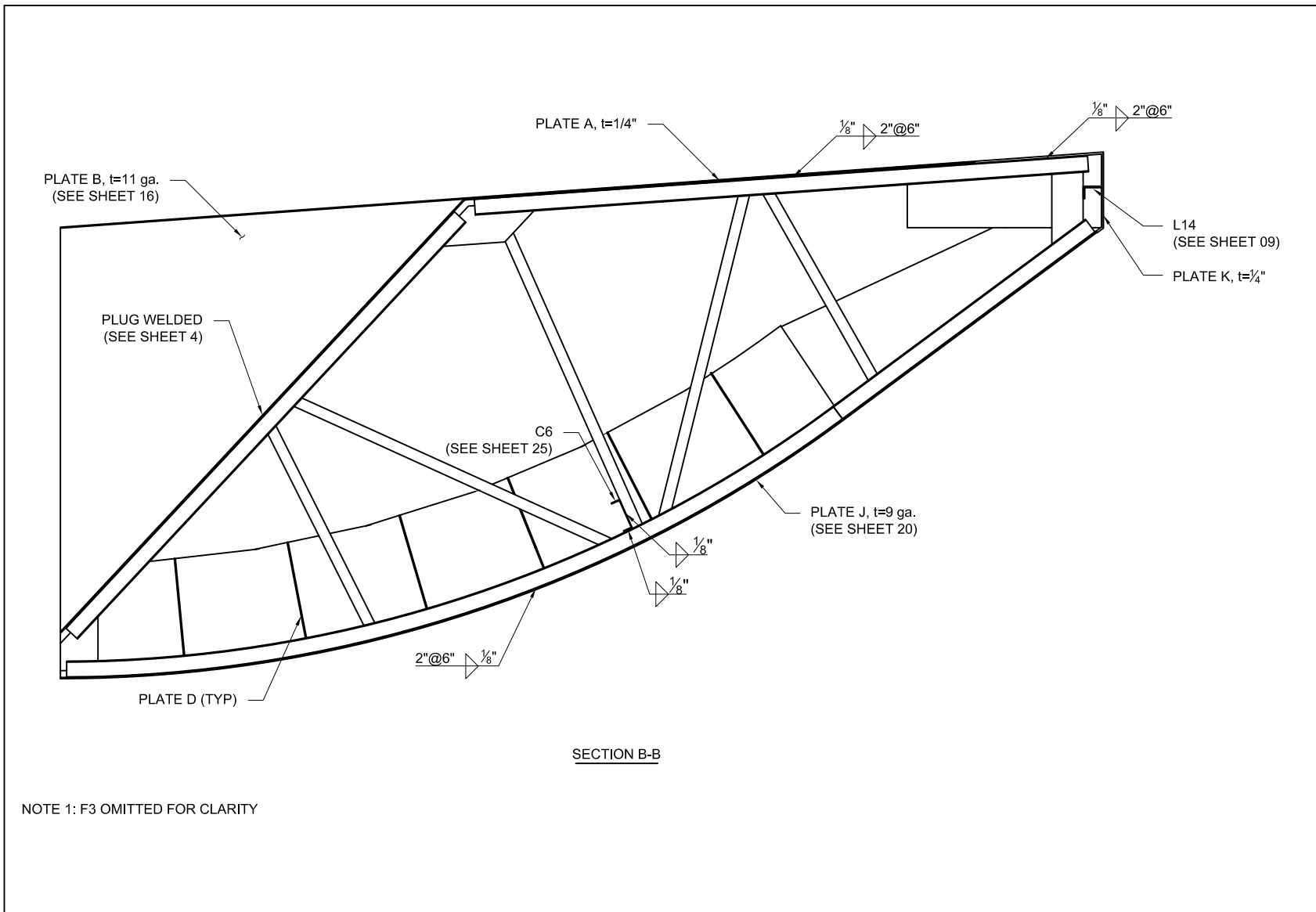
<i>Reduced Scale Barge Bow Fabrication Plans</i>				<i>Revisions:</i>		
<i>Elevation view</i>	<i>2013-12-11</i>	<i>University of Florida</i>	<i>Sheet 05 of 25</i>			



SECTION A-A

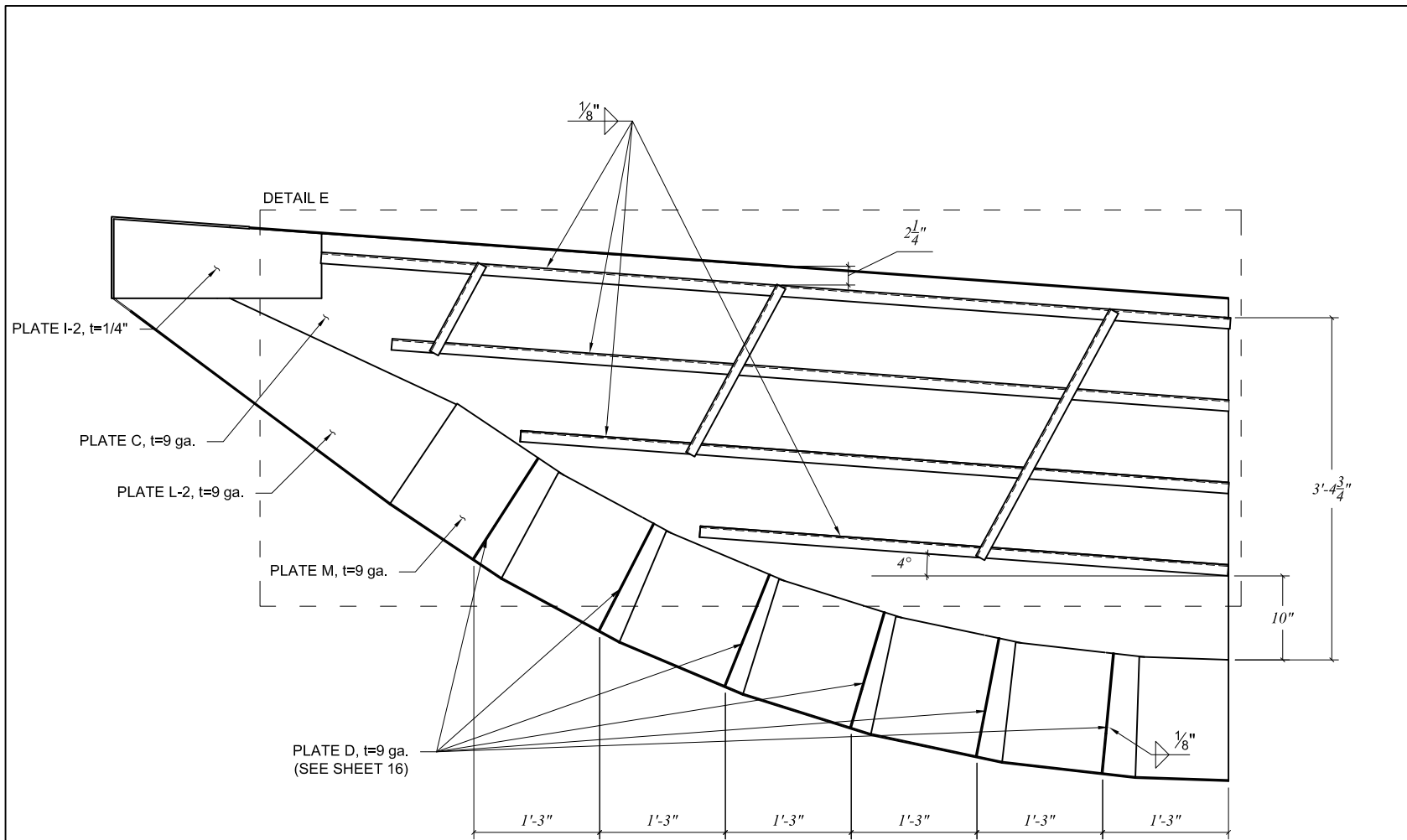
NOTE: LONG LEG OF ANGLES SHALL BE WELDED TO PLATE C WITH 1/8" FILLETS.

<i>Reduced Scale Barge Bow Fabrication Plans</i>				<i>Revisions:</i>		
<i>Section view A-A</i>	<i>2013-12-11</i>	<i>University of Florida</i>	<i>Sheet 06 of 25</i>			



NOTE 1: F3 OMITTED FOR CLARITY

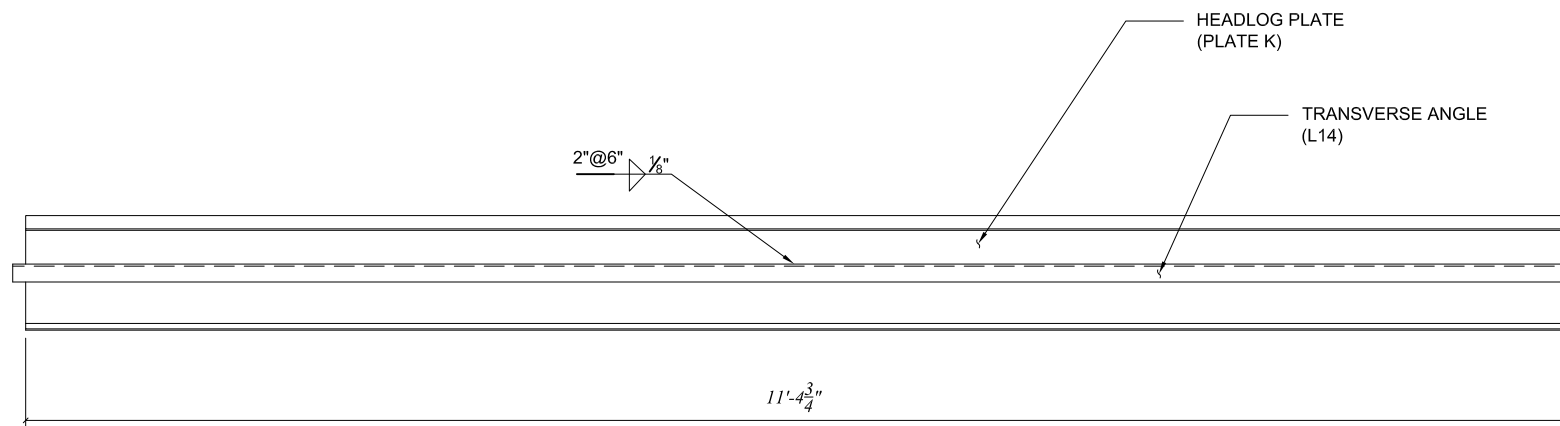
<i>Reduced Scale Barge Bow Fabrication Plans</i>				<i>Revisions:</i>	<i>2013-08-26</i>	
<i>Section view B-B</i>	<i>2013-12-11</i>	<i>University of Florida</i>	<i>Sheet 07 of 25</i>			



SECTION C-C

NOTE: LONG LEG OF ANGLES SHALL BE WELDED TO PLATE C WITH $\frac{1}{8}$ " FILLETS.

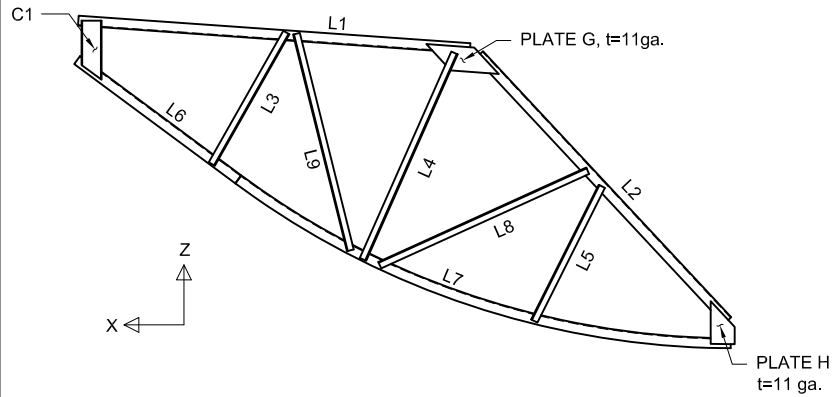
<i>Reduced Scale Barge Bow Fabrication Plans</i>				Revisions:		
<i>Section view C-C</i>	<i>2013-12-11</i>	<i>University of Florida</i>	<i>Sheet 08 of 25</i>			



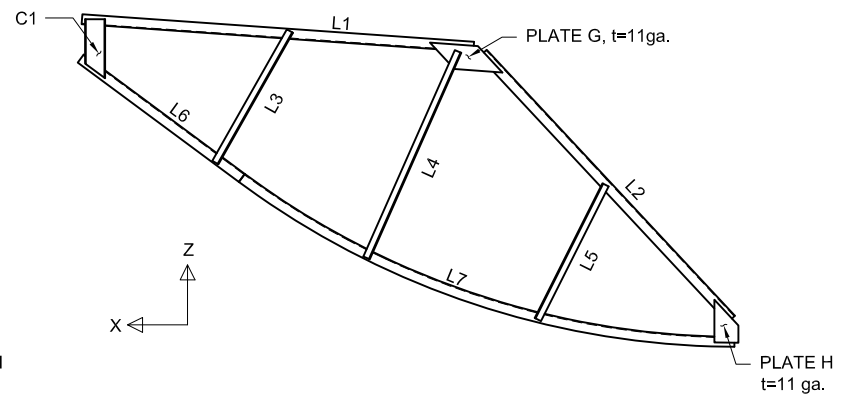
SECTION D-D

NOTE 1: PLATES I AND L REMOVED FOR CLARITY
 NOTE 2: LONG LEG OF ANGLE WELDED TO HEADLOG PLATE.

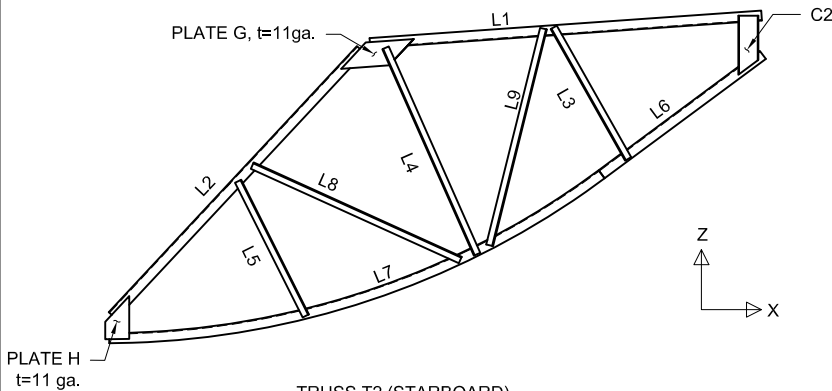
<i>Reduced Scale Barge Bow Fabrication Plans</i>				<i>Revisions:</i>		
<i>Section view D-D</i>	<i>2013-12-11</i>	<i>University of Florida</i>	<i>Sheet 09 of 25</i>			



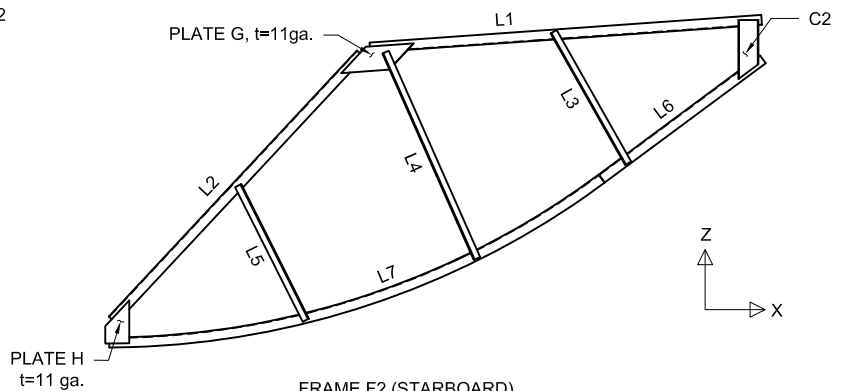
(4) TRUSS T1 (PORT SIDE)
(QTY: 4 PER BARGE BOW)



FRAME F1 (PORT SIDE)
(QTY: 3 PER BARGE BOW)



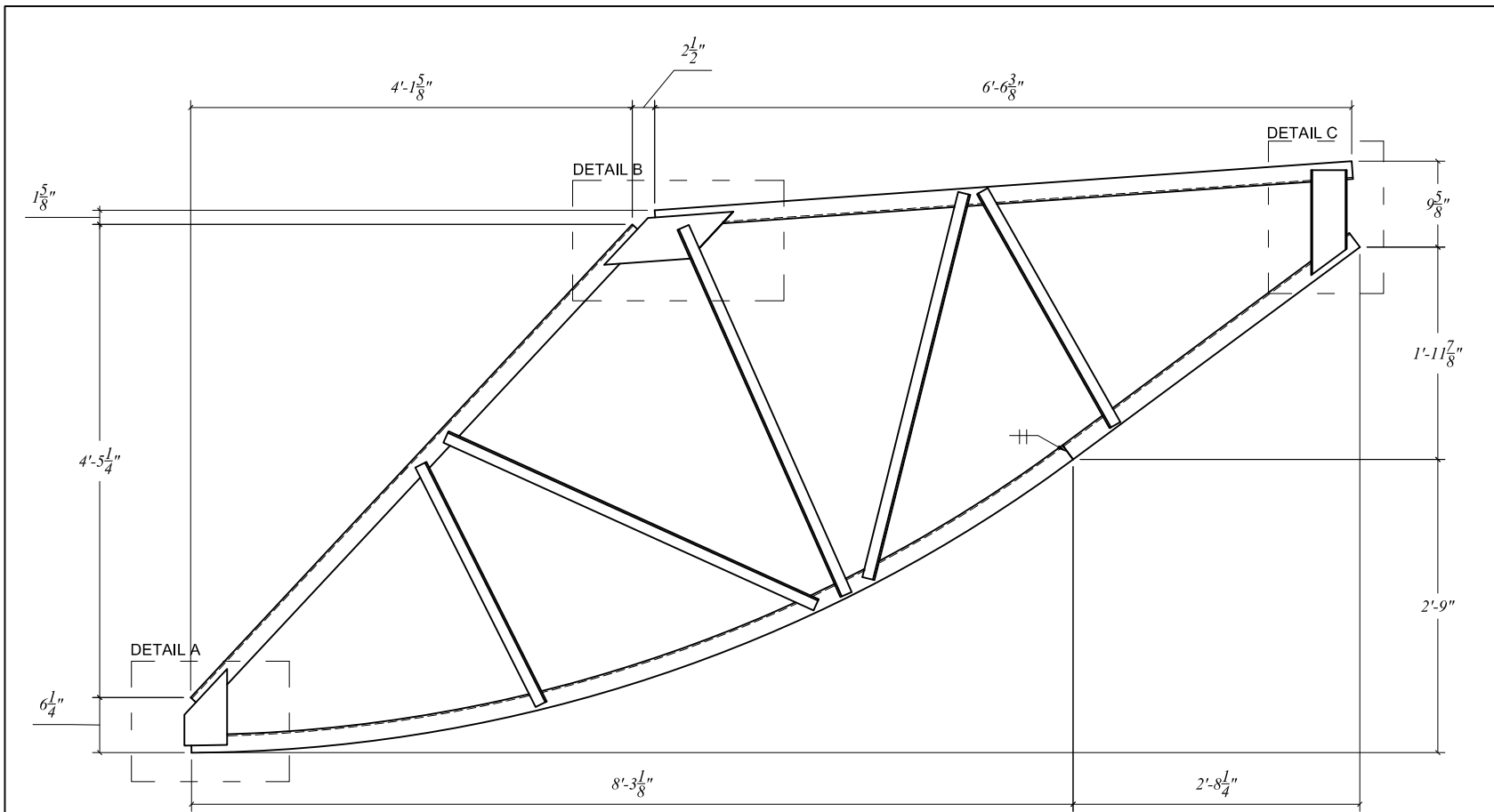
TRUSS T2 (STARBOARD)
(QTY: 4 PER BARGE BOW)



FRAME F2 (STARBOARD)
(QTY: 3 PER BARGE BOW)

NOTE 1: SEE SHEET 25 FOR MEMBER LENGTHS
 NOTE 2: LONG LEGS OF ALL ANGLE MEMBERS SHALL BE FILLET WELDED TO ADJOINING COMPONENTS WITH 1/8" FILLET WELDS
 NOTE 3: SHORT LEGS OF ALL L2 ANGLE MEMBERS SHALL BE PLUG WELDED TO PLATE E (SEE SHEET 4)

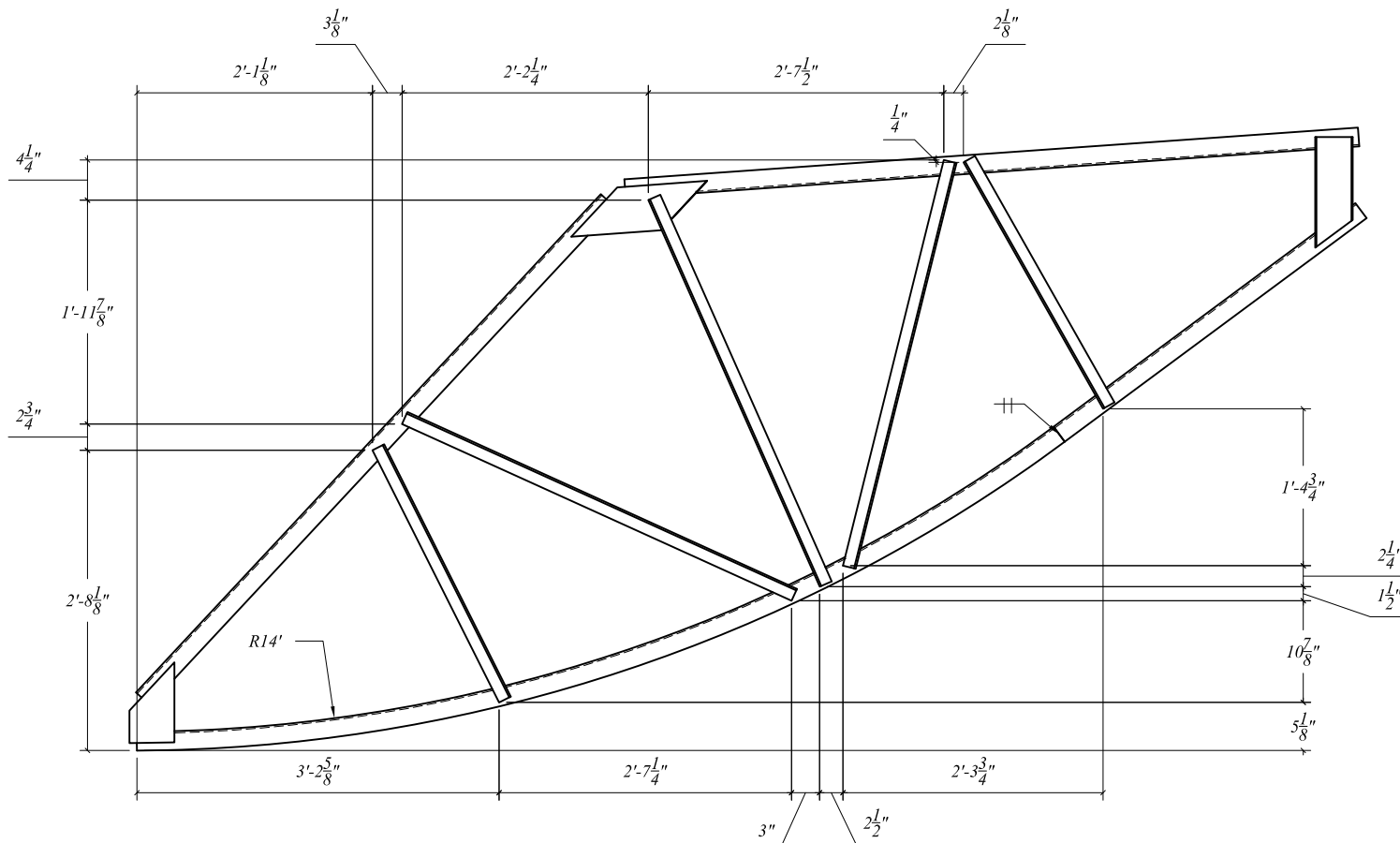
<i>Reduced Scale Barge Bow Fabrication Plans</i>				Revisions:	2013-08-26	
<i>Truss member layouts</i>	2013-12-11	<i>University of Florida</i>	<i>Sheet 10 of 25</i>			



TYPICAL TRUSS OR FRAME

- NOTE 1: DIMENSIONS FOR TOP AND BOTTOM CHORDS OF T1, T2, F1, AND F2
 NOTE 2: LONG LEGS OF ALL ANGLE MEMBERS SHALL BE FILLET WELDED TO ADJOINING COMPONENTS WITH $\frac{1}{8}"$ FILLET WELDS
 NOTE 3: SHORT LEGS OF ALL L2 ANGLE MEMBERS SHALL BE PLUG WELDED TO PLATE E (SEE SHEET 4)

<i>Reduced Scale Barge Bow Fabrication Plans</i>				<i>Revisions:</i>	<i>2013-08-26</i>	
<i>Truss chord dimensions</i>	<i>2013-12-11</i>	<i>University of Florida</i>	<i>Sheet 11 of 25</i>			



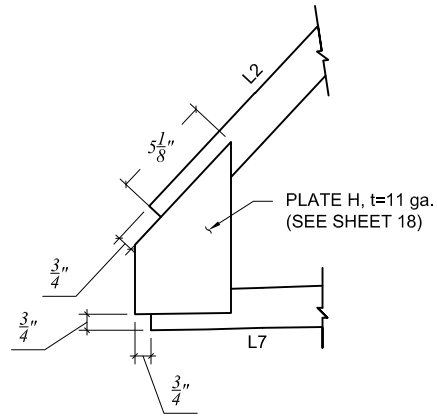
TYPICAL TRUSS OR FRAME

NOTE 1: DIMENSIONS FOR WEB MEMBERS OF T1, T2, F1, AND F2

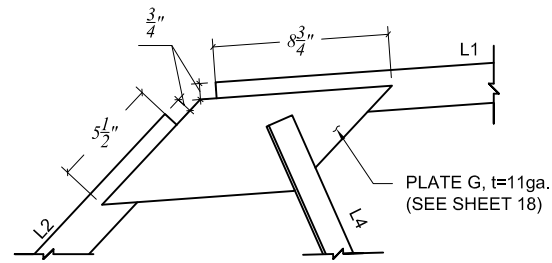
NOTE 2: LONG LEGS OF ALL ANGLE MEMBERS SHALL BE FILLET WELDED TO ADJOINING COMPONENTS WITH 1/8" FILLET WELDS

NOTE 3: SHORT LEGS OF ALL L2 ANGLE MEMBERS SHALL BE PLUG WELDED TO PLATE E (SEE SHEET 4)

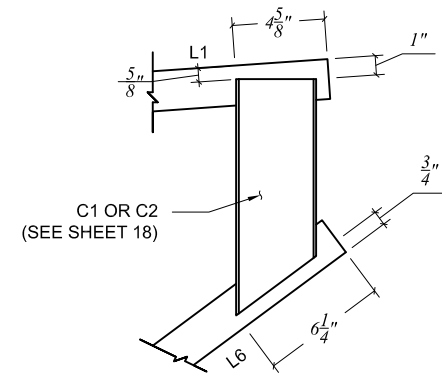
<i>Reduced Scale Barge Bow Fabrication Plans</i>				Revisions:	2013-08-26	
<i>Truss web dimensions</i>	2013-12-11	<i>University of Florida</i>	<i>Sheet 12 of 25</i>			



DETAIL A
ASSEMBLY OF PLATE H



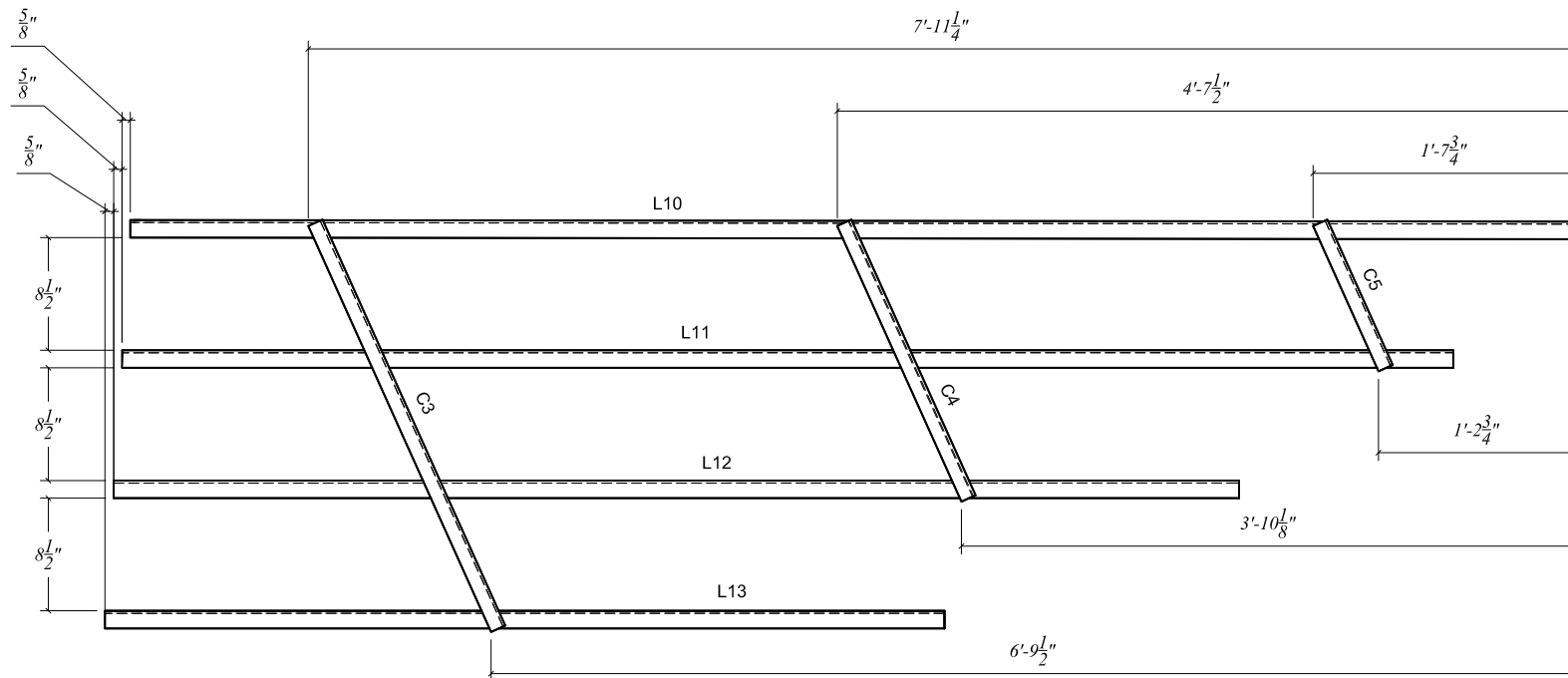
DETAIL B
ASSEMBLY OF PLATE G



DETAIL C
ASSEMBLY OF C1

NOTE: ALL ANGLE-TO-PLATE AND ANGLE-TO-CHANNEL CONNECTIONS SHALL BE WELDED AROUND THE ENTIRE INTERFACE(FRONT AND BACK) WITH $\frac{1}{8}$ " FILLET WELDS.

<i>Reduced Scale Barge Bow Fabrication Plans</i>				<i>Revisions:</i>		
<i>Truss details</i>	<i>2013-12-11</i>	<i>University of Florida</i>	<i>Sheet 13 of 25</i>			

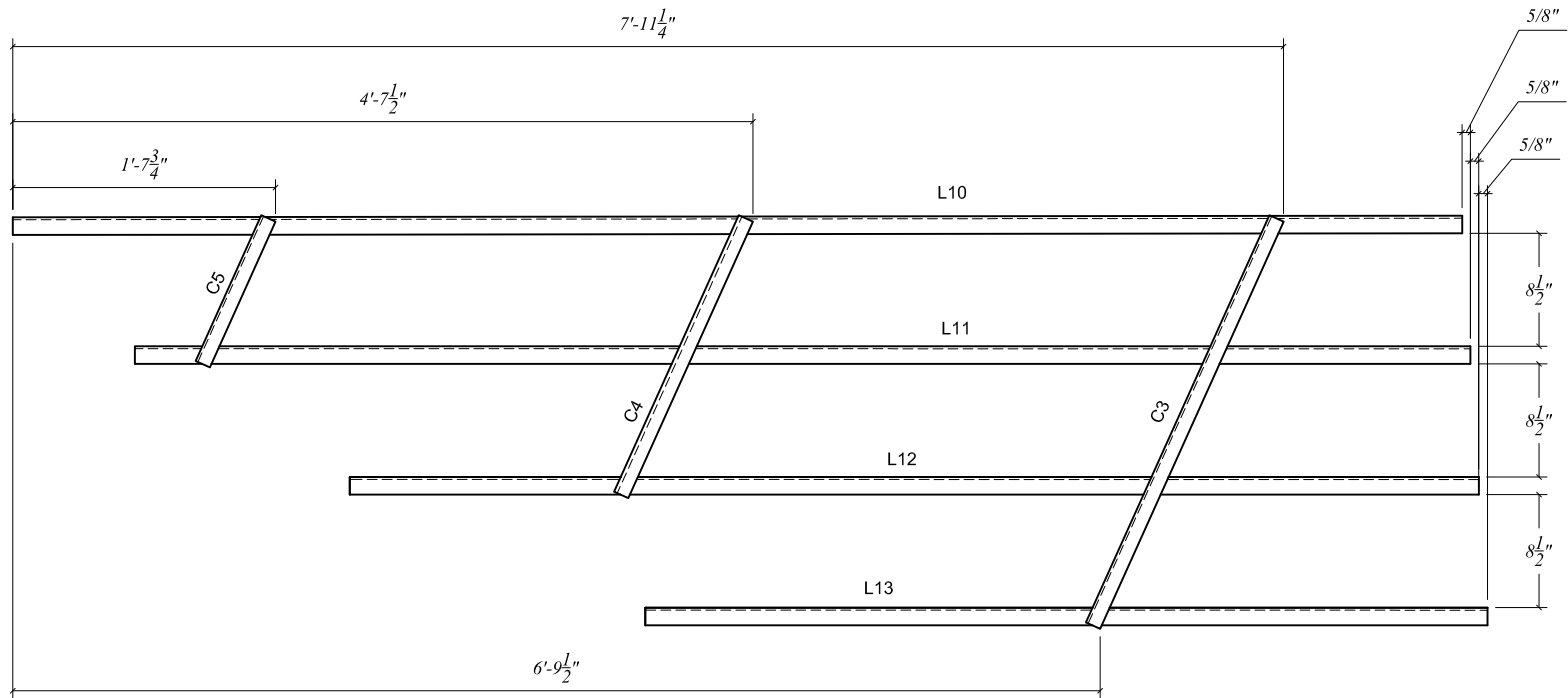


DETAIL D
F3- SIDE FRAME

NOTE 1: SEE SHEET 21 FOR MEMBER LENGTHS.

NOTE 2: SHORT LEG OF ANGLES SHALL BE FILLET WELDED TO CHANNELS WITH $\frac{1}{8}$ " FILLETS.

<i>Reduced Scale Barge Bow Fabrication Plans</i>				<i>Revisions:</i>		
<i>Side frame detail D</i>	<i>2013-12-11</i>	<i>University of Florida</i>	<i>Sheet 14 of 25</i>			



DETAIL E
F4- SIDE FRAME

NOTE 1: SEE SHEET 21 FOR MEMBER LENGTHS

NOTE 2: SHORT LEG OF ANGLES SHALL BE FILLET WELDED TO CHANNELS WITH $\frac{1}{8}$ " FILLETS

<i>Reduced Scale Barge Bow Fabrication Plans</i>				<i>Revisions:</i>		
<i>Side frame detail E</i>	<i>2013-12-11</i>	<i>University of Florida</i>	<i>Sheet 15 of 25</i>			

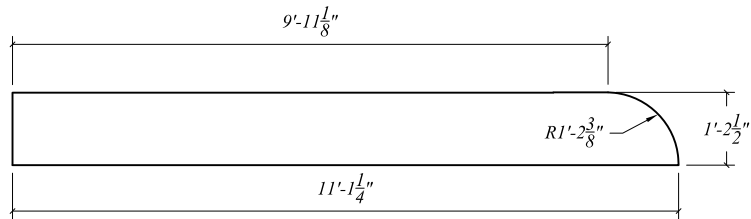


PLATE A
(QTY: 2 PER BARGE BOW)
GRADE A36, t=1/4"

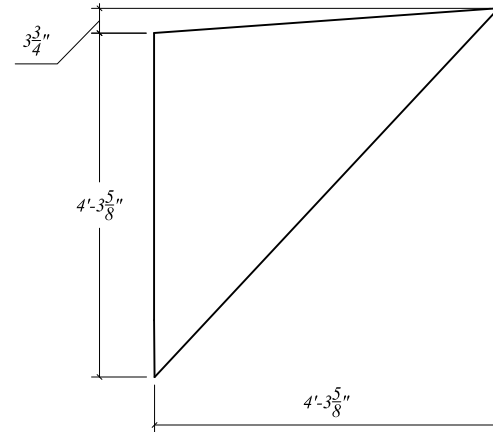


PLATE B
(QTY: 2 PER BARGE BOW)
GRADE A1011 CS B, t=11 ga.

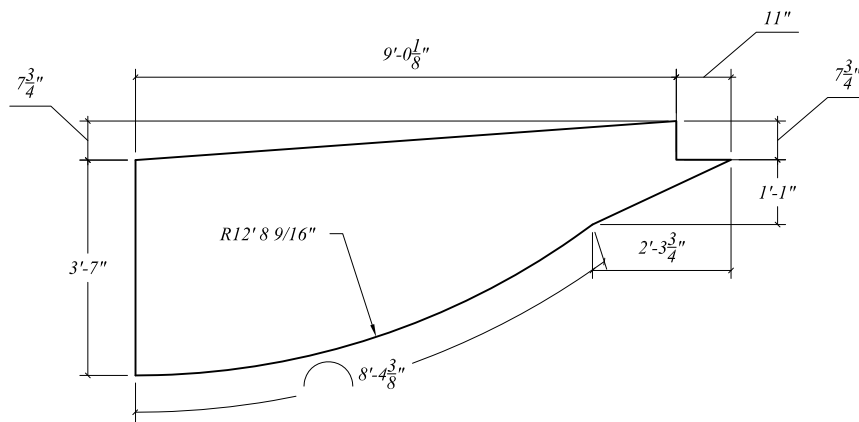


PLATE C
(QTY: 2 PER BARGE BOW)
GRADE A1011 CS B, t=9 ga.

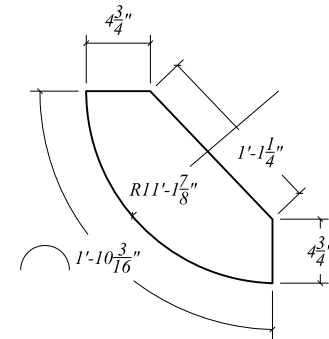


PLATE D
(QTY: 12 PER BARGE BOW)
GRADE A1011 CS B, t=9 ga.

Reduced Scale Barge Bow Fabrication Plans

Plate dimensions 1

2013-12-11

University of Florida

Sheet 16 of 25

Revisions:

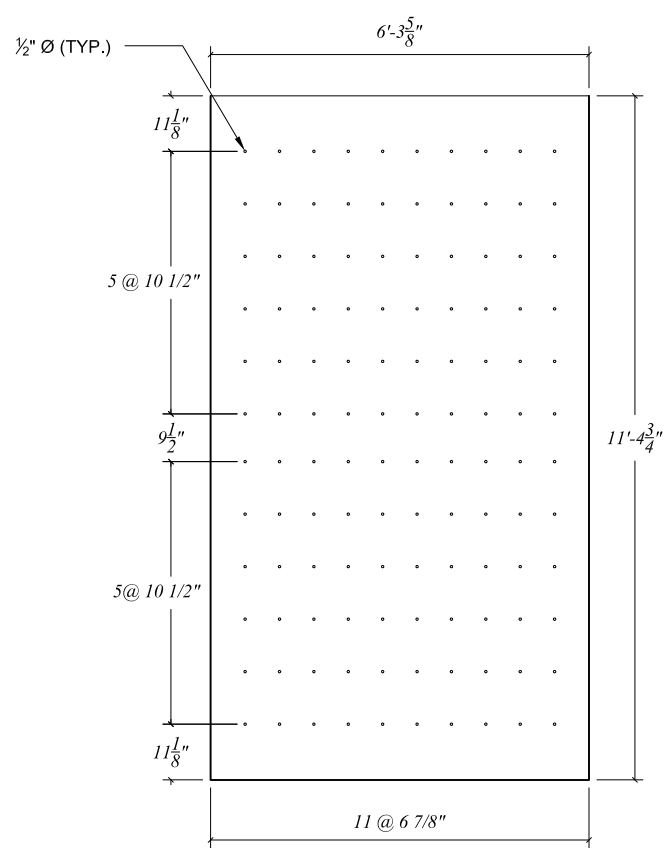


PLATE E
GRADE A1011 CS B, t=11 ga.

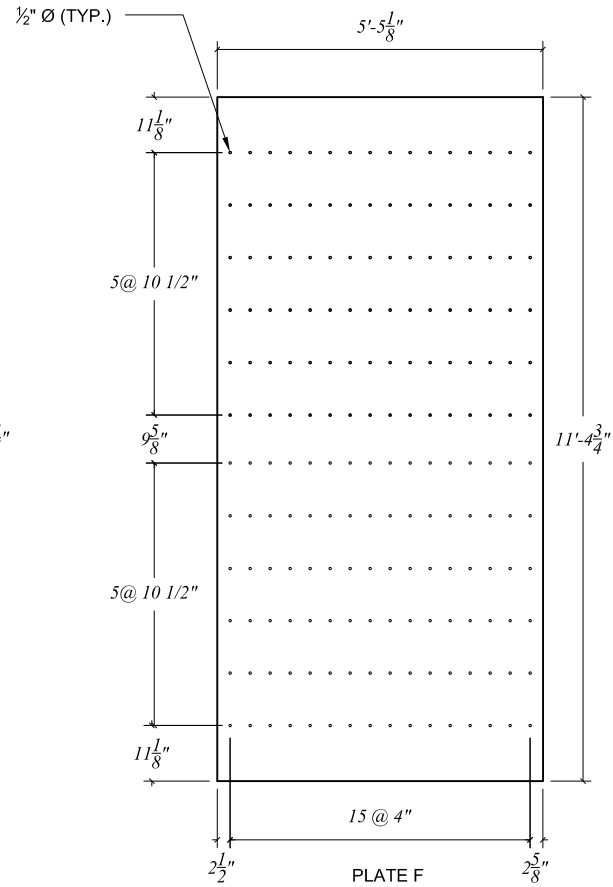


PLATE F
GRADE A1011 CS B, t=11 ga.

NOTE: IF PLATE WITH THE DIMENSIONS INDICATED ABOVE IS UNAVAILABLE, PLATES E AND/OR F MAY BE CONSTRUCTED BY BUTT-WELDING (2) SMALLER RECTANGULAR PLATES TOGETHER. CONSULT WITH OWNER FOR APPROVAL.

PLATE LIST- TOP HULL

<i>Reduced Scale Barge Bow Fabrication Plans</i>				<i>Revisions:</i>	2013-08-26	
					2013-09-17	
<i>Plate dimensions 2</i>	2013-12-11	<i>University of Florida</i>	<i>Sheet 17 of 25</i>			

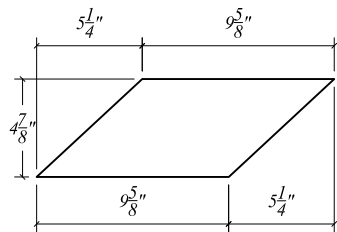


PLATE G
 (QTY: 14 PER BARGE BOW)
 GRADE A1011 CS B, t=11 ga.

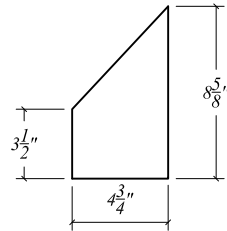
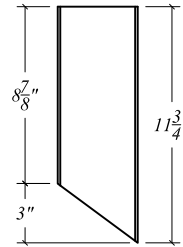
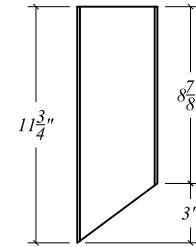


PLATE H
 (QTY: 14 PER BARGE BOW)
 GRADE A1011 CS B, t=11 ga.



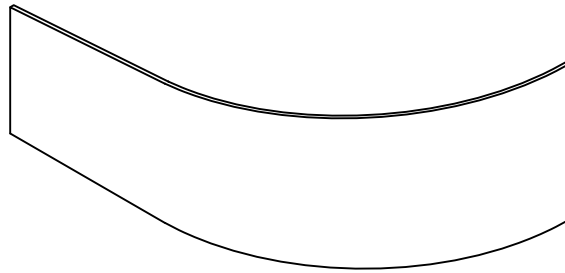
C1
 (QTY: 7 PER BARGE BOW)
 GRADE A36



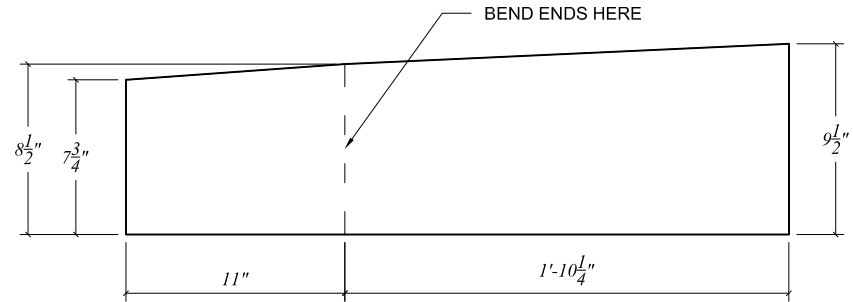
C2
 (QTY: 7 PER BARGE BOW)
 GRADE A36

PLATE LIST- TRUSS AND FRAMES

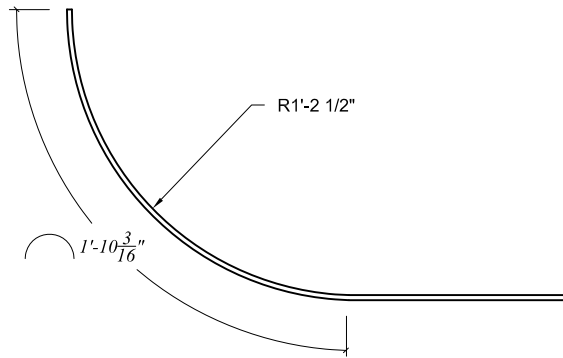
<i>Reduced Scale Barge Bow Fabrication Plans</i>				<i>Revisions:</i>		
<i>Plate dimensions 3</i>	<i>2013-12-11</i>	<i>University of Florida</i>	<i>Sheet 18 of 25</i>			



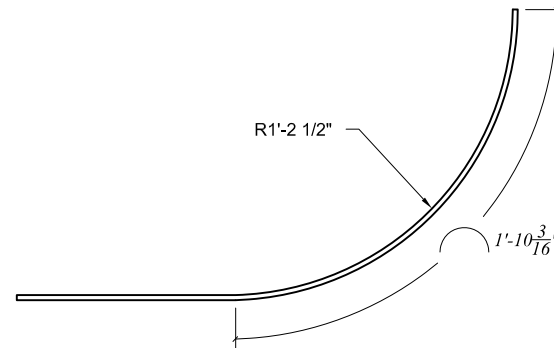
ISOMETRIC VIEW



FLAT PLATE DIMENSIONS



PLAN VIEW - PLATE I-1

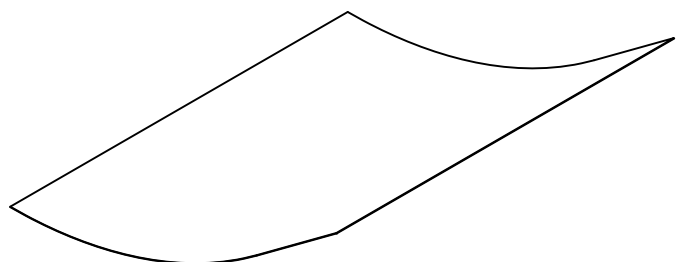


PLAN VIEW - PLATE I-2

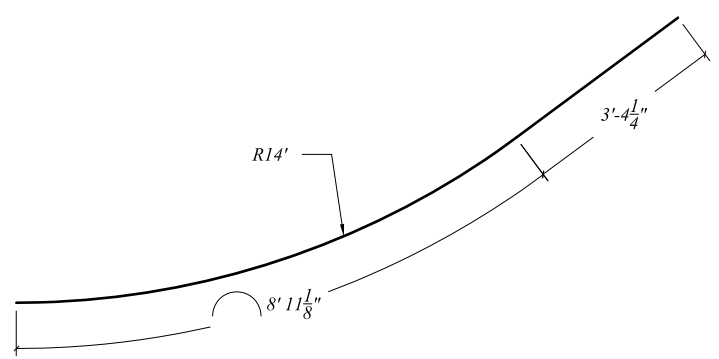
PLATE I
 (QTY: 2 PER BARGE BOW - SEE NOTE ON THIS PAGE)
 GRADE A36, t=1/4"

NOTE: TWO OF PLATE "I" SHALL BE CONSTRUCTED (I-1, I-2) AS MIRROR IMAGES TO EACH OTHER, ROLLED TO CONFORM TO THE RADII INDICATED ON THIS SHEET.

<i>Reduced Scale Barge Bow Fabrication Plans</i>				<i>Revisions:</i>		
<i>Bent plate I</i>	<i>2013-12-11</i>	<i>University of Florida</i>	<i>Sheet 19 of 25</i>			

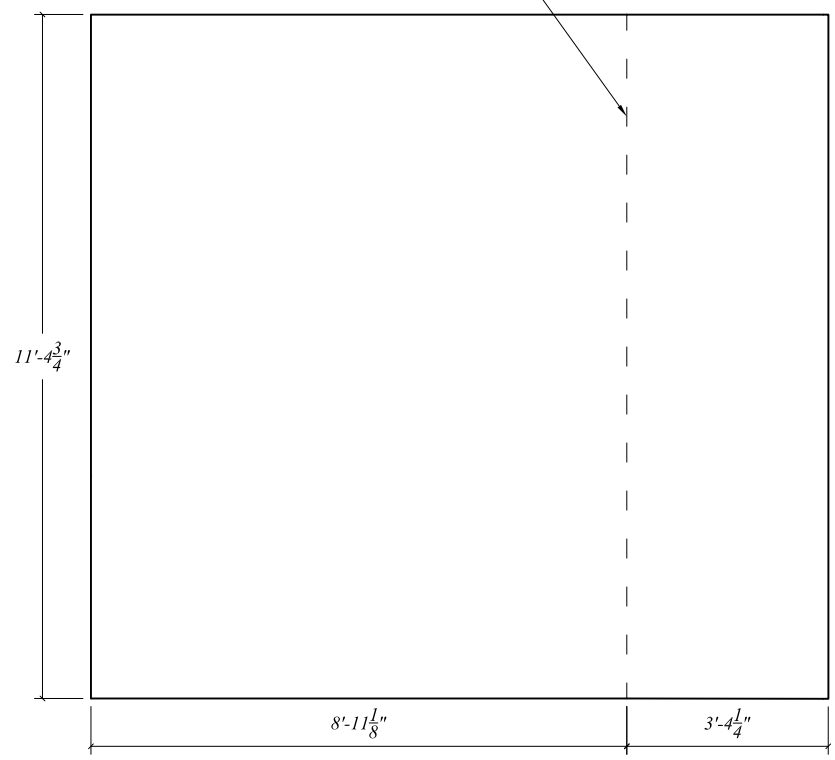


ISOMETRIC VIEW



PLAN VIEW

BEND ENDS HERE

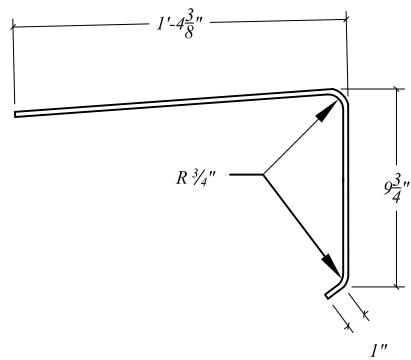


FLAT PLATE DIMENSIONS

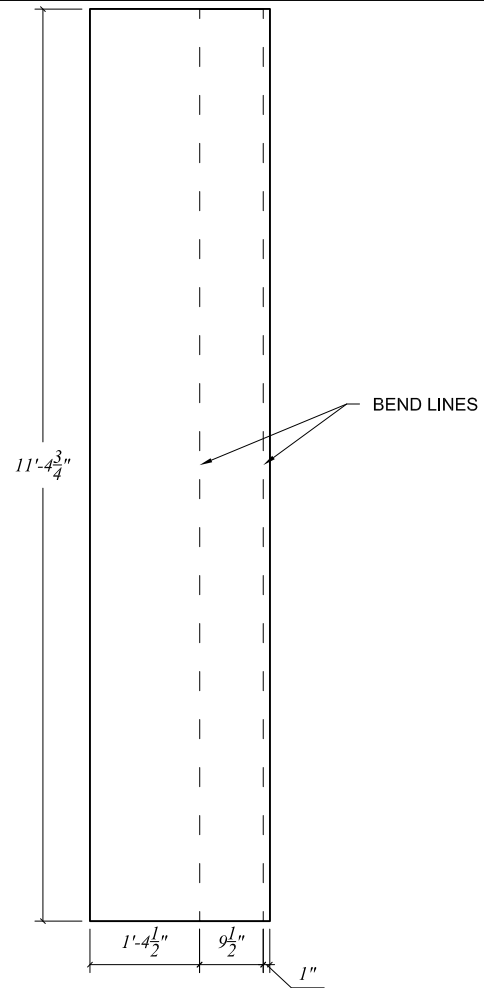
NOTE: IF FLAT PLATE WITH THE DIMENSIONS INDICATED ABOVE IS UNAVAILABLE, PLATE J MAY BE CONSTRUCTED BY BUTT-WELDING SMALLER RECTANGULAR PLATES TOGETHER.

PLATE J
GRADE A1011 CS B, t=9 ga.

<i>Reduced Scale Barge Bow Fabrication Plans</i>				<i>Revisions:</i>		
<i>Bent plate J</i>	<i>2013-12-11</i>	<i>University of Florida</i>	<i>Sheet 20 of 25</i>			



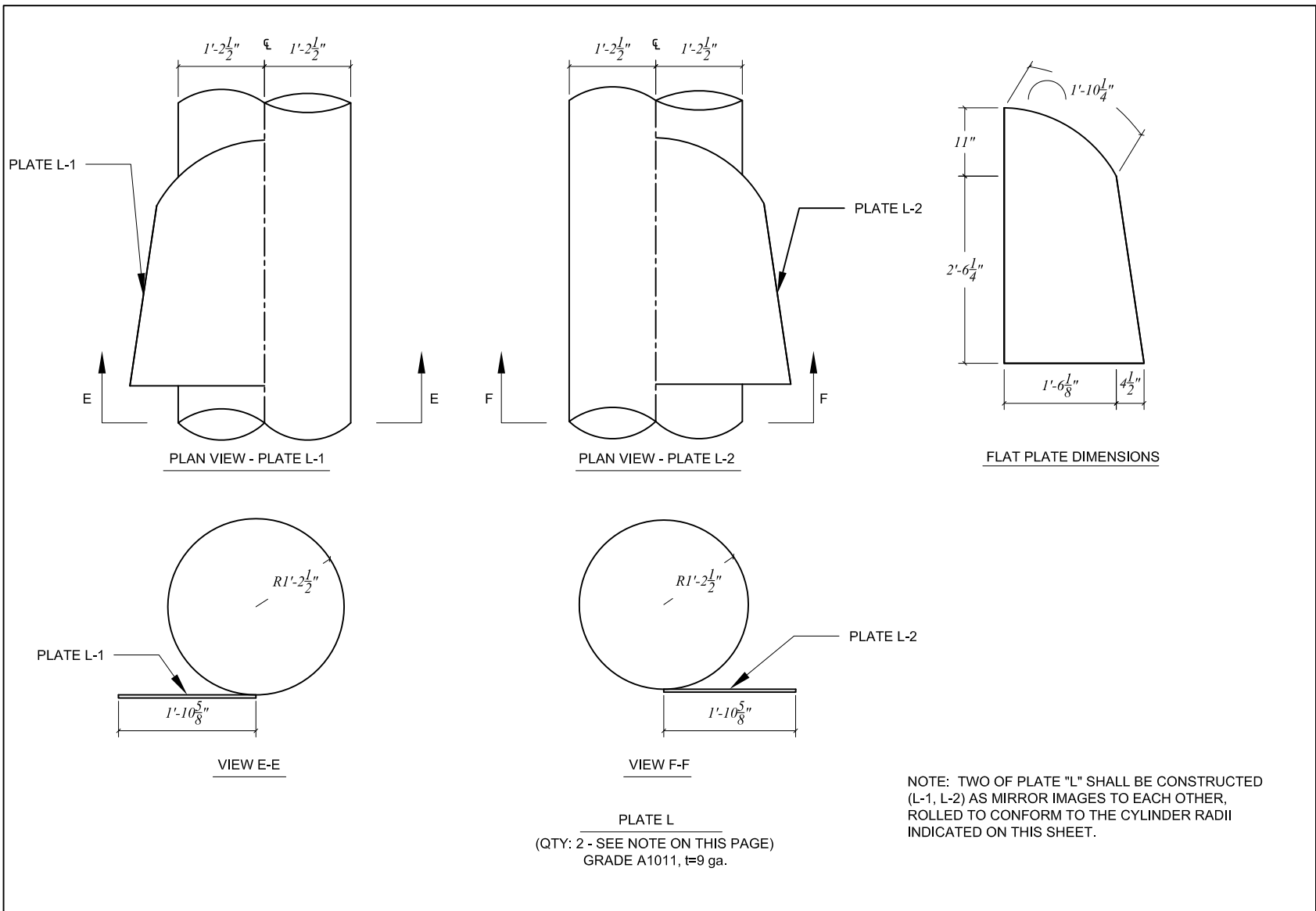
PLAN VIEW



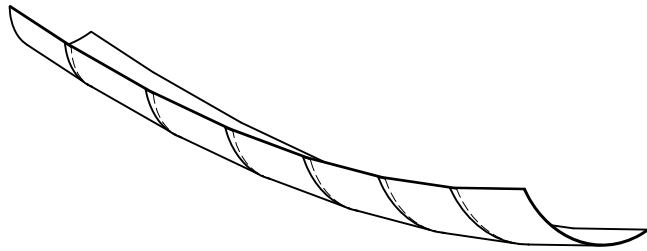
FLAT PLATE DIMENSIONS

PLATE K
GRADE A36, t=1/4"

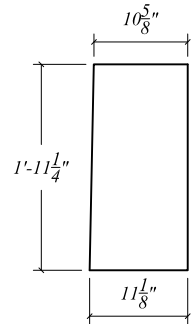
<i>Reduced Scale Barge Bow Fabrication Plans</i>				<i>Revisions:</i>		
<i>Bent plate K</i>	<i>2013-12-11</i>	<i>University of Florida</i>	<i>Sheet 21 of 25</i>			



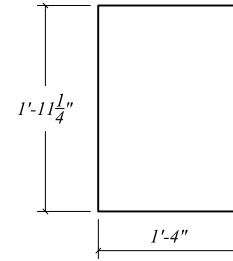
<i>Reduced Scale Barge Bow Fabrication Plans</i>				<i>Revisions:</i>		
<i>Bent Plate L</i>	2013-12-11	<i>University of Florida</i>	<i>Sheet 22 of 25</i>			



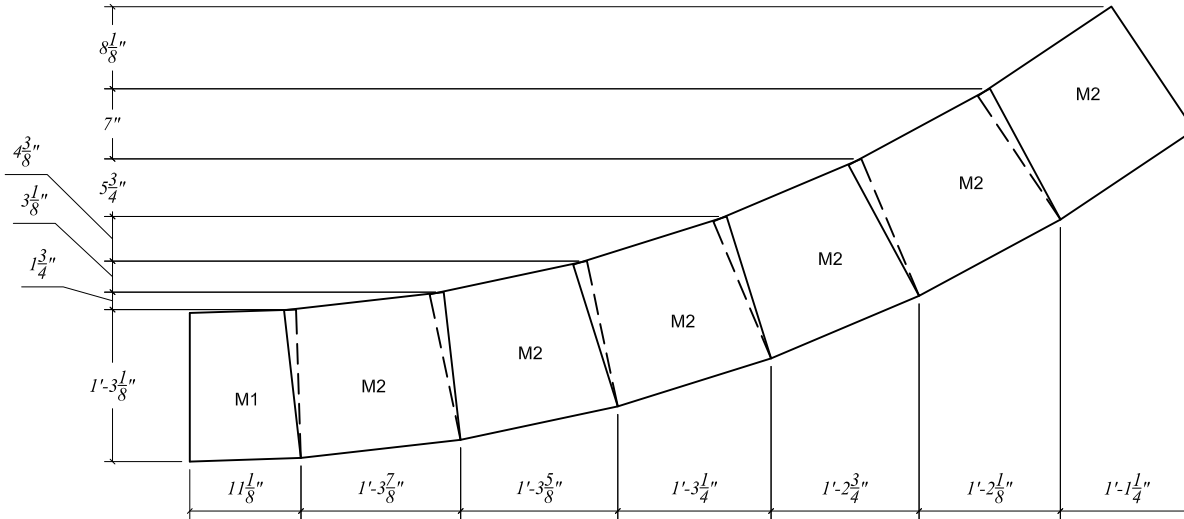
ISOMETRIC VIEW



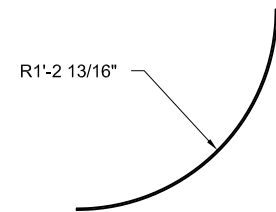
M1 FLAT PLATE DIMENSIONS



M2 FLAT PLATE DIMENSIONS
(QTY: 6 PER BARGE BOW)



ELEVATION VIEW



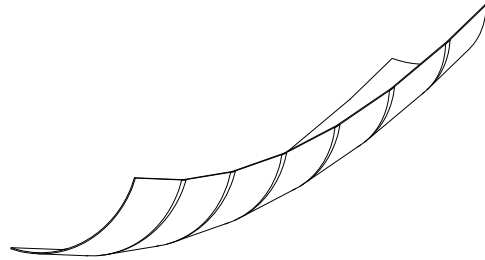
M PLATE CURVATURE

NOTE 1: PLATE M IS CONSTRUCTED BY OVERLAPPING PLATES M1 AND M2 ACCORDING TO THE LAYOUT DEPICTED ABOVE. NOTE THAT THE PLATE BEING OVERLAPPED ALTERNATES

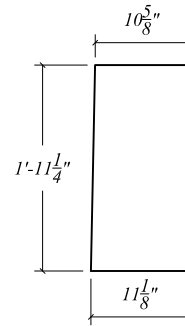
NOTE 2: ALL PLATE OVERLAPS SHALL BE WELDED WITH 1/8" FILLET WELD (BOTH SIDES).

PLATE M
GRADE A1011, t=9 ga.

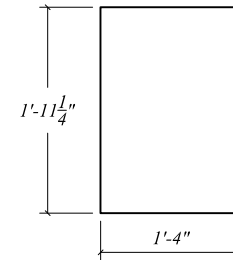
<i>Reduced Scale Barge Bow Fabrication Plans</i>				Revisions:		
<i>Bent Plate M</i>	2013-12-11	University of Florida	Sheet 23 of 25			



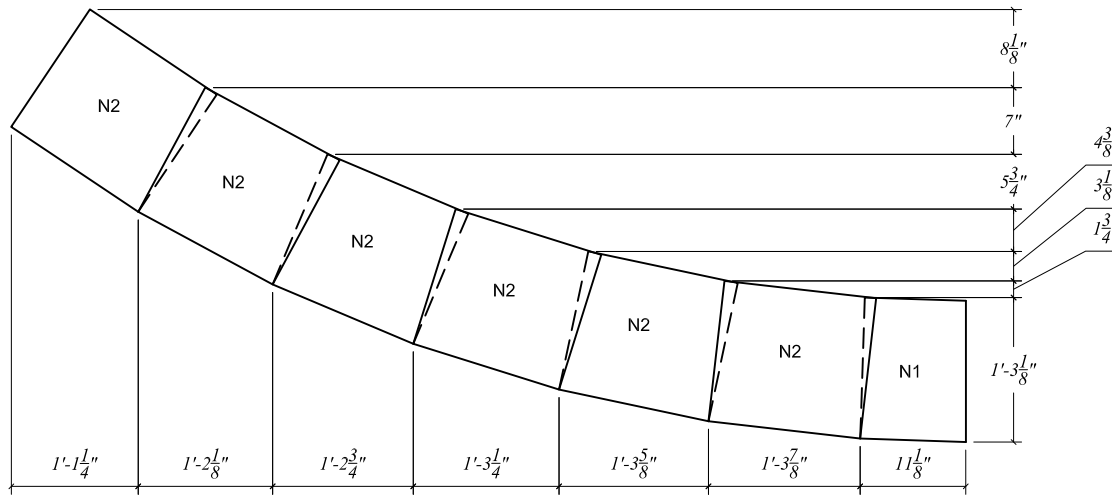
ISOMETRIC VIEW



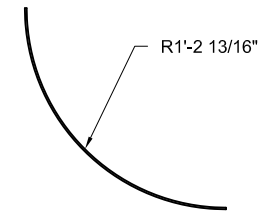
N1 FLAT PLATE DIMENSIONS



N2 FLAT PLATE DIMENSIONS
(QTY: 6 PER BARGE BOW)



ELEVATION VIEW



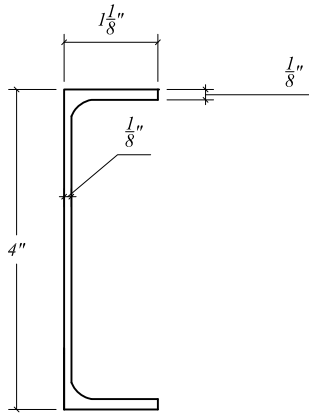
N PLATE CURVATURE

NOTE 1: PLATE N IS CONSTRUCTED BY OVERLAPPING PLATES N1 AND N2 ACCORDING TO THE LAYOUT DEPICTED ABOVE. NOTE THAT THE PLATE BEING OVERLAPPED ALTERNATES.

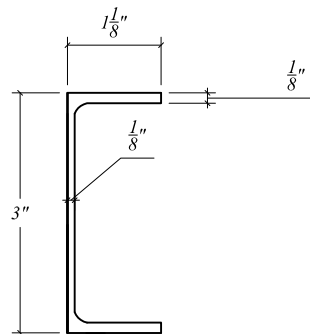
NOTE 2: ALL PLATE OVERLAPS SHALL BE WELDED WITH 1/8" FILLET WELD (BOTH SIDES).

PLATE N
GRADE A1011, t=9 ga.

<i>Reduced Scale Barge Bow Fabrication Plans</i>				<i>Revisions:</i>		
<i>Bent Plate N</i>	<i>2013-12-11</i>	<i>University of Florida</i>	<i>Sheet 24 of 25</i>			



CHANNEL A
GRADE A36



CHANNEL B
GRADE A36

SCHEDULE OF MEMBERS					
NAME	SIZE	LENGTH	QTY (PER BARGE BOW)	TOTAL	NOTES
L1	L2x1.2x $\frac{1}{8}$ "	6'-6 $\frac{1}{2}$ "	14	91'-7"	
L2	L2x1.2x $\frac{1}{8}$ "	6'-0 $\frac{3}{4}$ "	14	84'-10 $\frac{1}{2}$ "	
L3	L1.5x1.4x $\frac{1}{8}$ "	2'-6 $\frac{1}{4}$ "	14	35'-3 $\frac{1}{2}$ "	
L4	L1.5x1.4x $\frac{1}{8}$ "	3'-9 $\frac{1}{8}$ "	14	52'-7 $\frac{3}{4}$ "	
L5	L1.5x1.4x $\frac{1}{8}$ "	2'-6 $\frac{1}{8}$ "	14	35'-1 $\frac{3}{4}$ "	
L6	L2x1.2x $\frac{1}{8}$ "	3'-4 $\frac{1}{8}$ "	14	46'-9 $\frac{3}{4}$ "	
L7	L2x1.2x $\frac{1}{8}$ "	8'-10 $\frac{3}{16}$ "	14	123'-10 $\frac{5}{8}$ "	THIS MEMBER BENT AROUND RADIUS OF 14'
L8	L1.5x1.4x $\frac{1}{8}$ "	3'-9 $\frac{11}{16}$ "	8	30'-5 $\frac{1}{2}$ "	
L9	L1.5x1.4x $\frac{1}{8}$ "	3'-8 $\frac{5}{8}$ "	8	29'-9"	
L10	L2x1.2x $\frac{1}{8}$ "	9'-0 $\frac{1}{16}$ "	2	18'-1 $\frac{3}{8}$ "	
L11	L2x1.2x $\frac{1}{8}$ "	8'-4 $\frac{3}{16}$ "	2	16'-8 $\frac{3}{8}$ "	
L12	L2x1.2x $\frac{1}{8}$ "	7'-0 $\frac{1}{16}$ "	2	14'-1 $\frac{3}{8}$ "	
L13	L2x1.2x $\frac{1}{8}$ "	5'-3 $\frac{3}{16}$ "	2	10'-6 $\frac{3}{8}$ "	
L14	L2.3x1.6x $\frac{3}{16}$ "	11'-7 $\frac{3}{4}$ "	1	11'-7 $\frac{3}{4}$ "	
C1	CHANNEL A	11 $\frac{1}{16}$ "	7	6'-10 $\frac{11}{16}$ "	THIS MEMBER MODIFIED SEE PLATE DETAIL SHEET 18
C2	CHANNEL A	11 $\frac{1}{16}$ "	7	6'-10 $\frac{11}{16}$ "	THIS MEMBER MODIFIED SEE PLATE DETAIL SHEET 18
C3	CHANNEL B	2'-9 $\frac{1}{2}$ "	2	5'-7"	
C4	CHANNEL B	1'-10 $\frac{3}{4}$ "	2	3'-9 $\frac{1}{2}$ "	
C5	CHANNEL B	1'	2	2'-0"	
C6	CHANNEL A	11'-7 $\frac{3}{4}$ "	1	11'-7 $\frac{3}{4}$ "	

Reduced Scale Barge Bow Fabrication Plans

Schedule of members

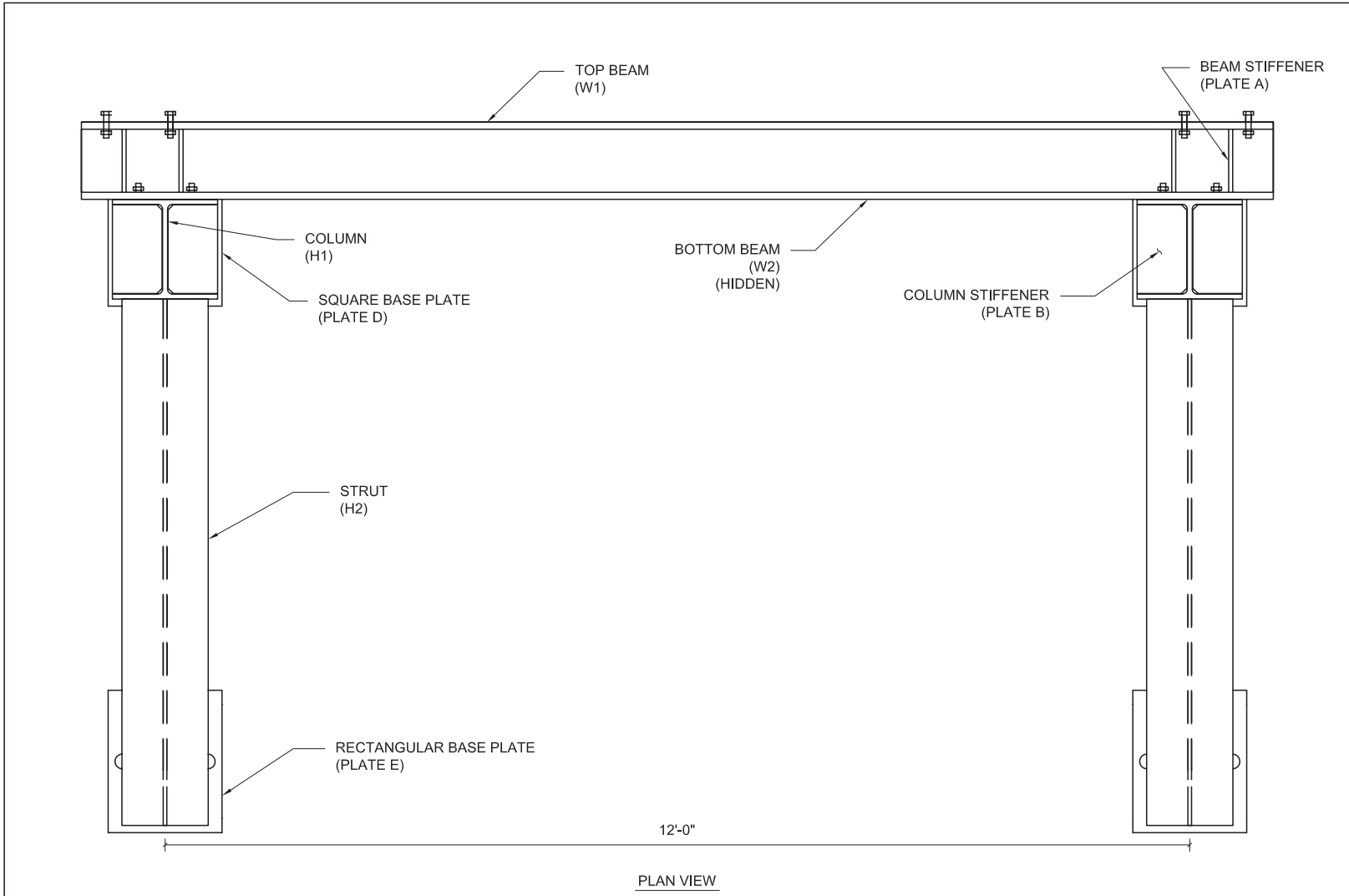
2013-12-11

University of Florida

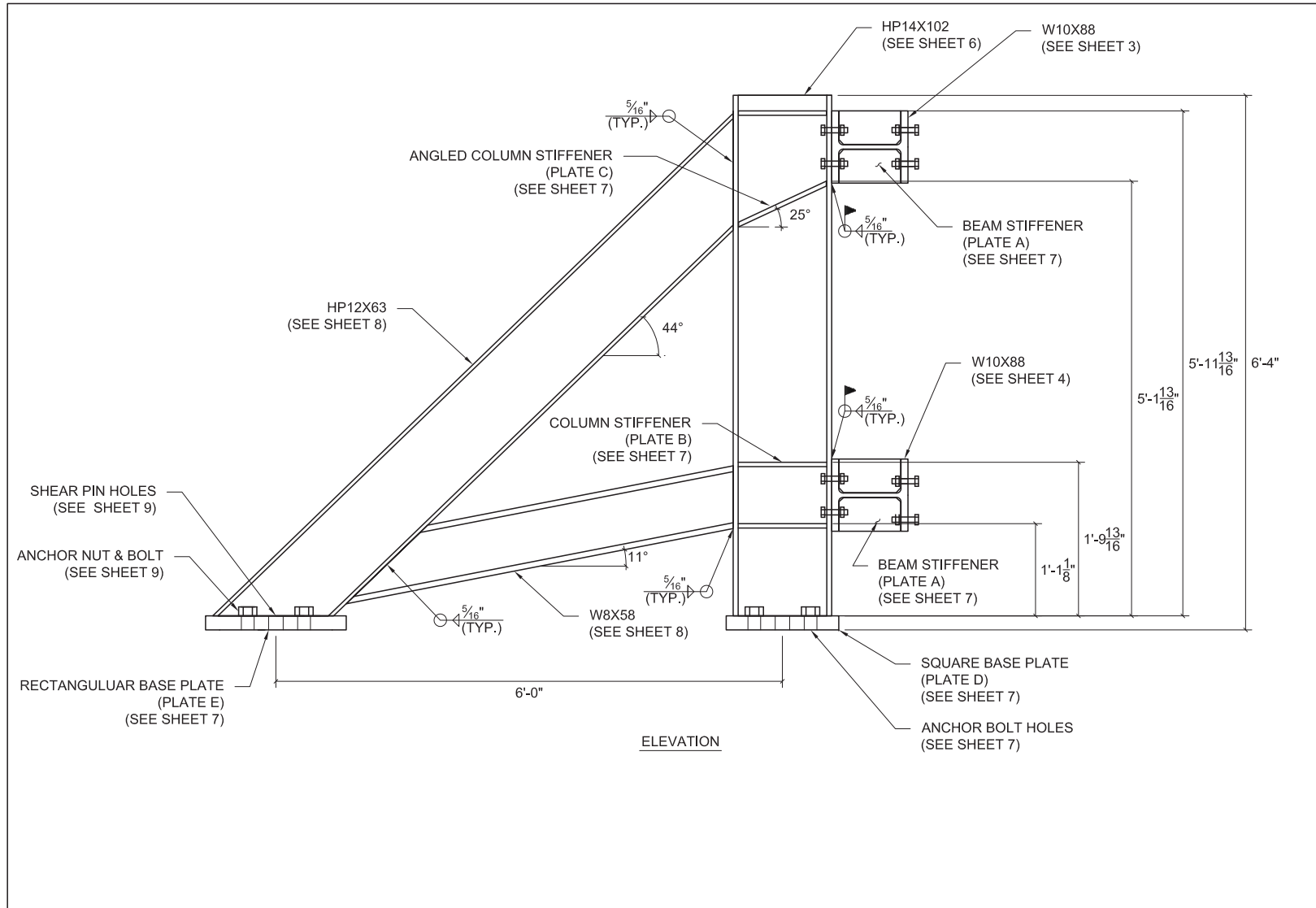
Sheet 25 of 25

Revisions:

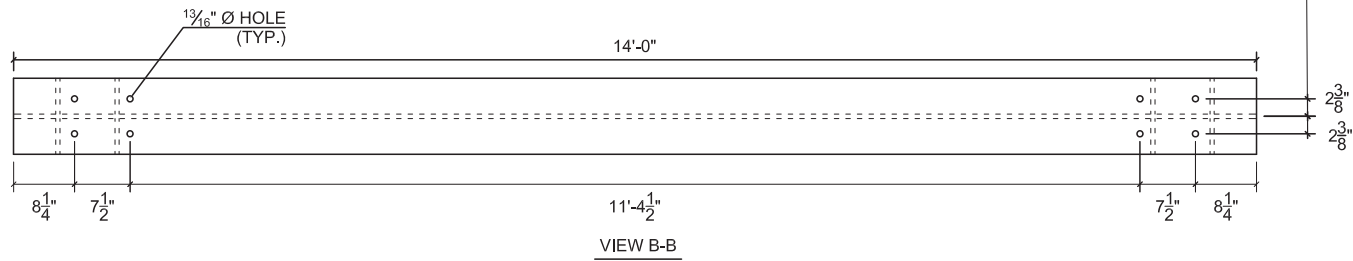
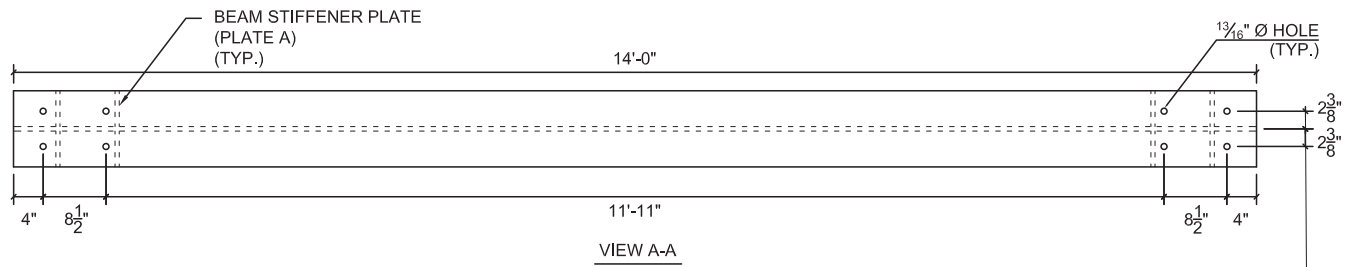
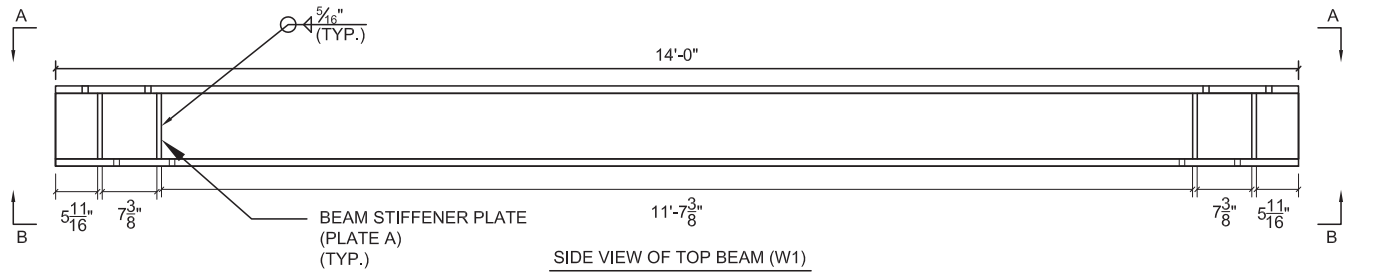
APPENDIX G
BARGE BOW REACTION FRAME FABRICATION DRAWINGS



<i>Validation and Implementation of Bridge Design Specifications for Barge Impact Loading (Reaction Frame)</i>				<i>Revisions:</i>	
<i>Plan View</i>	<i>2013-03-11</i>	<i>University of Florida</i>	<i>Sheet 01 of 12</i>		



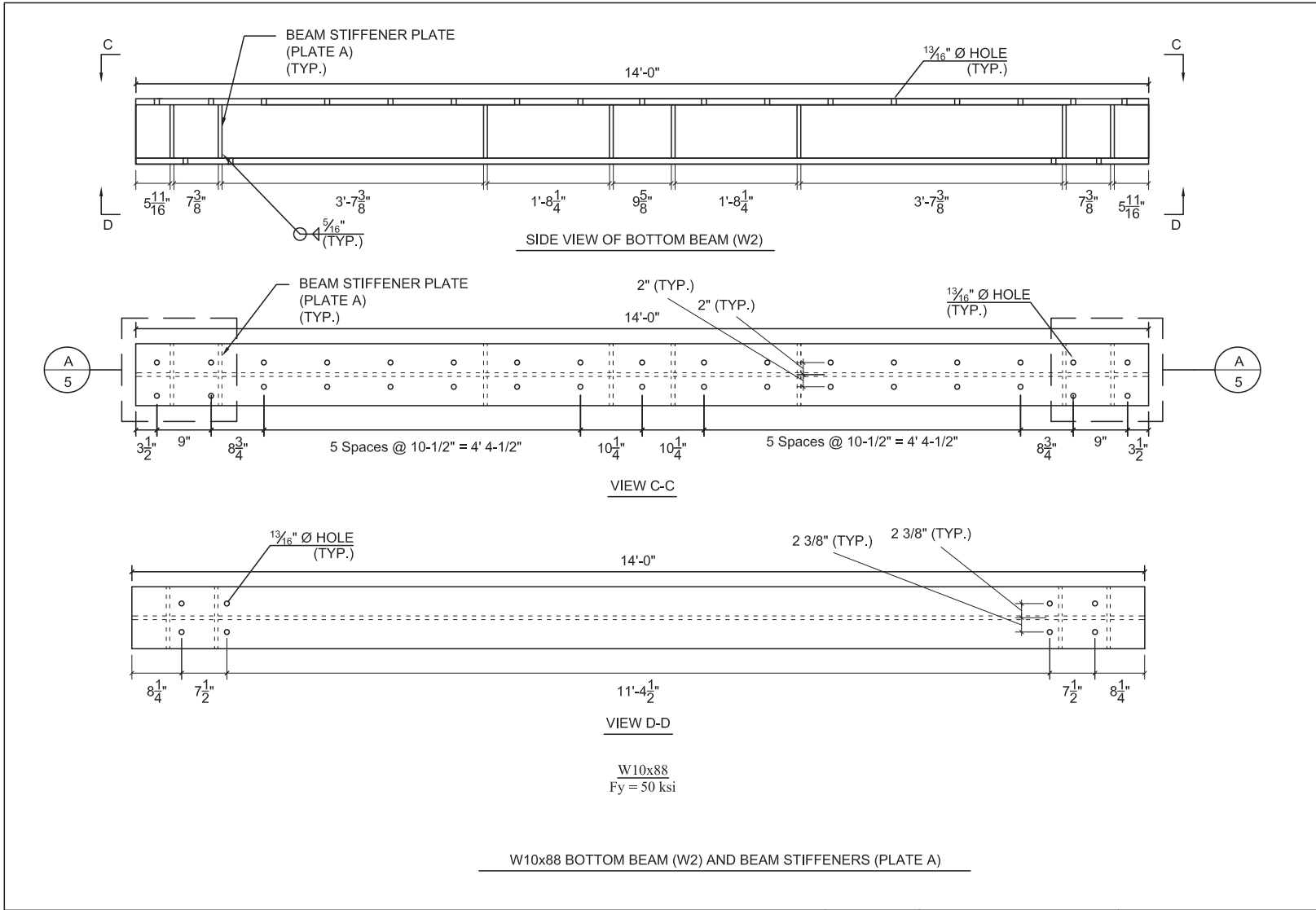
<i>Validation and Implementation of Bridge Design Specifications for Barge Impact Loading (Reaction Frame)</i>				<i>Revisions:</i>		
<i>Elevation View</i>	<i>2013-03-11</i>	<i>University of Florida</i>	<i>Sheet 02 of 12</i>			



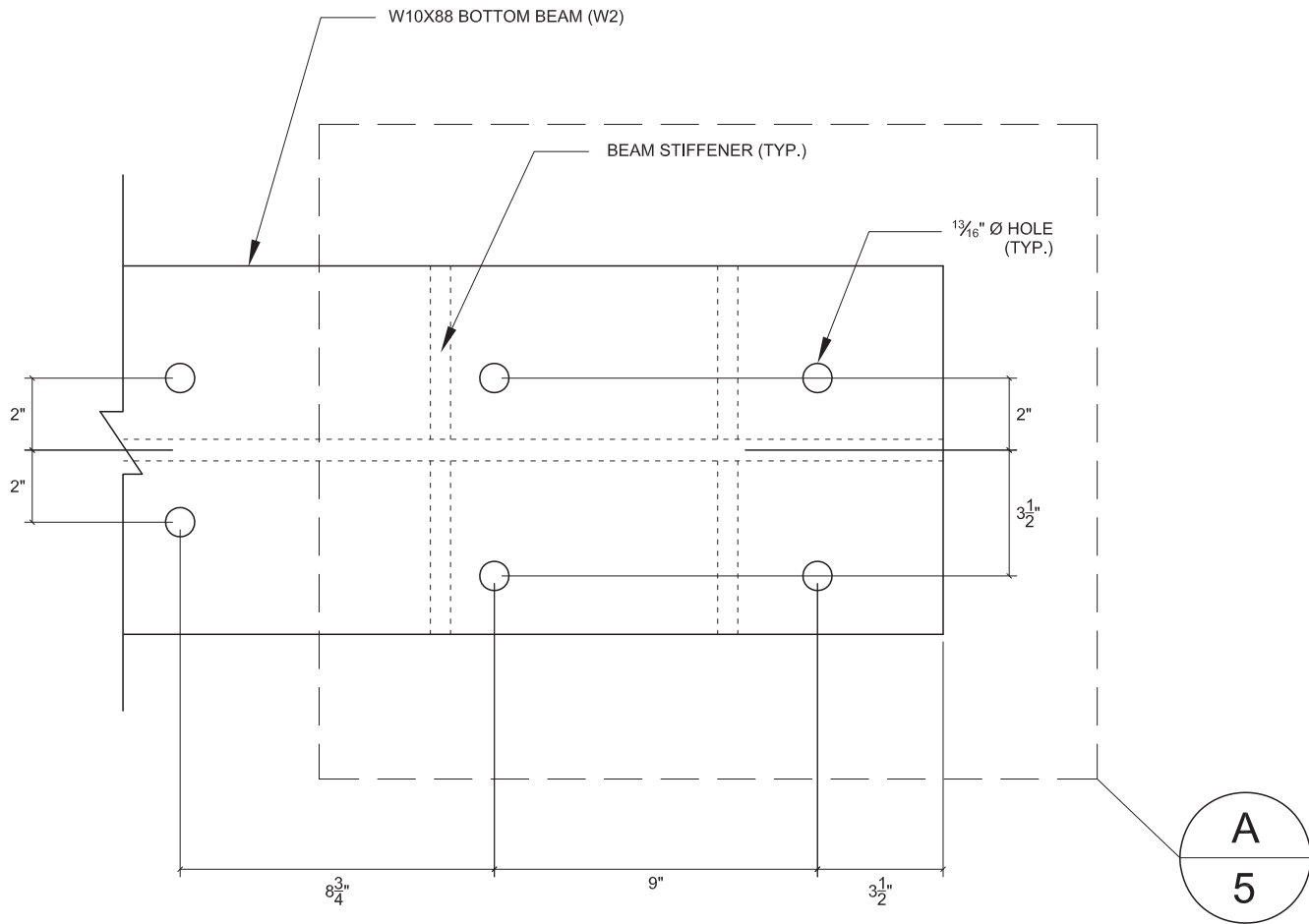
W10x88
F_y = 50 ksi

W10x88 TOP BEAM (W1) AND BEAM STIFFENER (PLATE A)

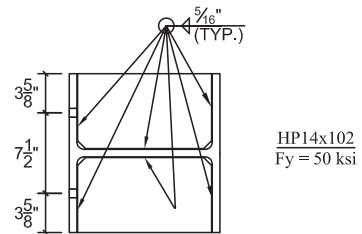
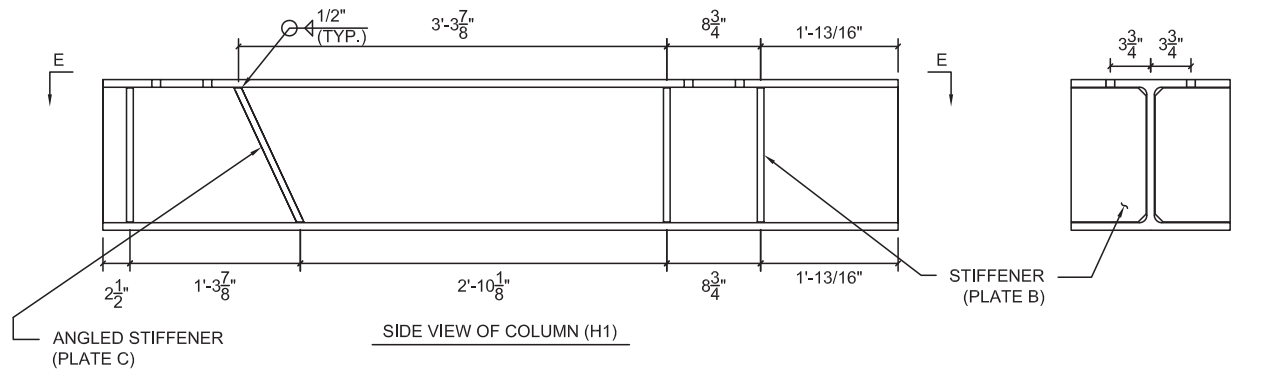
Validation and Implementation of Bridge Design Specifications for Barge Impact Loading (Reaction Frame)				Revisions:		
Top Beam (W1) Details	2013-03-11	University of Florida	Sheet 03 of 12			



Validation and Implementation of Bridge Design Specifications for Barge Impact Loading (Reaction Frame)				Revisions:		
Bottom Beam (W2) Details	2013-03-11	University of Florida	Sheet 04 of 12			

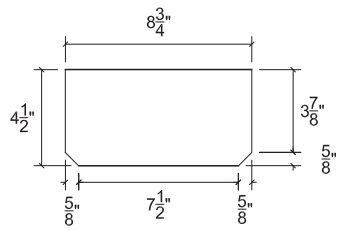


<i>Validation and Implementation of Bridge Design Specifications for Barge Impact Loading (Reaction Frame)</i>				<i>Revisions:</i>		
<i>Bottom Beam End Detail</i>	<i>2013-03-11</i>	<i>University of Florida</i>	<i>Sheet 05 of 12</i>			

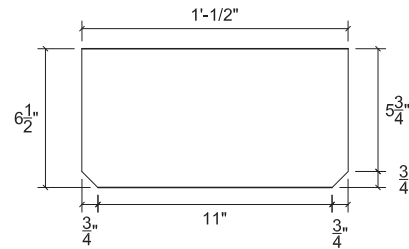


HP14x102 COLUMN (H1), COLUMN STIFFENERS (PLATE B) AND ANGLED COLUMN STIFFENERS (PLATE C)

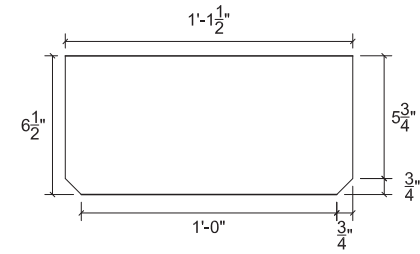
Validation and Implementation of Bridge Design Specifications for Barge Impact Loading (Reaction Frame)				Revisions:		
Column Details	2013-03-11	University of Florida	Sheet 06 of 12			



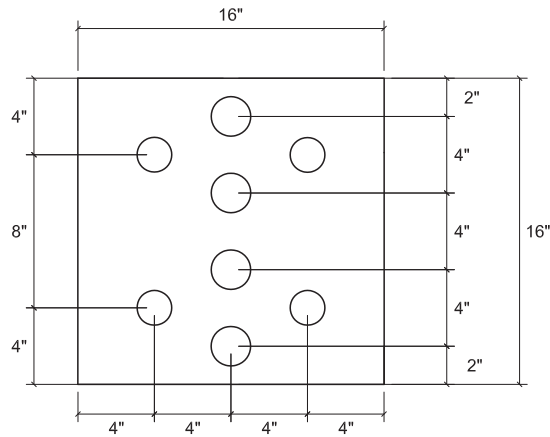
BEAM STIFFENER (PLATE A)
(Fy = 50 ksi, t = 5/8")



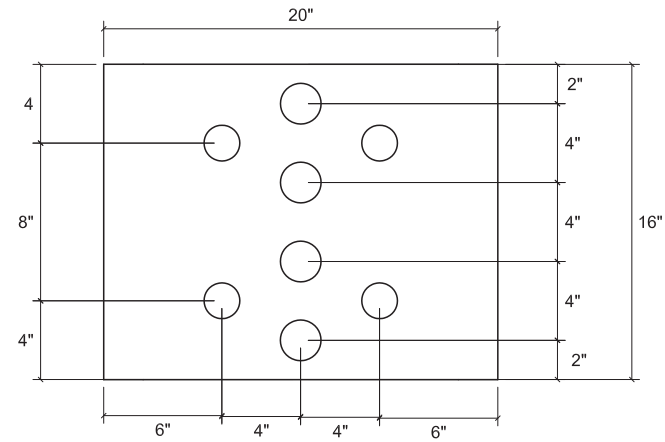
COLUMN STIFFENER (PLATE B)
(Fy = 50 ksi, t = 3/8")



ANGLED COLUMN STIFFENER (PLATE C)
(Fy = 50 ksi, t = 5/8")



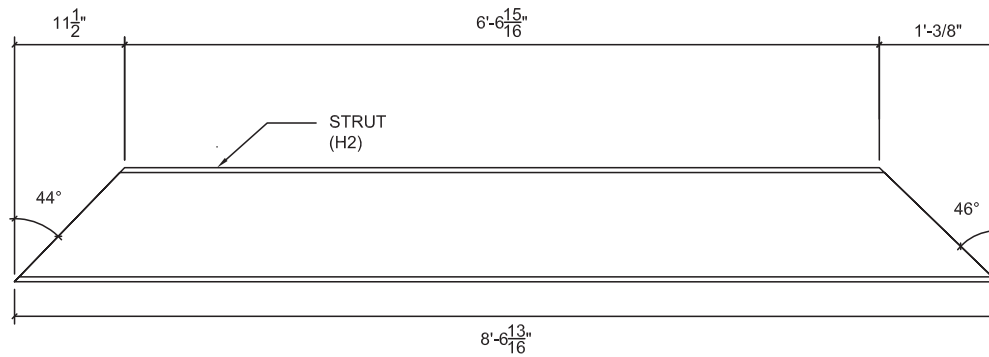
SQUARE BASE PLATE (PLATE D)
(Fy = 50 ksi, t = 2")



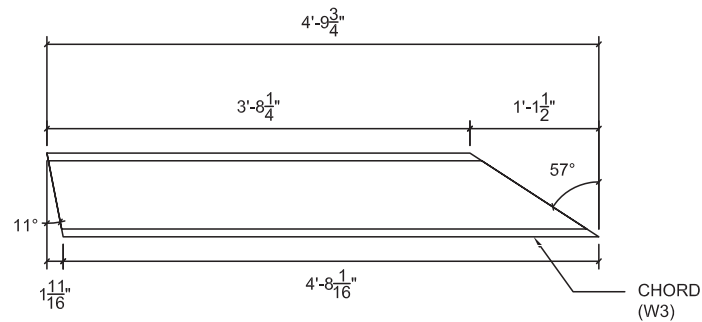
RECTANGULAR BASE PLATE (PLATE E)
(Fy = 50 ksi, t = 2")

BEAM STIFFENER (PLATE A), COLUMN STIFFENER (PLATE B), ANGLED COLUMN STIFFENER (PLATE C), SQUARE BASE PLATE (PLATE D) AND RECTANGULAR BASE PLATE (PLATE E)

<i>Validation and Implementation of Bridge Design Specifications for Barge Impact Loading (Reaction Frame)</i>				<i>Revisions:</i>		
<i>Plate Details</i>	<i>2013-03-11</i>	<i>University of Florida</i>	<i>Sheet 07 of 12</i>			



STRUT H2
 HP12x63
 Fy = 50 ksi

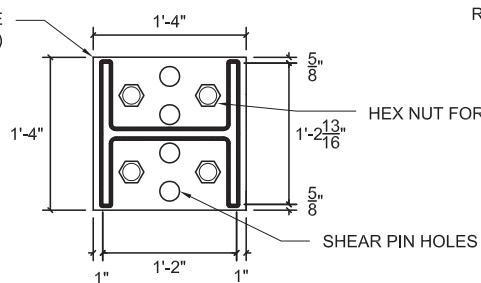


CHORD W3
 W8x58
 Fy = 50 ksi

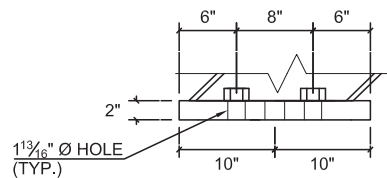
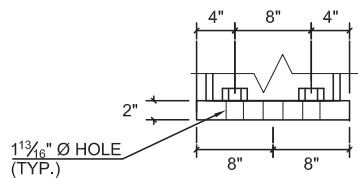
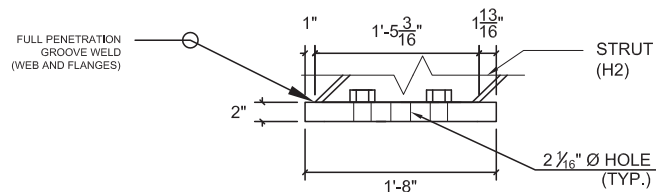
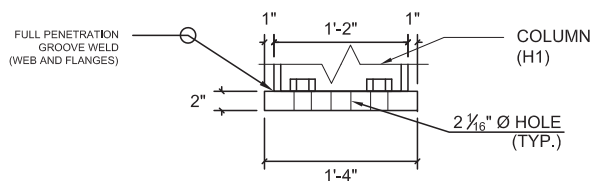
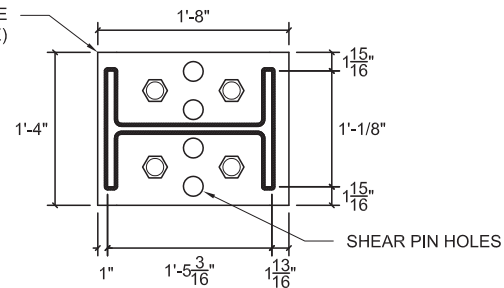
HP12x63 STRUT (H2) AND W8x58 CHORD (W3)

<i>Validation and Implementation of Bridge Design Specifications for Barge Impact Loading (Reaction Frame)</i>				<i>Revisions:</i>		
<i>Strut and Chord Details</i>	<i>2013-03-11</i>	<i>University of Florida</i>	<i>Sheet 08 of 12</i>			

SQUARE BASE PLATE
(PLATE D)



RECTANGULAR BASE PLATE
(PLATE E)



SQUARE BASE PLATE (PLATE D) AND RECTANGULAR BASE PLATE (PLATE E)

Validation and Implementation of Bridge Design Specifications for Barge Impact Loading (Reaction Frame)

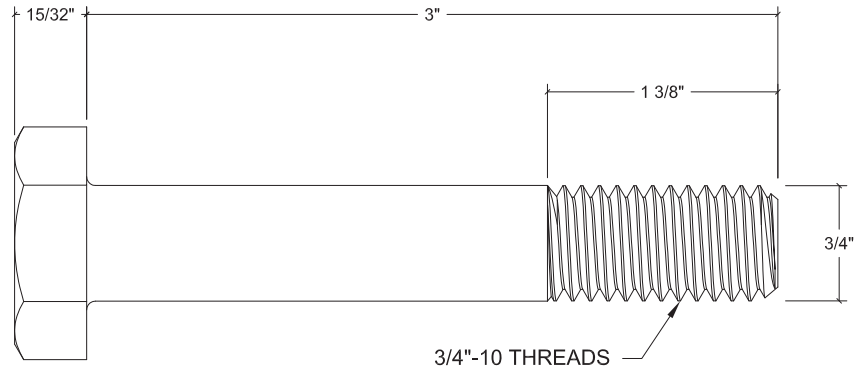
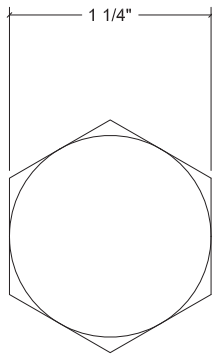
Anchor Plate Details

2013-03-11

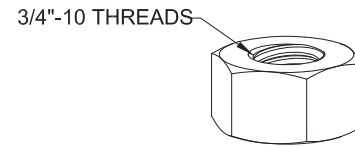
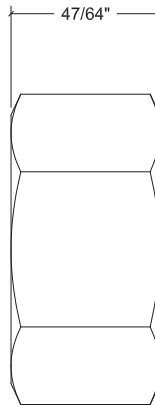
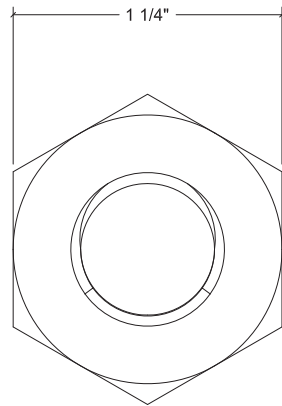
University of Florida

Sheet 09 of 12

Revisions:



Bolt Details



Nut Details

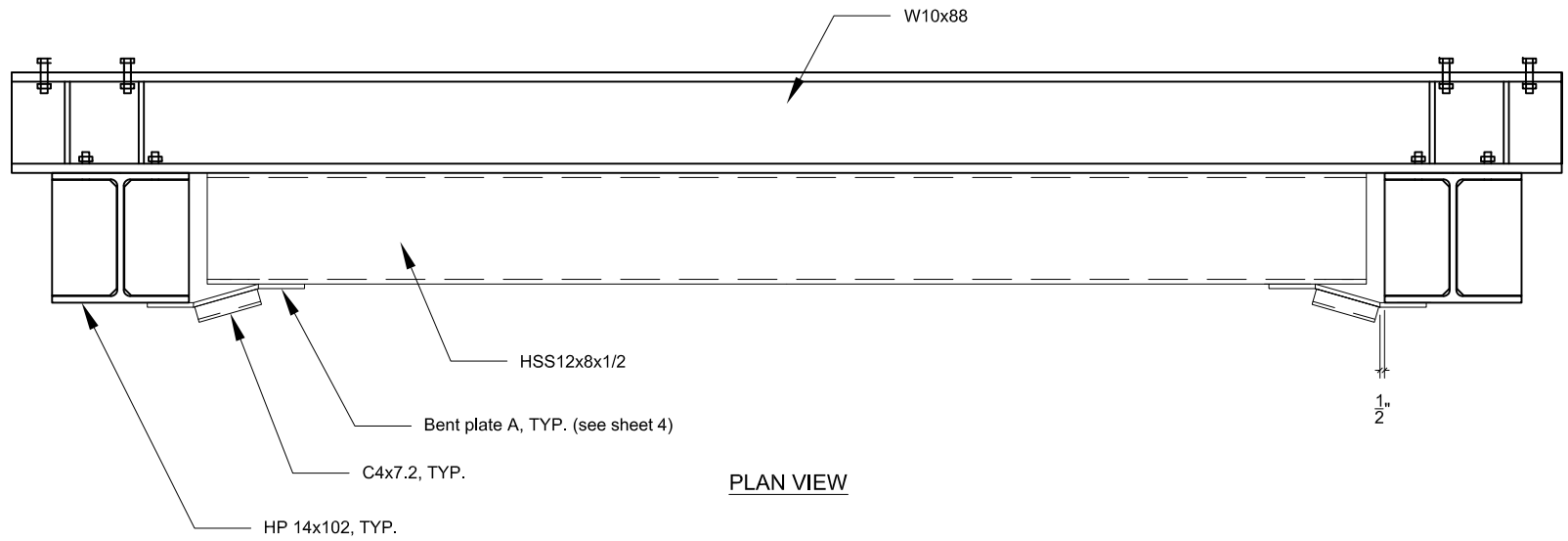
<i>Validation and Implementation of Bridge Design Specifications for Barge Impact Loading (Reaction Frame)</i>				<i>Revisions:</i>		
<i>Bolt and Nut Details</i>	<i>2013-03-11</i>	<i>University of Florida</i>	<i>Sheet 10 of 12</i>			

SCHEDULE OF MEMBERS					
NAME	SIZE	LENGTH	QTY	TOTAL LENGTH	NOTES
W1	W10x88	14'	1	14'-0"	TOP BEAM, Fy = 50 ksi
W2	W10x88	14'	1	14'-0"	BOTTOM BEAM, Fy = 50 ksi
W3	W8x58	4'-9 3/4"	2	9'-7 1/2"	CHORD (HORIZONTAL COMPRESSION) MEMBER, Fy = 50ksi
H1	HP14x102	6'-4"	2	12'-8"	COLUMNS, Fy = 50 ksi
H2	HP12x63	8'-6 13/16"	2	17'-1 5/8"	STRUT MEMBERS, Fy = 50 ksi
BOLTS	3/4" Ø x 3" Long	3"	50	-	CONNECTING PLATES, BEAMS AND COLUMNS, A325
NUTS	3/4" Ø	-	50	-	CONNECTING PLATES, BEAMS AND COLUMNS, A563

<i>Validation and Implementation of Bridge Design Specifications for Barge Impact Loading (Reaction Frame)</i>				<i>Revisions:</i>		
<i>Schedule of Members</i>	<i>2013-03-11</i>	<i>University of Florida</i>	<i>Sheet 11 of 12</i>			

SCHEDULE OF PLATES		
NAME	QTY	NOTES
PLATE A	16	STIFFENERS FOR TOP AND BOTTOM BEAMS, Fy = 50 ksi
PLATE B	12	STIFFENERS FOR COLUMNS, Fy = 50ksi
PLATE C	4	ANGLED STIFFENERS FOR COLUMNS, Fy = 50ksi
PLATE D	2	SQUARE BASE PLATES, Fy = 50 ksi
PLATE E	2	RECTANGULAR BASE PLATES, Fy = 50 ksi

<i>Validation and Implementation of Bridge Design Specifications for Barge Impact Loading (Reaction Frame)</i>				<i>Revisions:</i>		
<i>Schedule of Plates</i>	<i>2013-03-11</i>	<i>University of Florida</i>	<i>Sheet 12 of 12</i>			



NOTE 1: Chords, struts, and base plates visually removed for clarity.

Validation and Implementation of Bridge Design Specifications for Barge Impact Loading (Reaction Frame)

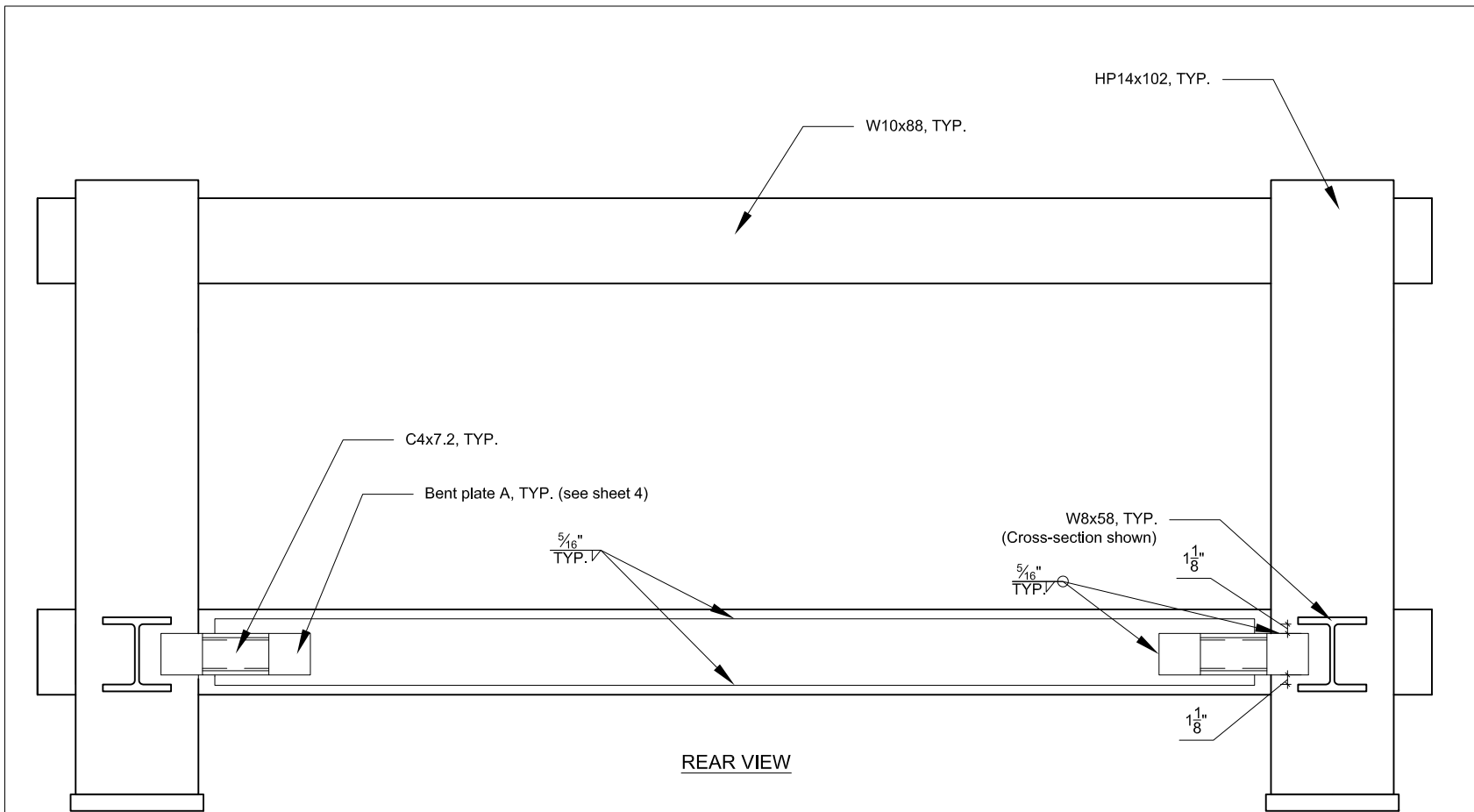
Backer Beam Connection Details I

2013-10-28

University of Florida

Sheet 01 of 04

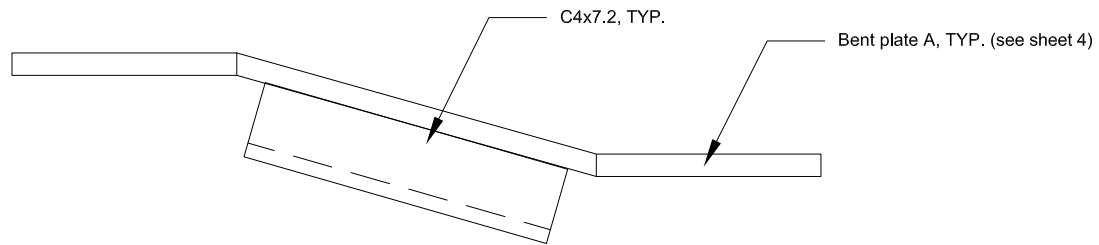
Revisions:



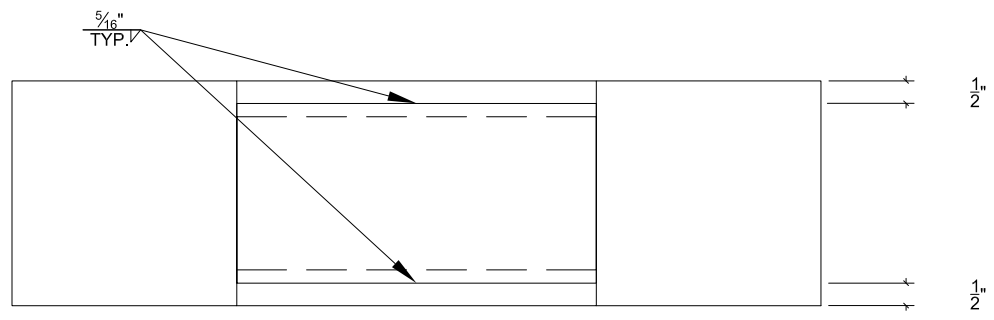
NOTE 1: Struts removed for clarity.

NOTE 2: Each bent plate shall be centered on the webs of the chord members such that the edge distance between the top of the bent plate and the top flange of the chord member is the same as the edge distance between the bottom of the bent plate and the bottom flange of the chord member, as indicated on this sheet.

<i>Validation and Implementation of Bridge Design Specifications for Barge Impact Loading (Reaction Frame)</i>				<i>Revisions:</i>		
<i>Backer Beam Connection Details II</i>	<i>2013-10-28</i>	<i>University of Florida</i>	<i>Sheet 02 of 04</i>			

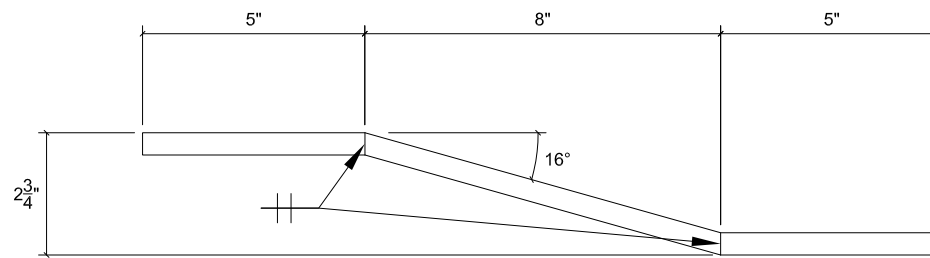


BENT PLATE ASSEMBLY - TOP VIEW

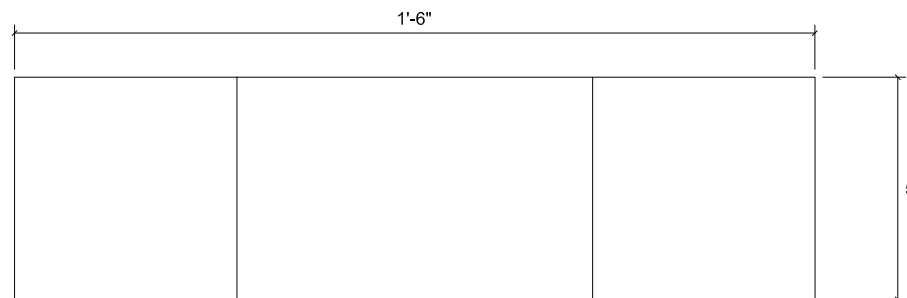


BENT PLATE ASSEMBLY - REAR VIEW

<i>Validation and Implementation of Bridge Design Specifications for Barge Impact Loading (Reaction Frame)</i>				<i>Revisions:</i>		
<i>Backer Beam Connection Details III</i>	<i>2013-10-28</i>	<i>University of Florida</i>	<i>Sheet 03 of 04</i>			



TOP VIEW



REAR VIEW

BENT PLATE A
A572-50, $t = \frac{1}{2}$ ", QUANTITY = 2

Validation and Implementation of Bridge Design Specifications for Barge Impact Loading (Reaction Frame)

Backer Beam Connection Details IV

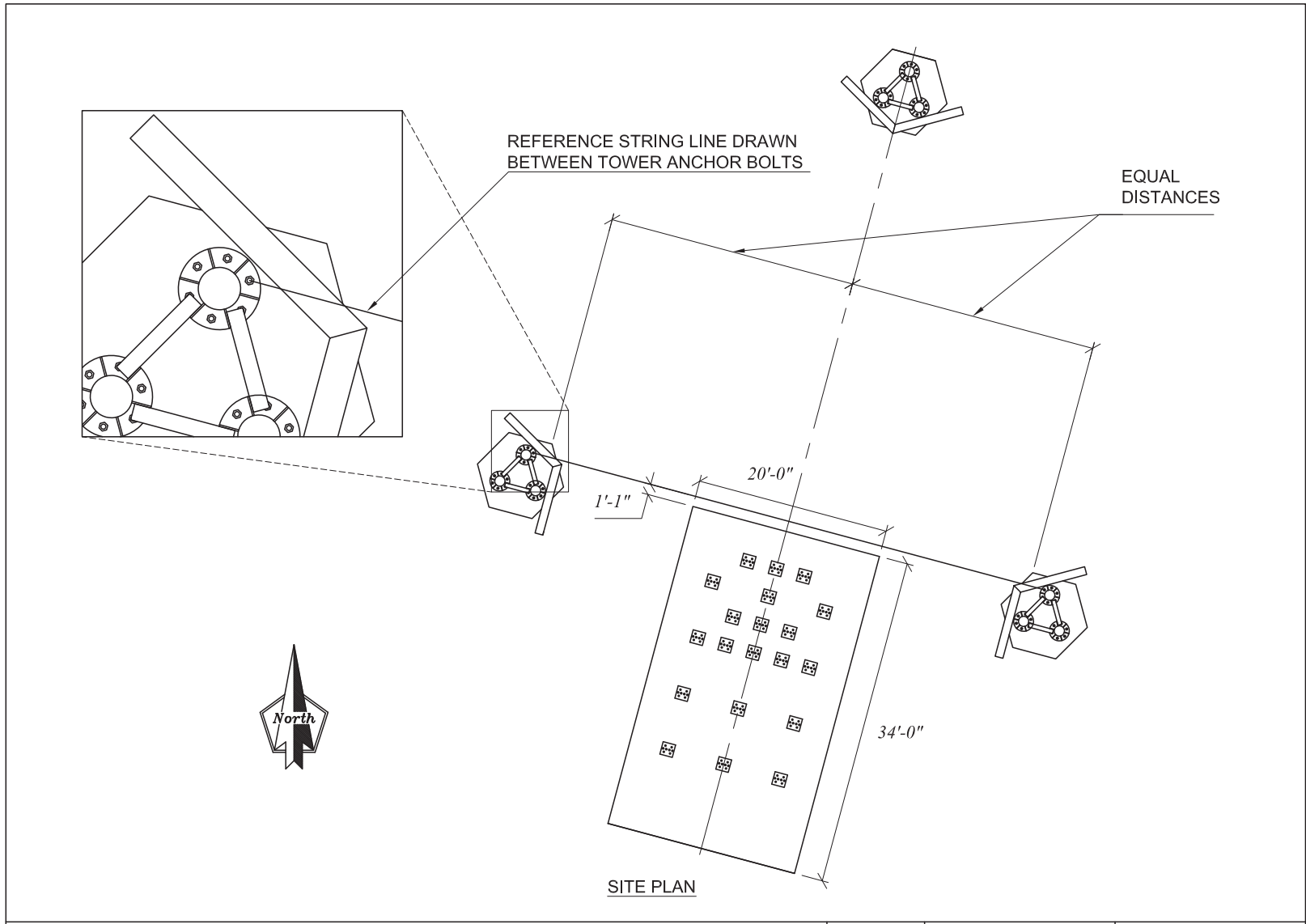
2013-10-28

University of Florida

Sheet 04 of 04

Revisions:

APPENDIX H
UNIVERSAL PENDULUM FOUNDATION FABRICATION DRAWINGS



<i>Universal Pendulum Foundation and Anchor System (as-built drawings)</i>				<i>Revisions:</i>		
<i>Site plan</i>	<i>2013-05-07</i>	<i>University of Florida</i>	<i>Sheet 01 of 18</i>			

General Notes:

Concrete shall have a minimum f'_c (28 day) = 5,000 psi.

Mild reinforcement shall be ASTM A615 grade 60 ($f_y = 60$ ksi).

Top of foundation elevation to be 1' - 0" below bottom surface of pendulum tower base plates. Final position subject to change based on site survey.

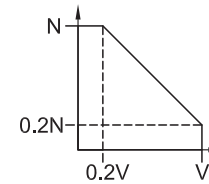
Foundation concrete to be poured in three lifts, approximately 1' - 0" each.

Concrete cylinders were cast from each concrete delivery. Breaking strengths (psi) were measured at 28 days as shown in the table below.

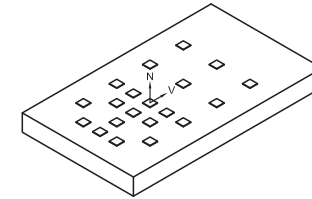
CYLINDER	LIFT #1	LIFT #2	LIFT #3
1	5,779	5,025	6,556
2	5,841	7,982	7,241
3	5,507	7,593	8,137
4	6,416	6,858	8,705
5	7,135	7,317	7,625
6	6,491	6,161	8,085
7	5,637	8,261	
8	4,837	8,271	
9	5,779		
10	6,039		
11	6,217		
AVERAGE	5,938	7,183	7,725

Loads applied to the embedded anchors shall not exceed the interaction envelope shown to the right, with uplift force (N) and shear force (V) as defined in the diagrams. Note that capacities are valid for any anchor row, not only the row shown in the diagrams.

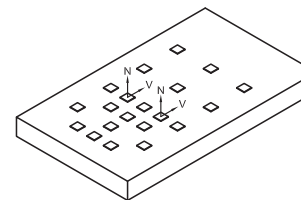
SHEAR-UPLIFT (V-N) INTERACTION ENVELOPE



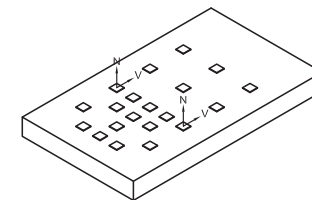
LOAD CASE 1 (1) anchor loaded alone



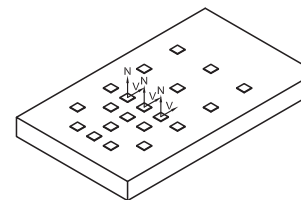
LOAD CASE 2A (2) anchors 6' O.C. together



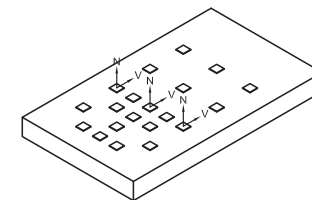
LOAD CASE 2B (2) anchors 12' O.C. together



LOAD CASE 3A (3) anchors 3' O.C. together



LOAD CASE 3B (3) anchors 6' O.C. together



LOAD CASE	N (kips)	V (kips)
1	320	190
2A	270	190
2B	310	190
3A	180	140
3B	250	190

Universal Pendulum Foundation and Anchor System (as-built drawings)

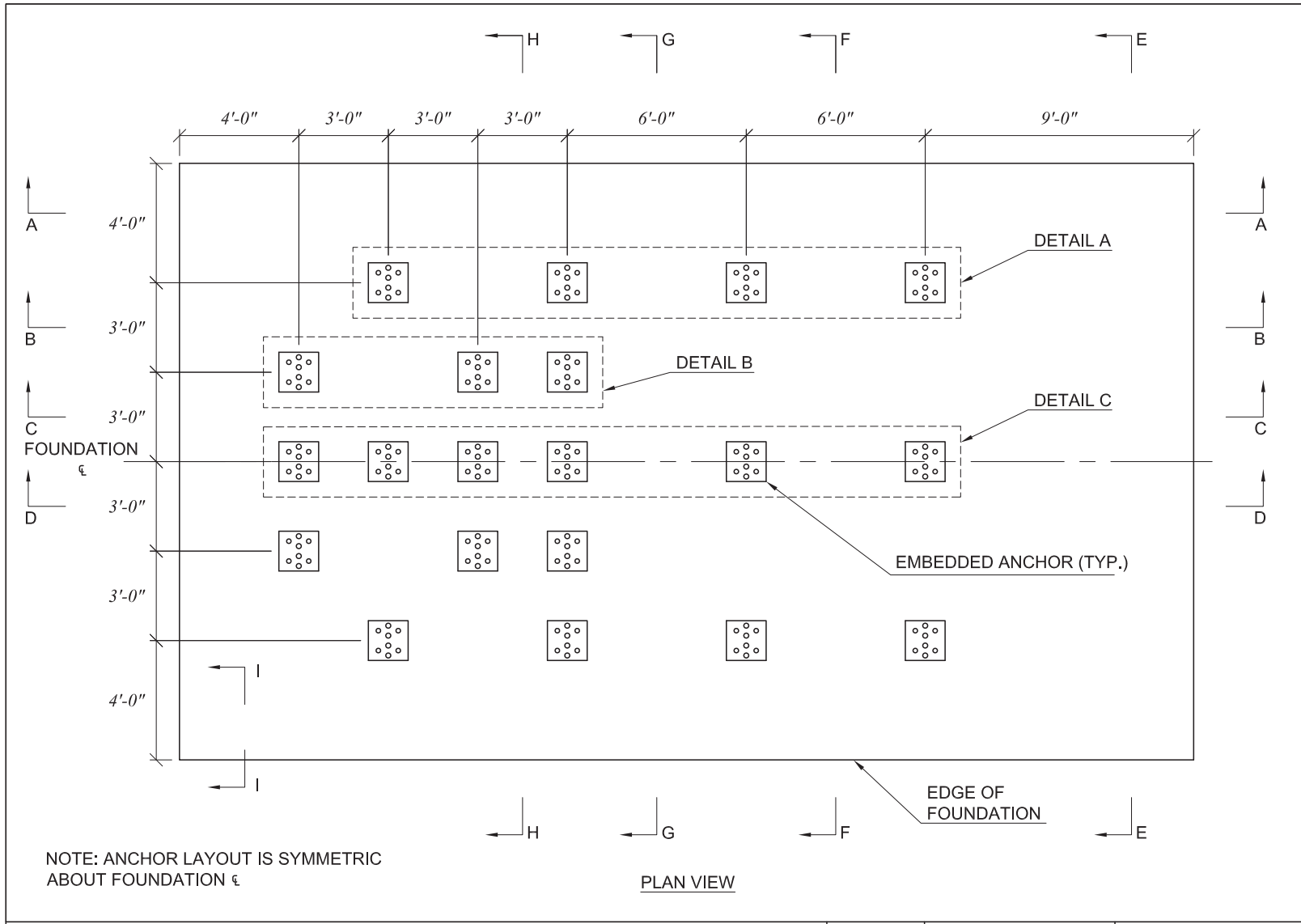
General notes

2013-05-07

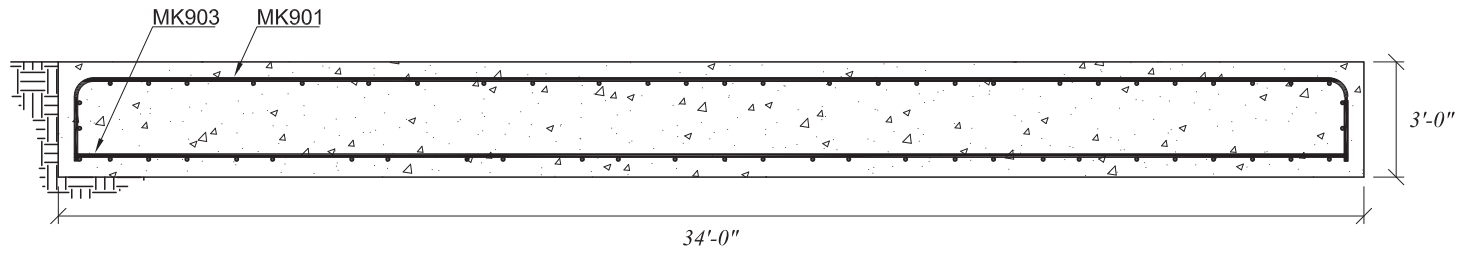
University of Florida

Sheet 02 of 19

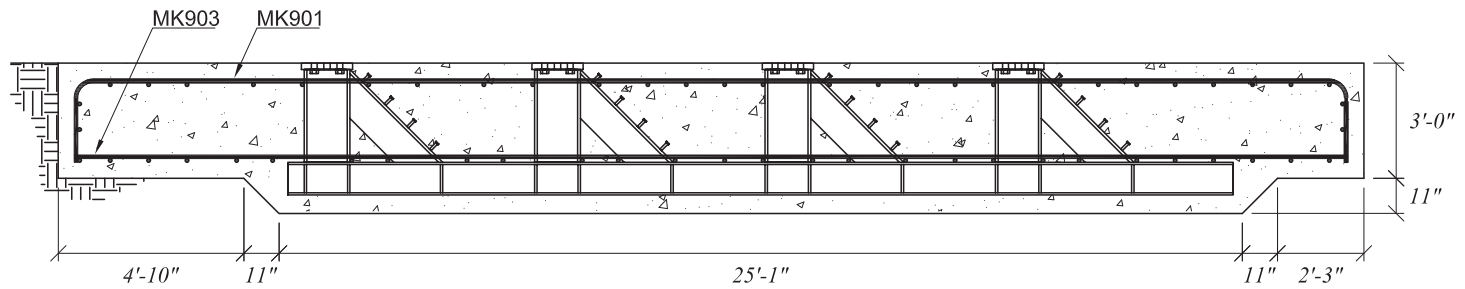
Revisions:



<i>Universal Pendulum Foundation and Anchor System (as-built drawings)</i>				Revisions:		
<i>Foundation plan view</i>	<i>2013-05-07</i>	<i>University of Florida</i>	<i>Sheet 03 of 19</i>			

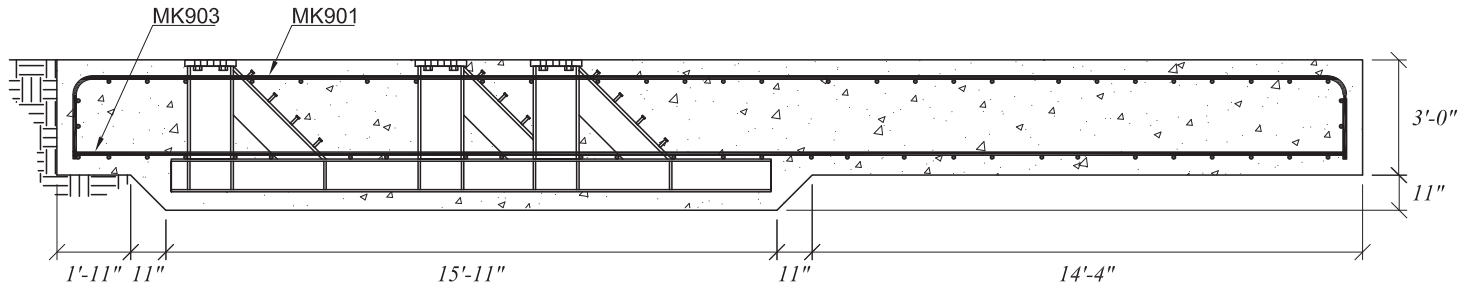


SECTION A-A

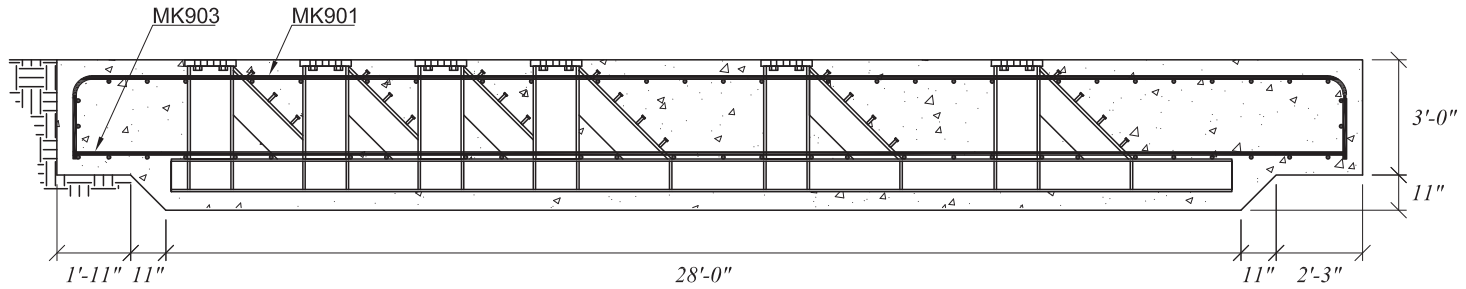


SECTION B-B

<i>Universal Pendulum Foundation and Anchor System (as-built drawings)</i>				<i>Revisions:</i>		
<i>Foundation sections</i>	<i>2013-05-07</i>	<i>University of Florida</i>	<i>Sheet 04 of 19</i>			

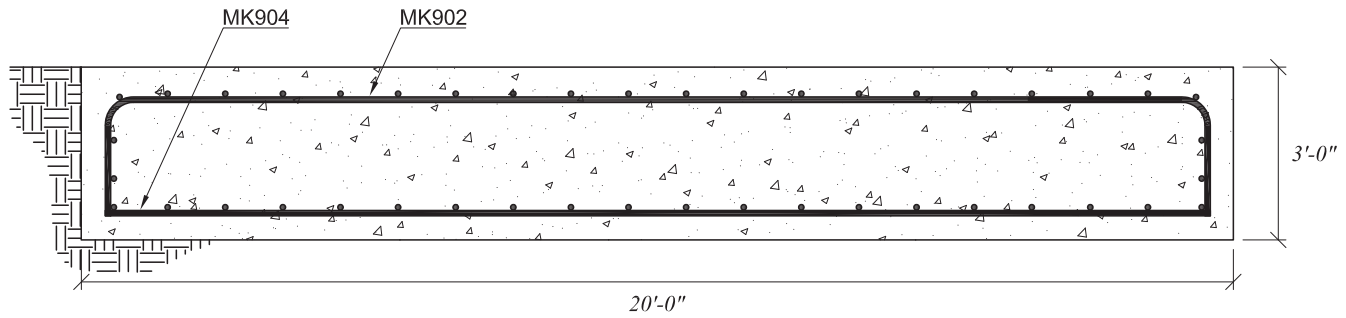


SECTION C-C

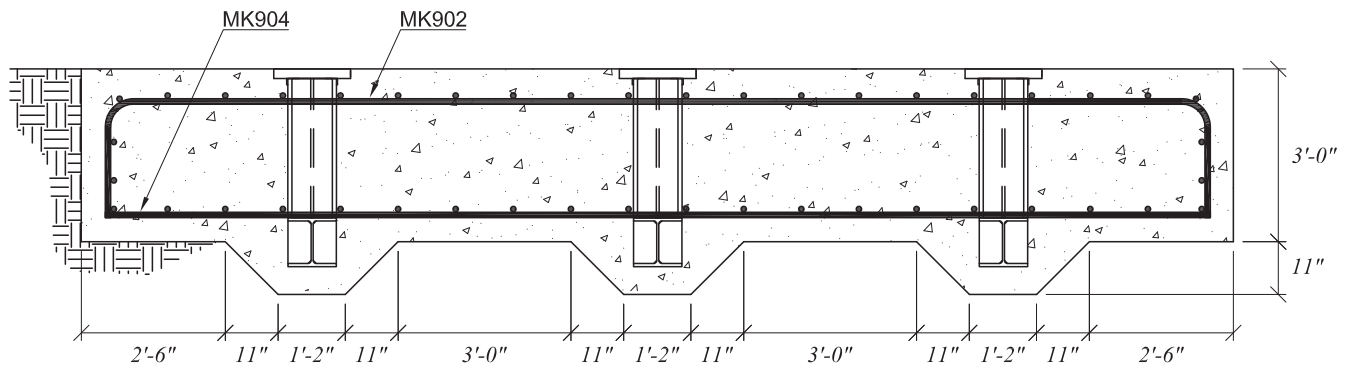


SECTION D-D

<i>Universal Pendulum Foundation and Anchor System (as-built drawings)</i>				Revisions:		
<i>Foundation sections</i>	2013-05-07	<i>University of Florida</i>	<i>Sheet 05 of 19</i>			

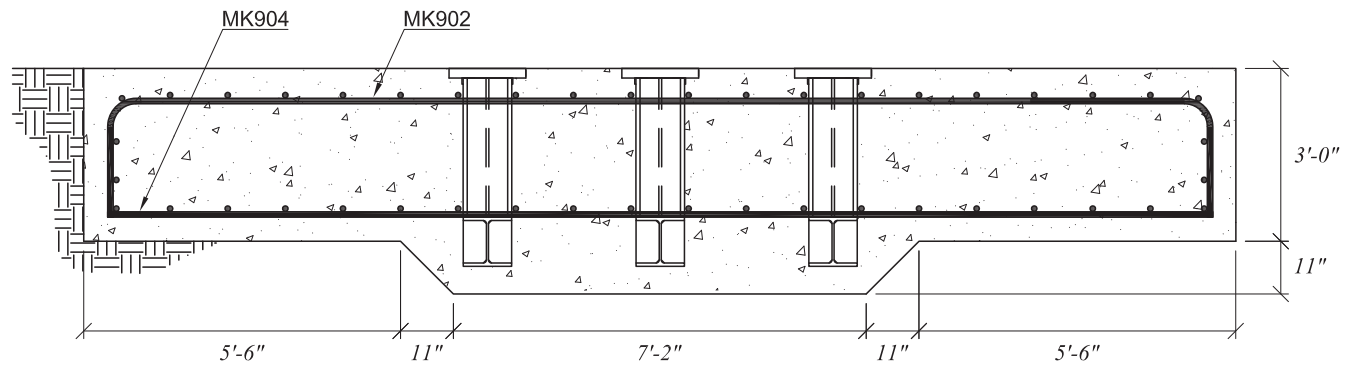
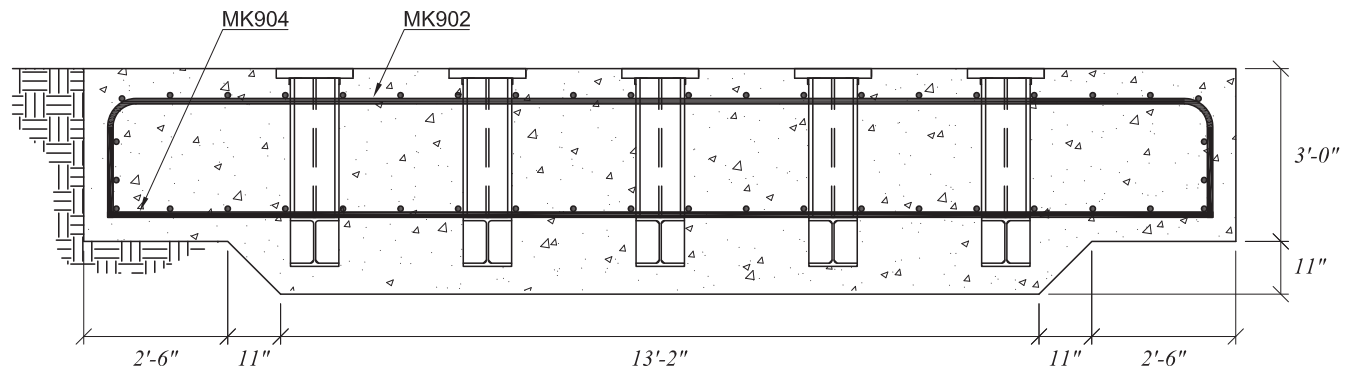


SECTION E-E

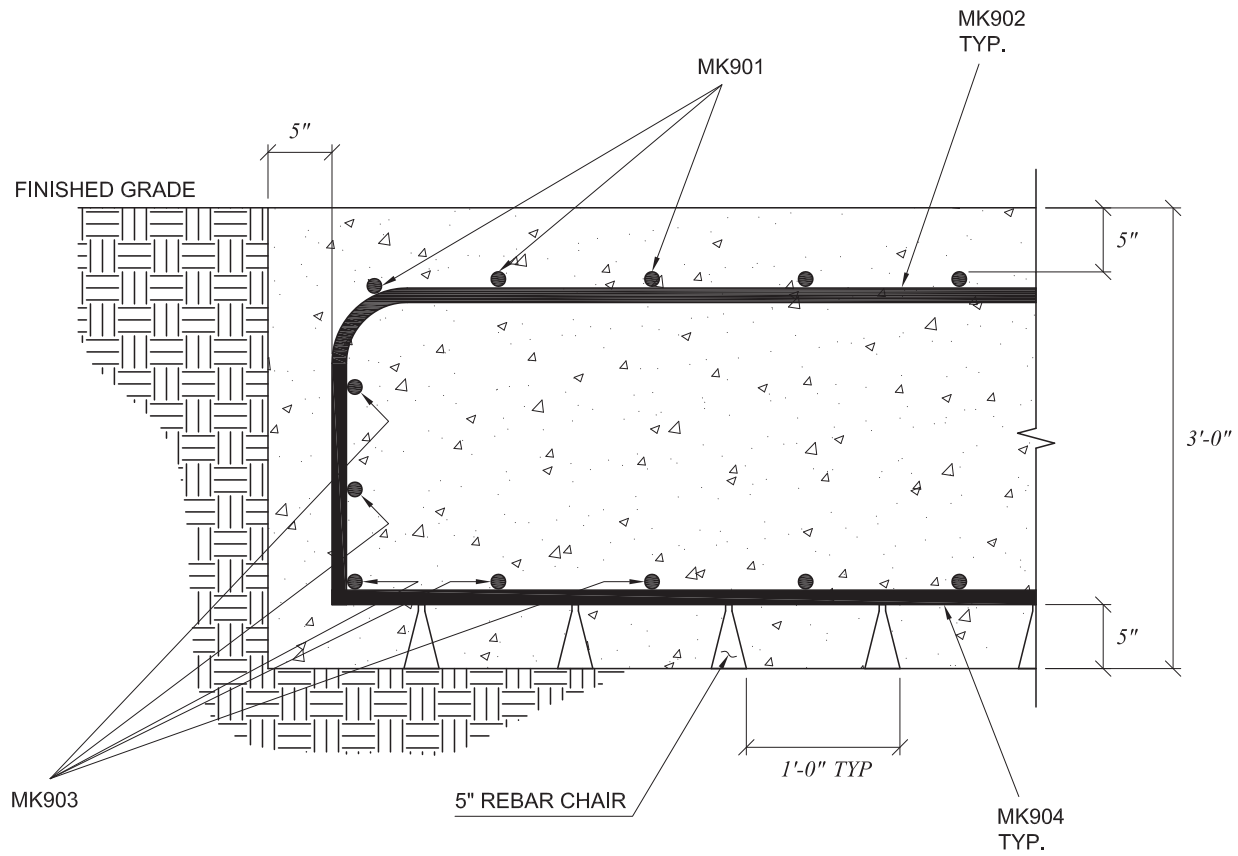


SECTION F-F

<i>Universal Pendulum Foundation and Anchor System (as-built drawings)</i>				<i>Revisions:</i>		
<i>Foundation sections</i>	<i>2013-05-07</i>	<i>University of Florida</i>	<i>Sheet 06 of 19</i>			

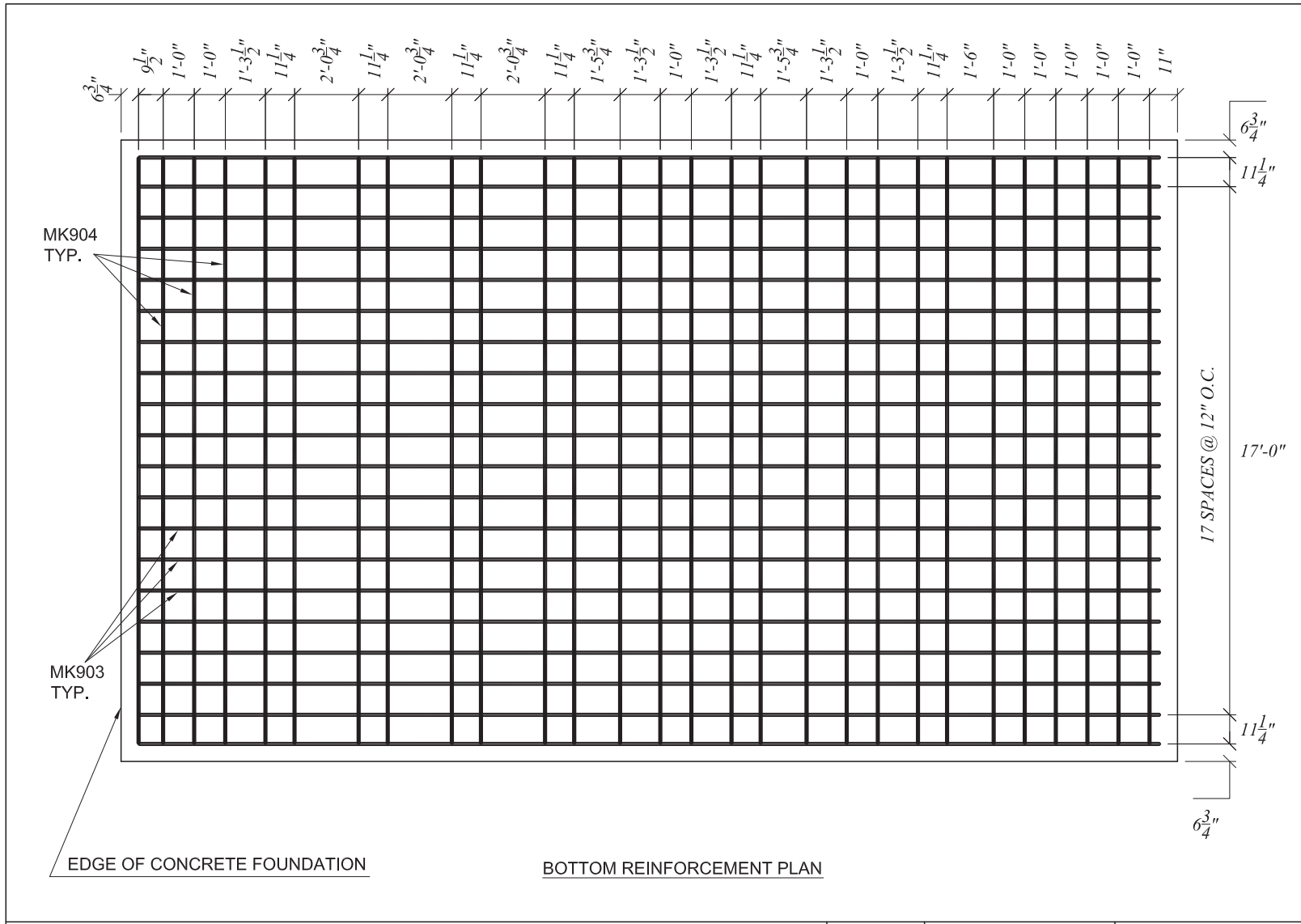


<i>Universal Pendulum Foundation and Anchor System (as-built drawings)</i>				Revisions:		
<i>Foundation sections</i>	<i>2013-05-07</i>	<i>University of Florida</i>	<i>Sheet 07 of 19</i>			

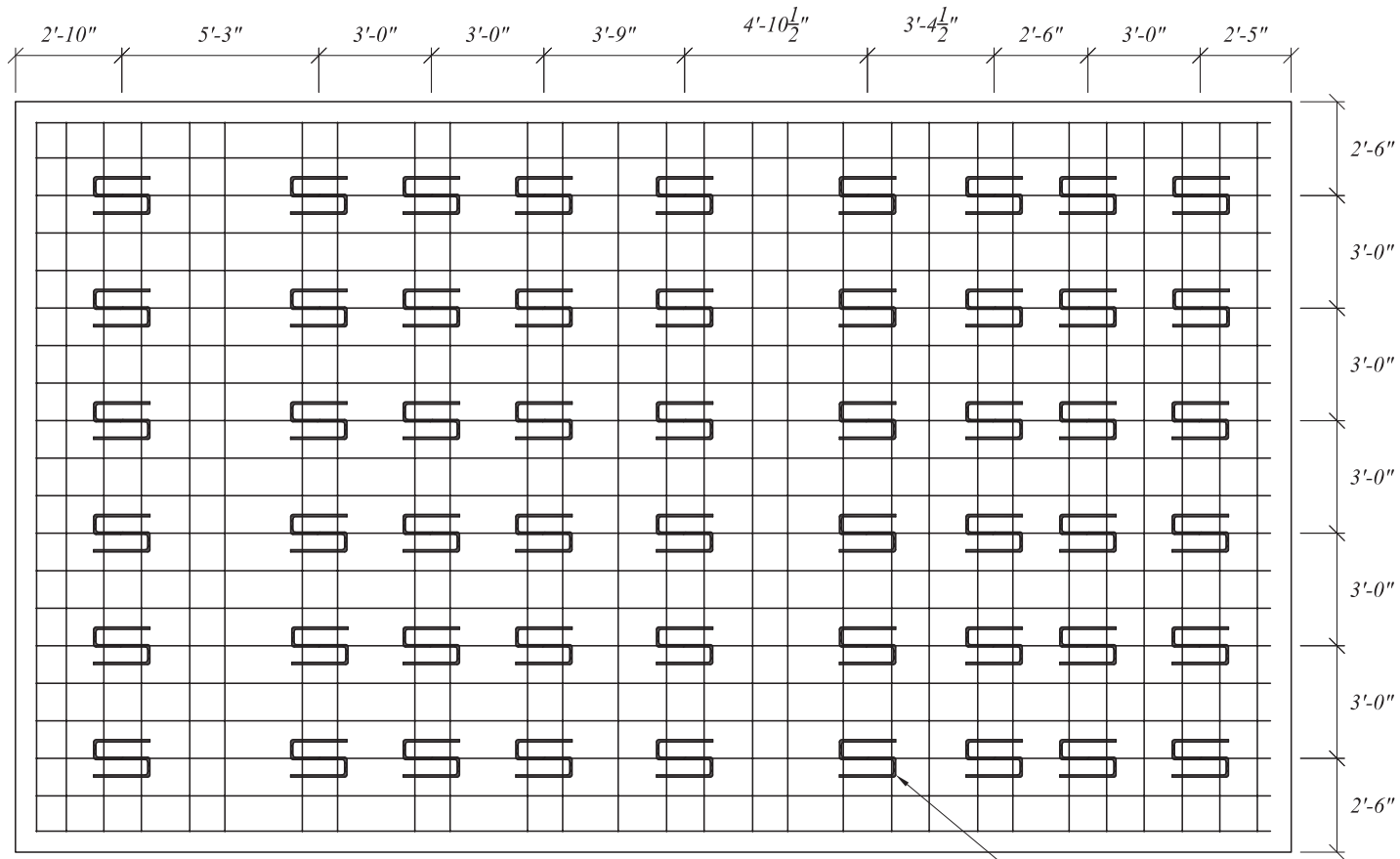


SECTION I-I

<i>Universal Pendulum Foundation and Anchor System (as-built drawings)</i>				<i>Revisions:</i>		
<i>Foundation section details</i>	<i>2013-05-07</i>	<i>University of Florida</i>	<i>Sheet 08 of 19</i>			



<i>Universal Pendulum Foundation and Anchor System (as-built drawings)</i>				Revisions:		
<i>Bottom reinforcement layout</i>	2013-05-07	University of Florida	Sheet 10 of 19			

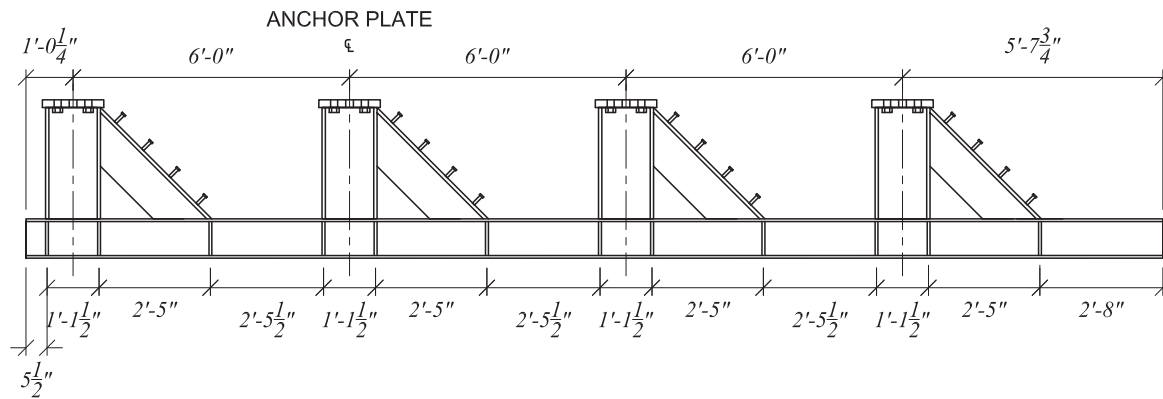
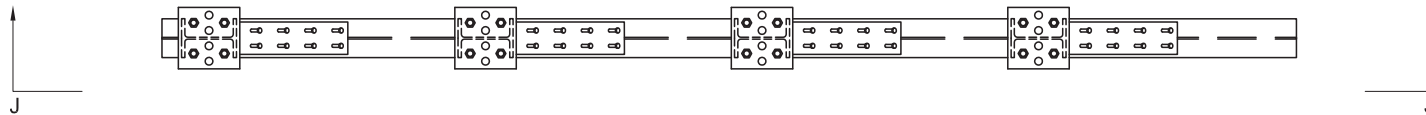


NOTE: MK601 STANDEES SIT ON
 BOTTOM REINFORCEMENT BARS MK904
 AND SUPPORT TOP BARS MK902

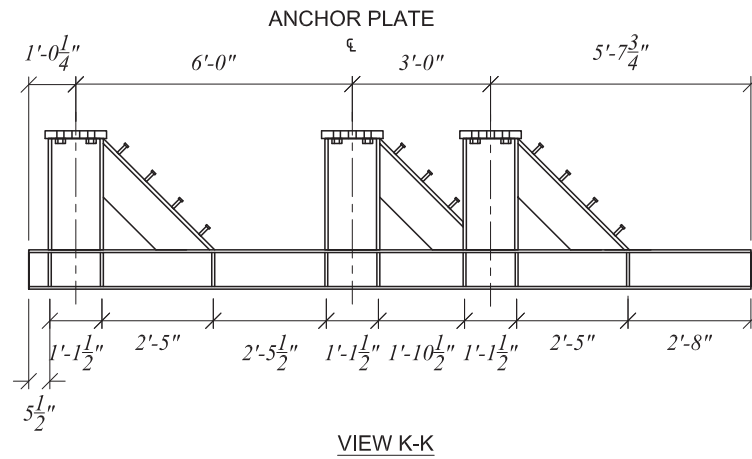
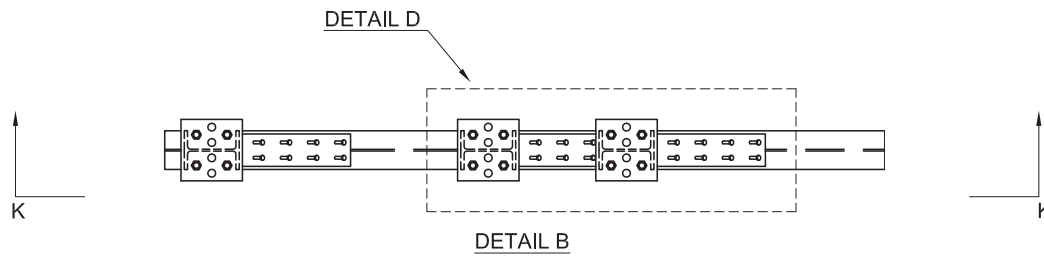
REBAR STAND PLAN
 TOP REINFORCEMENT OMITTED FOR CLARITY

MK601 STANDEE (TYP)

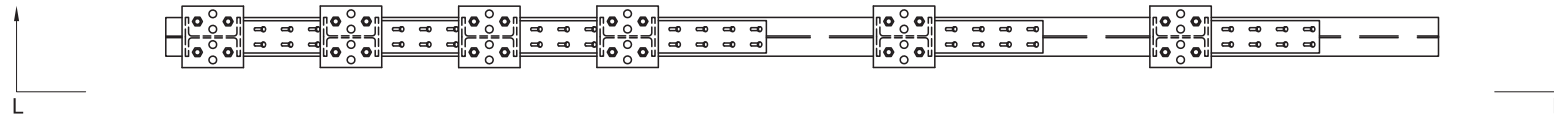
<i>Universal Pendulum Foundation and Anchor System (as-built drawings)</i>				Revisions:		
<i>Rebar stand layout</i>	2013-05-07	<i>University of Florida</i>	<i>Sheet 11 of 19</i>			



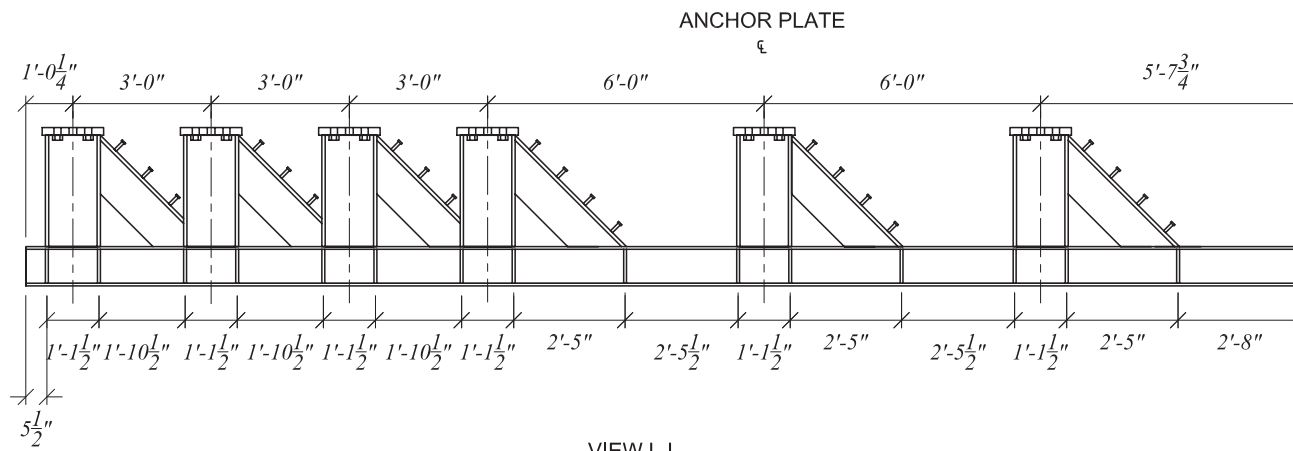
Universal Pendulum Foundation and Anchor System (as-built drawings)				Revisions:		
Anchor unit details	2013-05-07	University of Florida	Sheet 12 of 19			



<i>Universal Pendulum Foundation and Anchor System (as-built drawings)</i>				<i>Revisions:</i>		
<i>Anchor unit details</i>	<i>2013-05-07</i>	<i>University of Florida</i>	<i>Sheet 13 of 19</i>			

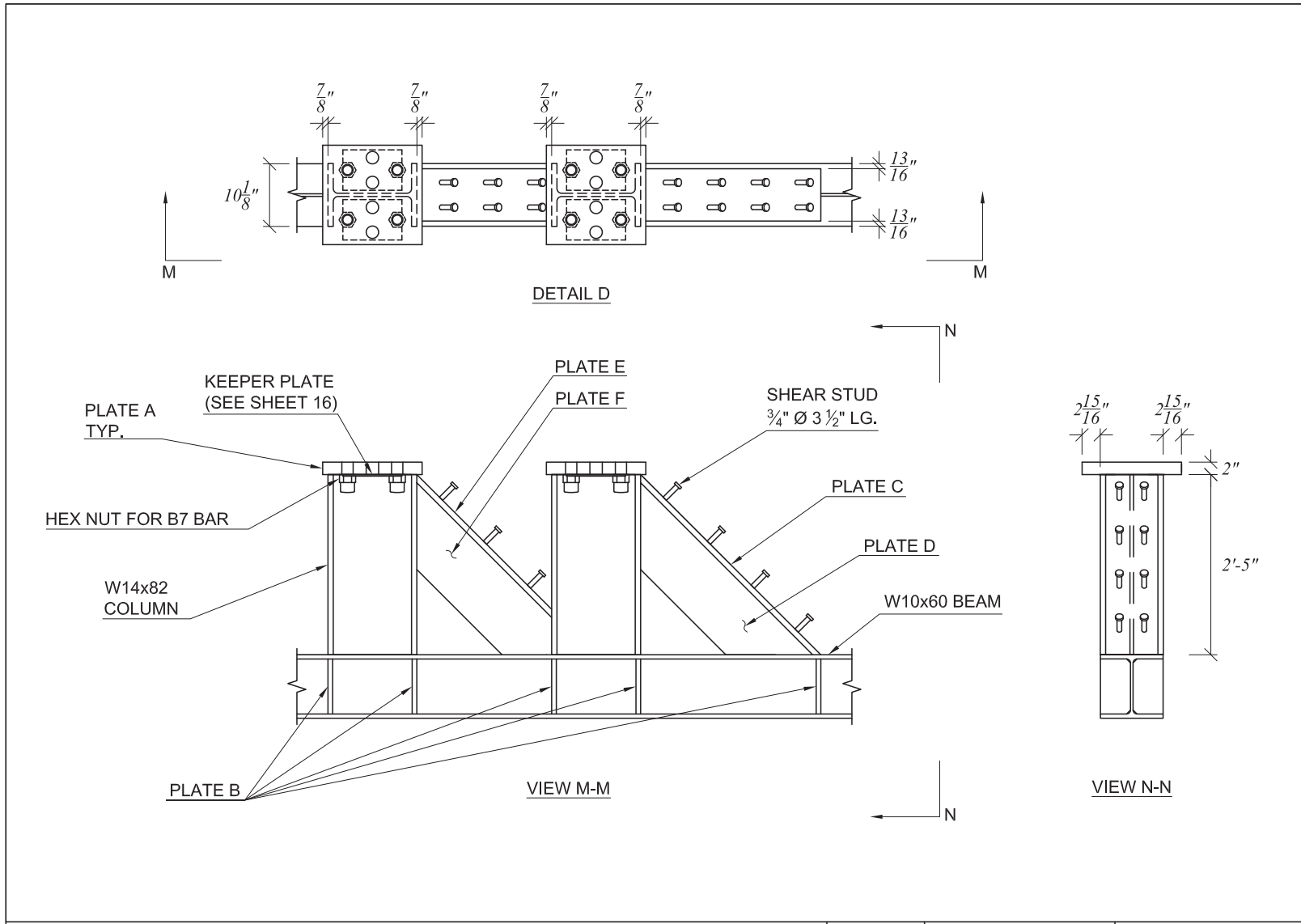


DETAIL C

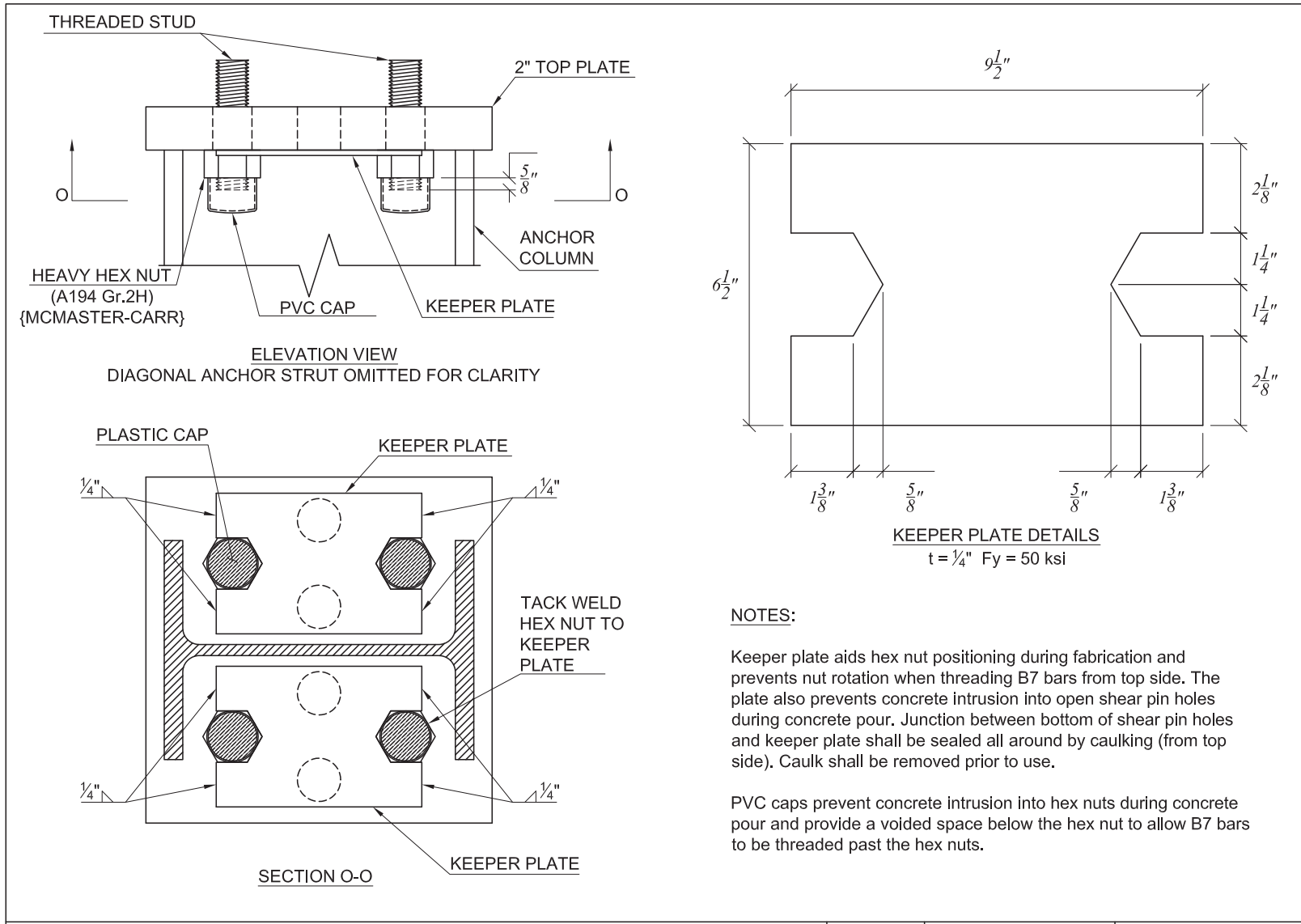


VIEW L-L

Universal Pendulum Foundation and Anchor System (as-built drawings)				Revisions:		
Anchor unit details	2013-05-07	University of Florida	Sheet 14 of 19			



<i>Universal Pendulum Foundation and Anchor System (as-built drawings)</i>				Revisions:		
<i>Anchor details</i>	2013-05-07	University of Florida	Sheet 15 of 19			

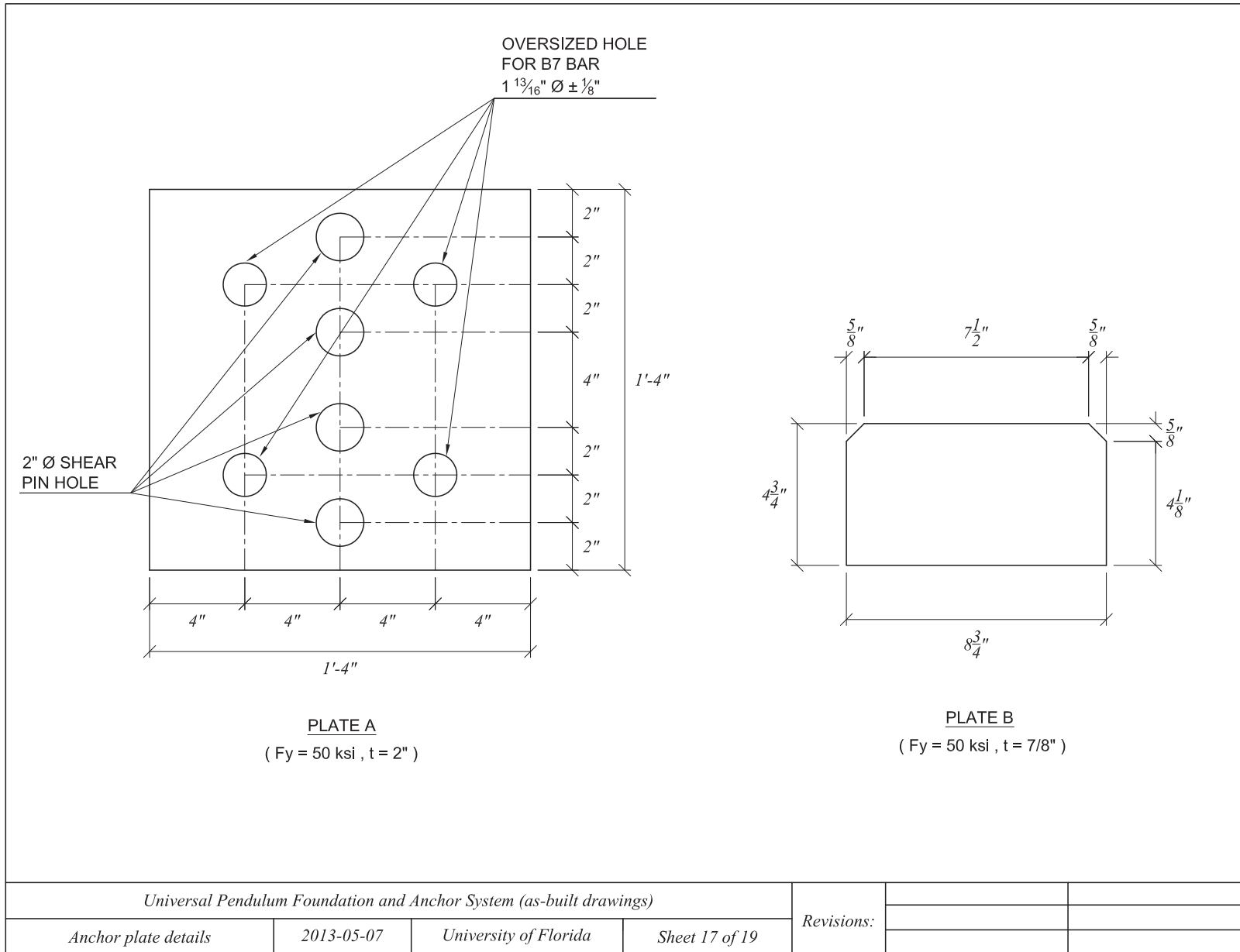


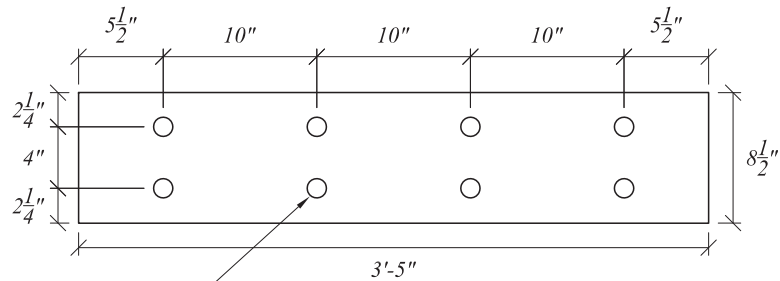
NOTES:

Keeper plate aids hex nut positioning during fabrication and prevents nut rotation when threading B7 bars from top side. The plate also prevents concrete intrusion into open shear pin holes during concrete pour. Junction between bottom of shear pin holes and keeper plate shall be sealed all around by caulking (from top side). Caulk shall be removed prior to use.

PVC caps prevent concrete intrusion into hex nuts during concrete pour and provide a voided space below the hex nut to allow B7 bars to be threaded past the hex nuts.

<i>Universal Pendulum Foundation and Anchor System (as-built drawings)</i>				<i>Revisions:</i>		
<i>Hex nut keeper plate details</i>	<i>2013-05-07</i>	<i>University of Florida</i>	<i>Sheet 16 of 19</i>			





SHEAR STUD
 $\frac{3}{4}$ " \varnothing 3 $\frac{1}{2}$ " LG.

PLATE C

(Fy = 50 ksi , t = 1")

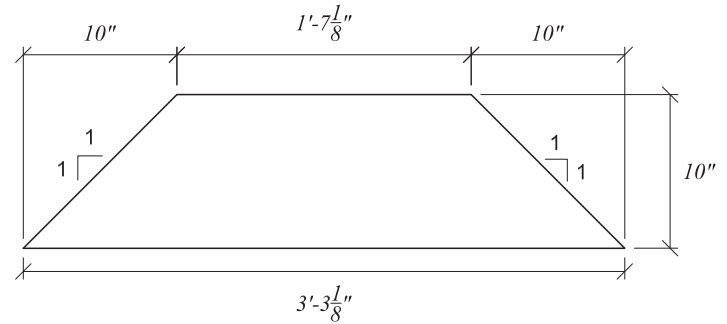
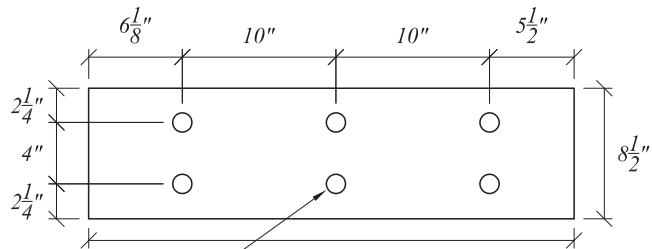


PLATE D

(Fy = 50 ksi , t = 1/2")



SHEAR STUD
 $\frac{3}{4}$ " \varnothing 3 $\frac{1}{2}$ " LG.

PLATE E

(Fy = 50 ksi , t = 1")

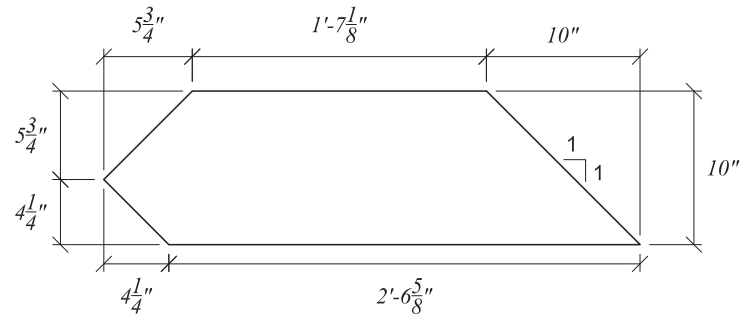
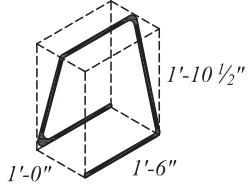
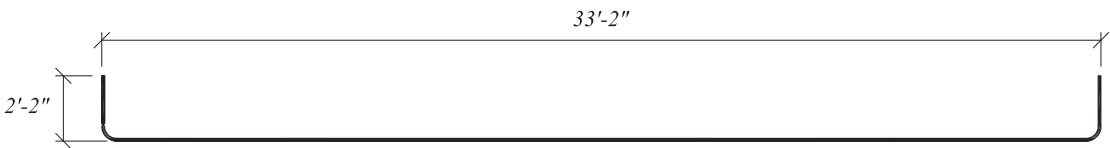
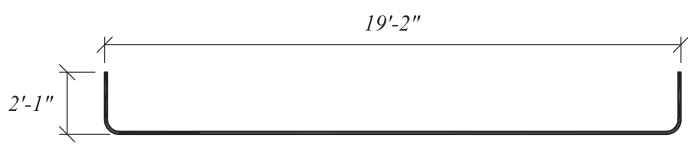
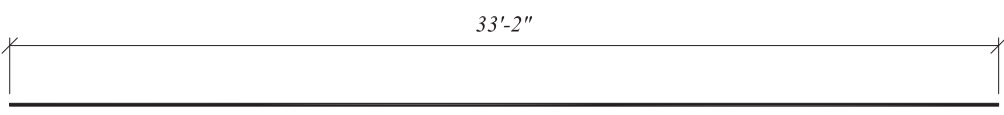
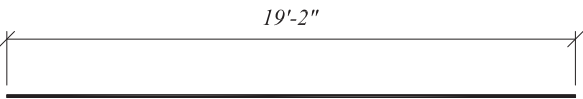


PLATE F

(Fy = 50 ksi , t = 1/2")

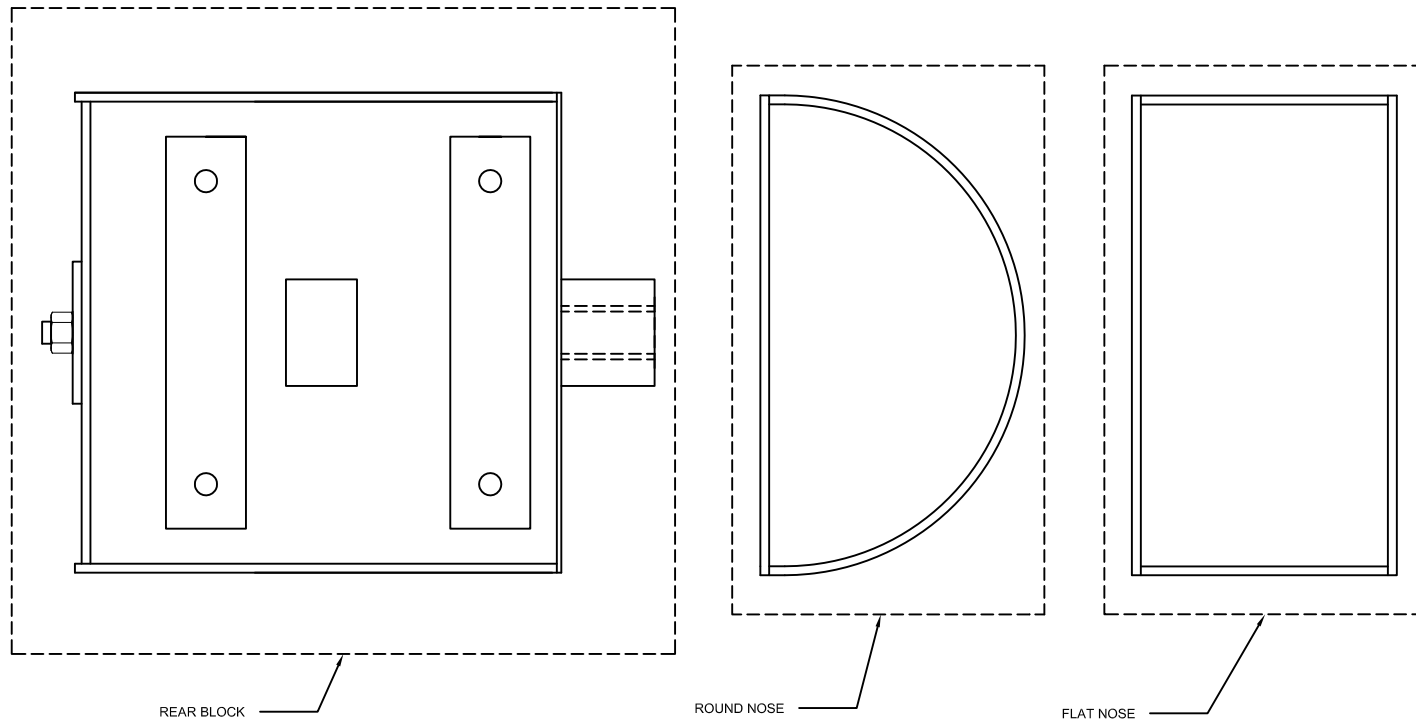
Universal Pendulum Foundation and Anchor System (as-built drawings)				Revisions:		
Anchor plate details	2013-05-07	University of Florida	Sheet 18 of 19			

BAR SIZE	DETAILS	MARK NO.	QTY
#6	 <p>TYPICAL STANDEE (ISO VIEW)</p>	MK601	54
#9		MK901	20
#9		MK902	27
#9		MK903	24
#9		MK904	32
<i>Universal Pendulum Foundation and Anchor System (as-built drawings)</i>		<i>Revisions:</i>	
<i>Rebar details</i>	<i>2013-05-07</i>		<i>University of Florida</i>

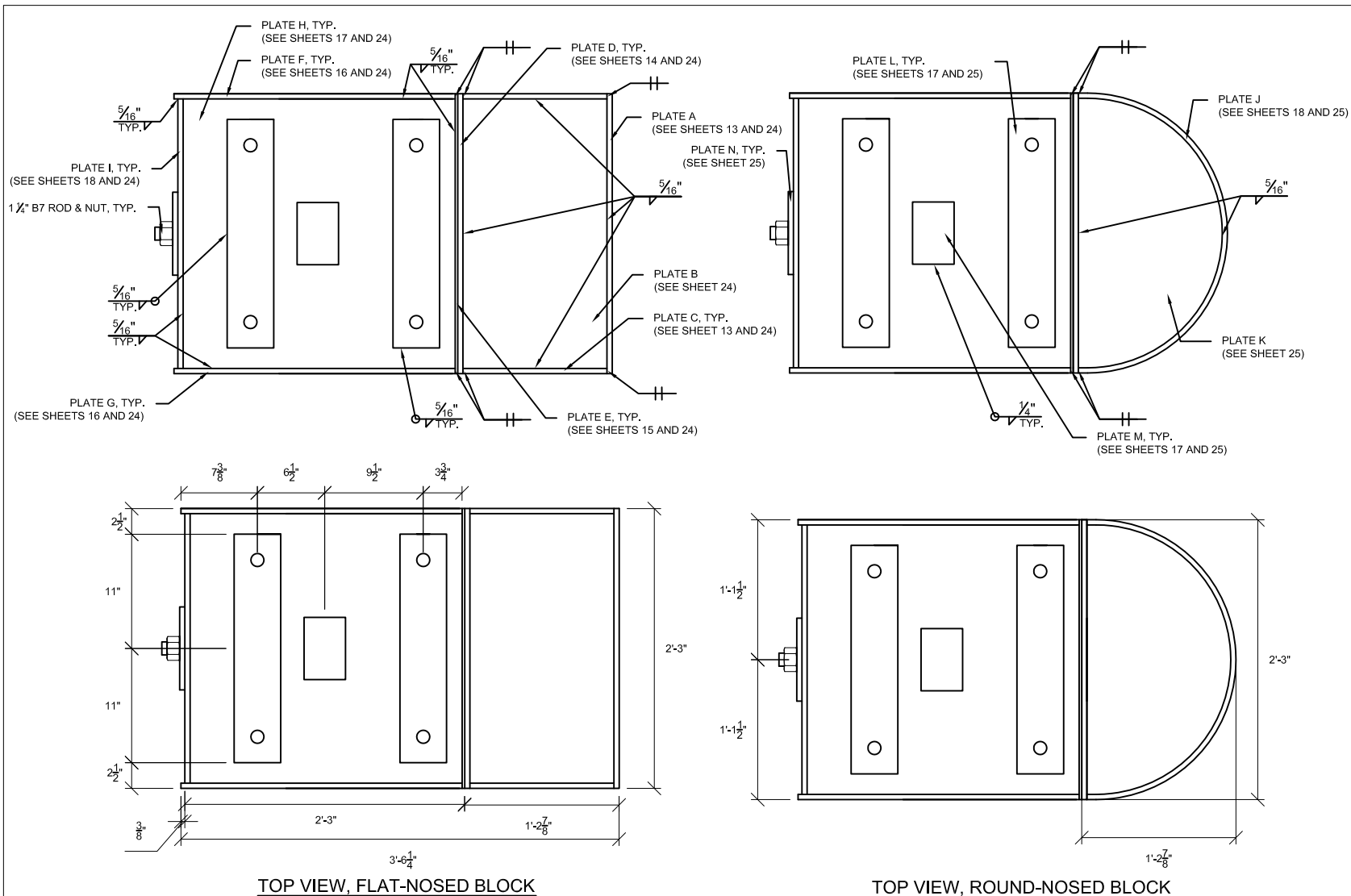
APPENDIX I
IMPACT BLOCK FABRICATION DRAWINGS

GENERAL NOTES

- 1) Concrete shall have a minimum f_c (28 day) of 4,000 psi
- 2) Mild reinforcement shall be #4 bar, ASTM A615 Grade 60 ($F_y = 60$ ksi)
- 3) As named in this drawing set, "plate assemblies" consist of the plate with the same letter designation as the assembly, and all components welded to the faces of that plate (i.e. plate assembly "A" consists of plate A and all components welded to plate A).
- 4) All $\frac{1}{4}$ " \varnothing shear studs shall be fillet welded all-around to connecting components with $\frac{1}{4}$ " fillet welds. All $\frac{1}{2}$ " \varnothing shear studs shall be fillet welded all-around to connecting components with $\frac{5}{16}$ " fillet welds.
- 5) The impact block consists of three major components - a rear block and two interchangeable noses (one rounded, and one flat-faced), as depicted on this sheet.

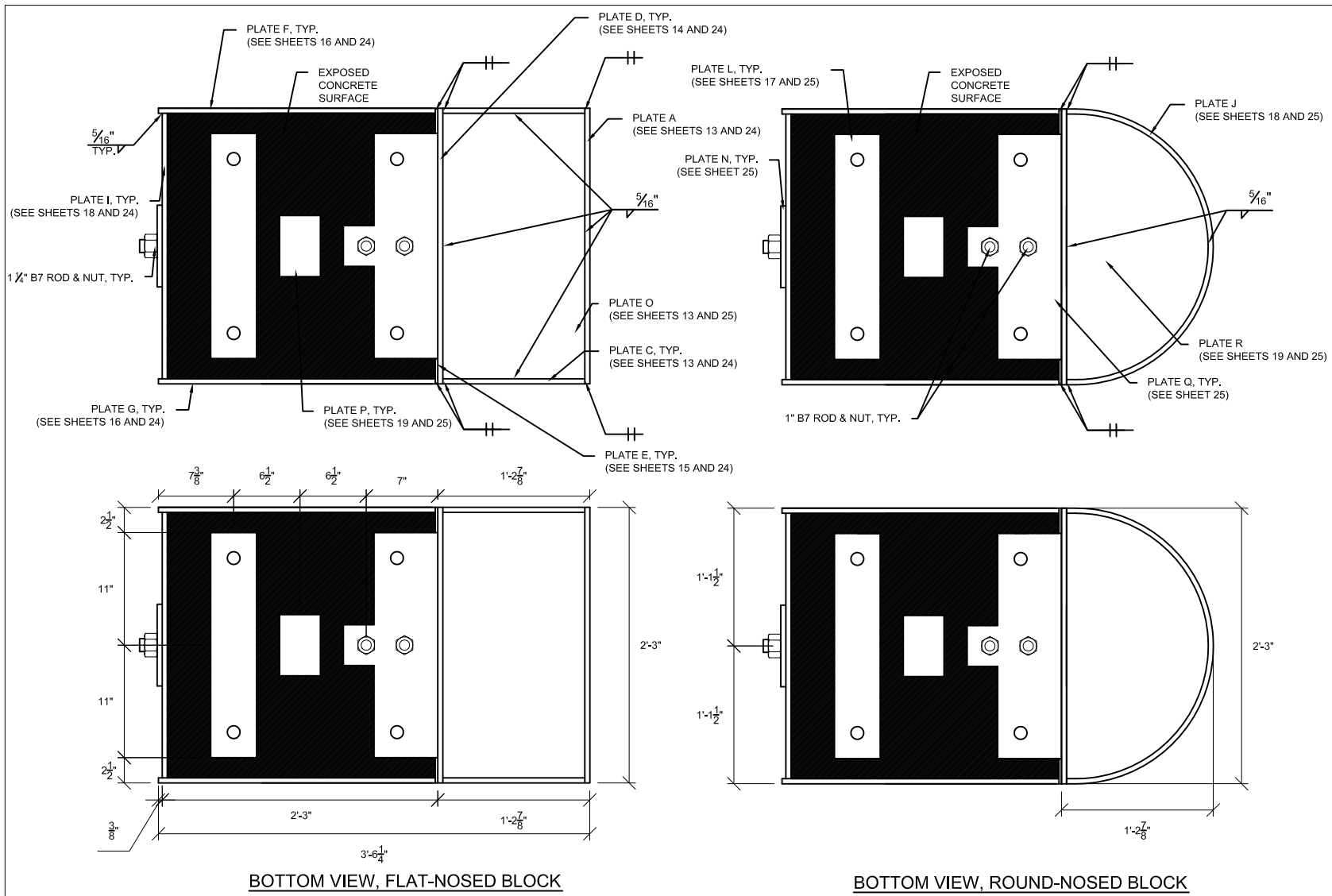


Impact Block				Revisions:		
General Notes	2013-12-31	University of Florida	Sheet 01 of 30			



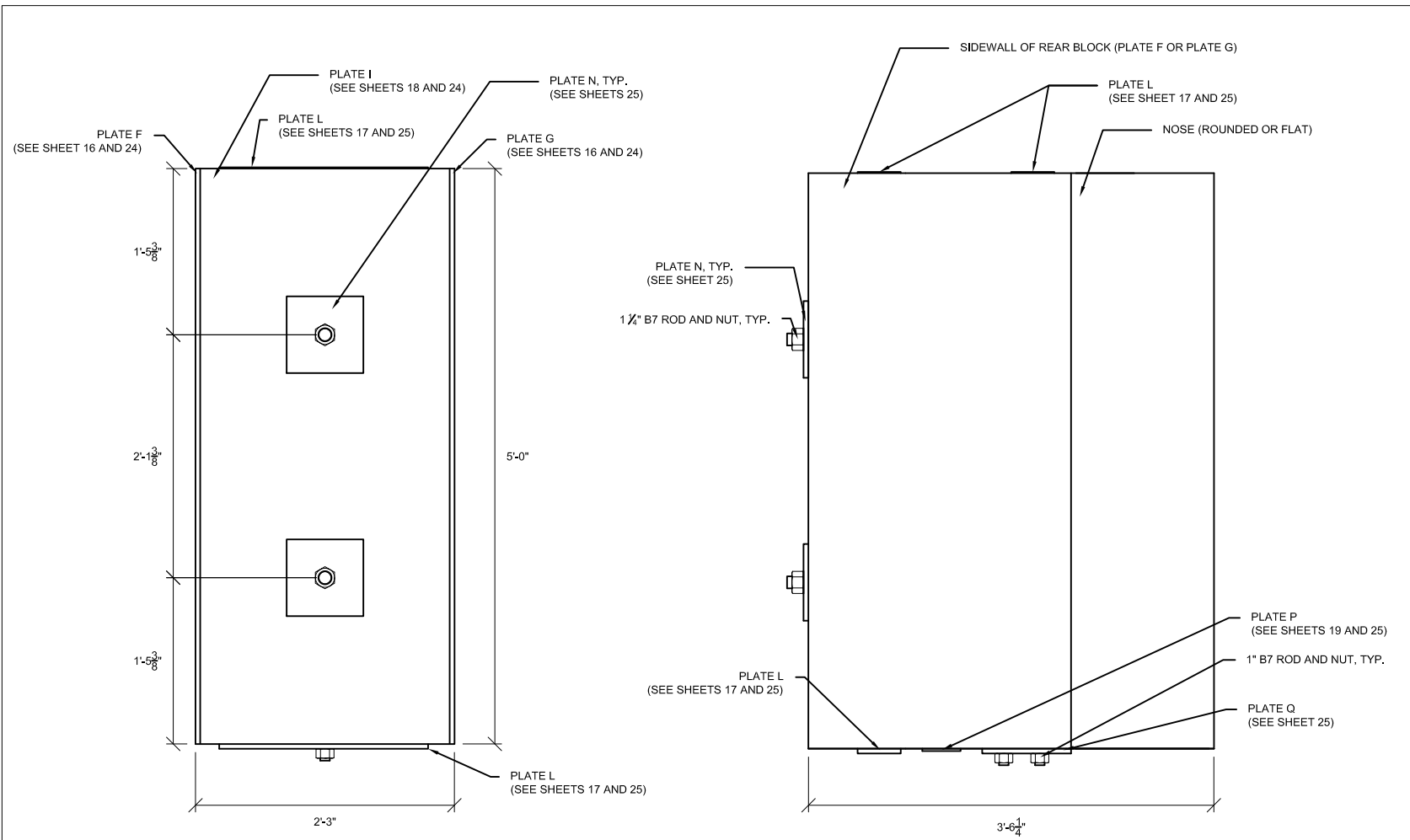
NOTE: ALL TYPICAL DETAILS ARE APPLICABLE FOR BOTH THE ROUND-NOSED AND FLAT-NOSED VARIANTS OF THE IMPACT BLOCK

Impact Block				Revisions:		
Top View	2013-12-31	University of Florida	Sheet 02 of 30			



NOTE: ALL TYPICAL DETAILS ARE APPLICABLE FOR BOTH THE ROUND-NOSED AND FLAT-NOSED VARIANTS OF THE IMPACT BLOCK

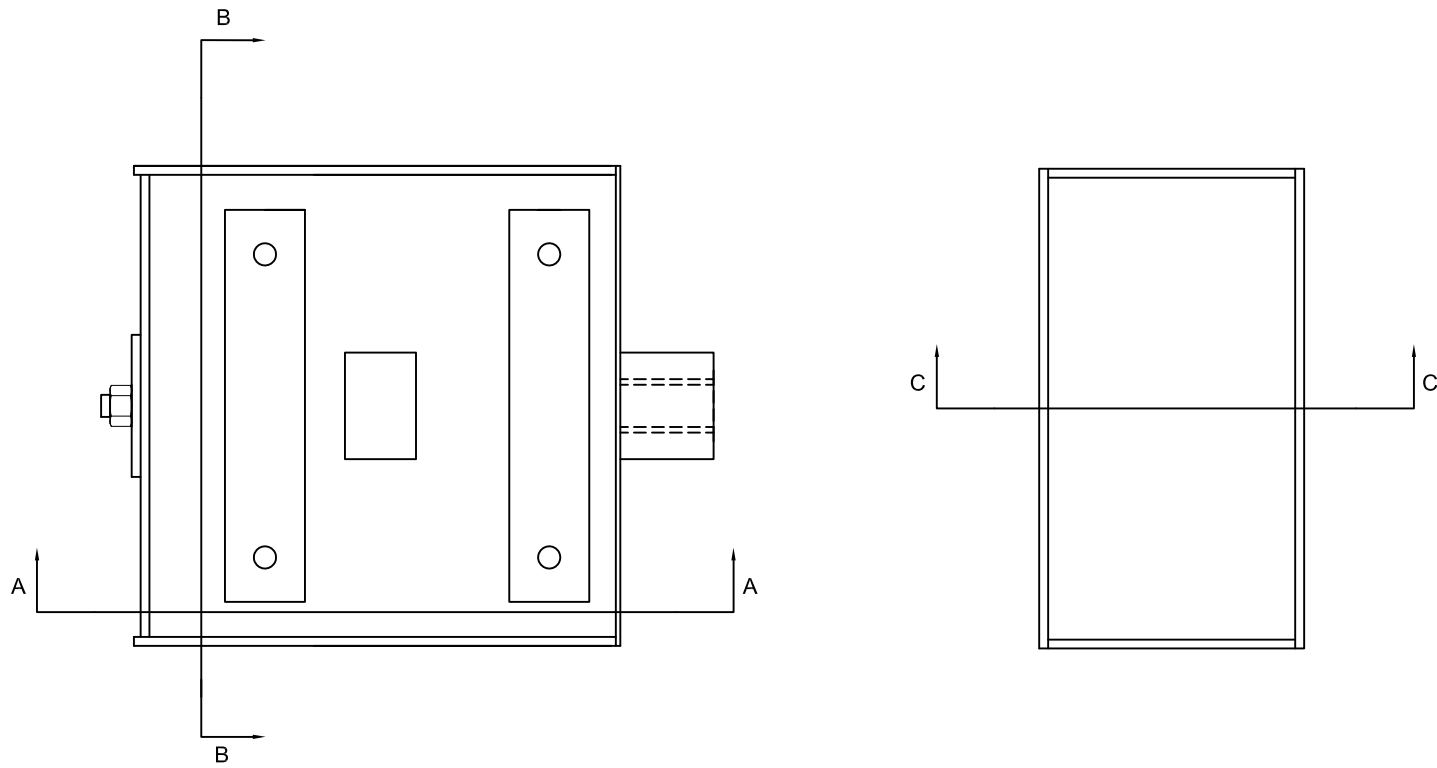
Impact Block				Revisions:		
Bottom View	2013-12-31	University of Florida	Sheet 03 of 30			



REAR VIEW

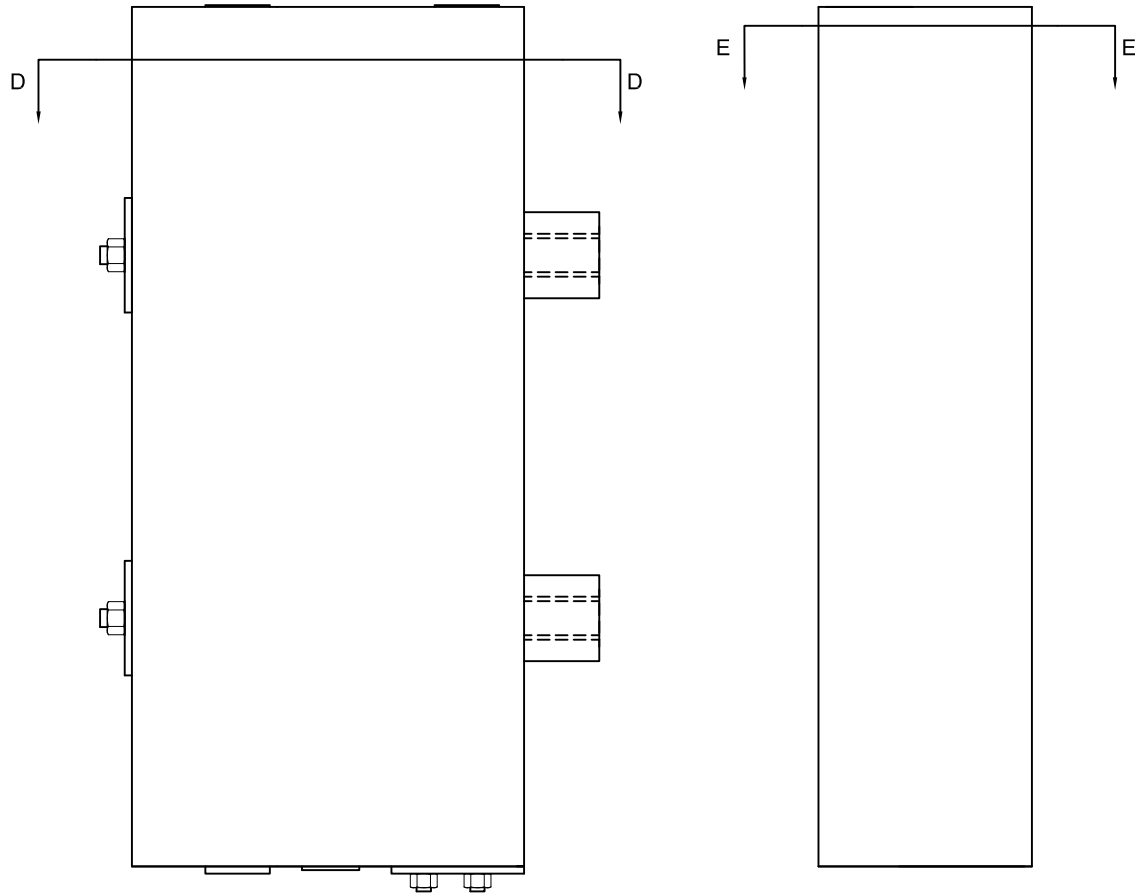
SIDE VIEW

Impact Block				Revisions:		
Elevation Views	2013-12-31	University of Florida	Sheet 04 of 30			

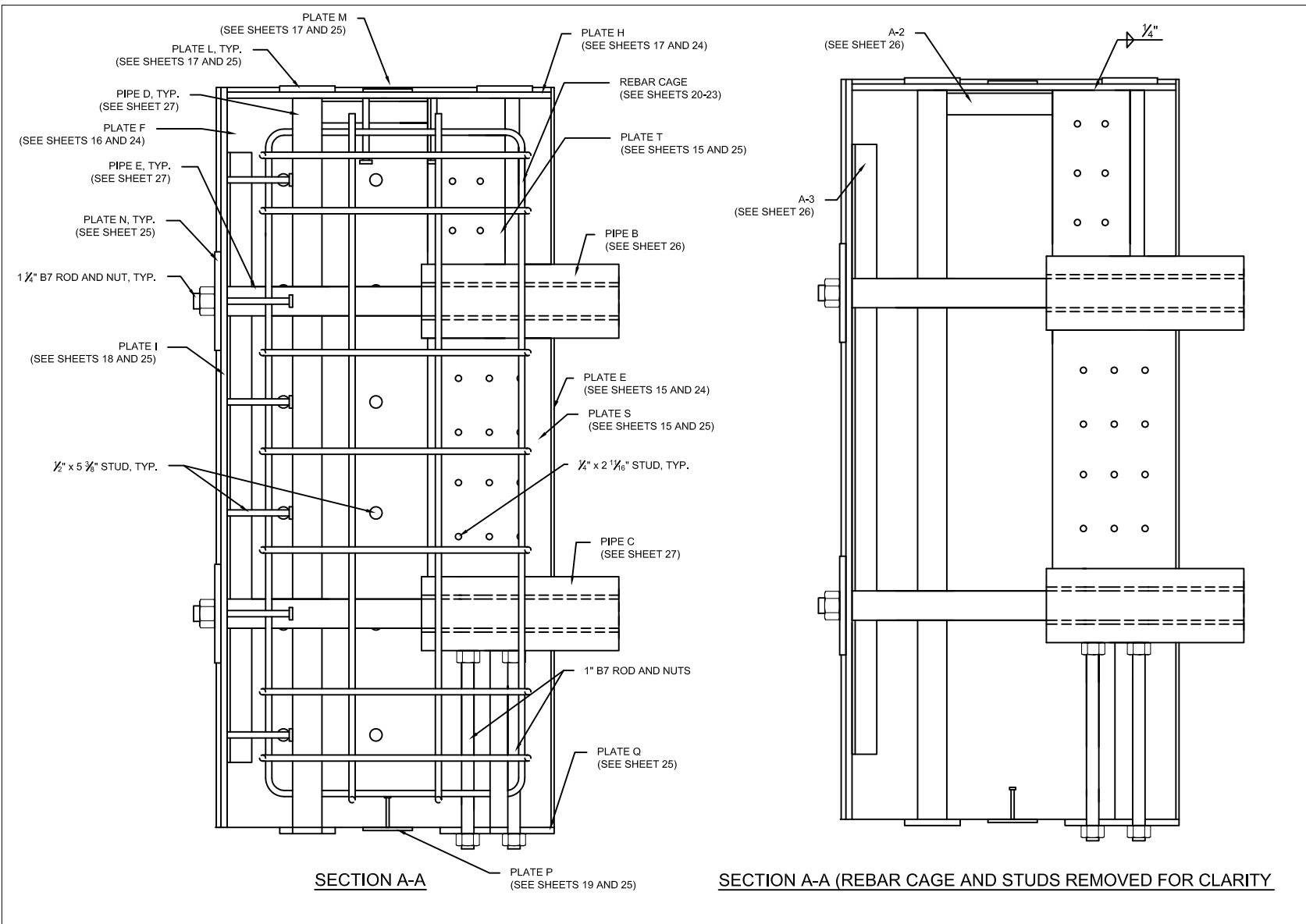


NOTE: SECTION C-C APPEARS SIMILAR FOR BOTH THE ROUND AND FLAT-NOSES.

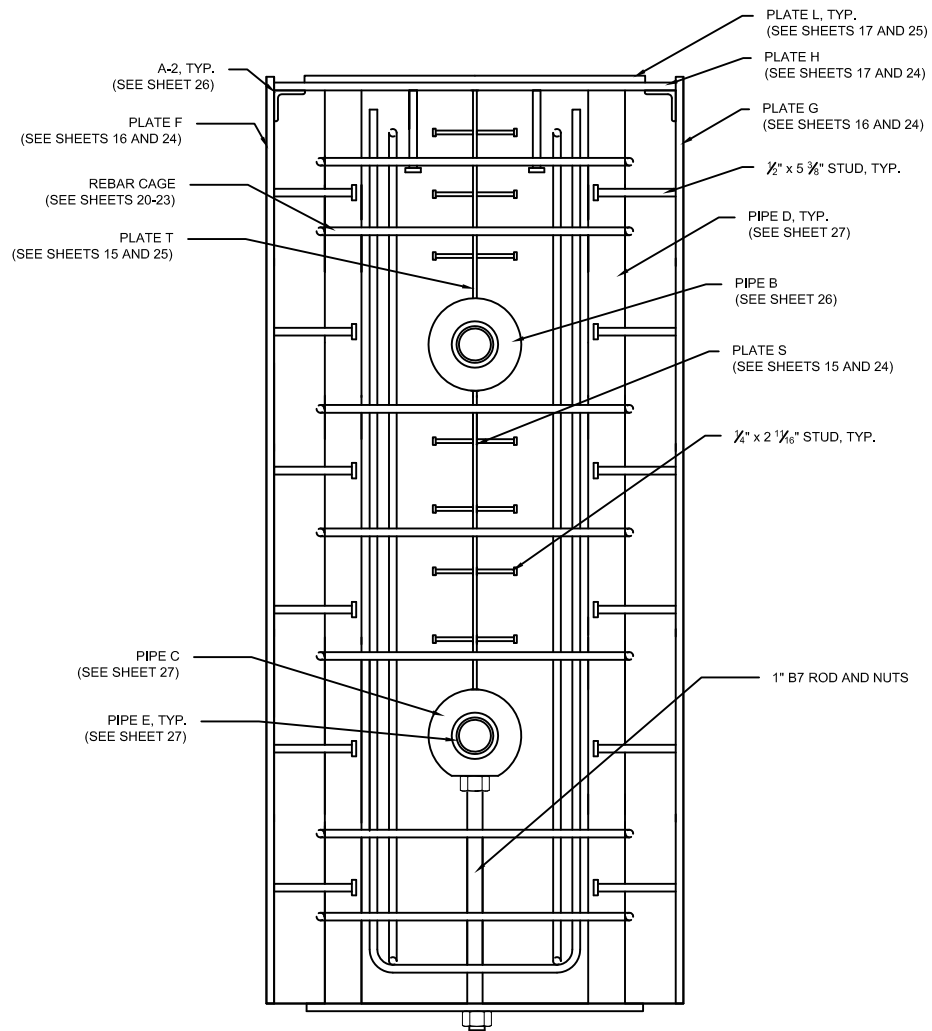
Impact Block				Revisions:		
Section Designations I	2013-12-31	University of Florida	Sheet 05 of 30			



Impact Block				Revisions:		
Section Designations II	2013-12-31	University of Florida	Sheet 06 of 30			

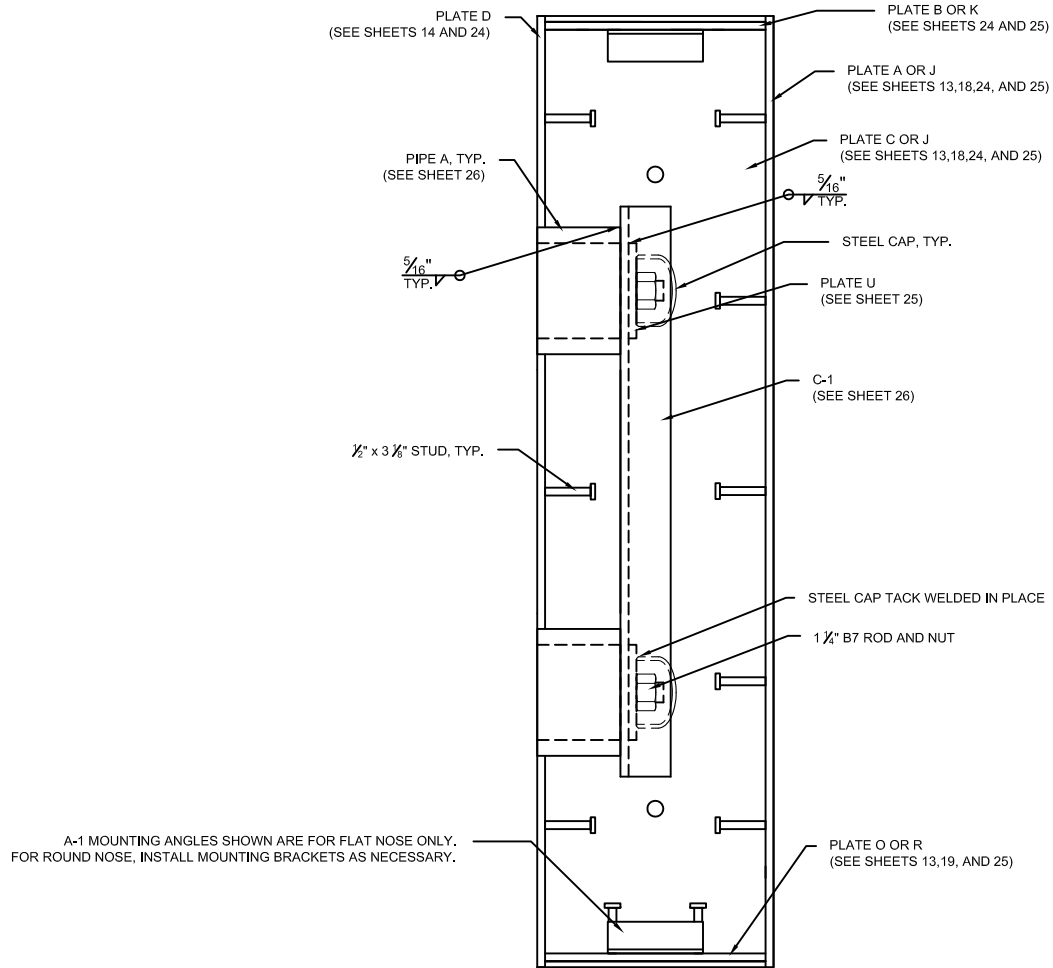


Impact Block				Revisions:		
Section Views I	2013-12-31	University of Florida	Sheet 07 of 30			



SECTION B-B

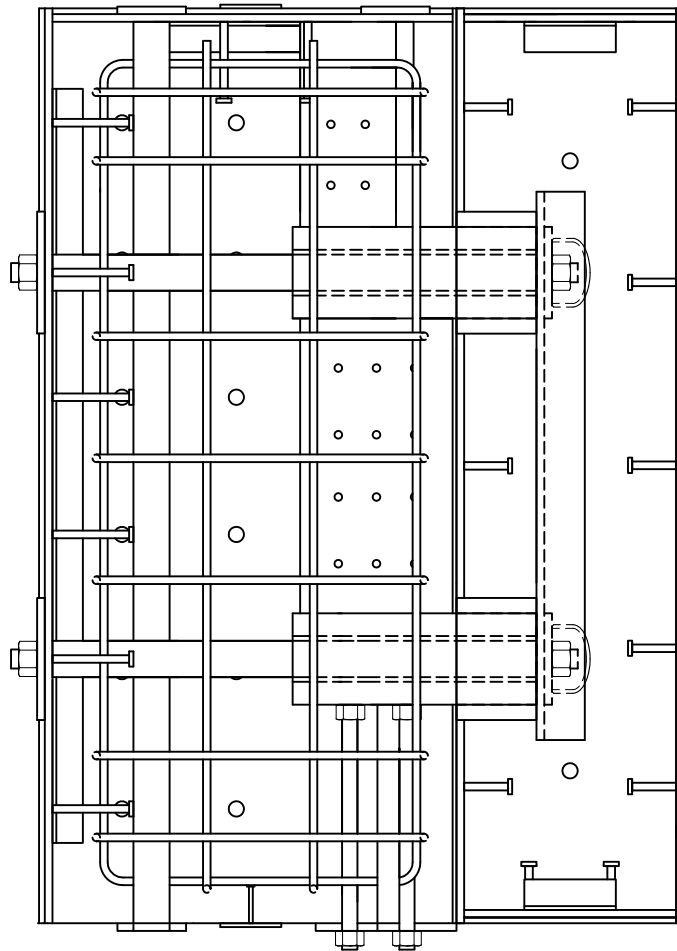
Impact Block				Revisions:		
Section Views II	2013-12-31	University of Florida	Sheet 08 of 30			



SECTION C-C

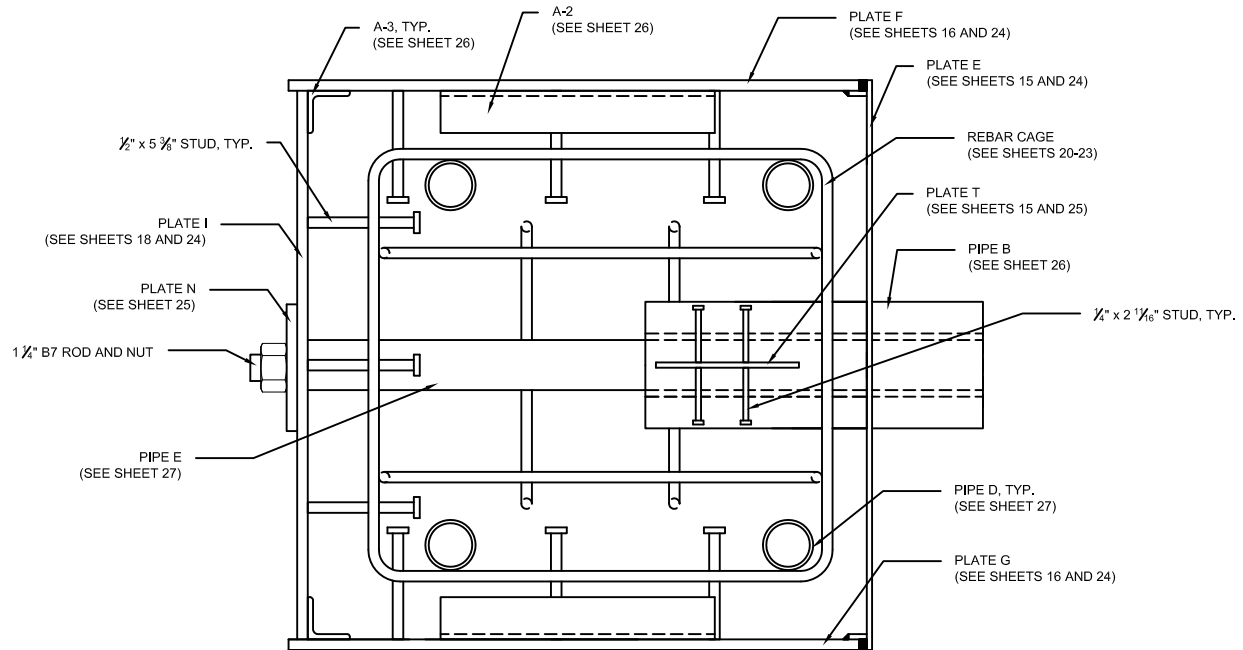
NOTE: SECTION C-C APPEARS SIMILAR FOR BOTH THE ROUND AND FLAT-NOSES.

Impact Block				Revisions:		
Section Views III	2013-12-31	University of Florida	Sheet 09 of 30			



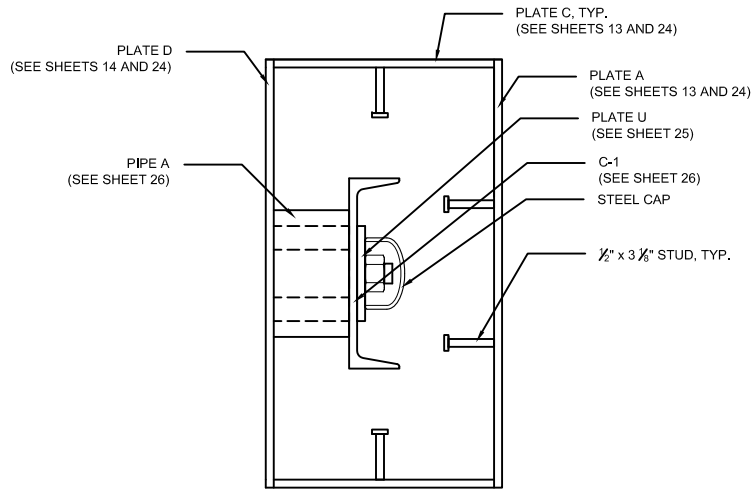
NOTE: THIS SECTION VIEW DEPICTS CROSS SECTIONS A-A AND C-C WHEN THE NOSE OF THE IMPACT BLOCK IS CONNECTED TO THE REAR BLOCK USING 1 1/4" B7 ROD.

Impact Block				Revisions:		
Section Views IV	2013-12-31	University of Florida	Sheet 10 of 30			

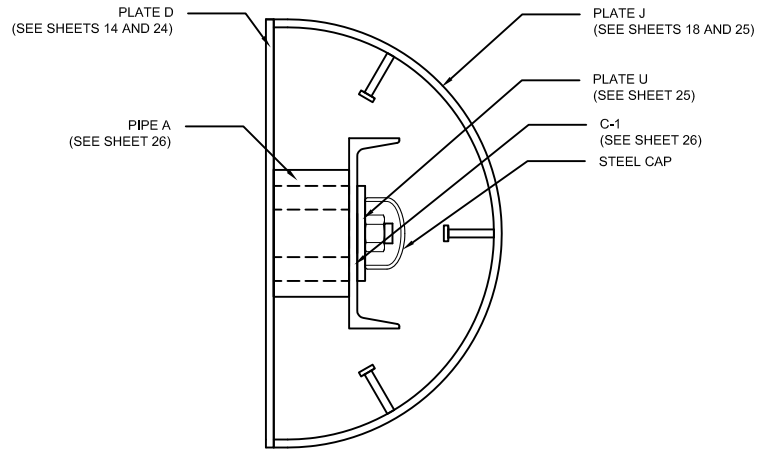


SECTION D-D

Impact Block				Revisions:		
Section Views V	2013-12-31	University of Florida	Sheet 11 of 30			



SECTION E-E (FLAT NOSE)



SECTION E-E (ROUND NOSE)

Impact Block				Revisions:		
Section Views VI	2013-12-31	University of Florida	Sheet 12 of 30			

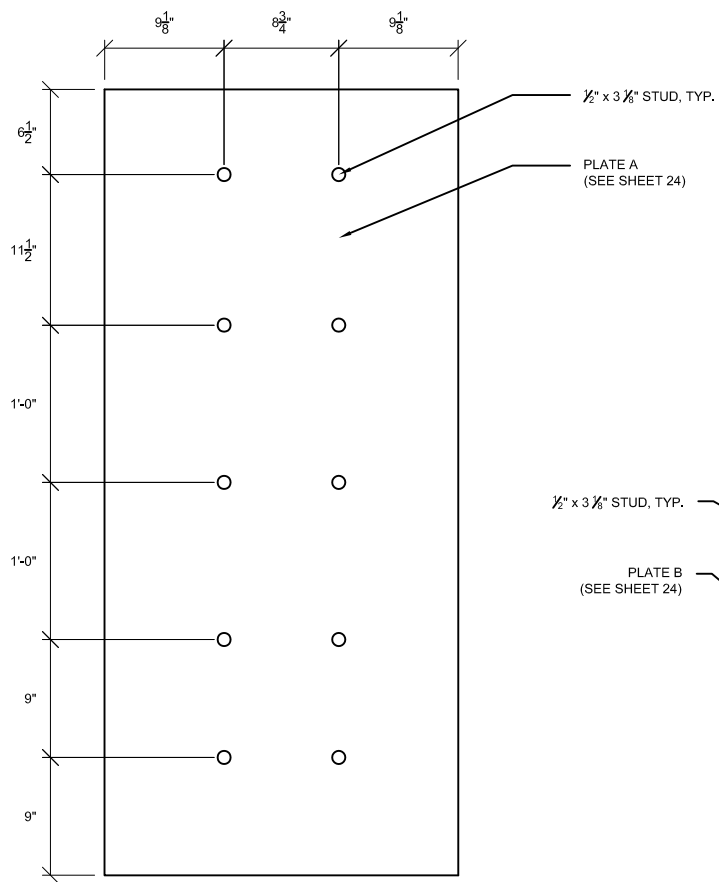


PLATE ASSEMBLY A

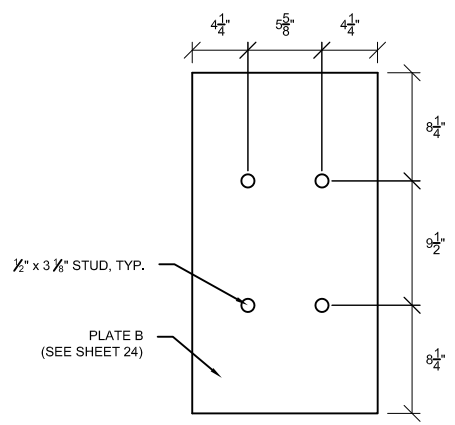


PLATE ASSEMBLY O

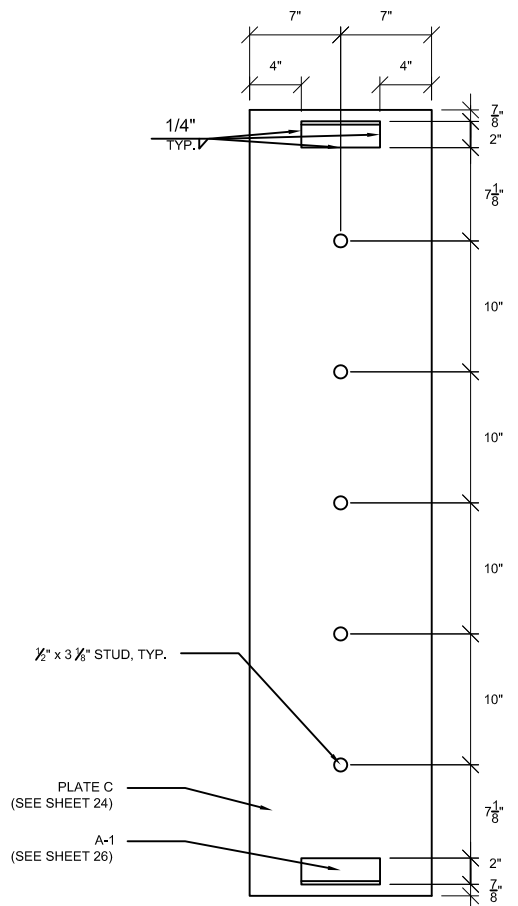


PLATE ASSEMBLY C

NOTE 1: FRONT VIEW OF PLATES SHOWN. PLATES A, C, AND O HAVE NO COMPONENTS WELDED TO THE REAR SIDE

Impact Block				Revisions:		
Plate Assemblies I	2013-12-31	University of Florida	Sheet 13 of 30			

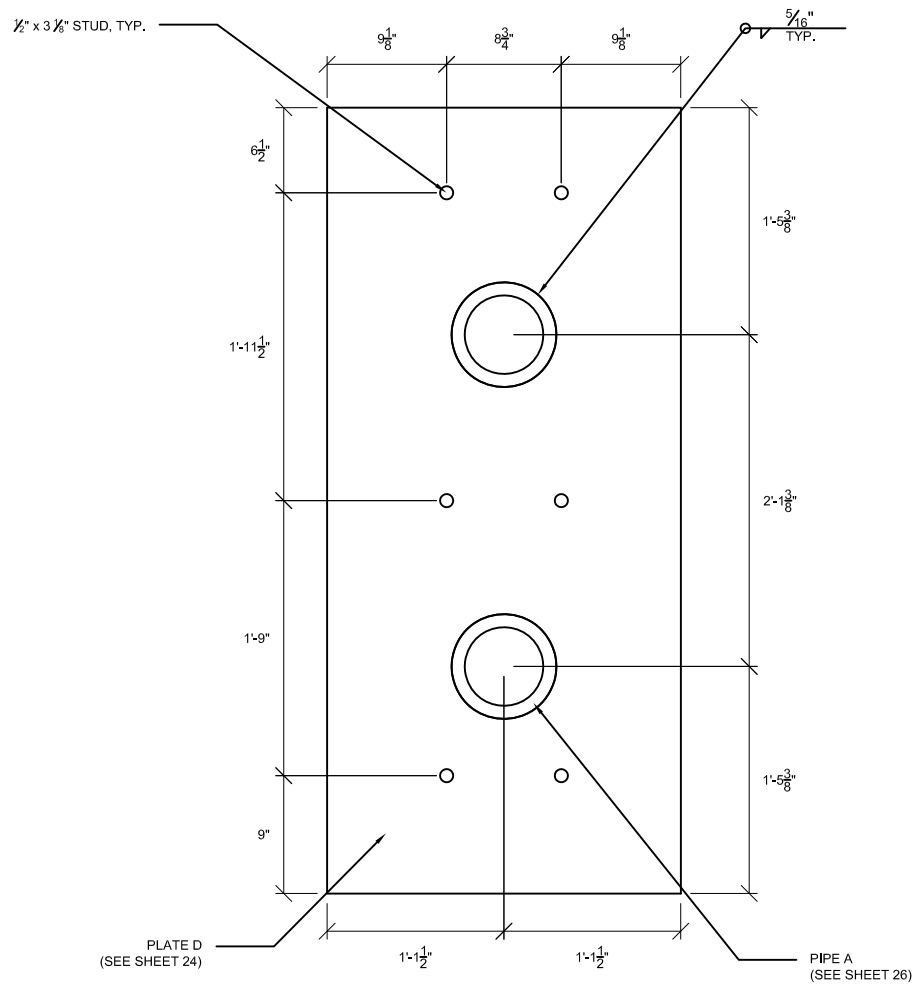


PLATE ASSEMBLY D

NOTE: FRONT VIEW OF PLATE SHOWN. PLATE D HAS NO COMPONENTS WELDED TO THE REAR SIDE.

Impact Block				Revisions:		
Plate Assemblies II	2013-12-31	University of Florida	Sheet 14 of 30			

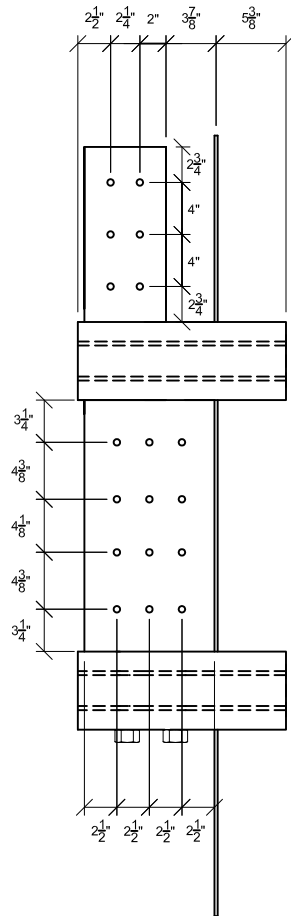


PLATE ASSEMBLY E, ELEVATION VIEW

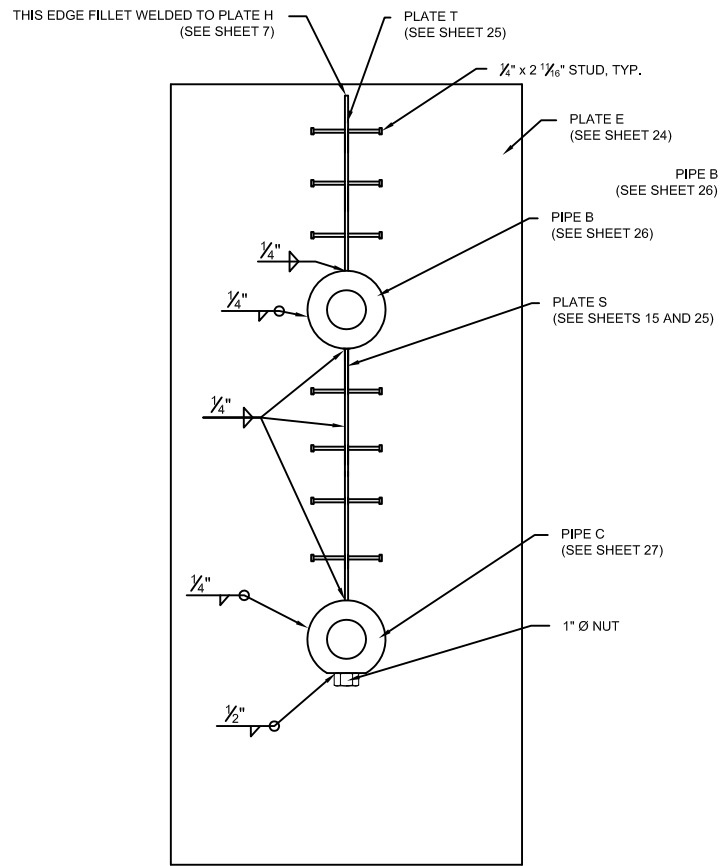


PLATE ASSEMBLY E, REAR VIEW

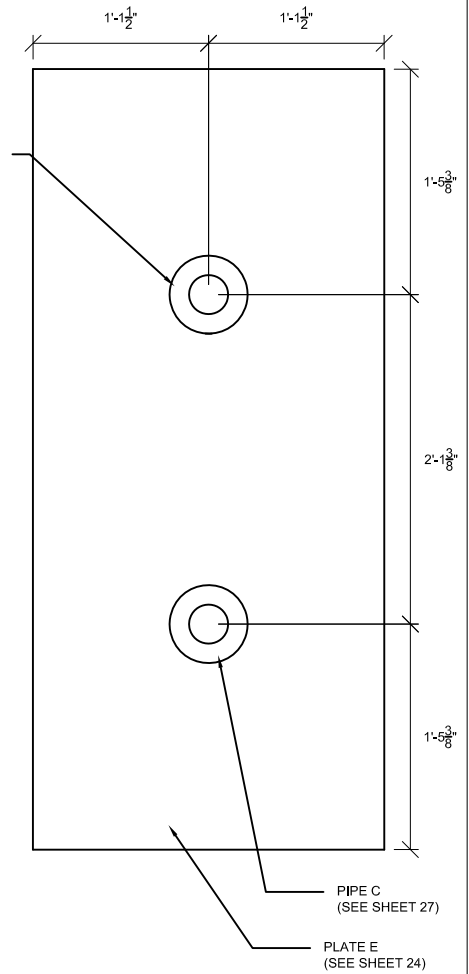
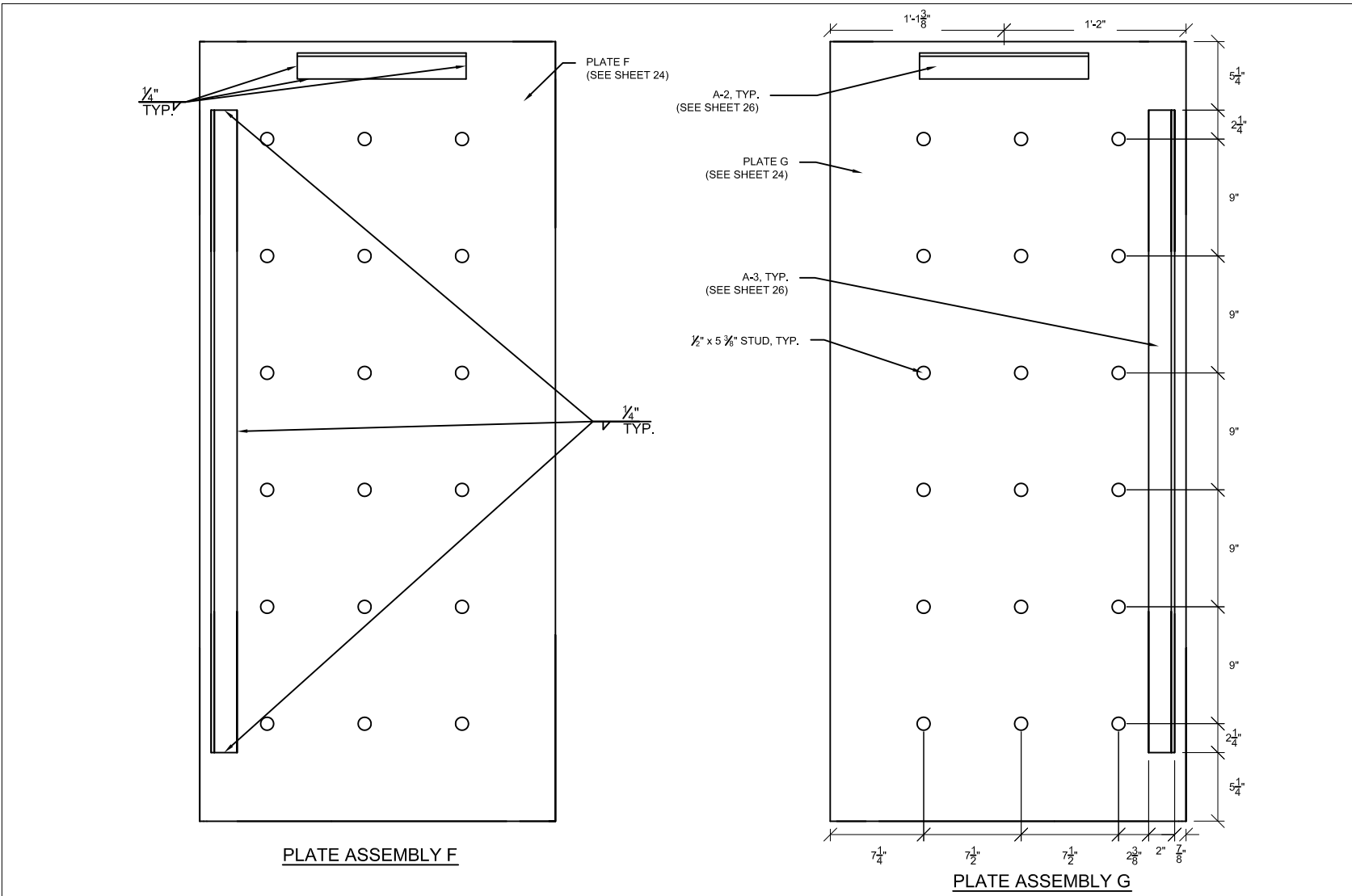


PLATE ASSEMBLY E, FRONT VIEW

Impact Block				Revisions:		
Plate Assemblies III	2013-12-31	University of Florida	Sheet 15 of 30			



NOTE 1: FRONT VIEW OF PLATES SHOWN. PLATES F AND G HAVE NO COMPONENTS WELDED TO THE REAR SIDE
 NOTE 2: SINCE PLATES F AND G ARE MIRROR IMAGES OF EACH OTHER, TYPICAL DETAILS AND DIMENSIONS APPLY FOR BOTH PLATES..

Impact Block				Revisions:		
Plate Assemblies IV	2013-12-31	University of Florida	Sheet 16 of 30			

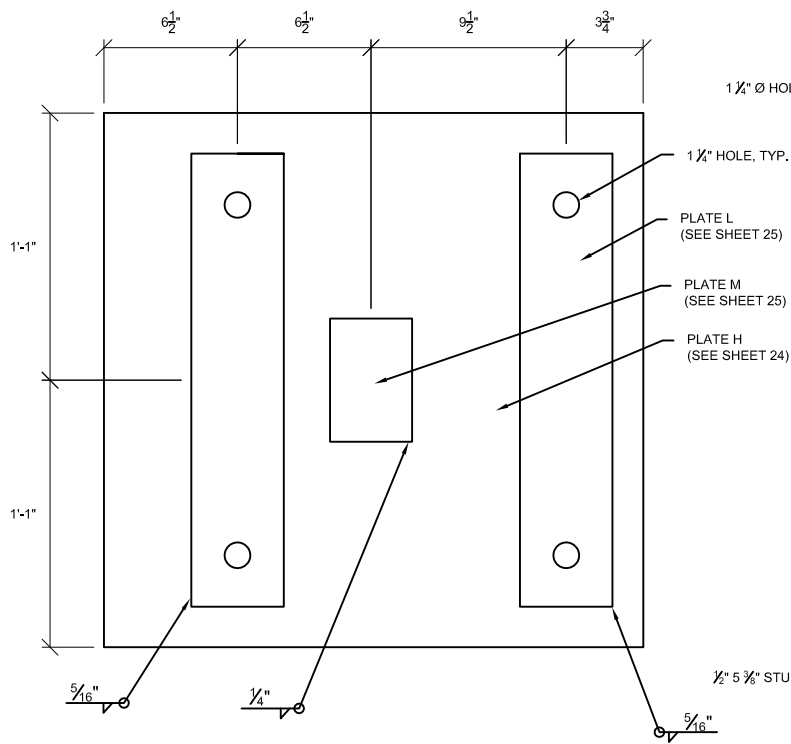


PLATE ASSEMBLY H - TOP VIEW

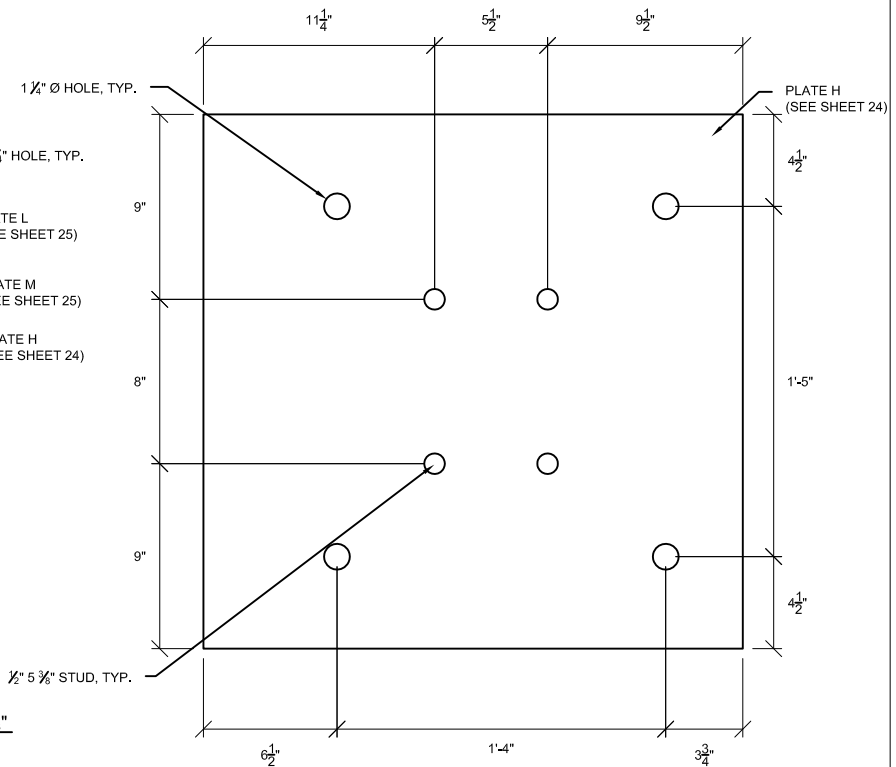
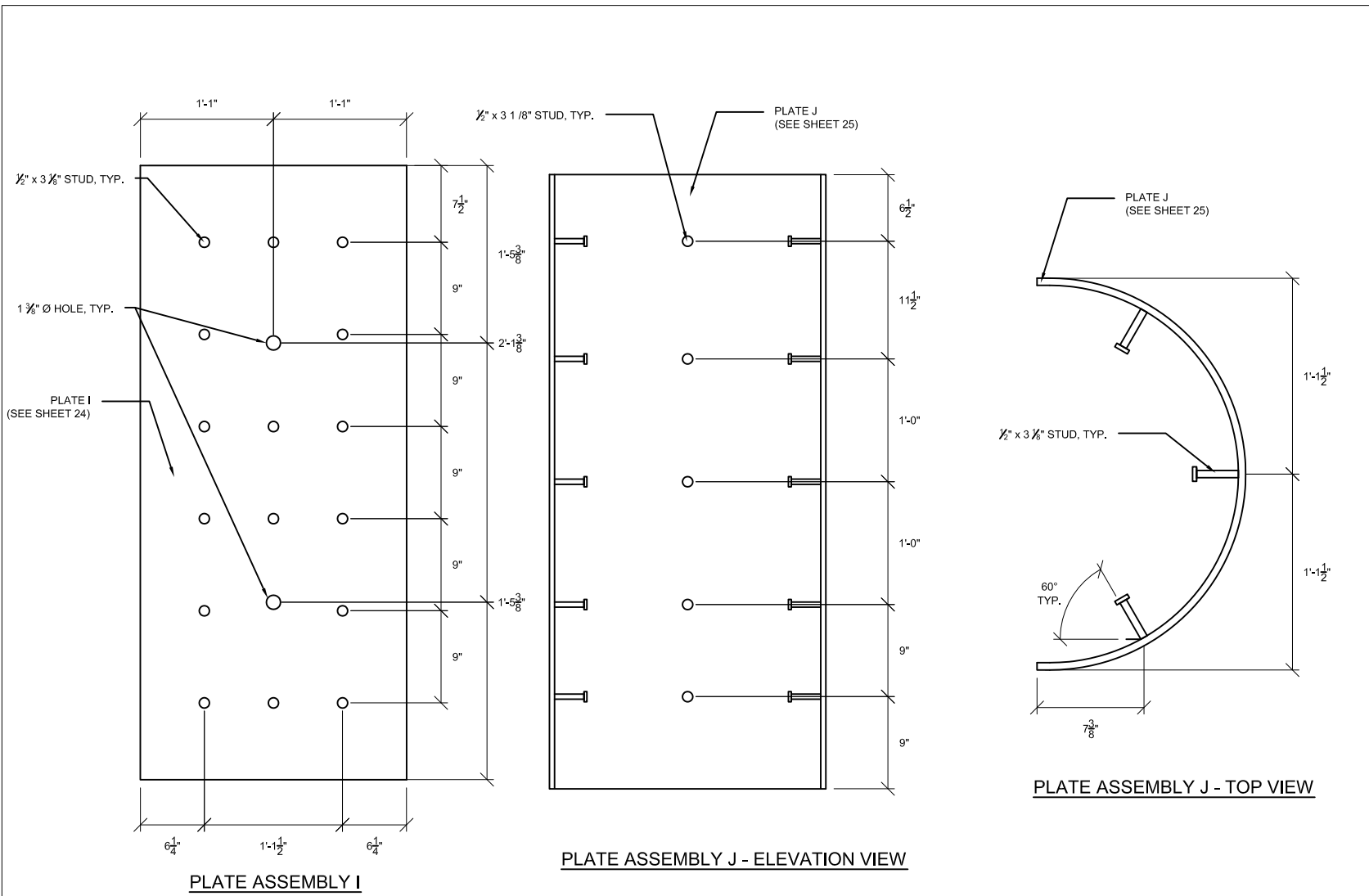


PLATE ASSEMBLY H - BOTTOM VIEW

Impact Block				Revisions:		
Plate Assemblies V	2013-12-31	University of Florida	Sheet 17 of 30			



NOTE: FRONT VIEW OF PLATES SHOWN. PLATES I AND J HAVE NO COMPONENTS WELDED TO THE REAR SIDE.

Impact Block				Revisions:		
Plate Assemblies VI	2013-12-31	University of Florida	Sheet 18 of 30			

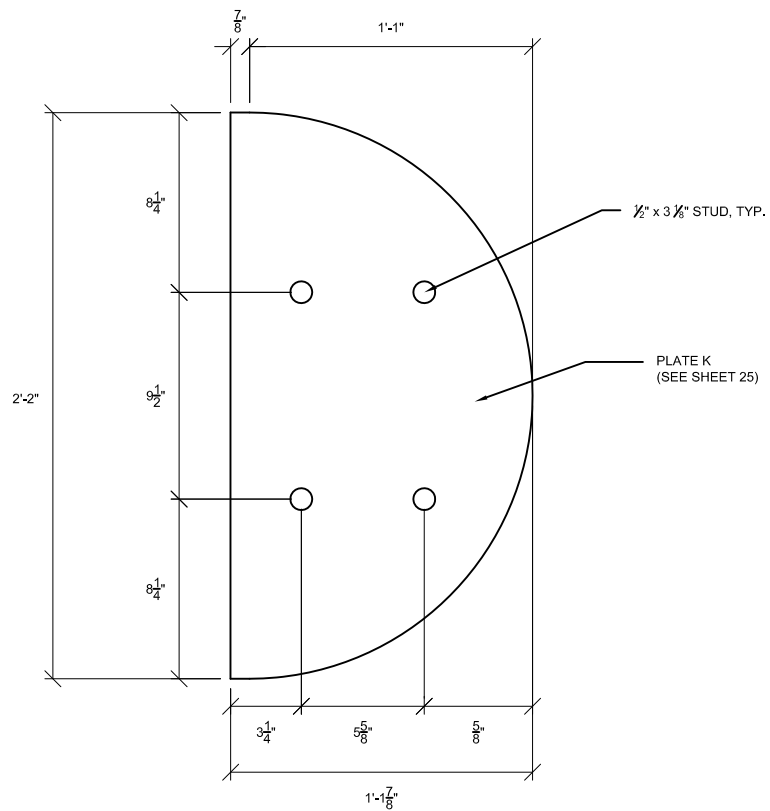


PLATE ASSEMBLY R

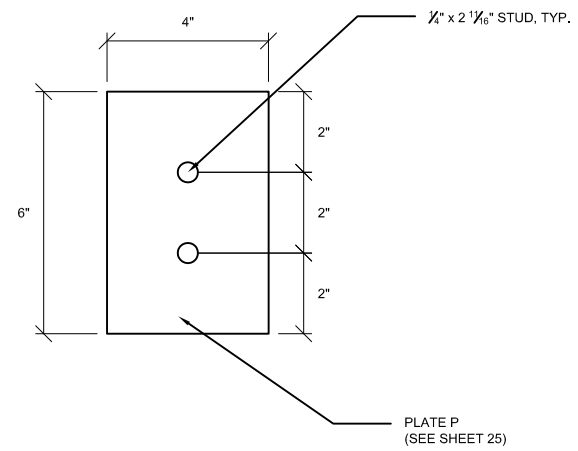
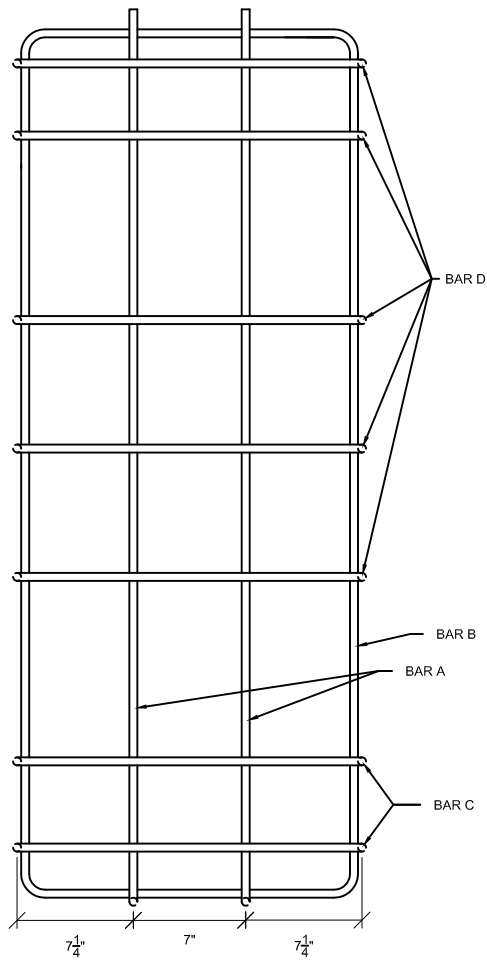


PLATE ASSEMBLY P

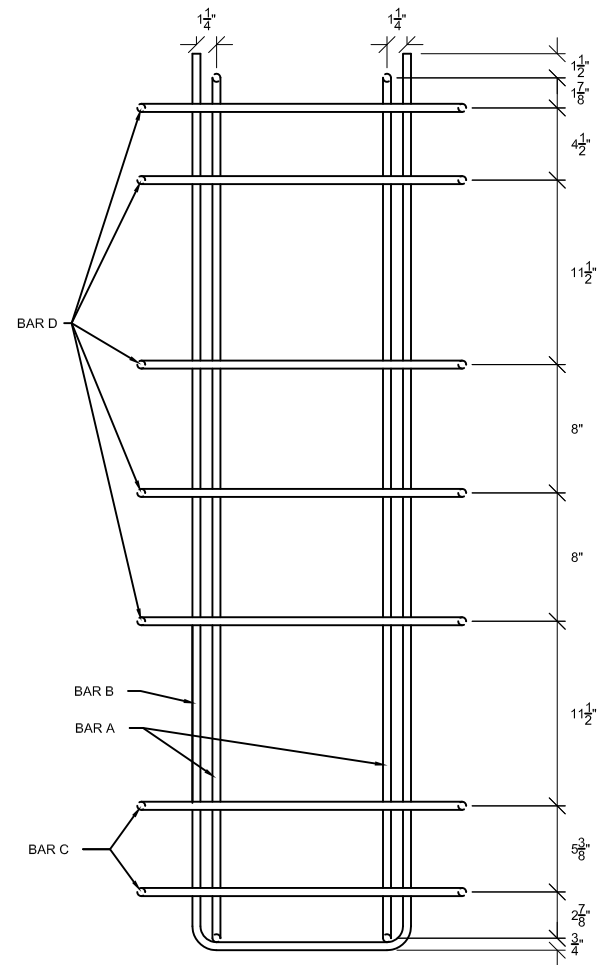
NOTE 1: FRONT VIEW OF PLATES SHOWN. PLATES P AND R HAVE NO COMPONENTS WELDED TO THE REAR SIDE.

NOTE 2: PLATE R HAS A 7/8" LONG STRAIGHT PORTION AND A 26" Ø HALF-CIRCULAR PORTION

Impact Block				Revisions:		
Plate Assemblies VII	2013-12-31	University of Florida	Sheet 19 of 30			

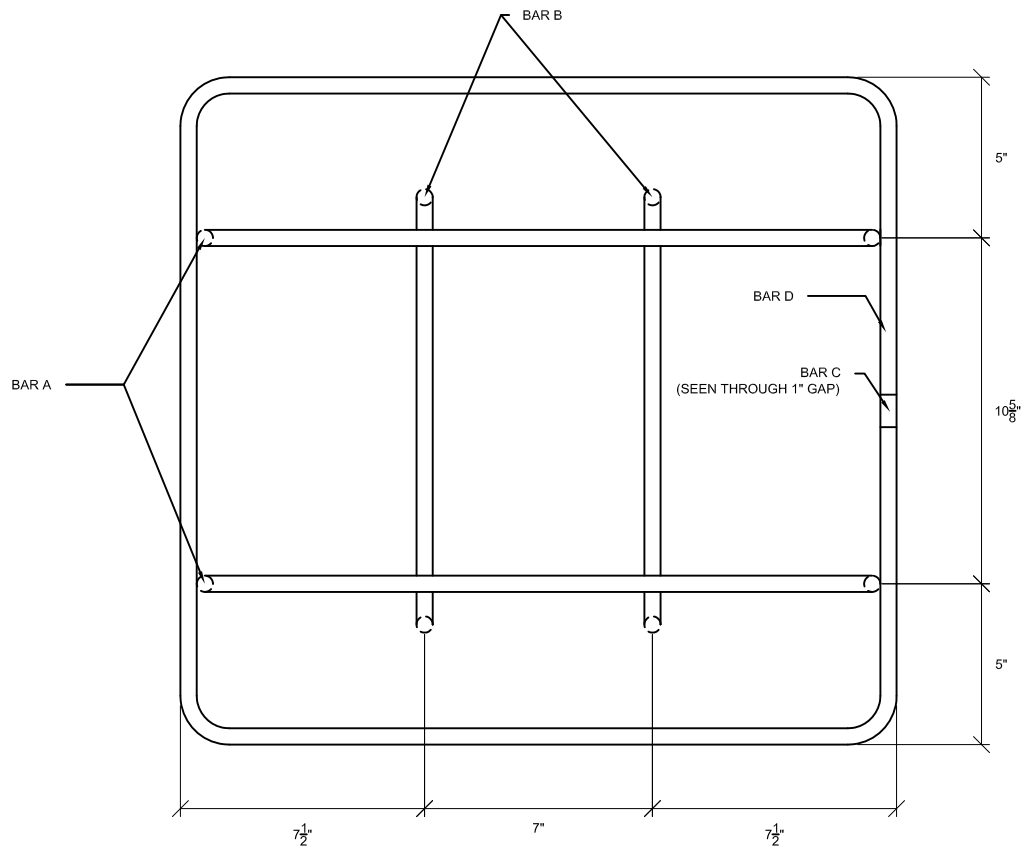


SIDE VIEW



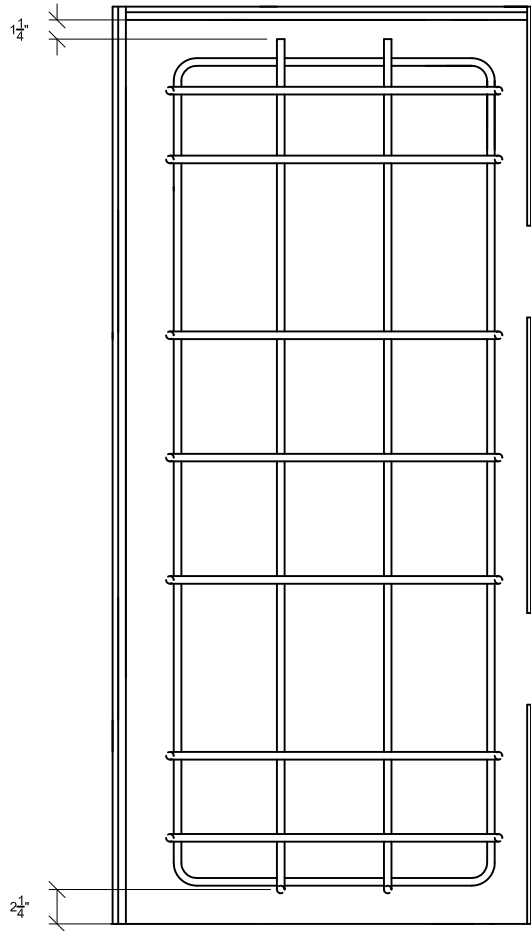
REAR VIEW

Impact Block				Revisions:		
Rebar Details I	2013-12-31	University of Florida	Sheet 20 of 30			

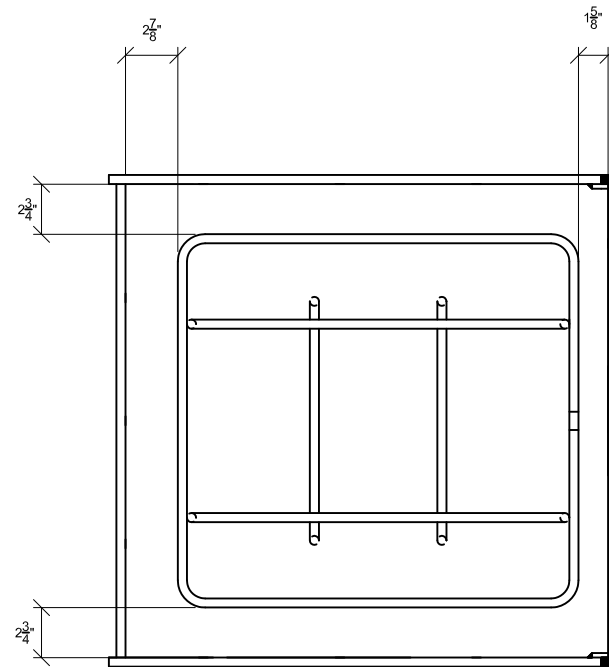


TOP VIEW

Impact Block				Revisions:		
Rebar Details II	2013-12-31	University of Florida	Sheet 21 of 30			

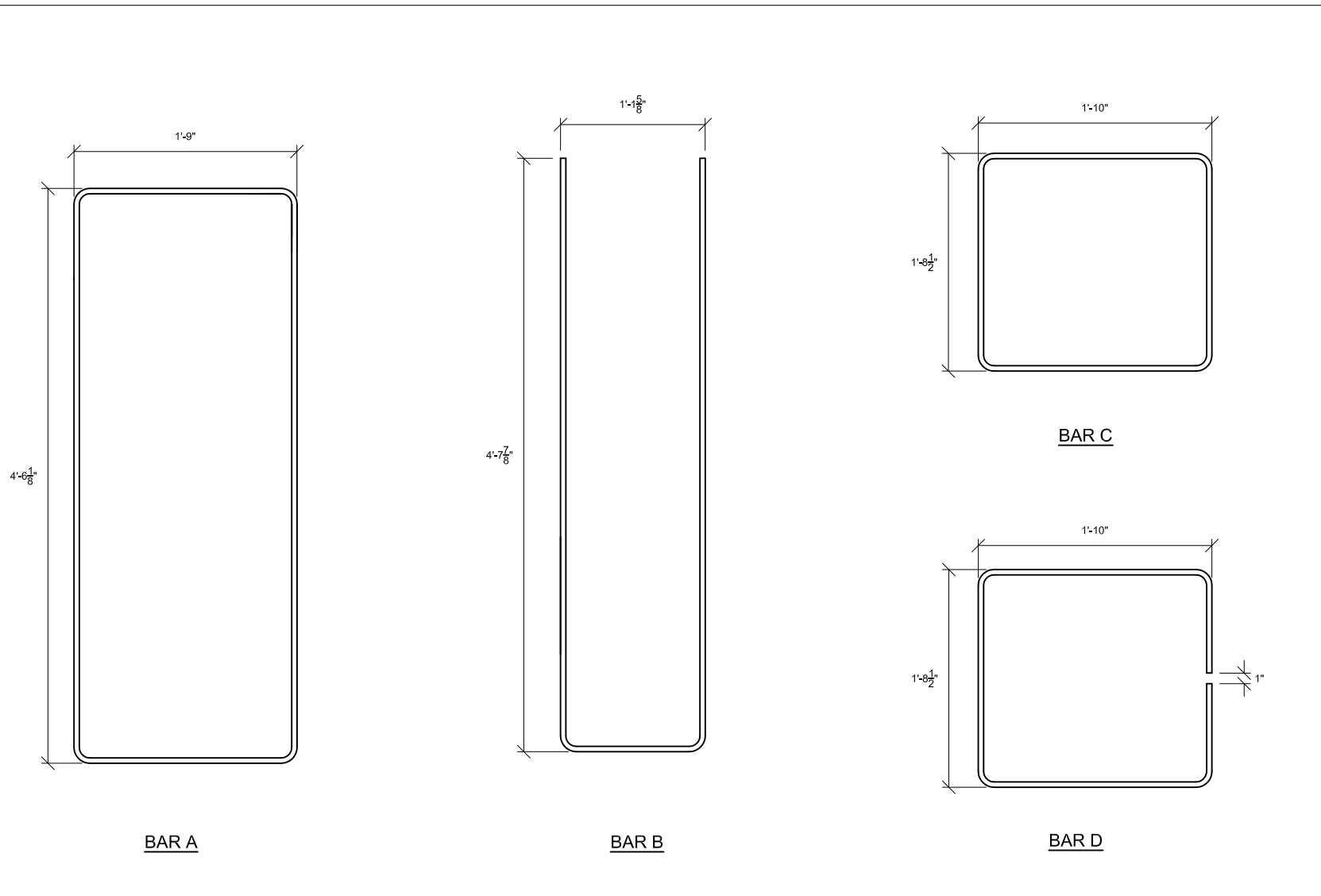


ELEVATION VIEW DEPICTING VERTICAL CLEAR DISTANCES BETWEEN REBAR CAGE AND STEEL SHELL



TOP VIEW DEPICTING CLEAR DISTANCES BETWEEN REBAR CAGE AND STEEL SHELL

Impact Block				Revisions:		
Rebar Details III	2013-12-31	University of Florida	Sheet 22 of 30			



NOTE: All reinforcement shall be #4 bar.

Impact Block				Revisions:		
Rebar Details IV	2013-12-31	University of Florida	Sheet 23 of 30			

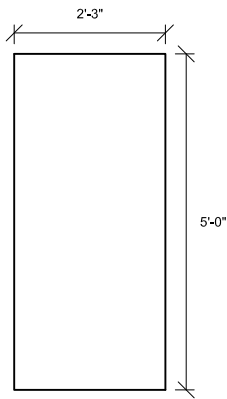


PLATE A
Fy = 50 ksi, t = 1/2"

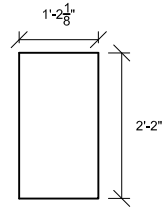


PLATE B
Fy = 50 ksi, t = 1/2"

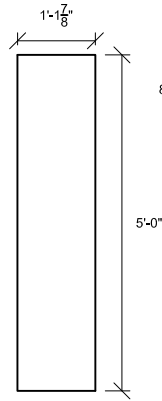


PLATE C
Fy = 50 ksi, t = 1/2"

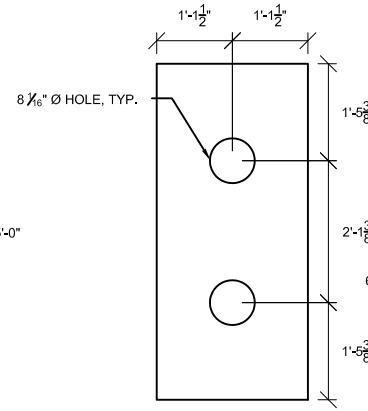


PLATE D
Fy = 50 ksi, t = 1/2"

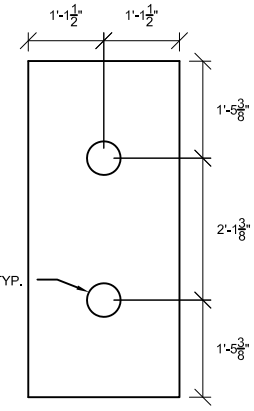


PLATE E
Fy = 50 ksi, t = 1/4"

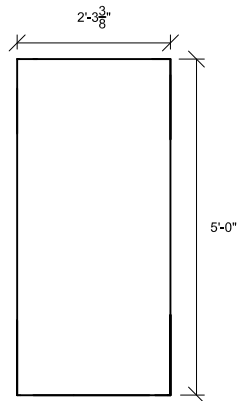


PLATE F
Fy = 50 ksi, t = 1/2"

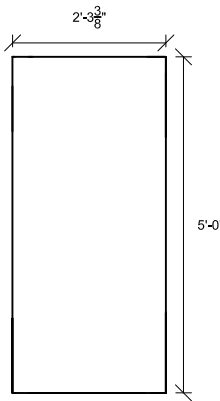


PLATE G
Fy = 50 ksi, t = 1/2"

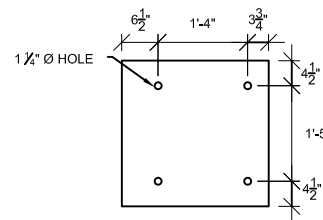


PLATE H
Fy = 50 ksi, t = 1/2"

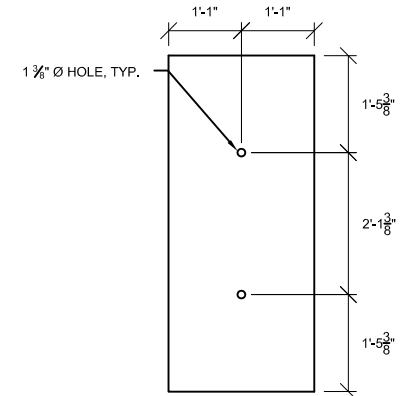
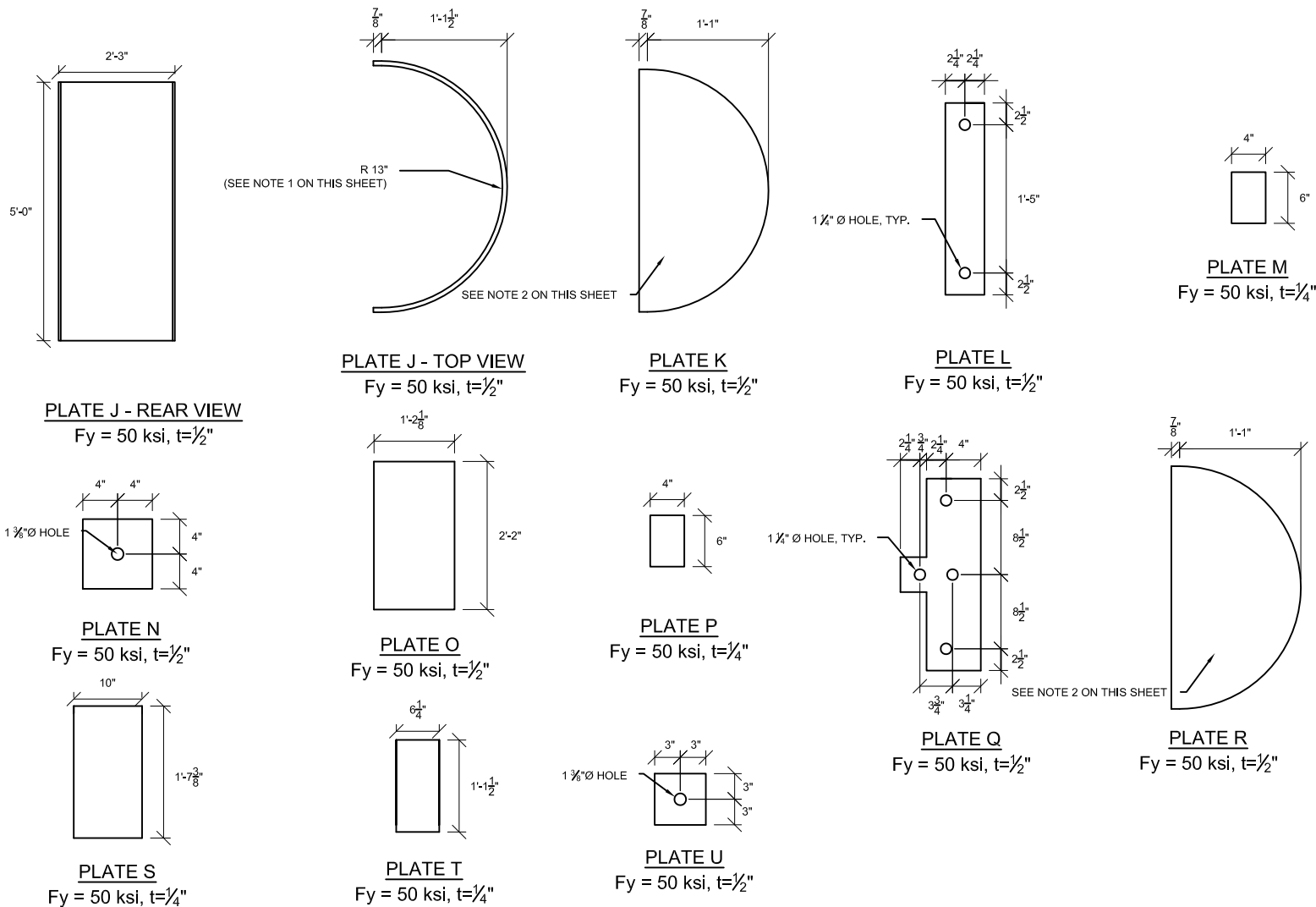


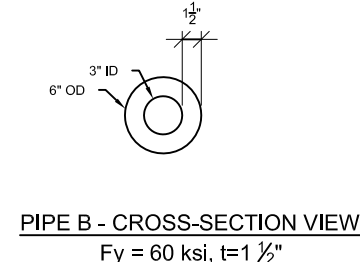
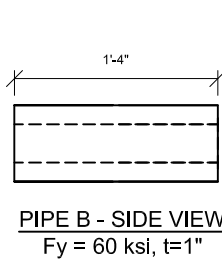
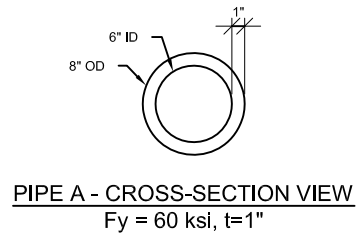
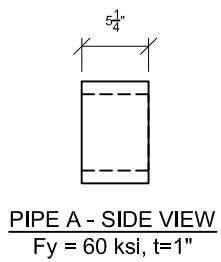
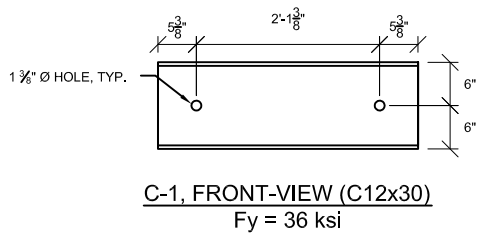
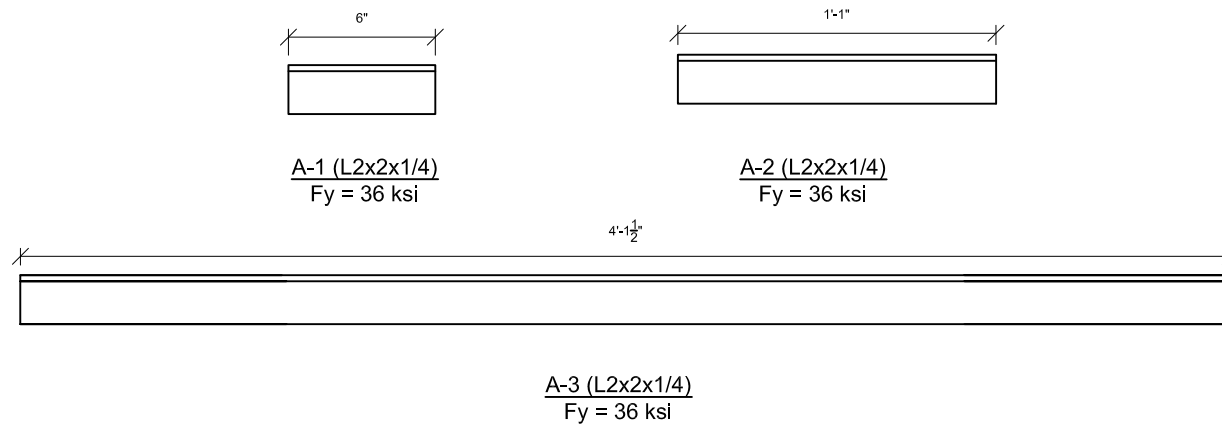
PLATE I
Fy = 50 ksi, t = 1/2"

Impact Block				Revisions:		
Plate Details I	2013-12-31	University of Florida	Sheet 24 of 30			

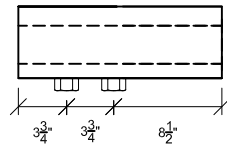


NOTE 1: PLATE J CONSISTS OF A 1/2" ROLLED PLATE WITH AN INTERNAL RADIUS OF 13" WITH TWO 7/8" STRAIGHT PORTIONS.
 NOTE 2: PLATES K AND R HAVE A 7/8" LONG STRAIGHT PORTION AND A 26" Ø HALF-CIRCULAR PORTION.

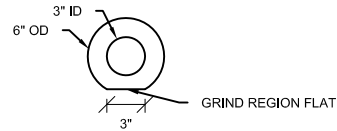
Impact Block				Revisions:		
Plate Details II	2013-12-31	University of Florida	Sheet 25 of 30			



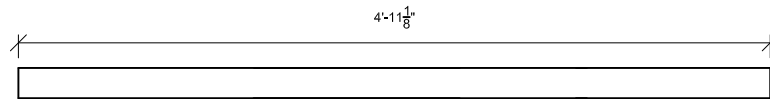
Impact Block				Revisions:		
Component Details I	2013-12-31	University of Florida	Sheet 26 of 30			



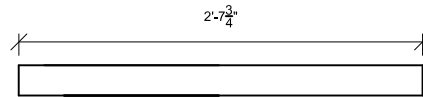
PIPE C - SIDE VIEW
 $F_y = 60 \text{ ksi}, t = 1''$



PIPE C - CROSS-SECTION VIEW
 (NUTS NOT SHOWN FOR CLARITY)
 $F_y = 60 \text{ ksi}, t = 1 \frac{1}{2}''$



PIPE D - SIDE VIEW (#2 SCH 40 PVC PIPE)



PIPE E - SIDE VIEW (#2 SCH 40 PVC PIPE)

Impact Block				Revisions:		
Component Details II	2013-12-31	University of Florida	Sheet 27 of 30			

SCHEDULE OF PLATES		
NAME	QTY	NOTES
PLATE A	1	A572-50
PLATE B	1	A572-50
PLATE C	2	A572-50
PLATE D	2	A572-50
PLATE E	1	A572-50
PLATE F	1	A572-50
PLATE G	1	A572-50
PLATE H	1	A572-50
PLATE I	1	A572-50
PLATE J	1	A572-50
PLATE K	1	A572-50
PLATE L	3	A572-50
PLATE M	1	A572-50
PLATE N	2	A572-50
PLATE O	1	A572-50
PLATE P	1	A572-50
PLATE Q	1	A572-50
PLATE R	1	A572-50
PLATE S	1	A572-50
PLATE T	1	A572-50
PLATE U	4	A572-50

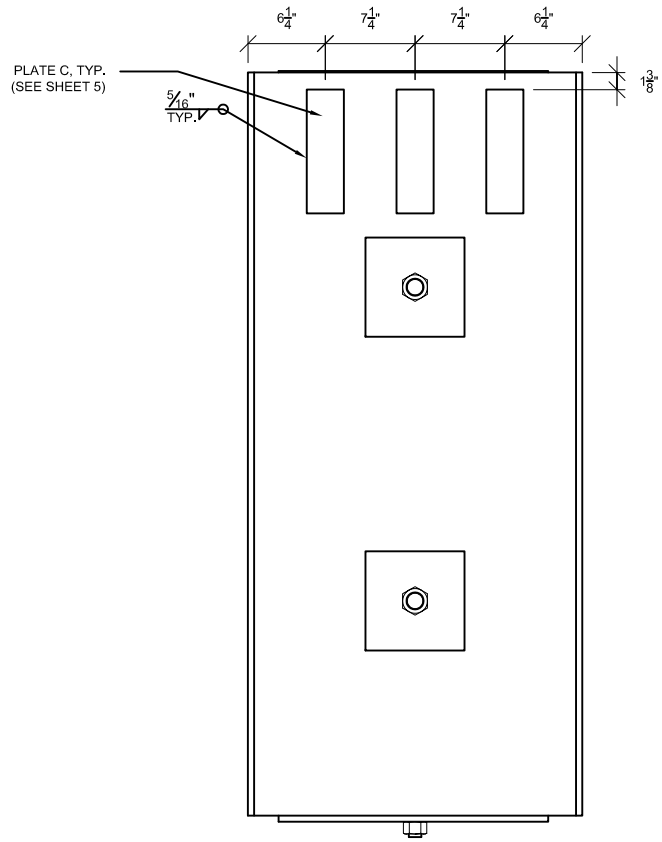
Impact Block				Revisions:		
Schedule of Plates	2013-12-31	University of Florida	Sheet 28 of 30			

SCHEDULE OF MEMBERS					
NAME	SIZE	LENGTH	QTY	TOTAL LENGTH	NOTES
A-1	L2x2x $\frac{1}{4}$	6"	4	2'-0"	A36
A-2	L2x2x $\frac{1}{4}$	1'-1"	2	2'-2"	A36
A-3	L2x2x $\frac{1}{4}$	1'-1 $\frac{1}{2}$ "	2	2'-3"	A36
C-1	C12x30	3'	2	6'-0"	A36
PIPE A	8" OD (6" ID)	5 $\frac{1}{4}$ "	4	1'-9"	A519 GRADE 1026
PIPE B	6" OD (3" ID)	1'-4"	1	1'-4"	A519 GRADE 1026
PIPE C	6" OD (3" ID)	1'-4"	1	1'-4"	A519 GRADE 1026
PIPE D	#2, SCH 40	4'-11 $\frac{1}{8}$ "	4	19'-8 $\frac{1}{2}$ "	PVC
PIPE E	#2, SCH 40	2'-7 $\frac{3}{4}$ "	2	5'-3 $\frac{1}{2}$ "	PVC
B7 ROD	1 $\frac{1}{4}$ " \emptyset	3'-1 $\frac{1}{8}$ "	2	6'-2 $\frac{1}{4}$ "	A193 GRADE B7
B7 ROD	1 \emptyset	1'-4"	2	2'-8"	A193 GRADE B7
NUTS	1 $\frac{1}{4}$ " \emptyset	-	10	-	A563
NUTS	1 \emptyset	-	10	-	A563
STUDS	$\frac{1}{2}$ " \emptyset	5 $\frac{3}{8}$ "	65	-	-
STUDS	$\frac{1}{2}$ " \emptyset	3 $\frac{1}{8}$ "	55	-	-
STUDS	$\frac{1}{4}$ " \emptyset	2 $\frac{1}{16}$ "	45	-	-

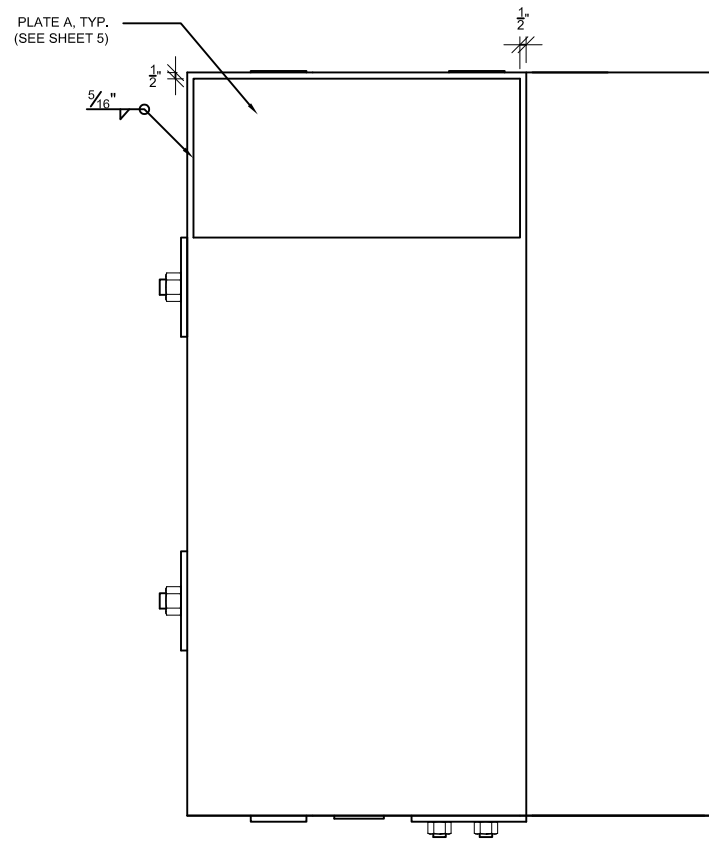
Impact Block				Revisions:		
Schedule of Members	2013-12-31	University of Florida	Sheet 29 of 30			

REINFORCING BAR SCHEDULE	
NAME	QTY
BAR A	2
BAR B	2
BAR C	2
BAR D	5

Impact Block				Revisions:		
Reinforcing Bar Schedule	2013-12-31	University of Florida	Sheet 30 of 30			

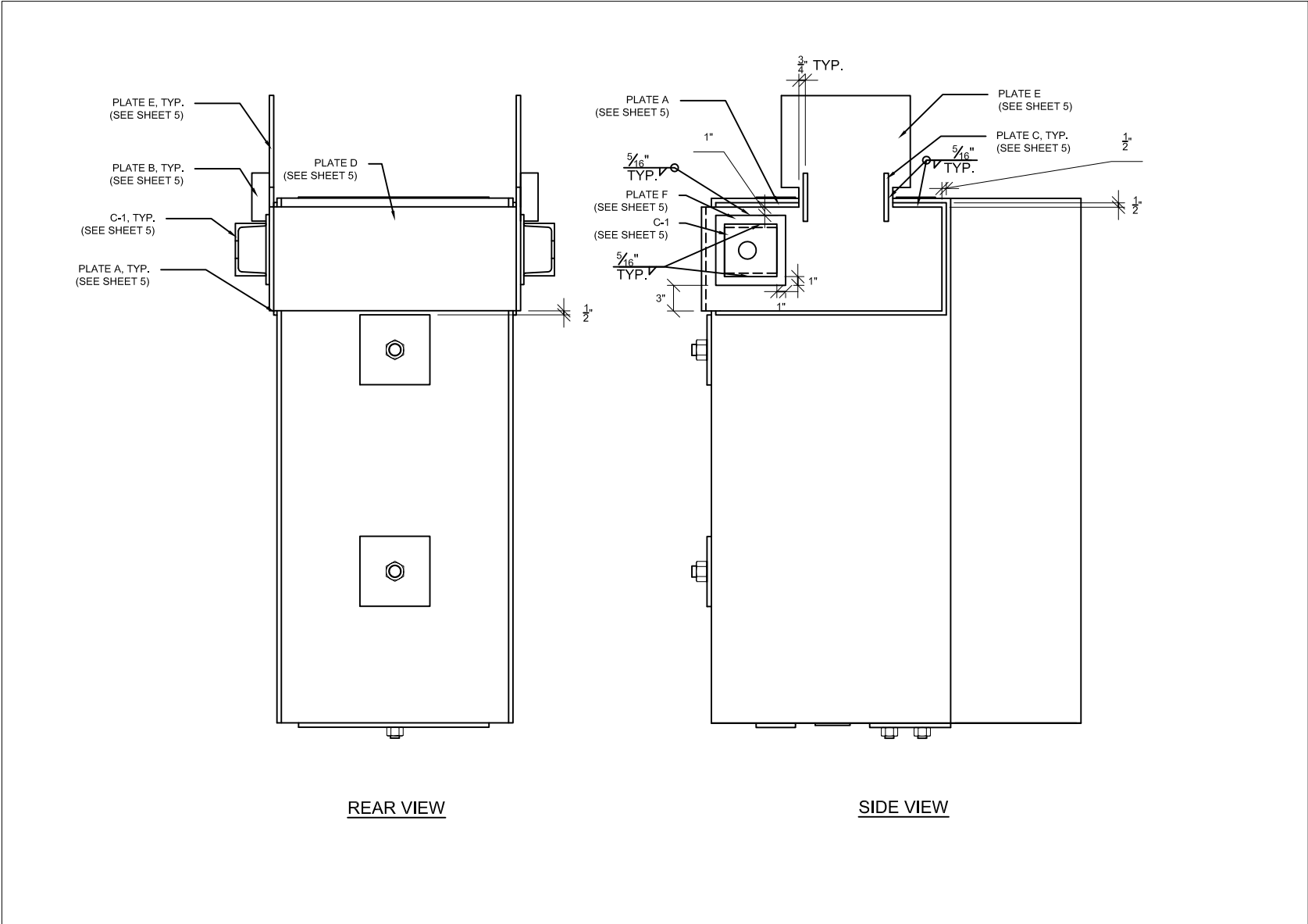


REAR VIEW - ONLY SPACER PLATES SHOWN

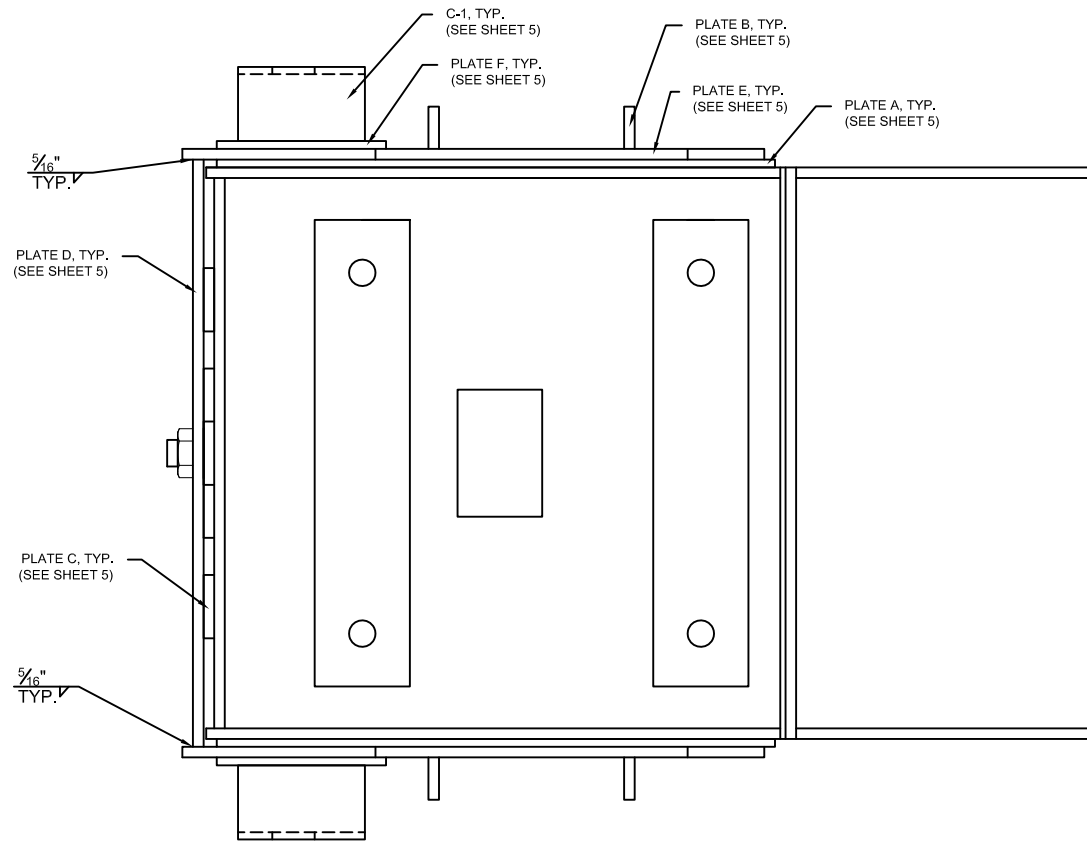


SIDE VIEW - ONLY SPACER PLATES SHOWN

Impact Block				Revisions:		
External Connections I	2013-12-31	University of Florida	Sheet 01 of 05			

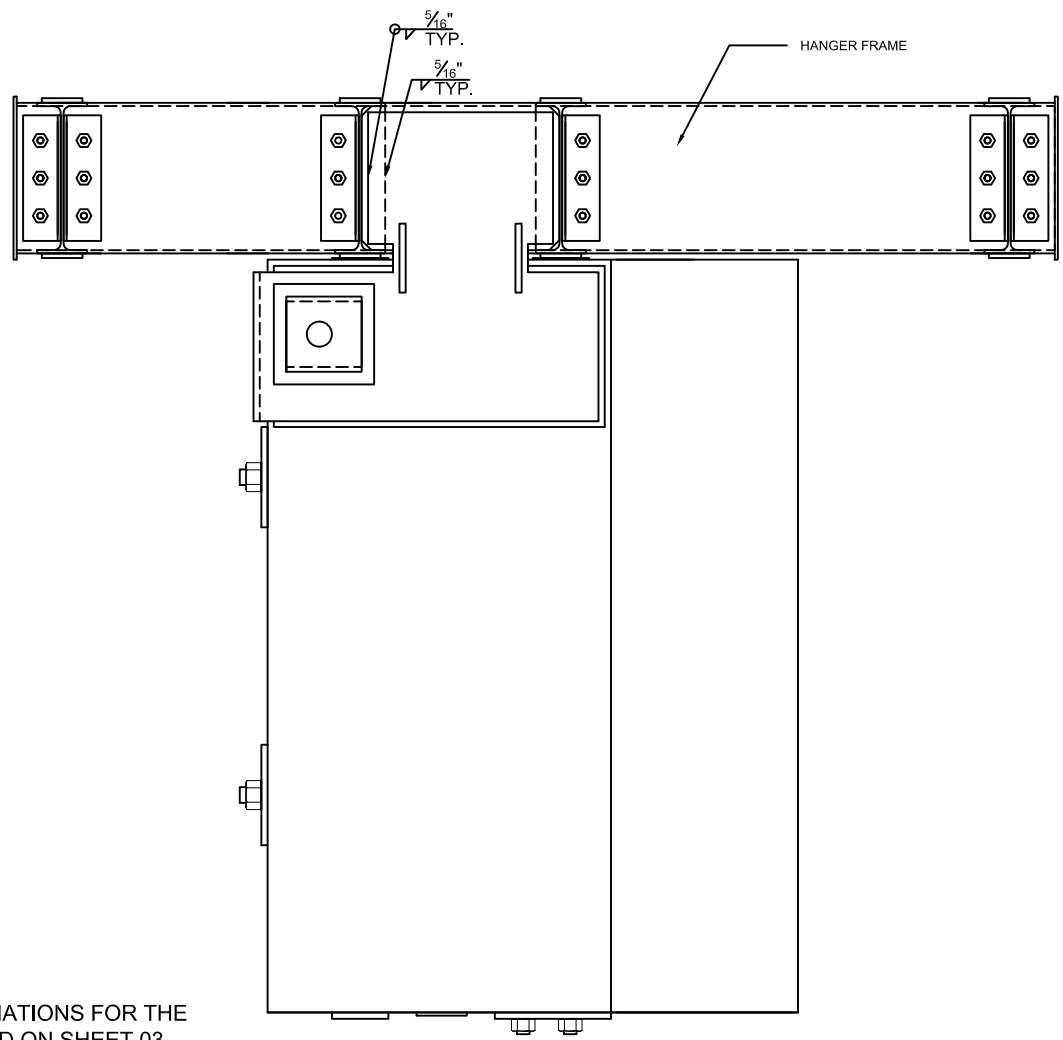


Impact Block				Revisions:		
External Connections II	2013-12-31	University of Florida	Sheet 02 of 05			



TOP VIEW

Impact Block				Revisions:		
External Connections III	2013-12-31	University of Florida	Sheet 03 of 05			



NOTE 1: COMPONENT DESIGNATIONS FOR THE IMPACT BLOCK MAY BE FOUND ON SHEET 03.

SIDE VIEW - CONNECTION WITH FRAME SHOWN

Impact Block				Revisions:		
External Connections IV	2013-12-31	University of Florida	Sheet 04 of 05			

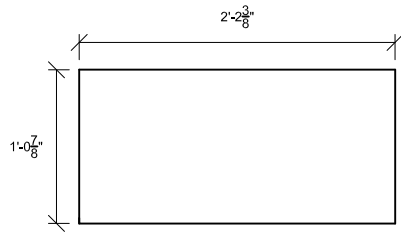


PLATE A
A572-50,t=3/8"
QUANTITY=2

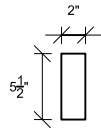


PLATE B
A572-50,t=1/2"
QUANTITY=4

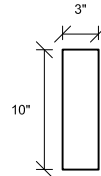


PLATE C
A572-50,t=1/2"
QUANTITY=3

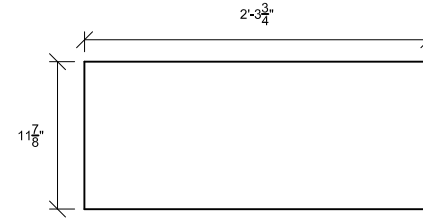


PLATE D
A572-50,t=1/2"
QUANTITY=1

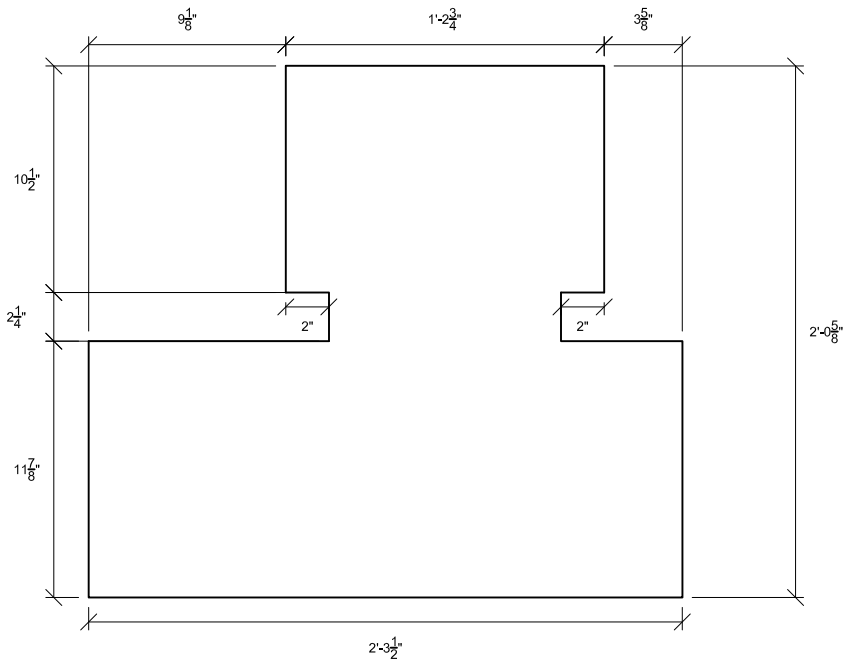


PLATE E
A572-50,t=1/2"
QUANTITY=2

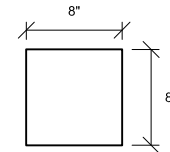
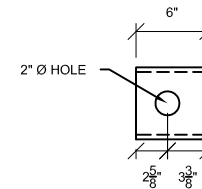


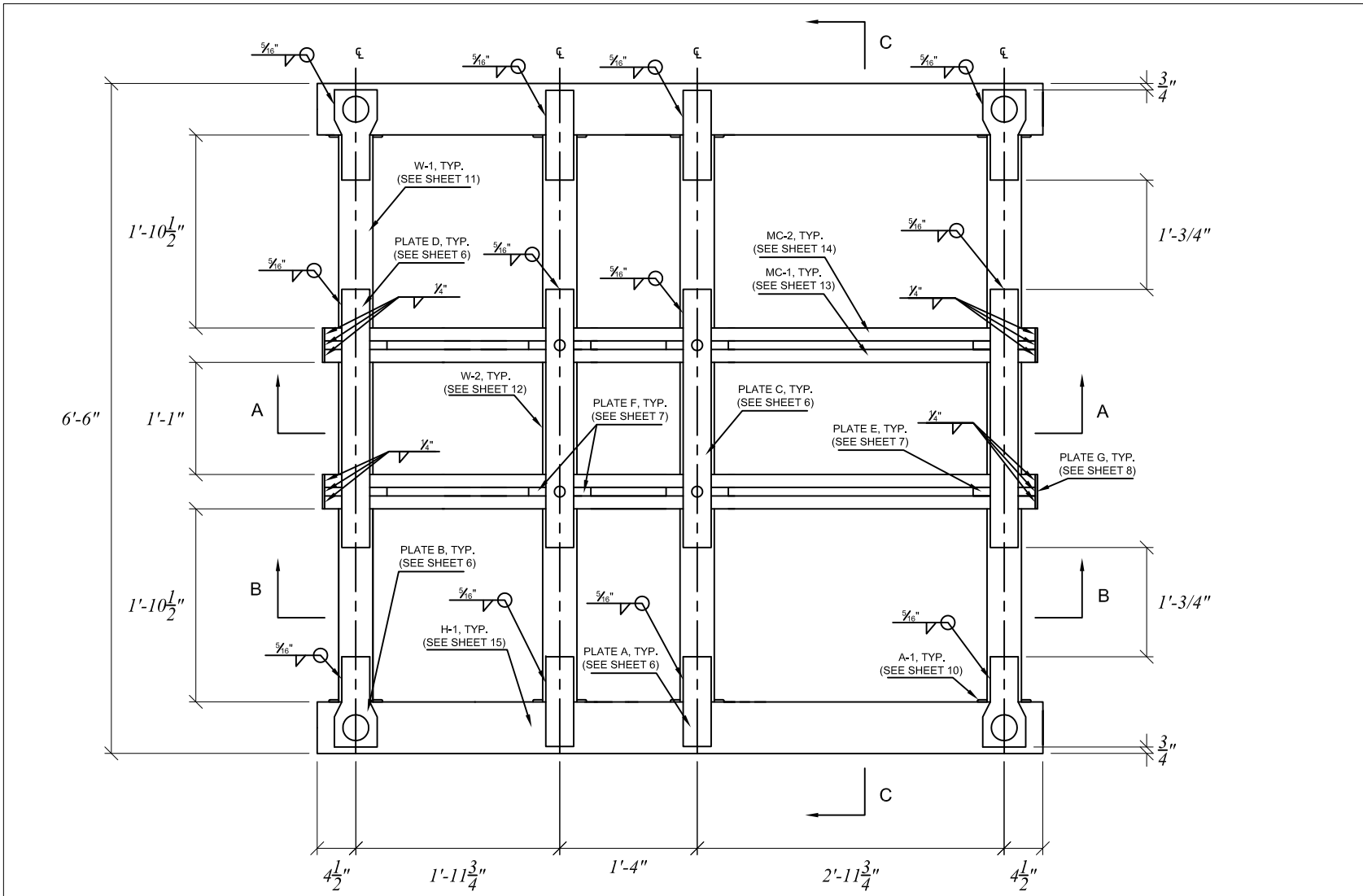
PLATE F
A36,t=3/8"
QUANTITY=2



C-1
MC6x15.3
QUANTITY=2

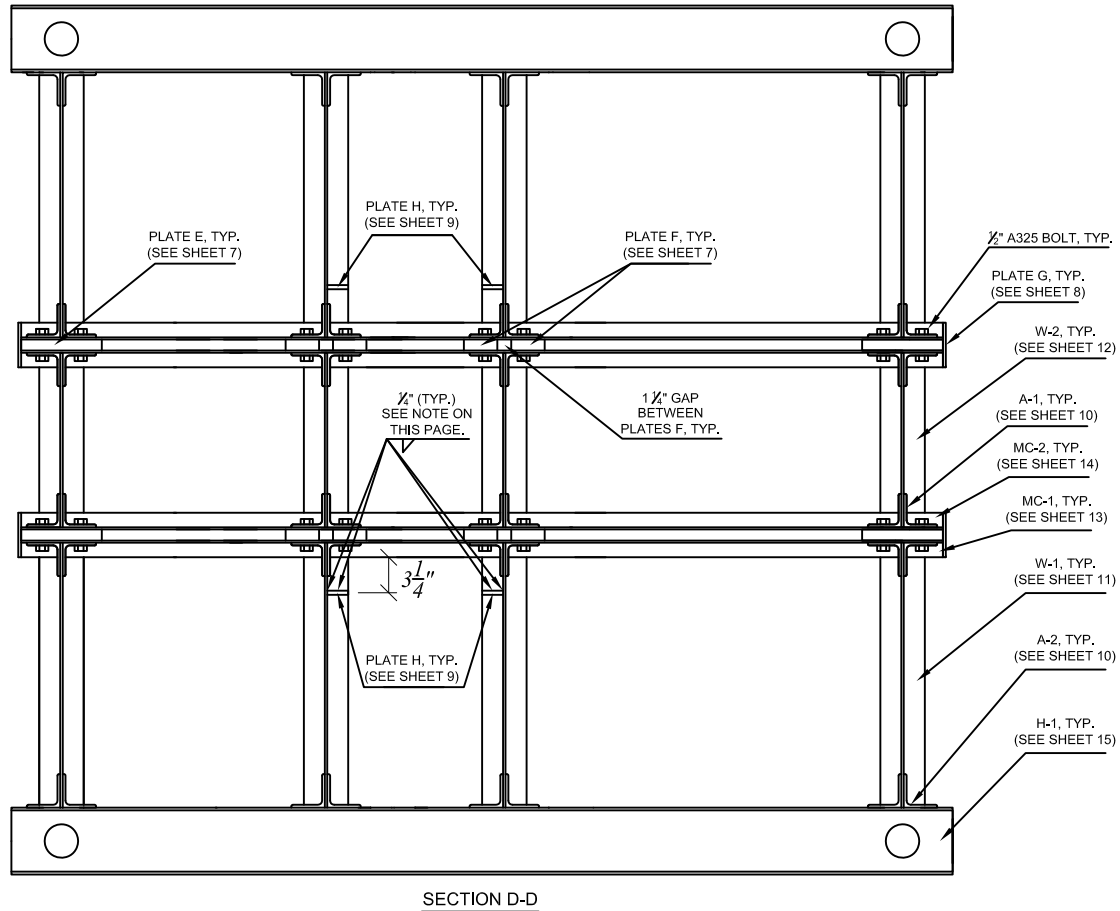
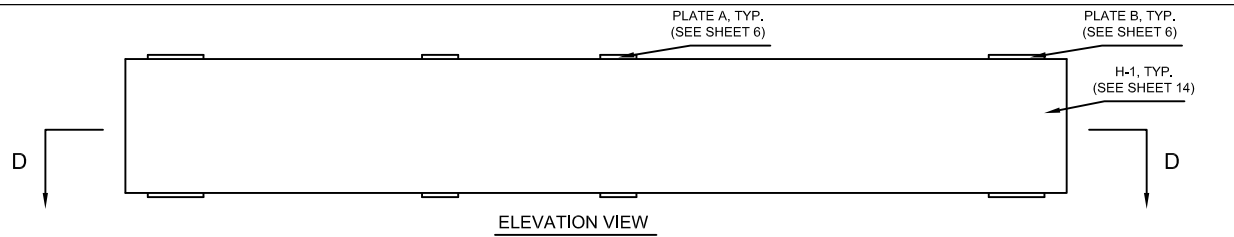
Impact Block				Revisions:		
External Connections V	2013-12-31	University of Florida	Sheet 05 of 05			

APPENDIX J
HANGER FRAME FABRICATION DRAWINGS



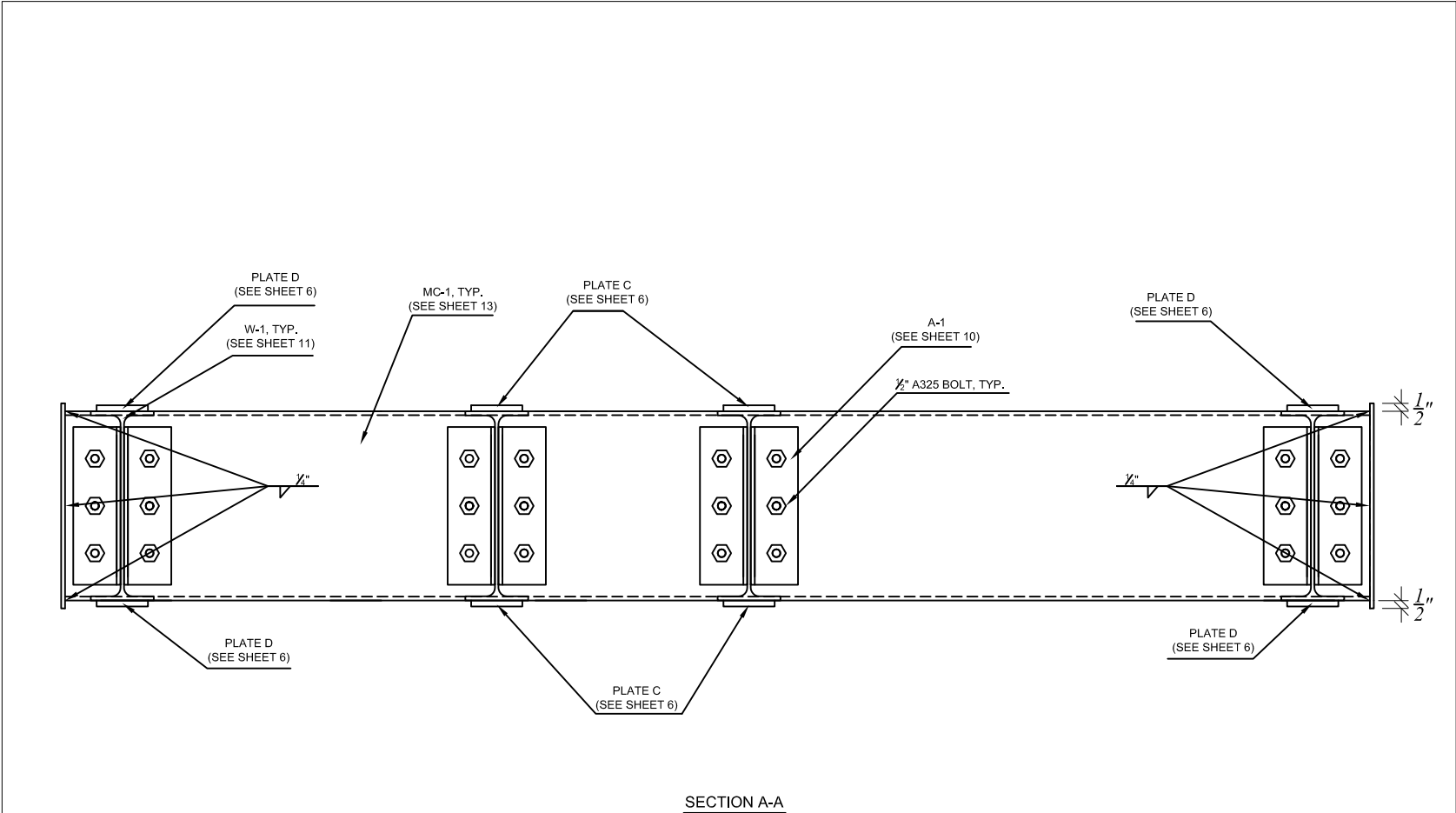
NOTE 1: PLATES A, B, C, AND D SHARE THE CENTERLINES DESIGNATED ABOVE WITH MEMBERS W-1 AND W-2.
 NOTE 2: THE BOTTOM VIEW OF THE STRUCTURE IS IDENTICAL TO THE PLAN VIEW PROVIDED ON THIS SHEET.

<i>Hanger Frame</i>				<i>Revisions:</i>		
<i>Plan View</i>	2014-01-02	University of Florida	Sheet 01 of 17			



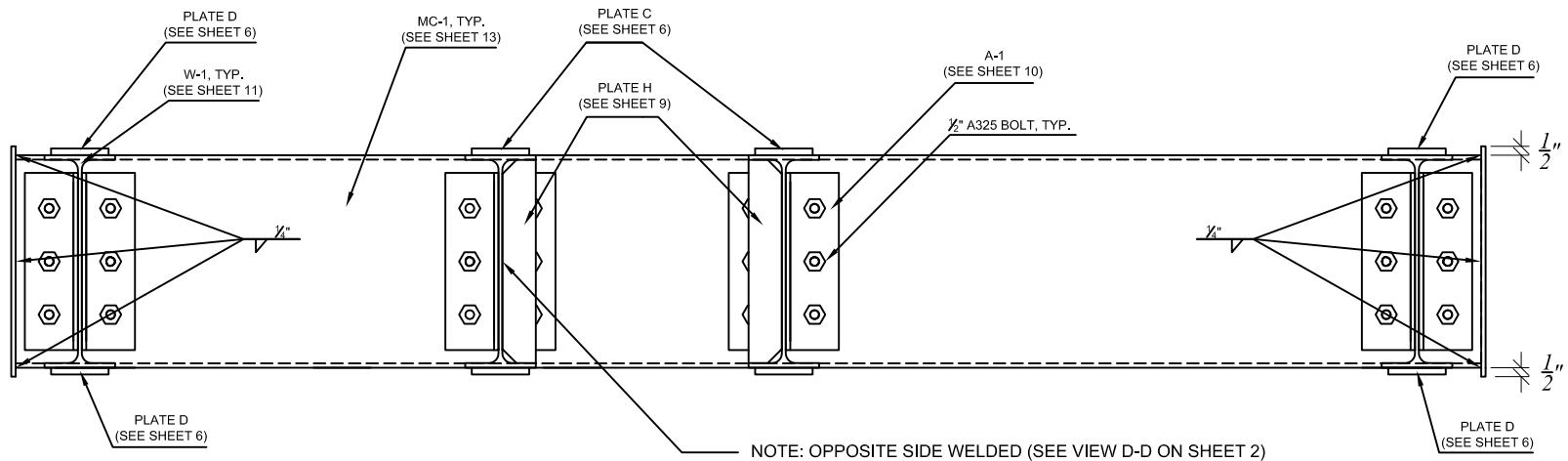
NOTE: PLATE H IS WELDED ON ONE SIDE ONLY TO THE WEB AND FLANGES OF MEMBER W-1, AS INDICATED ON THIS SHEET.

<i>Hanger Frame</i>				<i>Revisions:</i>		
<i>Elevation View</i>	<i>2014-01-02</i>	<i>University of Florida</i>	<i>Sheet 02 of 17</i>			

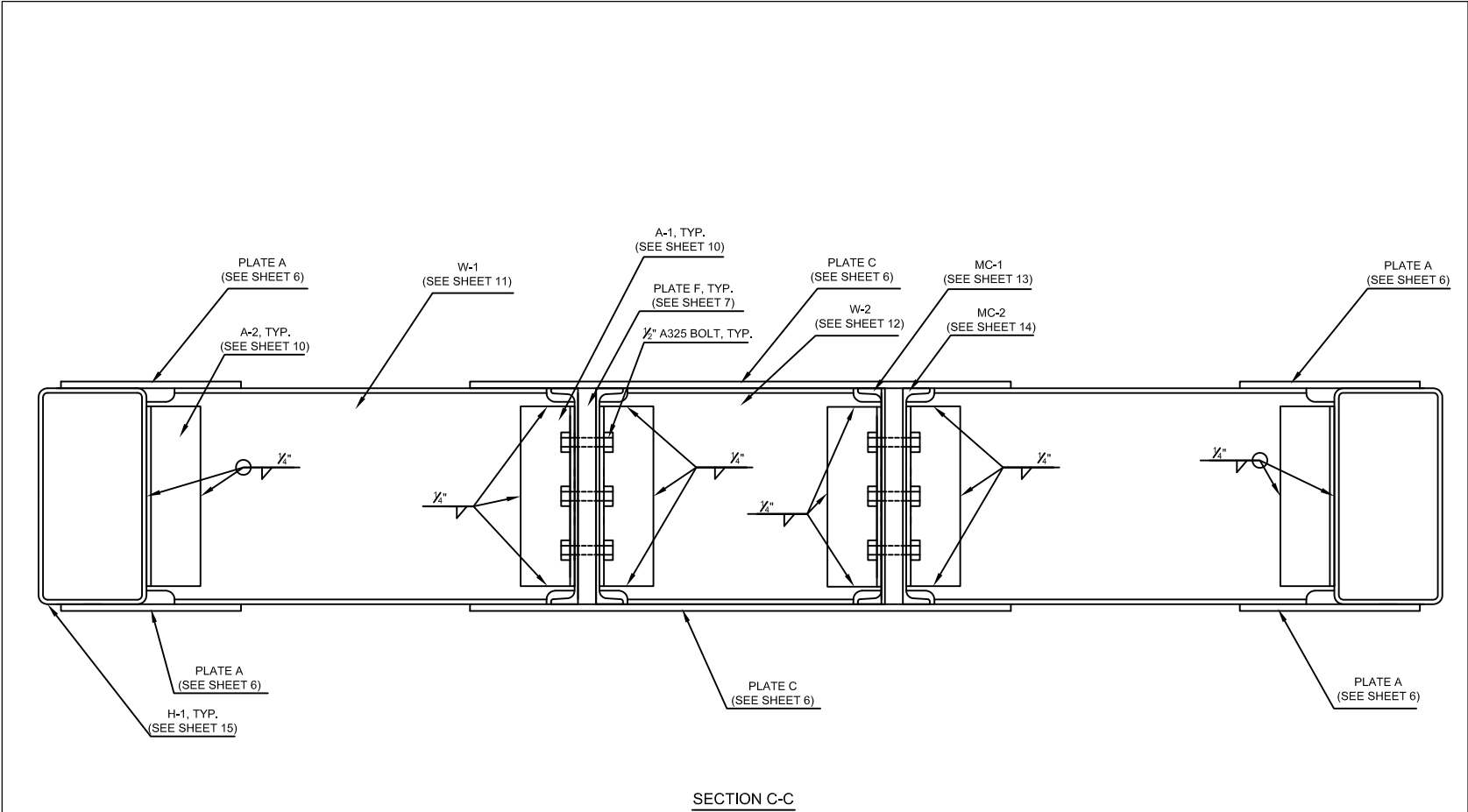


SECTION A-A

<i>Hanger Frame</i>				<i>Revisions:</i>		
<i>Section A-A</i>	<i>2014-01-02</i>	<i>University of Florida</i>	<i>Sheet 03 of 17</i>			



<i>Hanger Frame</i>				<i>Revisions:</i>		
<i>Section B-B</i>	<i>2014-01-02</i>	<i>University of Florida</i>	<i>Sheet 04 of 17</i>			



<i>Hanger Frame</i>				<i>Revisions:</i>		
<i>Section C-C</i>	<i>2014-01-02</i>	<i>University of Florida</i>	<i>Sheet 05 of 17</i>			

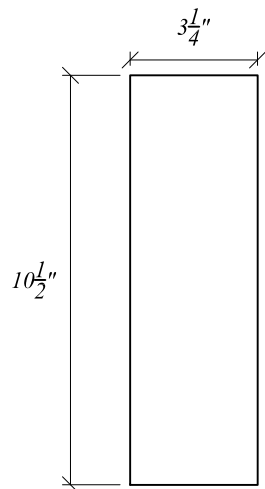


PLATE A
(t = 3/8", A572-50, QTY: 8)

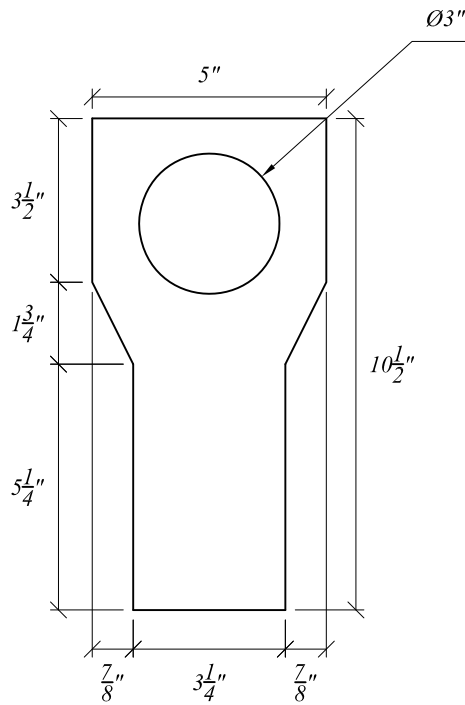


PLATE B
(t = 3/8", A572-50, QTY: 8)

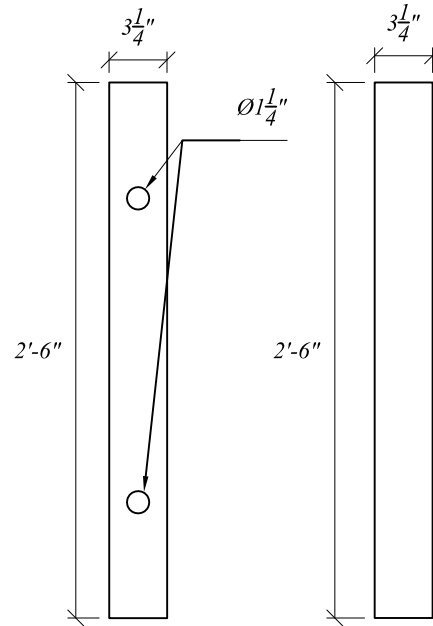
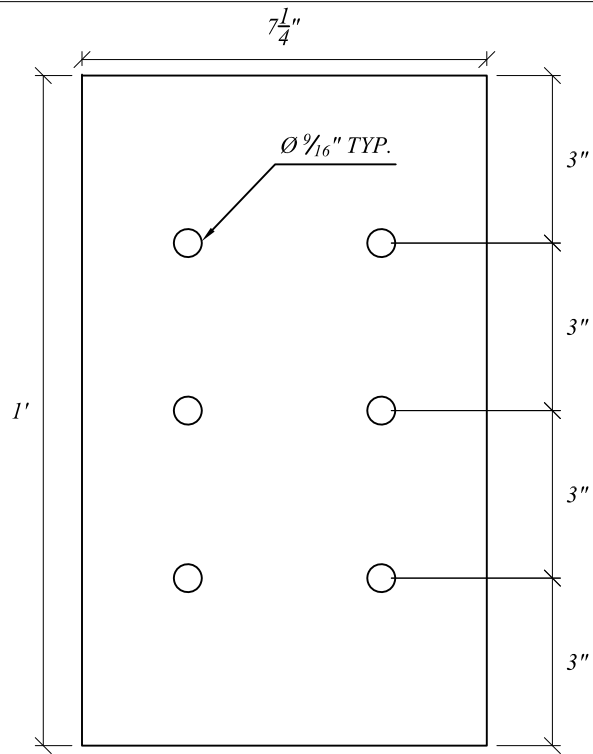


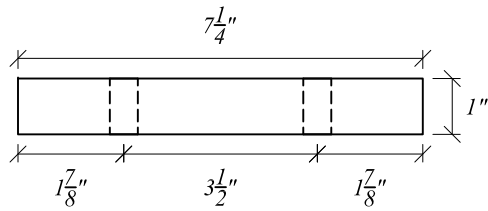
PLATE C
(t = 3/8", A572-50, QTY: 4)

PLATE D
(t = 3/8", A572-50, QTY: 4)

<i>Hanger Frame</i>				<i>Revisions:</i>		
<i>Flange Plate Details</i>	<i>2014-01-02</i>	<i>University of Florida</i>	<i>Sheet 06 of 17</i>			

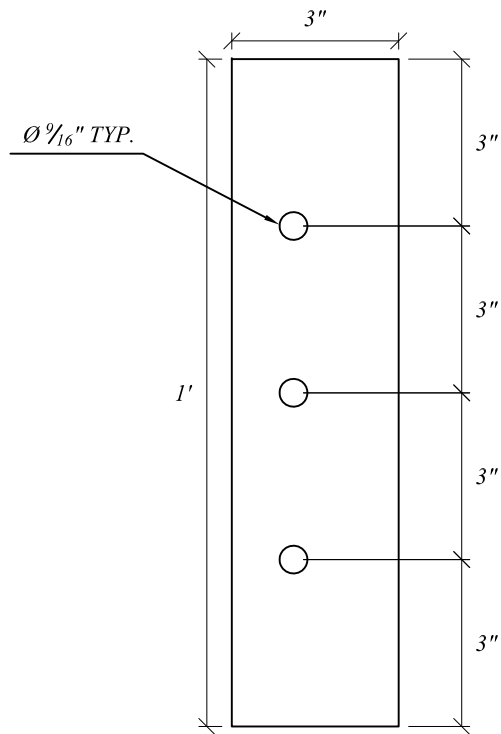


ELEVATION VIEW

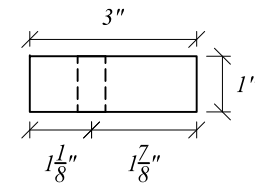


PLAN VIEW

PLATE E
(t = 1", A572-50, QTY: 4)



ELEVATION VIEW



PLAN VIEW

PLATE F
(t = 1", A572-50, QTY: 8)

<i>Hanger Frame</i>				<i>Revisions:</i>		
<i>Spacer Plate Details</i>	<i>2014-01-02</i>	<i>University of Florida</i>	<i>Sheet 07 of 17</i>			

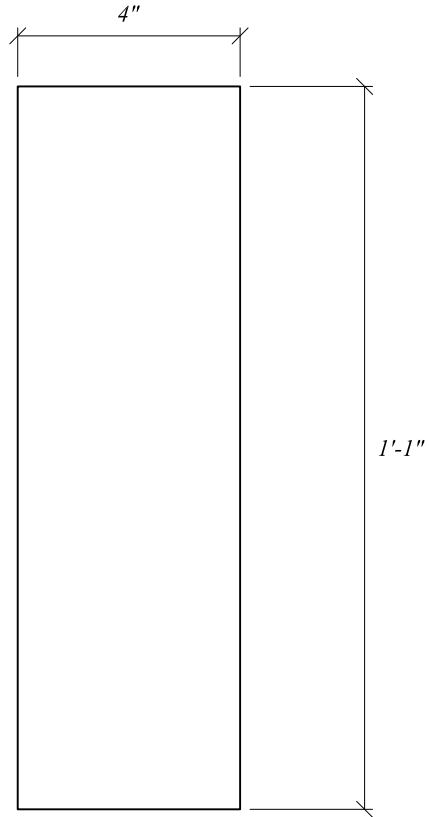


PLATE G
 (t = 1/4", A572-50, QTY: 4)

<i>Hanger Frame</i>				<i>Revisions:</i>		
<i>End Plate Details</i>	<i>2014-01-02</i>	<i>University of Florida</i>	<i>Sheet 08 of 17</i>			

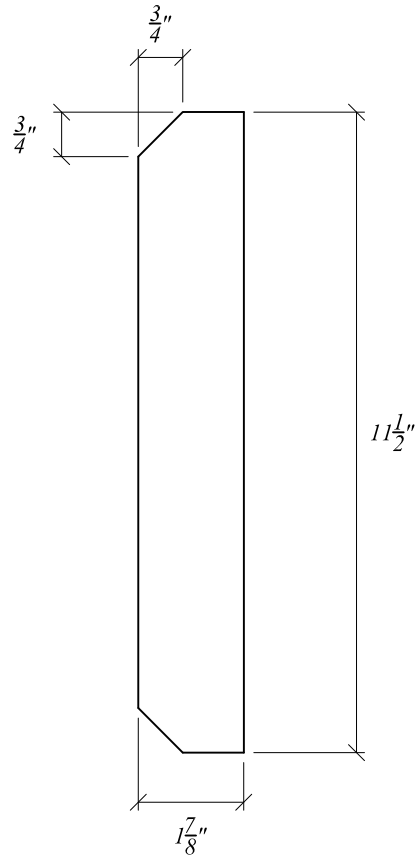
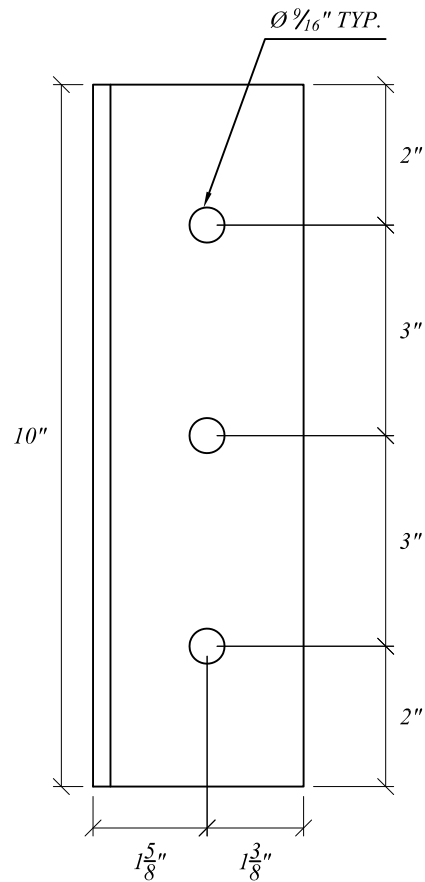


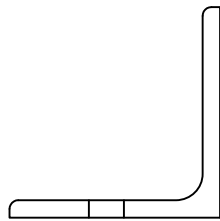
PLATE H
 (t = 3/8", A572-50, QTY: 4)

<i>Hanger Frame</i>				<i>Revisions:</i>		
<i>Stiffener Plate Details</i>	<i>2014-01-02</i>	<i>University of Florida</i>	<i>Sheet 09 of 17</i>			

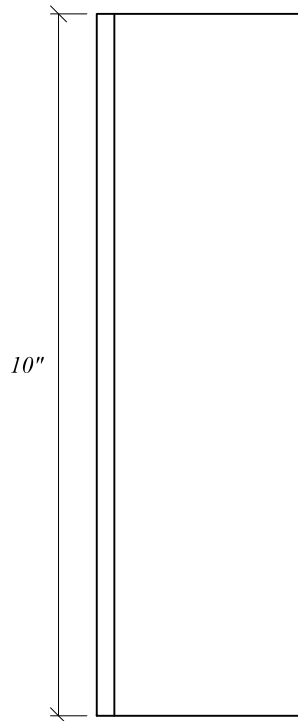


ELEVATION VIEW

A-1
(L3x3x1/4, A36)

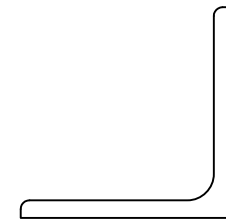


CROSS-SECTION VIEW



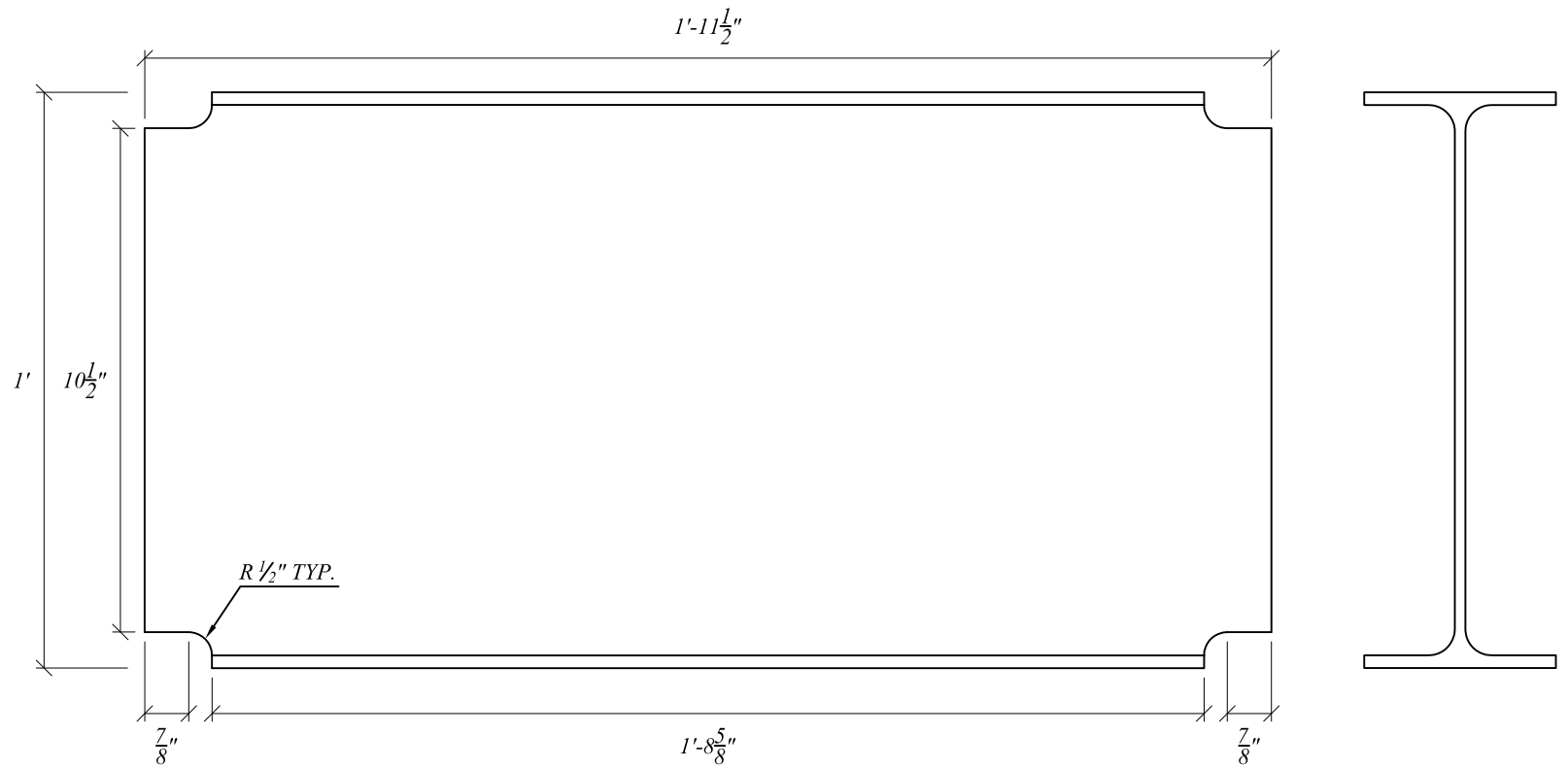
ELEVATION VIEW

A-2
(L3x3x1/4, A36)



CROSS-SECTION VIEW

<i>Hanger Frame</i>				<i>Revisions:</i>		
<i>Angle Details</i>	<i>2014-01-02</i>	<i>University of Florida</i>	<i>Sheet 10 of 17</i>			

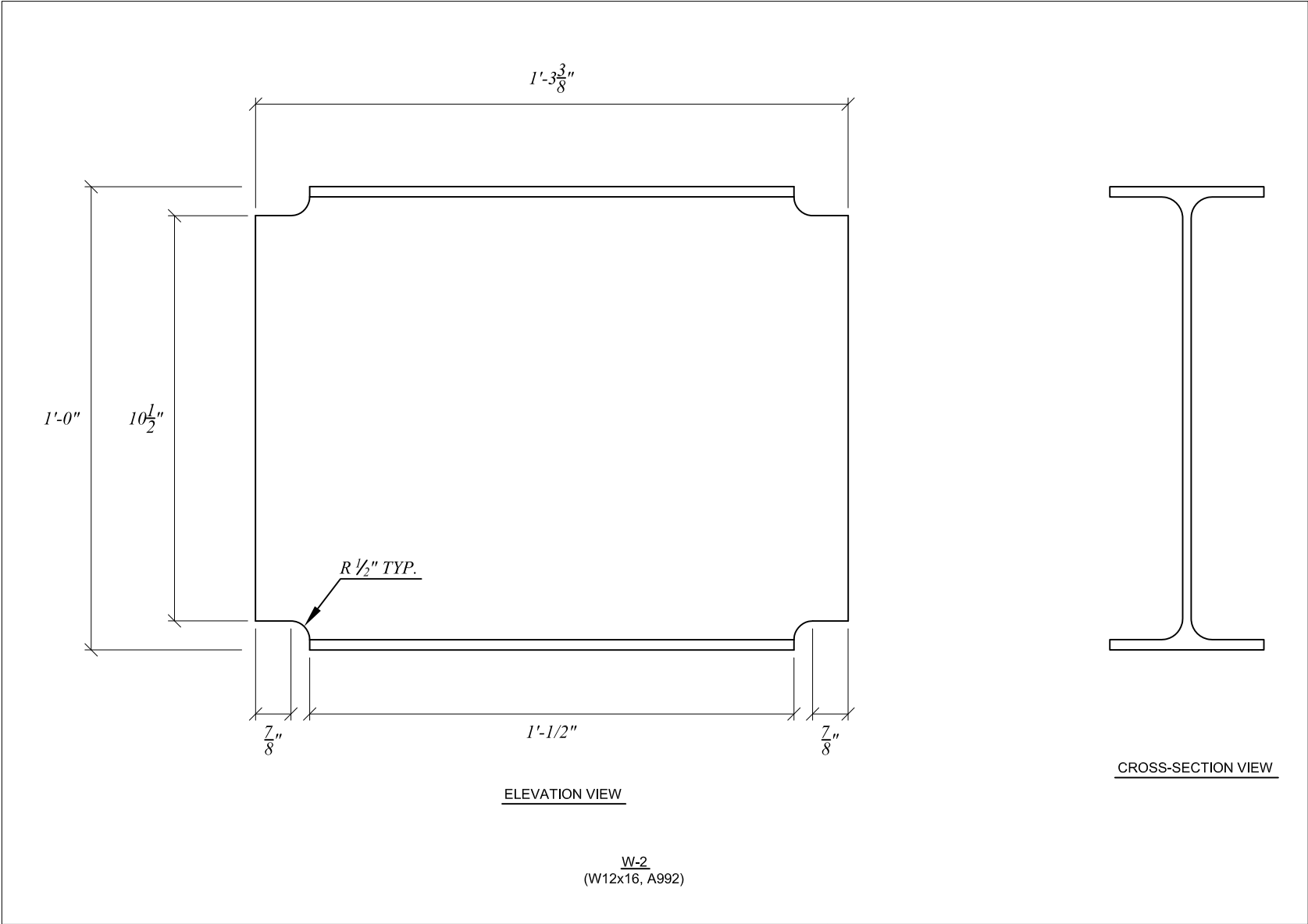


ELEVATION VIEW

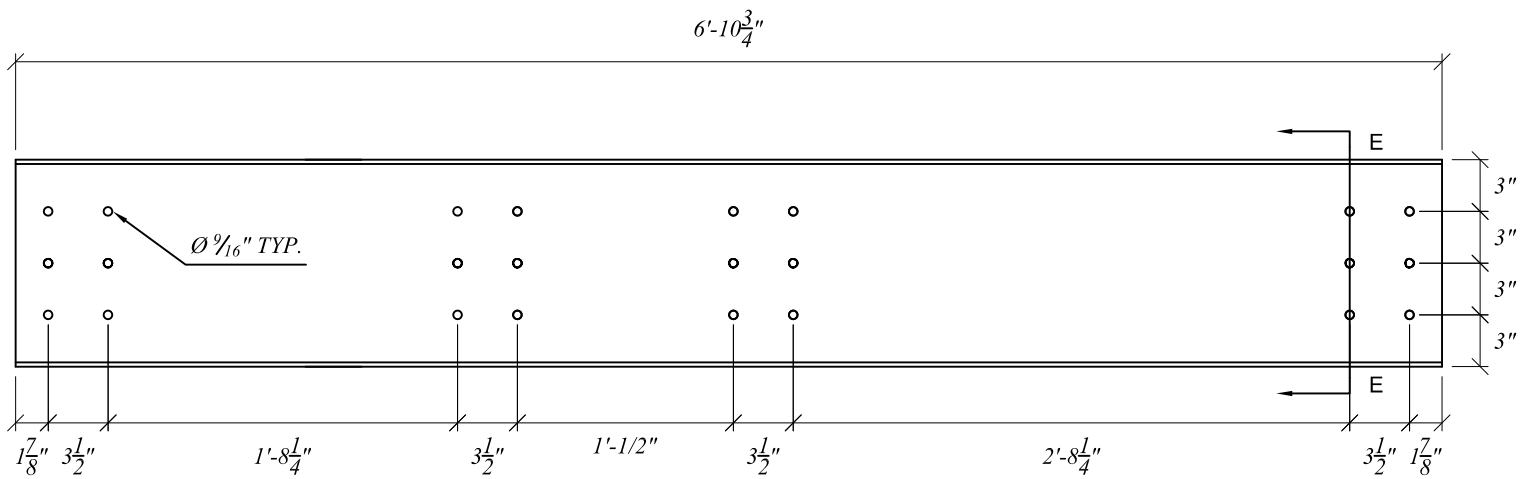
CROSS-SECTION VIEW

W-1
(W12x16, A992)

<i>Hanger Frame</i>				<i>Revisions:</i>		
<i>Transverse Beam (W-1) Detail</i>	<i>2014-01-02</i>	<i>University of Florida</i>	<i>Sheet 11 of 17</i>			



<i>Hanger Frame</i>				<i>Revisions:</i>		
<i>Transverse Beam (W-2) Detail</i>	<i>2014-01-02</i>	<i>University of Florida</i>	<i>Sheet 12 of 17</i>			



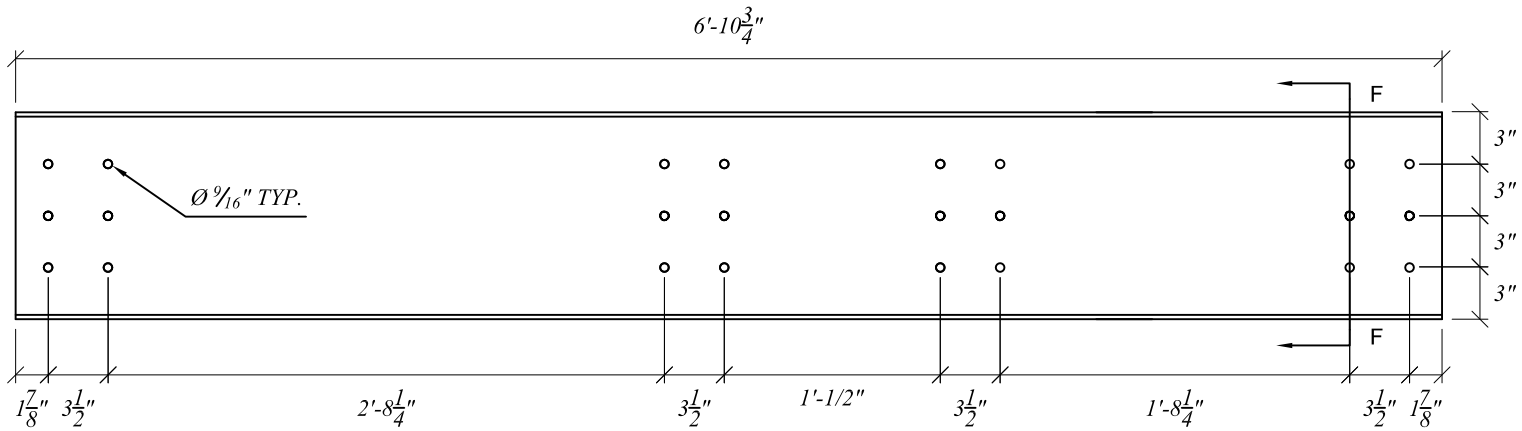
ELEVATION VIEW



CROSS-SECTION VIEW E-E

MC-1
(MC12x10.6, A36)

<i>Hanger Frame</i>				<i>Revisions:</i>		
<i>Channel (MC-1) Details</i>	<i>2014-01-02</i>	<i>University of Florida</i>	<i>Sheet 13 of 17</i>			



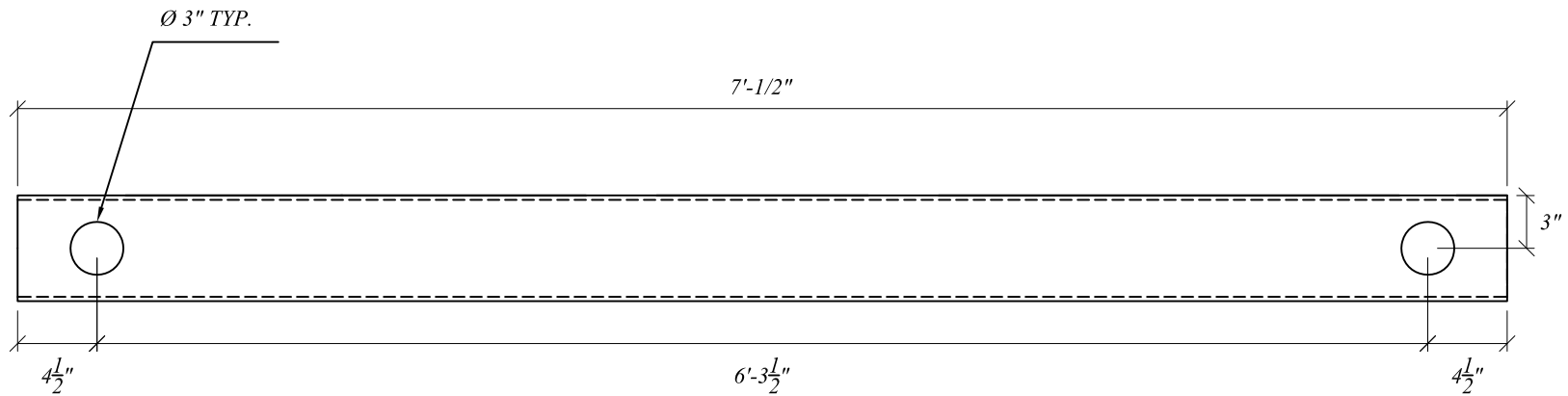
ELEVATION VIEW



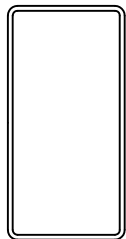
CROSS-SECTION VIEW F-F

MC-2
(MC12x10.6, A36)

<i>Hanger Frame</i>				<i>Revisions:</i>		
<i>Channel (MC-2) Details</i>	<i>2014-01-02</i>	<i>University of Florida</i>	<i>Sheet 14 of 17</i>			



PLAN VIEW



CROSS-SECTION VIEW

H-1
(HSS12x6x1/4, A-500 Grade B)

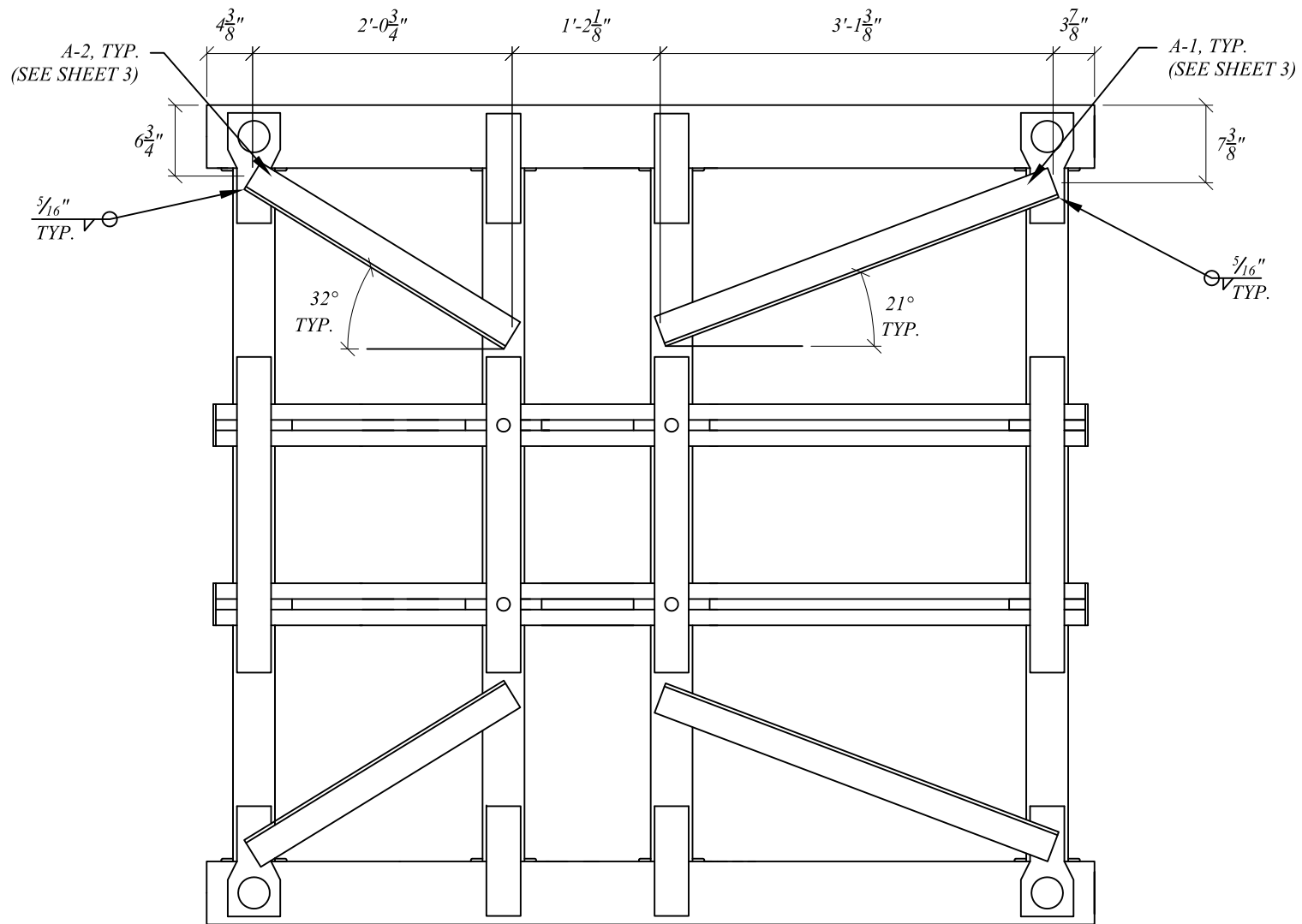
<i>Hanger Frame</i>				<i>Revisions:</i>		
<i>External Beam Details</i>	<i>2014-01-02</i>	<i>University of Florida</i>	<i>Sheet 15 of 17</i>			

SCHEDULE OF PLATES		
NAME	QTY	NOTES
PLATE A	8	A572-50
PLATE B	8	A572-50
PLATE C	4	A572-50
PLATE D	4	A572-50
PLATE E	4	A572-50
PLATE F	8	A572-50
PLATE G	4	A572-50
PLATE H	4	A572-50

<i>Hanger Frame</i>				<i>Revisions:</i>		
<i>Schedule of Plates</i>	<i>2014-01-02</i>	<i>University of Florida</i>	<i>Sheet 16 of 17</i>			

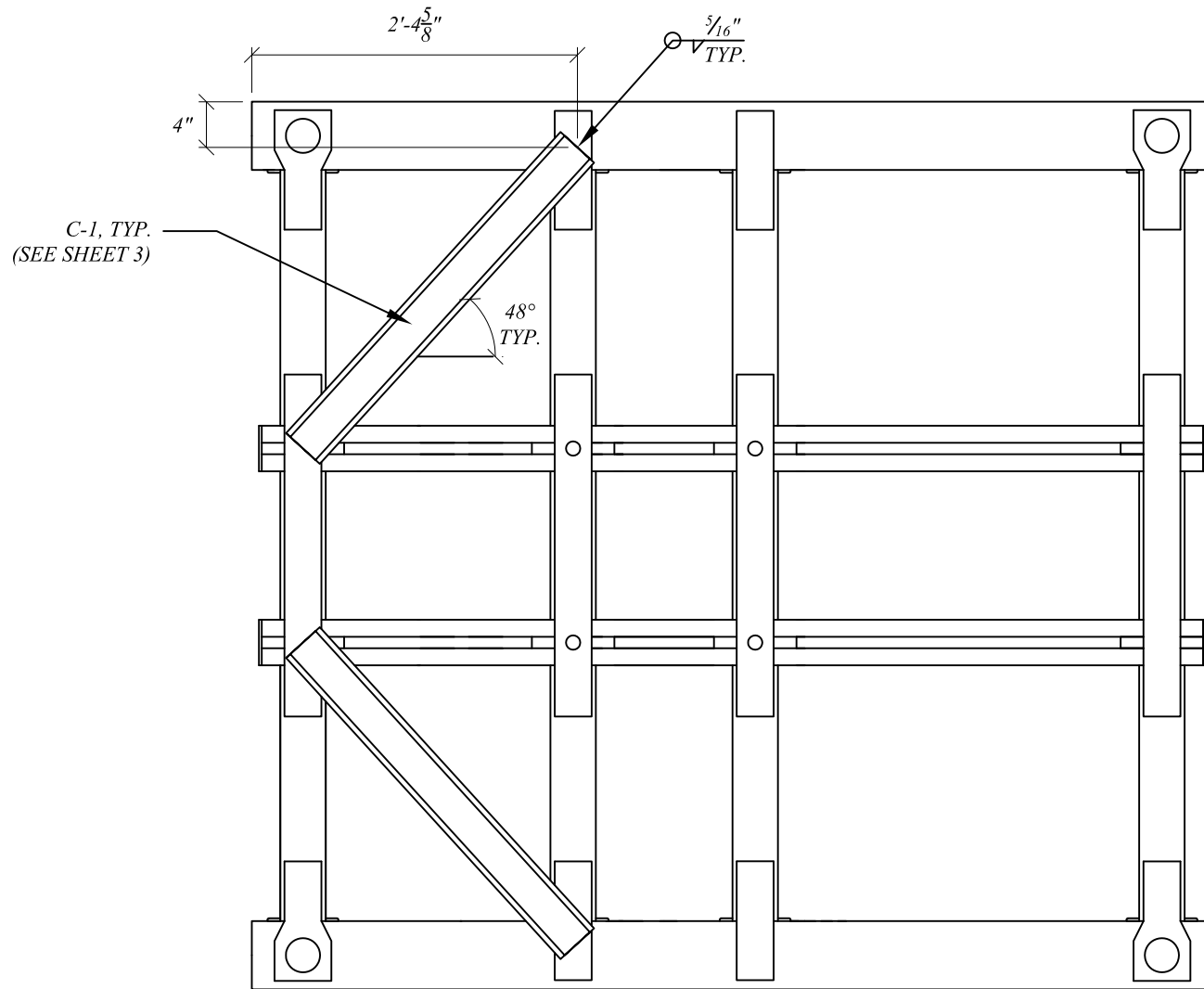
SCHEDULE OF MEMBERS					
NAME	SIZE	LENGTH	QTY	TOTAL LENGTH	NOTES
A-1	L3x3x $\frac{1}{4}$	10"	32	26'-8"	A36
A-2	L3x3x $\frac{1}{4}$	10"	16	13'-4"	A36
H-1	HSS12x6x $\frac{1}{4}$	7'-1/2"	2	14'-1"	A-500 Gr. B
MC-1	MC12x10.6	6'-10 3/4"	2	13'-9 1/2"	A36
MC-2	MC12x10.6	6'-10 3/4"	2	13'-9 1/2"	A36
W-1	W12x16	1'-11 1/2"	8	15'-8"	A992
W-2	W12x16	1'-3 3/8"	4	5'-1 1/2"	A992
BOLTS	$\frac{1}{2}$ " \emptyset x 2 1/2" Long	2 1/2"	54	-	A325
NUTS	1/2" \emptyset	-	54	-	A563

<i>Hanger Frame</i>				<i>Revisions:</i>		
<i>Schedule of Members</i>	<i>2014-01-02</i>	<i>University of Florida</i>	<i>Sheet 17 of 17</i>			



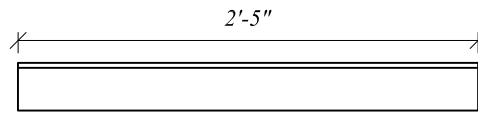
TOP VIEW
 (bottom braces not shown for clarity)

<i>Hanger Frame</i>				<i>Revisions:</i>		
<i>Bracing Scheme</i>	<i>2014-01-02</i>	<i>University of Florida</i>	<i>Sheet 01 of 03</i>			

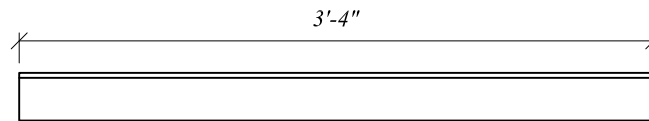


BOTTOM VIEW
(top braces not shown for clarity)

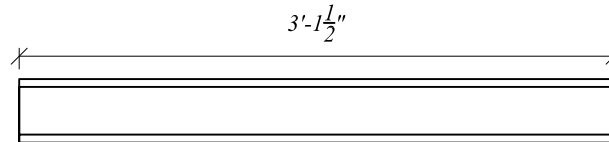
<i>Hanger Frame</i>				<i>Revisions:</i>		
<i>Bracing Scheme</i>	<i>2014-01-02</i>	<i>University of Florida</i>	<i>Sheet 02 of 03</i>			



A-2
L3x3x $\frac{5}{16}$
QTY: 2



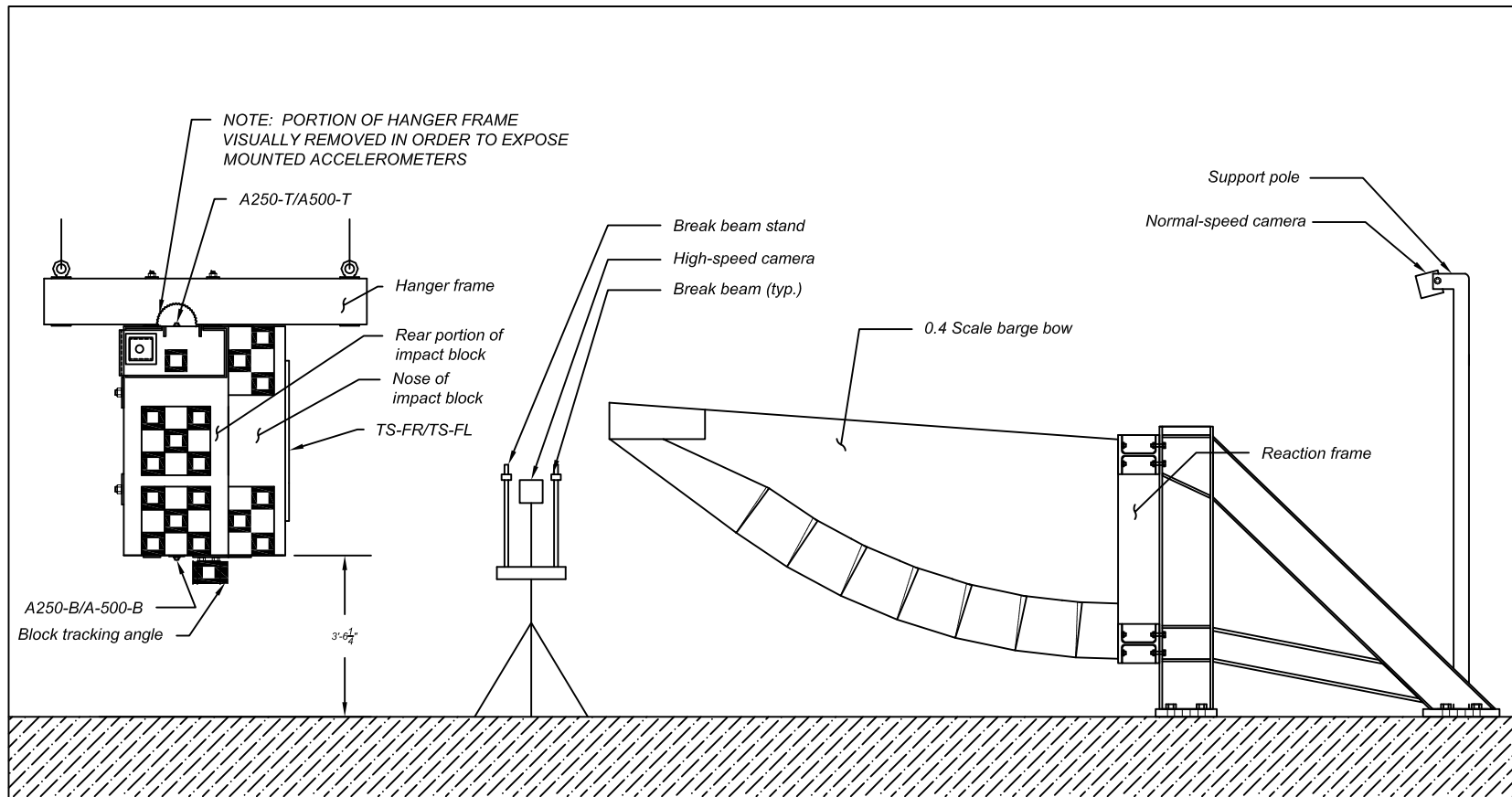
A-1
L3x3x $\frac{5}{16}$
QTY: 2



C-1
MC4x13.8
QTY: 2

<i>Hanger Frame</i>				<i>Revisions:</i>		
<i>Bracing Scheme</i>	2014-01-02	University of Florida	Sheet 03 of 03			

**APPENDIX K
INSTRUMENTATION PLAN**



Naming System

T-L where:

T = Instrument type

- A500: +/- 500g range
- A250: +/- 250g range
- TS: Tape switch

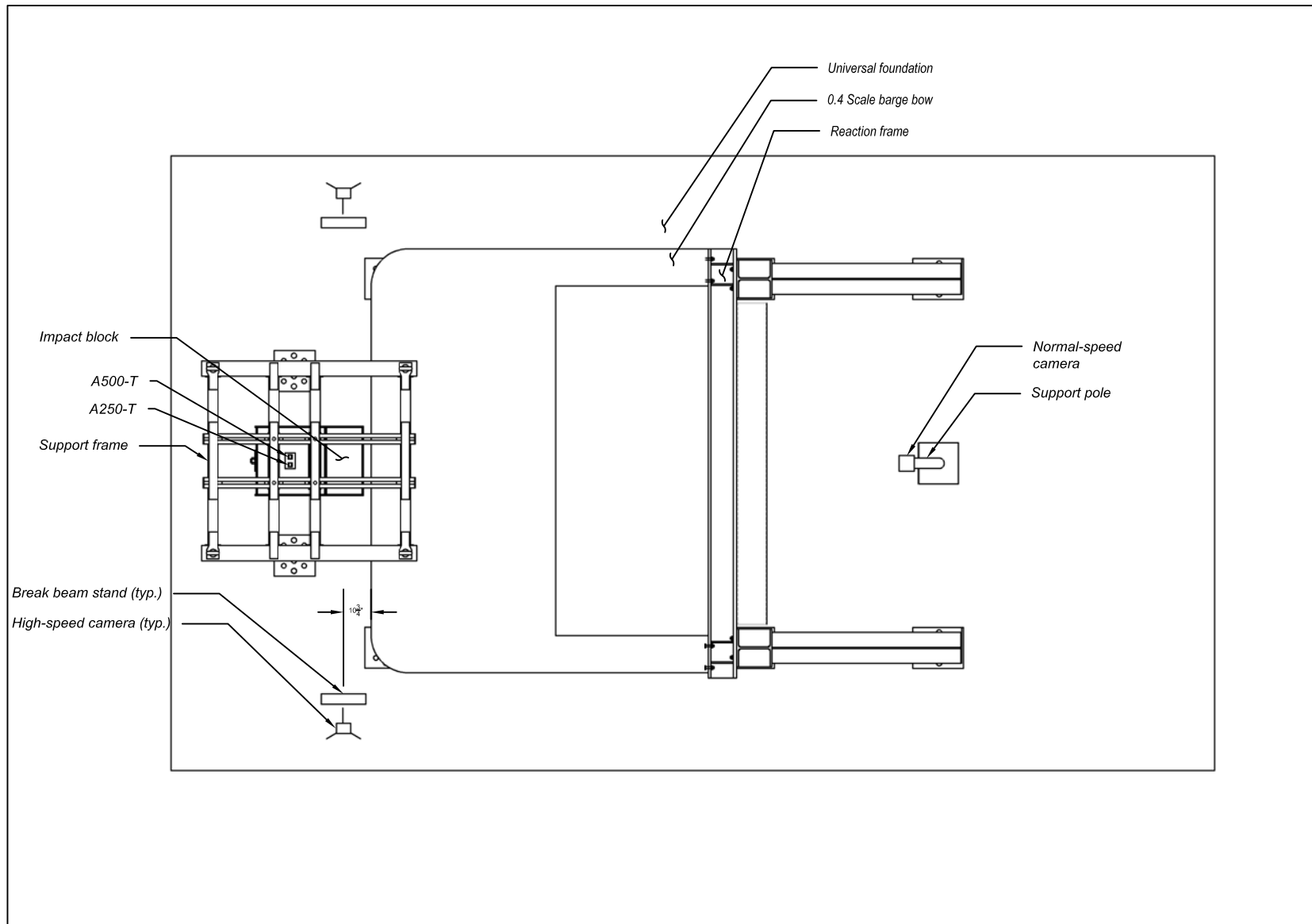
L = Location of instrument

- T: Top of impact block
- B: Bottom of impact block
- FR: Front of nose of impact block, right side
- FL: Front of nose of impact block, left side

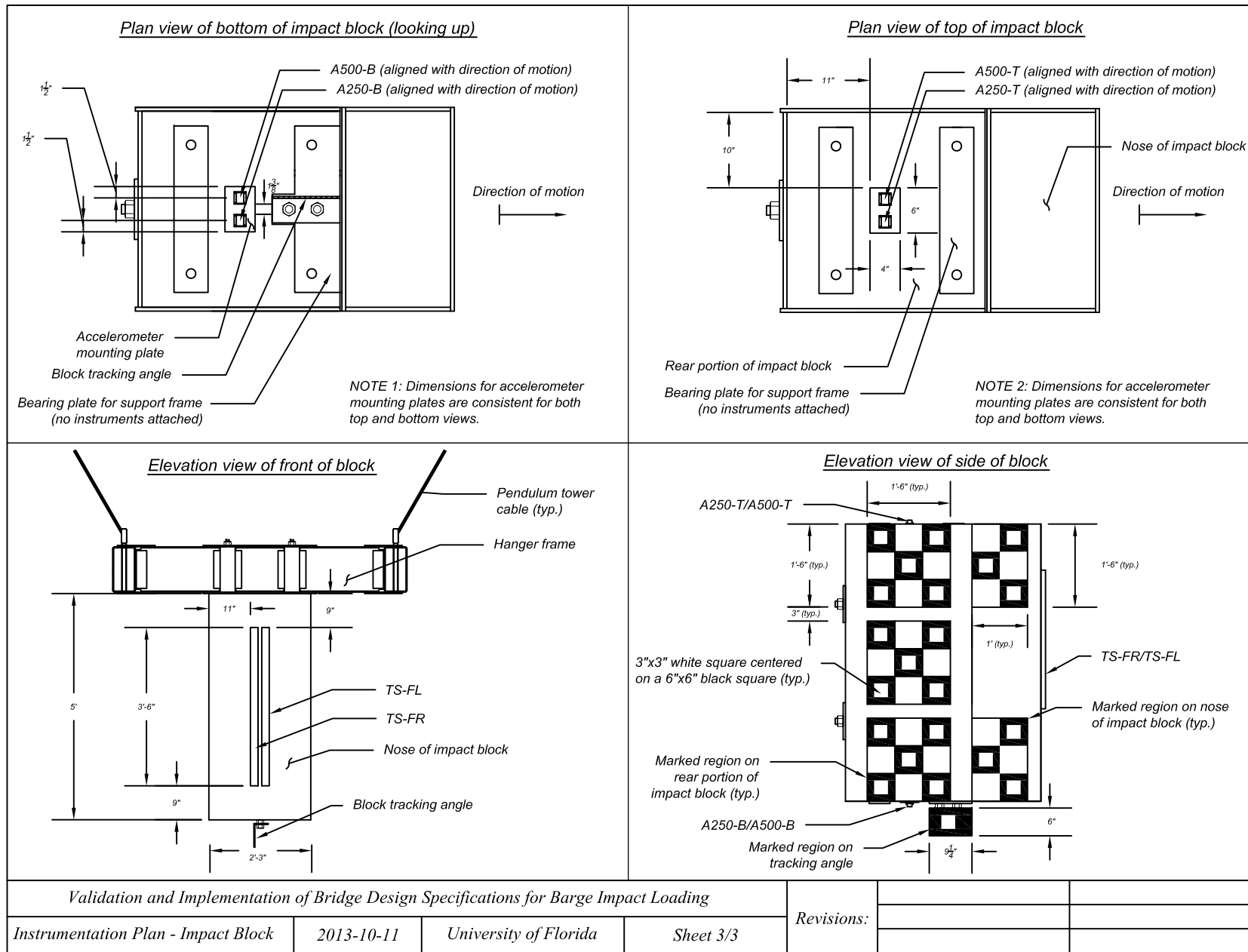
Instrumentation Summary

- A250-T
- A250-B
- A500-T
- A500-B
- TS-FR
- TS-FL

<i>Validation and Implementation of Bridge Design Specifications for Barge Impact Loading</i>				Revisions:		
Instrumentation Plan - Elevation View	2013-10-11	University of Florida	Sheet 1/3			



<i>Validation and Implementation of Bridge Design Specifications for Barge Impact Loading</i>				<i>Revisions:</i>		
<i>Instrumentation Plan - Plan View</i>	<i>2013-10-11</i>	<i>University of Florida</i>	<i>Sheet 2/3</i>			



APPENDIX L CONSIDERATION OF LRFD APPROACH TO VESSEL COLLISION DESIGN

L.1 Introduction

A literature review was carried out pertaining to the development of LRFD design procedures for vessel collision. The following sections summarize the design philosophy of the existing AASHTO design procedures for vessel impact and compare this to the overall analysis methodologies employed by Nowak (1999) to calibrate the dead, live, and vehicle impact load factors in the AASHTO LRFD code, and Nowak et al. (2008) to calibrate the resistance factors in ACI-318.

L.2 AASHTO Vessel Collision Risk Assessment

In general, the annual frequency of bridge collapse (AF) is computed as:

$$AF = (N)(PA)(PG)(PC)(PF) \quad (\text{L.1})$$

where N is the number of vessel transits, PA is the probability of aberrancy, PG is the geometric probability, PC is the probability of collapse, and PF is a protection factor. However, because AF is the annual frequency of *bridge* collapse (not *pier* collapse), it is computed as a sum of the annual frequency of pier collapse for each pier within the navigation zone (6 x LOA range, centered on the transit path). Furthermore, vastly different vessel types navigate most waterways. Thus, the pier annual frequency of collapse is computed for each vessel type (vessel group) that traverses the bridge. Consequently, in practice, AF is computed as:

$$AF = \sum_{i=1}^{N_{VG}} \left[N_i \times PA_i \sum_{j=1}^{N_P} (PG_{ij} \times PC_{ij} \times PF_{ij}) \right] \quad (\text{L.2})$$

where N_{VG} is the total number of vessel groups, and N_P is the number of piers in the navigation zone. Thus, AF is the total annual probability of *any* pier in the bridge collapsing as a result of *all* possible vessel impact scenarios.

In the AASHTO provisions, AF is limited to a specific value based on the relative importance of the bridge (0.001 for typical bridges, and 0.0001 for critical bridges). In other words, the acceptable return period for bridge failure from vessel collision is 1,000 years for typical bridges and 10,000 years for critical bridges.

L.3 LRFD Calibration Methodology

While the AASHTO risk acceptance criterion for vessel collision is based on structural reliability (probabilistic) principles, it is quite different in nature to LRFD criteria used for other loading conditions. For more common loading conditions (e.g., dead, live, wind), acceptance criteria that are used to derive load and resistance factors are based on acceptable probabilities of *member* failure within the design life of the structure (Nowak 1999; Nowak et al. 2008). Specifically, the goal of any LRFD procedure is to develop load factors (γ_i) and resistance factors (ϕ) such that:

$$\phi R_n \geq \sum \gamma_i Q_i \quad (\text{L.3})$$

where R_n is the nominal member resistance (e.g., moment) computed based on the code-prescribed procedure, and Q_i are load effects. During LRFD calibration, ϕ and γ_i are chosen such that the target member reliability is achieved. Reliability is typically quantified by probabilistic analysis of perhaps hundreds of structures that have been designed using current code procedures (Nowak 1999; Nowak et al. 2008).

To perform reliability analysis, consider a particular limit state function (g):

$$g = R - Q \quad (\text{L.4})$$

where R is the member resistance, and Q is the load effect. In this form, member failure occurs when $Q > R$. Thus, the probability of failure p_f is defined as:

$$p_f = P(R - Q < 0) = P(g < 0) \quad (\text{L.5})$$

Let the R and Q be defined as random variables with mean μ_R and μ_Q , respectively. Thus, the limit state can be redefined as a random variable (Z), corresponding to the safety margin, as follows:

$$Z = R - Q \quad (\text{L.6})$$

The objective of LRFD calibration then is to choose ϕ and γ_i such that:

$$p_f = P\left(\phi \mu_R - \sum \gamma_i \mu_Q < 0\right) \leq p_f^{\text{target}} \quad (\text{L.7})$$

for all possible combinations of load effects. The target probability of failure is chosen based on the design life of the structure (75 years for bridges), and a target reliability index (β_T) where:

$$\beta_T = -\Phi^{-1}\left(p_f^{\text{target}}\right) \quad (\text{L.8})$$

Φ^{-1} represents in the inverse cumulative distribution function (CDF) for a standard normal distribution. The target value for β_T set forth by AASHTO is 3.5 for a 75-year design life. Thus, if designed according to the AASHTO LRFD code, all bridge members should be expected to have a probability of failure no higher than 0.00023 in the 75-year design life (assuming that the safety margin, Z , is Gaussian distributed).

L.4 Applicability of LRFD Procedures to AASHTO Acceptable Vessel Collision Risk

Both procedures detailed above—AASHTO vessel collision risk assessment, and typical LRFD calibration—are based on probabilistic assessment of structural response to variable loads. However, there are important differences between the risk acceptance criteria and overall design philosophy that make transference of the current procedure (or UF/FDOT-proposed procedure) to an LRFD procedure difficult.

Foremost is the difference between *bridge* reliability (central to the AASHTO vessel collision procedure) and *bridge member* reliability (central to LRFD). For illustration purposes, assume that the existing AASHTO vessel collision procedure is exactly correct, and annual bridge failure frequencies (AF) are equal to 0.001 or 0.0001 (depending on bridge importance). Therefore, the 1-year probability of failure is ($p_f^{1\text{yr.}}$) is equal to 0.001 or 0.0001. However, LRFD calibration is performed using the 75-year probability ($p_f^{75\text{yr.}}$) where:

$$p_f^{75\text{yr.}} = 75 AF \quad (\text{L.9})$$

Thus, the LRFD-style reliability index (β) can simply be computed as:

$$\beta = -\Phi^{-1}(75 AF) \quad (\text{L.10})$$

Computed in this manner, the 75-year β is equal to only 1.44 for typical bridges ($AF = 0.001$) and 2.43 for critical bridges ($AF = 0.0001$). Both reliability indices are far lower than the AASHTO-stated target of $\beta = 3.5$ for other load conditions. The very low reliability is a consequence of the difference between failure acceptance. The existing AASHTO AF quantity is based upon *bridge* failure, while LRFD is based on *member* failure.

Assume instead that we base the LRFD-style calibration on *pier* failure instead of bridge failure—i.e. we treat the pier instead of the bridge as the “member.” In this case, the 75-year probability of failure ($p_f^{75\text{yr.}}$) is dependent on the number of bridge piers in the navigation zone (N_P) such that:

$$p_f^{75\text{yr.}} = \frac{75 AF}{N_P} \quad (\text{L.11})$$

Note that the above expression assumes uniform risk distribution among all the piers in the navigation zone. Recall that the navigation zone is defined by a 6 x LOA wide region, centered on the navigation channel. Consequently, the reliability index can now be computed as:

$$\beta = -\Phi^{-1} \left(\frac{75 AF}{N_P} \right) \quad (\text{L.12})$$

The above expression demonstrates that β is strongly dependent on the number of piers that can reasonably expect to be struck (N_P). Thus, reliability indices were computed for a range of N_P and reported in Table L.1. Note β values increase dramatically when reliability is assessed based on pier failure, rather than bridge failure. β values range from 1.78 – 2.67 for typical bridges, and 2.67 – 3.37 for critical bridges. Note that still, 75-year β values fall short of the 3.5 target set forth by AASHTO.

Of course, the process of computing reliability indices (and resulting load factors) that is most consistent with past LRFD calibration efforts (Nowak 1999, Nowak et al. 2008) is to directly compute bridge *member* reliabilities (not bridge or pier reliabilities). Interestingly, it might be that, if pier reliabilities are in the 2.0 – 3.0 range, member reliabilities are notably higher (perhaps equal to or higher than the target 3.5), because piers are a conglomeration of many structural members. However, prohibiting member failure is a stricter design standard than prohibiting pier collapse, because multiple members can exceed the design capacity without the pier collapsing. Thus, these two effects may offset each other, resulting in individual member reliabilities that are on par with the pier reliability (or even lower).

Table L.1. *Pier* reliability index (75-year β) for various numbers of piers

Number of piers in navigation zone (6 x LOA wide)	β for typical bridges ($AF = 0.001$)	β for critical bridges ($AF = 0.0001$)
2	1.78	2.67
4	2.08	2.90
6	2.24	3.02
8	2.35	3.11
10	2.43	3.17
12	2.50	3.23
14	2.55	3.27
16	2.60	3.31
18	2.64	3.34
20	2.67	3.37

L.5 Conclusions

Unfortunately, there is no simple process of transference between the existing AASHTO bridge-based reliability assessment and a more traditional member-based assessment. Note that even the more rational PC expression developed by recently by Consolazio et al. (2010a) is based upon pier failure, not individual member failure. Thus, to develop load factors that ensure similar member reliability to the other AASHTO LRFD load conditions, many reliability analyses (perhaps 100 or more) would be required. Such reliability assessments would need to include nonlinear dynamic structural analyses, similar to those conducted by Consolazio et al (2010).

Aside from the computational effort that would be required, the process of forming load factors is cumbersome. Unlike dead loads or live loads, vessel collision loads are *highly* variable because of a variety of factors: vessel traffic, route geometry, structural configuration, etc. Thus, two options are possible in forming load factors:

- Option 1: Develop load factors that encompass these uncertainties. Such load factors could become *very* large (thus very conservative), but the design process would probably be much simpler than it is currently, or;
- Option 2: Develop load factors that are dependent on these uncertainties (i.e., variable load factors). This would significantly reduce conservatism relative to Option 1, but the design process would probably be effectively as complicated as the current process.

Option 1 above is probably not practical, given the likely conservatism. The only benefit to Option 2 is that the load formulation would be based upon member reliability rather than bridge reliability, which is more consistent with other loading conditions considered in the AASHTO LRFD code.

Typical LRFD calibration procedures are compared to the existing AASHTO vessel collision methodology in Table L.2 for the purpose of summarizing potential obstacles in applying LRFD principles to the vessel collision problem. Many of these issues have been discussed in detail above.

Table L.2. Comparison of LRFD and AASHTO vessel collision design methodologies

Typical LRFD provisions	AASHTO vessel collision provisions
<p>Based on member-by-member assessment of</p> $\phi R_n \geq \sum \gamma_i Q_i$ <p>(factored resistance > factored load effects)</p> <p>Load and resistance factors are formulated such that the probability of <i>member failure</i> is below a maximum target value <i>within the lifetime of the structure</i> (typically 75 years for bridges).</p> <p>Probabilistic descriptions of loads exist in literature for use in reliability analysis (e.g., for code calibration).</p> <p>Loads and load probabilities are fairly similar for most structures (based on use).</p> <p>Code calibration can (and should) be executed using structures designed in accordance with the existing design provisions.</p>	<p>Based on structural collapse assessment of the <i>full bridge</i>. Load effects on individual members are permitted to exceed the factored resistance.</p> <p>Structural risk assessment ensures that the probability of <i>bridge failure</i> is held below a target <i>annual frequency</i> (1/1,000 or 1/10,000).</p> <p>Probabilistic descriptions of loads do not exist for use in reliability analysis. Expensive reliability analysis including dynamic simulations is required.</p> <p>Loads and load probabilities vary considerably between structures, based on vessel traffic, bridge layout, etc.</p> <p>No structures have been designed in accordance with UF/FDOT proposed changes to vessel collision design.</p>

In the opinion of the author, developing an LRFD vessel collision design procedure may exceed the intended scope of the current project: develop revised design procedures that incorporate recent UF/FDOT research findings. By developing an LRFD procedure, not only would UF/FDOT research be incorporated into the design code, but the fundamental risk acceptance criteria would be dramatically altered. Depending on the opinions of AASHTO committee members, this might impede adoption of the revised design provisions, relative to more targeted changes. Furthermore, the complicated reliability analyses including dynamic analysis would need to be analyzed *multiple times* (once for each trial combination of load factors), and more cases are probably necessary for proper calibration. Recent UF/FDOT research findings can instead be more easily incorporated into the existing AASHTO design framework (considering overall bridge reliability). Therefore, it is proposed that incremental changes to the *existing* design procedure be executed that reflect UF/FDOT research findings.

APPENDIX M
SR-300 BRIDGE VESSEL COLLISION RISK ASSESSMENT DATA

M.1 Introduction

In this appendix, detailed data are presented for vessel collision risk assessments of the Bryant Grady Patton Bridge (SR-300) over Apalachicola Bay, Florida. The associated risk assessments are discussed in Chapter 9. Tables M.1 – M.18 present risk assessment input parameters and results for every combination of pier (35 – 60) and vessel group (1 – 11). Figures M.1 – M.26 show barge impact force-time histories computed by the CVIA and AVIL analysis methods for each combination of pier (35 – 60) and barge vessel group (1 – 8). See Chapter 9 for descriptions of piers and vessel groups.

Table M.1 Vessel impact velocities (v_i) (knots)

VG	P35	P36	P37	P38	P39	P40	P41	P42	P43	P44	P45	P46	P47
1	1.00	1.00	1.00	1.00	1.00	1.00	1.00	1.00	1.02	1.82	2.63	3.83	5.31
2	1.00	1.00	1.00	1.00	1.00	1.00	1.08	1.53	1.99	2.45	2.91	3.59	4.44
3	1.00	1.00	1.00	1.00	1.00	1.00	1.00	1.00	1.38	1.94	2.51	3.35	4.40
4	1.00	1.00	1.00	1.00	1.00	1.08	1.48	1.89	2.30	2.70	3.11	3.71	4.46
5	1.00	1.00	1.12	1.57	2.02	2.48	2.93	3.38	3.83	4.28	4.74	5.41	6.24
6	1.23	1.53	1.84	2.14	2.45	2.75	3.06	3.36	3.67	3.97	4.28	4.73	5.29
7	1.00	1.00	1.00	1.24	1.63	2.02	2.41	2.80	3.19	3.58	3.97	4.54	5.26
8	1.00	1.00	1.28	1.63	1.98	2.33	2.69	3.04	3.39	3.75	4.10	4.62	5.27
9	1.00	1.00	1.00	1.00	1.00	1.00	1.00	1.00	1.00	1.00	1.00	1.00	5.37
10	1.00	1.00	1.00	1.00	1.00	1.00	1.00	1.00	1.00	1.00	1.00	1.00	6.47
11	1.00	1.00	1.00	1.00	1.00	1.00	1.00	1.00	1.00	1.00	1.00	1.00	6.86
VG	P48	P49	P50	P51	P52	P53	P54	P55	P56	P57	P58	P59	P60
1	5.31	3.83	2.63	1.82	1.02	1.00	1.00	1.00	1.00	1.00	1.00	1.00	1.00
2	4.44	3.59	2.91	2.45	1.99	1.53	1.08	1.00	1.00	1.00	1.00	1.00	1.00
3	4.40	3.35	2.51	1.94	1.38	1.00	1.00	1.00	1.00	1.00	1.00	1.00	1.00
4	4.46	3.71	3.11	2.70	2.30	1.89	1.48	1.08	1.00	1.00	1.00	1.00	1.00
5	6.24	5.41	4.74	4.28	3.83	3.38	2.93	2.48	2.02	1.57	1.12	1.00	1.00
6	5.29	4.73	4.28	3.97	3.67	3.36	3.06	2.75	2.45	2.14	1.84	1.53	1.23
7	5.26	4.54	3.97	3.58	3.19	2.80	2.41	2.02	1.63	1.24	1.00	1.00	1.00
8	5.27	4.62	4.10	3.75	3.39	3.04	2.69	2.33	1.98	1.63	1.28	1.00	1.00
9	5.37	1.00	1.00	1.00	1.00	1.00	1.00	1.00	1.00	1.00	1.00	1.00	1.00
10	6.47	1.00	1.00	1.00	1.00	1.00	1.00	1.00	1.00	1.00	1.00	1.00	1.00
11	6.86	1.00	1.00	1.00	1.00	1.00	1.00	1.00	1.00	1.00	1.00	1.00	1.00

Table M.2 Geometric probability of impact (PG)

VG	P35	P36	P37	P38	P39	P40	P41	P42	P43	P44	P45	P46	P47
1	0.000	0.000	0.000	0.000	0.000	0.000	0.000	0.000	0.002	0.006	0.018	0.059	0.127
2	0.000	0.000	0.000	0.000	0.000	0.000	0.001	0.004	0.009	0.019	0.035	0.069	0.106
3	0.000	0.000	0.000	0.000	0.000	0.000	0.000	0.001	0.003	0.009	0.023	0.062	0.116
4	0.000	0.000	0.000	0.000	0.000	0.001	0.003	0.006	0.013	0.023	0.038	0.065	0.091
5	0.000	0.000	0.001	0.002	0.003	0.006	0.009	0.014	0.022	0.031	0.041	0.056	0.068
6	0.001	0.002	0.003	0.005	0.007	0.011	0.016	0.021	0.029	0.037	0.044	0.056	0.064
7	0.000	0.000	0.000	0.001	0.002	0.004	0.007	0.012	0.020	0.028	0.038	0.055	0.068
8	0.000	0.001	0.001	0.003	0.004	0.008	0.013	0.019	0.028	0.038	0.049	0.066	0.079
9	0.000	0.000	0.000	0.000	0.000	0.000	0.000	0.000	0.000	0.000	0.000	0.000	0.107
10	0.000	0.000	0.000	0.000	0.000	0.000	0.000	0.000	0.000	0.000	0.000	0.002	0.151
11	0.000	0.000	0.000	0.000	0.000	0.000	0.000	0.000	0.000	0.000	0.000	0.000	0.139
VG	P48	P49	P50	P51	P52	P53	P54	P55	P56	P57	P58	P59	P60
1	0.127	0.059	0.018	0.006	0.002	0.000	0.000	0.000	0.000	0.000	0.000	0.000	0.000
2	0.106	0.069	0.035	0.019	0.009	0.004	0.001	0.000	0.000	0.000	0.000	0.000	0.000
3	0.116	0.062	0.023	0.009	0.003	0.001	0.000	0.000	0.000	0.000	0.000	0.000	0.000
4	0.091	0.065	0.038	0.023	0.013	0.006	0.003	0.001	0.000	0.000	0.000	0.000	0.000
5	0.068	0.056	0.041	0.031	0.022	0.014	0.009	0.006	0.003	0.002	0.001	0.000	0.000
6	0.064	0.056	0.044	0.037	0.029	0.021	0.016	0.011	0.007	0.005	0.003	0.002	0.001
7	0.068	0.055	0.038	0.028	0.020	0.012	0.007	0.004	0.002	0.001	0.000	0.000	0.000
8	0.079	0.066	0.049	0.038	0.028	0.019	0.013	0.008	0.004	0.003	0.001	0.001	0.000
9	0.107	0.000	0.000	0.000	0.000	0.000	0.000	0.000	0.000	0.000	0.000	0.000	0.000
10	0.151	0.002	0.000	0.000	0.000	0.000	0.000	0.000	0.000	0.000	0.000	0.000	0.000
11	0.139	0.000	0.000	0.000	0.000	0.000	0.000	0.000	0.000	0.000	0.000	0.000	0.000

Table M.3 Vessel impact forces (kips): AASHTO (1991) methods

VG	P35	P36	P37	P38	P39	P40	P41	P42	P43	P44	P45	P46	P47
1	367	367	367	367	367	367	367	367	380	1,209	2,032	2,102	2,216
2	1,230	1,230	1,230	1,230	1,230	1,230	1,419	2,335	2,384	2,444	2,513	2,628	2,790
3	1,219	1,219	1,219	1,219	1,219	1,219	1,219	1,219	2,011	2,069	2,143	2,275	2,470
4	2,145	2,144	2,144	2,143	2,143	2,149	2,206	2,278	2,362	2,456	2,559	2,723	2,942
5	669	669	836	1,633	2,033	2,067	2,107	2,152	2,201	2,255	2,312	2,403	2,523
6	2,494	2,541	2,596	2,658	2,726	2,799	2,878	2,960	3,045	3,134	3,225	3,364	3,542
7	1,801	1,801	1,801	1,831	1,892	1,966	2,050	2,143	2,243	2,350	2,461	2,634	2,858
8	2,924	2,923	2,998	3,110	3,240	3,347	3,486	3,633	3,790	3,951	4,116	4,365	4,682
9	240	240	240	240	240	240	240	240	240	240	240	240	1,291
10	258	258	258	258	258	258	258	258	258	258	258	258	1,670
11	198	198	198	198	198	198	198	198	198	198	198	198	1,358
VG	P48	P49	P50	P51	P52	P53	P54	P55	P56	P57	P58	P59	P60
1	2,216	2,102	2,032	1,209	380	367	367	367	367	367	367	367	367
2	2,790	2,628	2,513	2,444	2,384	2,335	1,419	1,230	1,230	1,230	1,230	1,230	1,230
3	2,470	2,275	2,143	2,069	2,011	1,219	1,219	1,219	1,219	1,219	1,219	1,219	1,219
4	2,942	2,723	2,559	2,456	2,362	2,278	2,206	2,149	2,143	2,143	2,144	2,144	2,145
5	2,523	2,403	2,312	2,255	2,201	2,152	2,107	2,067	2,033	1,633	836	669	669
6	3,542	3,364	3,225	3,134	3,045	2,960	2,878	2,799	2,726	2,658	2,596	2,541	2,494
7	2,858	2,634	2,461	2,350	2,243	2,143	2,050	1,966	1,892	1,831	1,801	1,801	1,801
8	4,682	4,365	4,116	3,951	3,790	3,633	3,486	3,347	3,240	3,110	2,998	2,923	2,924
9	1,291	240	240	240	240	240	240	240	240	240	240	240	240
10	1,670	258	258	258	258	258	258	258	258	258	258	258	258
11	1,358	198	198	198	198	198	198	198	198	198	198	198	198

Table M.4 Capacity-demand ratios (H/P): AASHTO (1991) methods

VG	P35	P36	P37	P38	P39	P40	P41	P42	P43	P44	P45	P46	P47
1	2.93	2.93	2.93	4.09	4.09	6.27	6.27	6.27	7.24	2.27	1.35	1.55	1.47
2	0.87	0.87	0.87	1.22	1.22	1.87	1.62	0.99	1.15	1.13	1.09	1.24	1.17
3	0.88	0.88	0.88	1.23	1.23	1.89	1.89	1.89	1.37	1.33	1.28	1.43	1.32
4	0.50	0.50	0.50	0.70	0.70	1.07	1.04	1.01	1.16	1.12	1.07	1.20	1.11
5	1.61	1.61	1.29	0.92	0.74	1.11	1.09	1.07	1.25	1.22	1.19	1.35	1.29
6	0.43	0.42	0.41	0.56	0.55	0.82	0.80	0.78	0.90	0.88	0.85	0.97	0.92
7	0.60	0.60	0.60	0.82	0.79	1.17	1.12	1.07	1.23	1.17	1.12	1.24	1.14
8	0.37	0.37	0.36	0.48	0.46	0.69	0.66	0.63	0.73	0.70	0.67	0.75	0.70
9	4.47	4.47	4.47	6.24	6.24	9.57	9.57	9.57	11.45	11.45	11.45	13.55	2.52
10	4.16	4.16	4.16	5.81	5.81	8.91	8.91	8.91	10.65	10.65	10.65	12.61	1.95
11	5.43	5.43	5.43	7.58	7.58	11.62	11.62	11.62	13.89	13.89	13.89	16.44	2.40
VG	P48	P49	P50	P51	P52	P53	P54	P55	P56	P57	P58	P59	P60
1	1.47	1.55	1.35	2.27	7.24	6.27	6.27	6.27	4.09	4.09	2.93	2.93	2.93
2	1.17	1.24	1.09	1.13	1.15	0.99	1.62	1.87	1.22	1.22	0.87	0.87	0.87
3	1.32	1.43	1.28	1.33	1.37	1.89	1.89	1.89	1.23	1.23	0.88	0.88	0.88
4	1.11	1.20	1.07	1.12	1.16	1.01	1.04	1.07	0.70	0.70	0.50	0.50	0.50
5	1.29	1.35	1.19	1.22	1.25	1.07	1.09	1.11	0.74	0.92	1.29	1.61	1.61
6	0.92	0.97	0.85	0.88	0.90	0.78	0.80	0.82	0.55	0.56	0.41	0.42	0.43
7	1.14	1.24	1.12	1.17	1.23	1.07	1.12	1.17	0.79	0.82	0.60	0.60	0.60
8	0.70	0.75	0.67	0.70	0.73	0.63	0.66	0.69	0.46	0.48	0.36	0.37	0.37
9	2.52	13.55	11.45	11.45	11.45	9.57	9.57	9.57	6.24	6.24	4.47	4.47	4.47
10	1.95	12.61	10.65	10.65	10.65	8.91	8.91	8.91	5.81	5.81	4.16	4.16	4.16
11	2.40	16.44	13.89	13.89	13.89	11.62	11.62	11.62	7.58	7.58	5.43	5.43	5.43

Table M.5 Probability of collapse (*PC*): AASHTO (1991) methods

VG	P35	P36	P37	P38	P39	P40	P41	P42	P43	P44	P45	P46	P47
1	0.000	0.000	0.000	0.000	0.000	0.000	0.000	0.000	0.000	0.000	0.000	0.000	0.000
2	0.000	0.000	0.000	0.000	0.000	0.000	0.000	0.002	0.000	0.000	0.000	0.000	0.000
3	0.000	0.000	0.000	0.000	0.000	0.000	0.000	0.000	0.000	0.000	0.000	0.000	0.000
4	0.000	0.000	0.000	0.000	0.000	0.000	0.000	0.000	0.000	0.000	0.000	0.000	0.000
5	0.000	0.000	0.000	0.009	0.029	0.000	0.000	0.000	0.000	0.000	0.000	0.000	0.000
6	0.063	0.064	0.065	0.048	0.050	0.020	0.022	0.025	0.011	0.014	0.016	0.004	0.009
7	0.000	0.000	0.000	0.020	0.023	0.000	0.000	0.000	0.000	0.000	0.000	0.000	0.000
8	0.000	0.000	0.071	0.058	0.060	0.035	0.038	0.041	0.030	0.034	0.037	0.028	0.034
9	0.000	0.000	0.000	0.000	0.000	0.000	0.000	0.000	0.000	0.000	0.000	0.000	0.000
10	0.000	0.000	0.000	0.000	0.000	0.000	0.000	0.000	0.000	0.000	0.000	0.000	0.000
11	0.000	0.000	0.000	0.000	0.000	0.000	0.000	0.000	0.000	0.000	0.000	0.000	0.000
VG	P48	P49	P50	P51	P52	P53	P54	P55	P56	P57	P58	P59	P60
1	0.000	0.000	0.000	0.000	0.000	0.000	0.000	0.000	0.000	0.000	0.000	0.000	0.000
2	0.000	0.000	0.000	0.000	0.000	0.002	0.000	0.000	0.000	0.000	0.000	0.000	0.000
3	0.000	0.000	0.000	0.000	0.000	0.000	0.000	0.000	0.000	0.000	0.000	0.000	0.000
4	0.000	0.000	0.000	0.000	0.000	0.000	0.000	0.000	0.000	0.000	0.000	0.000	0.000
5	0.000	0.000	0.000	0.000	0.000	0.000	0.000	0.000	0.029	0.009	0.000	0.000	0.000
6	0.009	0.004	0.016	0.014	0.011	0.025	0.022	0.020	0.050	0.048	0.065	0.064	0.063
7	0.000	0.000	0.000	0.000	0.000	0.000	0.000	0.000	0.023	0.020	0.000	0.000	0.000
8	0.034	0.028	0.037	0.034	0.030	0.041	0.038	0.035	0.060	0.058	0.071	0.000	0.000
9	0.000	0.000	0.000	0.000	0.000	0.000	0.000	0.000	0.000	0.000	0.000	0.000	0.000
10	0.000	0.000	0.000	0.000	0.000	0.000	0.000	0.000	0.000	0.000	0.000	0.000	0.000
11	0.000	0.000	0.000	0.000	0.000	0.000	0.000	0.000	0.000	0.000	0.000	0.000	0.000

Table M.6 Vessel impact forces (kips): AASHTO (2009) methods

VG	P35	P36	P37	P38	P39	P40	P41	P42	P43	P44	P45	P46	P47
1	367	367	367	367	367	367	367	367	380	1,209	1,415	1,485	1,599
2	1,230	1,230	1,230	1,230	1,230	1,230	1,387	1,425	1,475	1,534	1,603	1,719	1,880
3	1,219	1,219	1,219	1,219	1,219	1,219	1,219	1,219	1,410	1,468	1,541	1,674	1,868
4	1,412	1,412	1,411	1,410	1,410	1,417	1,474	1,546	1,630	1,724	1,826	1,990	2,209
5	669	669	836	1,393	1,421	1,455	1,494	1,539	1,588	1,642	1,699	1,790	1,910
6	1,438	1,485	1,539	1,602	1,670	1,743	1,822	1,904	1,989	2,078	2,169	2,308	2,486
7	1,408	1,408	1,408	1,438	1,499	1,573	1,657	1,750	1,850	1,957	2,068	2,241	2,465
8	1,482	1,482	1,557	1,669	1,798	1,905	2,044	2,192	2,348	2,509	2,674	2,924	3,241
9	240	240	240	240	240	240	240	240	240	240	240	240	1,291
10	258	258	258	258	258	258	258	258	258	258	258	258	1,670
11	198	198	198	198	198	198	198	198	198	198	198	198	1,358
VG	P48	P49	P50	P51	P52	P53	P54	P55	P56	P57	P58	P59	P60
1	1,599	1,485	1,415	1,209	380	367	367	367	367	367	367	367	367
2	1,880	1,719	1,603	1,534	1,475	1,425	1,387	1,230	1,230	1,230	1,230	1,230	1,230
3	1,868	1,674	1,541	1,468	1,410	1,219	1,219	1,219	1,219	1,219	1,219	1,219	1,219
4	2,209	1,990	1,826	1,724	1,630	1,546	1,474	1,417	1,410	1,410	1,411	1,412	1,412
5	1,910	1,790	1,699	1,642	1,588	1,539	1,494	1,455	1,421	1,393	836	669	669
6	2,486	2,308	2,169	2,078	1,989	1,904	1,822	1,743	1,670	1,602	1,539	1,485	1,438
7	2,465	2,241	2,068	1,957	1,850	1,750	1,657	1,573	1,499	1,438	1,408	1,408	1,408
8	3,241	2,924	2,674	2,509	2,348	2,192	2,044	1,905	1,798	1,669	1,557	1,482	1,482
9	1,291	240	240	240	240	240	240	240	240	240	240	240	240
10	1,670	258	258	258	258	258	258	258	258	258	258	258	258
11	1,358	198	198	198	198	198	198	198	198	198	198	198	198

Table M.7 Capacity-demand ratios (H/P): AASHTO (2009) methods

VG	P35	P36	P37	P38	P39	P40	P41	P42	P43	P44	P45	P46	P47
1	2.93	2.93	2.93	4.09	4.09	6.27	6.27	6.27	7.24	2.27	1.94	2.19	2.04
2	0.87	0.87	0.87	1.22	1.22	1.87	1.66	1.61	1.86	1.79	1.72	1.89	1.73
3	0.88	0.88	0.88	1.23	1.23	1.89	1.89	1.89	1.95	1.87	1.78	1.94	1.74
4	0.76	0.76	0.76	1.06	1.06	1.62	1.56	1.49	1.69	1.60	1.51	1.64	1.47
5	1.61	1.61	1.29	1.08	1.06	1.58	1.54	1.49	1.73	1.67	1.62	1.82	1.70
6	0.75	0.72	0.70	0.94	0.90	1.32	1.26	1.21	1.38	1.32	1.27	1.41	1.31
7	0.76	0.76	0.76	1.04	1.00	1.46	1.39	1.31	1.49	1.41	1.33	1.45	1.32
8	0.73	0.73	0.69	0.90	0.83	1.21	1.13	1.05	1.17	1.10	1.03	1.11	1.00
9	4.47	4.47	4.47	6.24	6.24	9.57	9.57	9.57	11.45	11.45	11.45	13.55	2.52
10	4.16	4.16	4.16	5.81	5.81	8.91	8.91	8.91	10.65	10.65	10.65	12.61	1.95
11	5.43	5.43	5.43	7.58	7.58	11.62	11.62	11.62	13.89	13.89	13.89	16.44	2.40
VG	P48	P49	P50	P51	P52	P53	P54	P55	P56	P57	P58	P59	P60
1	2.04	2.19	1.94	2.27	7.24	6.27	6.27	6.27	4.09	4.09	2.93	2.93	2.93
2	1.73	1.89	1.72	1.79	1.86	1.61	1.66	1.87	1.22	1.22	0.87	0.87	0.87
3	1.74	1.94	1.78	1.87	1.95	1.89	1.89	1.89	1.23	1.23	0.88	0.88	0.88
4	1.47	1.64	1.51	1.60	1.69	1.49	1.56	1.62	1.06	1.06	0.76	0.76	0.76
5	1.70	1.82	1.62	1.67	1.73	1.49	1.54	1.58	1.06	1.08	1.29	1.61	1.61
6	1.31	1.41	1.27	1.32	1.38	1.21	1.26	1.32	0.90	0.94	0.70	0.72	0.75
7	1.32	1.45	1.33	1.41	1.49	1.31	1.39	1.46	1.00	1.04	0.76	0.76	0.76
8	1.00	1.11	1.03	1.10	1.17	1.05	1.13	1.21	0.83	0.90	0.69	0.73	0.73
9	2.52	13.55	11.45	11.45	11.45	9.57	9.57	9.57	6.24	6.24	4.47	4.47	4.47
10	1.95	12.61	10.65	10.65	10.65	8.91	8.91	8.91	5.81	5.81	4.16	4.16	4.16
11	2.40	16.44	13.89	13.89	13.89	11.62	11.62	11.62	7.58	7.58	5.43	5.43	5.43

Table M.8 Probability of collapse (PC): AASHTO (2009) methods

VG	P35	P36	P37	P38	P39	P40	P41	P42	P43	P44	P45	P46	P47
1	0.000	0.000	0.000	0.000	0.000	0.000	0.000	0.000	0.000	0.000	0.000	0.000	0.000
2	0.000	0.000	0.000	0.000	0.000	0.000	0.000	0.000	0.000	0.000	0.000	0.000	0.000
3	0.000	0.000	0.000	0.000	0.000	0.000	0.000	0.000	0.000	0.000	0.000	0.000	0.000
4	0.000	0.000	0.000	0.000	0.000	0.000	0.000	0.000	0.000	0.000	0.000	0.000	0.000
5	0.000	0.000	0.000	0.000	0.000	0.000	0.000	0.000	0.000	0.000	0.000	0.000	0.000
6	0.028	0.031	0.034	0.007	0.011	0.000	0.000	0.000	0.000	0.000	0.000	0.000	0.000
7	0.000	0.000	0.000	0.000	0.000	0.000	0.000	0.000	0.000	0.000	0.000	0.000	0.000
8	0.000	0.000	0.034	0.011	0.018	0.000	0.000	0.000	0.000	0.000	0.000	0.000	0.000
9	0.000	0.000	0.000	0.000	0.000	0.000	0.000	0.000	0.000	0.000	0.000	0.000	0.000
10	0.000	0.000	0.000	0.000	0.000	0.000	0.000	0.000	0.000	0.000	0.000	0.000	0.000
11	0.000	0.000	0.000	0.000	0.000	0.000	0.000	0.000	0.000	0.000	0.000	0.000	0.000
VG	P48	P49	P50	P51	P52	P53	P54	P55	P56	P57	P58	P59	P60
1	0.000	0.000	0.000	0.000	0.000	0.000	0.000	0.000	0.000	0.000	0.000	0.000	0.000
2	0.000	0.000	0.000	0.000	0.000	0.000	0.000	0.000	0.000	0.000	0.000	0.000	0.000
3	0.000	0.000	0.000	0.000	0.000	0.000	0.000	0.000	0.000	0.000	0.000	0.000	0.000
4	0.000	0.000	0.000	0.000	0.000	0.000	0.000	0.000	0.000	0.000	0.000	0.000	0.000
5	0.000	0.000	0.000	0.000	0.000	0.000	0.000	0.000	0.000	0.000	0.000	0.000	0.000
6	0.000	0.000	0.000	0.000	0.000	0.000	0.000	0.000	0.011	0.007	0.034	0.031	0.028
7	0.000	0.000	0.000	0.000	0.000	0.000	0.000	0.000	0.000	0.000	0.000	0.000	0.000
8	0.000	0.000	0.000	0.000	0.000	0.000	0.000	0.000	0.018	0.011	0.034	0.000	0.000
9	0.000	0.000	0.000	0.000	0.000	0.000	0.000	0.000	0.000	0.000	0.000	0.000	0.000
10	0.000	0.000	0.000	0.000	0.000	0.000	0.000	0.000	0.000	0.000	0.000	0.000	0.000
11	0.000	0.000	0.000	0.000	0.000	0.000	0.000	0.000	0.000	0.000	0.000	0.000	0.000

Table M.9 Maximum vessel impact forces (kips): UF/FDOT methods (CVIA)

VG	P35	P36	P37	P38	P39	P40	P41	P42	P43	P44	P45	P46	P47
1	1,044	997	992	1,023	1,018	1,300	1,297	1,284	1,424	2,508	3,148	3,148	3,148
2	1,965	1,962	1,663	2,100	2,066	2,352	2,518	3,145	3,148	3,148	3,148	3,148	3,148
3	1,959	1,955	1,658	2,093	2,059	2,340	2,363	2,325	3,148	3,148	3,148	3,148	3,148
4	2,418	2,345	1,975	2,547	2,507	3,148	3,148	3,148	3,148	3,148	3,148	3,148	3,148
5	1,483	1,473	1,392	2,141	2,449	3,148	3,148	3,148	3,148	3,148	3,148	3,148	3,148
6	2,555	2,555	2,555	2,555	2,555	3,148	3,148	3,148	3,148	3,148	3,148	3,148	3,148
7	2,429	2,349	1,980	2,555	2,555	3,148	3,148	3,148	3,148	3,148	3,148	3,148	3,148
8	2,555	2,555	2,555	2,555	2,555	3,148	3,148	3,148	3,148	3,148	3,148	3,148	3,148
9	240	240	240	240	240	240	240	240	240	240	240	240	1,291
10	258	258	258	258	258	258	258	258	258	258	258	258	1,670
11	198	198	198	198	198	198	198	198	198	198	198	198	1,358
VG	P48	P49	P50	P51	P52	P53	P54	P55	P56	P57	P58	P59	P60
1	3,148	3,148	3,148	2,585	1,447	1,308	1,292	1,289	1,018	1,029	1,006	1,076	1,123
2	3,148	3,148	3,148	3,148	3,148	3,148	2,472	2,429	2,092	2,100	1,836	2,075	2,081
3	3,148	3,148	3,148	3,148	3,148	2,371	2,322	2,417	2,085	2,093	1,831	2,069	2,074
4	3,148	3,148	3,148	3,148	3,148	3,148	3,148	3,148	2,534	2,554	2,268	2,518	2,555
5	3,148	3,148	3,148	3,148	3,148	3,148	3,148	3,148	2,514	2,146	1,565	1,581	1,588
6	3,148	3,148	3,148	3,148	3,148	3,148	3,148	3,148	2,555	2,555	2,555	2,555	2,555
7	3,148	3,148	3,148	3,148	3,148	3,148	3,148	3,148	2,555	2,555	2,274	2,525	2,555
8	3,148	3,148	3,148	3,148	3,148	3,148	3,148	3,148	2,555	2,555	2,555	2,555	2,555
9	1,291	240	240	240	240	240	240	240	240	240	240	240	240
10	1,670	258	258	258	258	258	258	258	258	258	258	258	258
11	1,358	198	198	198	198	198	198	198	198	198	198	198	198

Table M.10 Demand-capacity ratios (D/C): UF/FDOT methods (CVIA). Cases highlighted in grey indicate that D/C was controlled by pier column demands rather than pile demands

VG	P35	P36	P37	P38	P39	P40	P41	P42	P43	P44	P45	P46	P47
1	0.468	0.470	0.569	0.440	0.457	0.389	0.402	0.399	0.336	0.563	0.683	0.677	0.695
2	0.751	0.758	0.901	0.679	0.689	0.558	0.618	0.806	0.702	0.763	0.722	0.677	0.694
3	0.749	0.754	0.900	0.677	0.686	0.557	0.576	0.563	0.646	0.757	0.720	0.677	0.694
4	0.904	0.911	0.960	0.840	0.853	0.757	0.836	0.885	0.708	0.765	0.724	0.677	0.695
5	0.544	0.544	0.795	0.750	0.898	0.877	0.877	0.894	0.716	0.769	0.727	0.680	0.696
6	0.926	0.978	1.000	0.978	0.968	0.882	0.878	0.894	0.716	0.769	0.726	0.680	0.695
7	0.904	0.911	0.963	0.843	0.914	0.876	0.875	0.893	0.714	0.768	0.726	0.679	0.695
8	0.973	0.985	1.000	0.925	0.953	0.881	0.877	0.894	0.715	0.768	0.726	0.679	0.695
9	---	---	---	---	---	---	---	---	---	---	---	---	---
10	---	---	---	---	---	---	---	---	---	---	---	---	---
11	---	---	---	---	---	---	---	---	---	---	---	---	---
VG	P48	P49	P50	P51	P52	P53	P54	P55	P56	P57	P58	P59	P60
1	0.587	0.648	0.660	0.542	0.325	0.391	0.460	0.376	0.503	0.474	0.509	0.460	0.463
2	0.586	0.648	0.691	0.682	0.671	0.801	0.659	0.539	0.724	0.709	0.874	0.750	0.739
3	0.586	0.648	0.688	0.676	0.628	0.566	0.623	0.539	0.719	0.704	0.870	0.748	0.735
4	0.586	0.648	0.692	0.684	0.676	0.858	0.857	0.684	0.850	0.842	0.934	0.898	0.890
5	0.587	0.651	0.694	0.689	0.683	0.871	0.878	0.827	0.874	0.780	0.751	0.555	0.550
6	0.587	0.650	0.693	0.688	0.683	0.871	0.879	0.829	0.960	0.983	0.993	0.943	0.890
7	0.587	0.650	0.693	0.688	0.682	0.869	0.877	0.823	0.888	0.843	0.935	0.898	0.890
8	0.587	0.650	0.693	0.689	0.682	0.871	0.877	0.828	0.948	0.938	0.988	0.938	0.950
9	---	---	---	---	---	---	---	---	---	---	---	---	---
10	---	---	---	---	---	---	---	---	---	---	---	---	---
11	---	---	---	---	---	---	---	---	---	---	---	---	---

Table M.11 Probability of collapse (*PC*): UF/FDOT methods (CVIA). Cases highlighted in grey indicate *PC* = 1

VG	P35	P36	P37	P38	P39	P40	P41	P42	P43	P44	P45	P46	P47
1	0.001	0.001	0.004	0.001	0.001	0.000	0.000	0.000	0.000	0.004	0.017	0.016	0.020
2	0.041	0.044	0.285	0.016	0.018	0.003	0.007	0.082	0.021	0.048	0.028	0.015	0.019
3	0.039	0.042	0.281	0.015	0.017	0.003	0.004	0.004	0.010	0.044	0.027	0.015	0.019
4	0.295	0.325	0.613	0.129	0.152	0.044	0.122	0.231	0.023	0.049	0.028	0.016	0.019
5	0.003	0.003	0.072	0.040	0.275	0.208	0.209	0.260	0.026	0.051	0.030	0.016	0.020
6	0.395	0.769	1.000	0.769	0.676	0.223	0.211	0.260	0.026	0.051	0.029	0.016	0.020
7	0.295	0.325	0.633	0.134	0.338	0.205	0.203	0.258	0.025	0.051	0.029	0.016	0.020
8	0.721	0.848	1.000	0.389	0.556	0.220	0.209	0.260	0.025	0.051	0.029	0.016	0.020
9	0.000	0.000	0.000	0.000	0.000	0.000	0.000	0.000	0.000	0.000	0.000	0.000	0.000
10	0.000	0.000	0.000	0.000	0.000	0.000	0.000	0.000	0.000	0.000	0.000	0.000	0.000
11	0.000	0.000	0.000	0.000	0.000	0.000	0.000	0.000	0.000	0.000	0.000	0.000	0.000
VG	P48	P49	P50	P51	P52	P53	P54	P55	P56	P57	P58	P59	P60
1	0.005	0.011	0.012	0.003	0.000	0.000	0.001	0.000	0.002	0.001	0.002	0.001	0.001
2	0.005	0.011	0.019	0.017	0.014	0.077	0.012	0.003	0.029	0.024	0.200	0.040	0.035
3	0.005	0.011	0.018	0.015	0.008	0.004	0.008	0.003	0.027	0.022	0.190	0.039	0.033
4	0.005	0.011	0.019	0.017	0.015	0.162	0.160	0.017	0.147	0.132	0.436	0.272	0.247
5	0.005	0.011	0.019	0.018	0.017	0.192	0.211	0.108	0.201	0.059	0.041	0.003	0.003
6	0.005	0.011	0.019	0.018	0.017	0.192	0.214	0.111	0.613	0.821	0.935	0.488	0.247
7	0.005	0.011	0.019	0.018	0.016	0.189	0.208	0.103	0.239	0.134	0.443	0.272	0.247
8	0.005	0.011	0.019	0.018	0.017	0.192	0.209	0.110	0.521	0.457	0.876	0.457	0.538
9	0.000	0.000	0.000	0.000	0.000	0.000	0.000	0.000	0.000	0.000	0.000	0.000	0.000
10	0.000	0.000	0.000	0.000	0.000	0.000	0.000	0.000	0.000	0.000	0.000	0.000	0.000
11	0.000	0.000	0.000	0.000	0.000	0.000	0.000	0.000	0.000	0.000	0.000	0.000	0.000

Table M.12 Maximum vessel impact forces (kips): UF/FDOT methods (AVIL)

VG	P35	P36	P37	P38	P39	P40	P41	P42	P43	P44	P45	P46	P47
1	1,298	1,297	1,197	1,335	1,345	1,539	1,528	1,427	1,630	2,770	3,148	3,148	3,148
2	2,388	2,387	2,203	2,456	2,474	2,831	3,028	3,148	3,148	3,148	3,148	3,148	3,148
3	2,378	2,376	2,193	2,445	2,463	2,818	2,799	2,614	3,148	3,148	3,148	3,148	3,148
4	2,555	2,555	2,555	2,555	2,555	3,148	3,148	3,148	3,148	3,148	3,148	3,148	3,148
5	1,755	1,755	1,811	2,555	2,555	3,148	3,148	3,148	3,148	3,148	3,148	3,148	3,148
6	2,555	2,555	2,555	2,555	2,555	3,148	3,148	3,148	3,148	3,148	3,148	3,148	3,148
7	2,555	2,555	2,555	2,555	2,555	3,148	3,148	3,148	3,148	3,148	3,148	3,148	3,148
8	2,555	2,555	2,555	2,555	2,555	3,148	3,148	3,148	3,148	3,148	3,148	3,148	3,148
9	240	240	240	240	240	240	240	240	240	240	240	240	1,291
10	258	258	258	258	258	258	258	258	258	258	258	258	1,670
11	198	198	198	198	198	198	198	198	198	198	198	198	1,358
VG	P48	P49	P50	P51	P52	P53	P54	P55	P56	P57	P58	P59	P60
1	3,148	3,148	3,148	2,692	1,486	1,420	1,527	1,538	1,361	1,362	1,345	1,377	1,390
2	3,148	3,148	3,148	3,148	3,148	3,148	3,026	2,830	2,504	2,506	2,474	2,534	2,555
3	3,148	3,148	3,148	3,148	3,148	2,600	2,797	2,818	2,493	2,495	2,463	2,522	2,545
4	3,148	3,148	3,148	3,148	3,148	3,148	3,148	3,148	2,555	2,555	2,555	2,555	2,555
5	3,148	3,148	3,148	3,148	3,148	3,148	3,148	3,148	2,555	2,555	2,034	1,862	1,879
6	3,148	3,148	3,148	3,148	3,148	3,148	3,148	3,148	2,555	2,555	2,555	2,555	2,555
7	3,148	3,148	3,148	3,148	3,148	3,148	3,148	3,148	2,555	2,555	2,555	2,555	2,555
8	3,148	3,148	3,148	3,148	3,148	3,148	3,148	3,148	2,555	2,555	2,555	2,555	2,555
9	1,291	240	240	240	240	240	240	240	240	240	240	240	240
10	1,670	258	258	258	258	258	258	258	258	258	258	258	258
11	1,358	198	198	198	198	198	198	198	198	198	198	198	198

Table M.13 Demand-capacity ratios (D/C): UF/FDOT methods (AVIL). Cases highlighted in grey indicate that D/C was controlled by pier column demands rather than pile demands

VG	P35	P36	P37	P38	P39	P40	P41	P42	P43	P44	P45	P46	P47
1	0.481	0.524	0.669	0.513	0.543	0.447	0.510	0.434	0.378	0.625	0.712	0.678	0.696
2	0.889	0.905	1.000	0.802	0.846	0.709	0.758	0.877	0.708	0.764	0.724	0.678	0.695
3	0.883	0.903	1.000	0.799	0.843	0.706	0.708	0.662	0.688	0.761	0.721	0.678	0.695
4	0.950	0.978	1.000	0.890	0.913	0.848	0.861	0.887	0.710	0.765	0.725	0.679	0.695
5	0.650	0.678	0.930	0.943	0.955	0.882	0.878	0.894	0.717	0.769	0.728	0.680	0.697
6	0.985	1.000	1.000	0.983	0.968	0.883	0.879	0.894	0.717	0.769	0.727	0.680	0.696
7	0.950	0.978	1.000	0.943	0.955	0.880	0.876	0.893	0.716	0.768	0.726	0.680	0.696
8	0.985	0.995	1.000	0.973	0.963	0.882	0.877	0.893	0.716	0.769	0.727	0.680	0.696
9	---	---	---	---	---	---	---	---	---	---	---	---	---
10	---	---	---	---	---	---	---	---	---	---	---	---	---
11	---	---	---	---	---	---	---	---	---	---	---	---	---
VG	P48	P49	P50	P51	P52	P53	P54	P55	P56	P57	P58	P59	P60
1	0.587	0.649	0.677	0.556	0.321	0.410	0.558	0.437	0.595	0.561	0.685	0.524	0.495
2	0.587	0.649	0.690	0.682	0.670	0.844	0.802	0.658	0.846	0.827	1.000	0.888	0.885
3	0.587	0.649	0.686	0.676	0.641	0.629	0.758	0.656	0.846	0.826	1.000	0.888	0.879
4	0.587	0.649	0.691	0.684	0.676	0.858	0.871	0.793	0.884	0.908	1.000	0.948	0.930
5	0.587	0.652	0.693	0.689	0.683	0.871	0.879	0.828	0.955	0.958	0.905	0.674	0.651
6	0.587	0.651	0.693	0.689	0.683	0.871	0.879	0.828	0.963	0.988	0.993	0.993	0.970
7	0.587	0.651	0.693	0.688	0.682	0.869	0.877	0.827	0.950	0.988	0.998	0.948	0.933
8	0.587	0.651	0.693	0.688	0.682	0.869	0.878	0.828	0.960	0.980	0.993	0.963	0.955
9	---	---	---	---	---	---	---	---	---	---	---	---	---
10	---	---	---	---	---	---	---	---	---	---	---	---	---
11	---	---	---	---	---	---	---	---	---	---	---	---	---

Table M.14 Probability of collapse (PC): UF/FDOT methods (AVIL). Cases highlighted in grey indicate $PC = 1$

VG	P35	P36	P37	P38	P39	P40	P41	P42	P43	P44	P45	P46	P47
1	0.001	0.002	0.014	0.002	0.003	0.001	0.002	0.001	0.000	0.008	0.024	0.016	0.020
2	0.243	0.300	1.000	0.078	0.139	0.024	0.044	0.208	0.023	0.048	0.029	0.016	0.020
3	0.224	0.290	1.000	0.076	0.133	0.023	0.023	0.013	0.018	0.046	0.028	0.016	0.020
4	0.538	0.769	1.000	0.247	0.334	0.143	0.169	0.238	0.024	0.049	0.029	0.016	0.020
5	0.011	0.016	0.415	0.488	0.574	0.221	0.211	0.260	0.026	0.051	0.030	0.016	0.020
6	0.848	1.000	1.000	0.821	0.676	0.226	0.214	0.260	0.026	0.051	0.030	0.016	0.020
7	0.538	0.769	1.000	0.488	0.574	0.217	0.206	0.256	0.026	0.050	0.029	0.016	0.020
8	0.848	0.966	1.000	0.721	0.633	0.223	0.209	0.258	0.026	0.051	0.030	0.016	0.020
9	0.000	0.000	0.000	0.000	0.000	0.000	0.000	0.000	0.000	0.000	0.000	0.000	0.000
10	0.000	0.000	0.000	0.000	0.000	0.000	0.000	0.000	0.000	0.000	0.000	0.000	0.000
11	0.000	0.000	0.000	0.000	0.000	0.000	0.000	0.000	0.000	0.000	0.000	0.000	0.000
VG	P48	P49	P50	P51	P52	P53	P54	P55	P56	P57	P58	P59	P60
1	0.005	0.011	0.015	0.003	0.000	0.000	0.003	0.001	0.005	0.003	0.017	0.002	0.001
2	0.005	0.011	0.018	0.017	0.014	0.136	0.078	0.012	0.139	0.108	1.000	0.239	0.231
3	0.005	0.011	0.017	0.015	0.010	0.008	0.044	0.012	0.139	0.107	1.000	0.239	0.213
4	0.005	0.011	0.019	0.017	0.015	0.163	0.192	0.070	0.229	0.310	1.000	0.521	0.415
5	0.005	0.011	0.019	0.018	0.017	0.192	0.214	0.111	0.574	0.593	0.300	0.015	0.011
6	0.005	0.011	0.019	0.018	0.017	0.192	0.214	0.111	0.633	0.876	0.935	0.935	0.698
7	0.005	0.011	0.019	0.018	0.016	0.188	0.209	0.108	0.538	0.876	0.998	0.521	0.429
8	0.005	0.011	0.019	0.018	0.016	0.189	0.212	0.111	0.613	0.795	0.935	0.633	0.574
9	0.000	0.000	0.000	0.000	0.000	0.000	0.000	0.000	0.000	0.000	0.000	0.000	0.000
10	0.000	0.000	0.000	0.000	0.000	0.000	0.000	0.000	0.000	0.000	0.000	0.000	0.000
11	0.000	0.000	0.000	0.000	0.000	0.000	0.000	0.000	0.000	0.000	0.000	0.000	0.000

Table M.15 Maximum vessel impact forces (kips): UF/FDOT methods (SBIA)

VG	P35	P36	P37	P38	P39	P40	P41	P42	P43	P44	P45	P46	P47
1	1,298	1,297	1,197	1,335	1,345	1,539	1,528	1,427	1,630	2,770	3,148	3,148	3,148
2	2,388	2,387	2,203	2,456	2,474	2,831	3,028	3,148	3,148	3,148	3,148	3,148	3,148
3	2,378	2,376	2,193	2,445	2,463	2,818	2,799	2,614	3,148	3,148	3,148	3,148	3,148
4	2,555	2,555	2,555	2,555	2,555	3,148	3,148	3,148	3,148	3,148	3,148	3,148	3,148
5	1,755	1,755	1,811	2,555	2,555	3,148	3,148	3,148	3,148	3,148	3,148	3,148	3,148
6	2,555	2,555	2,555	2,555	2,555	3,148	3,148	3,148	3,148	3,148	3,148	3,148	3,148
7	2,555	2,555	2,555	2,555	2,555	3,148	3,148	3,148	3,148	3,148	3,148	3,148	3,148
8	2,555	2,555	2,555	2,555	2,555	3,148	3,148	3,148	3,148	3,148	3,148	3,148	3,148
9	240	240	240	240	240	240	240	240	240	240	240	240	1,291
10	258	258	258	258	258	258	258	258	258	258	258	258	1,670
11	198	198	198	198	198	198	198	198	198	198	198	198	1,358
VG	P48	P49	P50	P51	P52	P53	P54	P55	P56	P57	P58	P59	P60
1	3,148	3,148	3,148	2,692	1,486	1,420	1,527	1,538	1,361	1,362	1,345	1,377	1,390
2	3,148	3,148	3,148	3,148	3,148	3,148	3,026	2,830	2,504	2,506	2,474	2,534	2,555
3	3,148	3,148	3,148	3,148	3,148	2,600	2,797	2,818	2,493	2,495	2,463	2,522	2,545
4	3,148	3,148	3,148	3,148	3,148	3,148	3,148	3,148	2,555	2,555	2,555	2,555	2,555
5	3,148	3,148	3,148	3,148	3,148	3,148	3,148	3,148	2,555	2,555	2,034	1,862	1,879
6	3,148	3,148	3,148	3,148	3,148	3,148	3,148	3,148	2,555	2,555	2,555	2,555	2,555
7	3,148	3,148	3,148	3,148	3,148	3,148	3,148	3,148	2,555	2,555	2,555	2,555	2,555
8	3,148	3,148	3,148	3,148	3,148	3,148	3,148	3,148	2,555	2,555	2,555	2,555	2,555
9	1,291	240	240	240	240	240	240	240	240	240	240	240	240
10	1,670	258	258	258	258	258	258	258	258	258	258	258	258
11	1,358	198	198	198	198	198	198	198	198	198	198	198	198

Table M.16 Demand-capacity ratios (D/C): UF/FDOT methods (SBIA). Cases highlighted in grey indicate that D/C was controlled by pier column demands rather than pile demands

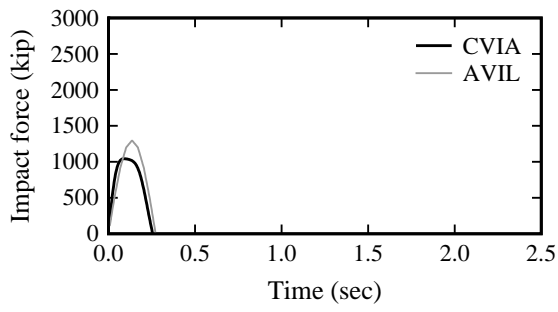
VG	P35	P36	P37	P38	P39	P40	P41	P42	P43	P44	P45	P46	P47
1	0.968	0.975	0.950	0.803	0.792	0.605	0.675	0.833	0.510	0.834	0.958	0.910	0.913
2	1.000	1.000	1.000	1.000	1.000	1.000	1.000	1.000	0.902	0.924	0.958	0.910	0.913
3	1.000	1.000	1.000	1.000	1.000	1.000	1.000	1.000	0.902	0.924	0.958	0.910	0.913
4	1.000	1.000	1.000	1.000	1.000	1.000	1.000	1.000	0.902	0.924	0.958	0.910	0.913
5	1.000	1.000	1.000	1.000	1.000	1.000	1.000	1.000	0.902	0.924	0.958	0.910	0.913
6	1.000	1.000	1.000	1.000	1.000	1.000	1.000	1.000	0.902	0.924	0.958	0.910	0.913
7	1.000	1.000	1.000	1.000	1.000	1.000	1.000	1.000	0.902	0.924	0.958	0.910	0.913
8	1.000	1.000	1.000	1.000	1.000	1.000	1.000	1.000	0.902	0.924	0.958	0.910	0.913
9	---	---	---	---	---	---	---	---	---	---	---	---	---
10	---	---	---	---	---	---	---	---	---	---	---	---	---
11	---	---	---	---	---	---	---	---	---	---	---	---	---
VG	P48	P49	P50	P51	P52	P53	P54	P55	P56	P57	P58	P59	P60
1	0.913	0.910	0.958	0.834	0.510	0.833	0.675	0.605	0.792	0.803	0.950	0.975	0.968
2	0.913	0.910	0.958	0.924	0.902	1.000	1.000	1.000	1.000	1.000	1.000	1.000	1.000
3	0.913	0.910	0.958	0.924	0.902	1.000	1.000	1.000	1.000	1.000	1.000	1.000	1.000
4	0.913	0.910	0.958	0.924	0.902	1.000	1.000	1.000	1.000	1.000	1.000	1.000	1.000
5	0.913	0.910	0.958	0.924	0.902	1.000	1.000	1.000	1.000	1.000	1.000	1.000	1.000
6	0.913	0.910	0.958	0.924	0.902	1.000	1.000	1.000	1.000	1.000	1.000	1.000	1.000
7	0.913	0.910	0.958	0.924	0.902	1.000	1.000	1.000	1.000	1.000	1.000	1.000	1.000
8	0.913	0.910	0.958	0.924	0.902	1.000	1.000	1.000	1.000	1.000	1.000	1.000	1.000
9	---	---	---	---	---	---	---	---	---	---	---	---	---
10	---	---	---	---	---	---	---	---	---	---	---	---	---
11	---	---	---	---	---	---	---	---	---	---	---	---	---

Table M.17 Probability of collapse (*PC*): UF/FDOT methods (SBIA). Cases highlighted in grey indicate *PC* = 1

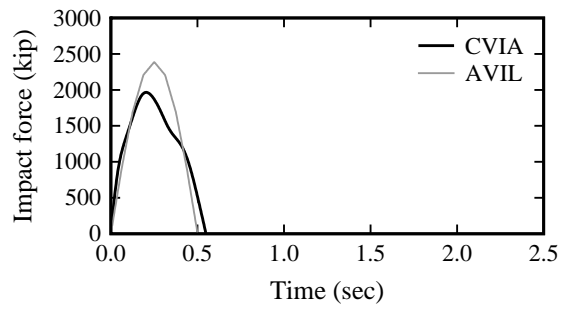
VG	P35	P36	P37	P38	P39	P40	P41	P42	P43	P44	P45	P46	P47
1	0.676	0.745	0.538	0.079	0.069	0.006	0.015	0.117	0.002	0.119	0.593	0.319	0.334
2	1.000	1.000	1.000	1.000	1.000	1.000	1.000	1.000	0.289	0.383	0.593	0.319	0.334
3	1.000	1.000	1.000	1.000	1.000	1.000	1.000	1.000	0.289	0.383	0.593	0.319	0.334
4	1.000	1.000	1.000	1.000	1.000	1.000	1.000	1.000	0.289	0.383	0.593	0.319	0.334
5	1.000	1.000	1.000	1.000	1.000	1.000	1.000	1.000	0.289	0.383	0.593	0.319	0.334
6	1.000	1.000	1.000	1.000	1.000	1.000	1.000	1.000	0.289	0.383	0.593	0.319	0.334
7	1.000	1.000	1.000	1.000	1.000	1.000	1.000	1.000	0.289	0.383	0.593	0.319	0.334
8	1.000	1.000	1.000	1.000	1.000	1.000	1.000	1.000	0.289	0.383	0.593	0.319	0.334
9	0.000	0.000	0.000	0.000	0.000	0.000	0.000	0.000	0.000	0.000	0.000	0.000	0.000
10	0.000	0.000	0.000	0.000	0.000	0.000	0.000	0.000	0.000	0.000	0.000	0.000	0.000
11	0.000	0.000	0.000	0.000	0.000	0.000	0.000	0.000	0.000	0.000	0.000	0.000	0.000
VG	P48	P49	P50	P51	P52	P53	P54	P55	P56	P57	P58	P59	P60
1	0.334	0.319	0.593	0.119	0.002	0.117	0.015	0.006	0.069	0.079	0.538	0.745	0.676
2	0.334	0.319	0.593	0.383	0.289	1.000	1.000	1.000	1.000	1.000	1.000	1.000	1.000
3	0.334	0.319	0.593	0.383	0.289	1.000	1.000	1.000	1.000	1.000	1.000	1.000	1.000
4	0.334	0.319	0.593	0.383	0.289	1.000	1.000	1.000	1.000	1.000	1.000	1.000	1.000
5	0.334	0.319	0.593	0.383	0.289	1.000	1.000	1.000	1.000	1.000	1.000	1.000	1.000
6	0.334	0.319	0.593	0.383	0.289	1.000	1.000	1.000	1.000	1.000	1.000	1.000	1.000
7	0.334	0.319	0.593	0.383	0.289	1.000	1.000	1.000	1.000	1.000	1.000	1.000	1.000
8	0.334	0.319	0.593	0.383	0.289	1.000	1.000	1.000	1.000	1.000	1.000	1.000	1.000
9	0.000	0.000	0.000	0.000	0.000	0.000	0.000	0.000	0.000	0.000	0.000	0.000	0.000
10	0.000	0.000	0.000	0.000	0.000	0.000	0.000	0.000	0.000	0.000	0.000	0.000	0.000
11	0.000	0.000	0.000	0.000	0.000	0.000	0.000	0.000	0.000	0.000	0.000	0.000	0.000

Table M.18 Protection factor (*PF*)

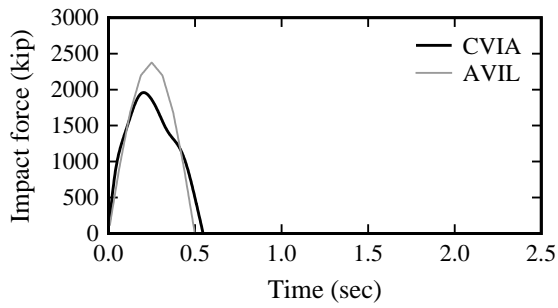
VG	P35	P36	P37	P38	P39	P40	P41	P42	P43	P44	P45	P46	P47
1	1.000	1.000	1.000	1.000	1.000	1.000	1.000	1.000	1.000	1.000	1.000	1.000	1.000
2	1.000	1.000	1.000	1.000	1.000	1.000	1.000	1.000	1.000	1.000	1.000	1.000	1.000
3	1.000	1.000	1.000	1.000	1.000	1.000	1.000	1.000	1.000	1.000	1.000	1.000	1.000
4	1.000	1.000	1.000	1.000	1.000	1.000	1.000	1.000	1.000	1.000	1.000	1.000	1.000
5	0.029	0.045	0.081	0.136	0.212	0.309	0.460	0.579	0.726	0.864	0.964	0.986	1.000
6	0.026	0.040	0.072	0.120	0.188	0.274	0.408	0.514	0.644	0.767	0.964	0.986	1.000
7	0.014	0.021	0.038	0.065	0.101	0.147	0.219	0.275	0.345	0.411	0.964	0.986	1.000
8	0.001	0.001	0.002	0.003	0.005	0.008	0.012	0.015	0.018	0.022	0.964	0.986	1.000
9	1.000	1.000	1.000	1.000	1.000	1.000	1.000	1.000	1.000	1.000	1.000	1.000	1.000
10	1.000	1.000	1.000	1.000	1.000	1.000	1.000	1.000	1.000	1.000	1.000	1.000	1.000
11	0.025	0.039	0.071	0.119	0.185	0.270	0.403	0.507	0.635	0.756	0.964	0.986	1.000
VG	P48	P49	P50	P51	P52	P53	P54	P55	P56	P57	P58	P59	P60
1	1.000	1.000	1.000	1.000	1.000	1.000	1.000	1.000	1.000	1.000	1.000	1.000	1.000
2	1.000	1.000	1.000	1.000	1.000	1.000	1.000	1.000	1.000	1.000	1.000	1.000	1.000
3	1.000	1.000	1.000	1.000	1.000	1.000	1.000	1.000	1.000	1.000	1.000	1.000	1.000
4	1.000	1.000	1.000	1.000	1.000	1.000	1.000	1.000	1.000	1.000	1.000	1.000	1.000
5	1.000	1.000	1.000	1.000	0.989	0.977	0.933	0.864	0.692	0.460	0.184	0.045	0.006
6	1.000	0.888	0.888	0.888	0.878	0.867	0.828	0.767	0.614	0.408	0.163	0.040	0.006
7	1.000	0.475	0.475	0.475	0.470	0.464	0.443	0.411	0.329	0.219	0.087	0.021	0.003
8	1.000	0.025	0.025	0.025	0.025	0.024	0.023	0.022	0.017	0.012	0.005	0.001	0.000
9	1.000	1.000	1.000	1.000	1.000	1.000	1.000	1.000	1.000	1.000	1.000	1.000	1.000
10	1.000	1.000	1.000	1.000	1.000	1.000	1.000	1.000	1.000	1.000	1.000	1.000	1.000
11	1.000	0.875	0.875	0.875	0.866	0.855	0.817	0.756	0.605	0.403	0.161	0.039	0.005



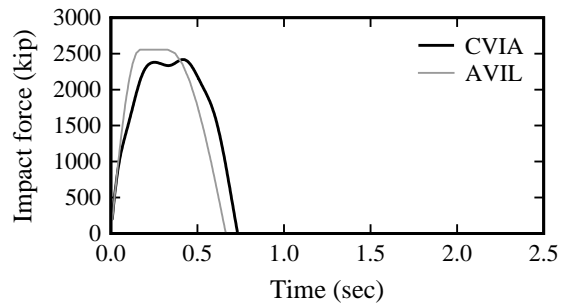
a) VG 1



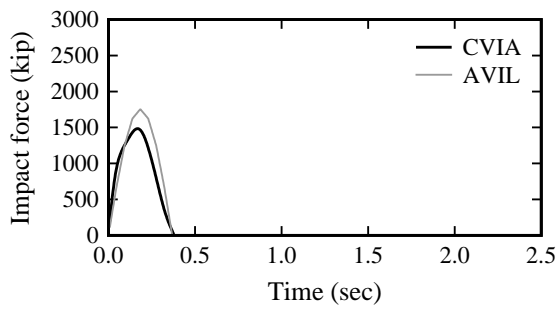
b) VG 2



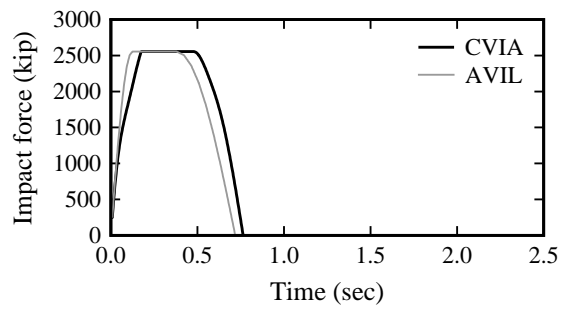
c) VG 3



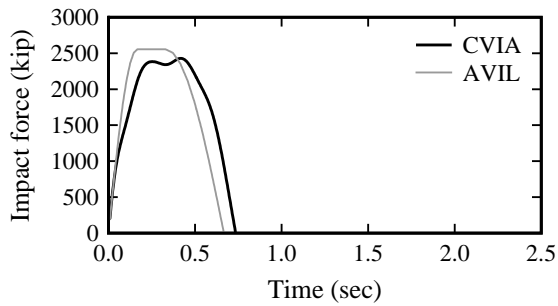
d) VG 4



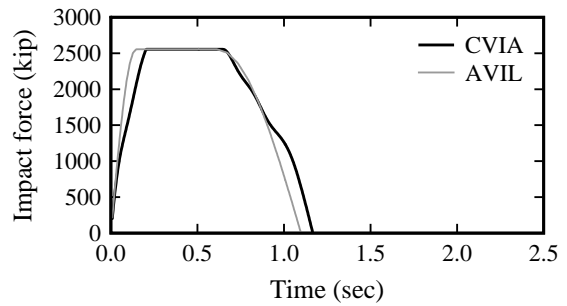
e) VG 5



f) VG 6

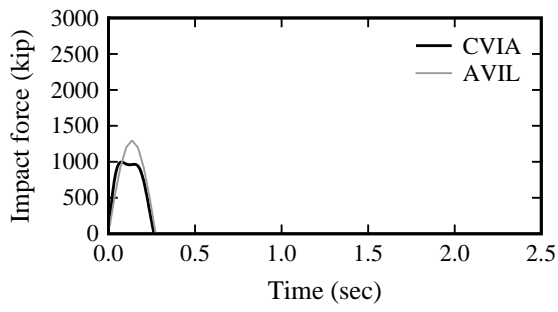


g) VG 7

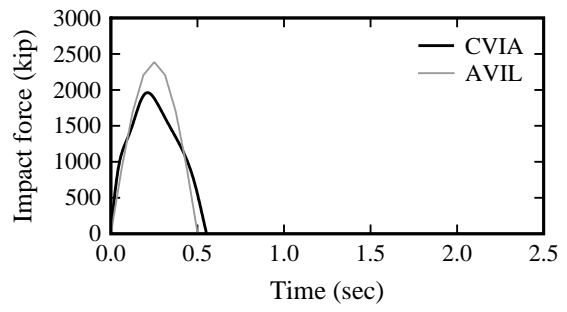


h) VG 8

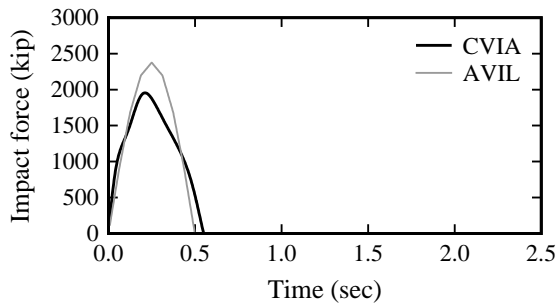
Figure M.1 Impact force-time histories: SR-300 Bridge, Pier 35



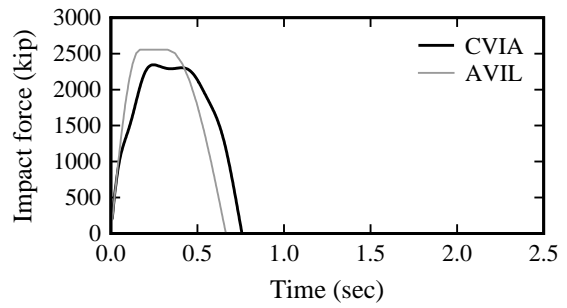
a) VG 1



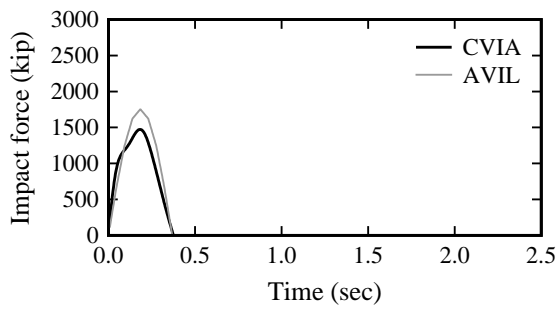
b) VG 2



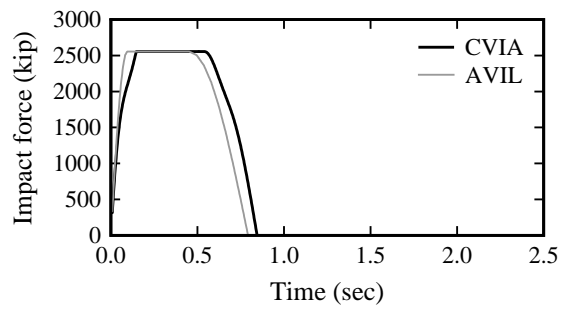
c) VG 3



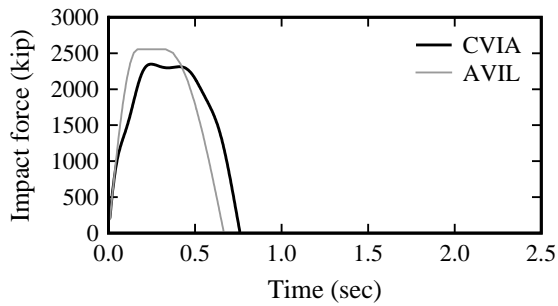
d) VG 4



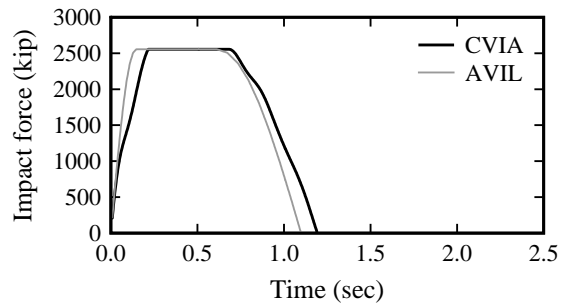
e) VG 5



f) VG 6

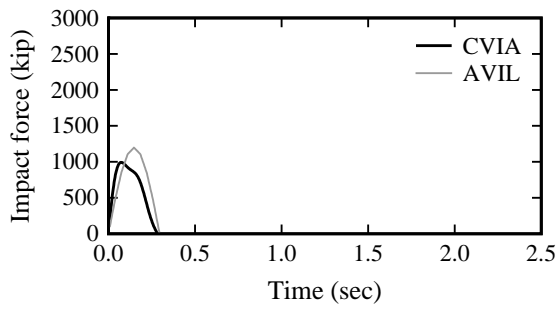


g) VG 7

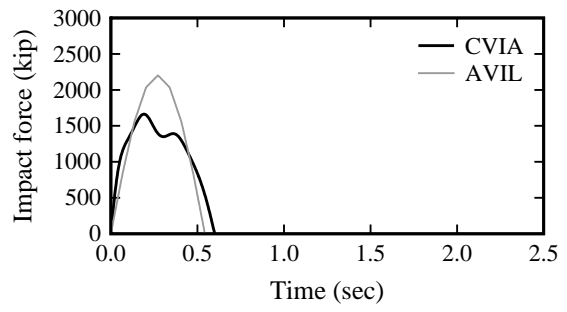


h) VG 8

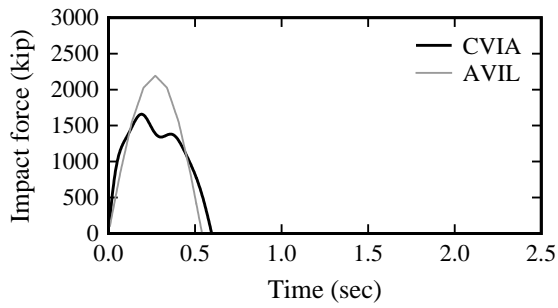
Figure M.2 Impact force-time histories: SR-300 Bridge, Pier 36



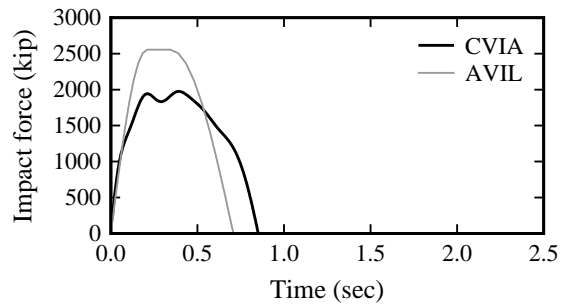
a) VG 1



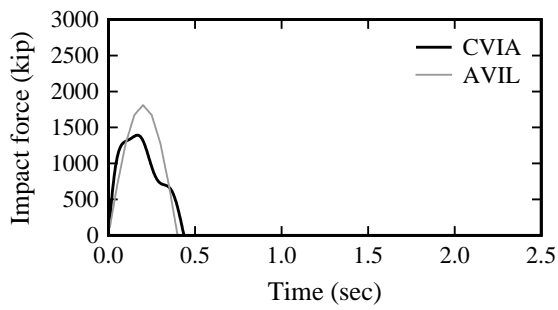
b) VG 2



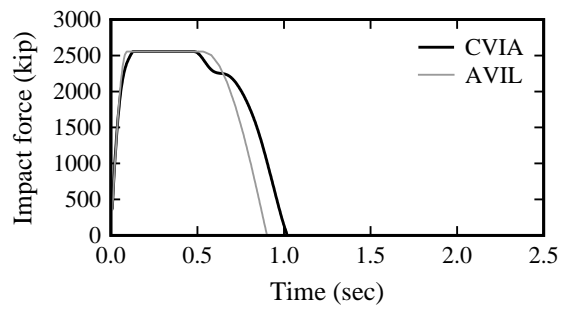
c) VG 3



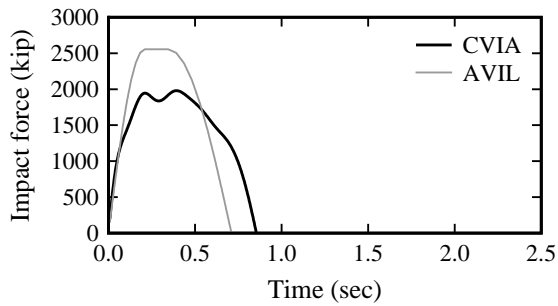
d) VG 4



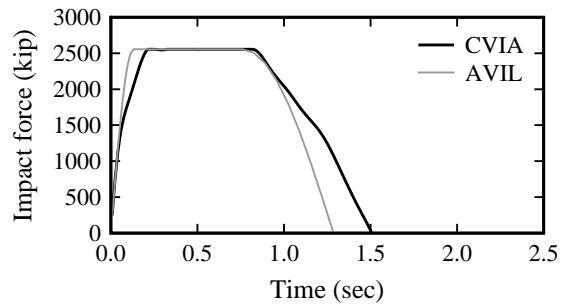
e) VG 5



f) VG 6

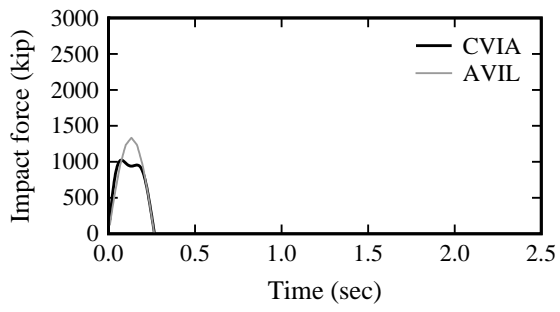


g) VG 7

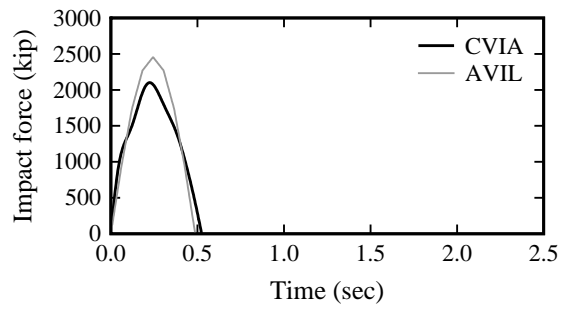


h) VG 8

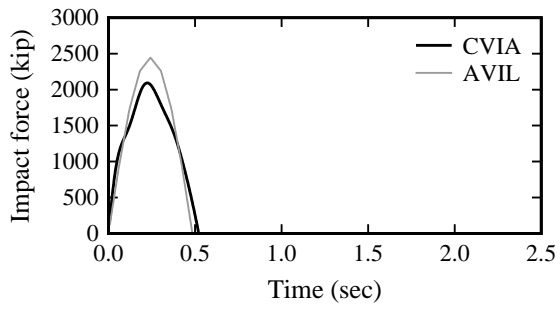
Figure M.3 Impact force-time histories: SR-300 Bridge, Pier 37



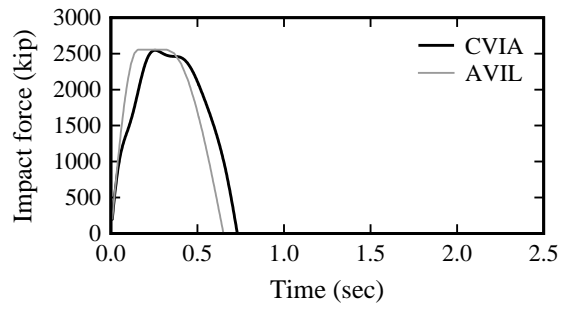
a) VG 1



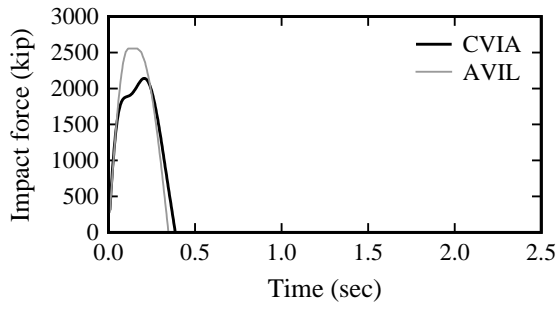
b) VG 2



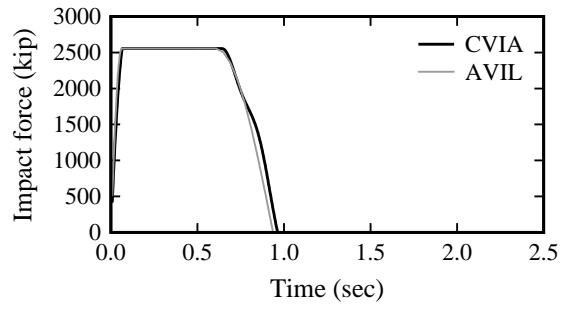
c) VG 3



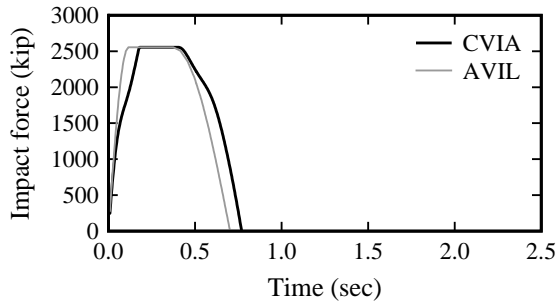
d) VG 4



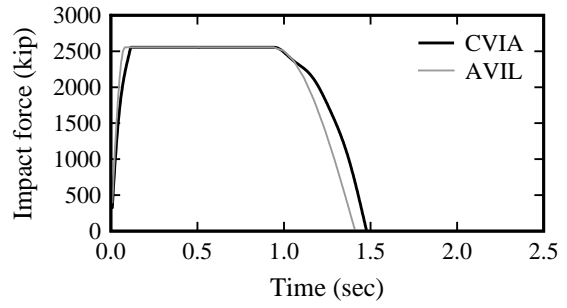
e) VG 5



f) VG 6

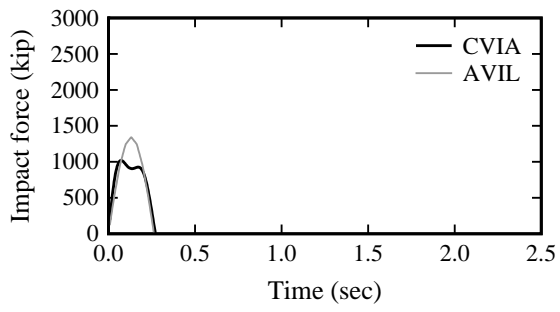


g) VG 7

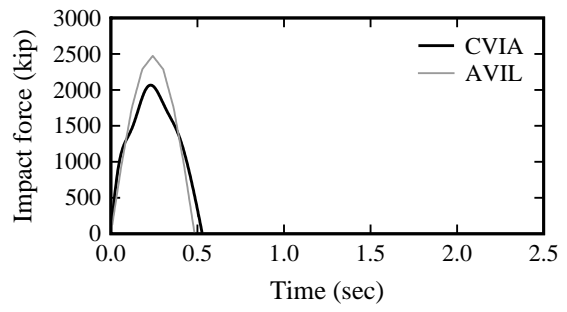


h) VG 8

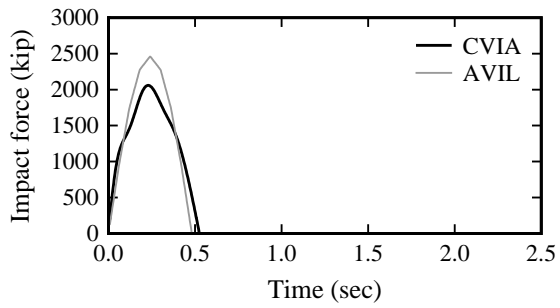
Figure M.4 Impact force-time histories: SR-300 Bridge, Pier 38



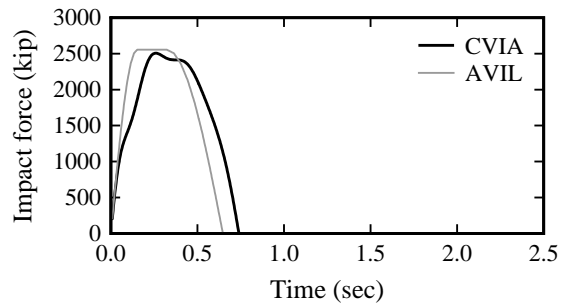
a) VG 1



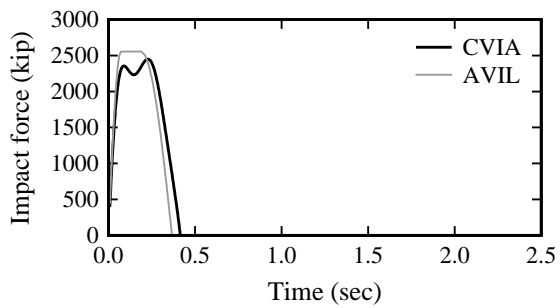
b) VG 2



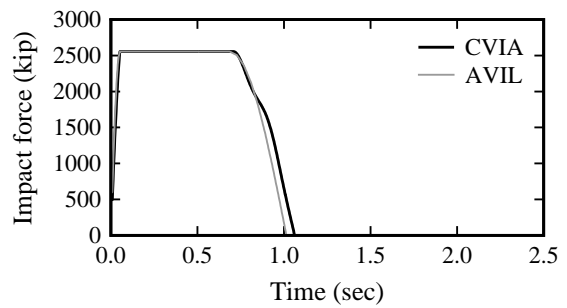
c) VG 3



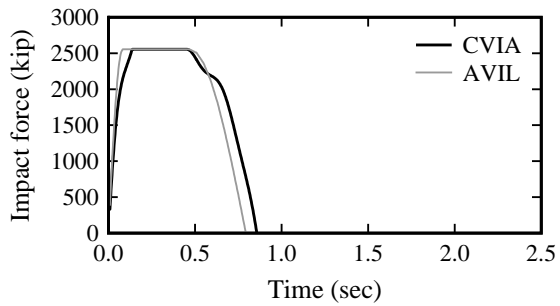
d) VG 4



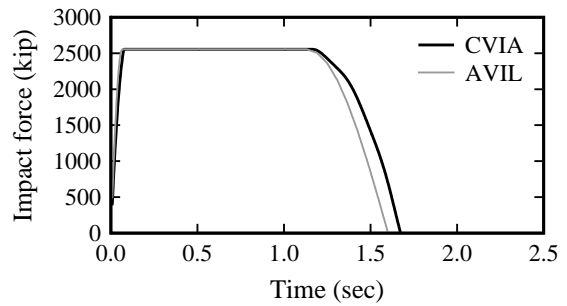
e) VG 5



f) VG 6

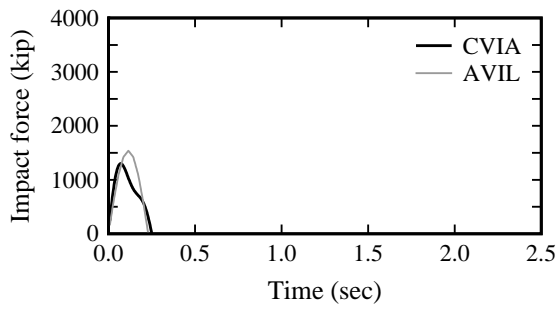


g) VG 7

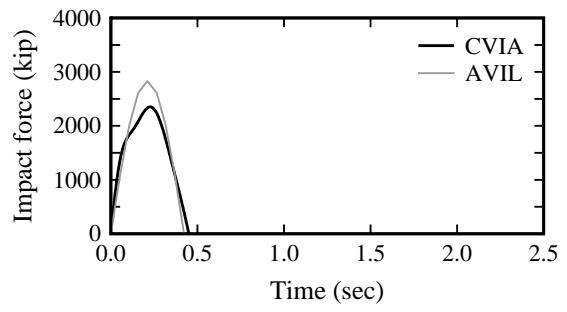


h) VG 8

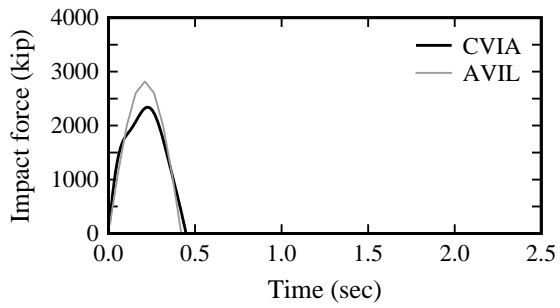
Figure M.5 Impact force-time histories: SR-300 Bridge, Pier 39



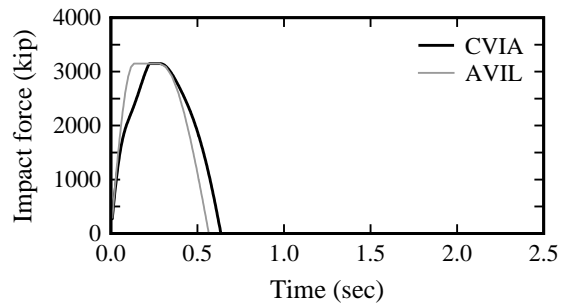
a) VG 1



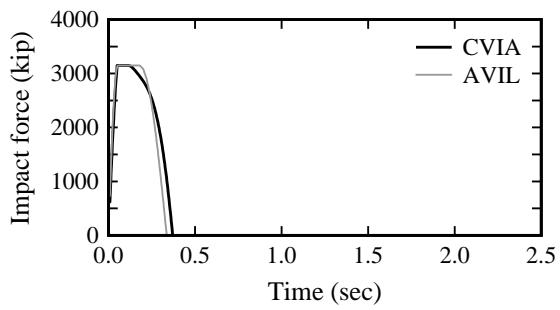
b) VG 2



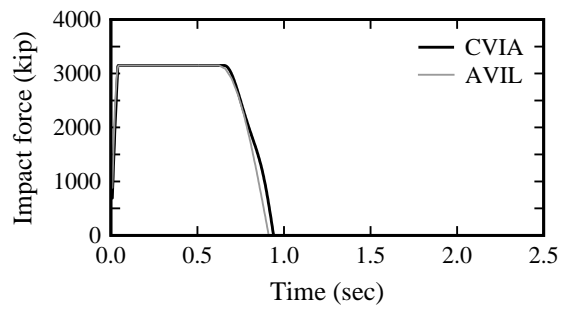
c) VG 3



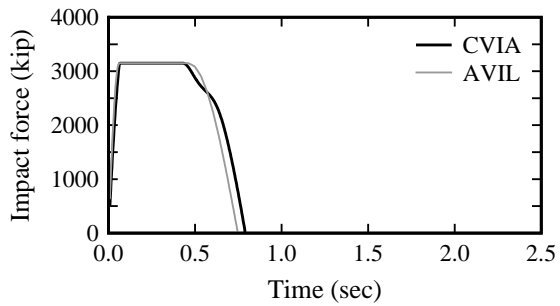
d) VG 4



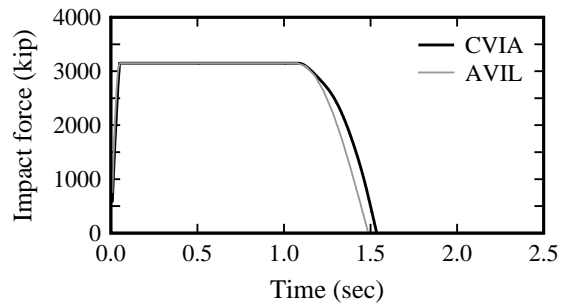
e) VG 5



f) VG 6

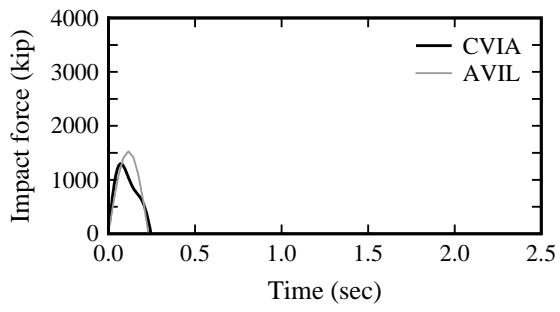


g) VG 7

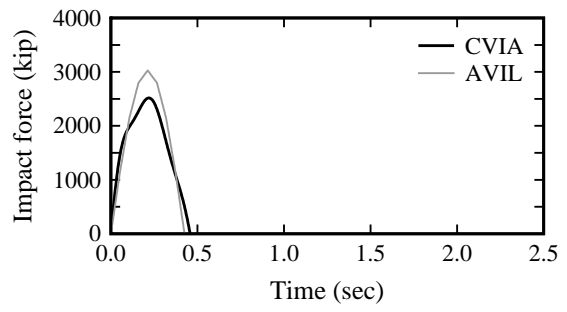


h) VG 8

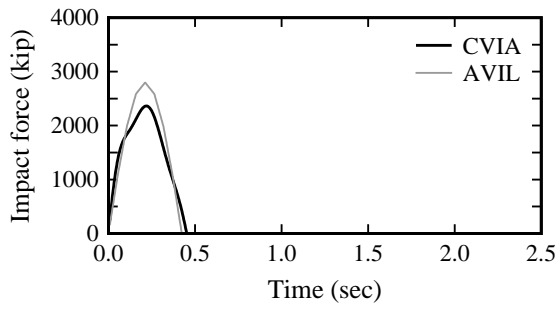
Figure M.6 Impact force-time histories: SR-300 Bridge, Pier 40



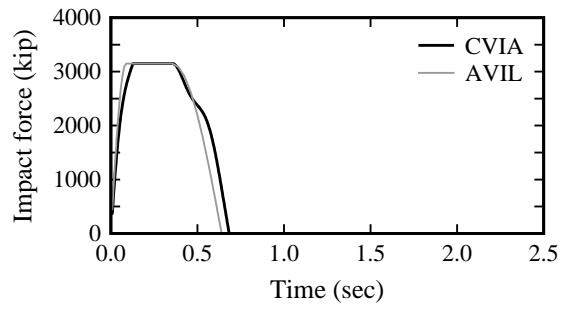
a) VG 1



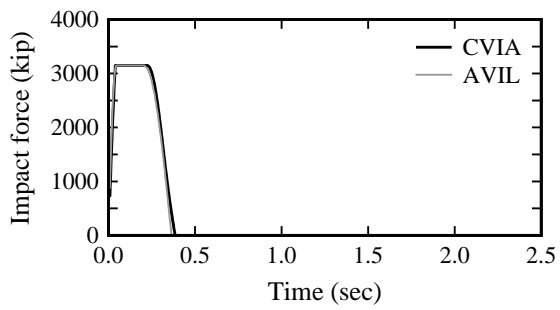
b) VG 2



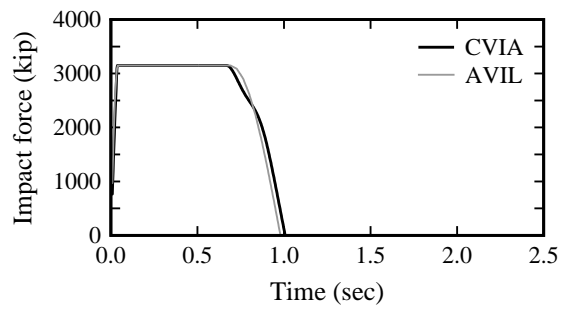
c) VG 3



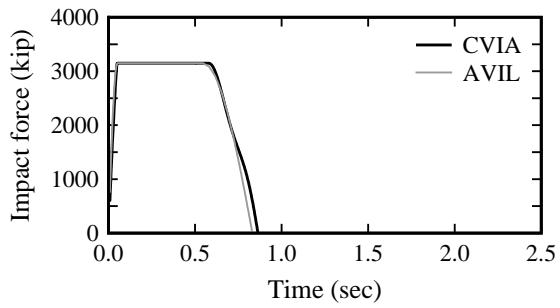
d) VG 4



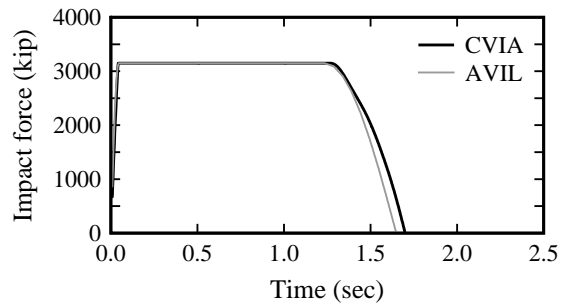
e) VG 5



f) VG 6

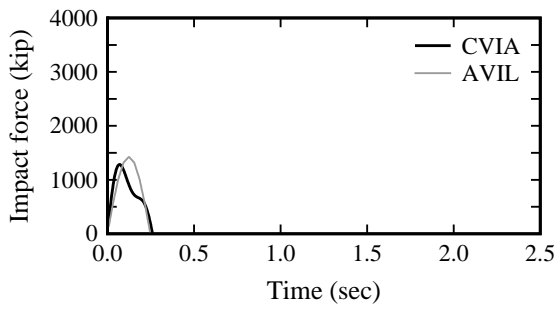


g) VG 7

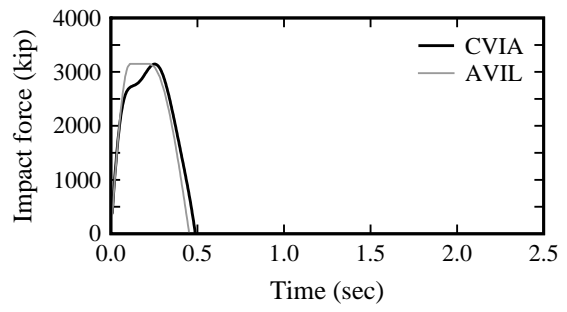


h) VG 8

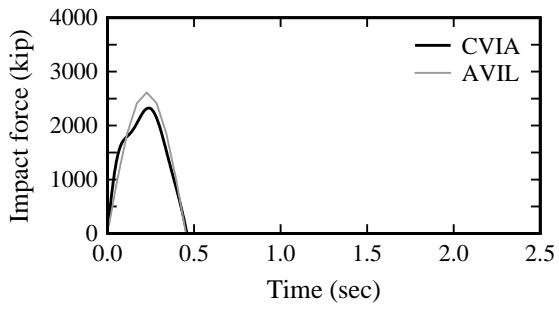
Figure M.7 Impact force-time histories: SR-300 Bridge, Pier 41



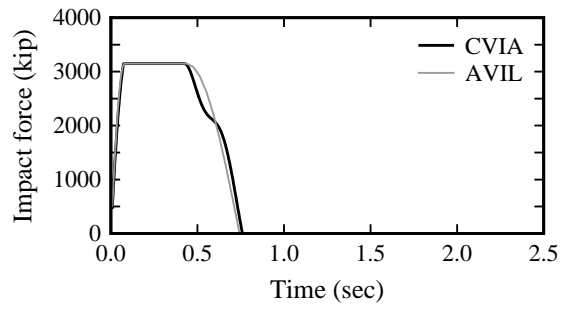
a) VG 1



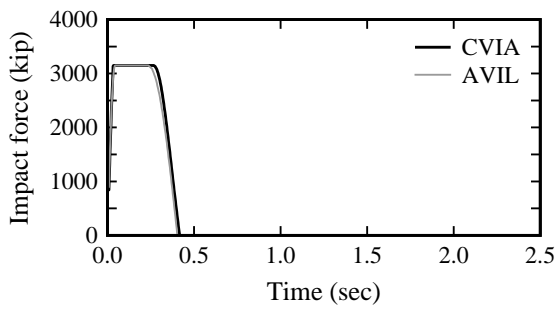
b) VG 2



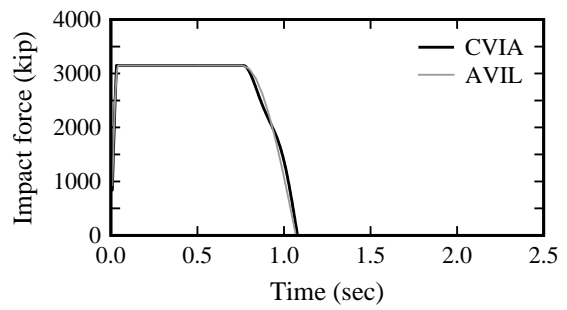
c) VG 3



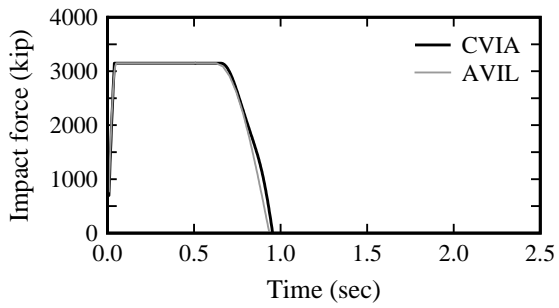
d) VG 4



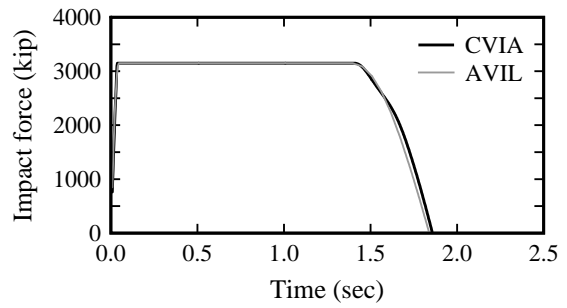
e) VG 5



f) VG 6

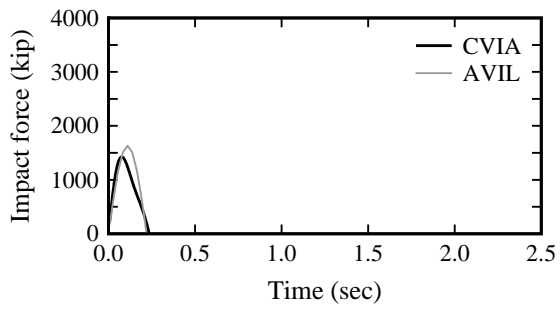


g) VG 7

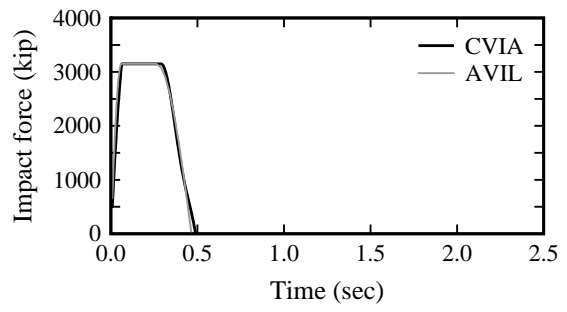


h) VG 8

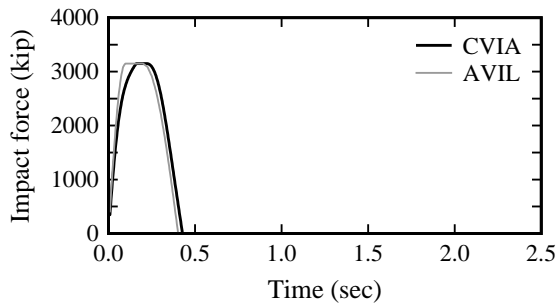
Figure M.8 Impact force-time histories: SR-300 Bridge, Pier 42



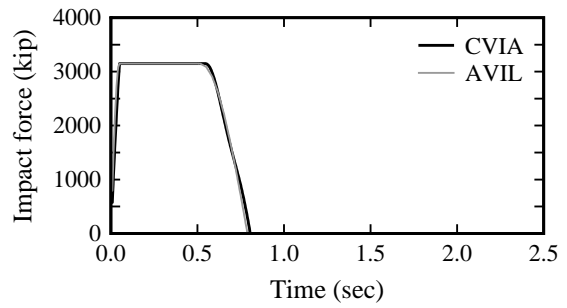
a) VG 1



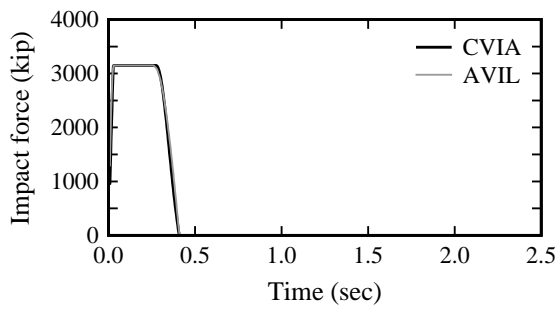
b) VG 2



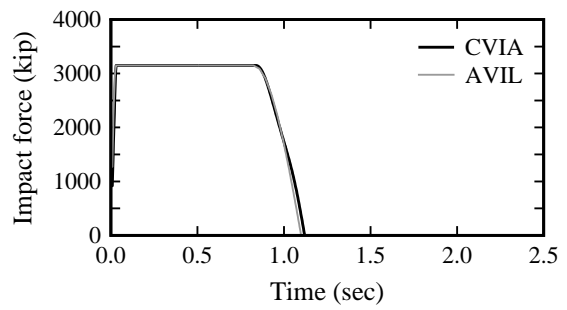
c) VG 3



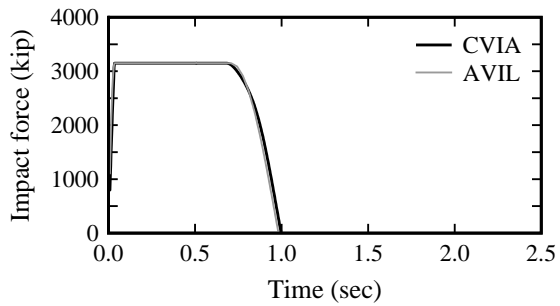
d) VG 4



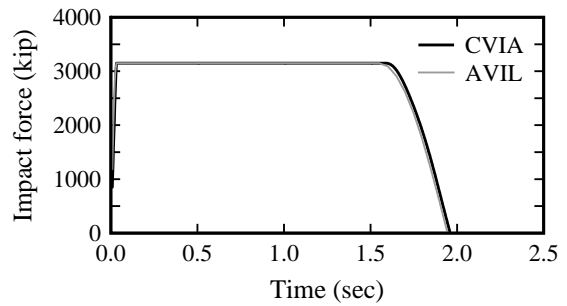
e) VG 5



f) VG 6

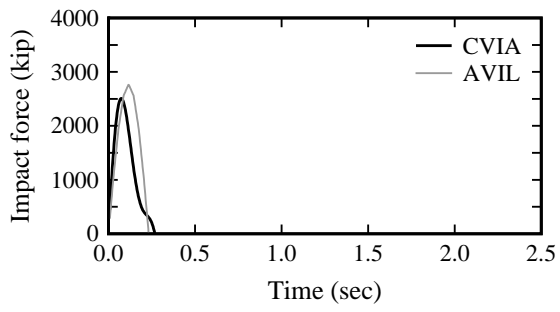


g) VG 7

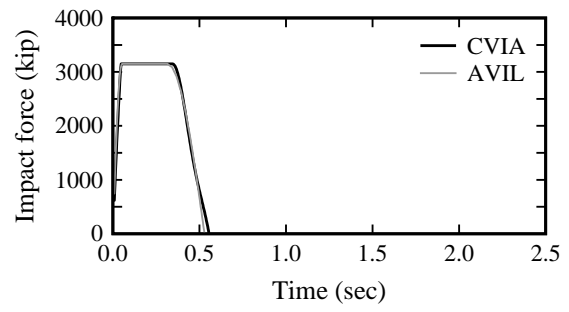


h) VG 8

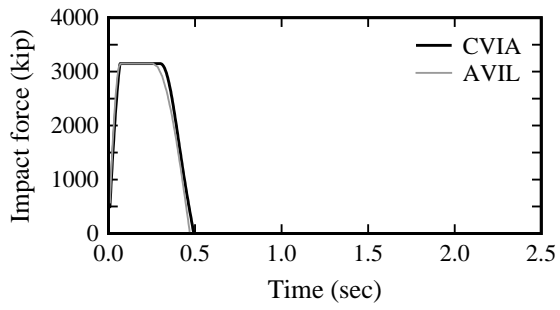
Figure M.9 Impact force-time histories: SR-300 Bridge, Pier 43



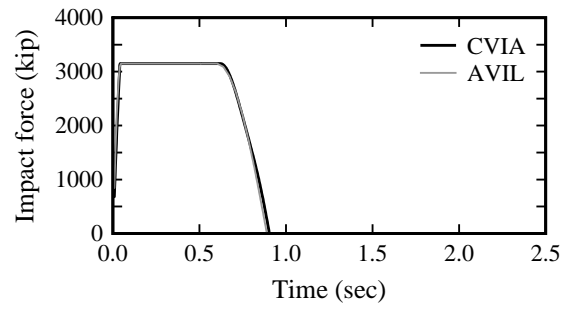
a) VG 1



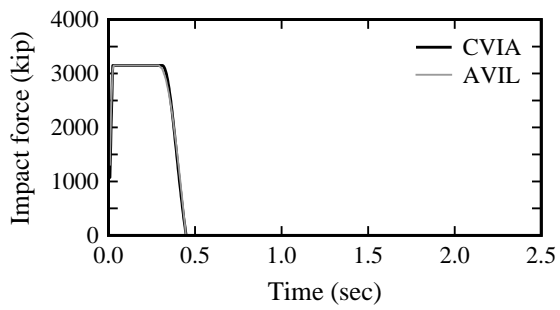
b) VG 2



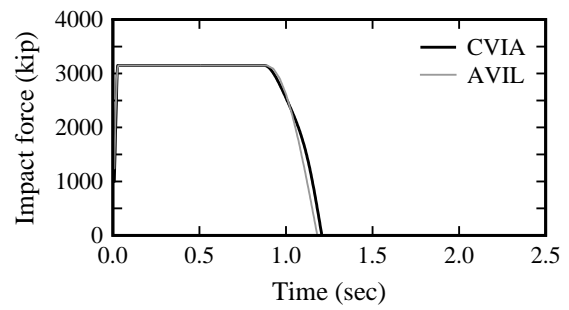
c) VG 3



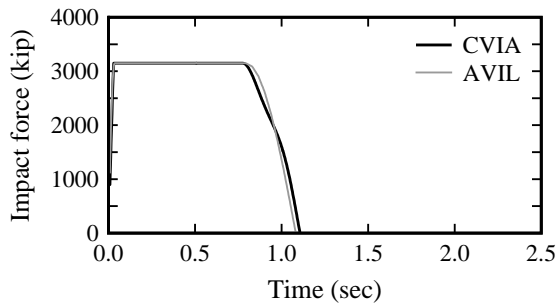
d) VG 4



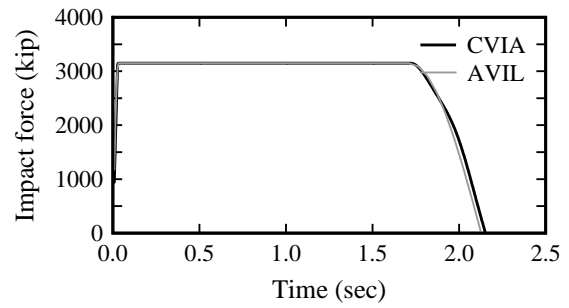
e) VG 5



f) VG 6

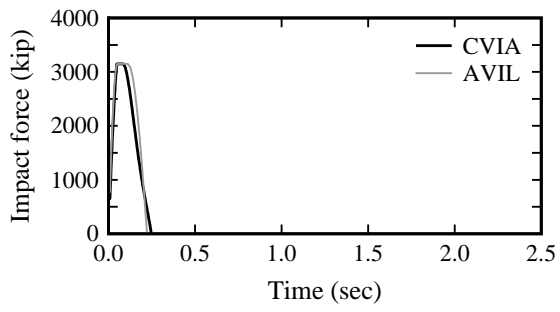


g) VG 7

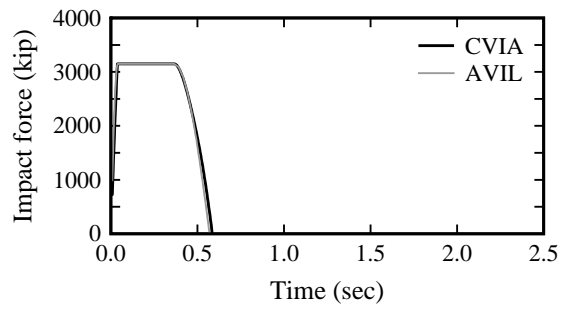


h) VG 8

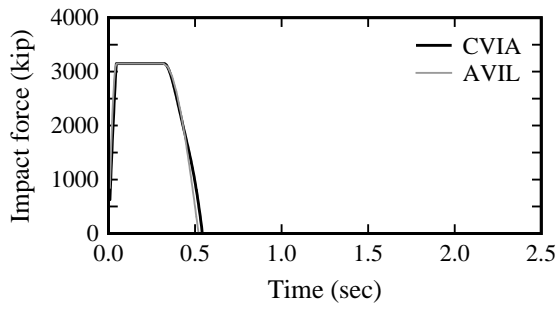
Figure M.10 Impact force-time histories: SR-300 Bridge, Pier 44



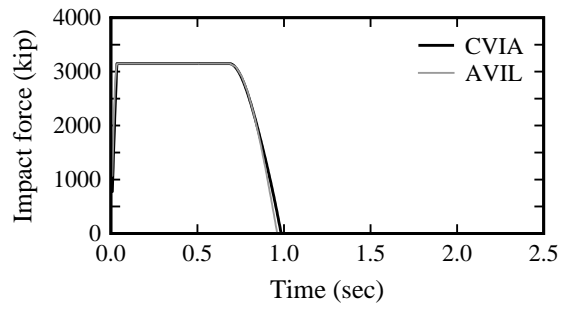
a) VG 1



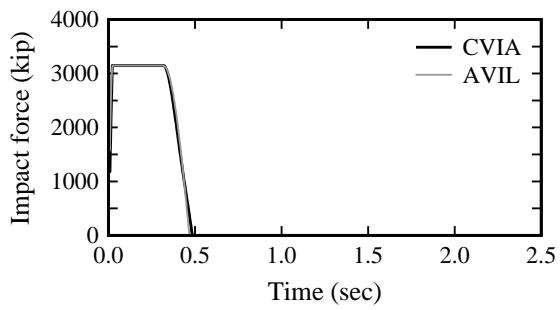
b) VG 2



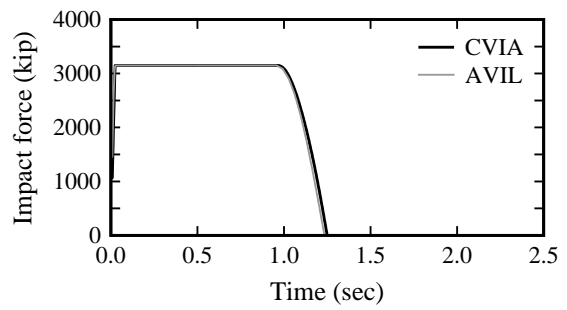
c) VG 3



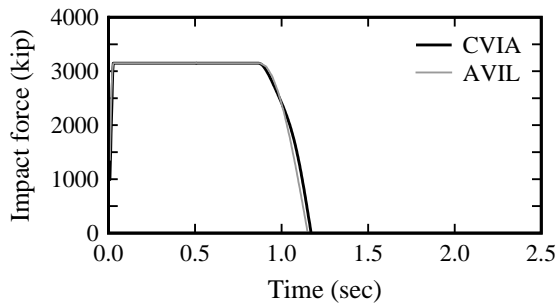
d) VG 4



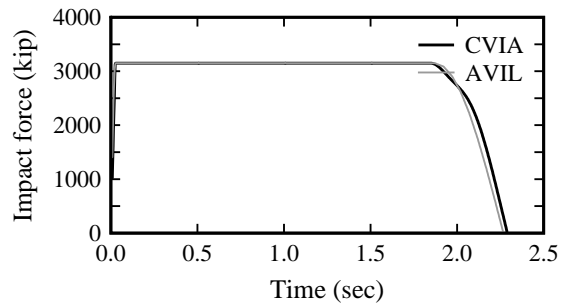
e) VG 5



f) VG 6

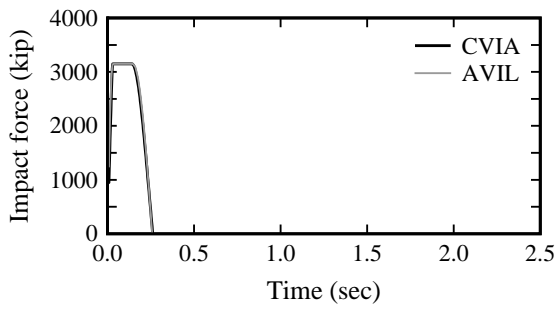


g) VG 7

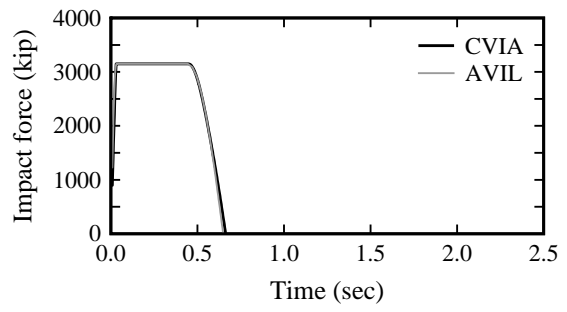


h) VG 8

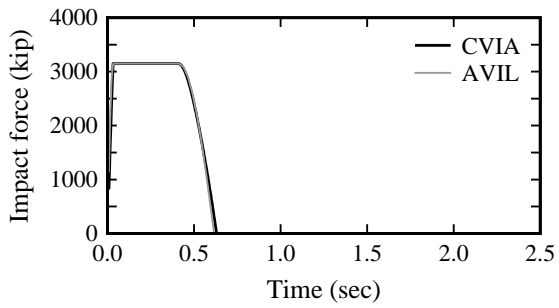
Figure M.11 Impact force-time histories: SR-300 Bridge, Pier 45



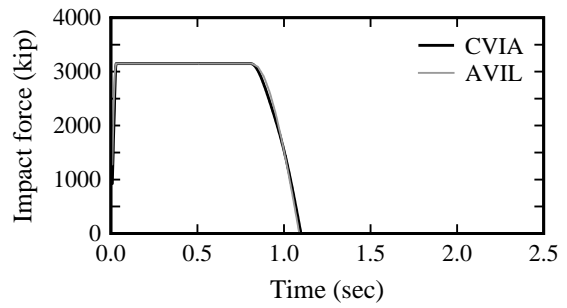
a) VG 1



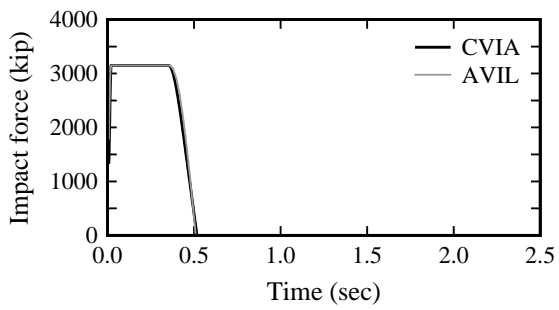
b) VG 2



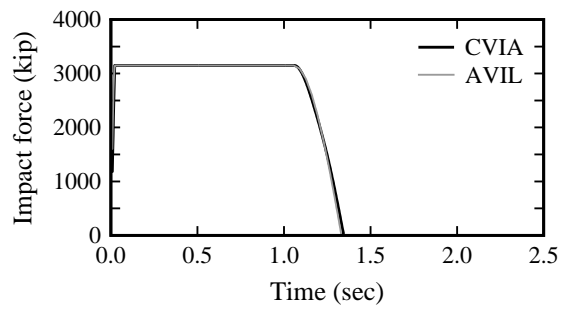
c) VG 3



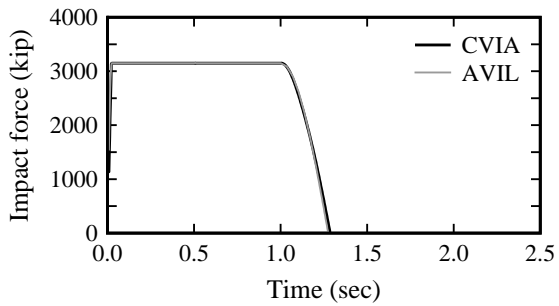
d) VG 4



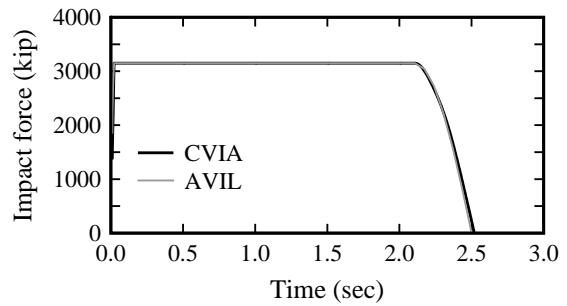
e) VG 5



f) VG 6

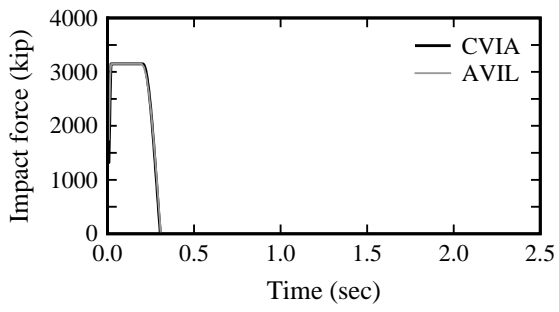


g) VG 7

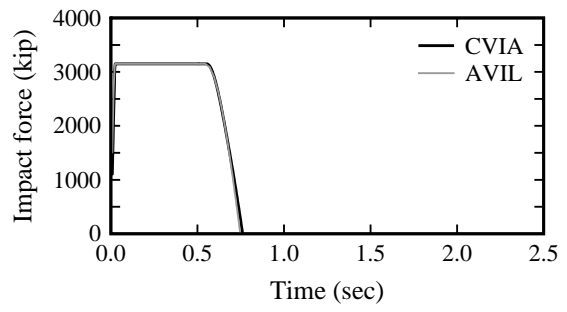


h) VG 8

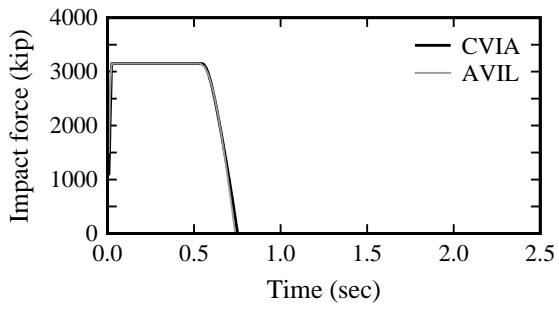
Figure M.12 Impact force-time histories: SR-300 Bridge, Pier 46



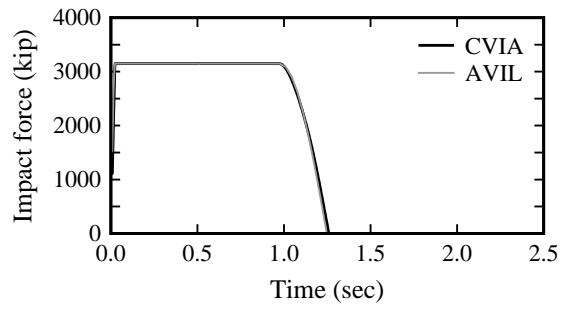
a) VG 1



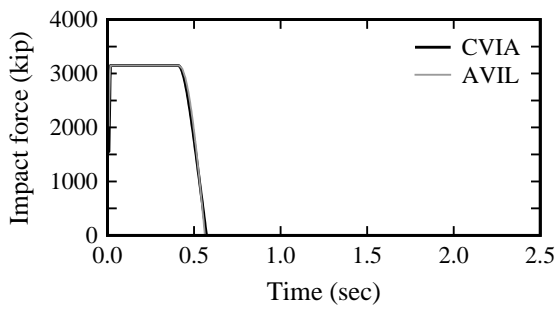
b) VG 2



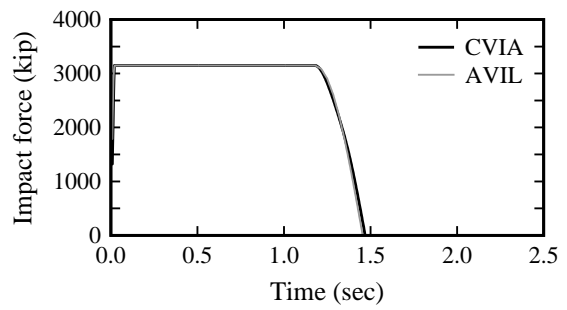
c) VG 3



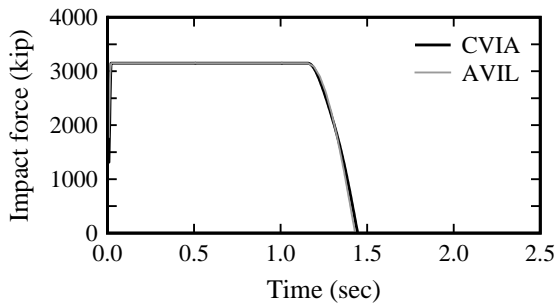
d) VG 4



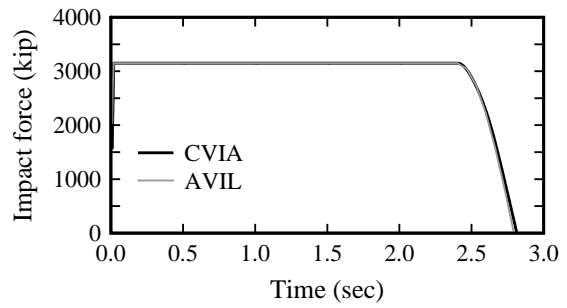
e) VG 5



f) VG 6

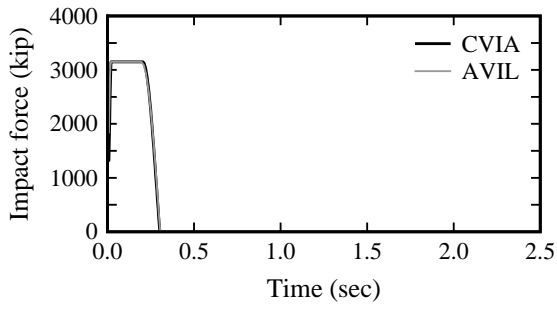


g) VG 7

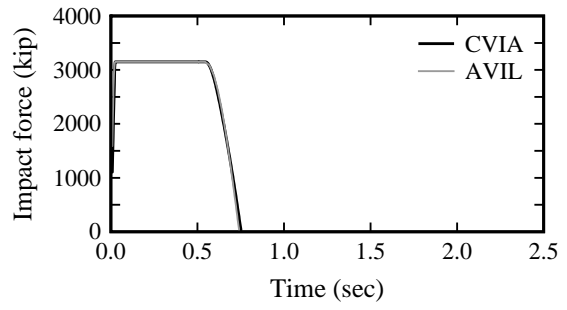


h) VG 8

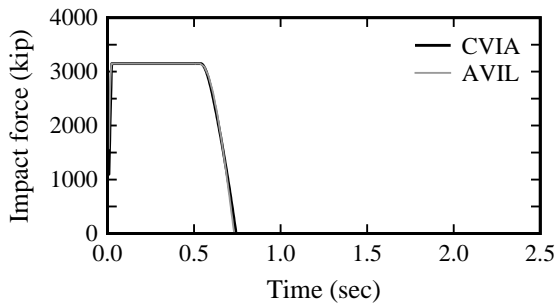
Figure M.13 Impact force-time histories: SR-300 Bridge, Pier 47



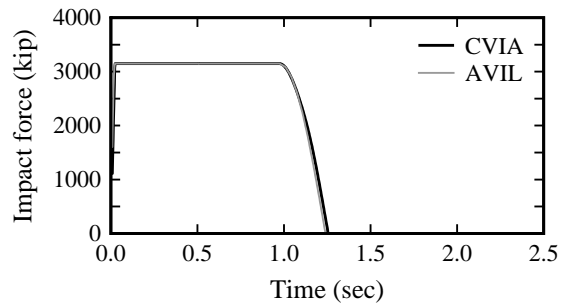
a) VG 1



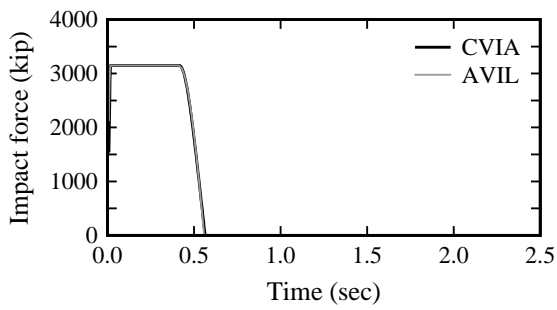
b) VG 2



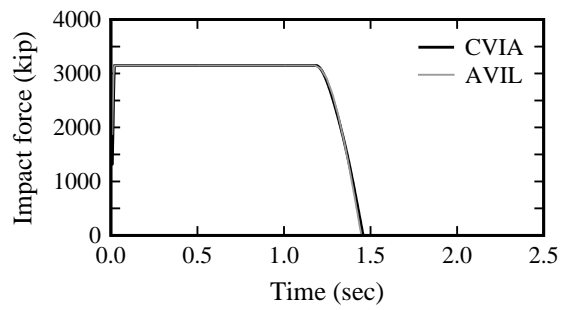
c) VG 3



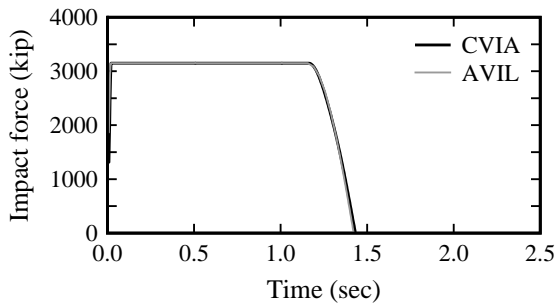
d) VG 4



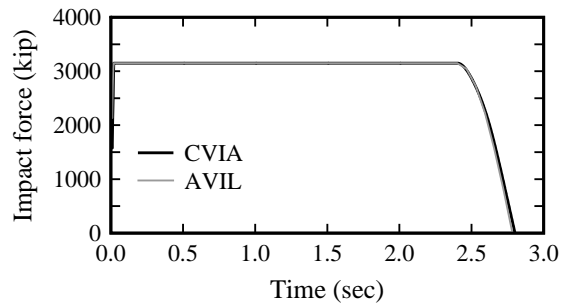
e) VG 5



f) VG 6

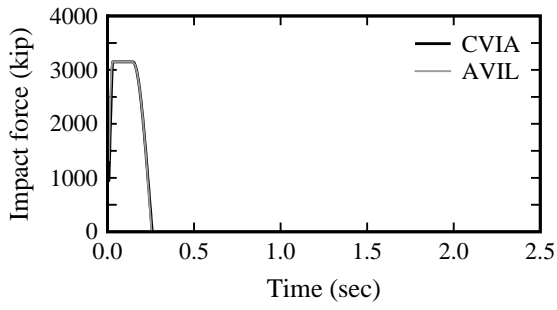


g) VG 7

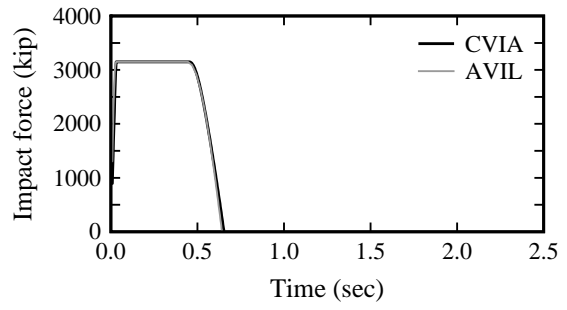


h) VG 8

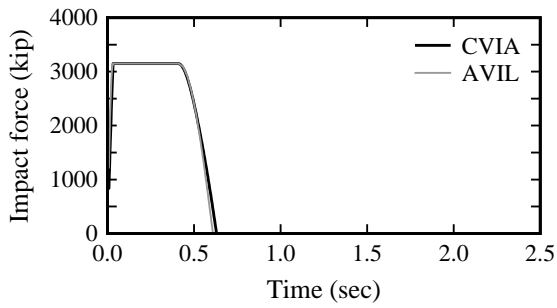
Figure M.14 Impact force-time histories: SR-300 Bridge, Pier 48



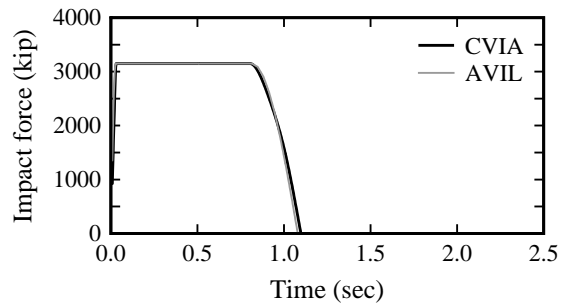
a) VG 1



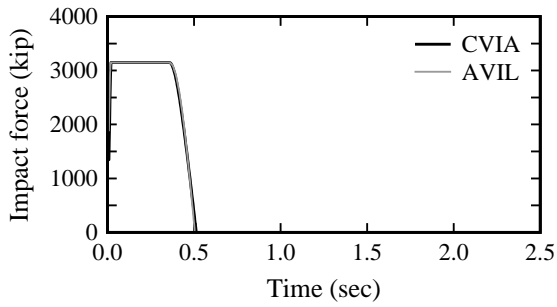
b) VG 2



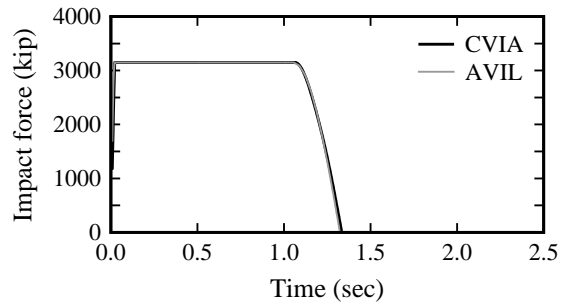
c) VG 3



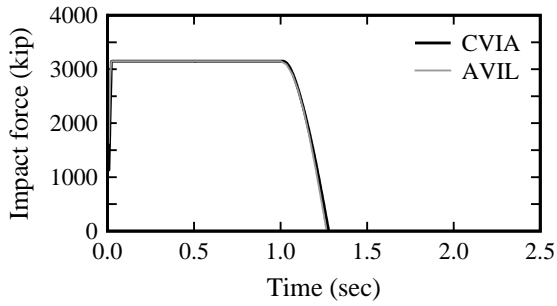
d) VG 4



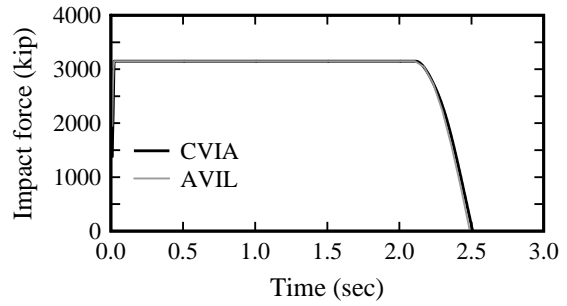
e) VG 5



f) VG 6

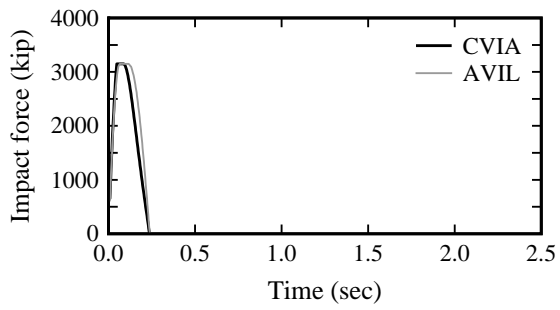


g) VG 7

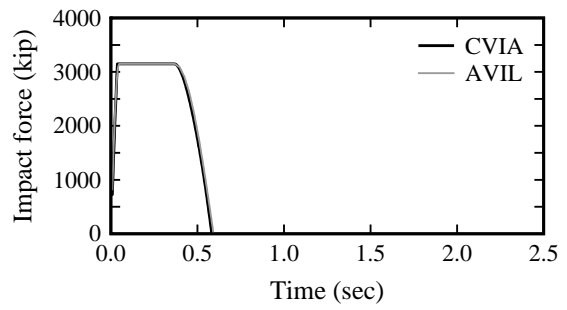


h) VG 8

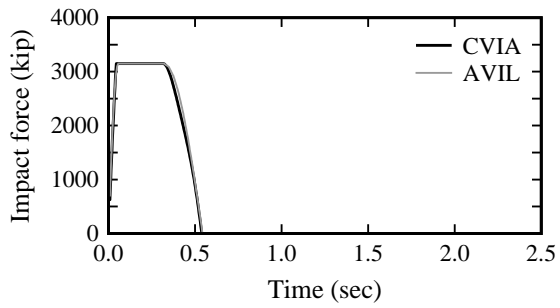
Figure M.15 Impact force-time histories: SR-300 Bridge, Pier 49



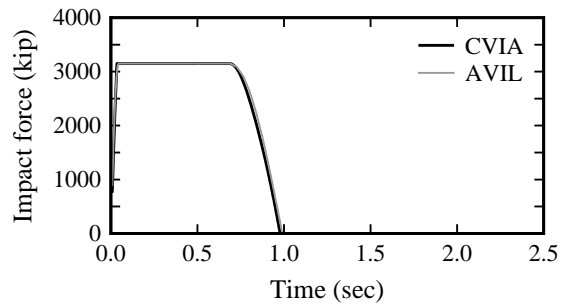
a) VG 1



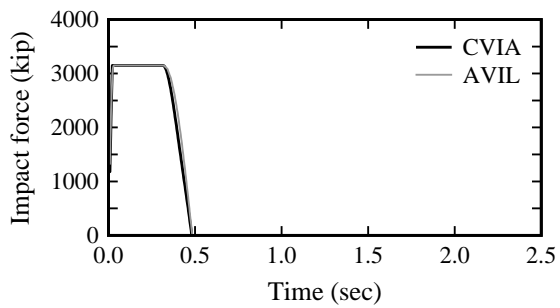
b) VG 2



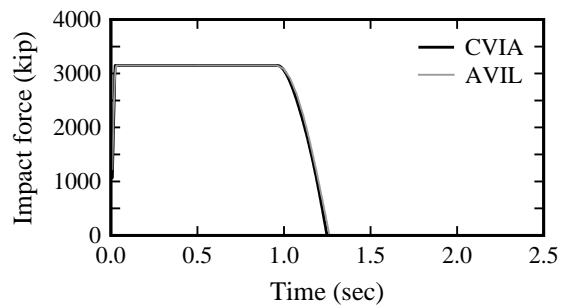
c) VG 3



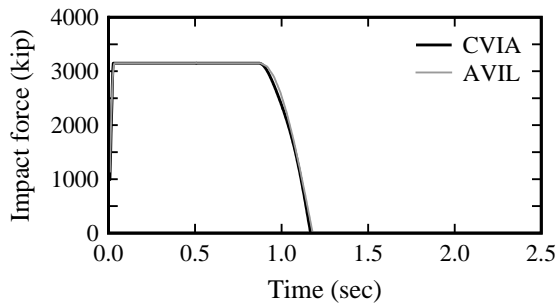
d) VG 4



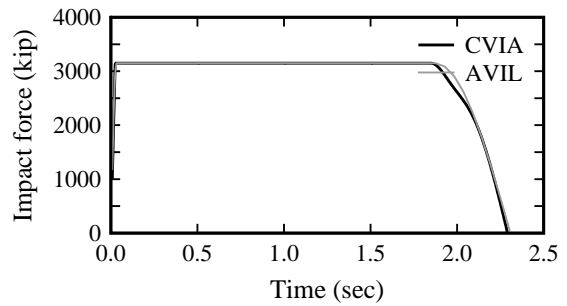
e) VG 5



f) VG 6

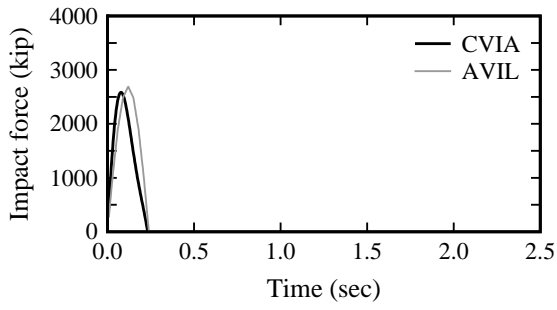


g) VG 7

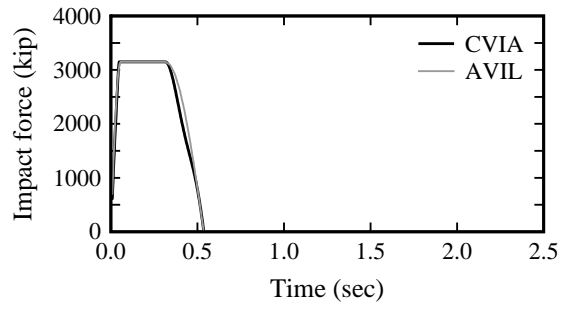


h) VG 8

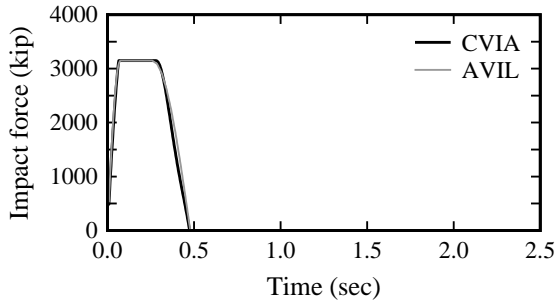
Figure M.16 Impact force-time histories: SR-300 Bridge, Pier 50



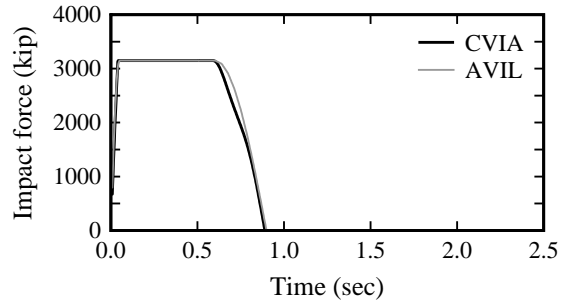
a) VG 1



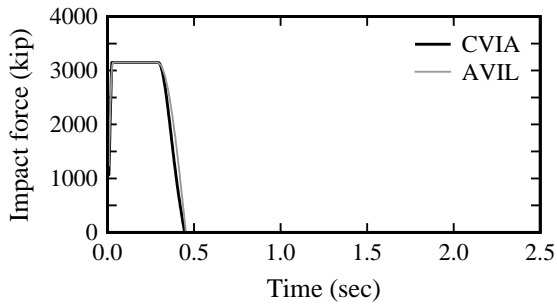
b) VG 2



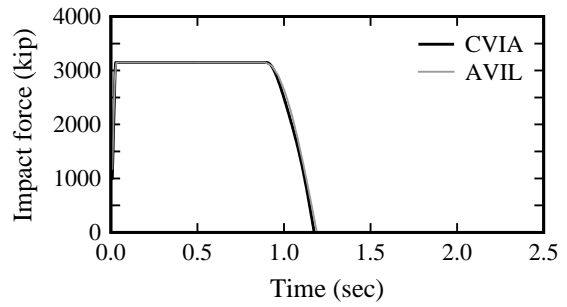
c) VG 3



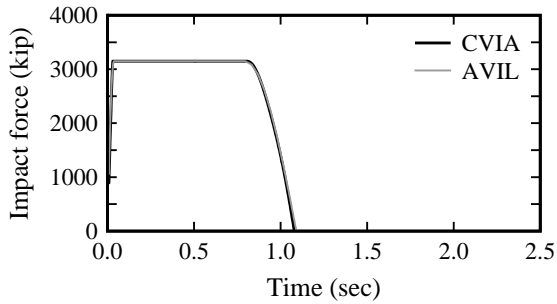
d) VG 4



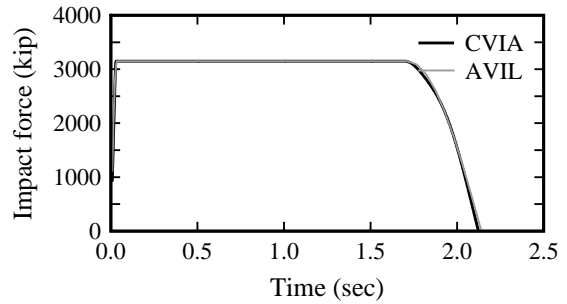
e) VG 5



f) VG 6

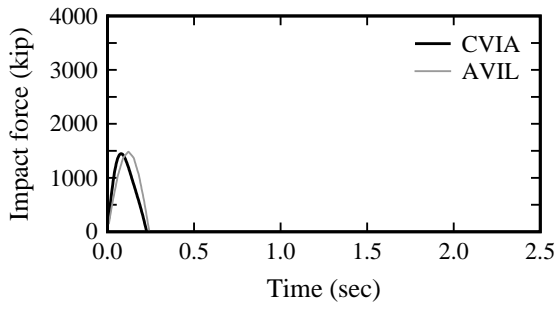


g) VG 7

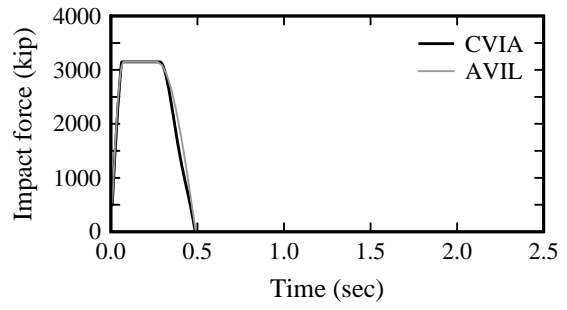


h) VG 8

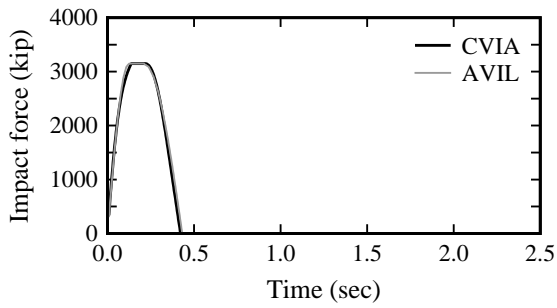
Figure M.17 Impact force-time histories: SR-300 Bridge, Pier 51



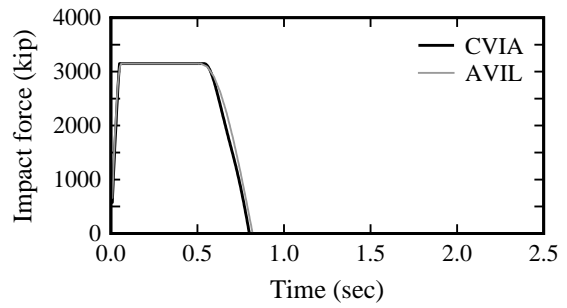
a) VG 1



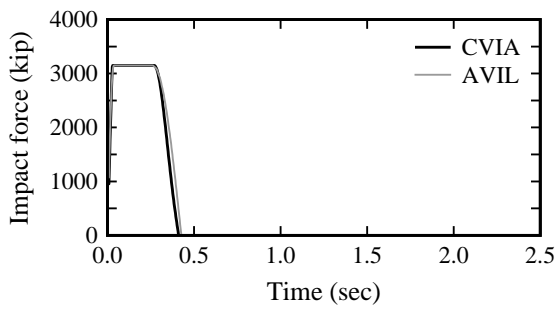
b) VG 2



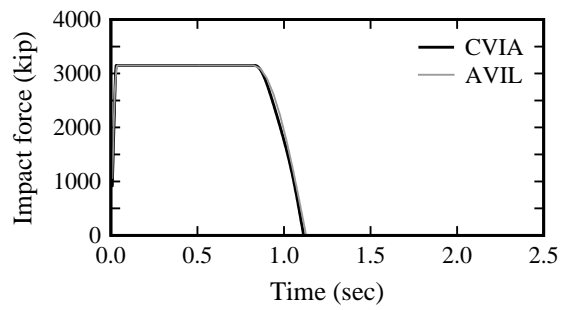
c) VG 3



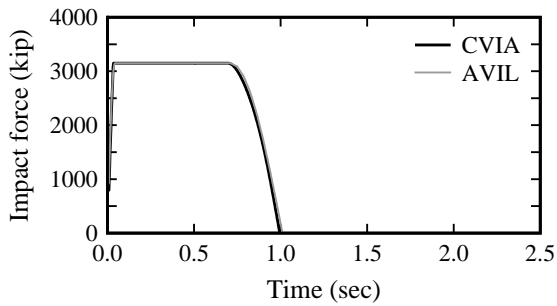
d) VG 4



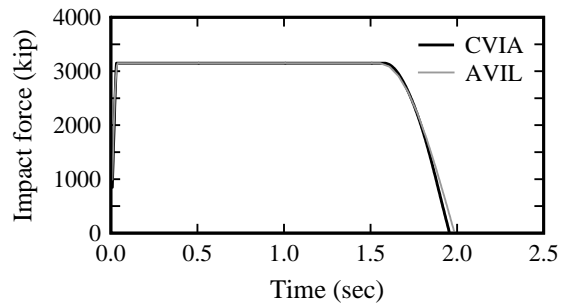
e) VG 5



f) VG 6

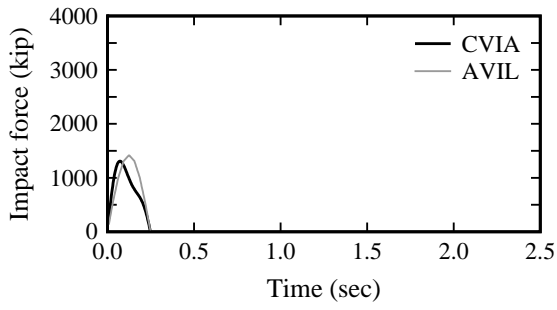


g) VG 7

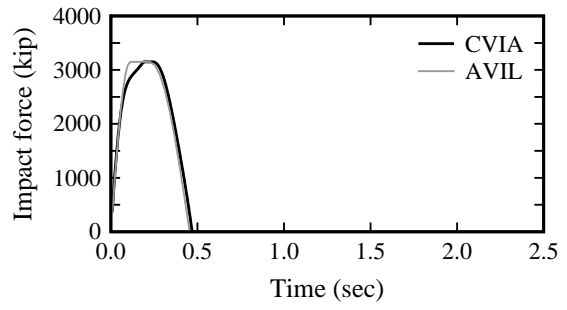


h) VG 8

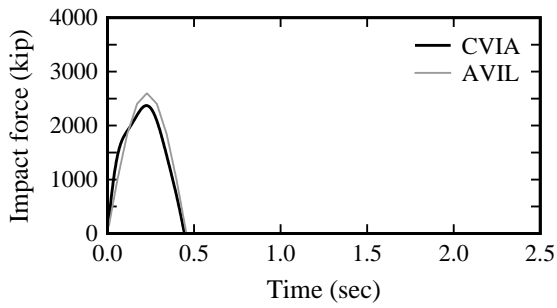
Figure M.18 Impact force-time histories: SR-300 Bridge, Pier 52



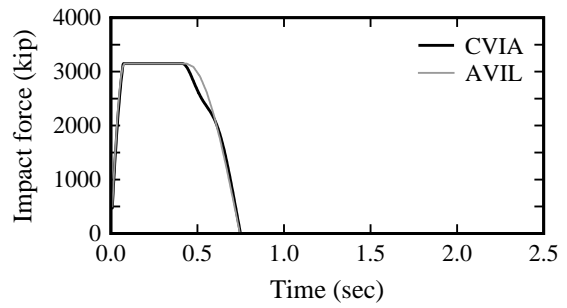
a) VG 1



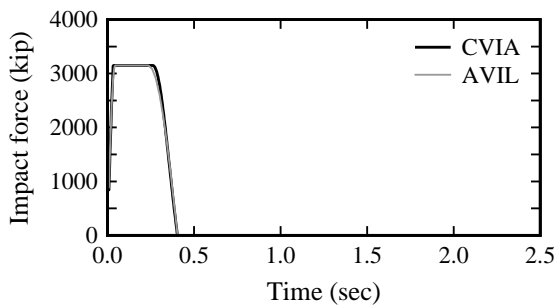
b) VG 2



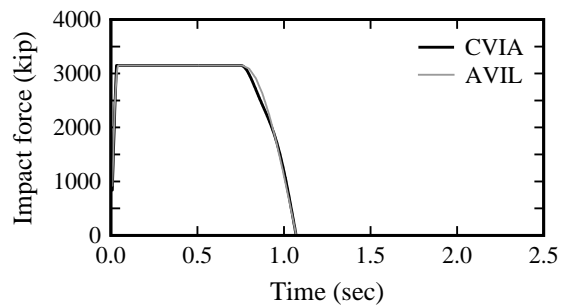
c) VG 3



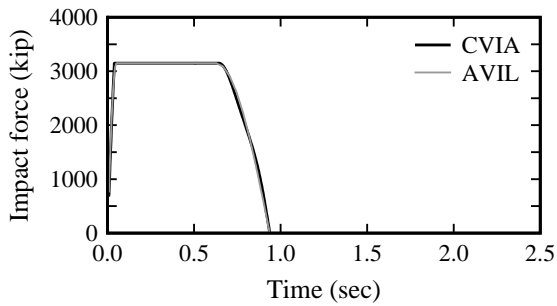
d) VG 4



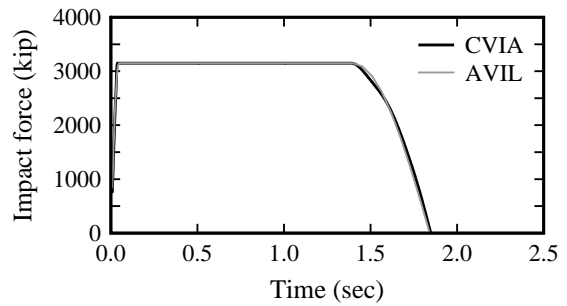
e) VG 5



f) VG 6

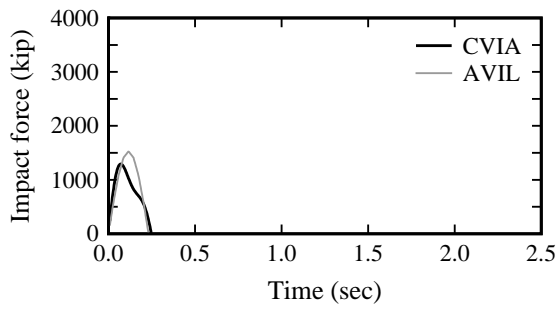


g) VG 7

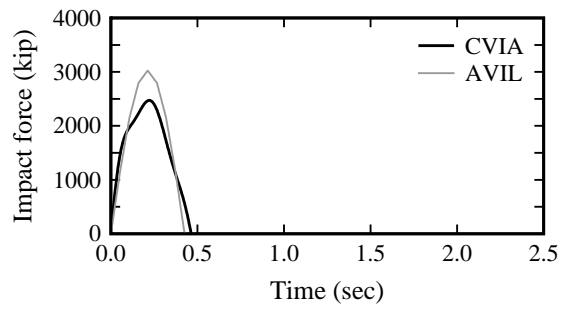


h) VG 8

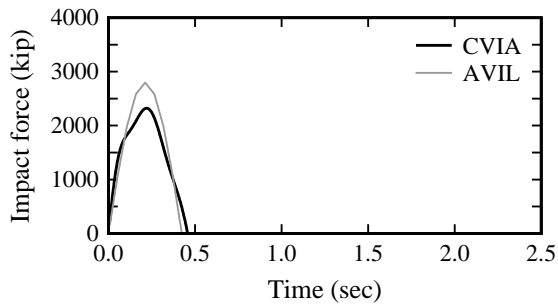
Figure M.19 Impact force-time histories: SR-300 Bridge, Pier 53



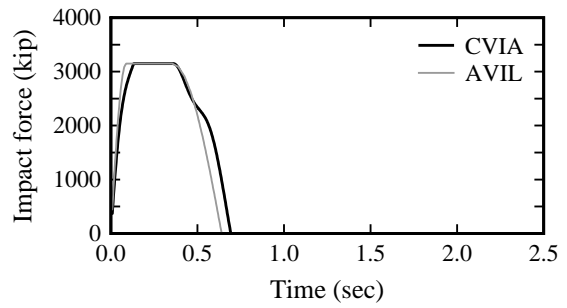
a) VG 1



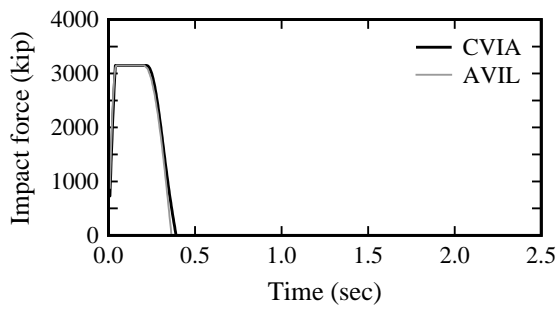
b) VG 2



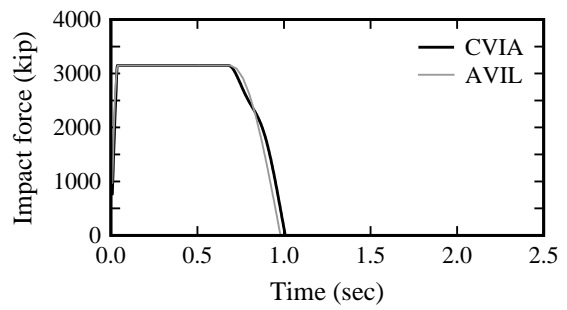
c) VG 3



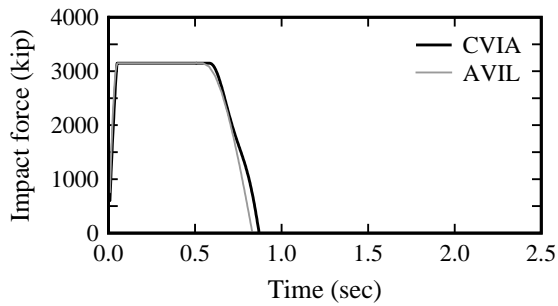
d) VG 4



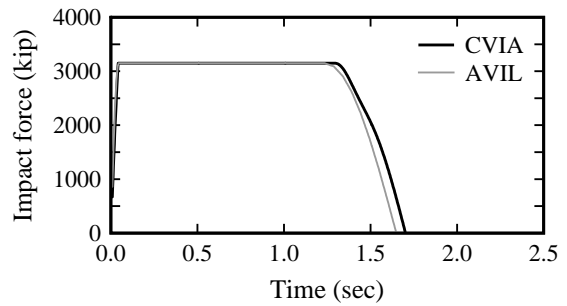
e) VG 5



f) VG 6

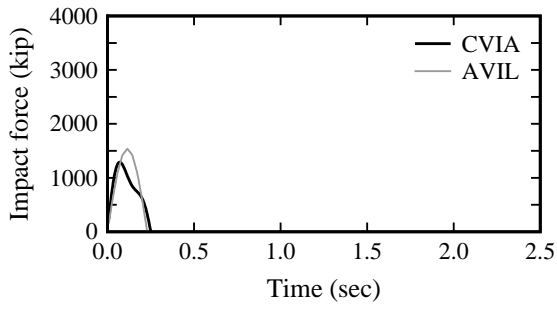


g) VG 7

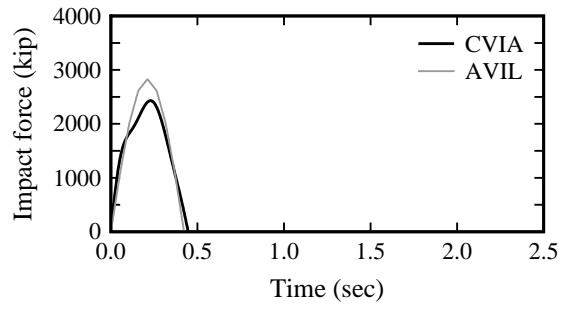


h) VG 8

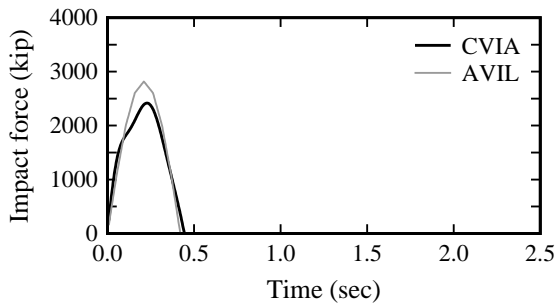
Figure M.20 Impact force-time histories: SR-300 Bridge, Pier 54



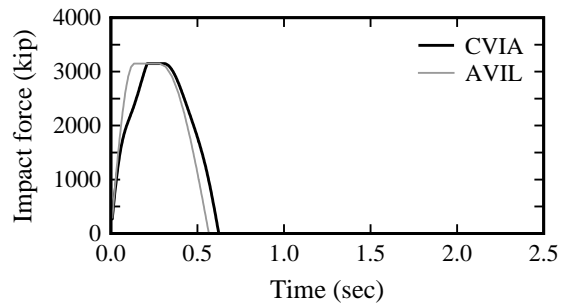
a) VG 1



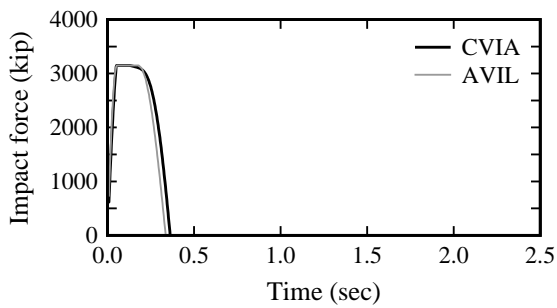
b) VG 2



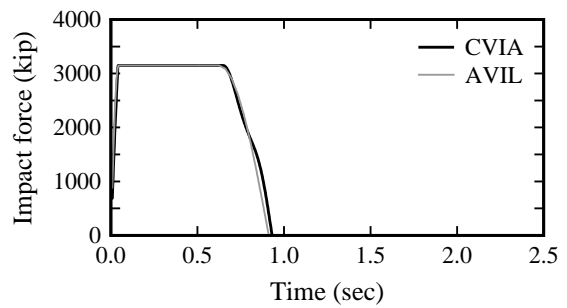
c) VG 3



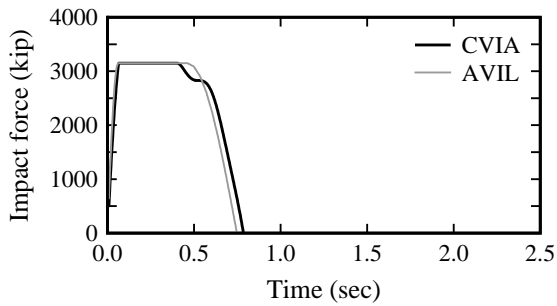
d) VG 4



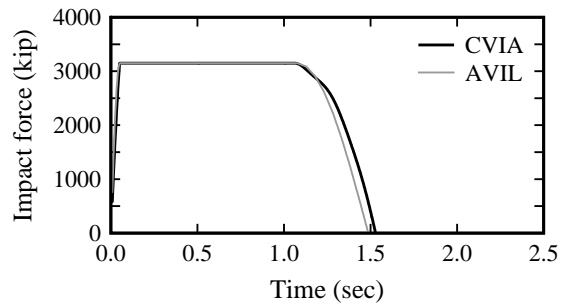
e) VG 5



f) VG 6

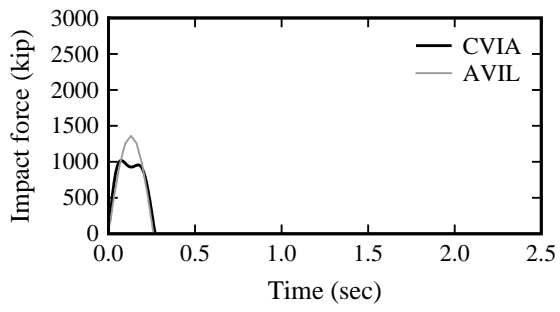


g) VG 7

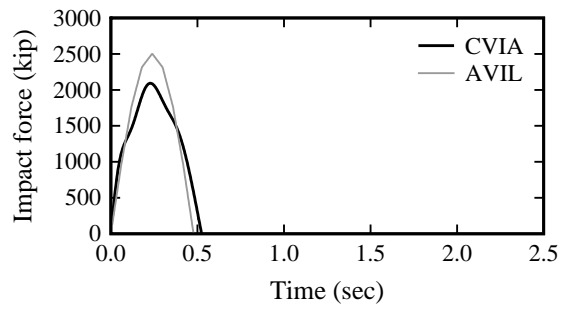


h) VG 8

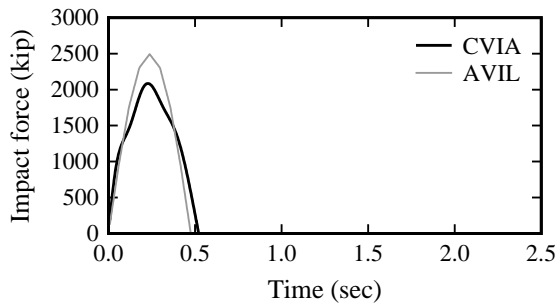
Figure M.21 Impact force-time histories: SR-300 Bridge, Pier 55



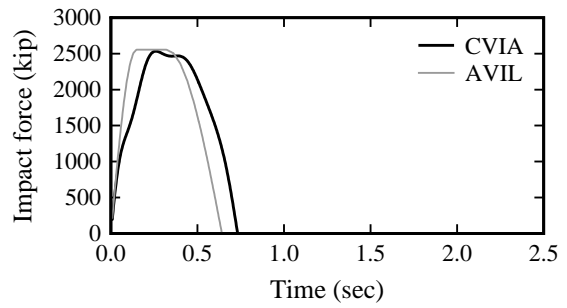
a) VG 1



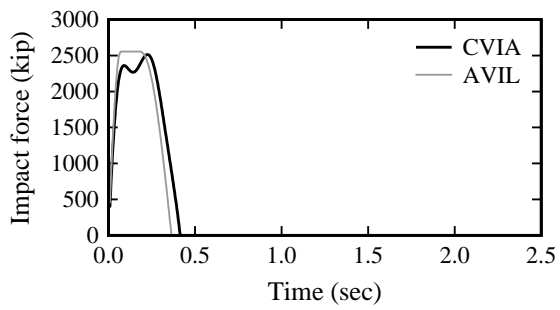
b) VG 2



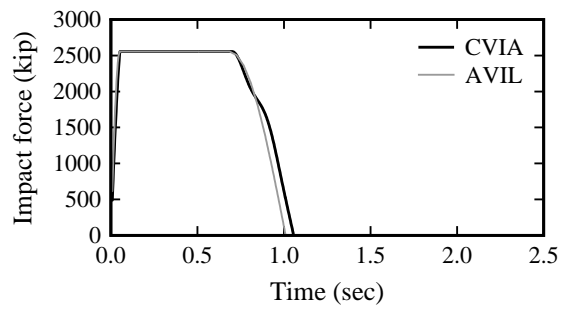
c) VG 3



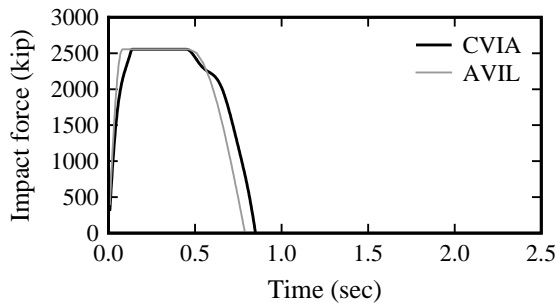
d) VG 4



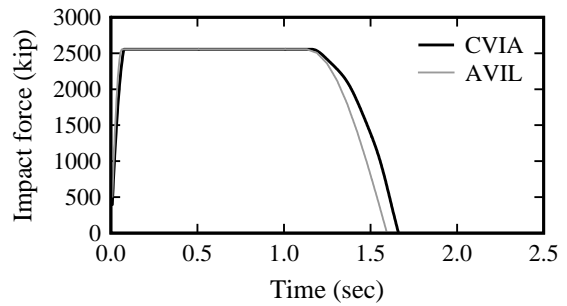
e) VG 5



f) VG 6

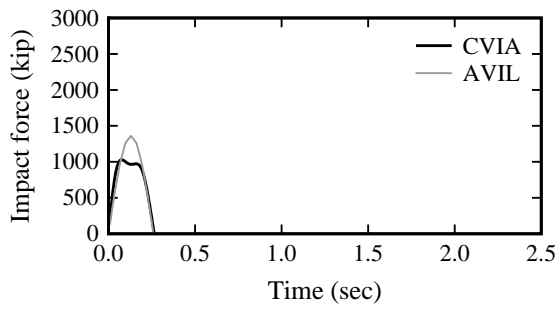


g) VG 7

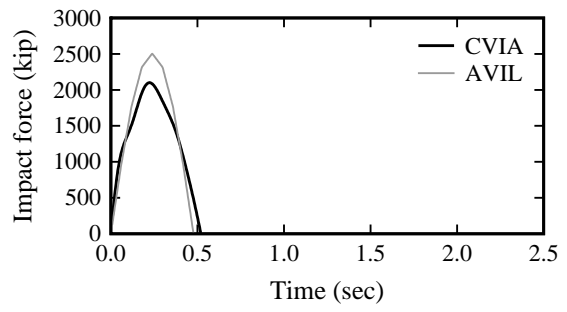


h) VG 8

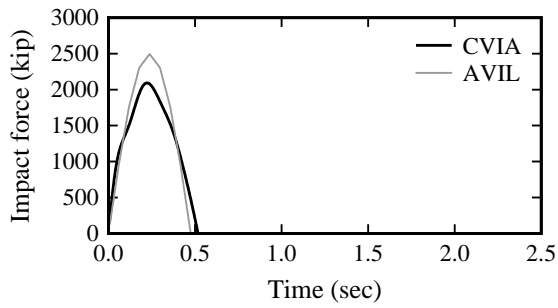
Figure M.22 Impact force-time histories: SR-300 Bridge, Pier 56



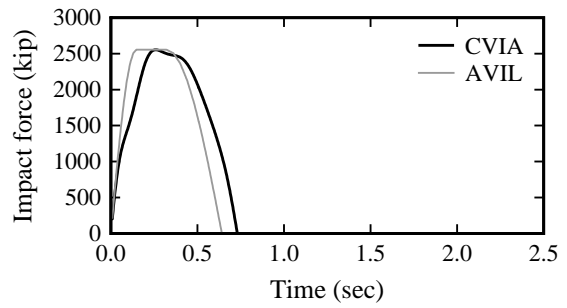
a) VG 1



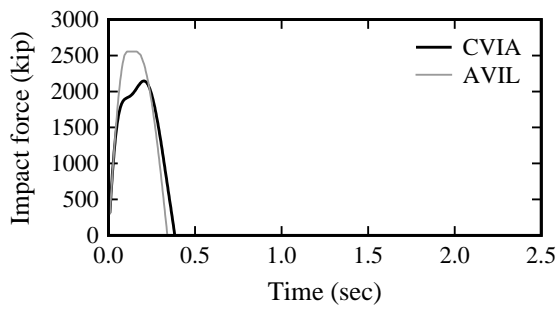
b) VG 2



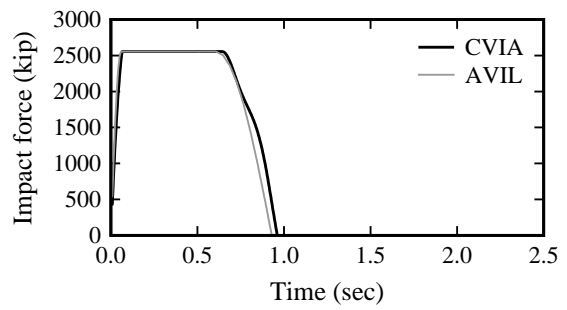
c) VG 3



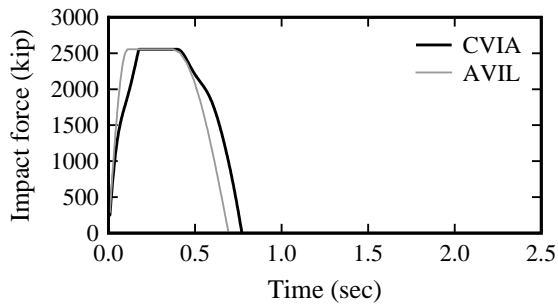
d) VG 4



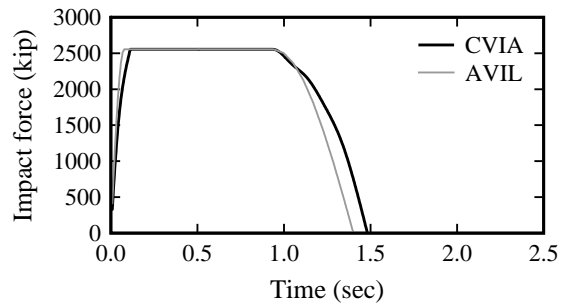
e) VG 5



f) VG 6

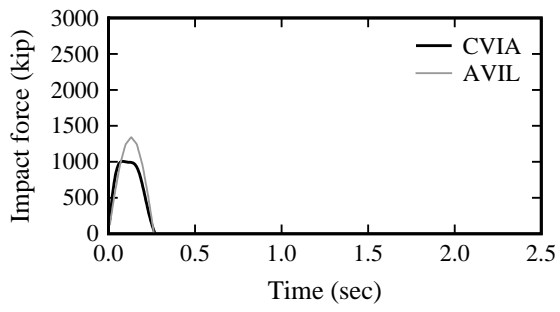


g) VG 7

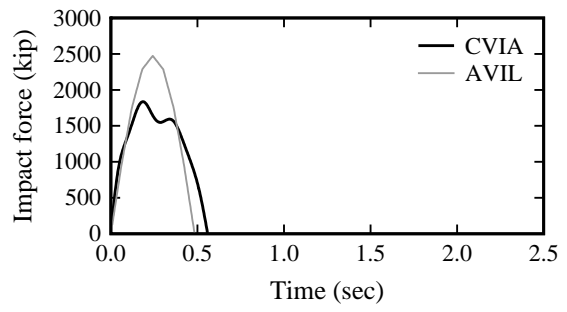


h) VG 8

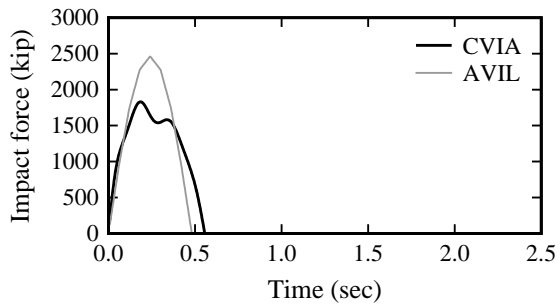
Figure M.23 Impact force-time histories: SR-300 Bridge, Pier 57



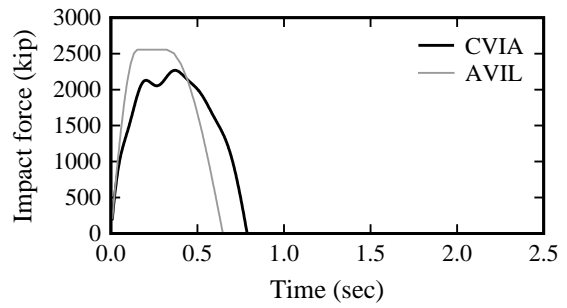
a) VG 1



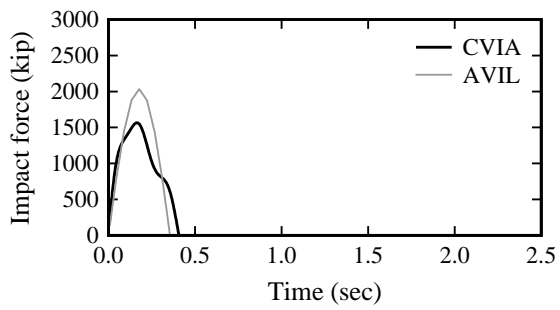
b) VG 2



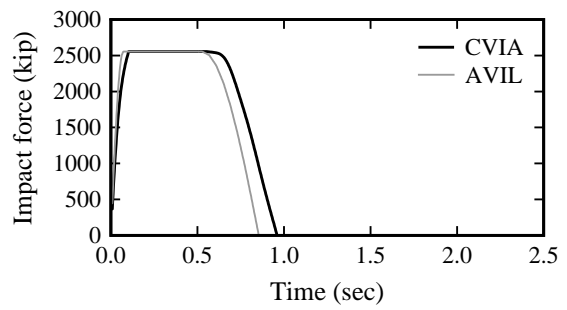
c) VG 3



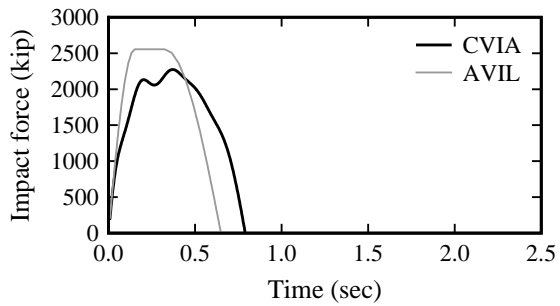
d) VG 4



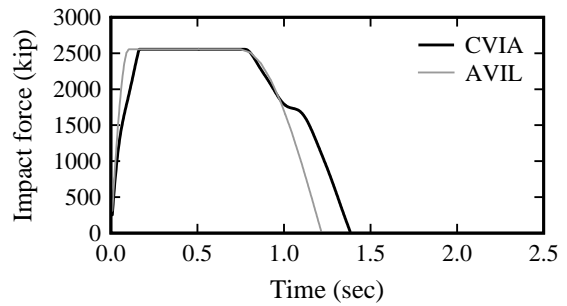
e) VG 5



f) VG 6

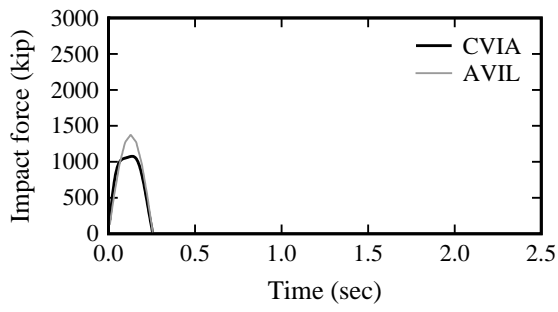


g) VG 7

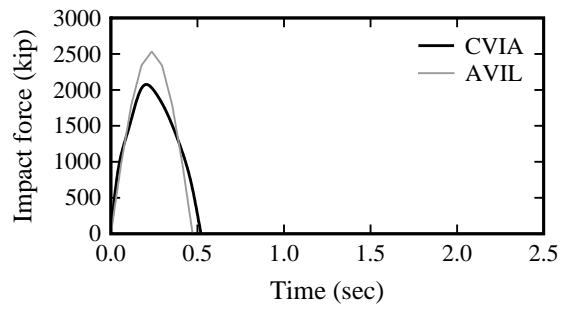


h) VG 8

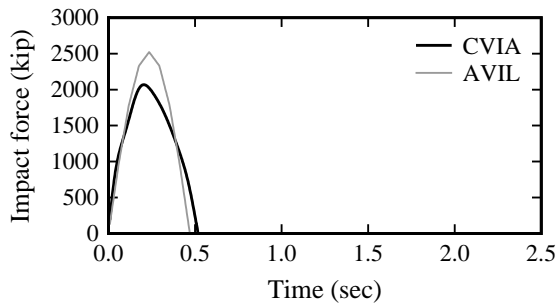
Figure M.24 Impact force-time histories: SR-300 Bridge, Pier 58



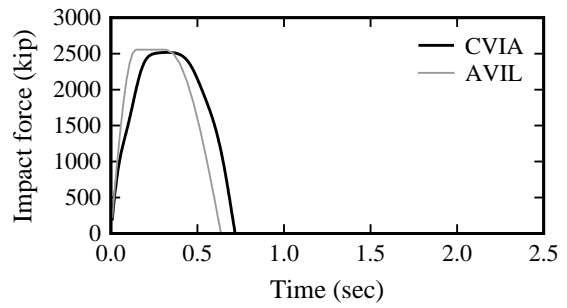
a) VG 1



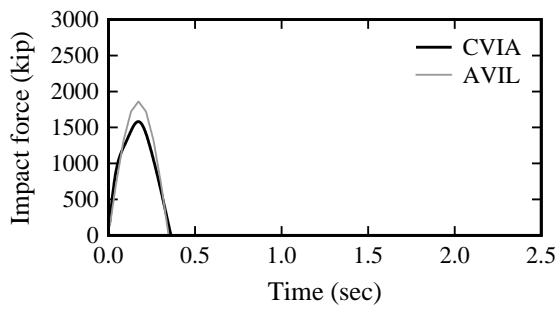
b) VG 2



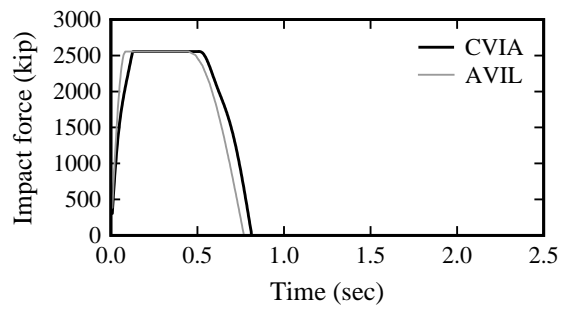
c) VG 3



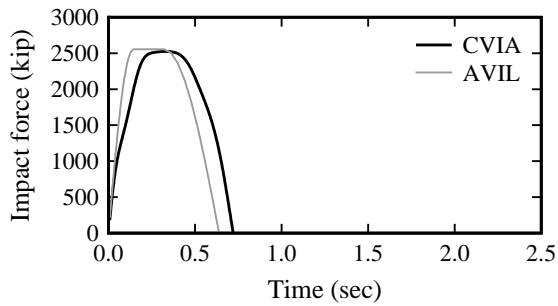
d) VG 4



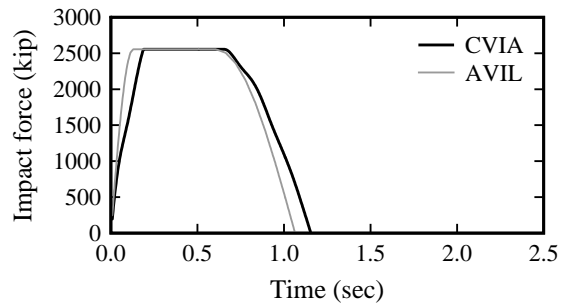
e) VG 5



f) VG 6

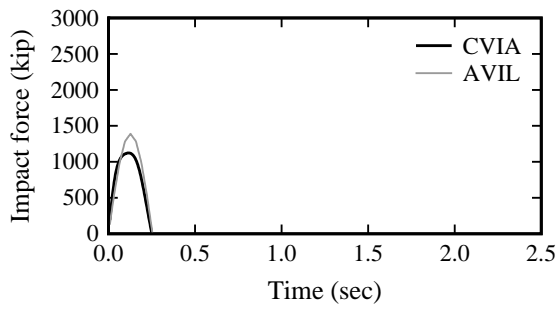


g) VG 7

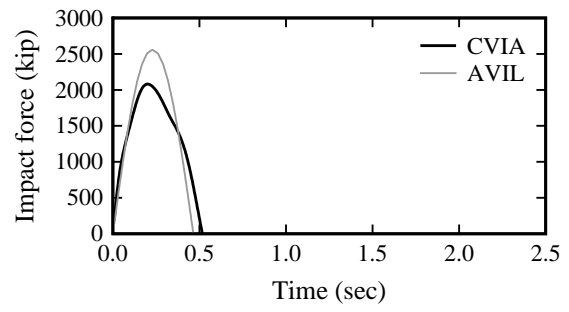


h) VG 8

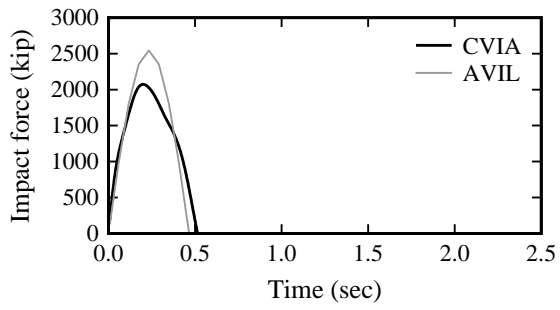
Figure M.25 Impact force-time histories: SR-300 Bridge, Pier 59



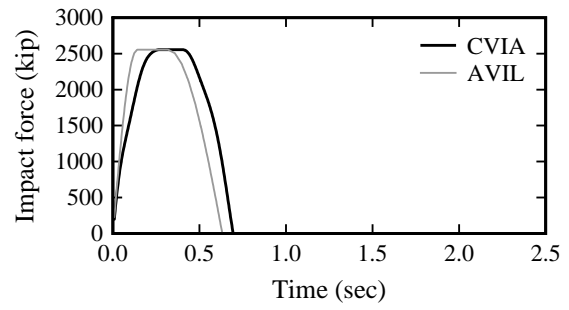
a) VG 1



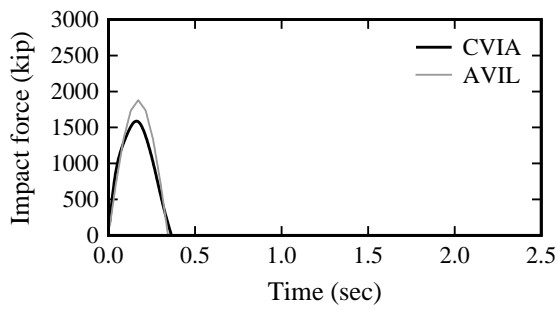
b) VG 2



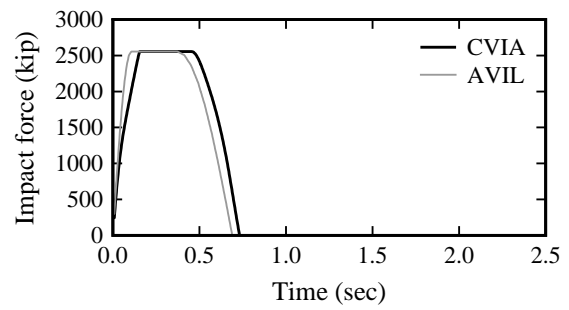
c) VG 3



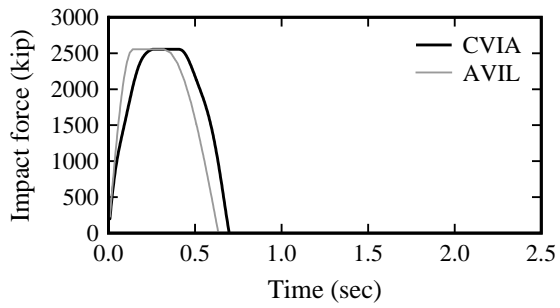
d) VG 4



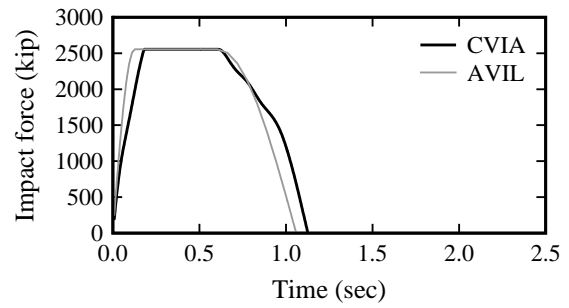
e) VG 5



f) VG 6



g) VG 7



h) VG 8

Figure M.26 Impact force-time histories: SR-300 Bridge, Pier 60

APPENDIX N
LA-1 BRIDGE VESSEL COLLISION RISK ASSESSMENT DATA

N.1 Introduction

In this appendix, detailed data are presented for vessel collision risk assessments of the Louisiana Highway 1 (LA-1) Bridge over Bayou Lafourche, Louisiana. The associated risk assessments are discussed in Chapter 10. Tables N.1 – N.16 present risk assessment input parameters and results for every combination of pier (2 – 4, 96 – 97) and vessel group (1 – 32). Figures N.1 – N.20 show barge impact force-time histories computed by the CVIA and AVIL analysis methods for each combination of pier (2 – 4, 96 – 97) and barge vessel group (1 – 32). See Chapter 10 for descriptions of piers and vessel groups.

Table N.1 Vessel impact velocities (v_i) (knots)

VG	P2	P3	P4	P96	P97	VG	P2	P3	P4	P96	P97
1	3.78	3.78	2.90	2.50	2.10	17	4.71	4.71	3.54	3.00	2.46
2	3.74	3.74	2.67	2.19	1.70	18	4.65	4.65	3.23	2.58	1.94
3	3.71	3.71	2.55	2.02	1.49	19	4.62	4.62	3.07	2.36	1.66
4	3.66	3.66	2.30	1.68	1.06	20	4.55	4.55	2.74	1.91	1.08
5	3.79	3.79	2.95	2.56	2.18	21	4.72	4.72	3.60	3.08	2.57
6	3.59	3.59	1.95	1.20	1.00	22	4.46	4.46	2.27	1.27	1.00
7	3.59	3.59	1.95	1.20	1.00	23	4.46	4.46	2.27	1.27	1.00
8	3.54	3.54	1.68	1.00	1.00	24	4.38	4.38	1.90	1.00	1.00
9	3.78	3.78	2.90	2.50	2.10	25	4.71	4.71	3.54	3.00	2.46
10	3.74	3.74	2.67	2.19	1.70	26	4.65	4.65	3.23	2.58	1.94
11	3.71	3.71	2.55	2.02	1.49	27	4.62	4.62	3.07	2.36	1.66
12	3.66	3.66	2.30	1.68	1.06	28	4.55	4.55	2.74	1.91	1.08
13	3.79	3.79	2.95	2.56	2.18	29	4.72	4.72	3.60	3.08	2.57
14	3.59	3.59	1.95	1.20	1.00	30	4.46	4.46	2.27	1.27	1.00
15	3.59	3.59	1.95	1.20	1.00	31	4.46	4.46	2.27	1.27	1.00
16	3.54	3.54	1.68	1.00	1.00	32	4.38	4.38	1.90	1.00	1.00

Table N.2 Geometric probability of impact (PG)

VG	P2	P3	P4	P96	P97	VG	P2	P3	P4	P96	P97
1	0.107	0.107	0.056	0.028	0.014	17	0.107	0.107	0.056	0.028	0.014
2	0.116	0.116	0.046	0.018	0.007	18	0.116	0.116	0.046	0.018	0.007
3	0.112	0.112	0.038	0.013	0.004	19	0.112	0.112	0.038	0.013	0.004
4	0.134	0.134	0.031	0.008	0.002	20	0.134	0.134	0.031	0.008	0.002
5	0.083	0.083	0.046	0.023	0.012	21	0.083	0.083	0.046	0.023	0.012
6	0.145	0.145	0.019	0.003	0.000	22	0.145	0.145	0.019	0.003	0.000
7	0.137	0.137	0.018	0.003	0.000	23	0.137	0.137	0.018	0.003	0.000
8	0.135	0.135	0.011	0.001	0.000	24	0.135	0.135	0.011	0.001	0.000
9	0.107	0.107	0.056	0.028	0.014	25	0.107	0.107	0.056	0.028	0.014
10	0.116	0.116	0.046	0.018	0.007	26	0.116	0.116	0.046	0.018	0.007
11	0.112	0.112	0.038	0.013	0.004	27	0.112	0.112	0.038	0.013	0.004
12	0.134	0.134	0.031	0.008	0.002	28	0.134	0.134	0.031	0.008	0.002
13	0.083	0.083	0.046	0.023	0.012	29	0.083	0.083	0.046	0.023	0.012
14	0.145	0.145	0.019	0.003	0.000	30	0.145	0.145	0.019	0.003	0.000
15	0.137	0.137	0.018	0.003	0.000	31	0.137	0.137	0.018	0.003	0.000
16	0.135	0.135	0.011	0.001	0.000	32	0.135	0.135	0.011	0.001	0.000

Table N.3 Barge impact forces (kips): AASHTO (1991) methods

VG	P2	P3	P4	P96	P97	VG	P2	P3	P4	P96	P97
1	2,368	2,368	2,250	2,174	2,106	17	2,564	2,564	2,383	2,270	2,167
2	2,021	2,021	1,904	1,839	1,784	18	2,171	2,171	1,989	1,891	1,809
3	1,590	1,590	1,490	1,440	1,399	19	1,705	1,705	1,548	1,471	1,410
4	1,830	1,830	1,723	1,675	855	20	1,932	1,932	1,763	1,691	888
5	1,415	1,415	1,348	1,304	1,265	21	1,539	1,539	1,432	1,365	1,305
6	1,644	1,644	1,387	532	368	22	1,696	1,696	1,592	593	386
7	1,480	1,480	1,397	686	475	23	1,545	1,545	1,413	765	475
8	1,215	1,215	593	211	211	24	1,244	1,244	762	211	211
9	2,035	2,035	1,992	1,806	1,279	25	2,090	2,090	2,022	1,996	1,754
10	1,783	1,783	1,699	1,145	697	26	1,828	1,828	1,762	1,589	900
11	1,407	1,407	1,048	660	361	27	1,438	1,438	1,389	899	444
12	1,676	1,676	856	459	183	28	1,706	1,706	1,204	590	190
13	1,237	1,237	1,206	1,194	1,015	29	1,279	1,279	1,229	1,210	1,194
14	1,599	1,599	645	246	170	30	1,629	1,629	870	274	170
15	1,346	1,346	403	153	106	31	1,404	1,404	543	171	106
16	1,197	1,197	351	125	125	32	1,219	1,219	451	125	125

Table N.4 Capacity-demand ratios (H/P): AASHTO (1991) methods

VG	P2	P3	P4	P96	P97	VG	P2	P3	P4	P96	P97
1	1.03	1.03	0.74	0.50	0.21	17	0.95	0.95	0.70	0.48	0.20
2	1.21	1.21	0.87	0.60	0.25	18	1.13	1.13	0.84	0.58	0.24
3	1.54	1.54	1.11	0.76	0.32	19	1.43	1.43	1.07	0.75	0.31
4	1.34	1.34	0.96	0.65	0.52	20	1.27	1.27	0.94	0.65	0.50
5	1.73	1.73	1.23	0.84	0.35	21	1.59	1.59	1.16	0.80	0.34
6	1.49	1.49	1.20	2.06	1.20	22	1.44	1.44	1.04	1.85	1.15
7	1.65	1.65	1.19	1.60	0.93	23	1.58	1.58	1.18	1.43	0.93
8	2.01	2.01	2.80	5.20	2.09	24	1.97	1.97	2.18	5.20	2.09
9	1.20	1.20	0.83	0.61	0.35	25	1.17	1.17	0.82	0.55	0.25
10	1.37	1.37	0.98	0.96	0.63	26	1.34	1.34	0.94	0.69	0.49
11	1.74	1.74	1.58	1.66	1.22	27	1.70	1.70	1.20	1.22	1.00
12	1.46	1.46	1.94	2.39	2.42	28	1.43	1.43	1.38	1.86	2.33
13	1.98	1.98	1.38	0.92	0.44	29	1.91	1.91	1.35	0.91	0.37
14	1.53	1.53	2.58	4.46	2.60	30	1.50	1.50	1.91	4.00	2.60
15	1.82	1.82	4.12	7.17	4.17	31	1.74	1.74	3.06	6.42	4.17
16	2.04	2.04	4.73	8.78	3.54	32	2.01	2.01	3.68	8.78	3.54

Table N.5 Probability of collapse (PC): AASHTO (1991) methods

VG	P2	P3	P4	P96	P97	VG	P2	P3	P4	P96	P97
1	0.000	0.000	0.029	0.055	0.088	17	0.005	0.005	0.034	0.057	0.088
2	0.000	0.000	0.014	0.045	0.084	18	0.000	0.000	0.018	0.047	0.084
3	0.000	0.000	0.000	0.027	0.076	19	0.000	0.000	0.000	0.028	0.076
4	0.000	0.000	0.004	0.038	0.054	20	0.000	0.000	0.006	0.039	0.056
5	0.000	0.000	0.000	0.018	0.072	21	0.000	0.000	0.000	0.022	0.074
6	0.000	0.000	0.000	0.000	0.000	22	0.000	0.000	0.000	0.000	0.000
7	0.000	0.000	0.000	0.000	0.008	23	0.000	0.000	0.000	0.000	0.008
8	0.000	0.000	0.000	0.000	0.000	24	0.000	0.000	0.000	0.000	0.000
9	0.000	0.000	0.019	0.044	0.073	25	0.000	0.000	0.020	0.050	0.083
10	0.000	0.000	0.003	0.005	0.041	26	0.000	0.000	0.006	0.034	0.057
11	0.000	0.000	0.000	0.000	0.000	27	0.000	0.000	0.000	0.000	0.001
12	0.000	0.000	0.000	0.000	0.000	28	0.000	0.000	0.000	0.000	0.000
13	0.000	0.000	0.000	0.009	0.063	29	0.000	0.000	0.000	0.010	0.070
14	0.000	0.000	0.000	0.000	0.000	30	0.000	0.000	0.000	0.000	0.000
15	0.000	0.000	0.000	0.000	0.000	31	0.000	0.000	0.000	0.000	0.000
16	0.000	0.000	0.000	0.000	0.000	32	0.000	0.000	0.000	0.000	0.000

Table N.6 Barge impact forces (kips): AASHTO (2009) methods

VG	P2	P3	P4	P96	P97	VG	P2	P3	P4	P96	P97
1	1,790	1,790	1,672	1,596	1,528	17	1,986	1,986	1,806	1,692	1,589
2	1,675	1,675	1,556	1,492	1,437	18	1,825	1,825	1,642	1,543	1,463
3	1,590	1,590	1,490	1,439	1,399	19	1,706	1,706	1,548	1,471	1,411
4	1,560	1,560	1,453	1,405	853	20	1,662	1,662	1,494	1,421	885
5	1,608	1,608	1,541	1,496	1,458	21	1,732	1,732	1,625	1,557	1,497
6	1,451	1,451	1,384	529	368	22	1,504	1,504	1,399	592	368
7	1,480	1,480	1,397	683	475	23	1,546	1,546	1,413	764	475
8	1,407	1,407	594	211	211	24	1,437	1,437	758	211	211
9	1,457	1,457	1,414	1,397	1,284	25	1,513	1,513	1,444	1,418	1,396
10	1,436	1,436	1,394	1,147	695	26	1,481	1,481	1,415	1,391	903
11	1,407	1,407	1,046	660	360	27	1,438	1,438	1,389	898	447
12	1,406	1,406	853	457	183	28	1,436	1,436	1,206	590	190
13	1,429	1,429	1,398	1,397	1,018	29	1,471	1,471	1,422	1,403	1,387
14	1,406	1,406	643	245	170	30	1,436	1,436	870	274	170
15	1,345	1,345	401	152	106	31	1,404	1,404	543	171	106
16	1,390	1,390	352	125	125	16	1,411	1,411	449	125	125

Table N.7 Capacity-demand ratios (H/P): AASHTO (2009) methods

VG	P2	P3	P4	P96	P97	VG	P2	P3	P4	P96	P97
1	1.37	1.37	0.99	0.69	0.29	17	1.23	1.23	0.92	0.65	0.28
2	1.46	1.46	1.07	0.74	0.31	18	1.34	1.34	1.01	0.71	0.30
3	1.54	1.54	1.11	0.76	0.32	19	1.43	1.43	1.07	0.75	0.31
4	1.57	1.57	1.14	0.78	0.52	20	1.47	1.47	1.11	0.77	0.50
5	1.52	1.52	1.08	0.73	0.30	21	1.41	1.41	1.02	0.70	0.30
6	1.69	1.69	1.20	2.07	1.20	22	1.63	1.63	1.19	1.85	1.20
7	1.65	1.65	1.19	1.61	0.93	23	1.58	1.58	1.18	1.44	0.93
8	1.74	1.74	2.80	5.20	2.09	24	1.70	1.70	2.19	5.20	2.09
9	1.68	1.68	1.17	0.79	0.34	25	1.62	1.62	1.15	0.77	0.32
10	1.70	1.70	1.19	0.96	0.64	26	1.65	1.65	1.17	0.79	0.49
11	1.74	1.74	1.59	1.66	1.23	27	1.70	1.70	1.20	1.22	0.99
12	1.74	1.74	1.95	2.40	2.42	28	1.70	1.70	1.38	1.86	2.33
13	1.71	1.71	1.19	0.79	0.43	29	1.66	1.66	1.17	0.78	0.32
14	1.74	1.74	2.58	4.48	2.60	30	1.70	1.70	1.91	4.00	2.60
15	1.82	1.82	4.14	7.22	4.17	31	1.74	1.74	3.06	6.42	4.17
16	1.76	1.76	4.72	8.78	3.54	32	1.73	1.73	3.70	8.78	3.54

Table N.8 Probability of collapse (PC): AASHTO (2009) methods

VG	P2	P3	P4	P96	P97	VG	P2	P3	P4	P96	P97
1	0.000	0.000	0.001	0.035	0.079	17	0.000	0.000	0.009	0.039	0.080
2	0.000	0.000	0.000	0.029	0.077	18	0.000	0.000	0.000	0.032	0.078
3	0.000	0.000	0.000	0.026	0.076	19	0.000	0.000	0.000	0.028	0.076
4	0.000	0.000	0.000	0.024	0.054	20	0.000	0.000	0.000	0.025	0.056
5	0.000	0.000	0.000	0.030	0.077	21	0.000	0.000	0.000	0.033	0.078
6	0.000	0.000	0.000	0.000	0.000	22	0.000	0.000	0.000	0.000	0.000
7	0.000	0.000	0.000	0.000	0.008	23	0.000	0.000	0.000	0.000	0.008
8	0.000	0.000	0.000	0.000	0.000	24	0.000	0.000	0.000	0.000	0.000
9	0.000	0.000	0.000	0.024	0.073	25	0.000	0.000	0.000	0.025	0.076
10	0.000	0.000	0.000	0.005	0.040	26	0.000	0.000	0.000	0.024	0.057
11	0.000	0.000	0.000	0.000	0.000	27	0.000	0.000	0.000	0.000	0.001
12	0.000	0.000	0.000	0.000	0.000	28	0.000	0.000	0.000	0.000	0.000
13	0.000	0.000	0.000	0.024	0.063	29	0.000	0.000	0.000	0.024	0.076
14	0.000	0.000	0.000	0.000	0.000	30	0.000	0.000	0.000	0.000	0.000
15	0.000	0.000	0.000	0.000	0.000	31	0.000	0.000	0.000	0.000	0.000
16	0.000	0.000	0.000	0.000	0.000	32	0.000	0.000	0.000	0.000	0.000

Table N.9 Minimum of barge width (B_B) and pier width (B_P) (ft)

VG	P2	P3	P4	P96	P97	VG	P2	P3	P4	P96	P97
1	48.0	48.0	34.5	28.0	28.0	17	48.0	48.0	34.5	28.0	28.0
2	44.0	44.0	34.5	28.0	28.0	18	44.0	44.0	34.5	28.0	28.0
3	35.0	35.0	34.5	28.0	28.0	19	35.0	35.0	34.5	28.0	28.0
4	42.0	42.0	34.5	28.0	28.0	20	42.0	42.0	34.5	28.0	28.0
5	30.0	30.0	30.0	28.0	28.0	21	30.0	30.0	30.0	28.0	28.0
6	40.0	40.0	34.5	28.0	28.0	22	40.0	40.0	34.5	28.0	28.0
7	35.0	35.0	34.5	28.0	28.0	23	35.0	35.0	34.5	28.0	28.0
8	30.0	30.0	30.0	28.0	28.0	24	30.0	30.0	30.0	28.0	28.0
9	48.0	48.0	34.5	28.0	28.0	25	48.0	48.0	34.5	28.0	28.0
10	44.0	44.0	34.5	28.0	28.0	26	44.0	44.0	34.5	28.0	28.0
11	35.0	35.0	34.5	28.0	28.0	27	35.0	35.0	34.5	28.0	28.0
12	42.0	42.0	34.5	28.0	28.0	28	42.0	42.0	34.5	28.0	28.0
13	30.0	30.0	30.0	28.0	28.0	29	30.0	30.0	30.0	28.0	28.0
14	40.0	40.0	34.5	28.0	28.0	30	40.0	40.0	34.5	28.0	28.0
15	35.0	35.0	34.5	28.0	28.0	31	35.0	35.0	34.5	28.0	28.0
16	30.0	30.0	30.0	28.0	28.0	32	30.0	30.0	30.0	28.0	28.0

Table N.10 Barge yield force (P_{BY}) (kip)

VG	P2	P3	P4	P96	P97	VG	P2	P3	P4	P96	P97
1	7,569	7,569	3,734	3,294	3,294	17	7,569	7,569	3,734	3,294	3,294
2	7,055	7,055	3,734	3,294	3,294	18	7,055	7,055	3,734	3,294	3,294
3	5,898	5,898	3,734	3,294	3,294	19	5,898	5,898	3,734	3,294	3,294
4	6,798	6,798	3,734	3,294	3,294	20	6,798	6,798	3,734	3,294	3,294
5	5,255	5,255	3,430	3,294	3,294	21	5,255	5,255	3,430	3,294	3,294
6	6,540	6,540	3,734	3,294	3,294	22	6,540	6,540	3,734	3,294	3,294
7	5,898	5,898	3,734	3,294	3,294	23	5,898	5,898	3,734	3,294	3,294
8	5,255	5,255	3,430	3,294	3,294	24	5,255	5,255	3,430	3,294	3,294
9	7,569	7,569	3,734	3,294	3,294	25	7,569	7,569	3,734	3,294	3,294
10	7,055	7,055	3,734	3,294	3,294	26	7,055	7,055	3,734	3,294	3,294
11	5,898	5,898	3,734	3,294	3,294	27	5,898	5,898	3,734	3,294	3,294
12	6,798	6,798	3,734	3,294	3,294	28	6,798	6,798	3,734	3,294	3,294
13	5,255	5,255	3,430	3,294	3,294	29	5,255	5,255	3,430	3,294	3,294
14	6,540	6,540	3,734	3,294	3,294	30	6,540	6,540	3,734	3,294	3,294
15	5,898	5,898	3,734	3,294	3,294	31	5,898	5,898	3,734	3,294	3,294
16	5,255	5,255	3,430	3,294	3,294	32	5,255	5,255	3,430	3,294	3,294

Table N.11 Maximum barge impact forces (P_{Bm}) (kip): UF/FDOT methods (CVIA)

VG	P2	P3	P4	P96	P97	VG	P2	P3	P4	P96	P97
1	7,569	7,569	3,734	3,294	3,294	17	7,569	7,569	3,734	3,294	3,294
2	7,055	7,055	3,734	3,294	2,965	18	7,055	7,055	3,734	3,294	3,294
3	5,898	5,898	3,734	3,286	2,426	19	5,898	5,898	3,734	3,294	2,701
4	6,798	6,798	3,734	2,670	1,693	20	6,798	6,798	3,734	3,021	1,720
5	5,255	5,255	3,430	3,294	3,294	21	5,255	5,255	3,430	3,294	3,294
6	6,540	6,540	2,893	1,555	1,294	22	6,540	6,540	3,367	1,638	1,294
7	5,898	5,898	3,179	1,685	1,404	23	5,898	5,898	3,734	1,776	1,404
8	5,196	5,204	1,922	1,061	1,060	24	5,255	5,255	2,173	1,061	1,060
9	7,569	7,569	3,734	3,161	2,651	25	7,569	7,569	3,734	3,294	3,104
10	7,055	7,055	3,601	2,594	2,013	26	7,055	7,055	3,734	3,047	2,292
11	5,513	5,519	2,912	2,062	1,518	27	5,898	5,898	3,508	2,406	1,693
12	5,801	5,816	2,628	1,719	1,084	28	6,798	6,798	3,129	1,948	1,102
13	5,255	5,255	3,430	2,908	2,476	29	5,255	5,255	3,430	3,294	2,918
14	5,716	5,724	2,270	1,253	1,043	30	6,540	6,540	2,643	1,320	1,043
15	4,337	4,345	1,839	1,030	857	31	5,390	5,396	2,549	1,085	857
16	4,398	4,404	1,647	920	919	32	5,255	5,255	1,862	920	919

Table N.12 Demand-capacity ratios (D/C): UF/FDOT methods (CVIA)

VG	P2	P3	P4	P96	P97	VG	P2	P3	P4	P96	P97
1	0.979	0.974	0.953	0.997	0.989	17	0.997	0.997	0.963	0.997	0.998
2	0.948	0.941	0.924	0.970	0.915	18	0.974	0.969	0.940	0.992	0.950
3	0.912	0.901	0.884	0.928	0.834	19	0.938	0.928	0.909	0.953	0.867
4	0.903	0.891	0.856	0.857	0.645	20	0.927	0.918	0.880	0.895	0.654
5	0.915	0.904	0.896	0.969	0.943	21	0.941	0.931	0.913	0.992	0.968
6	0.850	0.839	0.797	0.521	0.441	22	0.866	0.856	0.822	0.545	0.441
7	0.867	0.857	0.823	0.590	0.504	23	0.877	0.869	0.846	0.616	0.504
8	0.722	0.684	0.546	0.300	0.303	24	0.775	0.736	0.613	0.300	0.303
9	0.855	0.844	0.837	0.851	0.786	25	0.870	0.860	0.846	0.885	0.845
10	0.828	0.807	0.821	0.743	0.610	26	0.852	0.840	0.832	0.818	0.678
11	0.706	0.670	0.723	0.558	0.425	27	0.774	0.735	0.794	0.633	0.472
12	0.701	0.662	0.676	0.477	0.301	28	0.783	0.744	0.752	0.532	0.306
13	0.793	0.753	0.820	0.782	0.700	29	0.827	0.803	0.829	0.844	0.785
14	0.710	0.673	0.612	0.353	0.293	30	0.788	0.748	0.687	0.373	0.293
15	0.486	0.434	0.400	0.241	0.201	31	0.608	0.558	0.582	0.255	0.201
16	0.566	0.513	0.392	0.228	0.230	32	0.668	0.624	0.460	0.228	0.230

Table N.13 Probability of collapse (*PC*): UF/FDOT methods (CVIA)

VG	P2	P3	P4	P96	P97	VG	P2	P3	P4	P96	P97
1	0.779	0.733	0.562	0.994	0.897	17	0.989	0.988	0.633	0.994	1.000
2	0.524	0.476	0.383	0.699	0.343	18	0.735	0.684	0.475	0.927	0.535
3	0.327	0.284	0.227	0.403	0.119	19	0.462	0.406	0.317	0.558	0.183
4	0.293	0.251	0.159	0.161	0.010	20	0.399	0.353	0.215	0.264	0.011
5	0.341	0.294	0.266	0.690	0.488	21	0.479	0.419	0.334	0.930	0.684
6	0.147	0.126	0.074	0.002	0.001	22	0.181	0.159	0.102	0.003	0.001
7	0.183	0.160	0.103	0.005	0.002	23	0.207	0.188	0.140	0.007	0.002
8	0.028	0.017	0.003	0.000	0.000	24	0.055	0.033	0.007	0.000	0.000
9	0.157	0.135	0.123	0.149	0.064	25	0.189	0.166	0.139	0.231	0.137
10	0.111	0.084	0.100	0.036	0.006	26	0.150	0.128	0.116	0.096	0.016
11	0.023	0.014	0.028	0.003	0.001	27	0.055	0.033	0.071	0.009	0.001
12	0.021	0.013	0.015	0.001	0.000	28	0.061	0.037	0.041	0.002	0.000
13	0.069	0.042	0.099	0.061	0.021	29	0.108	0.079	0.111	0.135	0.063
14	0.024	0.015	0.007	0.000	0.000	30	0.065	0.039	0.018	0.000	0.000
15	0.001	0.001	0.000	0.000	0.000	31	0.006	0.003	0.004	0.000	0.000
16	0.004	0.002	0.000	0.000	0.000	32	0.014	0.008	0.001	0.000	0.000

Table N.14 Maximum dynamic impact force (P_{Bm}): UF/FDOT methods (AVIL)

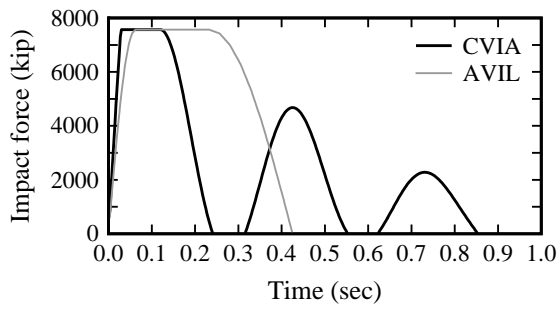
VG	P2	P3	P4	P96	P97	VG	P2	P3	P4	P96	P97
1	7,569	7,569	3,734	3,294	3,294	17	7,569	7,569	3,734	3,294	3,294
2	7,055	7,055	3,734	3,294	3,294	18	7,055	7,055	3,734	3,294	3,294
3	5,898	5,898	3,734	3,294	3,078	19	5,898	5,898	3,734	3,294	3,294
4	6,798	6,798	3,734	3,294	2,071	20	6,798	6,798	3,734	3,294	2,106
5	5,255	5,255	3,430	3,294	3,294	21	5,255	5,255	3,430	3,294	3,294
6	5,692	6,175	2,788	1,646	1,358	22	6,540	6,540	3,246	1,735	1,358
7	5,898	5,898	3,170	1,871	1,544	23	5,898	5,898	3,734	1,972	1,544
8	4,051	4,361	1,777	1,037	1,028	24	5,015	5,255	2,009	1,037	1,028
9	6,011	6,555	3,734	3,294	2,775	25	7,490	7,569	3,734	3,294	3,253
10	5,314	5,781	3,376	2,650	2,038	26	6,611	7,055	3,734	3,115	2,321
11	4,168	4,505	2,639	2,002	1,461	27	5,193	5,613	3,179	2,336	1,629
12	4,236	4,601	2,381	1,667	1,042	28	5,264	5,718	2,835	1,890	1,059
13	4,791	5,158	3,430	2,925	2,470	29	5,255	5,255	3,430	3,294	2,913
14	4,216	4,574	2,065	1,219	1,006	30	5,239	5,684	2,404	1,285	1,006
15	3,255	3,518	1,629	961	793	31	4,045	4,372	2,257	1,014	793
16	3,396	3,656	1,490	869	862	32	4,204	4,525	1,684	869	862

Table N.15 Demand-capacity ratios (*D/C*): UF/FDOT methods (AVIL)

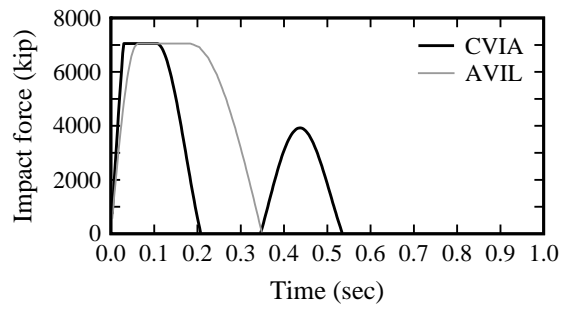
VG	P2	P3	P4	P96	P97	VG	P2	P3	P4	P96	P97
1	1.000	0.868	0.961	1.000	1.000	17	1.000	1.000	0.965	0.997	0.998
2	1.000	0.848	1.000	1.000	1.000	18	1.000	1.000	0.953	0.997	0.997
3	0.972	0.728	1.000	0.984	1.000	19	0.988	0.972	0.933	0.995	0.981
4	0.971	0.725	1.000	0.982	1.000	20	0.988	0.973	0.916	0.987	0.805
5	0.966	0.829	1.000	0.999	1.000	21	0.983	0.964	0.923	0.997	0.997
6	0.876	0.733	0.963	0.987	1.000	22	0.905	0.884	0.833	0.657	0.530
7	0.907	0.505	0.973	0.870	1.000	23	0.924	0.907	0.868	0.752	0.610
8	0.781	0.583	0.860	0.905	0.937	24	0.838	0.824	0.660	0.363	0.360
9	0.876	0.870	0.854	0.935	0.874	25	0.911	0.896	0.860	0.957	0.924
10	0.861	0.851	0.833	0.845	0.728	26	0.879	0.872	0.850	0.896	0.797
11	0.770	0.733	0.768	0.659	0.507	27	0.834	0.816	0.817	0.745	0.558
12	0.766	0.730	0.725	0.565	0.358	28	0.831	0.813	0.794	0.628	0.365
13	0.845	0.833	0.835	0.868	0.813	29	0.867	0.854	0.843	0.921	0.868
14	0.775	0.737	0.663	0.427	0.347	30	0.836	0.820	0.735	0.450	0.347
15	0.558	0.509	0.458	0.284	0.233	31	0.671	0.632	0.640	0.300	0.233
16	0.632	0.588	0.445	0.268	0.268	32	0.733	0.698	0.516	0.268	0.268

Table N.16 Probability of collapse (*PC*): UF/FDOT methods (AVIL)

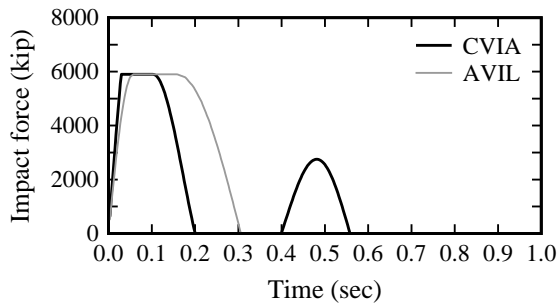
VG	P2	P3	P4	P96	P97	VG	P2	P3	P4	P96	P97
1	1.000	0.186	0.623	1.000	1.000	17	1.000	1.000	0.654	0.994	1.000
2	1.000	0.142	1.000	1.000	1.000	18	1.000	1.000	0.562	0.994	0.988
3	0.712	0.030	1.000	0.835	1.000	19	0.885	0.714	0.429	0.971	0.808
4	0.710	0.029	1.000	0.817	1.000	20	0.882	0.728	0.347	0.872	0.081
5	0.663	0.111	1.000	1.000	1.000	21	0.829	0.641	0.378	0.994	0.989
6	0.204	0.032	0.636	0.871	1.000	22	0.299	0.229	0.117	0.012	0.002
7	0.308	0.002	0.721	0.190	1.000	23	0.385	0.306	0.186	0.041	0.006
8	0.060	0.005	0.167	0.300	0.454	24	0.125	0.104	0.012	0.000	0.000
9	0.206	0.190	0.155	0.445	0.200	25	0.323	0.266	0.167	0.586	0.385
10	0.169	0.148	0.117	0.137	0.030	26	0.212	0.195	0.146	0.268	0.074
11	0.052	0.032	0.051	0.012	0.002	27	0.119	0.095	0.096	0.037	0.003
12	0.049	0.031	0.029	0.004	0.000	28	0.114	0.091	0.071	0.008	0.000
13	0.137	0.117	0.120	0.185	0.090	29	0.183	0.154	0.134	0.369	0.185
14	0.055	0.034	0.013	0.001	0.000	30	0.122	0.100	0.033	0.001	0.000
15	0.003	0.002	0.001	0.000	0.000	31	0.014	0.009	0.010	0.000	0.000
16	0.009	0.005	0.001	0.000	0.000	32	0.032	0.020	0.002	0.000	0.000



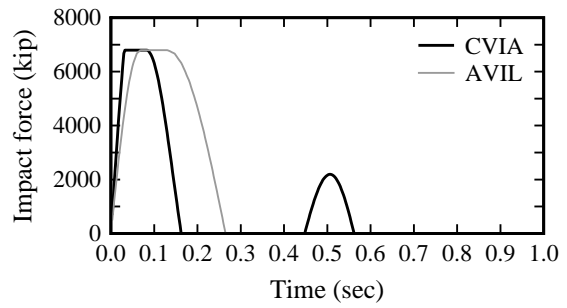
a) VG 1



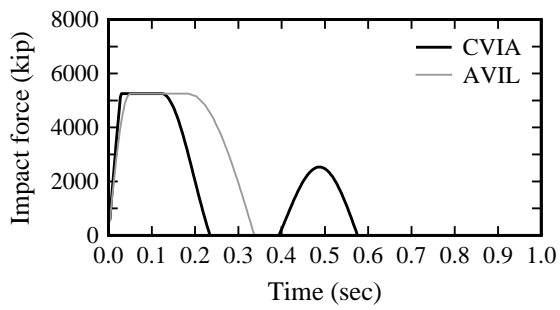
b) VG 2



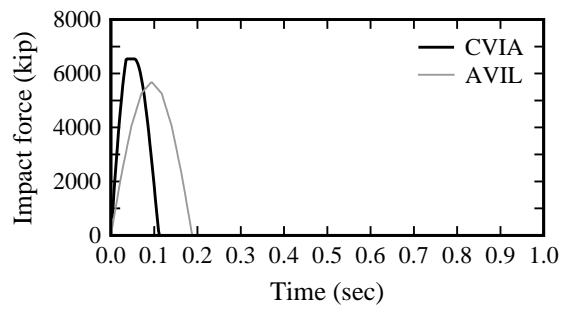
c) VG 3



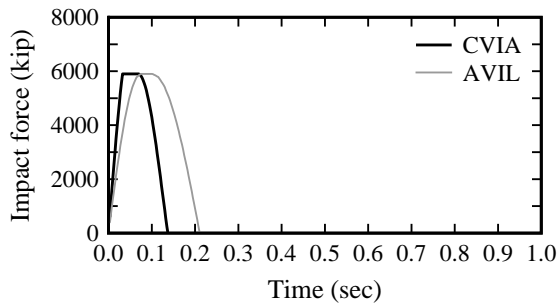
d) VG 4



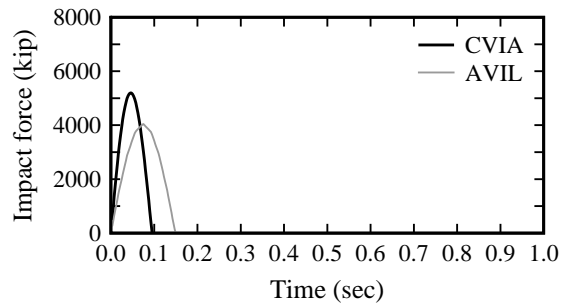
e) VG 5



f) VG 6

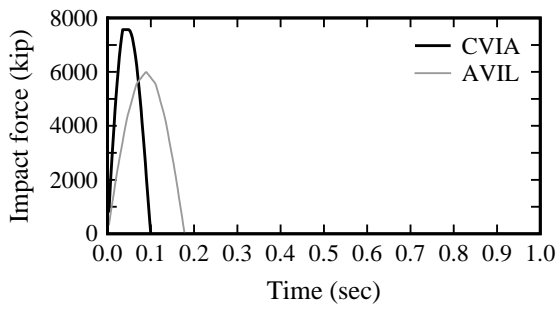


g) VG 7

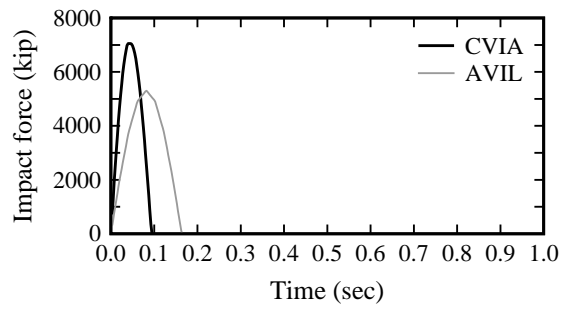


h) VG 8

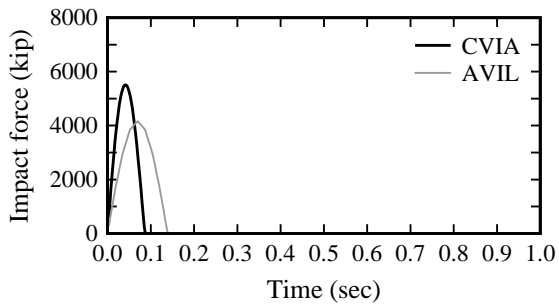
Figure N.1 Impact force-time histories: LA-1 Bridge, Pier 2, upbound traffic, fully loaded



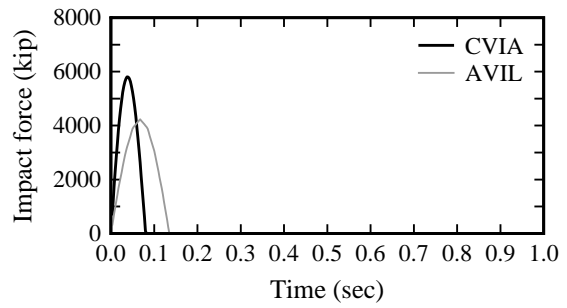
a) VG 9



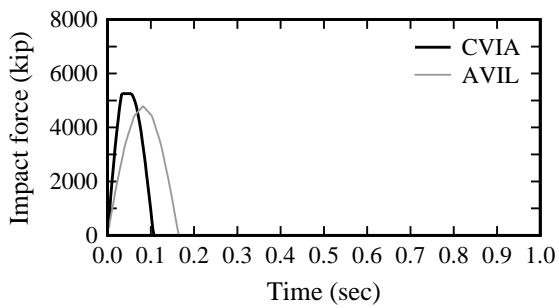
b) VG 10



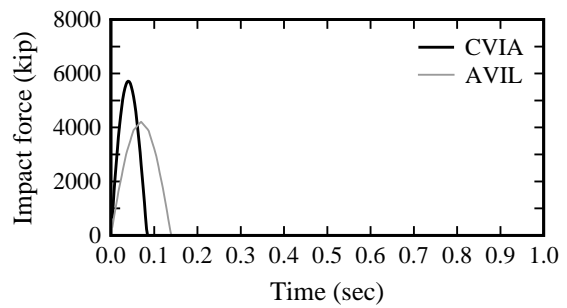
c) VG 11



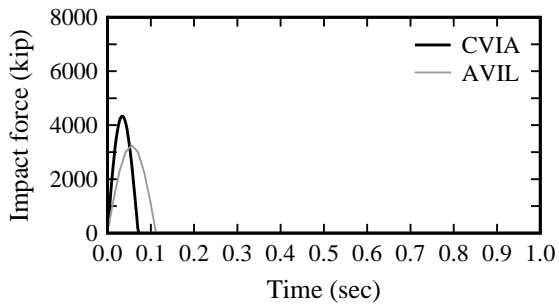
d) VG 12



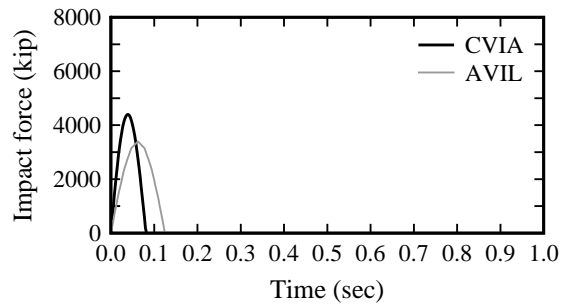
e) VG 13



f) VG 14

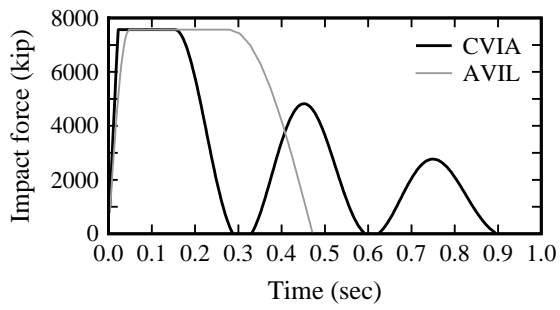


g) VG 15

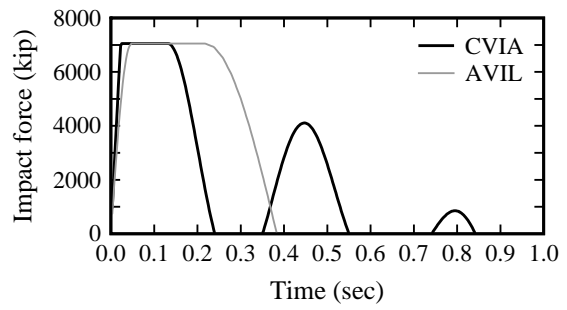


h) VG 16

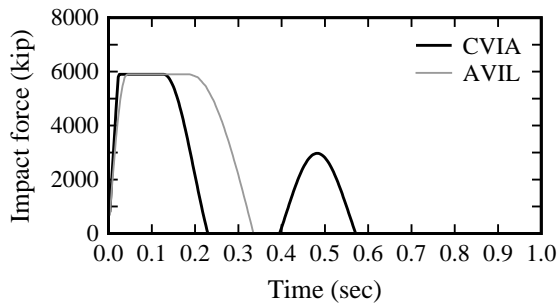
Figure N.2 Impact force-time histories: LA-1 Bridge, Pier 2, upbound traffic, lightly loaded



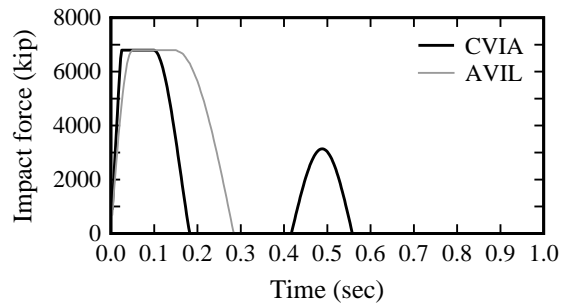
a) VG 17



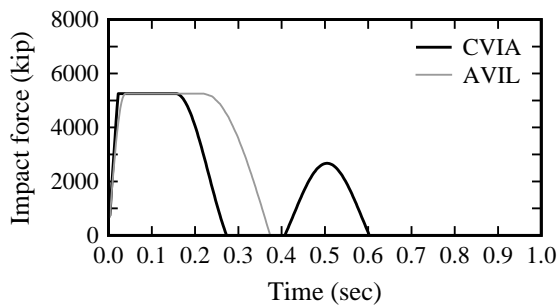
b) VG 18



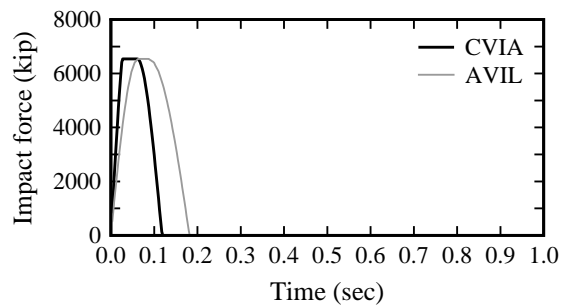
c) VG 19



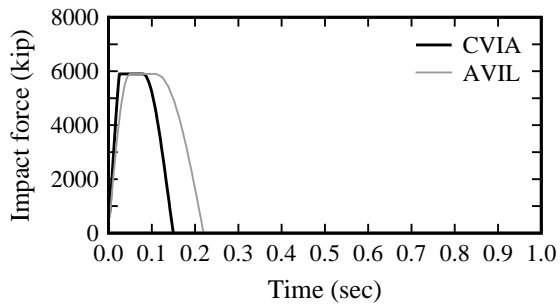
d) VG 20



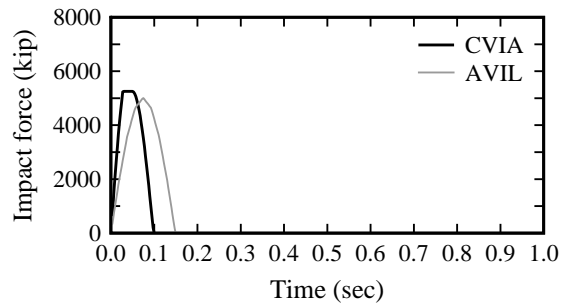
e) VG 21



f) VG 22

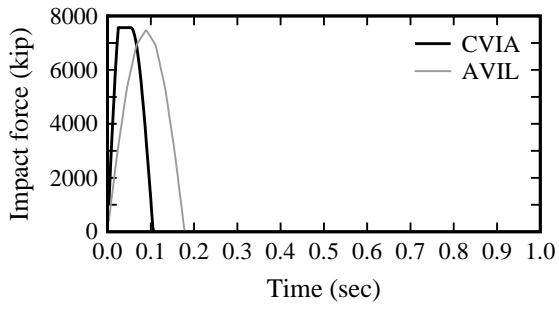


g) VG 23

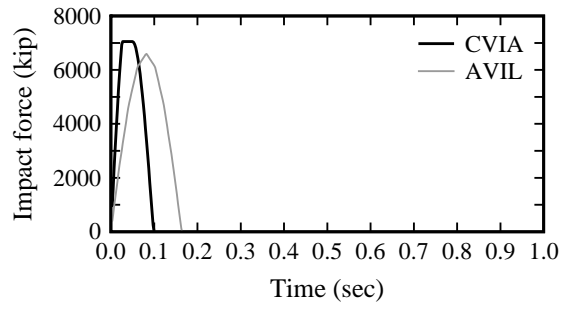


h) VG 24

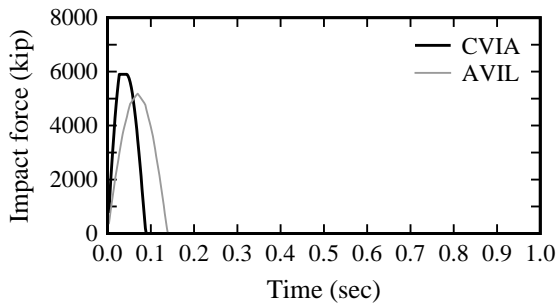
Figure N.3 Impact force-time histories: LA-1 Bridge, Pier 2, downbound traffic, fully loaded



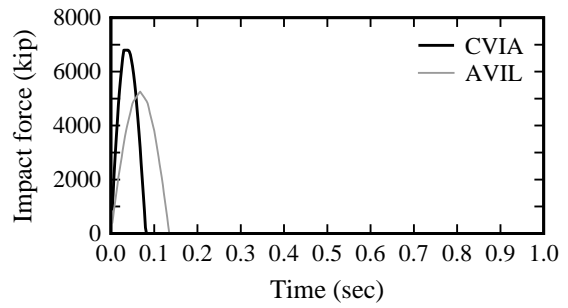
a) VG 25



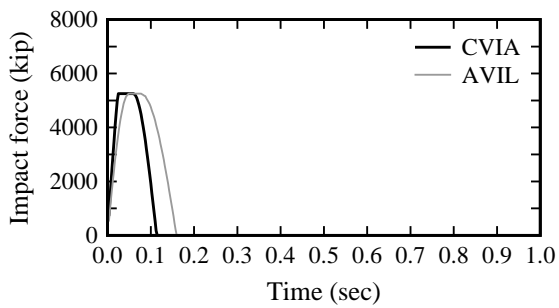
b) VG 26



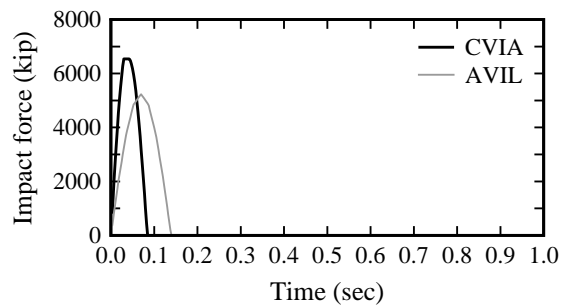
c) VG 27



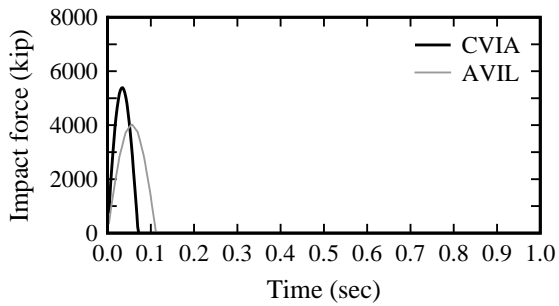
d) VG 28



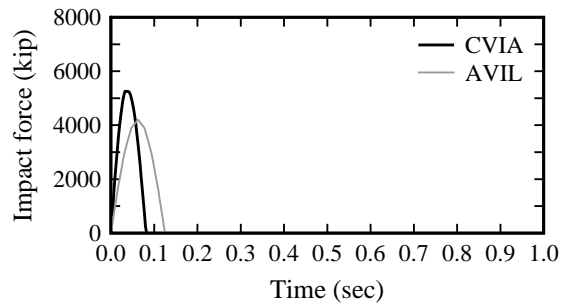
e) VG 29



f) VG 30

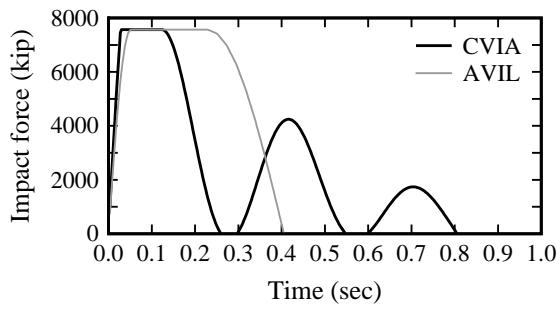


g) VG 31

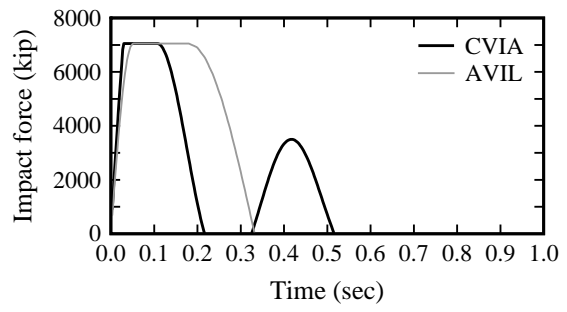


h) VG 32

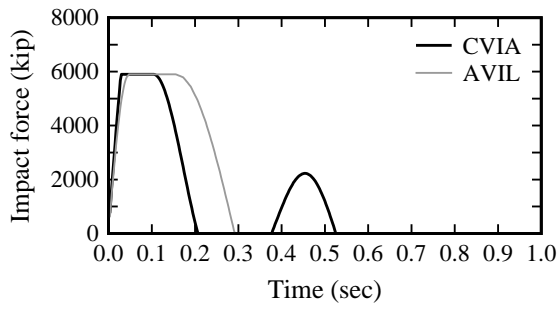
Figure N.4 Impact force-time histories: LA-1 Bridge, Pier 2, downbound traffic, lightly loaded



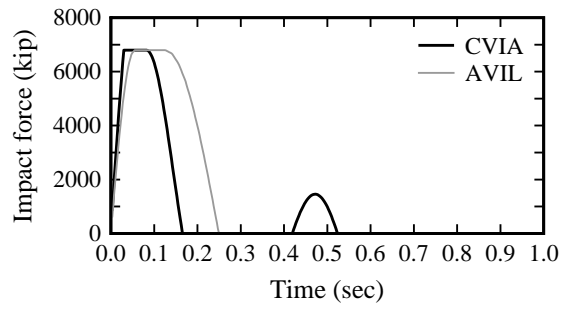
a) VG 1



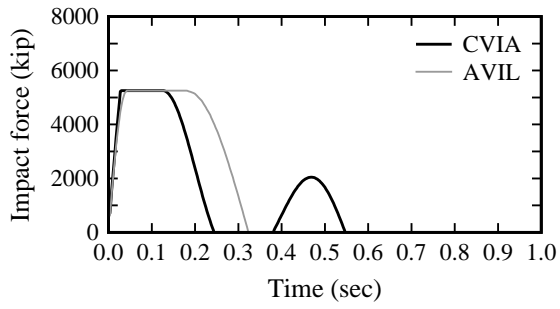
b) VG 2



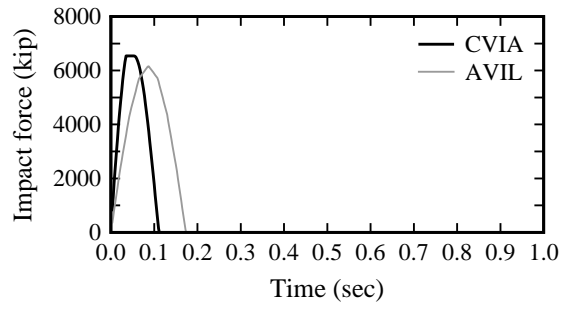
c) VG 3



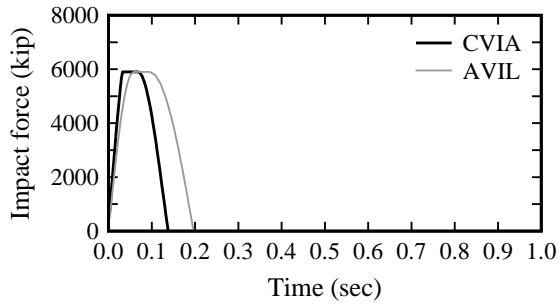
d) VG 4



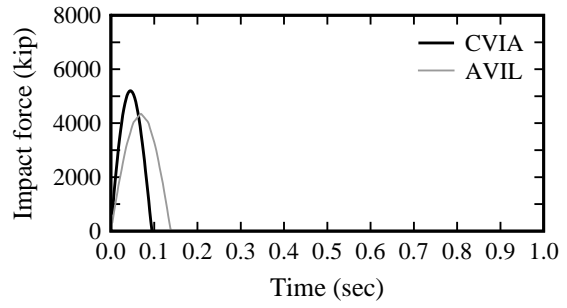
e) VG 5



f) VG 6

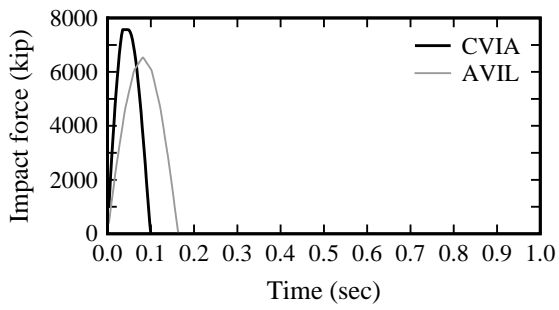


g) VG 7

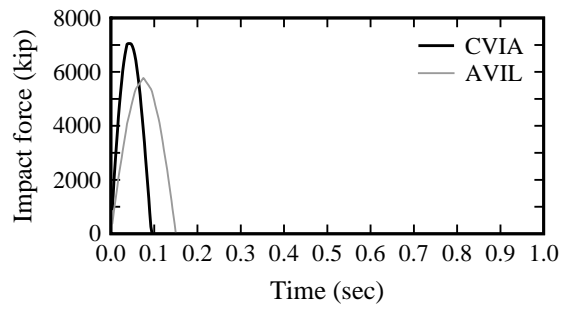


h) VG 8

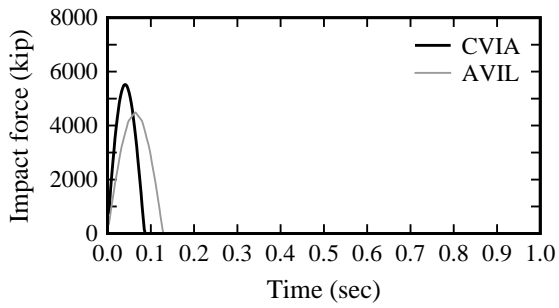
Figure N.5 Impact force-time histories: LA-1 Bridge, Pier 3, upbound traffic, fully loaded



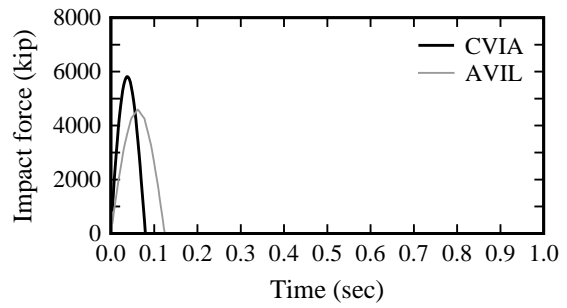
a) VG 9



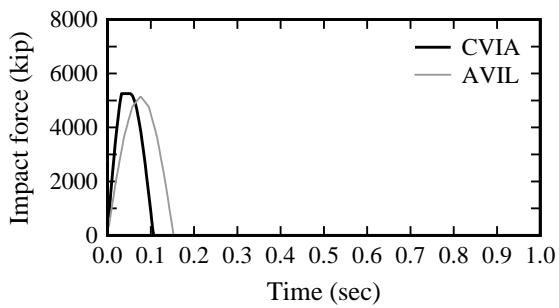
b) VG 10



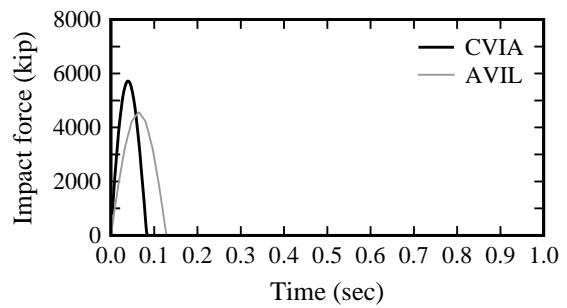
c) VG 11



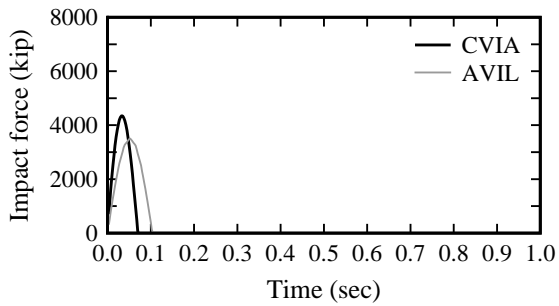
d) VG 12



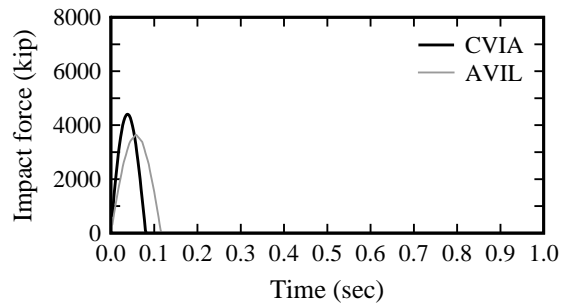
e) VG 13



f) VG 14

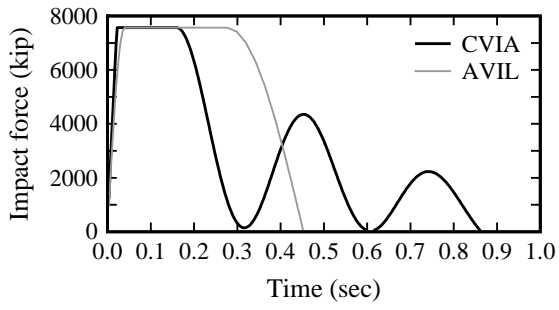


g) VG 15

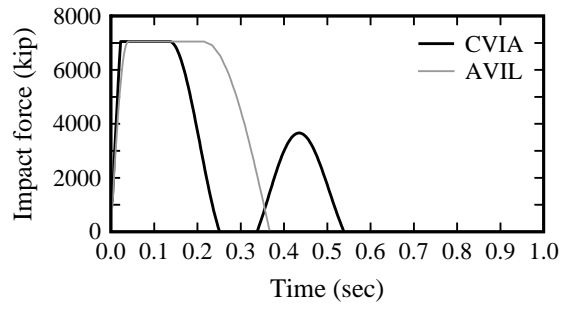


h) VG 16

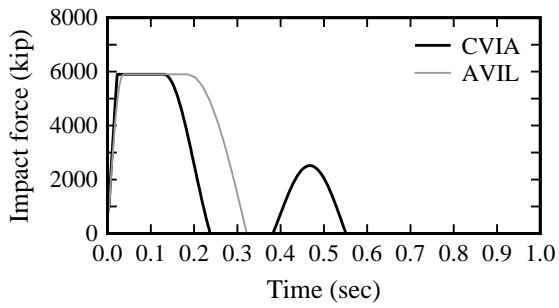
Figure N.6 Impact force-time histories: LA-1 Bridge, Pier 3, upbound traffic, lightly loaded



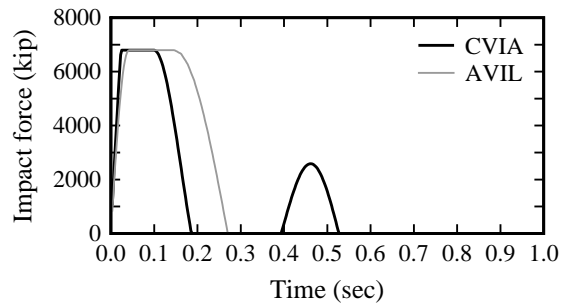
a) VG 17



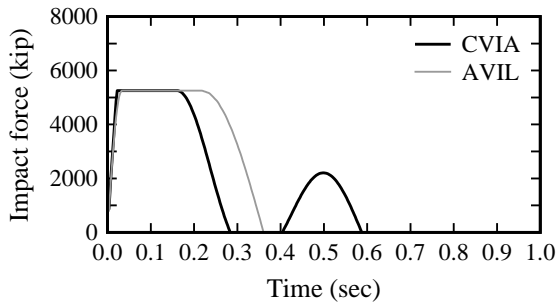
b) VG 18



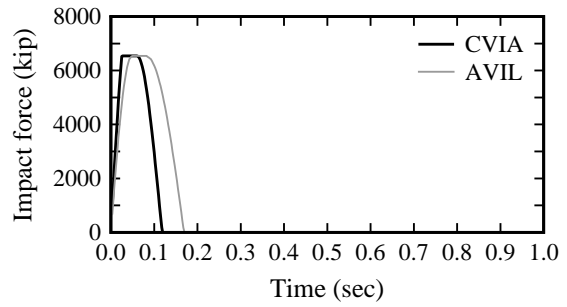
c) VG 19



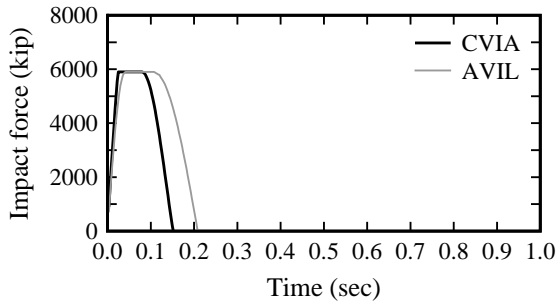
d) VG 20



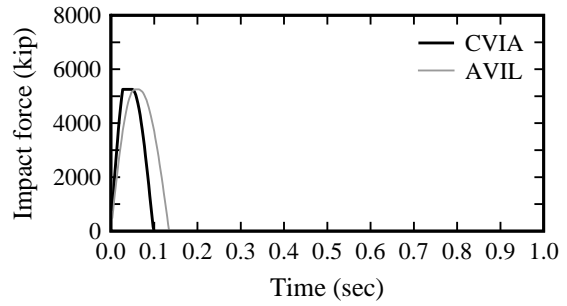
e) VG 21



f) VG 22

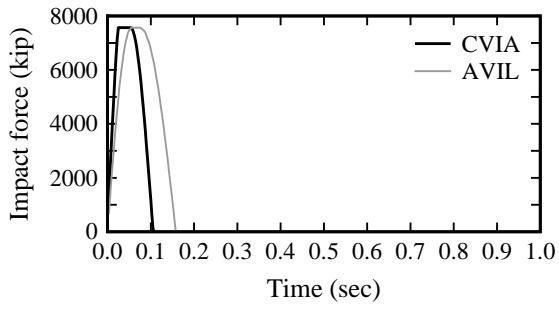


g) VG 23

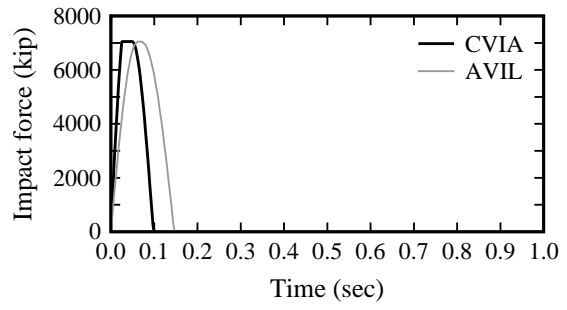


h) VG 24

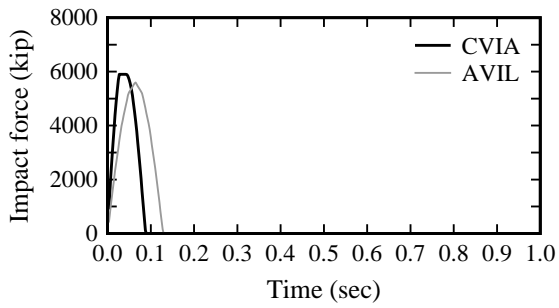
Figure N.7 Impact force-time histories: LA-1 Bridge, Pier 3, downbound traffic, fully loaded



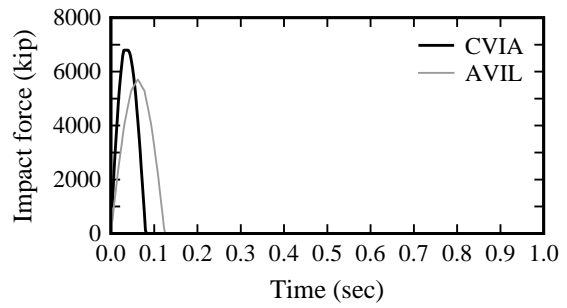
a) VG 25



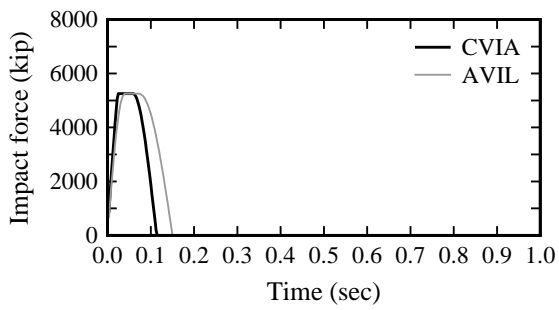
b) VG 26



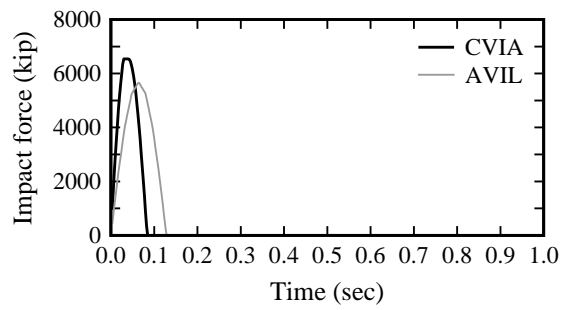
c) VG 27



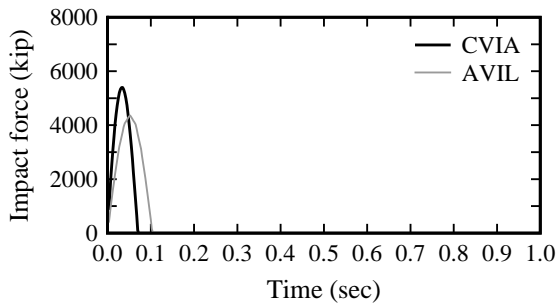
d) VG 28



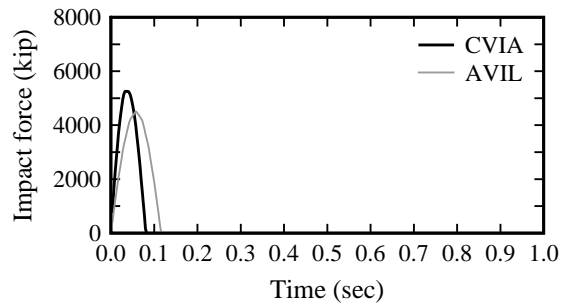
e) VG 29



f) VG 30

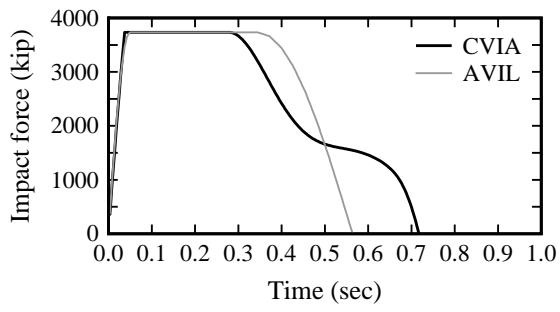


g) VG 31

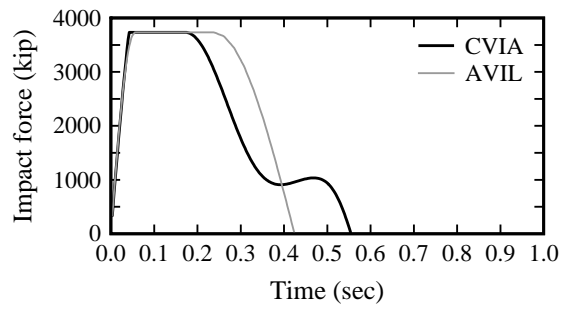


h) VG 32

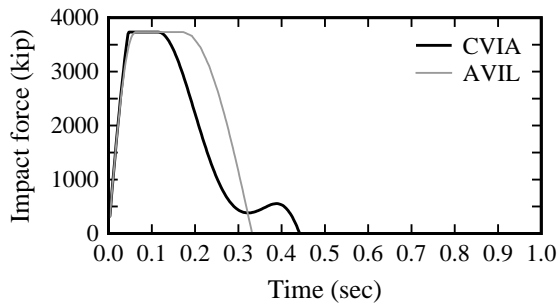
Figure N.8 Impact force-time histories: LA-1 Bridge, Pier 3, downbound traffic, lightly loaded



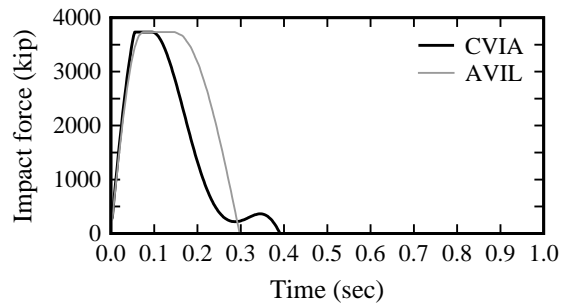
a) VG 1



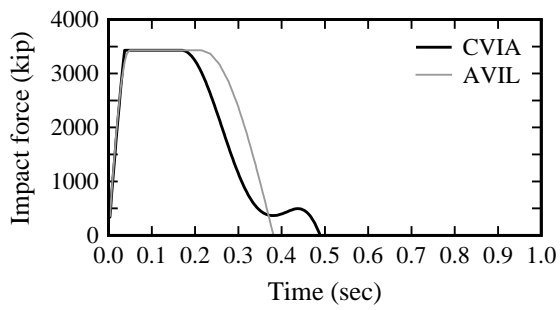
b) VG 2



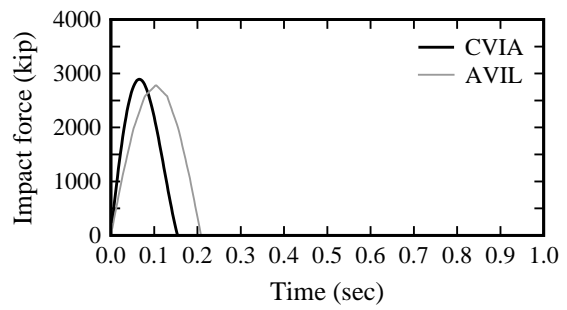
c) VG 3



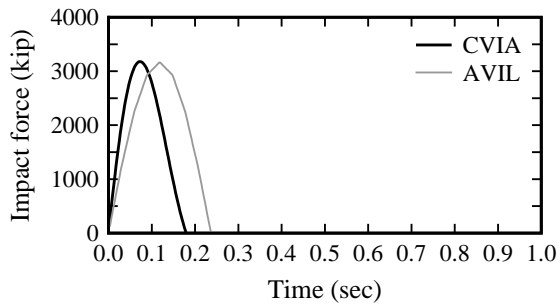
d) VG 4



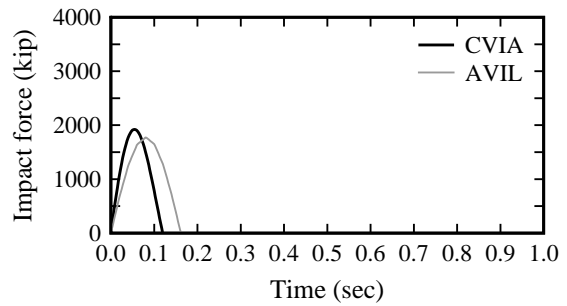
e) VG 5



f) VG 6

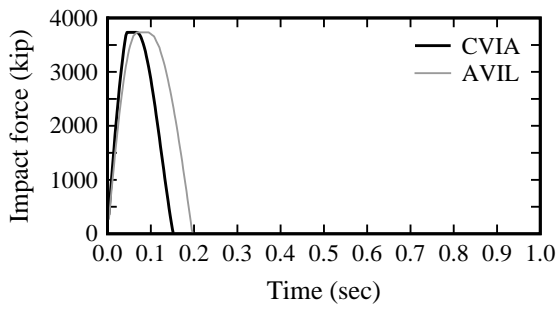


g) VG 7

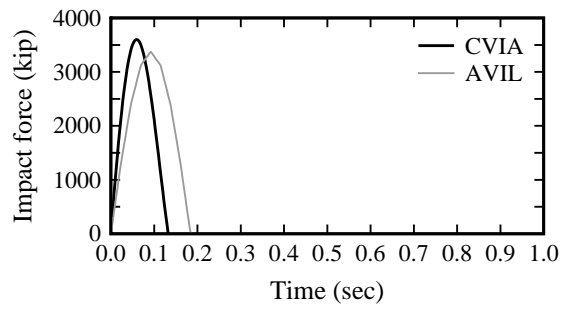


h) VG 8

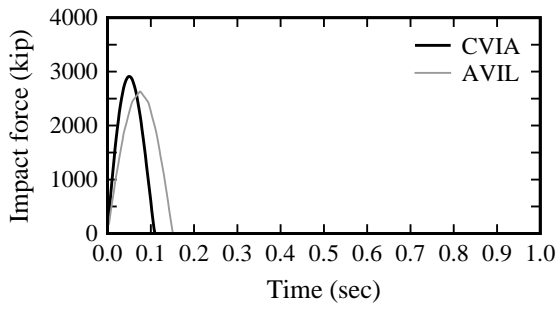
Figure N.9 Impact force-time histories: LA-1 Bridge, Pier 4, upbound traffic, fully loaded



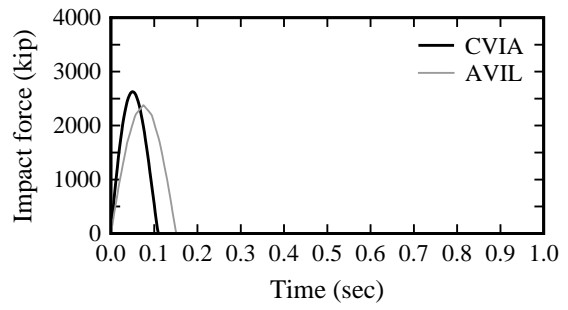
a) VG 9



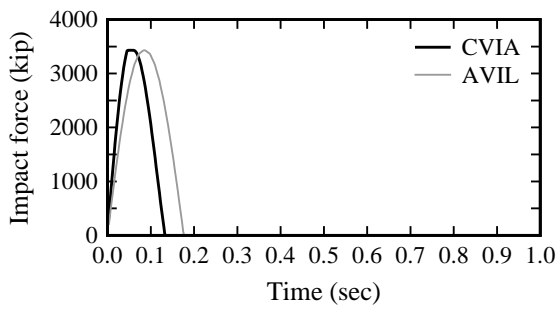
b) VG 10



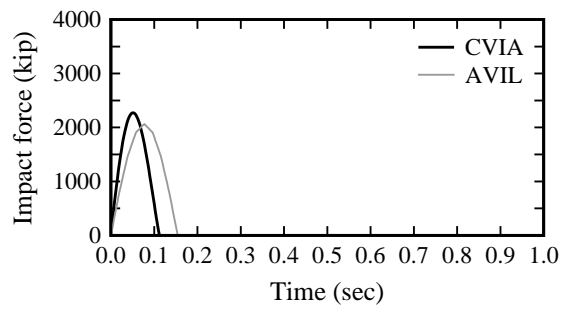
c) VG 11



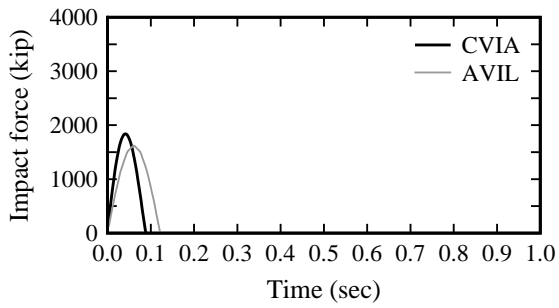
d) VG 12



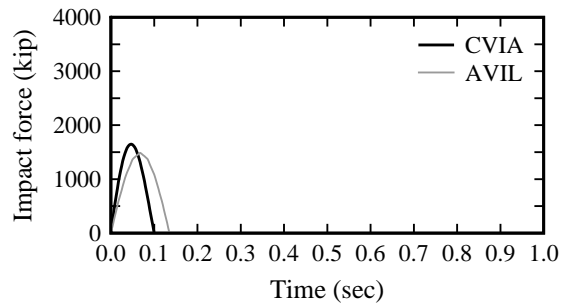
e) VG 13



f) VG 14

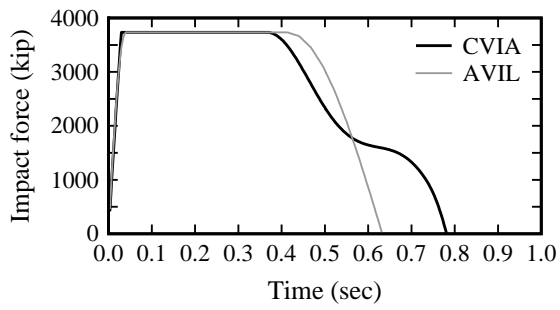


g) VG 15

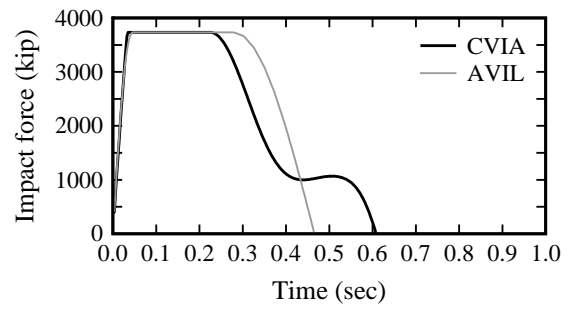


h) VG 16

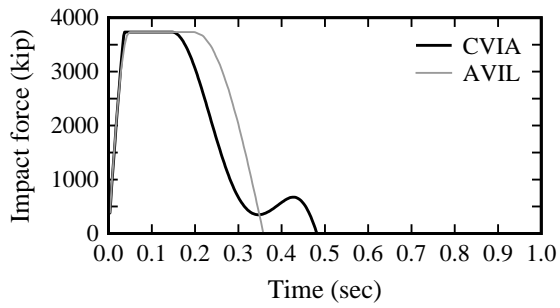
Figure N.10 Impact force-time histories: LA-1 Bridge, Pier 4, upbound traffic, lightly loaded



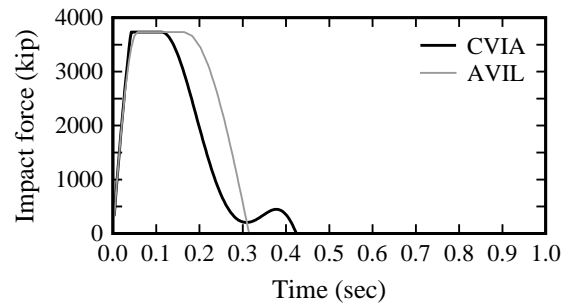
a) VG 17



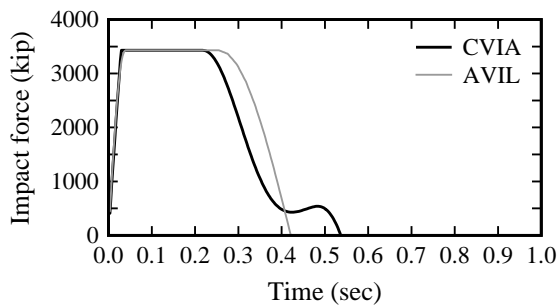
b) VG 18



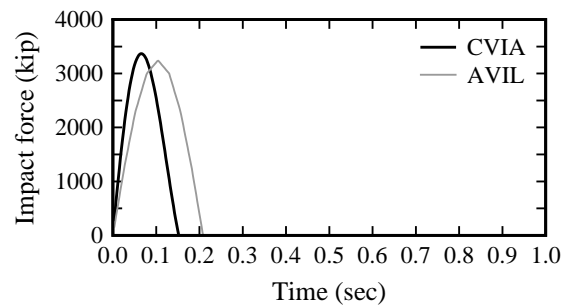
c) VG 19



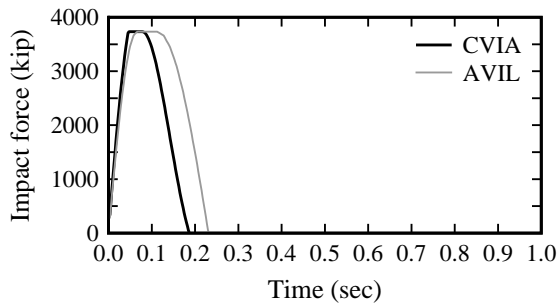
d) VG 20



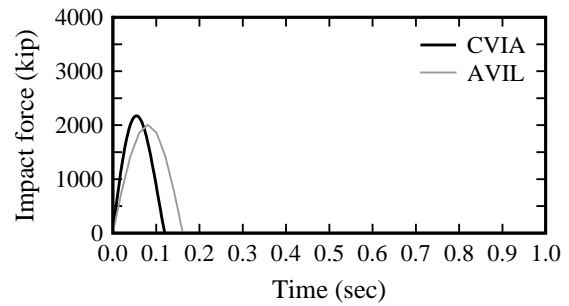
e) VG 21



f) VG 22

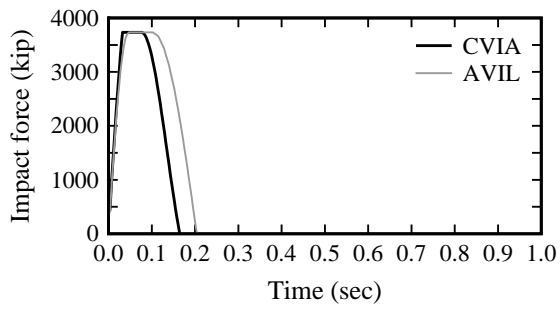


g) VG 23

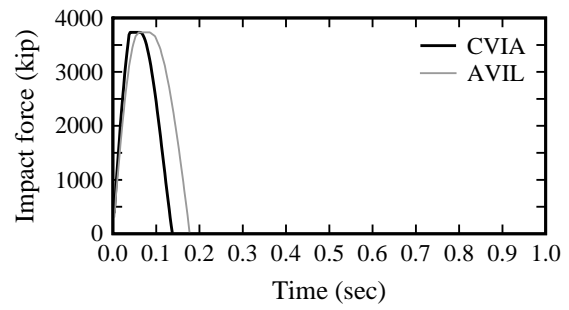


h) VG 24

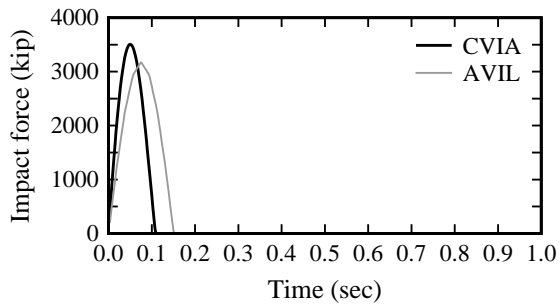
Figure N.11 Impact force-time histories: LA-1 Bridge, Pier 4, downbound traffic, fully loaded



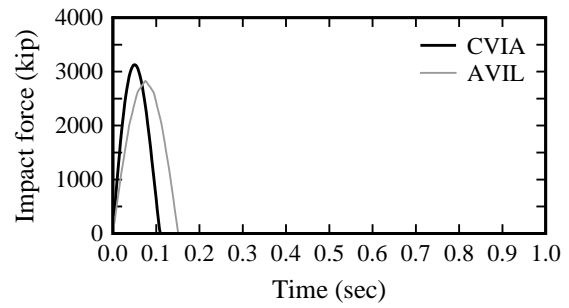
a) VG 25



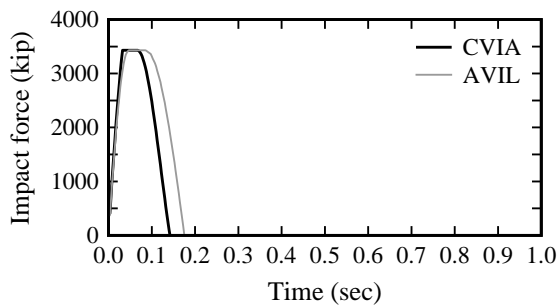
b) VG 26



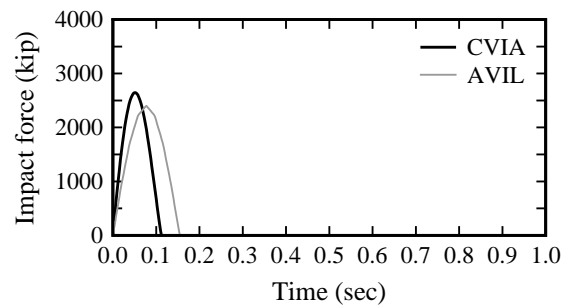
c) VG 27



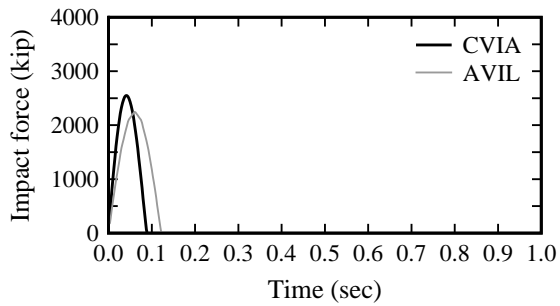
d) VG 28



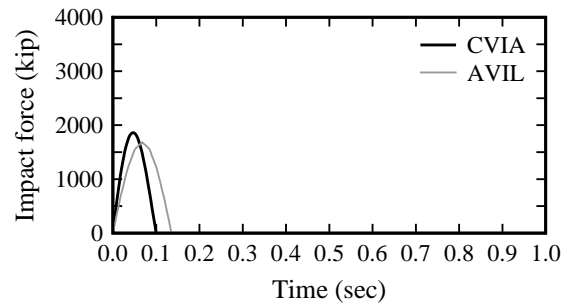
e) VG 29



f) VG 30

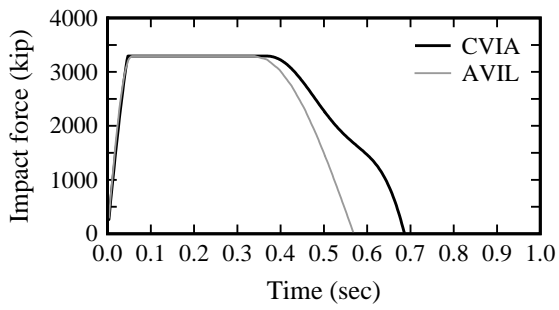


g) VG 31

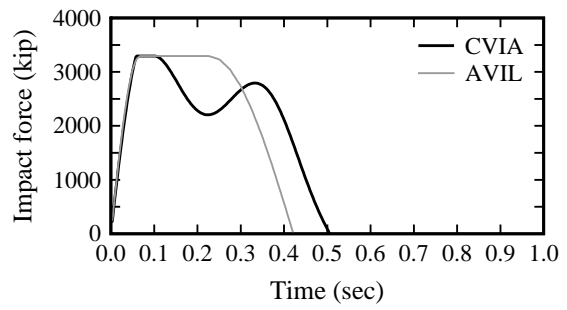


h) VG 32

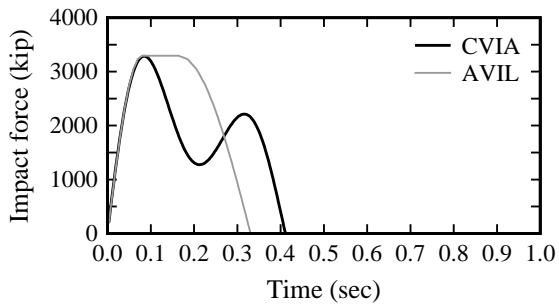
Figure N.12 Impact force-time histories: LA-1 Bridge, Pier 4, downbound traffic, lightly loaded



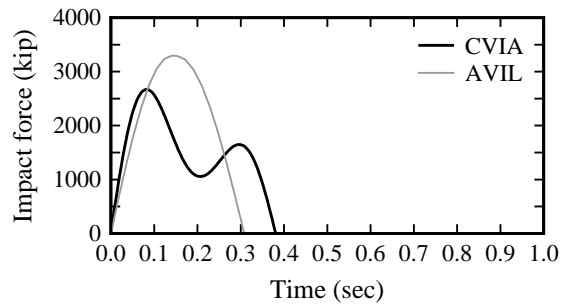
a) VG 1



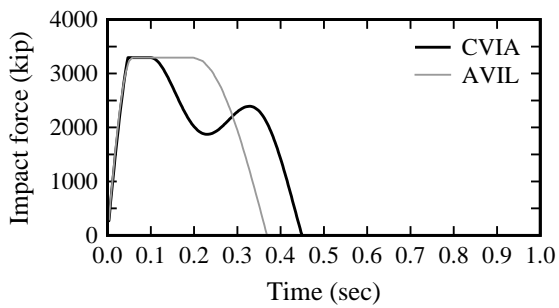
b) VG 2



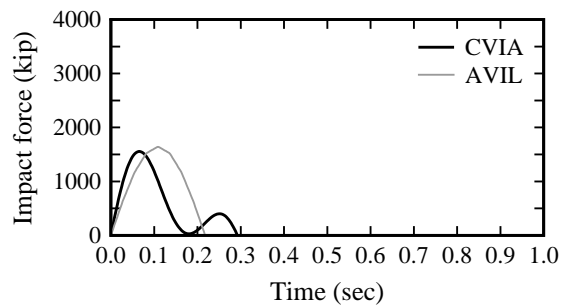
c) VG 3



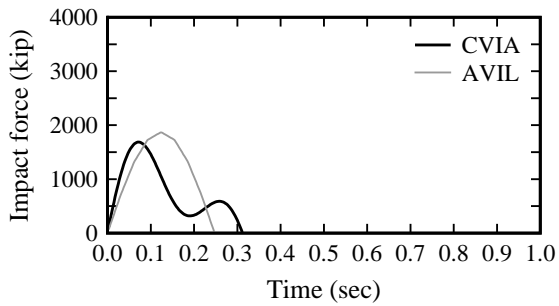
d) VG 4



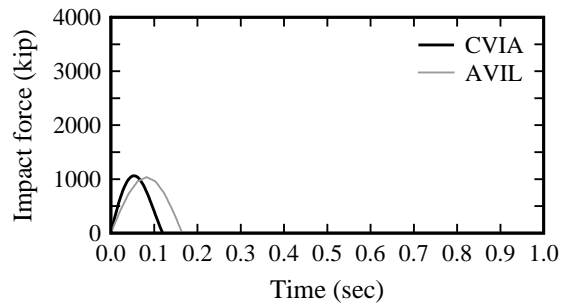
e) VG 5



f) VG 6

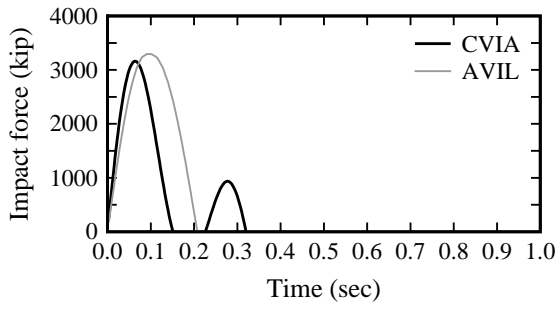


g) VG 7

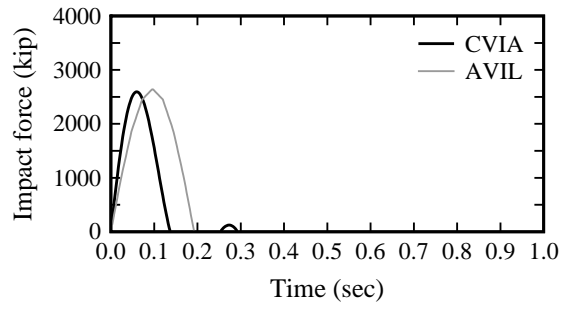


h) VG 8

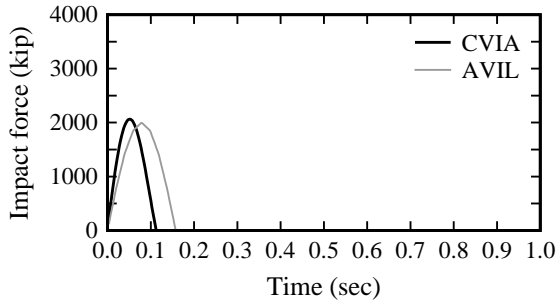
Figure N.13 Impact force-time histories: LA-1 Bridge, Pier 96, upbound traffic, fully loaded



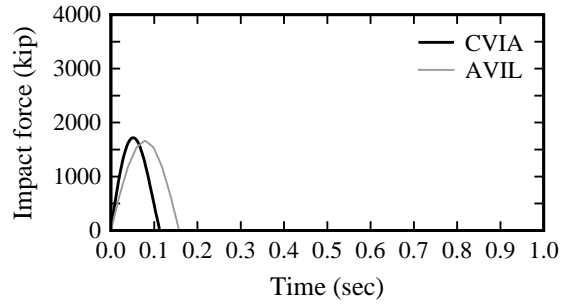
a) VG 9



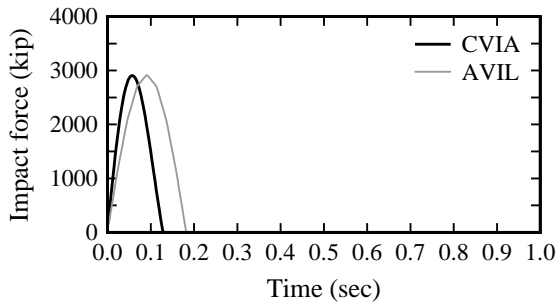
b) VG 10



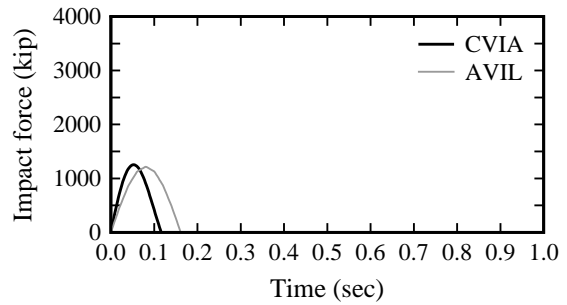
c) VG 11



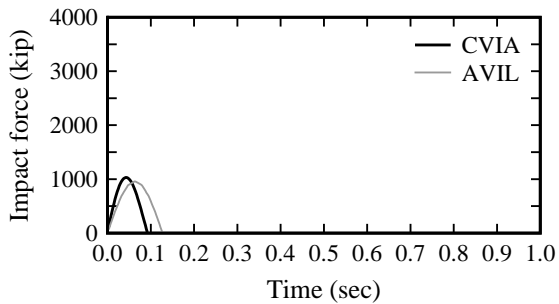
d) VG 12



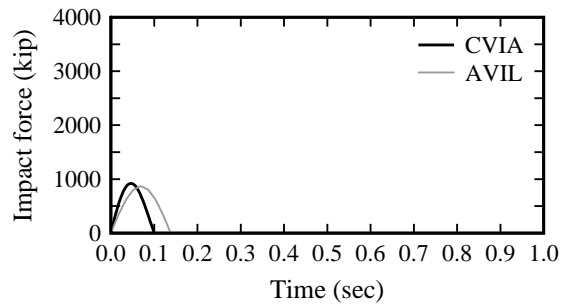
e) VG 13



f) VG 14

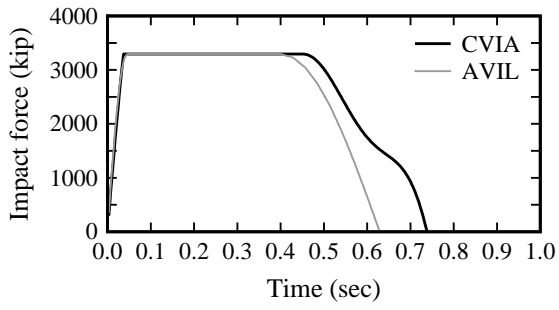


g) VG 15

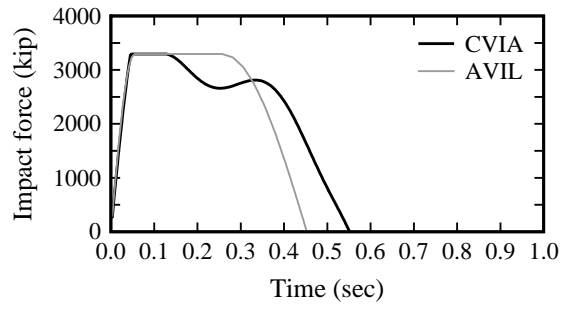


h) VG 16

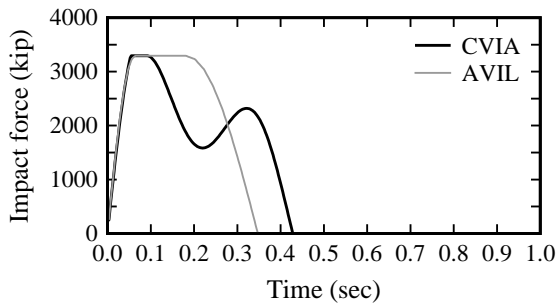
Figure N.14 Impact force-time histories: LA-1 Bridge, Pier 96, upbound traffic, lightly loaded



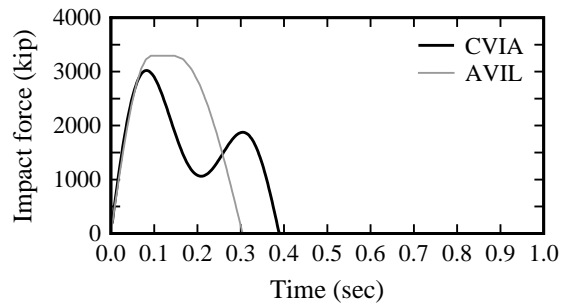
a) VG 17



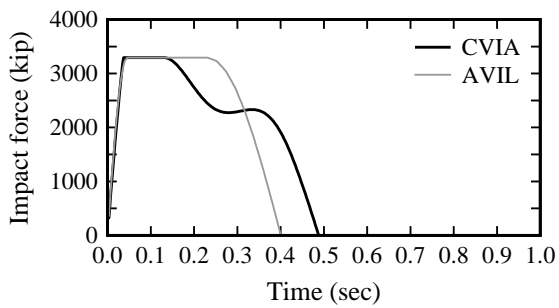
b) VG 18



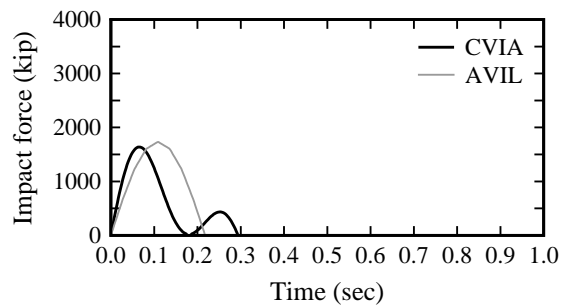
c) VG 19



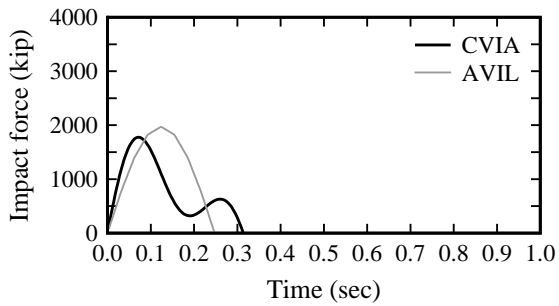
d) VG 20



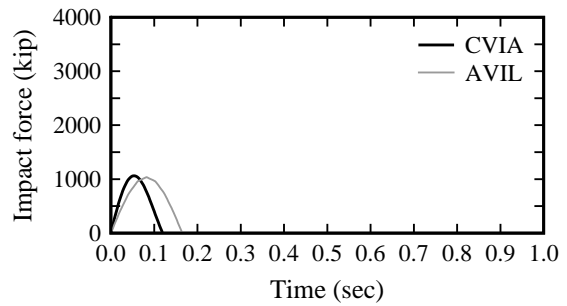
e) VG 21



f) VG 22

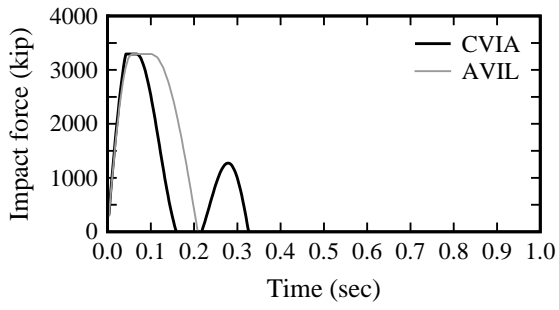


g) VG 23

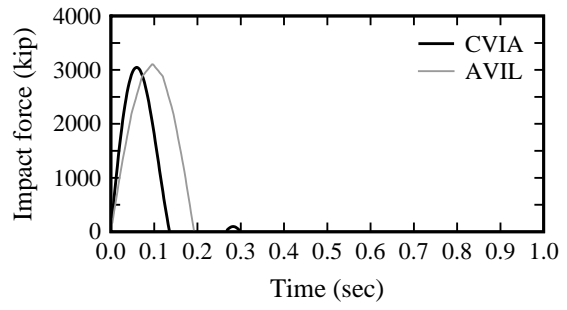


h) VG 24

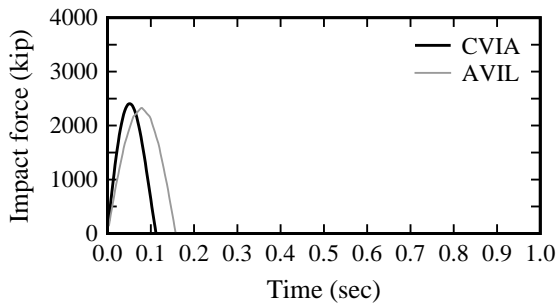
Figure N.15 Impact force-time histories: LA-1 Bridge, Pier 96, downbound traffic, fully loaded



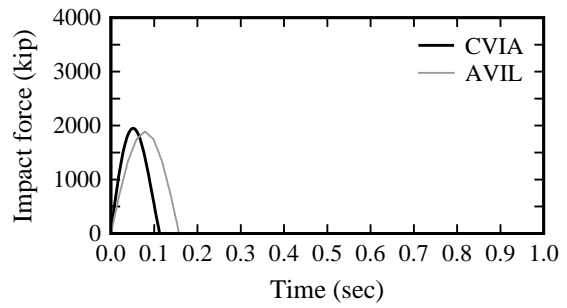
a) VG 25



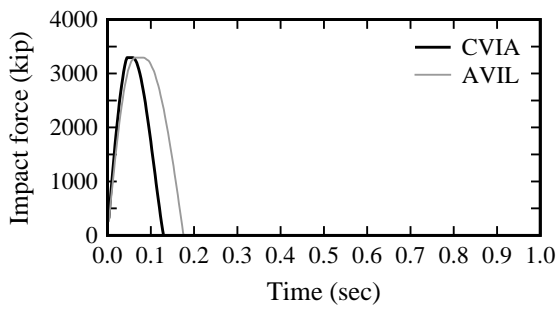
b) VG 26



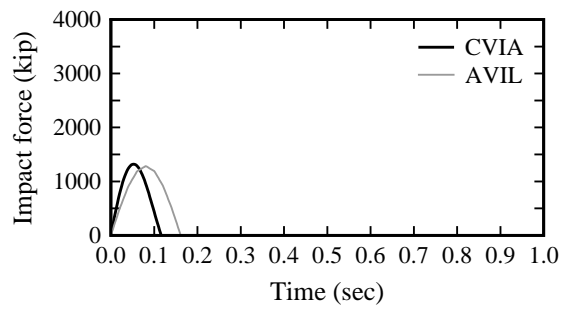
c) VG 27



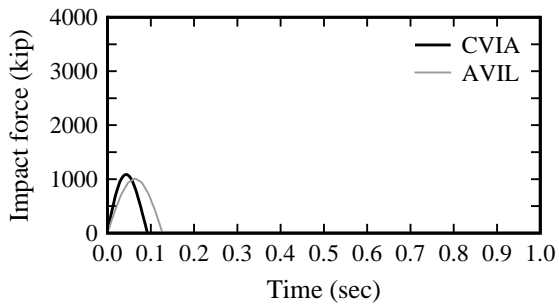
d) VG 28



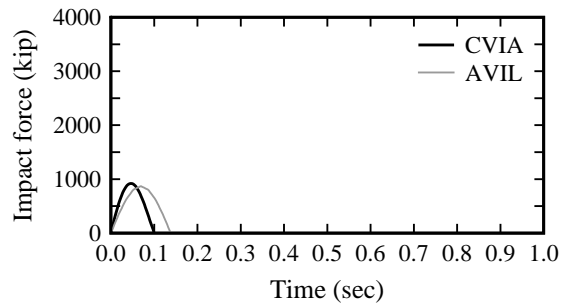
e) VG 29



f) VG 30

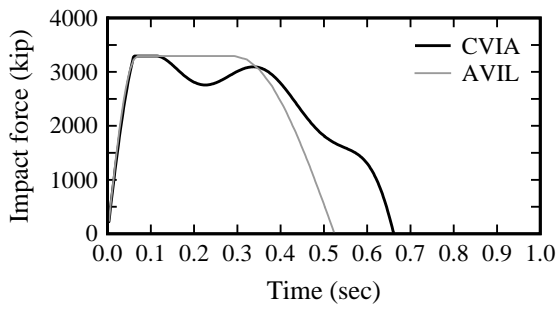


g) VG 31

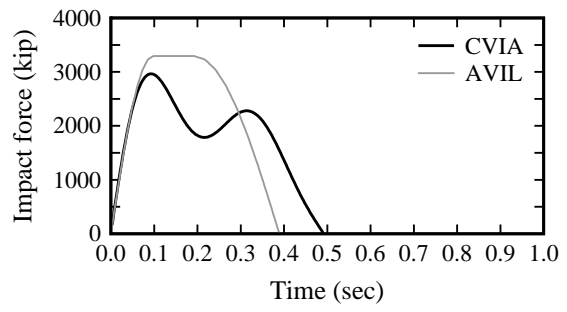


h) VG 32

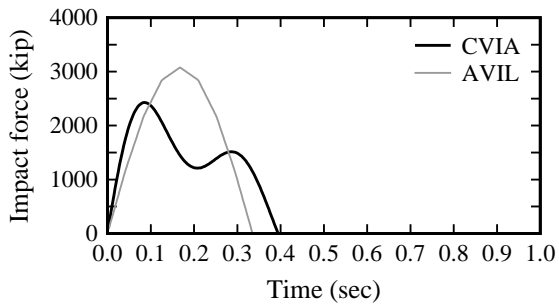
Figure N.16 Impact force-time histories: LA-1 Bridge, Pier 96, downbound traffic, lightly loaded



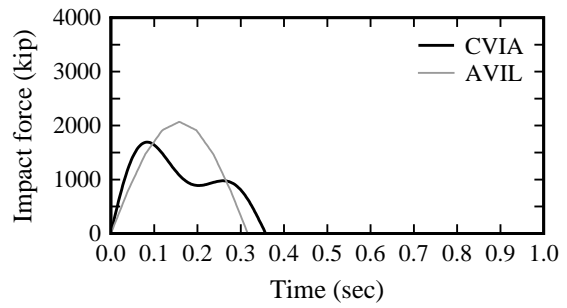
a) VG 1



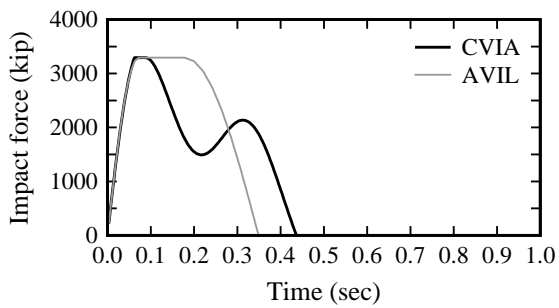
b) VG 2



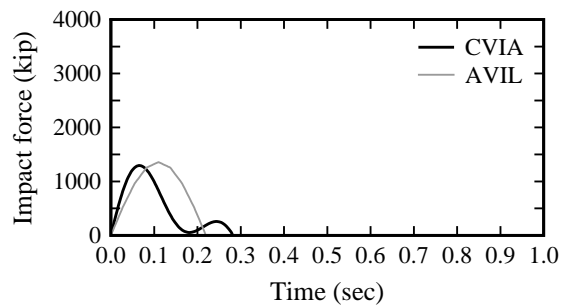
c) VG 3



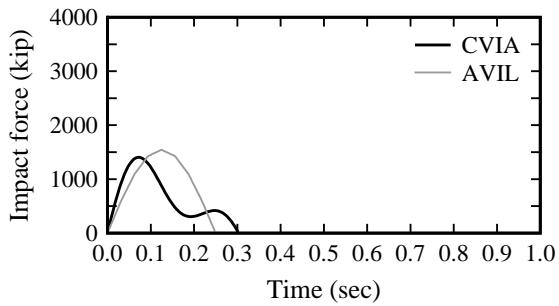
d) VG 4



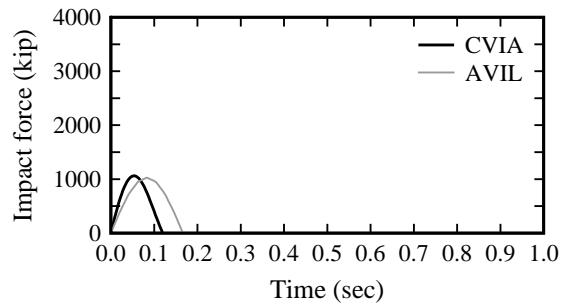
e) VG 5



f) VG 6

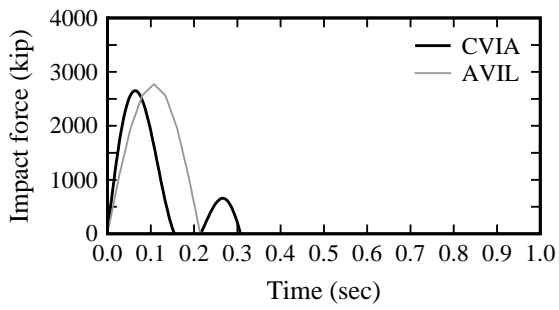


g) VG 7

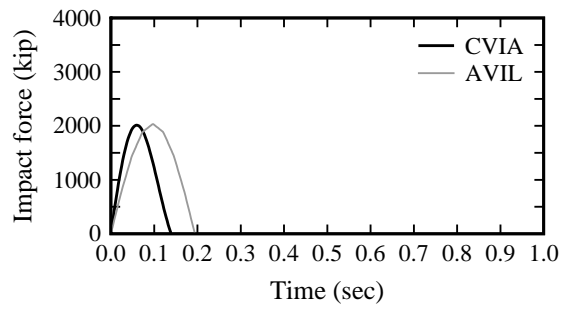


h) VG 8

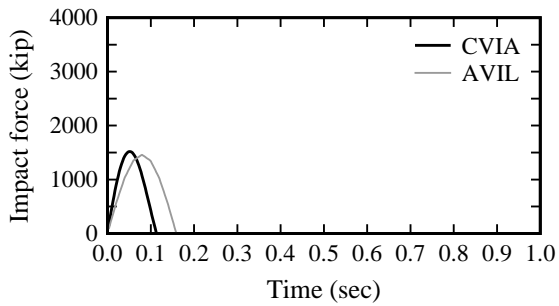
Figure N.17 Impact force-time histories: LA-1 Bridge, Pier 97, upbound traffic, fully loaded



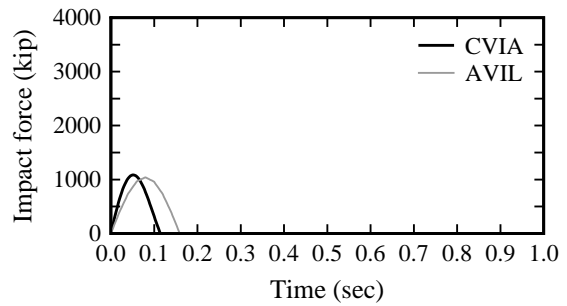
a) VG 9



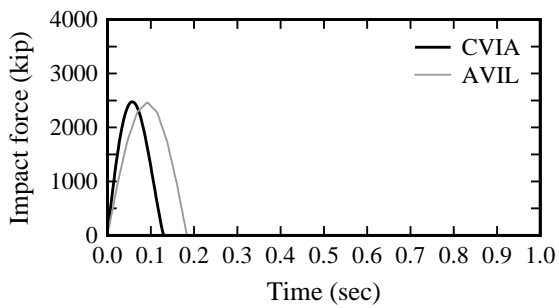
b) VG 10



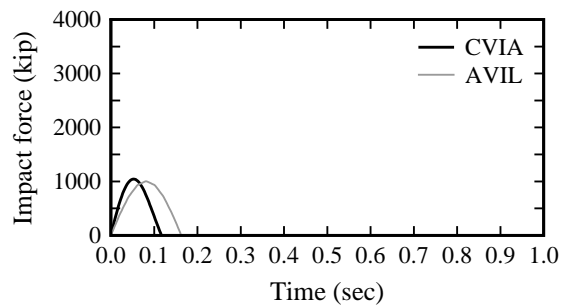
c) VG 11



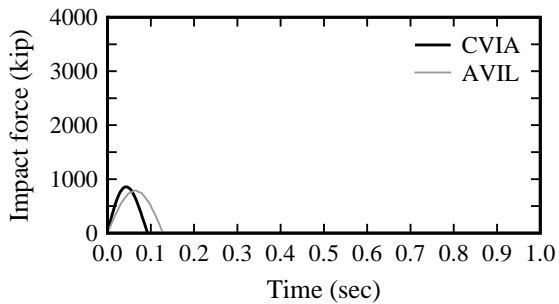
d) VG 12



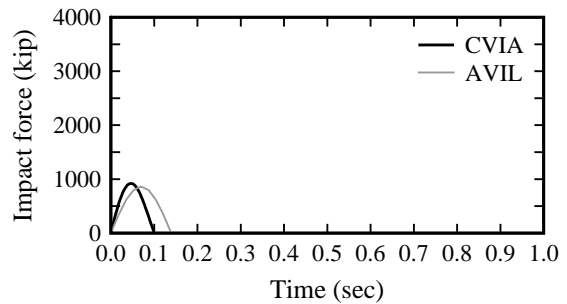
e) VG 13



f) VG 14

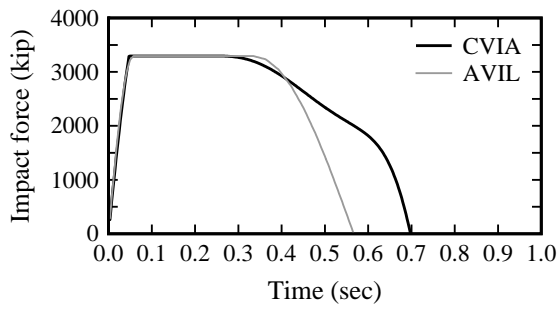


g) VG 15

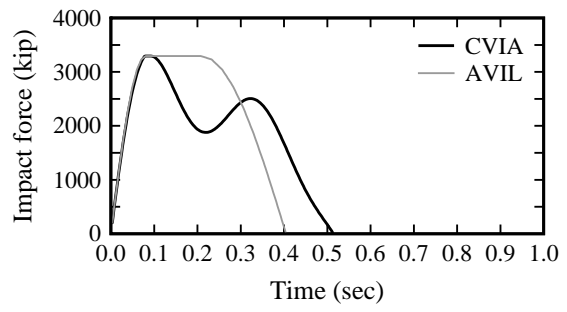


h) VG 16

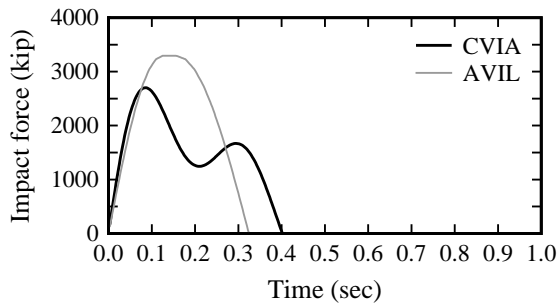
Figure N.18 Impact force-time histories: LA-1 Bridge, Pier 97, upbound traffic, lightly loaded



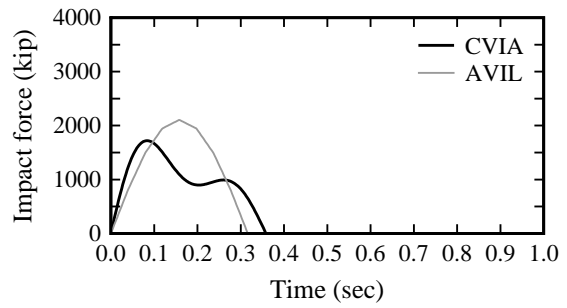
a) VG 17



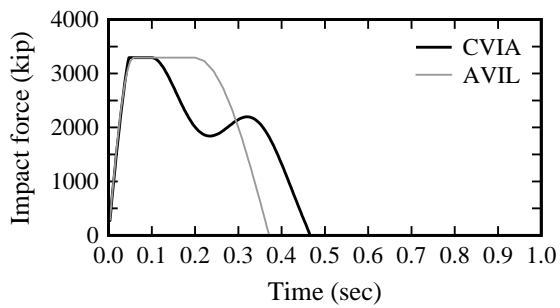
b) VG 18



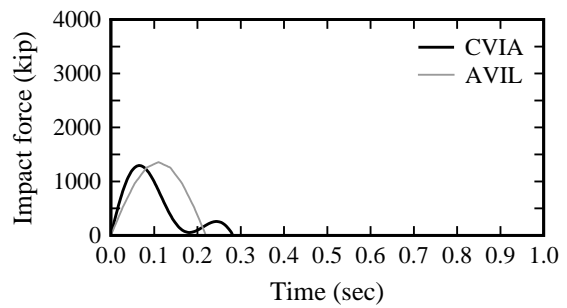
c) VG 19



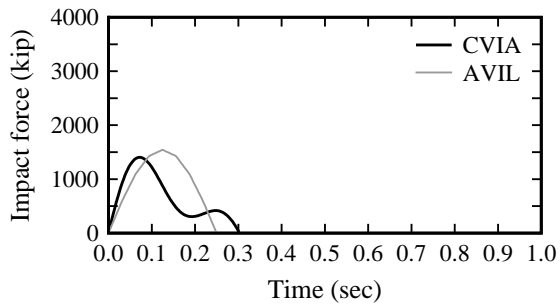
d) VG 20



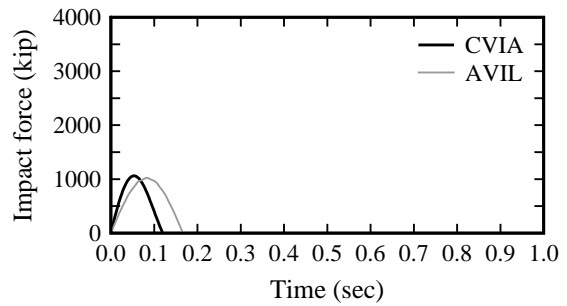
e) VG 21



f) VG 22

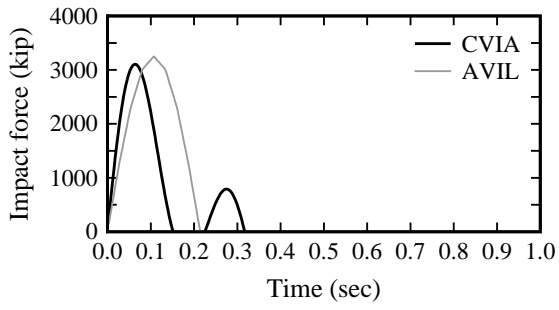


g) VG 23

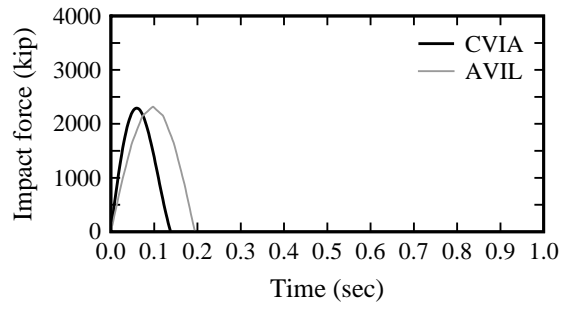


h) VG 24

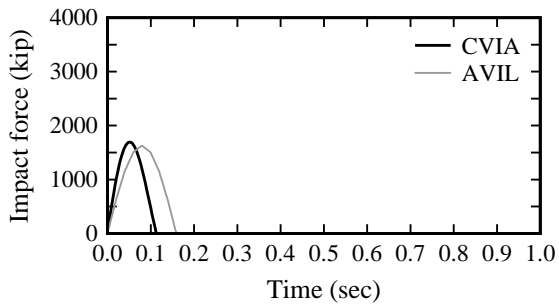
Figure N.19 Impact force-time histories: LA-1 Bridge, Pier 97, downbound traffic, fully loaded



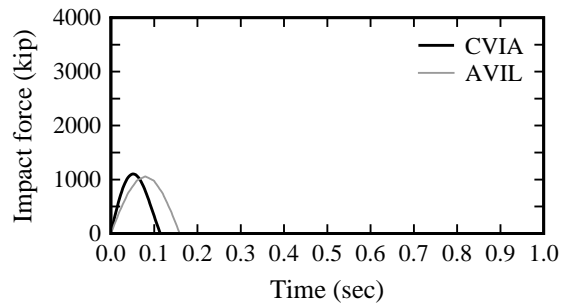
a) VG 25



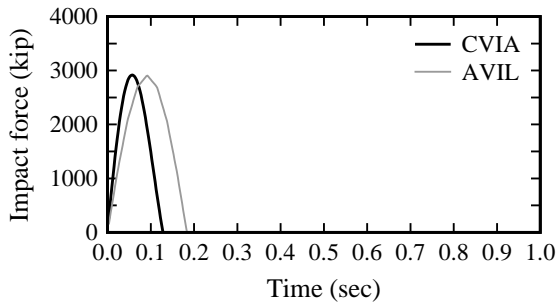
b) VG 26



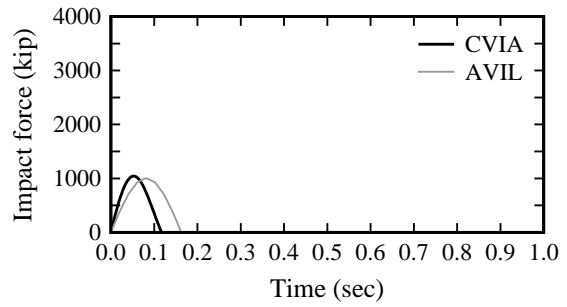
c) VG 27



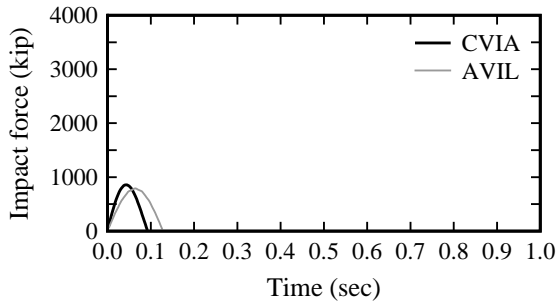
d) VG 28



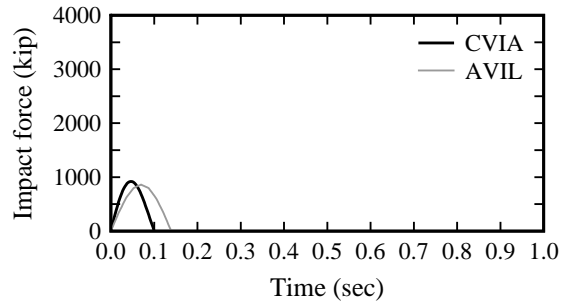
e) VG 29



f) VG 30



g) VG 31



h) VG 32

Figure N.20 Impact force-time histories: LA-1 Bridge, Pier 97, downbound traffic, lightly loaded